CONTENTS

ACI Structural Journal

July 2023, V. 120, No. 4

A JOURNAL OF THE AMERICAN CONCRETE INSTITUTE
AN INTERNATIONAL TECHNICAL SOCIETY

Contents continued on next page

Discussion is welcomed for all materials published in this issue and will appear ten months from this journal's date if the discussion is received within four months of the paper's print publication. Discussion of material received after specified dates will be considered individually for publication or private response. ACI Standards published in ACI Journals for public comment have discussion due dates printed with the Standard.

The *ACI Structural Journal* (ISSN 0889-3241) is published bimonthly by the American Concrete Institute. Publication office: 38800 Country Club Drive, Farmington Hills, MI 48331. Periodicals postage paid at Farmington, MI, and at additional mailing offices. Subscription rates: $192 per year, payable in advance. POSTMASTER: Send address changes to: *ACI Structural Journal*, 38800 Country Club Drive, Farmington Hills, MI 48331.

Canadian GST: R 1226213149.

Direct correspondence to 38800 Country Club Drive, Farmington Hills, MI 48331. Telephone: +1.248.848.3700. Facsimile (FAX): +1.248.848.3701. **Website: http://www.concrete.org.**

CONTENTS

MEETINGS

JULY 2023

17-18—ACI Professors' Workshop, Online, www.concrete.org/events/professorsworkshop.aspx

17-20—Bridge Engineering Institute Conference 2023 (BEI-2023), Rome, Italy, www.beibridge.org

20-23—ASCC Concrete Executive Leadership Forum, Beaver Creek, CO, USA, https://ascconline.org/events

AUGUST 2023

8-10—DFI S3: Slopes, Support and Stabilization, Boston, MA, USA, https://www.xcdsystem.com/dfi/program/3YFd0Di/index.cfm

10-12—World of Concrete Asia, Shanghai, China, https://en.wocasia.cn

14-18—The Twelfth International Structural Engineering and Construction Conference (ISEC 12), Chicago, IL, USA, www.isec-society.org/ISEC_12

ACI CONCRETE CONVENTION: FUTURE DATES

2023—Oct. 29-Nov. 2, Boston Convention Center & Westin Boston Waterfront, Boston, MA
2024—March 24-28, Hyatt Regency New Orleans, New Orleans, LA
2024—November 3-7, Marriott Philadelphia Downtown, Philadelphia, PA

For additional information, contact:
Event Services, ACI
38800 Country Club Drive
Farmington Hills, MI 48331
Telephone: +1.248.848.3795
email: conventions@concrete.org

ON COVER: 120-S63, p. 33, Fig. 3—Construction of bridge-deck slabs: (a) formwork; (b) meshes; (c) prepared formwork for casting; (d) mixing lightweight (LW) aggregates with water (pre-wetting) 3 days before casting; (e) casting; and (f) demolding.

Contributions to *ACI Structural Journal*

The *ACI Structural Journal* is an open forum on concrete technology and papers related to this field are always welcome. All material submitted for possible publication must meet the requirements of the "American Concrete Institute Publication Policy" and "Author Guidelines and Submission Procedures." Prospective authors should request a copy of the Policy and Guidelines from ACI or visit ACI's website at **www.concrete.org** prior to submitting contributions.

Papers reporting research must include a statement indicating the significance of the research.

The Institute reserves the right to return, without review, contributions not meeting the requirements of the Publication Policy.

All materials conforming to the Policy requirements will be reviewed for editorial quality and technical content, and every effort will be made to put all acceptable papers into the information channel. However, potentially good papers may be returned to authors when it is not possible to publish them in a reasonable time.

Discussion

All technical material appearing in the *ACI Structural Journal* may be discussed. If the deadline indicated on the contents page is observed, discussion can appear in the designated issue. Discussion should be complete and ready for publication, including finished, reproducible illustrations. Discussion must be confined to the scope of the paper and meet the ACI Publication Policy.

Follow the style of the current issue. Be brief—1800 words of double spaced, typewritten copy, including illustrations and tables, is maximum. Count illustrations and tables as 300 words each and submit them on individual sheets. As an approximation, 1 page of text is about 300 words. Submit one original typescript on 8-1/2 x 11 plain white paper, use 1 in. margins, and include two good quality copies of the entire discussion. References should be complete. Do not repeat references cited in original paper; cite them by original number. Closures responding to a single discussion should not exceed 1800-word equivalents in length, and to multiple discussions, approximately one half of the combined lengths of all discussions. Closures are published together with the discussions.

Discuss the paper, not some new or outside work on the same subject. Use references wherever possible instead of repeating available information.

Discussion offered for publication should offer some benefit to the general reader. Discussion which does not meet this requirement will be returned or referred to the author for private reply.

Send manuscripts to:
http://mc.manuscriptcentral.com/aci

Send discussions to:
Journals.Manuscripts@concrete.org

ACI STRUCTURAL JOURNAL TECHNICAL PAPER

Title No. 120-S61

Precast Concrete Frames with Emulative Connections Subjected to Progressive Collapse

by Kai Qian, Shi-Lin Liang, Lu Zhang, and Zhi Li

This paper documents an experimental study on load-transfer mechanisms of six precast concrete (PC) frames with different emulative connections to resist progressive collapse. Load-transfer mechanisms, such as compressive arch action (CAA) and catenary action (CA), were observed during the loading history, while the CA dominated the ultimate load capacity. The robustness of PC frames assembled by mechanical couplers or U-shaped bars was evaluated experimentally and analytically. To improve the robustness of PC frames assembled by U-shaped bars, two refined strategies were introduced: 1) adding additional straight bars in the trough connection; and 2) replacing U-shaped deformed bars with plain bars. It was found that, with the additional straight bars in the beam troughs, the CAA capacity, CA capacity, and deformation capacity can be increased. Replacing U-shaped deformed bars with plain bars can improve the CA capacity and deformation capacity effectively, while it may decrease the CAA capacity slightly. To further understand the load-transfer mechanisms of PC frames with different connections, an analytical elaboration was conducted. It was demonstrated that, at the CAA stage, shear force (related to flexural action) dominated the load-transfer mechanisms. At the CA stage, shear force still dominated the load-transfer mechanisms of the beam-side column interface, while tensile axial force dominated the load-transfer mechanisms of the beam-middle column interface.

Keywords: catenary action (CA); compressive arch action (CAA); emulative connection; precast concrete (PC); progressive collapse.

INTRODUCTION

Progressive collapse is defined as "the spread of an initial local failure from element to element, which eventually results in the collapse of an entire structure or a disproportionately large part of it."[1] Progressive collapse has drawn special attention from practical engineers since the collapse of Ronan Point in 1968. Afterward, several design methods (for example, the tie force method, local resistance method, and alternate load path method) were commonly proposed in guidelines[2,3]; among them, the alternate load path method is the most popular in design and academic studies because it is independent of the initial abnormal loads.

The alternate load path method is implemented by removing the target column notionally; the subsequent load redistribution behavior of the remaining structure can therefore be evaluated under the pushdown loading method. In the past decades, especially since the collapse of the Twin Towers in the World Trade Center in 2001, extensive studies have been performed to study the progressive collapse behavior of structures based on tests of beam-column joints,[4,5] multi-story buildings,[6-10] or beam-column substructures.[11-18] Qian and Li[4] and Quiel et al.[5] investigated the progressive collapse behavior of reinforced concrete (RC) or precast concrete (PC) beam-column joints with simplified boundary conditions subjected to monotonic loading. Sasani et al.,[6] Sasani and Sagiroglu,[7,8] Xiao et al.,[9] and Adam et al.[10] conducted dynamic tests on on-site multi-story buildings. The tested building survived various initial damage, such as the loss of a single interior, exterior, and corner column. Moreover, it was discovered that the load-transfer mechanisms included flexural action, compressive arch action (CAA), Vierendeel action, and catenary action (CA). Compared with beam-column joint tests and multi-story building tests, substructure tests on planar or three-dimensional beam-column subassemblages were much more prevalent. Su et al.,[11] Yu and Tan,[12] Sadek et al.,[13] and Deng et al.[14] evaluated the resilience of RC frames based on planar beam-column substructures with two beams, two side column stubs, and one middle column stub. Normally, the side column stub is enlarged to apply fixed boundary conditions. These efforts demonstrated that both CAA and CA were viable alternate load paths for RC frames to resist progressive collapse. To quantify the effects of boundary conditions, beam-column subframes subjected to different column removal scenarios were tested.[15,16] Studies on the effects of seismic design and detailing[17,18] demonstrated that complying with seismic design and increasing the seismic design category can significantly increase the load-resisting capacity of cast-in-place RC frames against progressive collapse, owing to the enlarged cross section of structural components and greater longitudinal reinforcement ratio. However, it will not obviously increase the deformation capacity of the frames. Guerrini[19] addressed the efficiency of designing structures against progressive collapse relying on ductility and redundancy. The need for increasing the length of the critical regions (plastic hinges) to resist progressive collapse was evaluated. As only planar beam-column substructures were investigated, the effects of slabs and transverse beams on the behavior of RC frames to resist progressive collapse were still unclear. For this purpose, Qian and Li[20,21] conducted several series of experimental programs at Nanyang Technological University in Singapore. It was found that including the slabs could increase the load-resisting capacity by 63%. The

ACI Structural Journal, V. 120, No. 4, July 2023.

MS No. S-2021-094.R2, doi: 10.14359/51738715, received October 19, 2022, and reviewed under Institute publication policies.

Table 1—Specimen details

Specimens	Connection details	Beam reinforcements				
		Beam ends			Midspan	
		Top	Middle	Bottom	Top	Bottom
MC-11	Mechanical coupler	3T12	—	2T12	2T12	
MC-13	Mechanical coupler	3T12	—	2T12		
UB-11	U-shaped deformed bar	3T12	—	2T12		
UB-R-11	U-shaped deformed bar and straight deformed bar	3T12	4T12	2T12		
UB-13	U-shaped deformed bar	3T12	—	2T12		
UB-R-13	U-shaped plain bar	3T12	—	2R12		
NSC-11	Lap splice	3T12	—	2T12	2T12	
NSC-13	Lap splice	3T12	—	2T12		

Note: NSC-11 and NSC-13 are RC specimens tested by Deng et al.[14]

development and contribution of compressive membrane action and tensile membrane action in RC slabs were evaluated by experimental and analytical studies. Moreover, to improve the robustness of RC structures that were designed in the 1970s or changed usable function, strengthening strategies were proposed and compared.[22,23] Recently, the additional load-transfer paths of masonry-infilled walls to improve the robustness of RC frames were investigated.[24,25] However, these tests were mainly focused on cast-in-place RC frames. PC frames were expected to be more vulnerable to progressive collapse, but their load-transfer mechanisms were still unclear.

Lew et al.[26] and Bao et al.[27] experimentally and numerically investigated the progressive collapse behavior of PC frames with welded connections. They found that the failure of the PC frames was caused by the welding fracture. Kang and Tan[28] reported the performance of a PC frame subjected to the loss of a middle column and concluded that the CAA and CA were also mobilized in PC frames to mitigate progressive collapse. Qian et al.[29,30] performed a series of tests on PC frames with unbonded post-tensioning connections to investigate their special load-transfer mechanisms to mitigate progressive collapse, and they found that the CAA and CA can develop simultaneously in PC frames with post-tensioning connections. The structural behavior of PC frames was highly correlated to the connection types; more tests should be carried out to investigate the load-transfer mechanisms of PC frames because many connection types are used in PC constructions. For this reason, six PC frames with different emulative connections were tested under a pushdown loading regime. Four of them were assembled by conventional mechanical couplers or U-shaped bars, while the other two specimens were assembled by the refined connections. The experimental results including failure modes, vertical load-displacement curves, and horizontal reaction-displacement curves are presented and discussed. Moreover, an analytical elaboration was performed to further understand the load-transfer mechanisms.

RESEARCH SIGNIFICANCE

The resilience of PC frames to resist progressive collapse highly depends on the connection type. Few relevant studies are reported in the literature. Furthermore, no special provisions are involved in the existing design guidelines for PC frames to resist progressive collapse (GSA[2] and DoD[3]). To resolve these issues, six beam-column substructures with different emulative connections were fabricated. The test results associated with the analytical model can help structural engineers understand the load-transfer mechanism of PC frames to resist progressive collapse. Moreover, the experimental results could provide some necessary information for numerical simulation. Furthermore, the conclusions or recommendations could help code writers refine existing progressive collapse guidelines by providing special design provisions for PC frames.

EXPERIMENTAL PROGRAM

Specimen design

To investigate the load-transfer mechanisms of PC frames with emulative connections subjected to the loss of an edge-column scenario, six half-scale PC beam-column substructures (MC-11, MC-13, UB-11, UB-R-11, UB-13, and UB-R-13) were designed and tested. The design details of the PC frames are shown in Table 1 and Fig. 1 (the shaded area indicates precast members and the cross-shaded area indicates the location of the beam trough). These specimens included three typical emulative connections and two span-depth ratios. As presented in Fig. 1(a), MC-11 had a span-depth ratio of 11 and a beam cross section of 250 x 150 mm (9.8 x 5.9 in.). The beam top reinforcements of 2T12 were continuous along the whole beam, while the beam bottom reinforcements of 2T12 were discontinuous at the joints. As seen in Fig. 2(a), for MC-11, the precast beams were seated on the precast columns first. Then, the discontinuous beam bottom reinforcements were connected through mechanical couplers at the joint zones, while the beam top reinforcements were installed passing through the stirrups continuously. Finally, the top layers were cast-in-place. T12 and R6 represent deformed reinforcement with a diameter of 12 mm (0.5 in.) and plain reinforcement with a diameter of 6 mm

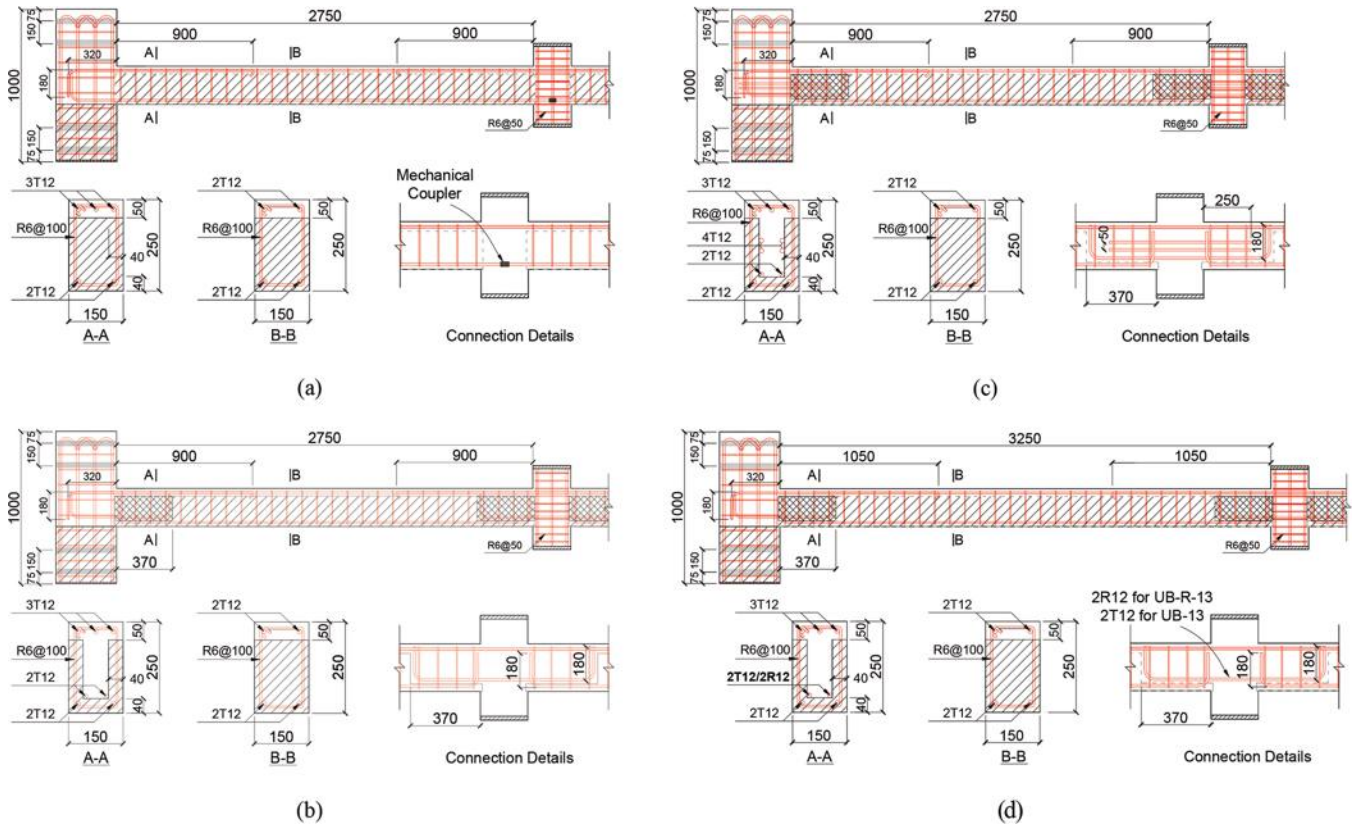

Fig. 1—Details of PC frames: (a) MC-11; (b) UB-11; (c) UB-R-11; and (d) UB-13 and UB-R-13. (Note: Units in mm; 1 in. = 25.4 mm.)

(0.2 in.), respectively. The enlarged side column stub with dimensions of 400 x 400 mm (15.7 x 15.7 in.) was designed for applying the fixed boundary properly. MC-13 had similar details to MC-11 but its span-depth ratio was 13. As shown in Fig. 1(b), the bottom reinforcements of UB-11 were bent up at the ends of the precast beams, while troughs were designed at the beam ends. As seen in Fig. 2(b), U-shaped bars of 2T12 were installed in the troughs to assemble the precast members. Correspondingly, UB-13 was similar to UB-11 but had a span-depth ratio of 13. To improve the performance of the connections, two refined reinforcement details were introduced for the UB-series specimens. As shown in Fig. 1(c), to increase the bending moment capacity of the beam ends, besides U-shaped bars of 2T12, additional straight bars of 4T12 were installed in the troughs of UB-R-11. For UB-R-13, the U-shaped bars of 2T12 in the troughs were replaced by 2R12. Thus, the only difference between UB-R-13 and UB-13 was the type of the U-shaped bars, as shown in Fig. 1(d). R12 represents plain reinforcement with a diameter of 12 mm (0.5 in.).

Based on cylinder tests, the average compressive strength of PC is 36 MPa, while the average compressive strength of cast-in-place concrete is 47 MPa. The mechanical properties of the reinforcements are summarized in Table 2.

Test setup and instrumentation

The test setup is shown in Fig. 3. The side columns were connected to the reaction frame by two horizontal chain rods. A pin support was applied at the bottom of each side column. Beneath the pin support, a series of steel rollers were placed to eliminate its horizontal constraints. Thus, the constraints applied at the side column were statically determined, and the horizontal and vertical reactions at the side columns can be measured directly. A hydraulic jack was employed to apply vertical force on the removed middle column. A steel assembly was installed below the hydraulic jack to eliminate possible out-of-plane failure. As shown in Fig. 3(b), to measure the vertical load applied by the hydraulic jack accurately, two load cells were installed above and below the jack (the average value was used hereafter). Moreover, a load cell was installed below each side column to monitor the vertical load redistribution history. A tension/compression load cell was installed in each horizontal chain rod to measure the horizontal reaction force. Seven linear variable displacement transducers (LVDTs) were installed along the beam (V1 to V7) to monitor the deflection profile of the beams. Four LVDTs (H1 to H4) were installed horizontally to measure the horizontal displacements of the side columns and to estimate the stiffness of the horizontal constraints, which was important for the evaluation of the load-transfer mechanisms. Moreover, four pairs of LVDTs (R1 to R8) were installed horizontally at potential plastic hinge zones to measure their rotations, which were essential for following analytical elaboration. To monitor the variation in reinforcing bar strain, a series of strain gauges were installed along the beam longitudinal reinforcing bars.

TEST RESULTS

Vertical load and failure mode

MC series—Table 3 summarizes the test results, whereas Fig. 4 shows the vertical load-displacement curves of the tested specimens. For MC-11, the yield load of 39 kN, owing to the yielding of beam bottom longitudinal reinforcement close to the middle column, was measured at a vertical displacement of 36 mm. It should be noted that the yield load was defined as the vertical load in accordance with the first yielding of the beam longitudinal reinforcements. At this stage, several flexural cracks occurred at the beam ends. Subsequently, more flexural cracks at the beam ends and some slight concrete crushing were observed. The initial peak load of 50 kN, also known as CAA capacity, was measured at a displacement of 80 mm. At this stage, the beam ends tended to move outward due to the change of the neutral axis, but they were restrained by the side column, resulting in the production of considerable compressive axial force in the beams. This will be further discussed in the subsequent section. After that, the load resistance began to drop due to the concrete crushing severer. At a displacement of 258 mm, 1.03 times of beam depth, the load resistance began to reascend because of the kicked-in CA. Accordingly, the compressive axial force in the beams began to convert to tensile force. At this stage, some cracks developed and penetrated the entire beam section, which explicitly reflected the development of tensile axial force in the beams. At the displacements of 429, 452, and 503 mm, beam bottom reinforcing bar fracture occurred at the beam end near the middle column in sequence. After that, the applied load was resisted by the CA, and dowel action developed in the beam top reinforcements. Finally, MC-11 failed at a displacement of 647 mm due to a complete fracture of the beam top reinforcements near the middle column. The CA capacity was 80 kN, which was 160% of the CAA capacity. Figure 5 shows the failure mode of MC-11. It was found that horizontal cracks occurred at the interface between the precast beam and the cast-in-place topping layer. Penetrating cracks were uniformly distributed along the beams. Additionally,

Table 2—Mechanical properties of reinforcements

Items		Yield load capacity, MPa (ksi)	Ultimate strength, MPa (ksi)	Elongation, %
Stirrups	R6	346 (50.2)	485 (70.5)	18.4
Longitudinal reinforcements	R12	445 (64.5)	595 (86.3)	16.2
	T12	438 (63.5)	576 (83.5)	15.3
	T16	466 (67.6)	603 (87.5)	16.8

Note: R6 and R12 represent plain bars with diameters of 6 and 12 mm (0.24 and 0.47 in.), respectively; T12 and T16 represent deformed reinforcing bars with diameters of 12 and 16 mm (0.47 and 0.63 in.), respectively.

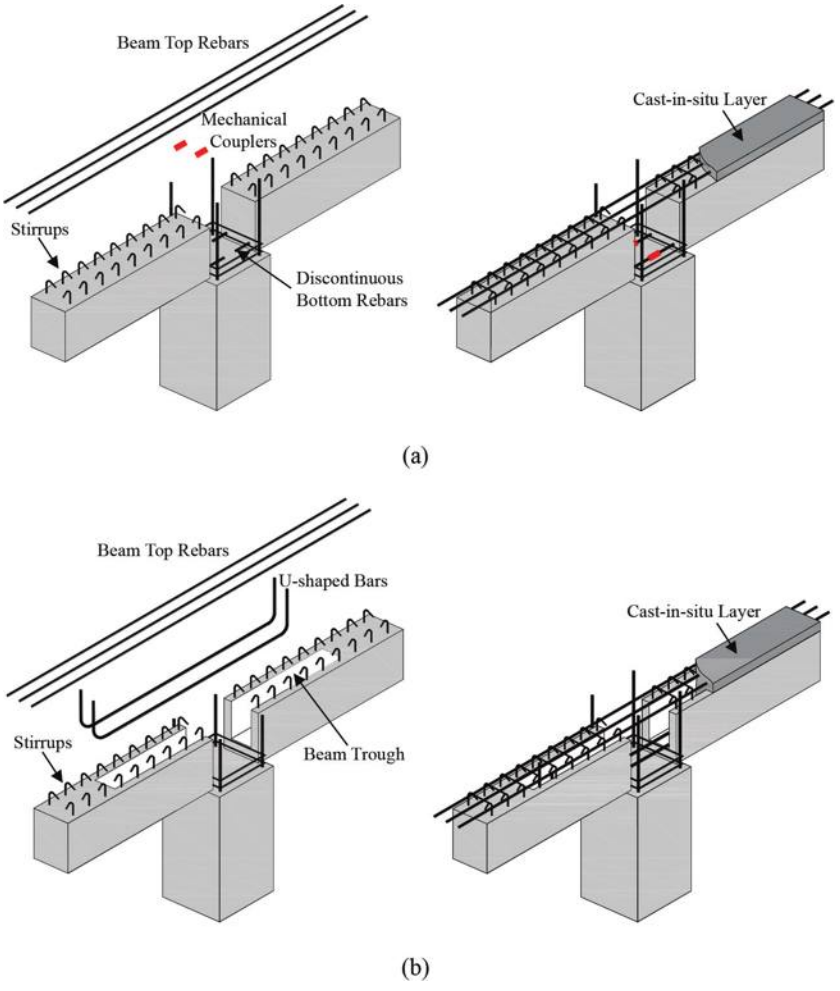

Fig. 2—Assembling of test specimens: (a) MC series; and (b) UB and UB-R series.

Table 3—Test results

Specimens	Critical displacements, mm (in.)			Critical loads, kN (kip)			MHCR, kN (kip)	MHTR, kN (kip)
	YL	CAA	CA	YL	CAA	CA		
MC-11	36 (1.2)	80 (3.1)	647 (25.5)	39 (8.8)	50 (11.2)	80 (18.0)	–171 (–38.4)	141 (31.7)
MC-13	58 (2.3)	106 (4.2)	736 (29.0)	35 (7.9)	45 (10.1)	80 (18.0)	–165 (–37.1)	144 (32.4)
UB-11	35 (1.4)	76 (3.0)	651 (25.6)	38 (8.3)	48 (10.8)	75 (16.9)	–169 (–38.0)	138 (31.0)
UB-R-11	36 (1.4)	69 (2.7)	700 (27.6)	45 (10.1)	57 (12.8)	85 (19.1)	–196 (–44.1)	155 (34.8)
UB-13	53 (2.1)	105 (4.1)	724 (28.5)	34 (7.6)	44 (9.9)	75 (16.9)	–159 (–35.7)	149 (33.5)
UB-R-13	60 (2.4)	103 (4.1)	731 (28.8)	34 (7.6)	43 (9.7)	86 (19.3)	–155 (–34.8)	172 (38.7)
NSC-11	36 (1.2)	79 (3.1)	712 (28.0)	37 (8.3)	52 (11.7)	94 (21.1)	–178 (–40.0)	154 (34.6)
NSC-13	45 (1.8)	108 (4.3)	731 (28.8)	33 (7.4)	43 (9.7)	81 (18.2)	–153 (–34.4)	148 (33.3)

Note: YL is yield load capacity; CAA is compressive arch action capacity; CA is catenary action capacity; MHCR is maximum horizontal compressive reaction; MHTR is maximum horizontal tensile reaction.

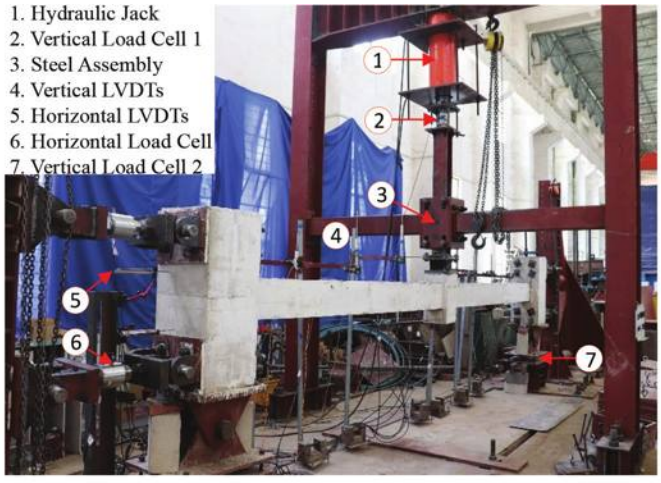

(a)

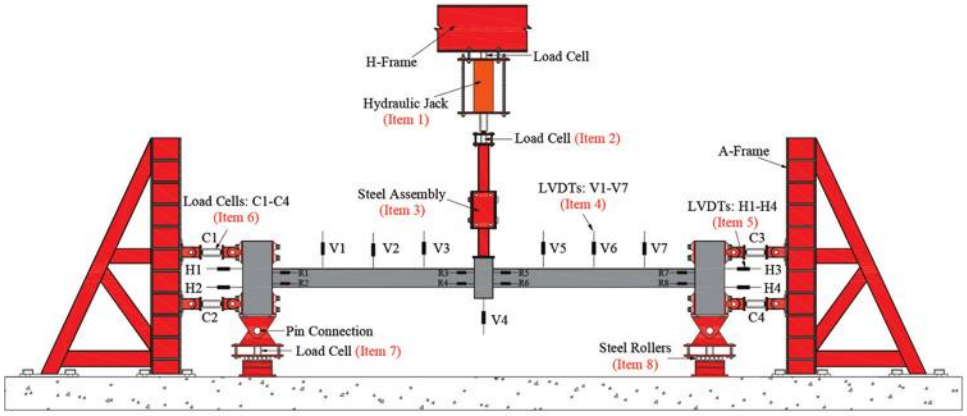

(b)

Fig. 3—Test setup and instrumentation: (a) photo; and (b) schematic view.

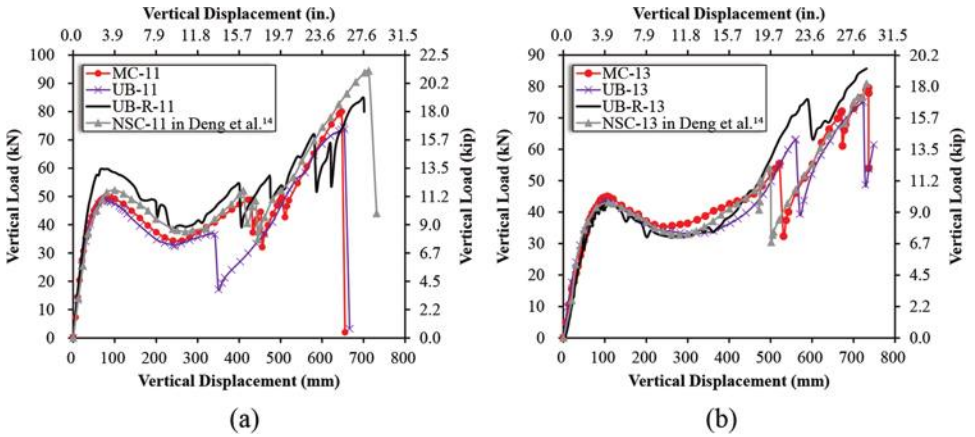

Fig. 4—Vertical load-displacement curves: (a) specimens with span-depth ratio of 11; and (b) specimens with span-depth ratio of 13.

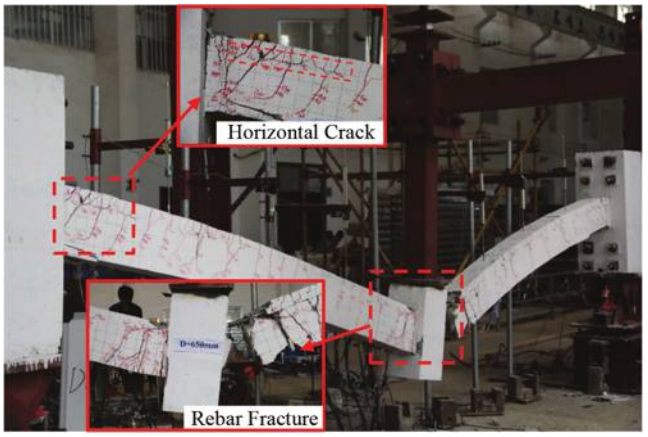

Fig. 5—Failure mode of MC-11.

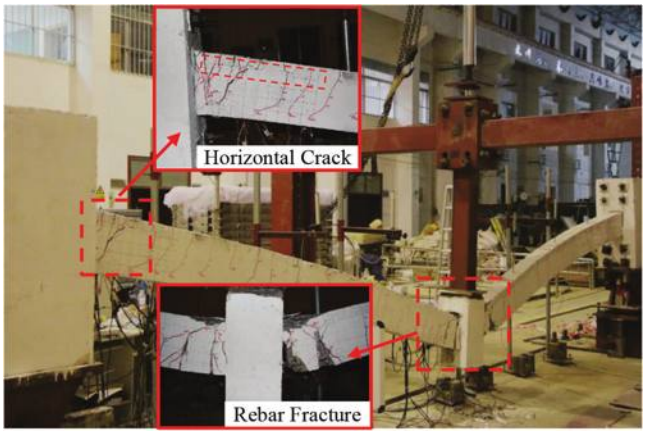

Fig. 6—Failure mode of MC-13.

the reinforcements at one of the beam ends near the middle column fractured completely. The general trend of the vertical load-displacement curve of MC-13 was similar to that of MC-11, as shown in Fig. 4(b). The yield load capacity of MC-13 was 35 kN, while the CAA capacity was 45 kN. Sequential fracture of three beam bottom reinforcements close to the middle column occurred at the displacements of 522, 672, and 736 mm. Due to the limitation of stroke capacity, the test was stopped at a displacement of 736 mm. The CA capacity of MC-13 was 80 kN. Note that MC-13 may obtain greater CA capacity if the hydraulic jack has greater stroke capacity. The failure mode of MC-13 was very similar to that of MC-11, as shown in Fig. 6.

UB series—The PC beams in the UB series had troughs at the beam ends, and U-shaped bars of 2T12 were installed in the troughs to assemble the PC beams and columns. Different from the MC-series frames, the first yield was measured at the U-shaped bars near the middle column. The yield load and CAA capacity of UB-11 were 38 kN and 48 kN, respectively. The failure of UB-11 occurred at a displacement of 651 mm, which corresponds to a CA capacity of 75 kN. It can be found that a wide crack occurred at the end of the trough (refer to Fig. 7) near the right-side column. In general, the failure mode of UB-11 was similar to that of MC-11. The yield load, CAA capacity, and CA capacity of UB-13 were 34, 44, and 75 kN, respectively, which were very close to

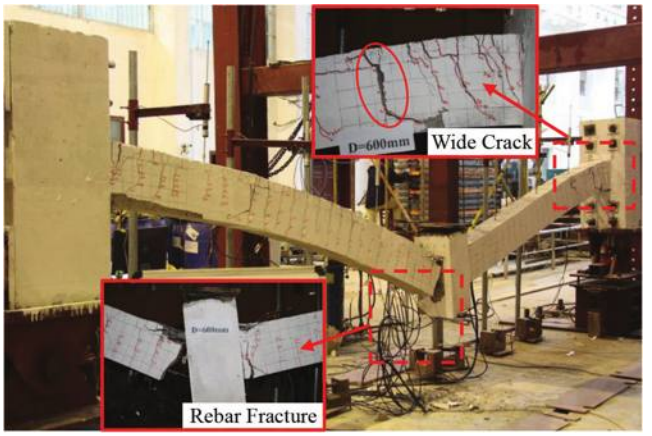

Fig. 7—Failure mode of UB-11.

MC-13. As shown in Fig. 8, the failure mode of UB-13 was similar to UB-11, except that no wide crack occurred at the end of the trough.

UB-R series—As mentioned previously, UB-R-11 had refined detailing compared with UB-11. 4T12 additional straight bars were installed in the beam troughs of UB-R-11. The yield load and CAA capacity of UB-R-11 were 45 kN and 57 kN, respectively. As a result of the refined detailing, the yield load and CAA capacity of UB-R-11 were 118% and 119% of that of UB-11, respectively. The test was stopped

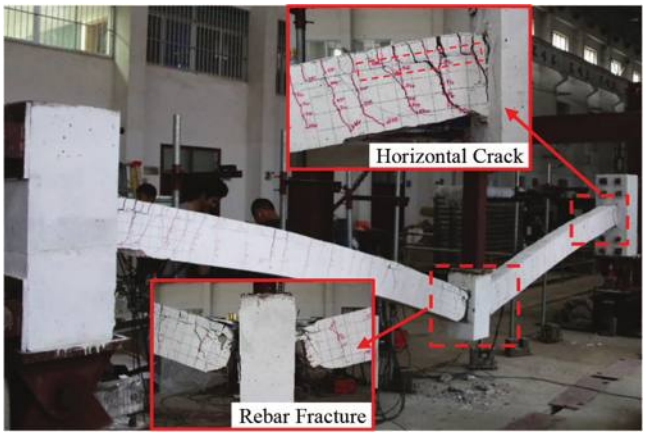

Fig. 8—Failure mode of UB-13.

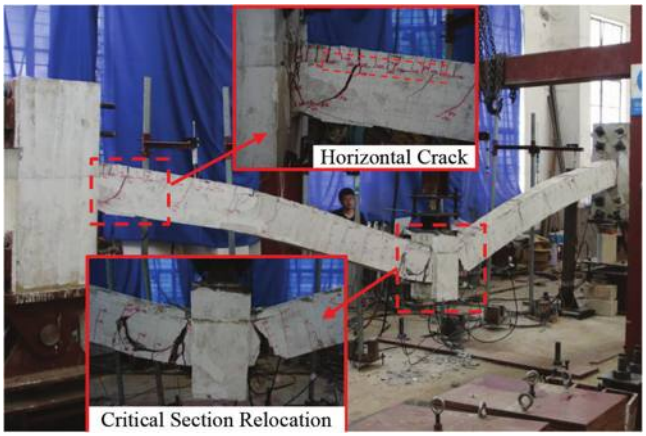

Fig. 9—Failure mode of UB-R-11.

at a displacement of 700 mm due to stroke limitation, and a CA capacity of 85 kN was obtained. Therefore, UB-R-11 achieved higher deformation and CA capacity than UB-11, which will be discussed later in detail. As shown in Fig. 9, the failure mode of UB-R-11 was quite different from that of UB-11. The reinforcing bar fracture occurred at the beam-middle column interfaces for UB-11. However, for UB-R-11, the reinforcing bar fracture occurred at the section 100 mm away from the beam-middle column interfaces.

Unlike UB-13, the plain bar of 2R12 was used in UB-R-13. As shown in Table 3 and Fig. 4(b), the yield load, CAA capacity, and CA capacity of UB-R-13 were 34, 43, and 86 kN, respectively. Therefore, the CA capacity of UB-R-13 was 15% higher than that of UB-13. Note that, different from UB-13, only one of the U-shaped plain bars near the middle column was fractured at a displacement of 590 mm. The difference was attributed to greater slip between the U-shaped plain bars and concrete in UB-R-13, which delayed the reinforcing bar fracture and increased the CA capacity. As shown in Fig. 10, the failure mode of UB-R-13 was similar to that of UB-13. However, due to less bond stress between the U-shaped plain reinforcing bars and the concrete, fewer cracks occurred within the length of the troughs near the middle column.

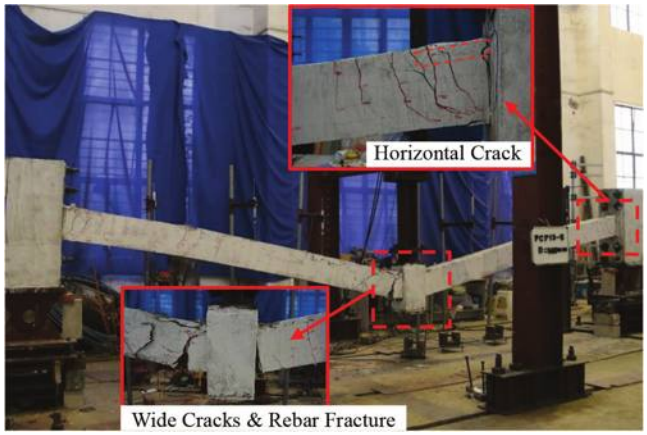

Fig. 10—Failure mode of UB-R-13.

Horizontal reaction

Figure 11(a) shows the total horizontal reaction versus the vertical displacement curves of the specimens with a span-depth ratio of 11. At the beginning of the test, the total horizontal reaction was close to 0 kN, indicating that the frames experienced a purely flexural condition. Subsequently, the horizontal compressive reaction was measured due to the mobilization of the CAA. When the horizontal compressive reaction reached its peak value, it began to decrease and finally transfer to a tensile reaction because of the development of the CA. Similar results were obtained in specimens with a span-depth ratio of 13. The maximum horizontal compressive/tensile reactions can be found in Table 3. Figure 11(b) decomposes the total horizontal reaction of UB-11. It was found that the majority of horizontal compressive reaction was measured in the bottom load cell, whereas the horizontal compressive reaction measured in the top load cell was too small to be ignored. This is because the hogging moment developed in the beam-side column interface was prone to pull the top of the side column inward and push the bottom of the side column outward (refer to Fig. 11(b)). At the CA stage, the horizontal tensile reaction in the top load cell was much larger than the one in the bottom load cell, which indicated that a considerable bending moment can still develop in the beam end near the side column. This will be further discussed in the following section on analytical elaboration.

Deformation measurement

Figure 12 shows the beam deflection shape of MC-11 at critical stages. The beam showed a symmetrical profile until the first reinforcing bar fracture at a displacement of 429 mm. After that, as the fracture of the beam bottom reinforcing bar first occurred at the beam end near the middle column, an asymmetrical profile appeared. Figure 13 illustrates the method to measure the rotation of the beam ends, while Fig. 14 presents the rotation of the beam ends of UB-11. The rotation of the beam end near the side column was less than the one near the middle column because the hogging moment capacity at the beam end near the side column was larger than the sagging moment capacity at the beam end near the middle column. However, as a concentrated load was applied at the middle column, the bending

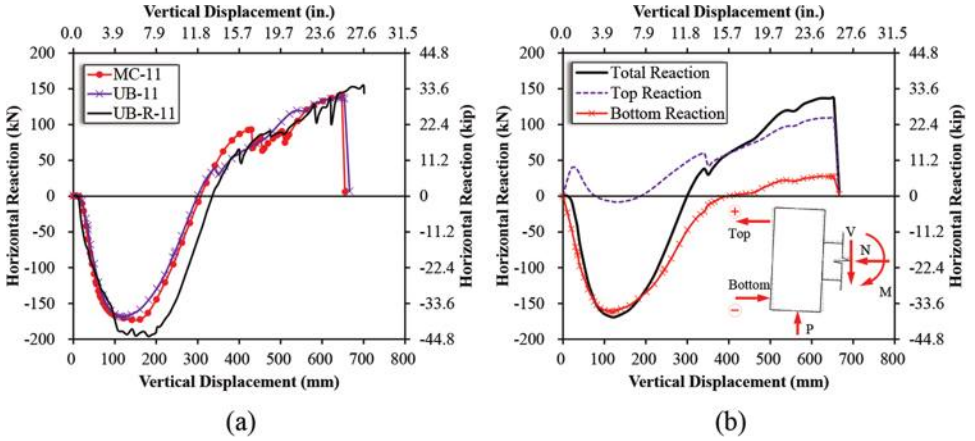

Fig. 11—Horizontal reaction-displacement curves: (a) specimens with span-depth ratio of 11; and (b) UB-11 contributions.

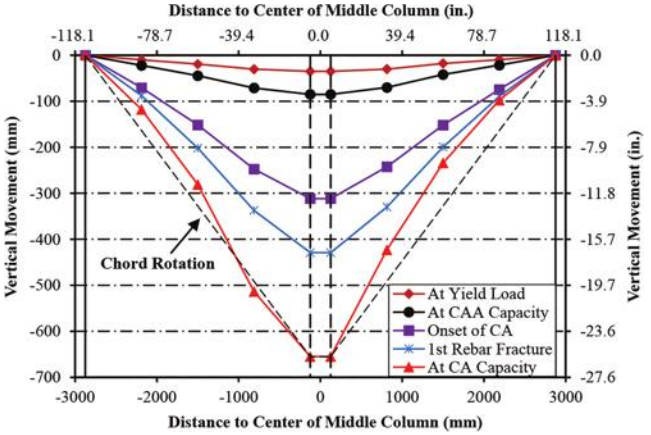

Fig. 12—Deflected shape of specimen MC-11 at selected loading stages.

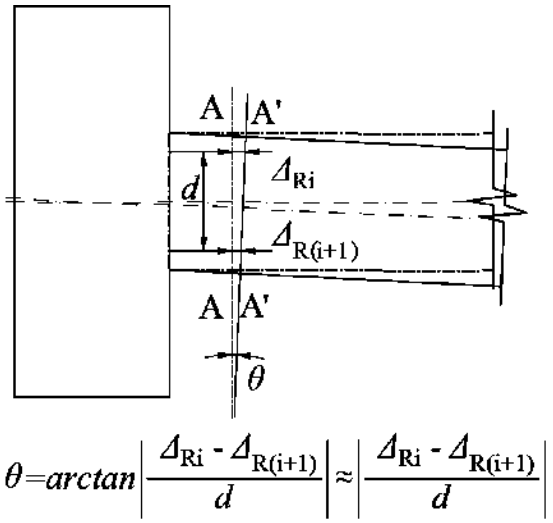

Fig. 13—Determination of rotation of beam end.

moment demand of the beam ends was similar. More serious damage happened in the beam end near the middle column. Moreover, the rotation of the beam end near the side column was less than the chord rotation, while the one near the middle column was greater than the chord rotation after the bottom reinforcing bars fractured. A similar observation was recorded for the other specimens.

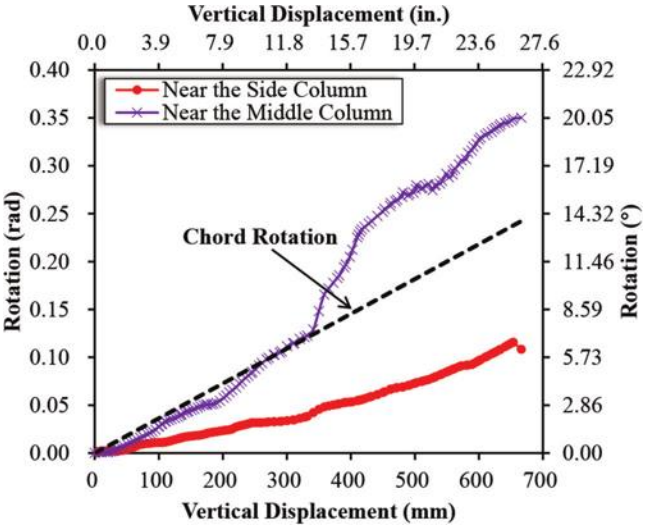

Fig. 14—Rotation of beam end of UB-11.

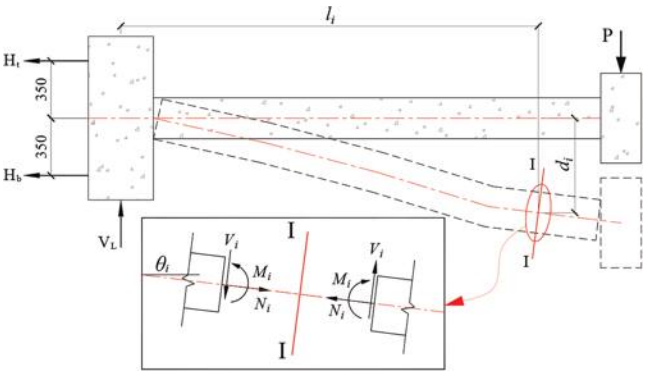

Fig. 15—Determination of internal forces in different beam sections.

ANALYTICAL ELABORATION AND DISCUSSION

Variation in internal forces in beams

An analytical investigation was performed to reveal the variation in the internal forces of the beams. As shown in Fig. 15, only one beam was extracted for analysis due to symmetry. For any beam section i, the bending moment M_i can be calculated as follows

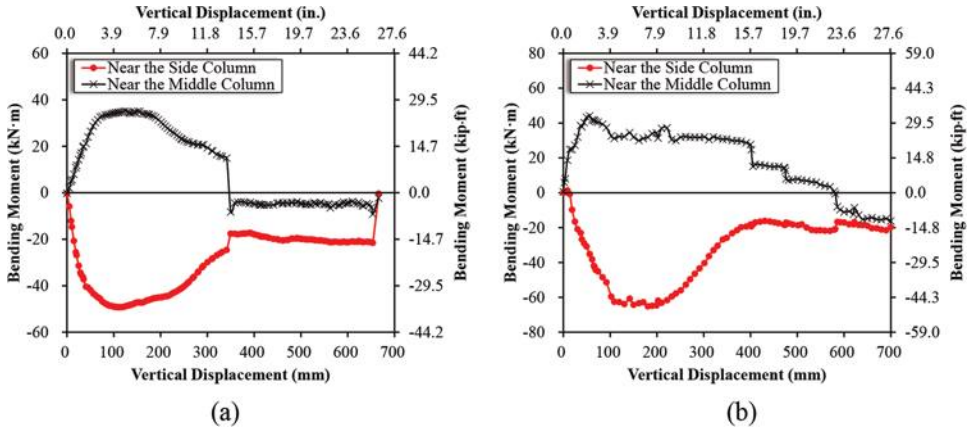

Fig. 16—Variation in bending moment at beam ends: (a) UB-11; and (b) UB-R-11.

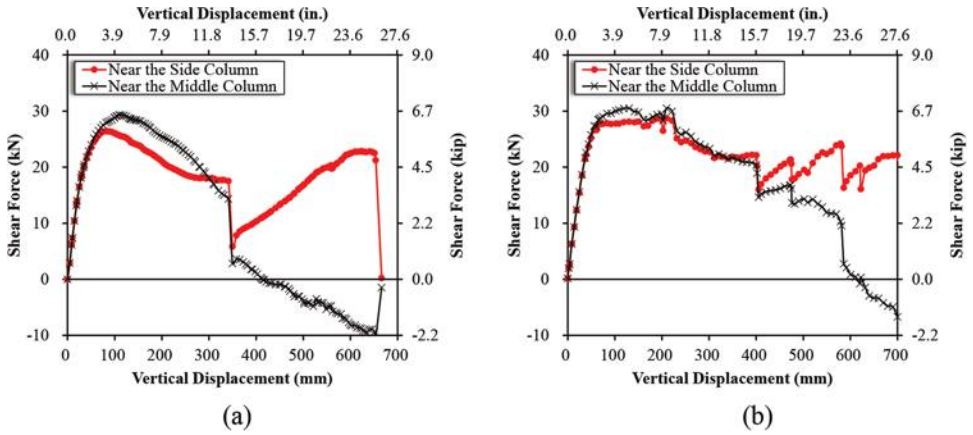

Fig. 17—Variation in shear force at beam ends: (a) UB-11; and (b) UB-R-11.

$$M_i = V_L l_i - H_t(d_i + 350) - H_b(d_i - 350) \quad (1)$$

According to force equilibrium along the beam axis, the axial force N_i is obtained as

$$N_i = V_L \sin\theta_i + (H_t + H_b)\cos\theta_i \quad (2)$$

According to force equilibrium in the vertical direction, the shear force V_i is obtained as

$$V_i = (V_L - N_i \sin\theta_i)/\cos\theta_i \quad (3)$$

The total vertical component of the axial force and the shear force of the section i can be obtained as

$$P_i = 2(N_i \sin\theta_i + V_i \cos\theta_i) \quad (4)$$

where V_L is the vertical reaction measured at the pin support; H_t and H_b are the horizontal reactions measured at the top and bottom roller, respectively; V_L is the vertical reaction measured at the pin support; d_i is the vertical displacement of section i; and θ_i is the rotation of section i.

As mentioned in the section "Deformation measurement," the rotation of the beam ends was measured, and thus the internal forces of the beam ends can be calculated by Eq. (1) to (4). UB-11 and UB-R-11 were selected to illustrate the variation in the internal forces. Figure 16 shows the bending moment-displacement history of the beam ends of UB-11 and UB-R-11. For UB-11, the bending moment reached its peak value at the CAA stage and then began to decrease with the increase in displacement. The sagging moment at the beam end near the middle column dropped sharply and changed into the hogging moment when the beam bottom reinforcing bars were fractured. Although no reinforcing bar was fractured, the bending moment at the beam end near the side column also dropped due to reinforcing bar fracture at the beam end near the middle column, which mitigated the rotation demand in the beam end near the side column. As shown in this figure, the bending moment at the beam end near the side column did not vanish after reinforcing bar fracture occurred at the beam end near the middle column, which agreed with the response of the horizontal reaction well. The bending moments of UB-R-11 exhibited a similar trend, while their peak values were higher because of the higher reinforcement ratio at the beam-column interfaces. Figure 17 shows the variation in shear force. Similar to the observation of the bending moment, the shear forces attained their peak values at the CAA stage. Reascending behavior was observed for the shear forces at the beam end near the side column at the large deformation stage, owing to the bending moment and dowel action of the reinforcing bars. Figure 18 shows the variation in axial force. It was found that the axial forces at the beam ends were very close to the total horizontal reactions. This is because the rotations

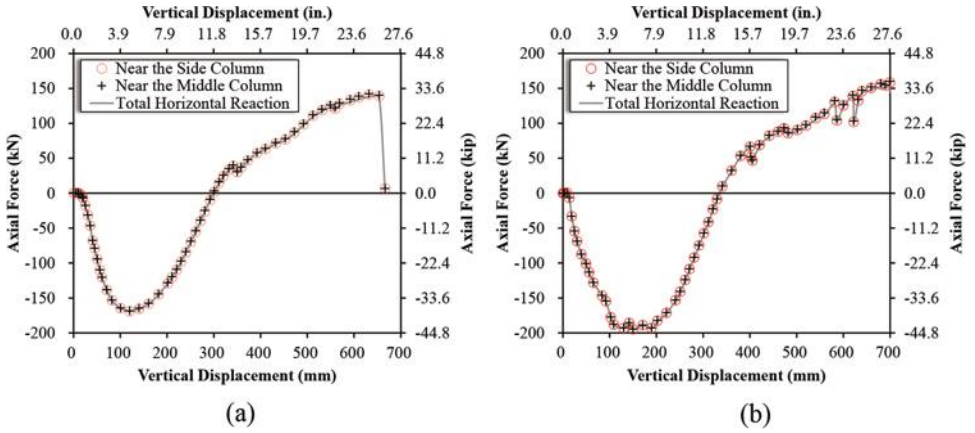

Fig. 18—Variation in axial force at beam ends: (a) UB-11; and (b) UB-R-11.

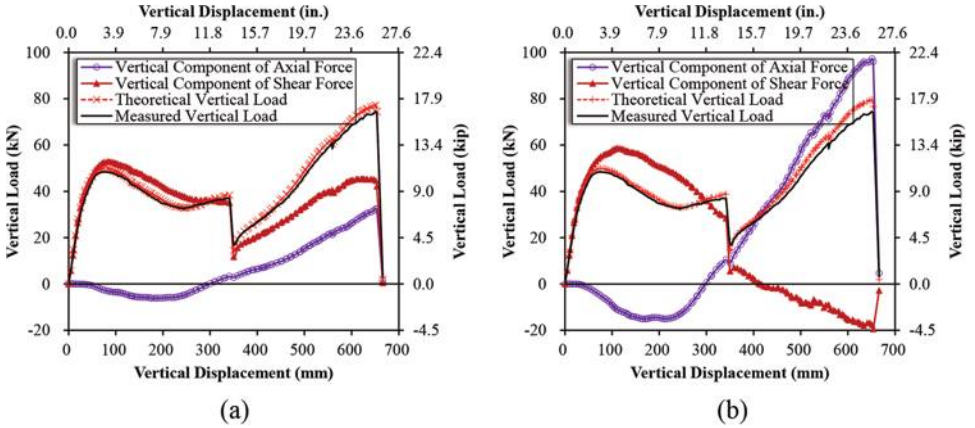

Fig. 19—Load-transfer behavior at different sections of UB-11: (a) at beam-side column interface; and (b) at beam-middle column interface.

of the beam ends were very small. Figure 19 compares the vertical load-transfer behaviors at different sections of UB-11. At the small deformation stage, the axial force made a negative contribution so that the shear force dominated the load-transfer process. At the CA stage, the shear force at the beam-side column interface still dominated the load-transfer behavior. However, tensile axial force at the beam-middle column interface dominated the load-transfer behavior. As expressed in Eq. (2) and (3), the axial and shear force were a function of the rotation of beam ends. Therefore, different load-transfer behavior could be attributed to the different rotation behavior of the beam ends. As shown in Fig. 14, the rotations of the beam ends near the middle column were greater than the ones near the side column, especially after the fracture of the beam bottom reinforcing bars.

Effects of connection type

In the current study, six PC specimens with different connection types were tested. The CAA capacity of MC-11, MC-13, UB-11, UB-13, UB-R-11, and UB-R-13 was 50, 45, 48, 44, 57, and 43 kN, respectively. Their CA capacity was 80, 80, 75, 75, 85, and 86 kN, respectively. Thus, PC specimens using mechanical couplers or U-shaped deformed bars (MC-11, MC-13, UB-11, and UB-13) achieved similar load-resisting behavior. Using U-shaped plain bars (UB-R-13) had little effect on CAA capacity. However, the CA capacity of UB-R-13 was upgraded by 15% compared with UB-13 as the slip of the plain bar delayed the reinforcing bar fracture. As a result of adding the additional straight bars, the CAA capacity of UB-R-11 was 19% higher than that of UB-11. Unexpectedly, the deformation capacity of UB-R-11 was also higher than that of UB-11. This is because the deformation capacity of the PC frame was controlled by the fracture of the beam top reinforcing bar. The additional straight bars in UB-R-11 can share parts of the tensile strength of the beam top reinforcing bar and mitigate the stress concentration at the critical sections.

To evaluate the robustness of PC frames with emulative connections, the cast-in-place RC specimens tested by authors (Deng et al.[14]) were briefly introduced for comparison. Two RC specimens (NSC-11 and NSC-13) had similar geometrical dimensions, reinforcement details, boundary conditions, as well as material properties to the tested PC frames. Note that "NSC" means normal-strength concrete, and the numerals 11 and 13 represent the span-depth ratio of the beams. The lap-splice technique (Class A splice in accordance with ACI 318-14[31]) was adopted to connect the beam bottom reinforcing bars. According to previous works,[14,17] Class A splices can satisfy the requirements of continuity of reinforcing bars—in other words, the beam bottom reinforcing bars of these two RC specimens can be regarded as continuous. For the detailed results of NSC-11 and NSC-13,

please refer to Deng et al.[14] The vertical load-displacement curves of these two RC specimens were compared with that of the PC specimens. As shown in Fig. 4(a), specimens MC-11 and UB-11 had a similar load-resisting capacity to the corresponding RC specimen NSC-11 before the beam top reinforcing bar fracture near the middle column. The ultimate load capacity of MC-11 and UB-11 was lower than that of NSC-11 because the reinforcing bar fracture in specimen NSC-11 was later, which may be attributed to the higher concrete strength (higher bond stress between concrete and reinforcing bars) of the topping layer of PC specimens. Due to the refined reinforcement details, UB-R-11 was able to develop greater CAA capacity than NSC-11. As seen in Fig. 4(b), specimens MC-13 and UB-13 showed similar performance to specimen NSC-13 during the whole loading process. In comparison, specimen UB-R-13 had a greater ultimate load capacity than specimen NSC-13 because the U-shaped plain reinforcing bars in the trough near the middle column did not fracture completely, and therefore they can make a contribution to the ultimate load capacity.

Effects of span-depth ratio

Compared with MC-13 and UB-13, the CAA capacity of MC-11 and UB-11 increased by over 10% due to a decreased span-depth ratio. However, due to the limited stroke capacity of the hydraulic jack, the CA capacity of MC-13 and UB-13 measured at the end of the tests was similar to MC-11 and UB-11. It was believed that the specimens with a greater span-depth ratio could achieve higher CA capacity if the jack with a higher stroke capacity was used for tests.

Dynamic progressive collapse resistance

Based on the energy-based framework proposed by Izzuddin et al.,[32] the quasi-static vertical load-displacement curve can be used to determine their dynamic resistance. As shown in Fig. 20, similar to the quasi-static curve, the dynamic resistance curves experienced a resistance softening stage after the first peak load. Reascending behavior was also observed in the dynamic resistance curves. Finally, the dynamic resistance of specimens MC-11, MC-13, UB-11, UB-13, UB-R-11, UB-R-13, NSC-11, and NSC-13 was obtained as 46, 46, 42, 44, 53, 47, 52, and 42 kN, respectively. Thus, the PC specimens that adopted the refined reinforcement details (UB-R series) achieved greater dynamic resistance than the RC specimens. The dynamic resistance of both MC-11 and MC-13 was 46 kN. However, it was believed that MC-13 could achieve higher dynamic resistance if the hydraulic jack has greater stroke capacity. Compared with UB-11 and UB-13, the dynamic resistance of UB-R-11 and UB-R-13 increased by 26% and 7%, respectively.

CONCLUSIONS

Based on the experimental and analytical results, the following conclusions were drawn:

1. Similar to the conventional reinforced concrete (RC) frames, compressive arch action (CAA) and catenary action (CA) were the main load-transfer mechanisms for the precast concrete (PC) frame with typical emulative connections to resist progressive collapse, while the CA dominated the ultimate load capacity.

2. PC frames assembled by mechanical couplers or additional U-shaped bars achieved similar CAA capacity, CA capacity, and deformation capacity. When the U-shaped deformed bars were replaced by U-shaped plain reinforcing bars, little effects were observed for CAA capacity. However, higher deformation capacity and CA capacity will be achieved due to lower bond strength between the plain bars and the concrete, which can delay the fracture of the reinforcing bars.

3. The CAA capacity of UB-R-11 was 19% higher than that of UB-11. Thus, adding the additional straight bars in the beam troughs can significantly improve the CAA capacity. Unexpectedly, UB-R-11 achieved higher deformation capacity than UB-11 as the additional straight bar can decrease the tensile stress concentrated in the beam top reinforcing bar at the critical sections, which can also delay the reinforcing bar fracture.

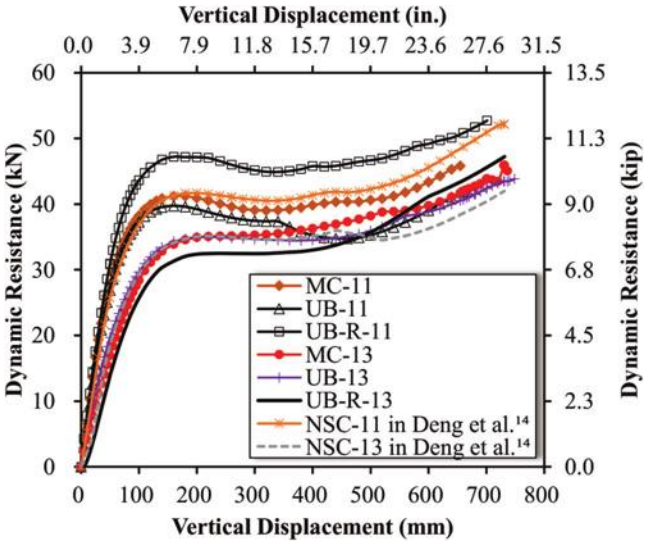

Fig. 20—Dynamic load resistance of specimens.

AUTHOR BIOS

ACI member **Kai Qian** *is a Professor in the College of Civil Engineering and Architecture at Guilin University of Technology, Guilin, Guangxi, China. He received his MSc and PhD from Nanyang Technological University, Singapore. His research interests include reinforced concrete and prestressed concrete structures design, particularly in the areas of progressive collapse and blast resistance.*

Shi-Lin Liang *is a Research Student in the College of Civil Engineering and Architecture at Guangxi University, Nanning, Guangxi, China. His research interests include precast concrete and prestressed concrete design, particularly in the area of progressive collapse.*

Lu Zhang *is a Professor in the College of Civil Engineering and Architecture at Guilin University of Technology. He received his PhD from the University of Illinois Chicago, Chicago, IL. His research interests include integrating structural design with damage-detection philosophies for more resilient and sustainable infrastructure systems.*

Zhi Li *is a Research Fellow in the College of Civil Engineering and Architecture at Guilin University of Technology. He received his PhD from Guangxi University. His research interests include steel structure and composite structure design, particularly in the area of progressive collapse.*

ACKNOWLEDGMENTS

This research was supported by a research grant provided by the National Natural Science Foundation of China (No. 52022024 and 51778153). Any opinions, findings, and conclusions expressed in this paper do not necessarily reflect the view of the National Natural Science Foundation of China.

REFERENCES

1. ASCE/SEI 7-05, "Minimum Design Loads for Buildings and Other Structures," Structural Engineering Institute, American Society of Civil Engineers, Reston, VA, 2005, 424 pp.

2. GSA, "Progressive Collapse Analysis and Design Guidelines for New Federal Office Buildings and Major Modernization Projects," U.S. General Services Administration, Washington, DC, 2009.

3. DoD, "Design of Buildings to Resist Progressive Collapse," UFC 4-023-03, Unified Facilities Criteria, U.S. Department of Defense, Washington, DC, 2009, 245 pp.

4. Qian, K., and Li, B., "Experimental and Analytical Assessment on RC Interior Beam-Column Subassemblages for Progressive Collapse," *Journal of Performance of Constructed Facilities*, ASCE, V. 26, No. 5, Oct. 2012, pp. 576-589. doi: 10.1061/(ASCE)CF.1943-5509.0000284

5. Quiel, S. E.; Naito, C. J.; and Fallon, C. T., "A Non-Emulative Moment Connection for Progressive Collapse Resistance in Precast Concrete Building Frames," *Engineering Structures*, V. 179, Jan. 2019, pp. 174-188. doi: 10.1016/j.engstruct.2018.10.027

6. Sasani, M.; Bazan, M.; and Sagiroglu, S., "Experimental and Analytical Progressive Collapse Evaluation of Actual Reinforced Concrete Structure," *ACI Structural Journal*, V. 104, No. 6, Nov.-Dec. 2007, pp. 731-739.

7. Sasani, M., and Sagiroglu, S., "Progressive Collapse Resistance of Hotel San Diego," *Journal of Structural Engineering*, ASCE, V. 134, No. 3, Mar. 2008, pp. 478-488. doi: 10.1061/(ASCE)0733-9445(2008)134:3(478)

8. Sasani, M., and Sagiroglu, S., "Gravity Load Redistribution and Progressive Collapse Resistance of 20-Story Reinforced Concrete Structure following Loss of Interior Column," *ACI Structural Journal*, V. 107, No. 6, Nov.-Dec. 2010, pp. 636-644.

9. Xiao, Y.; Kunnath, S.; Li, F. W.; Zhao, Y. B.; Lew, H. S.; and Bao, Y., "Collapse Test of Three-Story Half-Scale Reinforced Concrete Frame Building," *ACI Structural Journal*, V. 112, No. 4, July-Aug. 2015, pp. 429-438. doi: 10.14359/51687746

10. Adam, J. M.; Buitrago, M.; Bertolesi, E.; Sagaseta, J.; and Moragues, J. J., "Dynamic Performance of a Real-Scale Reinforced Concrete Building Test under A Corner-Column Failure Scenario," *Engineering Structures*, V. 210, May 2020, Article No. 110414. doi: 10.1016/j.engstruct.2020.110414

11. Su, Y.; Tian, Y.; and Song, X., "Progressive Collapse Resistance of Axially-Restrained Frame Beams," *ACI Structural Journal*, V. 106, No. 5, Sept.-Oct. 2009, pp. 600-607.

12. Yu, J., and Tan, K. H., "Structural Behavior of RC Beam-Column Subassemblages under a Middle Column Removal Scenario," *Journal of Structural Engineering*, ASCE, V. 139, No. 2, Feb. 2013, pp. 233-250. doi: 10.1061/(ASCE)ST.1943-541X.0000658

13. Sadek, F.; Main, J. A.; Lew, H. S.; and Bao, Y., "Testing and Analysis of Steel and Concrete Beam-Column Assemblies under a Column Removal Scenario," *Journal of Structural Engineering*, ASCE, V. 137, No. 9, Sept. 2011, pp. 881-892. doi: 10.1061/(ASCE)ST.1943-541X.0000422

14. Deng, X.-F.; Liang, S.-L.; Fu, F.; and Qian, K., "Effects of High-Strength Concrete on Progressive Collapse Resistance of Reinforced Concrete Frame," *Journal of Structural Engineering*, ASCE, V. 146, No. 6, June 2020, p. 04020078. doi: 10.1061/(ASCE)ST.1943-541X.0002628

15. Yu, J., and Tan, K. H., "Structural Behavior of Reinforced Concrete Frames Subjected to Progressive Collapse," *ACI Structural Journal*, V. 114, No. 1, Jan.-Feb. 2017, pp. 63-74. doi: 10.14359/51689424

16. Qian, K.; Liang, S.-L.; Fu, F.; and Fang, Q., "Progressive Collapse Resistance of Precast Concrete Beam-Column Sub-Assemblages with High-Performance Dry Connections," *Engineering Structures*, V. 198, Nov. 2019, Article No. 109552. doi: 10.1016/j.engstruct.2019.109552

17. Yu, J., and Tan, K.-H., "Experimental and Numerical Investigation on Progressive Collapse Resistance of Reinforced Concrete Beam-Column Sub-Assemblages," *Engineering Structures*, V. 55, Oct. 2013, pp. 90-106. doi: 10.1016/j.engstruct.2011.08.040

18. Lew, H. S.; Bao, Y.; Pujol, S.; and Sozen, M. A., "Experimental Study of Reinforced Concrete Assemblies under Column Removal Scenario," *ACI Structural Journal*, V. 111, No. 4, July-Aug. 2014, pp. 881-892. doi: 10.14359/51686739

19. Guerrini, G., "Two Critical Issues in Detailing Reinforced Concrete Frames for Ductility," *Proceedings of the 1st* fib *Italy YMG Symposium on Concrete and Concrete Structures*, M. Del Zoppo, I. G. Colombo, and F. Vecchi, eds., Parma, Italy, Oct. 2019, pp. 154-161.

20. Qian, K., and Li, B., "Slab Effects on Response of Reinforced Concrete Substructures after Loss of Corner Column," *ACI Structural Journal*, V. 109, No. 6, Nov.-Dec. 2012, pp. 845-855.

21. Qian, K., and Li, B., "Quantification of Slab Influences on the Dynamic Performance of RC Frames against Progressive Collapse," *Journal of Performance of Constructed Facilities*, ASCE, V. 29, No. 1, Feb. 2015, p. 04014029. doi: 10.1061/(ASCE)CF.1943-5509.0000488

22. Qian, K.; Weng, Y.-H.; and Li, B., "Improving Behavior of Reinforced Concrete Frames to Resist Progressive Collapse through Steel Bracings," *Journal of Structural Engineering*, ASCE, V. 145, No. 2, Feb. 2019, p. 04018248. doi: 10.1061/(ASCE)ST.1943-541X.0002263

23. Qian, K., and Li, B., "Strengthening of Multibay Reinforced Concrete Flat Slabs to Mitigate Progressive Collapse," *Journal of Structural Engineering*, ASCE, V. 141, No. 6, June 2015, p. 04014154. doi: 10.1061/(ASCE)ST.1943-541X.0001125

24. Li, S.; Kose, M. M.; Shan, S.; and Sezen, H., "Modeling Methods for Collapse Analysis of Reinforced Concrete Frames with Infill Walls," *Journal of Structural Engineering*, ASCE, V. 145, No. 4, Apr. 2019, p. 04019011. doi: 10.1061/(ASCE)ST.1943-541X.0002285

25. Qian, K.; Lan, D.-Q.; Fu, F.; and Li, B., "Effects of Infilled Wall Opening on Load Resisting Capacity of RC Frames to Mitigate Progressive Collapse Risk," *Engineering Structures*, V. 223, Nov. 2020, Article No. 111196. doi: 10.1016/j.engstruct.2020.111196

26. Lew, H. S.; Main, J. A.; Bao, Y.; Sadek, F.; Chiarito, V. P.; Robert, S. D.; and Torres, J. O., "Performance of Precast Concrete Moment Frames Subjected to Column Removal: Part 1, Experimental Study," *PCI Journal*, V. 62, No. 5, Sept.-Oct. 2017, pp. 35-52. doi: 10.15554/pcij62.5-02

27. Bao, Y.; Main, J. A.; Lew, H. S.; and Sadek, F., "Performance of Precast Concrete Moment Frames Subjected to Column Removal: Part 2, Computational Analysis," *PCI Journal*, V. 62, No. 5, Sept.-Oct. 2017, pp. 53-74. doi: 10.15554/pcij62.5-01

28. Kang, S.-B., and Tan, K. H., "Behaviour of Precast Concrete Beam–Column Sub-Assemblages Subject to Column Removal," *Engineering Structures*, V. 93, June 2015, pp. 85-96. doi: 10.1016/j.engstruct.2015.03.027

29. Qian, K.; Liang, S.-L.; Xiong, X.-Y.; Fu, F.; and Fang, Q., "Quasi-Static and Dynamic Behavior of Precast Concrete Frames with High Performance Dry Connections Subjected to Loss of a Penultimate Column Scenario," *Engineering Structures*, V. 205, Feb. 2020, Article No. 110115. doi: 10.1016/j.engstruct.2019.110115

30. Qian, K.; Liang, S.-L.; Feng, D.-C.; Fu, F.; and Wu, G., "Experimental and Numerical Investigation on Progressive Collapse Resistance of Post-Tensioned Precast Concrete Beam-Column Subassemblages," *Journal of Structural Engineering*, ASCE, V. 146, No. 9, Sept. 2020, p. 04020170. doi: 10.1061/(ASCE)ST.1943-541X.0002714

31. ACI Committee 318, "Building Code Requirements for Structural Concrete (ACI 318-14) and Commentary (ACI 318R-14)," American Concrete Institute, Farmington Hills, MI, 2014, 520 pp.

32. Izzuddin, B. A.; Vlassis, A. G.; Elghazouli, A. Y.; and Nethercot, D. A., "Progressive Collapse of Multi-Storey Buildings Due to Sudden Column Loss—Part I: Simplified Assessment Framework," *Engineering Structures*, V. 30, No. 5, May 2008, pp. 1308-1318. doi: 10.1016/j.engstruct.2007.07.011

ACI STRUCTURAL JOURNAL TECHNICAL PAPER

Title No. 120-S62

Vibration Behavior of Post-Tensioned Concrete Slabs

by Fady Ibrahim Ezzat Aziz, Amr Abdelrahman, and Ezzeldin Yazeed Sayed-Ahmed

Post-tensioned concrete flat slabs with high span-depth ratios are susceptible to vibration problems. Although the issue was addressed in previous research, there is no final agreement on the effect of prestress level on the fundamental frequency of post-tensioned concrete slabs. Through numerical modeling using Abaqus software, this paper presents the effect of prestressing forces on the fundamental frequencies of slabs. This paper also examines the applicability and accuracy of the available mathematical models to estimate the fundamental frequency of concrete slabs. Finally, the paper presents two newly proposed mathematical models created by a neural designer program. The first model estimates the fundamental frequencies of uncracked concrete slabs, and it is more accurate than the currently available equations. The second proposed model estimates the peak acceleration of uncracked concrete slabs, and it is applicable for the dynamic motion of a forcing frequency of 2 Hz and a damping ratio of 2%.

Keywords: flat slabs; fundamental frequency; peak vertical acceleration; post-tensioned floors; prestressed concrete; static deflection method; vibration.

INTRODUCTION

Post-tensioned concrete flat slabs are extensively used nowadays in various projects worldwide for the system's advantages such as saving reinforcement quantities, less slab thickness, much less susceptibility to deflection, uncracked sections under service loads, and less construction time. Slabs of small thickness and long spans make the section slender, which raises the significance of vibration analysis as excessive vibration causes discomfort to building users due to human footfall. Post-tensioned flat slabs of low values of natural frequency are very critical to high dynamic displacement and resonance phenomena due to low forcing frequency values of human walking of an average frequency of 2 Hz. In addition, the dynamic behavior of uncracked concrete slabs is studied to evaluate the peak vertical acceleration to achieve the required comfort level for the floor's occupants. Simplified equations are available and can help check the vibration and dynamic characteristics of post-tensioned flat slabs; however, detailed calculations can present more precise equations in case simplified equations have shown a vibration problem might happen.

This research focuses on the impact of various parameters on the fundamental frequency of post-tensioned flat slabs and concludes with two mathematical models. The first model predicts the fundamental frequency of uncracked concrete slabs, while the second model predicts the peak vertical acceleration of uncracked concrete slabs due to the dynamic motion of a forcing frequency of 2 Hz. The parameters to be studied are the prestress level, span-depth ratio, slab aspect ratio, the ratio between the long side and short side, and effective mass on the slab.

Vibration limits due to human motion

Slab vibration is a consequence of any motion over the floor induced by either humans or machines. Excessive floor vibration causes discomfort to its occupants resembling in many forms the feeling that the building is collapsing. Different references[1,2] state the acceleration limits for different activities on floors to achieve the suitable comfort level for floor occupants, as stated in Table 1.

In addition to people's discomfort and annoyance, the fundamental frequency of the structure and the forcing frequency should be evaluated to avoid high dynamic displacement and resonance phenomena. Bachmann et al.[3] stated the threshold minimum fundamental frequency (f) for floors according to the functions and type of motion on that floor, as shown in Table 2.

First mode and fundamental frequency

For an undamped structure of stiffness K subjected to a dynamic force of amplitude (F_o), the amplitude displacement (U) of the structure follows Eq. (1).

$$U = \frac{F_o/K}{1 - r^2} \tag{1}$$

Table 1—Acceleration limits for different rhythmic activities[2]

Occupancies affected by vibration	Acceleration limit, m/s^2
Office or residential or shopping malls	0.04 to 0.07
Dining	0.15 to 0.25
Weightlifting	0.15 to 0.25
Dance rhythmic activities	0.4 to 0.7

Table 2—Minimum fundamental frequencies of slabs with different functions,[3] in Hz

Floor type	Walking areas	Sport floors	Dance floors	Soft-pop concerts	Hard-pop concerts
Reinforced concrete	7.5	7.5	6.5	3.4	6.5
Prestressed concrete	7.5	8.0	7.0	3.4	6.5
Composite	7.5	8.5	7.5	3.4	6.5
Steel	7.5	9.0	8.0	3.4	6.5

ACI Structural Journal, V. 120, No. 4, July 2023.

MS No. S-2021-437.R5, doi: 10.14359/51738716, received December 18, 2022, and reviewed under Institute publication policies.

where r is the ratio between the natural frequency of the acting force (ω') and the natural frequency of the structure (ω). When ω' comes very close to ω, the value of r is nearly equal to one, leading the denominator of Eq. (1) to be too small—very close to zero. As a result, the amplitude displacement value (U) becomes too high, very near to infinity (∞), causing sudden failure of the whole structure; this phenomenon is called "resonance." The first vibrational mode always exhibits the lowest comfort feeling for the floor occupants because it has the lowest natural frequency value; therefore, the first modal shape for the vertical displacement component is most critical, and its frequency (f) should not be lower than the threshold minimum frequency to avoid the resonance phenomenon.

Dependent factors of floor's fundamental frequency

For the undamped single degree of freedom (SDOF), the natural frequency (ω_n) of any element is linked to its frequency (f) through Eq. (2) and (3).

$$\omega_n = \sqrt{\frac{K}{m}} \tag{2}$$

$$f = \frac{\sqrt{\frac{K}{m}}}{2\pi} \tag{3}$$

The natural frequency of any structure is dependent on its stiffness (K) and effective modal mass (m), and the structural element's stiffness is a function of the material modulus of elasticity (E_c), section inertia (I), and the span length (L). The section inertia (I) for a solid concrete slab is equal to ($bh^3/12$), where b is the section or slab strip width, which is 1 m for slabs, and h is the effective uncracked section's depth or slab's thickness; thus, concrete tensile cracks decrease the effective slab thickness and its inertia.

When a concrete section is subjected to compressive stress, the stress-strain relationship starts linearly, having the elastic modulus (E_c) as its slope until the compressive stress roughly reaches $0.5f_c'$, where f_c' is the 28-day concrete cylinder compressive strength. Dynamic loading increases the stress rate, which in turn increases the elastic modulus, and with various research stating different values for the dynamic elastic modulus of concrete, it is recommended that the concrete dynamic elastic modulus is 20% higher than the static modulus.[1,4]

The concrete compressive stress-strain relationship tends to be nonlinear when the stress exceeds $0.5f_c'$, and nonlinear strains tend to increase at a faster rate than stresses, which in turn reduces the slope value of the elastic modulus and the stiffness of the concrete structural element, as shown in Fig. 1; this phenomenon is known as "compression softening." Most international codes[4] and other references require post-tensioned concrete structures to be uncracked in most cases under service loads, and compressive stresses not to exceed $0.5f_c'$ to avoid compression softening.

RESEARCH SIGNIFICANCE

It is interesting to note that there are controversies in the current literature regarding the effect of prestressing force on the natural frequency of concrete structures. The analysis and design of post-tensioned flat slabs are performed using finite element modeling (FEM) programs such as ADAPT-Builder,[6] RAM Concept,[7] and PLPAK.[8] The different hypotheses for the prestress effect on the frequencies of slabs are outlined in the following sections. In addition, the static deflection method is stated to present conservative values for the fundamental frequencies of concrete slabs. Further, a simple mathematical model is needed to estimate the peak vertical acceleration of the floor to achieve a suitable comfort level for occupants.

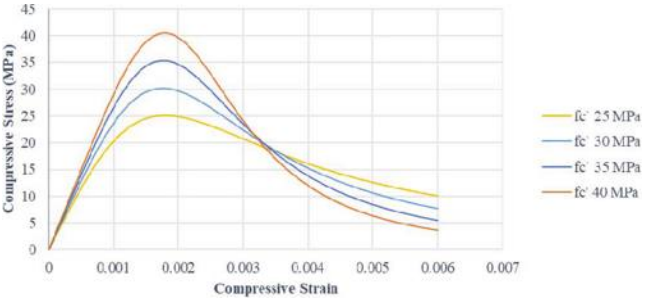

Fig. 1—General concrete compressive stress-strain plot.[5]

IMPACT OF PRESTRESS LEVEL ON FUNDAMENTAL FREQUENCY OF SLABS

Fundamental frequency is directly proportional to prestress level

Lu and Law[9] performed laboratory experimental work for a simply supported 4.0 m long prestressed concrete beam, and they concluded that the beam's fundamental frequency increased after applying prestressing force; however, the fundamental frequency increased only by 0.43%.

Jang et al.[10] carried out six laboratory tests for 8.0 m long beams with six different prestress levels. However, the bending moment induced by the beam's own weight at its midspan is enough to initiate tensile cracks at the beam's bottom fibers under no prestress, and extra loads of equipment and sensors on the beam will produce more cracks; therefore, prestressing forces reduced the tensile cracks and stiffened the beam by increasing its effective inertia. At the point where prestressing force could diminish all tensile cracks, the beam's fundamental frequency did not increase significantly by increasing the prestress level.

Noble et al.[11] studied the effect of prestressing force on the fundamental frequency of cracked concrete beams by implementing experimental tests for concrete beams with nine different eccentricities and 11 prestress levels, and it was concluded that the prestress level is directly proportional to the beam's fundamental frequencies for closing tensile cracks and increasing the section stiffness.

Fundamental frequency is inversely proportional to prestress level

Law and Lu[12] created a simulation for a prestressed concrete beam to monitor its fundamental frequency under different prestress levels, and the authors confirmed that the relationship between prestressing force and the beam's fundamental frequency is inversely proportional. However, the applied prestressing force is huge enough to cause compression softening. As a result, the beam's stiffness was

reduced for reducing the concrete elastic modulus due to compression softening.

Fundamental frequency is independent of prestress level

Noble et al.[13] used the same experimental data mentioned in their former research,[11] but for uncracked beams, to monitor the impact of the prestress level on uncracked beams' fundamental frequency through static and dynamic tests. The dynamic tests revealed that the tendon's eccentricity and the prestressing force have no impact on the fundamental frequency of uncracked concrete beams.

Goh et al.[14] examined the impact of several parameters on the fundamental frequency of prestressed concrete beams using the Structural Dynamics Toolbox (SDT) and MATLAB, and the magnitude of the prestressing force is among these parameters. Through the simulation of a simple prestressed panel with a span of 2.7 m and the application of five different prestress levels, Goh et al. confirmed that the magnitude of the prestress level has no impact on the fundamental frequency of prestressed concrete panels.

Bonopera et al.[15] applied three different prestress levels on a prestressed concrete beam where the authors confirmed no compression softening or buckling occurs, and the beam is uncracked under the applied prestress levels; thus, Bonopera et al. assured that concrete behaves linearly in compression and tension in this beam. It was found that the fundamental frequency of the beam only changed by 2%, confirming there is no significant impact of the prestress level on the concrete beam's frequency. The same conclusion was confirmed by Hamed and Frostig[16] through developing a nonlinear mathematical model to predict the impact of prestressing forces on the fundamental frequency of uncracked prestressed concrete beams where no compression softening occurs.

Fundamental frequency is directly proportional to low prestress levels and inversely proportional to high prestress levels

Breccolotti[17] studied various research in this debate on the impact of prestress level on the fundamental frequency of prestressed concrete structures. Breccolotti summed up the findings of his research that prestressing force increases the beam's fundamental frequency as it diminishes microcracks and may tend to decrease the prestressed concrete beam's fundamental frequency if it induced excessive compressive stresses on the beam for compression softening. This also concludes that prestressing force has no impact on a prestressed concrete beam's fundamental frequency if the beam is already uncracked and no compression softening occurs.

NUMERICAL MODELS FOR POST-TENSIONED CONCRETE SLABS

Finite element analysis is performed using Abaqus[18] to simulate post-tensioned concrete slabs of different geometries and applied loads. Post-tensioned concrete slabs are modeled as solid elements—also known as "rectangular hexahedral"—which is a three-dimensional (3-D) stress brick element composed of eight nodes, one at each corner, and each node has three displacement degrees of freedom (u, υ, w) in the directions of (x, y, z), respectively.

Prestressing steel tendons are modeled as "truss elements" in parabolic profiles. Truss elements—also known as "elastic rods" or "bar elements"—are modeled to represent elements supporting axial forces only.

Flat slabs of 13 different geometries are modeled in 3 x 3 bays following Fig. 2 and Table 3, where 12 slab geometries follow Khan,[19] whose experimental on-site readings for fundamental frequencies of slabs are used for verification of Abaqus FEM results.

The fundamental frequency of concrete slabs is obtained from Abaqus following these steps:

1. The second user-defined step "linear perturbation, frequency" is created to estimate the modal frequencies and modal shapes of the assembled structure, and the first modal frequency and modal shape of the whole structure is in the vertical direction, which is this research's target. This step is linked to its previous steps and reads all data defined in previous steps.

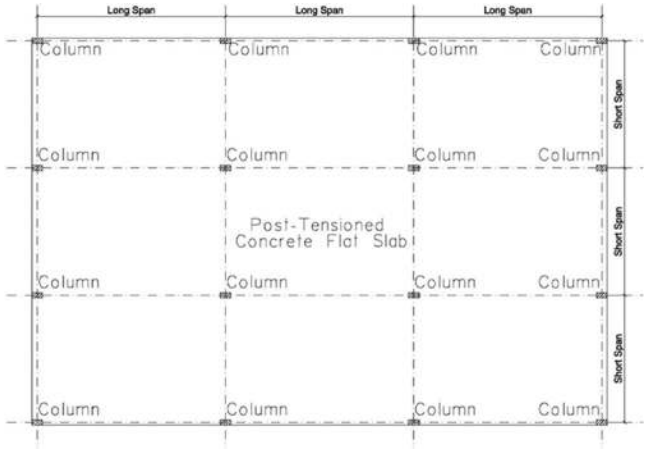

Fig. 2—Layout of 3 x 3 bay flat slab.

Table 3—Geometries of modeled post-tensioned concrete slabs, in m

Model number	Slab thickness	Slab long span	Slab short span	Column length	Column width
Model 1	0.28	10	10	0.4	0.4
Model 2	0.225	8.4	7.2	0.36	0.36
Model 3	0.225	10.7	7.2	0.6	0.3
Model 4	0.225	7.2	7.2	0.45	0.45
Model 5	0.375	8	8	0.4	0.4
Model 6	0.25	8.4	7.2	0.45	0.45
Model 7	0.25	9.55	7.2	0.4	0.4
Model 8	0.225	8	7.5	0.45	0.45
Model 9	0.35	8	7.5	0.45	0.45
Model 10	0.3	9	9	0.6	0.6
Model 11	0.3	9	7.5	0.6	0.6
Model 12	0.2	7.5	6	0.45	0.25
Model 13	0.275	9	8	0.45	0.45

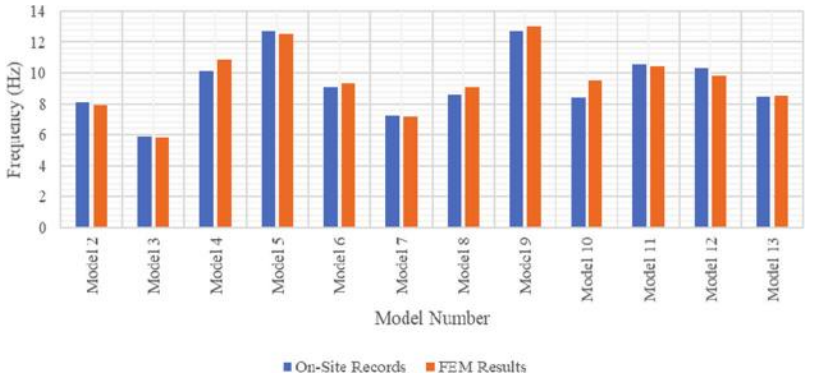

Fig. 3—Comparison between on-site and FEM results.

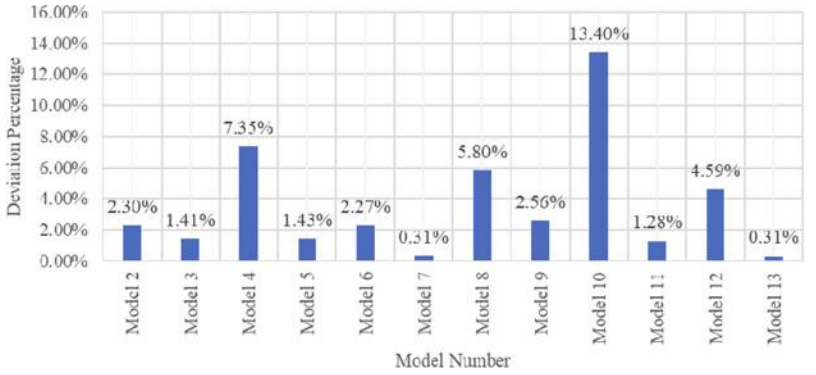

Fig. 4—Deviation percentage of FEM results for verification.

Table 4—Concrete parameters[19]

Concrete unit weight, kN/m^3	23.544	Eccentricity	0.1
Concrete dynamic elastic modulus, MPa	34.79 × 10^3	f_{bo}/f_{co}	1.16
Poisson's ratio (υ)	0.2	K	0.6667
Dilation angle	5	Viscosity parameter	0.0001

2. The calculation of the structure's modal frequencies requires the definition of the modal mass, and the modal mass is composed of the structure's own mass and the mass of external loads. The mass of the externally applied load is defined from the "engineering features" and "inertia" options, and "nonstructural mass" is selected.

3. The fundamental frequency and modal shapes can be derived from the "linear perturbation, frequency" step.

Figure 3 shows the comparison between on-site and FEM outputs, where all the results are close, except the results of Model 10 with a difference of 13.40%, as presented in Fig. 4, where the on-site slab was mentioned to have voids and be more flexible than modeled. The tendon's layouts were not mentioned in the reference,[19] so banded-banded distribution is used with 1.5 m maximum spacing and 0.5 m minimum spacing between the tendons, and each tendon is three to five strands.

Materials properties

Concrete is defined as an isotropic material with the parameters in Table 4 following Khan.[19] Linear-elastic behavior for any material requires the definition of its unit weight, elastic modulus, and Poisson's ratio, while other parameters as well

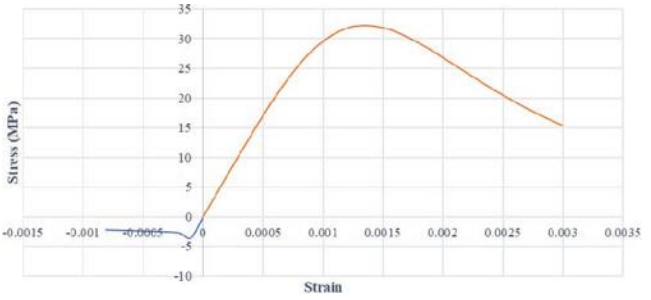

Fig. 5—Concrete stress-strain plot.[5]

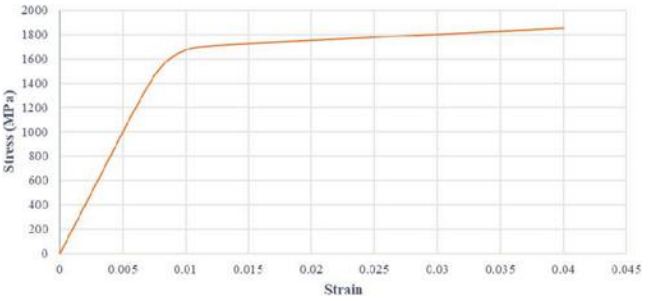

Fig. 6—Prestressing steel stress-strain plot.[5]

as compression and tension damage parameters are needed to achieve nonlinear behavior for concrete, in addition to full stress-strain curves, as shown in Fig. 5 for concrete and Fig. 6 for prestressing steel. The unit weight of prestressing steel is 76.518 kN/m^3, the elastic modulus (E_s) is 200 GPa, and Poisson's ratio (υ) is zero. The dilation angle is recommended to be five by Michał and Andrzej[20] to represent the actual behavior of concrete based on experimental tests. The

author of the cited research has used different values for dilation angle from 5 to 30, and the concrete behavior and strains were almost the same with those different values.

RESULTS

Impact of prestress on fundamental frequency of uncracked post-tensioned concrete slabs

Three different prestress levels are applied to the previously mentioned 13 flat slabs, where each strand is jacked with 1395 MPa in full prestress, between 700 and 900 MPa in moderate prestress, and zero prestress in the third level. It is shown in Fig. 7 that the fundamental frequency of uncracked post-tensioned concrete flats slabs is not influenced by the prestressing forces under the effect of the slabs' own weight only.

Table 5—Fundamental frequencies of cracked post-tensioned concrete flat slabs in Model 1, in Hz

Materials behavior	Prestress activity	Externally applied loads		
		Zero	3 kN/m^2	4.5 kN/m^2
Nonlinear	Inactive	6.127	4.807	4.274
	Active	6.214	5.077	4.675
Linear elastic	Inactive	6.265	5.187	4.820

Impact of prestress on fundamental frequency of cracked post-tensioned concrete slabs

To discuss this point, an analysis of Model 1 with applied loads of 3 and 4.5 kN/m^2 in addition to the slabs' own weight has been performed, and results are presented in Table 5.

The gap between the slab's fundamental frequencies whether with or without the prestressing force gets bigger for higher applied loads for more initiation of tensile cracks to occur. Figure 8 shows the tremendous tension damage on slab top fibers under external loads of 4.5 kN/m^2, while Fig. 9 demonstrates the impact of prestressing force in reducing concrete tension damage and minimizing tensile cracks. Thus, the slab's fundamental frequency increased by activating the prestressing force to minimize the tensile cracks, which increases the section's inertia and stiffness.

Impact of materials behavior (linear elastic and nonlinear) on section's stiffness

Most international codes require prestressed concrete structures to be uncracked under service loads, and they specify certain limits to prestress levels and compressive stresses to avoid compression softening. Therefore, concrete behaves linearly in such a range in Fig. 10, and the fundamental frequency of post-tensioned concrete flat slabs with nonlinear material properties should be equal to that

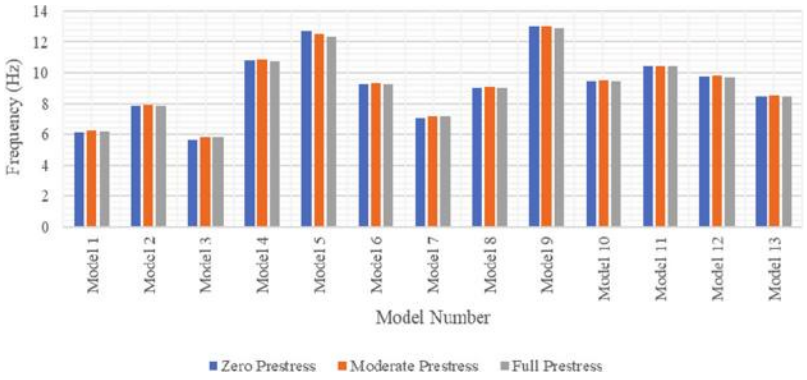

Fig. 7—Fundamental frequencies of uncracked post-tensioned concrete flat slabs.

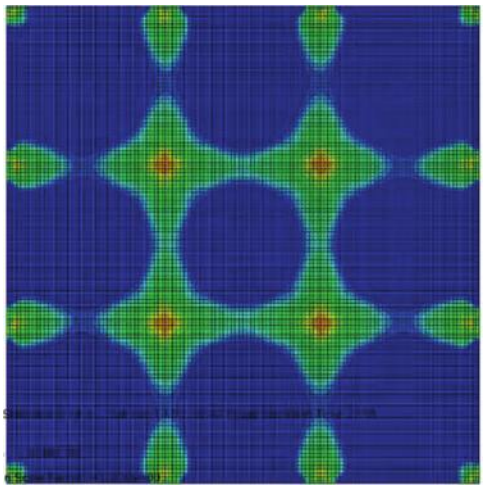

Fig. 8—Tension damage at slab top fibers with zero prestress and applied load of 4.5 kN/m^2.

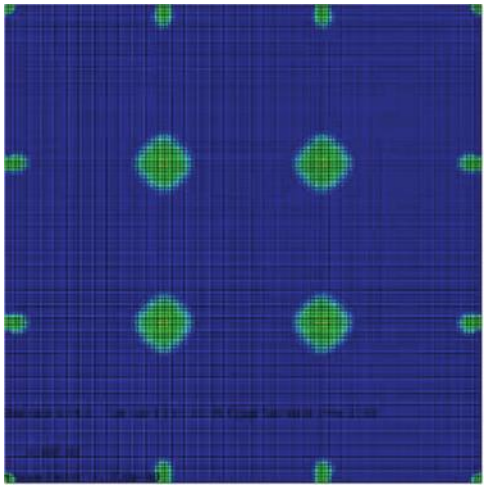

Fig. 9—Tension damage at slab top fibers with prestress and applied load of 4.5 kN/m^2.

produced from numerical models of linear-elastic material properties.

This concept is confirmed by the results shown in Fig. 11, where the fundamental frequencies of slab models of linear-elastic materials and no prestressing forces are equal to that produced from numerical analysis of uncracked slabs and nonlinear material behavior.

In addition, Fig. 12 to 14 present comparisons between fundamental frequencies of slabs with linear-elastic material behavior under differed applied loads. The results boost the idea that prestress levels have no remarkable impact on fundamental frequencies of uncracked prestressed concrete slabs, and there is no need to model the materials with their nonlinear parameters if the section is uncracked and no compression softening occurs.

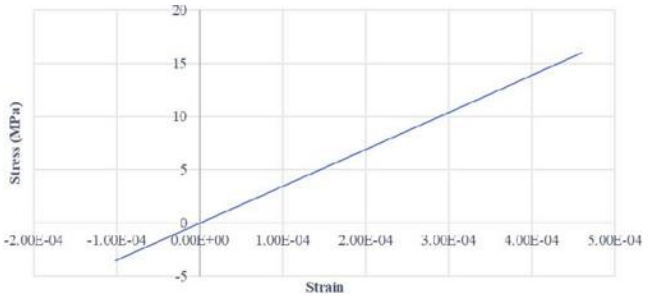

Fig. 10—Concrete compressive and tensile stress-strain linear-elastic behavior.

MATHEMATICAL MODEL OF FUNDAMENTAL FREQUENCY OF UNCRACKED CONCRETE SLABS

Proposed mathematical model

There are different available methods and mathematical models to estimate the fundamental frequency of concrete

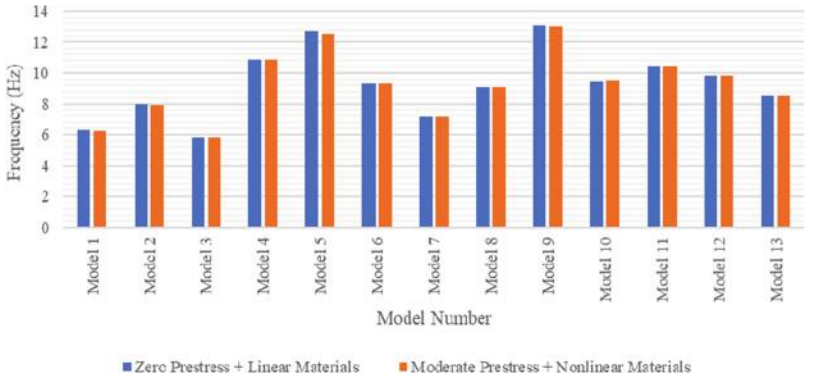

Fig. 11—Impact of prestress and material behavior on fundamental frequency of uncracked concrete slabs.

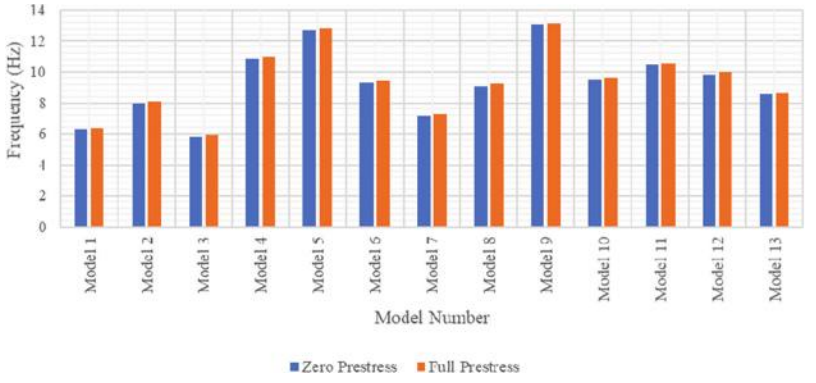

Fig. 12—Fundamental frequencies of concrete slabs with linear-elastic material behavior and no applied loads.

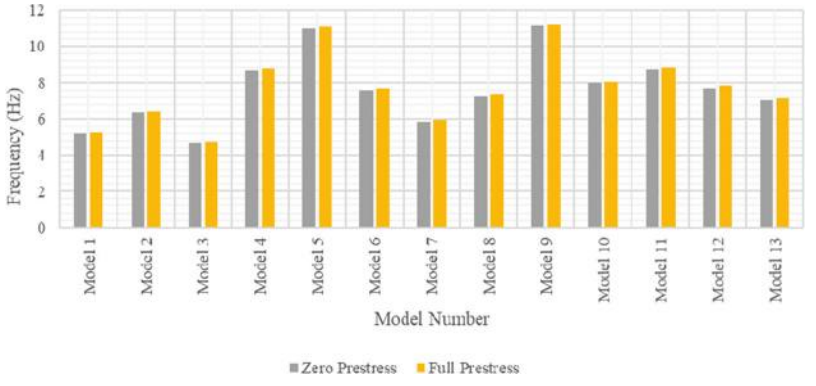

Fig. 13—Fundamental frequencies of concrete slabs with linear-elastic material behavior and 3 kN/m^2 applied load.

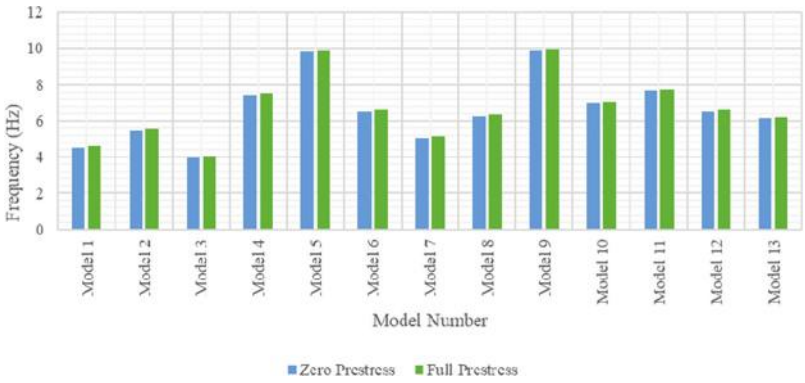

Fig. 14—Fundamental frequencies of concrete slabs with linear material behavior and applied load of 6 kN/m^2.

slabs, such as the "rectangular plate method"; however, most of these models require the slab to be rectangular and the column pattern to be regular, and these models miss the effect of some parameters such as voids, drop panels, and marginal beams. Thus, these mathematical models are not applicable to modern architectural and structural requirements. Nevertheless, the static deflection method is an equation used to estimate the fundamental frequency (f) of concrete slabs, and it can be applicable to all slab geometries as it is only dependent on the deflection (Δ) in meters due to sustained loads including own weight, permanent loads, and quasi-permanent loads without the effect of prestress following Eq. (4).

$$f = 0.18\sqrt{\frac{g}{\Delta}} \tag{4}$$

Results presented in Fig. 12 to 14 for numerical FEM analysis with linear-elastic material behavior and no prestress are used to test the accuracy of the static deflection method, where linear-elastic material behavior represents the uncracked slab, and prestress is inactive as it has no impact on the fundamental frequency. For example, Table 6 presents an evaluation of the precision of the static deflection method to predict the fundamental frequency of uncracked concrete slabs using data from Model 10.

The static deflection method does not provide an accurate estimation of fundamental frequencies of concrete slabs, and it gets much less accurate and more conservative by increasing the magnitude of total loads; therefore, it is worth trying to create a new mathematical model to estimate the fundamental frequency of post-tensioned concrete slabs with more accurate results than the static deflection method. More models are created using the previously mentioned 13 slab geometries with applied load increments of 1.5 kN/m^2 from zero to 9 kN/m^2, forming a total of 91 models, then data are exported to neural designer software[21] using artificial neural networks (ANNs) to create a new mathematical model. Iterations take place for the model's inputs, type of equations—whether linear, hyperbolic, or polynomial—number of equation layers in the mathematical model, and number of neurons per layer. Accordingly, the software analyzes the data and corresponding results, concludes a mathematical model with a set of equations that can be plotted in a graph, and presents a linear regression analysis for the mathematical model. After applying multiple iterations, the neural designer software concluded a mathematical model composed of a set of equations that can be simplified in Fig. 15 through sensitivity analysis. The inputs of this mathematical model are "sustained loads, kN/m^2" and its corresponding "deflection, mm" without considering the prestressing force camber, and the output is the "fundamental frequency of the slab, Hz".

Table 6—Evaluation of accuracy of static deflection method to predict fundamental frequency of uncracked concrete slabs using data from Model 10

Applied loads, kN/m^2	No load	3	6
FEM fundamental frequency, Hz	9.50	7.9597	6.984
Deflection, mm	3.84	7.084	10.33
Static deflection method frequency, Hz	9.10	6.70	5.55
Error %	4.22%	15.85%	20.58%

The same figure also demonstrates that the impact of the sustained load's parameter starts to decrease for higher deflection values; however, it is very influential for small and moderate values of deflection. The sensitivity of the load's parameter is shown in Fig. 15 as the relationship between deflection and the slab's fundamental frequency is not the same for different loads as assumed in the static deflection method, but it varies according to the magnitude of sustained loads. The reason behind this idea could be that a slab of a specific sustained load and deflection is stiffer than a slab of the same specific deflection but less sustained load. Figure 15 is used to determine the fundamental frequency of a concrete slab such that the maximum deformation is concluded from FEM in mm, without accounting for the prestress effect, which is the x-axis, and the total area load on the slab in kN/m^2 is a user's input, where Fig. 15 has different curves for different area loads. A vertical projection goes up from the x-axis to the curve of the area load value, then moves horizontally straight to the y-axis to get the fundamental frequency of the slab at that point.

Linear regression analysis

Linear regression analysis in Fig. 16 for the proposed model demonstrates that the average slope between the real and estimated numbers of slabs' frequencies is 99.97%, which is almost 100% with no error exceeding 10% and a mean error of 3.29%, while Fig. 17 for the static deflection method shows more scattered points with an average slope

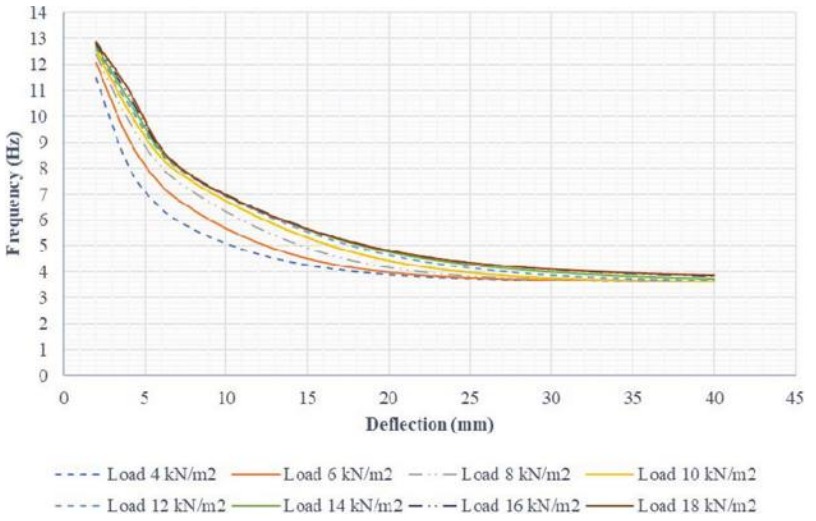

Fig. 15—Proposed model to predict fundamental frequency of uncracked concrete slabs.

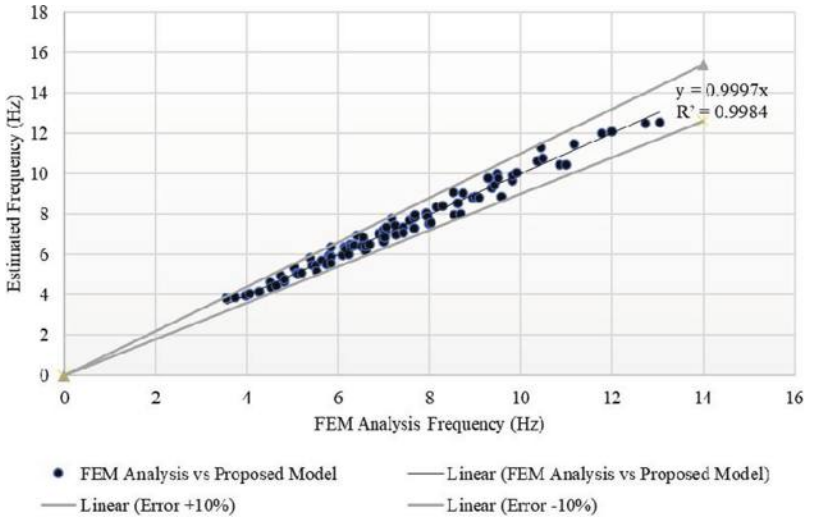

Fig. 16—Linear regression analysis for proposed mathematical model.

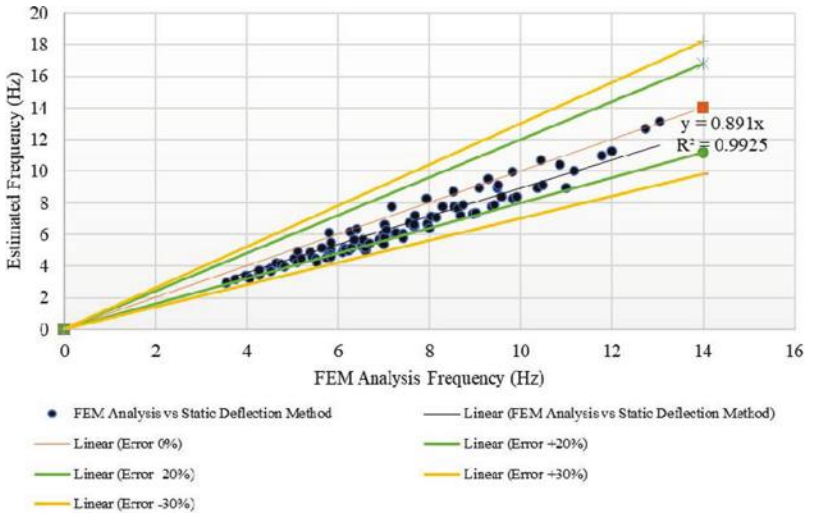

Fig. 17—Linear regression analysis for static deflection method.

between the real and estimated slabs' frequencies of 89.1% with errors exceeding 25% and a mean error of 12.99%, tending to be uneconomic.

Validity of proposed mathematical model for solid slabs

The applicability of the proposed mathematical model is tested for solid slab structural systems where all columns are

connected through marginal and internal beams with linear-elastic material behavior and slab geometries as shown in Fig. 18 and Table 7.

Applied loads of 4.5 and 9 kN/m^2 are applied for each slab, so a total of four models of solid slabs are studied, and results are presented in Fig. 19. The proposed mathematical model presents more accurate results than the static deflection method for solid slabs; however, the error percentage reached 17%, which makes the proposed model less applicable for solid slabs supported by rigid beams than for flat slabs.

Validity of proposed mathematical model for ribbed slabs

A one-way ribbed slab is modeled in Abaqus to examine the accuracy of the proposed mathematical model to estimate the fundamental frequency of post-tensioned concrete ribbed slabs, where 16 post-tensioned concrete ribs are supported by stiff edges following Fig. 20 and the properties in Table 8.

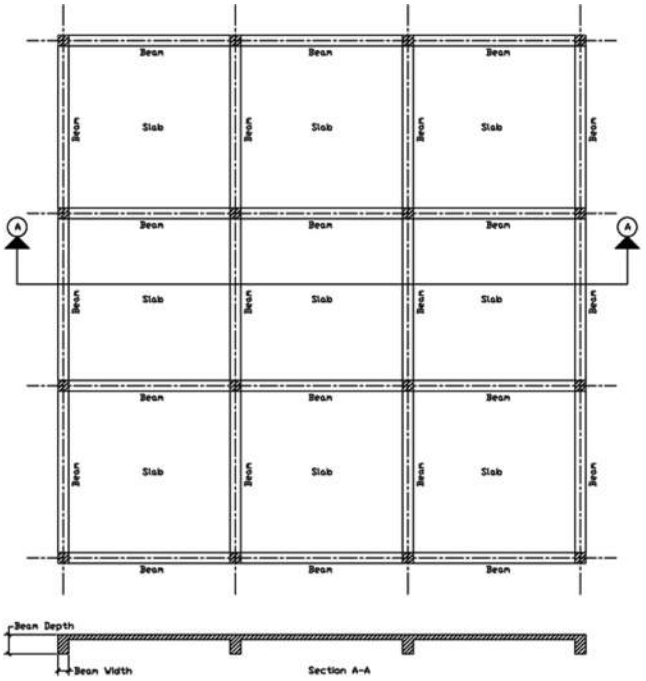

Fig. 18—Plan view and section of solid slabs.

Results presented in Table 9 confirm that the proposed mathematical model could precisely predict the fundamental frequency of uncracked post-tensioned concrete ribbed slabs, while the static deflection method produced a conservative estimation with an error of 16.51%.

Validity of proposed mathematical model for flat slabs with drop panels

The proposed mathematical model is tested for uncracked concrete flat slabs with drop panels using linear-elastic concrete behavior and slab geometry as shown in Fig. 21 and Table 10 under applied loads of 4.5 and 6 kN/m^2.

The proposed mathematical model produces an accurate estimation of fundamental frequencies of slabs with drop panels with error percentages of 1.7% for applied loads of 4.5 kN/m^2 and 3.56% for applied loads of 6 kN/m^2, while the static deflection method gives conservative and less accurate results with error percentages of 17.61% and 19.40% under applied loads of 4.5 kN/m^2 and 6 kN/m^2, respectively, as presented in Fig. 22. Thus, the proposed model is fit to estimate the fundamental frequency of uncracked concrete flat slabs with drop panels.

Impact of other parameters on frequencies of uncracked concrete slabs

To ensure that sustained loads and deflection are the only two parameters impacting the fundamental frequencies of concrete slabs, two different slabs are modeled with the different properties mentioned in Table 11.

Although all the structural and geometric parameters are different between both slabs except sustained loads and deflection, the fundamental frequencies produced from FEM analysis and the proposed model are almost the same, with an error of less than 1.65%. Therefore, there are no parameters

Table 7—Properties of modeled solid slabs

Slab properties	Solid slab (1)	Solid slab (2)
Slab thickness, m	0.225	0.16
Beam depth, m	0.8	0.7
Column dimensions, m	0.45 x 0.45	0.45 x 0.45
Beam width, m	0.45	0.45
Long span, m	7.2	7.2
Short span, m	7.2	7.2

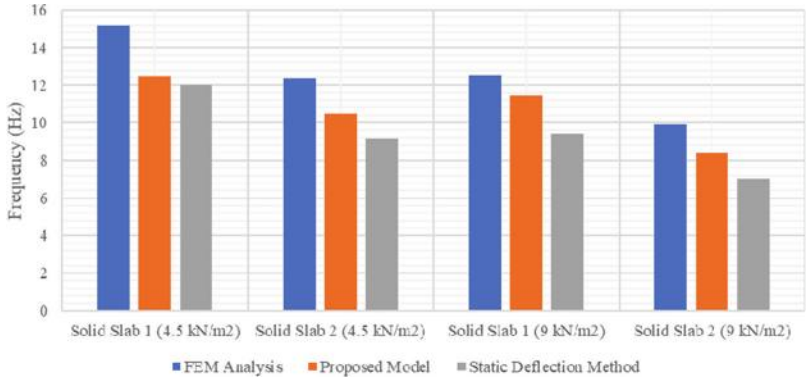

Fig. 19—Fundamental frequencies of concrete solid slabs using different methods.

Table 8—Properties of post-tensioned concrete ribbed slab

Concrete dynamic elastic modulus, MPa	29.1×10^3	Concrete Poisson's ratio	0.2
		Concrete unit weight, kN/m^3	23.544
Concrete compressive strength, MPa	35	Concrete tensile modulus of rupture, MPa	3.7
Reinforcing bar yield strength, MPa	420	Strand yield strength, MPa	1674
Ribs CL-CL span, m	15.7	Ribs CL-CL spacing, m	1
Rib width, m	0.35	Rib depth, m	0.6
Slab thickness, m	0.1	Slab mesh reinforcing bar	T10@300 mm
Rib top reinforcing bar	3T12	Beam bottom reinforcing bar	3T12
Strand area, mm^2	98	Number of strands per rib	8
Tendon profile	Parabolic	Jacking stress, MPa	1395
Stirrups at first and last third of ribs	T10@150 mm	Stirrups at middle-third of ribs	T10@200 mm
Dead loads, kN/m^2	2	Live loads, kN/m^2	2

Table 9—Fundamental frequency of linear-elastic concrete ribbed slab

		FEM results	Proposed model		Static deflection method	
Deflection, mm	Sustained load, kN/m^2	Frequency, Hz	Frequency, Hz	Error %	Frequency, Hz	Error %
13.52	10.81	5.8077	5.8073	0.01%	4.85	16.51%

Table 10—Properties of flat slab with drop panels

Slab thickness, m	0.25
Drop panel thickness, m	0.4
Column dimensions, m	0.4 x 0.4
Long span, m	10
Short span, m	10
Interior drop panels, m	3.5 x 3.5
Edge drop panels, m	3.5 x 2.0
Corner drop panels, m	2.0 x 2.0

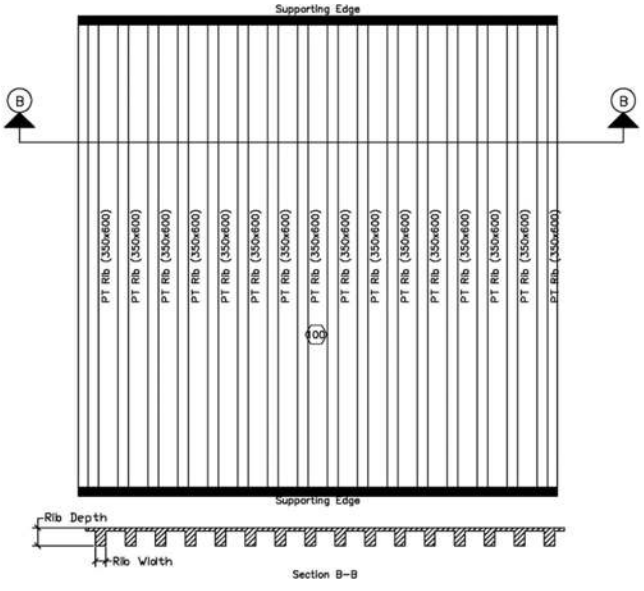

Fig. 20—Plan view and section of post-tensioned concrete ribbed slab.

other than sustained loads and deflection influencing the fundamental frequency of uncracked post-tensioned concrete slabs of different structural systems.

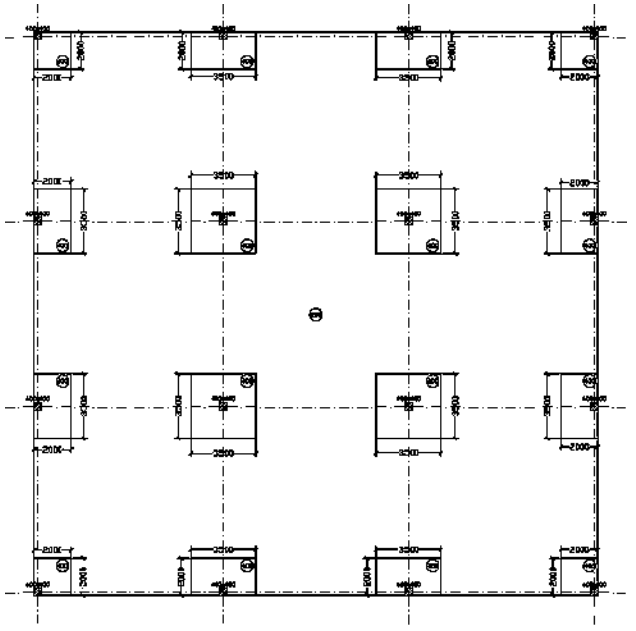

Fig. 21—Layout of flat slab with drop panels.

MATHEMATICAL MODEL OF PEAK VERTICAL ACCELERATION OF UNCRACKED CONCRETE SLABS

Slab peak acceleration is an important parameter to be explored to assess the behavior of the slab under dynamic motion and to achieve the desired comfort level for the floor's users. Dynamic loads are assigned to different slab geometries from Table 3 with a forcing frequency of 2 Hz to represent human walking[3] and a conservative damping ratio of 2%.[2] The dynamic motion follows a sinusoidal wave pattern as per Fig. 23, and it starts with an initial displacement equal to the maximum deflection/camber of the slab due to sustained static loads, dynamic loads, and the prestressing force.

Values of peak acceleration under different parameters are presented in Table 12, and these data are inserted in neural network software to create a mathematical model to predict the peak acceleration of concrete slabs. Slabs are assumed to behave linearly elastic in both tension and compression.

The neural designer software concluded a mathematical model where the inputs are "fundamental frequency, Hz" of the concrete slab and "initial displacement, mm" due to service loads including the prestressing force camber, while the output is "acceleration per dynamic load of 1 kN/m^2, m/s^2." The proposed mathematical model to predict the peak vertical acceleration is presented in Fig. 24, and its linear regression analysis is shown in Fig. 25. Figure 24 is used to determine the peak vertical acceleration of a concrete slab such that the maximum deformation is concluded from FEM in mm, considering the prestress effect, which is the x-axis, and the fundamental frequency of the concrete slab at that point is also concluded from the proposed model in Fig. 15,

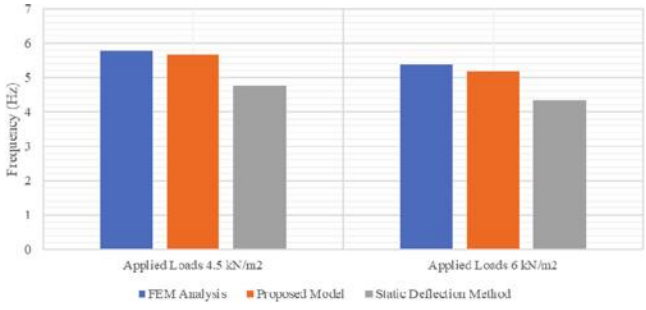

Fig. 22—Fundamental frequencies of flat slabs with drop panels using different methods.

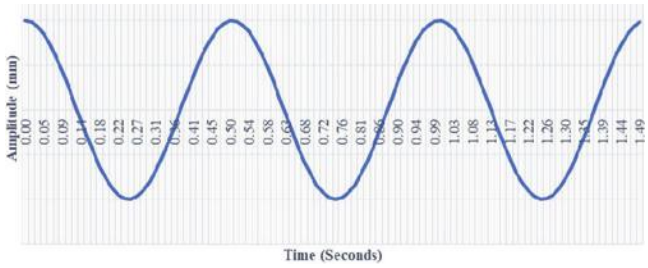

Fig. 23—Sinusoidal wave of dynamic load motion of frequency of 2 Hz.

where Fig. 24 has different curves for different frequencies. A vertical projection goes up from the x-axis to the curve of the fundamental frequency value curve, then moves horizontally straight to the y-axis to get the peak vertical acceleration per unit of dynamic load (1 kN/m^2) at that point.

CONCLUSIONS

According to the investigation of the vibration behavior of post-tensioned concrete slabs, it is concluded that the prestress level does not influence the fundamental frequency of uncracked concrete slabs if the prestress level is not high enough to cause compression softening. However, for cracked post-tensioned concrete slabs, the prestressing force increases the inertia and the fundamental frequency of the slab by closing all tensile cracks until these cracks diminish on the condition that no compression softening occurs. If the prestress level is high and compression softening occurs, which is unlikely to happen as per design codes, the concrete elastic modulus and the fundamental frequency of the slab decrease. Moreover, prestressing steel behaves linearly if the jacking stress does not exceed the yield stress, and concrete

Table 11—Properties of concrete slabs with different parameters

Slab structural system	Flat slab	Flat slab with drop panels
Concrete dynamic elastic modulus, MPa	34.79 × 10^3	43 × 10^3
Slab thickness, m	0.2	0.25
Drop panel thickness, m	Not applied	0.4
Drop panel dimensions, m	Not applied	Table 10
Long span, m	7.5	10
Short span, m	6	10
Column length, m	0.45	0.4
Column width, m	0.25	0.4
External applied loads, kN/m^2	6	4.5
Sustained loads, kN/m^2	10.7088	10.8484
Deflection, mm	11.38	11.37
FEM frequency, Hz	6.5025	6.4298
Proposed model frequency, Hz	6.3968	6.4146
Error %	1.63%	0.24%

Table 12—Peak vertical acceleration of different slab geometries for dynamic motion of frequency of 2 Hz

Model number	Prestress activity	Total applied load, kN/m^2	Dynamic load, kN/m^2	Initial displacement, mm	Fundamental frequency, Hz	Acceleration, m/s^2
Model 1	Inactive	1.5	1.5	12.05	5.65	0.31
Model 1	Inactive	3	3	15.82	5.19	0.63
Model 1	Inactive	4.5	1.5	19.59	4.82	0.32
Model 1	Inactive	6	3	23.37	4.52	0.55
Model 1	Inactive	6	6	23.37	4.52	1.09
Model 1	Inactive	7.5	1.5	27.15	4.27	0.27
Model 1	Inactive	9	3	30.93	4.06	0.72
Model 1	Inactive	9	6	30.93	4.06	1.43

Table 12 (cont.)—Peak vertical acceleration of different slab geometries for dynamic motion of frequency of 2 Hz

Model 1	Active	1.5	1.5	5.09	5.74	0.10
Model 1	Active	3	3	8.76	5.26	0.30
Model 1	Active	4.5	1.5	12.45	4.89	0.24
Model 1	Active	6	3	16.14	4.59	0.49
Model 1	Active	6	6	16.14	4.59	0.97
Model 1	Active	7.5	1.5	19.84	4.33	0.27
Model 1	Active	9	3	23.54	4.12	0.64
Model 1	Active	9	6	23.54	4.12	1.27
Model 2	Inactive	3	3	9.89	6.34	0.61
Model 2	Inactive	4.5	4.5	12.52	5.84	0.75
Model 2	Inactive	6	3	15.14	5.43	0.47
Model 2	Inactive	6	6	15.14	5.43	0.94
Model 2	Inactive	7.5	4.5	17.77	5.10	1.06
Model 2	Inactive	9	3	20.40	4.83	0.65
Model 2	Inactive	9	6	20.40	4.83	1.29
Model 2	Active	3	3	4.63	6.46	0.27
Model 2	Active	4.5	4.5	7.17	5.94	0.55
Model 2	Active	6	3	9.74	5.53	0.43
Model 2	Active	6	6	9.74	5.53	0.87
Model 2	Active	7.5	4.5	12.30	5.19	0.62
Model 2	Active	9	3	14.87	4.91	0.53
Model 2	Active	9	6	14.87	4.91	1.06
Model 6	Inactive	3	3	7.03	7.56	0.41
Model 6	Inactive	6	3	10.58	6.54	0.44
Model 6	Inactive	6	6	10.58	6.54	0.87
Model 6	Inactive	7.5	7.5	12.35	6.16	0.84
Model 6	Inactive	9	3	14.13	5.84	0.50
Model 6	Inactive	9	6	14.13	5.84	0.99
Model 6	Active	3	3	2.84	7.66	0.15
Model 6	Active	6	3	6.16	6.62	0.19
Model 6	Active	6	6	6.16	6.62	0.38
Model 6	Active	7.5	7.5	7.90	6.24	0.74
Model 6	Active	9	3	9.65	5.91	0.31
Model 6	Active	9	6	9.65	5.91	0.62
Model 11	Inactive	3	3	5.14	8.74	0.24
Model 11	Inactive	6	3	7.50	7.66	0.27
Model 11	Inactive	6	6	7.50	7.66	0.54
Model 11	Inactive	9	3	9.87	6.91	0.27
Model 11	Inactive	9	6	9.87	6.91	0.54
Model 11	Active	3	3	2.00	8.81	0.09
Model 11	Active	6	3	4.15	7.72	0.14
Model 11	Active	6	6	4.15	7.72	0.28
Model 11	Active	9	3	6.49	6.96	0.19
Model 11	Active	9	6	6.49	6.96	0.37

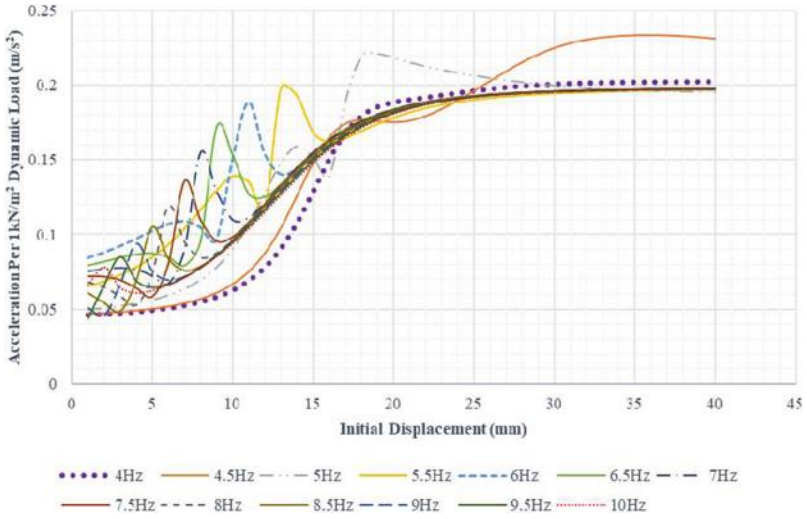

Fig. 24—Proposed mathematical model to estimate peak vertical acceleration of uncracked concrete slabs under dynamic motion of forcing frequency of 2 Hz.

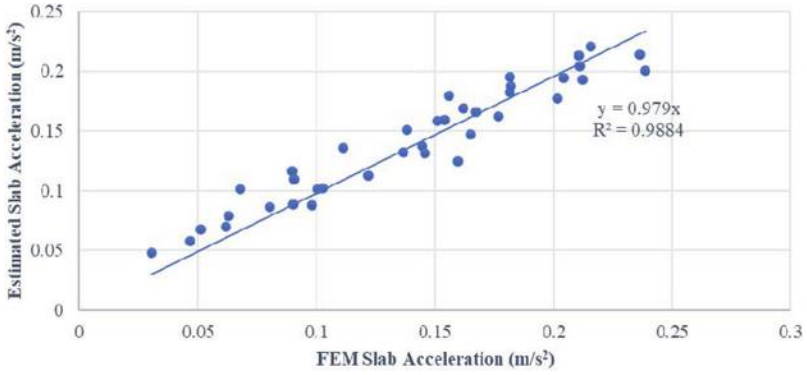

Fig. 25—Linear regression analysis for proposed mathematical model to estimate peak acceleration of uncracked concrete slabs for dynamic motion of forcing frequency of 2 Hz.

behaves linearly if compressive stresses do not exceed $0.5f_c'$ in the uncracked concrete section.

It is also concluded that the static deflection method presents conservative results for the fundamental frequencies of slabs, and the proposed mathematical model in Fig. 15 presents more accurate values for the fundamental frequency of uncracked concrete slabs of different structural systems. Further, no parameters other than sustained loads and deflection have an impact on the fundamental frequency of uncracked post-tensioned concrete slabs.

In addition, the newly proposed mathematical model in Fig. 24 is used to estimate the peak vertical acceleration value for uncracked concrete slabs under a dynamic area load of a forcing frequency of 2 Hz. The prestressing forces reduce the initial displacement of concrete slabs due to service loads, which in turn reduces the peak acceleration of slabs and achieves a better comfort level for the floor's occupants.

AUTHOR BIOS

Fady Ibrahim Ezzat Aziz *is an MSc Candidate in structural engineering at Ain Shams University, Cairo, Egypt. He received his BS from The American University in Cairo, Cairo, Egypt, in 2017.*

Amr Abdelrahman *is Chairman of the Structural Engineering Department and Professor of Concrete Structures at Ain Shams University. He received his BS and MS from Ain Shams University in 1986 and 1989, respectively, and his PhD from the University of Manitoba, Winnipeg, MB, Canada, in 1995. His research interests include reinforced and prestressed concrete structures.*

Ezzeldin Yazeed Sayed-Ahmed *is a Professor and Chairman of the Department of Construction Engineering at The American University in Cairo. He received his BSc and MSc from Ain Shams University in 1986 and 1990, respectively, and his PhD from the University of Calgary, Calgary, AB, Canada, in 1995. His research interests include the design and analysis of steel, reinforced concrete, and prestressed concrete structures as well as the vibration of lightweight bridges.*

ACKNOWLEDGMENTS

From the lead author to his father, Dr. Ibrahim Ezzat Aziz: Thank you for your continuous support to the whole family and your support to me since my first day at school. Thank you for your persistence to provide us with the best-quality environment to study and work, and this thesis is a result of all your efforts in raising me since I was born. I always hope to make you proud.

REFERENCES

1. CPCI, *CPCI Design Manual: Precast and Prestressed Concrete*, fourth edition, Canadian Precast/Prestressed Concrete Institute, Ottawa, ON, Canada, 2007, 546 pp.

2. PCI, *PCI Design Handbook*, seventh edition, Precast/Prestressed Concrete Institute, Chicago, IL, 2010.

3. Bachmann, H.; Ammann, W. J.; Deischl, F.; Eisenmann, J.; Floegl, I.; Hirsch, G. H.; Klein, G. K.; Lande, G. J.; Mahrenholtz, O.; Natke, H. G.; Nussbaumer, H.; Pretlove, A. J.; Rainer, J. H.; Saemann, E.-U.; and Steinbeisser, L., *Vibration Problems in Structures: Practical Guidelines*, Birkhäuser Verlag GmbH, Basel, Switzerland, 1995.

4. ACI Committee 318, "Building Code Requirements for Structural Concrete (ACI 318-19) and Commentary (ACI 318R-19) (Reapproved 2022)," American Concrete Institute, Farmington Hills, MI, 2019, 624 pp.

5. Collins, M. P., and Mitchell, D., *Prestressed Concrete Structures*, Response Publications, Canada, 1997.

6. RISA, "ADAPT-Builder: Fully Integrated Design for Concrete Buildings," v22.0.1, RISA Tech, Inc., Foothill Ranch, CA, 2022, https://risa.com/products/adapt-builder. (last accessed June 15, 2023)

7. Bentley Systems, "RAM Concept: Concrete Slab Design Software," Bentley Systems, Incorporated, Exton, PA, 2022, https://www.bentley.com/software/ram-concept/. (last accessed June 15, 2023)

8. Rashed, Y. F., "Boundary Element Analysis of Post-tensioned Slabs," *International Journal of Advanced Structural Engineering*, V. 7, No. 2, June 2015, pp. 143-158. doi: 10.1007/s40091-015-0088-3

9. Lu, Z. R., and Law, S. S., "Identification of Prestress Force from Measured Structural Responses," *Mechanical Systems and Signal Processing*, V. 20, No. 8, Nov. 2006, pp. 2186-2199. doi: 10.1016/j.ymssp.2005.09.001

10. Jang, J.-B.; Lee, H.-P.; Hwang, K.-M.; and Song, Y.-C., "A Sensitivity Analysis of the Key Parameters for the Prediction of the Prestress Force on Bonded Forces," *Nuclear Engineering and Technology*, V. 42, No. 3, June 2010, pp. 319-328. doi: 10.5516/NET.2010.42.3.319

11. Noble, D.; Nogal, M.; O'Connor, A. J.; and Pakrashi, V., "The Effect of Post-Tensioning Force Magnitude and Eccentricity on the Natural Bending Frequency of Cracked Post-Tensioned Concrete Beams," *Journal of Physics: Conference Series*, V. 628, Article No. 012047, 2015.

12. Law, S., and Lu, Z., "Time Domain Responses of a Prestressed Beam and Prestress Identification," *Journal of Sound and Vibration*, V. 288, No. 4-5, 2005, pp. 1011-1025. doi: 10.1016/j.jsv.2005.01.045

13. Noble, D.; Nogal, M.; O'Connor, A.; and Pakrashi, V., "The Effect of Prestress Force Magnitude and Eccentricity on the Natural Bending Frequencies of Uncracked Prestressed Concrete Beams," *Journal of Sound and Vibration*, V. 365, Mar. 2016, pp. 22-44. doi: 10.1016/j.jsv.2015.11.047

14. Goh, L. D.; Rahman, A. A.; Bakhary, N.; and Ahmad, B. H., "Factors Influencing Natural Frequencies in a Prestressed Concrete Panel for Damage Detection," *Jurnal Teknologi*, V. 69, No. 3, 2014, pp. 51-57. doi: 10.11113/jt.v69.3143

15. Bonopera, M.; Chang, K. C.; Chen, C. C.; Sung, Y. C.; and Tullini, N., "Experimental Study on the Fundamental Frequency of Prestressed Concrete Bridge Beams with Parabolic Unbonded Tendons," *Journal of Sound and Vibration*, V. 455, Sept. 2019, pp. 150-160. doi: 10.1016/j.jsv.2019.04.038

16. Hamed, E., and Frostig, Y., "Natural Frequencies of Bonded and Unbonded Prestressed Beams–Prestress Force Effects," *Journal of Sound and Vibration*, V. 295, No. 1-2, Aug. 2006, pp. 28-39. doi: 10.1016/j.jsv.2005.11.032

17. Breccolotti, M., "On the Evaluation of Prestress Loss in PRC Beams by Means of Dynamic Techniques," *International Journal of Concrete Structures and Materials*, V. 12, No. 1, 2018, Article No. 1. doi: 10.1186/s40069-018-0237-8

18. SIMULIA, "Abaqus: Finite Element Analysis for Mechanical Engineering and Civil Engineering," Dassault Systèmes, Vélizy-Villacoublay, France, 2022, https://www.3ds.com/products-services/simulia/products/abaqus/. (last accessed June 15, 2023)

19. Khan, A. Z., "Frequency Estimation of Pre-stressed and Composite Floors," PhD dissertation, City, University of London, London, UK, 1996, 204 pp.

20. Michał, S., and Andrzej, W., "Calibration of the CDP Model Parameters in Abaqus," *The 2015 World Congress on Advances in Structural Engineering and Mechanics (ASEM15)*, Incheon, South Korea, 2015, 11 pp.

21. Artelnics, "Neural Designer," Artificial Intelligence Techniques, Ltd., Salamanca, Castile and León, Spain, 2022, Neuraldesigner.com. (last accessed June 15, 2023)

ACI STRUCTURAL JOURNAL TECHNICAL PAPER

Title No. 120-S63

Design and Testing of Lightweight Self-Consolidating Concrete Bridge-Deck Slabs Reinforced with Glass Fiber-Reinforced Polymer Bars

by M. Aflakisamani, S. Mousa, H. M. Mohamed, E. A. Ahmed, and B. Benmokrane

Advances in new lightweight self-consolidating concrete (LWSCC) mixture designs have led to the construction of new concrete structures with much lower weight and higher strengths. The integration of glass fiber-reinforced polymer (GFRP) bars with LWSCC can be used effectively in Accelerated Bridge Construction (ABC) with longer spans and less shipping cost to build durable bridges with smaller cross sections and extended service lives. This study aimed at evaluating the effectiveness of this type of concrete for building concrete bridge-deck slabs with GFRP reinforcement. Five full-scale edge-restrained concrete bridge-deck slabs were fabricated, simulating a slab-on-girder bridge deck commonly used in North America. The bridge-deck slabs were 3000 mm (118.1 in.) in length, 2500 mm (98.4 in.) in width, and 200 mm (7.9 in.) in thickness. The test parameters included reinforcement type (sand-coated or helically wrapped GFRP and steel) and reinforcement ratio (ranging from 0.44 to 1.15%). The bridge-deck slabs were designed according to the Canadian Highway Bridge Design Code. The specimens were exposed to a concentrated load over a contact area of 250 x 600 mm (9.8 x 23.6 in.), which simulates the footprint of a sustained truck wheel load (87.5 kN CL-625 truck), as specified in Canadian standards. The test results indicate that the failure mode of all deck slabs was punching shear. The recorded ultimate load capacities for all specimens exceeded the design factored load, which validates the use of GFRP-reinforced LWSCC for the construction of bridge-deck slabs. It was also concluded that the surface conditions of the GFRP bars (sand coated or helically wrapped) had a minor effect on the cracking, deflection, and behavior of the tested LWSCC deck slabs. In addition, increasing the axial-reinforcement stiffness in the GFRP-reinforced slabs significantly increased the ultimate capacity and reduced maximum crack width, reinforcement strains, and midspan deflection at ultimate load.

Keywords: bridge-deck slab; cracking patterns and strains; design codes; glass fiber-reinforced polymer (GFRP) reinforcing bars; lightweight self-consolidating concrete (LWSCC); load-deflection; punching shear; ultimate capacity; wheel load.

INTRODUCTION

Concrete made with lightweight (LW) aggregates can have many significant applications, including the construction of bridge elements. This type of concrete reduces structure mass, consequently reducing the cross section and the reinforcement used in concrete structures. The weight of long-span bridges is considerably more than imposed traffic loads, so that minimizing the structure's dead load becomes an essential design parameter. Replacing normal aggregates with LW aggregates reduces the weight of the concrete by 25 to 35% while maintaining structural capacity (Harmon 2007).

Concrete bridge-deck slabs are more likely to deteriorate than any other bridge element because they experience harsh environmental conditions, including the routine use of deicing salts as well as traffic loads, freezing-and-thawing cycles, and wetting-and-drying cycles, all of which corrode steel reinforcing bars (Benmokrane et al. 2021a; Gooranorimi et al. 2019; Elgabbas et al. 2016; Arafa et al. 2016). As steel reinforcement corrodes when exposed to chlorides and deicing chemicals, fiber-reinforced polymer (FRP) bars are increasingly used in the construction industry, particularly for marine structures, concrete bridge-deck slabs, and parking garages (Benmokrane et al. 2021a; ACI Committee 440 2015; Benmokrane et al. 2007). FRP bars have many advantages compared to steel, such as high tensile strength and light weight (Mehany et al. 2021; Benmokrane et al. 2021b; Gooranorimi et al. 2019; Mousa et al. 2018; ACI Committee 440 2015). Besides, FRP bars help reduce the cost of maintenance, repair, and rehabilitation because of their noncorrodible nature (Benmokrane et al. 2021a). Using lightweight concrete (LWC) reinforced with FRP bars would be an effective solution to improve the strength-to-weight ratio and reduce the lifetime cost of the bridge-deck slabs (Billington et al. 2020). In addition, the use of LWC reinforced with FRP bars in Accelerated Bridge Construction (ABC) can minimize traffic disruptions, improve work-zone safety, minimize environmental impacts, improve constructability, enhance quality, and lower life-cycle costs (Youssef et al. 2019).

Limited experimental programs have been conducted to evaluate the behavior of GFRP-reinforced LWC members (ACI Committee 440 2015). Comparing the results of the shear behavior of one-way glass FRP (GFRP)-reinforced LWC slabs with the ACI 440.1R-06 (ACI Committee 440 2006) design provisions showed that these predictions are less conservative for LW concrete than for normalweight (NW) concrete (Pantelides et al. 2012a,b). Their experimental results, however, showed that the GFRP-reinforced LW panels behaved similar to the NW concrete (NWC)

ACI Structural Journal, V. 120, No. 4, July 2023.

MS No. S-2021-442.R1, doi: 10.14359/51738717, received May 12, 2022, and reviewed under Institute publication policies.

panels (Pantelides et al. 2012b). Canadian (CAN/CSA S806-02 2002) and Japanese (JSCE 1997) standards provide predictions of the shear strength of LW and NW concrete panels reinforced with GFRP bars with a lower degree of conservativism. Consequently, a reduction factor was determined to be unnecessary (Liu and Pantelides 2013). The "AASHTO LRFD Bridge Design Guide Specifications for GFRP-Reinforced Concrete" (AASHTO 2018) has no provisions for the use of LWC reinforced with GFRP bars because of the lack of experimental studies. This guide's specifications allow the use of LWC to improve the predicted values based on the experimental results obtained from tested LWC slabs reinforced with GFRP bars.

The results from past studies on FRP-reinforced bridge-deck slabs indicate that punching shear was the failure mode of the tested bridge-deck slabs (El-Gamal et al. 2005). They also show that reinforcement type (GFRP, carbon FRP [CFRP], and steel) had a negligible effect on the deflection behavior of these deck slabs (Ahmad et al. 1994; El-Gamal et al. 2005, 2007). Moreover, FRP reinforcement can improve the cracking performance of and induced strains in FRP-reinforced concrete (RC) slabs by enhancing the bond between the concrete and reinforcing bars (Hussein and El-Salakawy 2018; Elgabbas et al. 2016).

Laboratory tests on lightweight concrete panels

Pantelides et al. (2012a) implemented an experimental study focusing on the shear strength of GFRP-reinforced LWC panels. The specimens were subjected to a load simulating the wheel-load area of the AASHTO (2009) design truck with simply supported edges and center-to-center spacing of 2440 mm (96 in.). The results show that the LWC specimens obtained 80% of the ultimate shear strength of the NWC specimens and 89% of their maximum deflection. A reduction factor of 0.85 was proposed to modify the ACI 440.1R-06 shear equations for GFRP-reinforced LWC.

Liu and Pantelides (2013) extended the study mentioned previously by testing 12 LWC and eight NWC panels. All specimens were reinforced with GFRP bars and all obtained 1.3 times the predicted ultimate shear capacity provided by the ACI 440.1R-06 equation. In contrast, the Canadian (CAN/CSA S806-02) and Japanese (JSCE 1997) standards predicted the shear capacity of GFRP-reinforced NWC and LWC panels with similar degrees of conservatism that were less than that calculated according to ACI 440.1R-06 guidelines. Hence, a reduction factor of 0.8 was proposed to calculate the shear capacity of GFRP-reinforced LWC panels defined in ACI 440.1R-06 to acquire a similar degree of conservatism to that of NWC panels.

Experimental projects of FRP-reinforced bridge-deck slabs

Elgabbas et al. (2016) experimentally investigated the behavior of edge-restrained concrete bridge-deck slabs reinforced with basalt FRP (BFRP) bars. Seven full-scale slabs were tested under a concentrated load over a contact area of 250 x 600 mm (9.8 x 23.6 in.), simulating the footprint of a sustained truck wheel load (87.5 kN CL-625 truck). The results show that ACI 440.1R-15 (ACI Committee 2015) produced conservative predictions in terms of the punching-shear strength of BFRP-RC bridge-deck slabs, while CSA S806-12 (2017) yielded predictions with a lower degree of conservatism. Moreover, the reinforcement ratio of the bottom assembly in the transverse direction was recognized as the main parameter affecting the structural behavior (deflection, strains, and crack width). It is worth mentioning that El-Gamal et al. (2005) used a similar test procedure and specimen dimensions but with different reinforcing bars (GFRP and CFRP bars). In their study, punching shear was the failure mode for all the tested specimens. The recorded ultimate load capacities were more than three times the design factored load specified in CAN/CSA S6-10 (2010). Generally similar results were obtained from the investigation conducted by Bouguerra et al. (2011).

Table 1—Mixture proportions for LWSCC

Cement, kg/m^3	543
w/*c*	0.33
Lightweight coarse aggregate, kg/m^3	369
Lightweight sand, kg/m^3	488
Natural sand, kg/m^3	381
Air entrainment, mL/100 kg	70
High-range water-reducing admixture, L/m^3	3.51

RESEARCH SIGNIFICANCE

No research has yet been reported on the behavior of lightweight self-consolidating concrete (LWSCC) bridge-deck slabs reinforced with FRP bars. This study experimentally investigated the punching-shear behavior of a series of full-scale LWSCC bridge-deck slabs reinforced with different types of GFRP bars subjected to a concentrated load, simulating a truck wheel load. The experimental results were used to evaluate the FRP punching-shear design provisions in CSA S806-12 (R2017), ACI 440.1R-15, and AASHTO (2018). It also establishes a step toward developing design provisions and recommendations for engineers in designing LWSCC bridge-deck slabs with GFRP reinforcement. Moreover, the findings of this pioneering study will support the work of North American technical committees engaged in developing standards and design provisions for GFRP-RC deck slabs made with LWSCC.

EXPERIMENTAL PROGRAM

Material properties

Concrete—LWSCC was used in this study (refer to Table 1 for the mixture design). The mixture was made with LW coarse and fine aggregates according to the specifications in ASTM C330/C330M (2017) and natural NW sand. The coarse and fine aggregates had a maximum size of 14 and 5 mm (0.55 and 0.2 in.), respectively. The LW aggregates were expanded shale, as shown in Fig. 1(a). As the water-cement ratio (*w*/*c*) of 0.33 was chosen, the aggregates were submerged in water before mixing to maintain the desired ratio by saturation. The LWSCC was prepared using a cement containing 75% general-use (GU) cement, 20% fly ash (FA), and 5% silica fume (SF) complying with

Fig. 1—(a) Lightweight aggregates; and (b) GFRP reinforcing bars.

Table 2—Mechanical properties of reinforcing bars

Reinforcement type	Bar type	Bar size	d_b, mm	A_f^*, mm^2	E_f, GPa	f_{fu}, MPa	ε_{fu}, %	Surface configuration
GFRP	Type I	No. 5	15.9	199	61.8	1316	2.13	Sand-coated
	Type II	No. 5	15.9	199	64.1	1528	2.4	Helically wrapped
Steel†	—	M15	16	200	200	$f_y^\ddagger$ = 460	$\varepsilon_f^\ddagger$ = 0.23	Ribbed

*Nominal cross-sectional area.

†Manufacturer-provided tensile properties of steel bars.

‡f_y and ε_y are yield strength and strain of steel bars, respectively.

Note: Properties calculated based on nominal cross-sectional area; 1 mm = 0.0394 in.; 1 mm^2 = 0.00155 in.^{2}; 1 MPa = 0.145 ksi.

ASTM C150/C150M (2018). The equilibrium density of the LWSCC was 1906 kg/m^3 (119 lb/ft^3) as measured according to ASTM C567/C567M (2019). The LWSCC was designed with a target 28-day compressive strength of 40 MPa (5.8 ksi). The curing process was started after casting by covering specimens with polyethylene sheets. The slabs were unmolded 1 day after casting, and the water-curing process was performed for 7 days.

Reinforcing bars—The GFRP bars used in this study were Type I (No. 5) and Type II (No. 5). Type I bars had a sand-coated surface, while Type II bars had a helically wrapped surface, as shown in Fig. 1(b). The GFRP bars were made with vinyl ester resin and E-glass corrosion-resistant (E-CR) glass fibers, classified as Grade III according to CSA S807:19 (2019). The tensile strength and the modulus of elasticity of the GFRP reinforcement were determined according to ASTM D7205/D7205M (2016). Deformed steel bars (15M) were used in the control specimen. Table 2 presents the mechanical properties of the reinforcing bars.

Test specimens

Five full-scale concrete bridge-deck slabs measuring 3000 x 2500 x 200 mm (118.1 x 98.4 x 7.9 in.) were fabricated. Two parallel steel girders were used to support the deck slabs with 2000 mm center-to-center spacing, as shown in Fig. 2. The specimens had two rows of holes (27 mm [1.06 in.] in diameter) at each edge, 160 and 250 mm (6.3 and 9.8 in.) from the restrained edges. These holes were fitted with steel bolts to provide edge restraint. The top and bottom concrete cover for all specimens was kept constant at 30 and 25 mm (1.2 and 1 in.), respectively, as specified in Clause 16.4.5 of CSA S6:19 (2019). The ratio of supporting girder spacing to slab thickness was less than 18, as specified in Clause 8.18.3.1 of CSA S6:19. Slab length was defined to prevent one-way shear before punching failure and to consider the slab area affected by the wheel load. This area was assumed to be based on the outer diameter of the wedge formed during punching failure (El-Gamal et al. 2005). The chosen test parameters were: 1) reinforcement ratio in the transverse direction of the bottom reinforcement (0.44, 0.83, and 1.15%); 2) surface conditioning of the GFRP bars (sand coated or helically wrapped); and 3) reinforcement type (steel or GFRP bars).

Table 3 summarizes the reinforcement details of the tested slabs. Number 5 sand-coated GFRP bars were used in G1-150, G1-100, and G1-300. Number 5 helically wrapped GFRP bars were used in G2-300. Deformed M15 steel bars were used in S1-300 to serve as a control specimen. The amount of bottom transverse reinforcement used in the tested slabs satisfies the empirical and flexural design methods in CSA S6:19 and AASHTO (2018), with a minimum reinforcement ratio of 0.44% and a maximum bar spacing of 300 mm (11.8 in.). Specimens G1-150 and G1-100 had a bar spacing of 200 mm (7.9 in.) in the longitudinal and transverse directions of the top assembly. In the bottom assembly, the spacing between bars was 150 mm (5.9 in.) and 100 mm (3.9 in.) in the main direction (transverse direction) in G1-150 and G1-100, respectively, and 200 mm (7.9 in.) in the longitudinal direction in both slabs. Specimens G1-300, G2-300, and S1-300 had a bar spacing of 300 mm (11.8 in.) in the longitudinal and transverse directions of the top and bottom assembly. Figure 2 shows the geometry and the reinforcement details of the tested deck slabs. The location of some reinforcing bars has been modified to prevent conflicts between prefabricated holes and bars. Figure 3 shows the slab construction. The Appendix* presents how specimen G1-150 was designed according to CSA S6:19 provisions.

*The Appendix is available at **www.concrete.org/publications** in PDF format, appended to the online version of the published paper. It is also available in hard copy

Table 3—Reinforcement details of tested bridge-deck slabs

	Bottom reinforcement						Top reinforcement					
	Transverse direction			Longitudinal direction			Transverse direction			Longitudinal direction		
Slab ID*	Bars†	ρ, %	ρ × *E*, MPa	Bars†	ρ, %	ρ × *E*, MPa	Bars†	ρ, %	ρ × *E*, MPa	Bars†	ρ, %	ρ × *E*, MPa
G1-150	16 @ 150	0.83	513	16 @ 200	0.62	383	16 @ 200	0.6	371	16 @ 200	0.62	383
G1-100	16 @ 100	1.15	711	16 @ 200	0.62	383	16 @ 200	0.6	371	16 @ 200	0.62	383
G1-300	16 @ 300	0.44	272	16 @ 300	0.43	266	16 @ 300	0.44	272	16 @ 300	0.43	266
G2-300‡	16 @ 300	0.44	282	16 @ 300	0.43	276	16 @ 300	0.44	282	16 @ 300	0.43	276
S1-300	16 @ 300	0.44	880	16 @ 300	0.43	860	16 @ 300	0.44	880	16 @ 300	0.43	860

*Reinforcement type (GFRP Type I and Type II and steel) followed by reinforcement spacing (100, 150, or 300 mm).

†Bar diameter and spacing in mm (diameter in mm @ spacing in mm).

‡Helically wrapped GFRP bars (GFRP Type II).

Note: 1 MPa = 0.145 ksi; 1 mm = 0.0394 in.

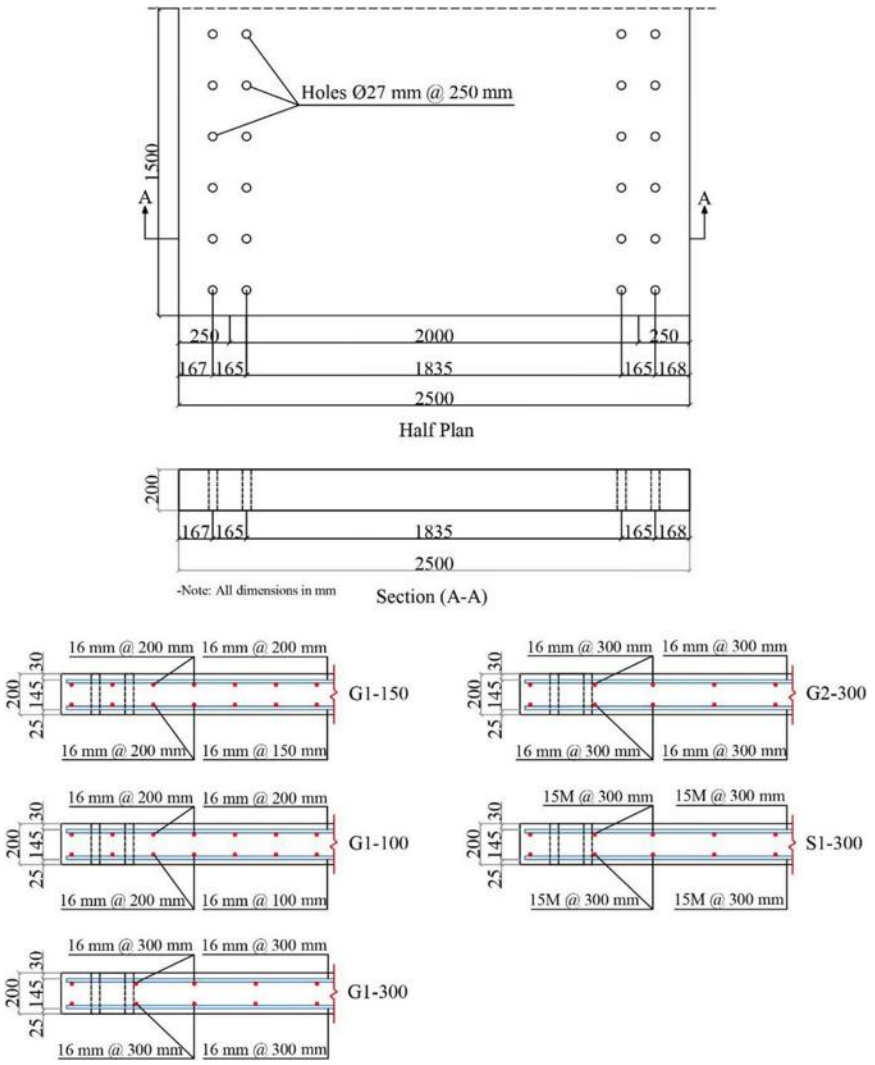

Fig. 2—Geometry of tested deck slabs and reinforcement details. (Note: 1 mm = 0.0394 in.)

Instrumentation

External and internal instrumentation was used in this study, as shown in Fig. 4. Fifteen strain gauges measuring 6 mm (0.24 in.) in length were installed on the surface of the top and bottom reinforcing bars, as shown in Fig. 4(a). Four electrical strain gauges measuring 60 mm (2.4 in.) in length were used around the loading plate to measure the concrete compressive strains. Seven potentiometers (POTs) (P1 to P7) were installed at different locations on the specimens to measure slab deflection, as shown in Fig. 4(b). Potentiometers P8 and P9 were installed to measure the side movements of specimens while testing. When the first three

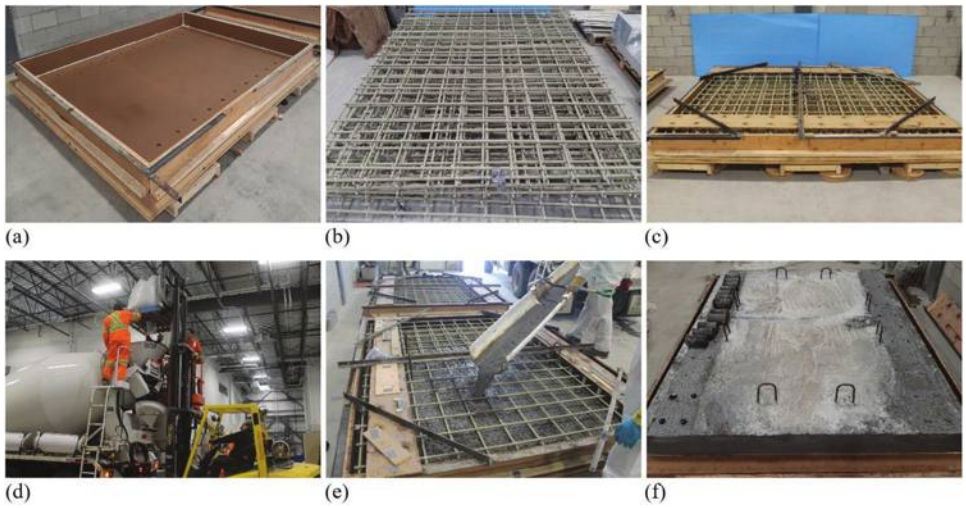

Fig. 3—Construction of bridge-deck slabs: (a) formwork; (b) meshes; (c) prepared formwork for casting; (d) mixing LW aggregates with water (pre-wetting) 3 days before casting; (e) casting; and (f) demolding.

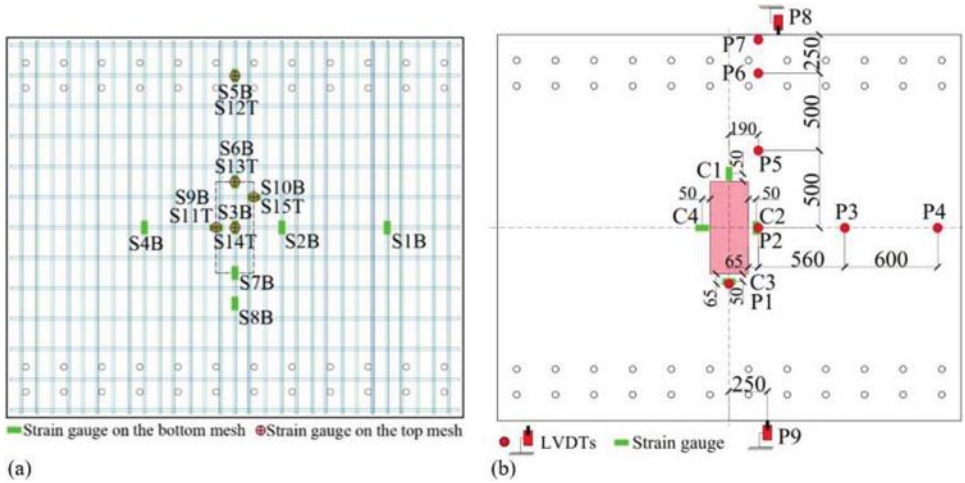

Fig. 4—Typical instrumentation of test slabs: (a) strain gauges on top (T) and bottom (B) reinforcing bars; and (b) LVDTs and strain gauges on top concrete surface. (Note: 1 mm = 0.0394 in.)

cracks appeared, three linear variable differential transducers (LVDTs), with a precision of 0.001 mm, were installed to measure the crack width. All the deflections, reinforcement and concrete strains, and loads were recorded by a data acquisition system connected to a computer.

Test setup and procedure

The specimens were tested up to failure under a concentrated monotonic load applied to the center of the slab with a servo-controlled, 1000 kN (224.8 kip) hydraulic actuator. The contact area of the applied load measured 250 x 600 mm (9.8 x 23.6 in.), which is specified in CSA S6:19 to simulate the footprint of a sustained truck wheel load (87.5 kN CL-625 truck). The load was applied at a displacement-controlled rate of 0.3 mm/min (0.01 in./min). A 10 mm (3.9 in.) thick sheet of neoprene was used under the loading plate to ensure uniform stresses on the concrete surface. The edges of the specimens were supported on two steel girders with a span of 2000 mm (78.7 in.), which is similar to the test setup of Elgabbas et al. (2016). Two neoprene strips 100 mm (3.9 in.) in width between the concrete surface and steel supports and two neoprene strips 100 mm (3.9 in.) in width between the concrete surface and steel channels were used. The strips were 3 and 10 mm (0.12 and 0.39 in.) thick, respectively. Figure 5 shows the test setup and data acquisition system. The corresponding loads were noted adjacent to each crack. The longitudinal edges of the slabs were partially restrained 22 mm (0.87 in.) diameter steel bolts that tied the deck slabs to the steel parts of the test setup. As shown in Fig. 2, four rows of holes 27 mm (1.06 in.) in diameter were prepared in the slabs during casting to fit the bolts. The steel bolts play the role of shear connectors between the specimens and girders in actual slab-on-girder bridges. The slabs were restrained by tightening the steel anchors with a torque moment of 160 N·m (116 lb·ft) to create uniform restraint along the slab edges. The torque moment was calculated to generate horizontal shear friction between the steel girder and the slab bottom surface above the horizontal component of the arching stress and to prevent lateral movement between the slab and girder.

Fig. 5—Overview of test setup.

TEST RESULTS AND DISCUSSION

The experimental results for the GFRP-reinforced LWSCC slabs consist of cracking patterns and failure mode, cracking and ultimate load capacity, concrete and reinforcement strains, and deflection behavior. Table 4 presents a summary of the test results.

Cracking patterns and loads

All the LWSCC specimens had similar cracking patterns despite their differences in reinforcement details. Figure 6 shows the cracking patterns of all the deck slabs. The formation and propagation of cracks were observed and identified from the beginning of loading. The first cracks appeared underneath the loading plate, mostly in the longitudinal direction. The cracks then propagated radially to the slab edges. The recorded cracking loads of the slabs were between 99.2 and 115.2 kN (22.3 and 25.9 kip). The average cracking load was 107.2 kN (24.1 kip), which is similar to the predicted service load (110.25 kN [24.8 kip]) according to the CSA S6:19 design provisions. Specimen G1-100 had the highest cracking load (115.2 kN [25.9 kip]) of the slabs. A comparison of the recorded cracking loads for G1-100 (115.2 kN [25.9 kip]), G1-150 (106.9 kN [24 kip]), and G1-300 (100.0 kN [22.5 kip]) confirms that reducing reinforcement spacing improved the cracking performance of the deck slabs. Cracking loads recorded for G1-300 and G2-300 were 100.0 and 114.5 kN (22.5 and 25.7 kip), respectively. This could be related to the effect of the GFRP bar surface treatment. Approximately similar cracking load values were recorded for G1-300 (100.0 kN [22.5 kip]) and S1-300 (99.2 kN [22.3 kip]). This can be attributed to the fact that the sand-coated GFRP bars significantly affected the cracking performance of the deck slabs.

Figure 7 shows the load-to-average-crack-width relationship for all the LWSCC specimens. Table 4 provides the values of the crack widths at the service, factored, and ultimate loads. The maximum measured crack widths for G1-150, G1-300, and S1-300 at the service designed load were 0.12, 0.2, and 0.1 mm (0.005, 0.008, and 0.004 in.), respectively. These values are less than the permissible value defined in ACI 440.1R-15 and CSA S6:19 of 0.5 mm (0.02 in.) for exterior exposure. The cracking loads for G1-100 and G1-300 were higher than the service load, which means that the first cracks appeared after the service load had been reached. Specimens G1-100 and S1-300 had similar levels of axial-reinforcement stiffness. Given the same load level, G1-100 had narrower average crack widths than S1-300. At the factored design load level, G1-100 and G1-150 behaved similarly to S1-300, while G1-300 and G2-300 had twice the crack width as S1-300. The crack-width values recorded for all specimens at the factored design load level did not exceed the limit (0.5 mm) defined in CSA S6:19.

At the ultimate load level, G1-100 showed the smallest crack width, followed by G1-150. Moreover, S1-300 and G1-100, which had similar axial-reinforcement stiffness ($\rho \times E$), exhibited different load-to-crack-width relationships. Spacing the GFRP bars at 100 mm (3.9 in.) in G1-100 enhanced the slab's cracking performance compared to the specimen with steel bars (S1-300) spaced at 300 mm (11.8 in.). In addition, G1-150 had lower axial-reinforcement stiffness and bar spacing than S1-300, but had a better load-to-crack-width relationship. This confirms that using lower bar spacing reduces crack width, even at lower levels of axial reinforcement (Elgabbas et al. 2016). Furthermore, it can be posited that having the same bottom reinforcement ratio and bar spacing might have led to S1-300, G1-300, and G2-300 having a similar load-to-crack-width relationship, as shown in Fig. 7. On the other hand, at the factored design load and ultimate load level, comparable crack-width values were recorded for G1-300 and G2-300, which indicates that using different bar surface treatments had a negligible effect on the cracking behavior of the tested specimens.

Ultimate load capacity and failure mode

Figure 6 shows that a similar cracking pattern appeared on the bottom surfaces of all LWSCC slabs after testing. All

Table 4—Test results and comparison to theoretical predictions of punching-shear capacities

ID	f'_c, MPa	σ_n, MPa	P_{cr}, kN	P_{max}, kN	Deflection, mm			FRP strain, με			Concrete strain, με			Crack width, mm			$P_{max,exp}/P_{max,pred}$				
					P_{serv}	P_{fact}	P_{max}	P_{serv}	P_{fact}	P_{max}	P_{serv}	P_{fact}	P_{max}	P_{serv}	P_{fact}	P_{max}	CSA (2012)	ACI (2015)*	ACI (2015)†	AASHTO (2018)‡	AASHTO (2018)§
G1-150	47.3	3.96	106.9	541.4	2.06	6.34	24.12	1239	3262	6719	–121	–236	–1305	0.12	0.27	0.82	1.18	1.53	1.37	1.40	1.40
G1-100	47.3	3.96	115.2	525.6	1.75	4.51	19.01	422	1600	4608	–181	–503	–1147	—	0.22	0.61	1.01	1.26	1.14	1.15	1.15
G1-300	42.4	3.25	100.0	442.8	2.24	8.2	25.81	90	2939	7051	–174	–698	–1119	0.20	0.60	1.68	1.22	1.64	1.48	1.78	1.59
G2-300	46.1	3.64	114.5	421.1	1.13	6.88	24.47	453	2159	7077	–123	–273	–944	—	0.49	1.89	1.11	1.53	1.37	1.47	1.41
S1-300	46.1	3.64	99.2	538.7	1.27	4.18	25.72	107	581	3892	–71	–151	–1206	0.10	0.30	2.01	—	—	—	—	—
Average	45.8	3.69	107.2	493.9	1.69	6.02	23.8	462	2108	5869	–134	–372	–1144	0.14	0.38	1.40	1.13	1.49	1.34	1.45	1.39
SD	2.0	0.3	7.6	57.4	0.5	1.7	2.8	466.3	1074	1506	44.9	224	132.7	0.1	0.2	0.6	0.1	0.2	0.1	0.3	0.2
CV, %	4.4	8.0	7.1	11.6	28.6	28	11.7	101	51	26	–34	–60	–11.6	37.8	43.0	45.8	8.1	10.9	10.7	17.9	13.0

*Considering concrete density reduction factor provided in ACI 440.1R-15.

†Without considering concrete density reduction factor provided in ACI 440.1R-15.

‡Considering concrete density reduction factor provided in AASHTO (2018).

§Without considering concrete density reduction factor provided in AASHTO (2018).

Note: σ_n, P_{cr}, and P_{max} are spitting tensile strength, cracking, and failure loads, respectively; service (P_{serv}) and factored (P_{fact}) design loads are calculated as follows: $P_{serv} = 1.4 \times 0.9 \times 87.5 = 110.25$ kN (24.8 kip), and $P_{fact} = 1.4 \times 1.7 \times 87.5 = 208.25$ kN (46.8 kip), respectively (CL-625 truck) (CSA S6:19); SD is standard deviation; CV is coefficient of variation. 1 kN = 0.225 kip; 1 MPa = 0.145 ksi; 1 mm = 0.0394 in.

the specimens experienced punching-shear failure around the loading plate. No signs of concrete crushing in the top surface or bar rupture were observed, which confirms punching shear as the failure mode. The maximum loads recorded were 541, 525, 442, 421, and 538 kN (121.6, 118, 99.4, 94.6, and 121 kip) for G1-150, G1-100, G1-300, G2-300, and S1-300, respectively. As expected, the slabs with wider GFRP bar spacing in the transverse direction of the bottom mesh showed lower punching-shear strengths. The recorded punching-shear capacities of the test specimens were 2.02 to 2.60 times the factored design load (208.25 kN [46.8 kip]) as estimated with the CSA S6:19 design provisions. This proves that the slabs experienced punching-shear failure despite being designed based on flexural failure. Similar to the findings of past studies on GFRP-, CFRP-, and BFRP-RC bridge-deck slabs, the ultimate capacity of the deck slabs exhibited a high level of conservativeness (Hewitt and Batchelor 1975; Perdikaris and Beim 1988; El-Gamal et al. 2005, 2007; Bouguerra et al. 2011; Elgabbas et al. 2016).

Table 4 presents the punching-shear strengths of all the LWSCC specimens. G1-100 and S1-300 showed similar punching-shear capacities (525 and 538 kN [118 and 121 kip], respectively) with close axial-reinforcement stiffness (711 and 880 MPa [103.1 and 127.6 ksi], respectively). The findings were similar for G1-300 and G2-300 with respect to axial-reinforcement stiffness (272 and 282 MPa [39.5 and 40.9 ksi], respectively) and ultimate loads (442 and 421 kN [99.4 and 94.6 kip]), respectively. This confirms that the slabs with similar degrees of axial-reinforcement stiffness could achieve similar levels of ultimate capacity.

Reinforcement and concrete strains

Table 4 presents the strains recorded by S3B (strain gauge located at the center of the middle bar in the bottom reinforcement of the LWSCC slabs) and C2 (strain gauge located on the top concrete surface near the loading plate), while Fig. 8 shows the load-to-strain graphs. The behavior of the strains in the graphs was linear up to the failure of the slabs. Generally, Fig. 8 confirms that increasing the axial-reinforcement stiffness reduced tensile strains in the bottom reinforcement. The effect of axial-reinforcement stiffness can be seen in G1-100, G1-150, and G1-300, which had reinforcement ratios of 1.15%, 0.83%, and 0.44%, respectively. At the maximum load level of each slab, the bottom reinforcement strains were 4600, 6700, and 7050 με for G1-100, and G1-150, G1-300, respectively. Reducing the reinforcement ratio from 1.15% to 0.83% and 0.44% increased the maximum reinforcement strains by 145.8% and 153.0%, respectively. Moreover, the axial-reinforcement stiffness significantly affected the maximum recorded values of bottom reinforcement strains in the tested slabs. Approximately the same level of reinforcement strain was recorded for G1-300 and G2-300 (7050 and 7100 με, respectively); the reinforcement had almost the same axial-reinforcement stiffness in the transverse direction of bottom reinforcement (272 and 282 MPa [39.5 and 40.9 ksi], respectively). This confirms that the GFRP bars' surface treatment had a negligible effect on the bottom transverse reinforcement.

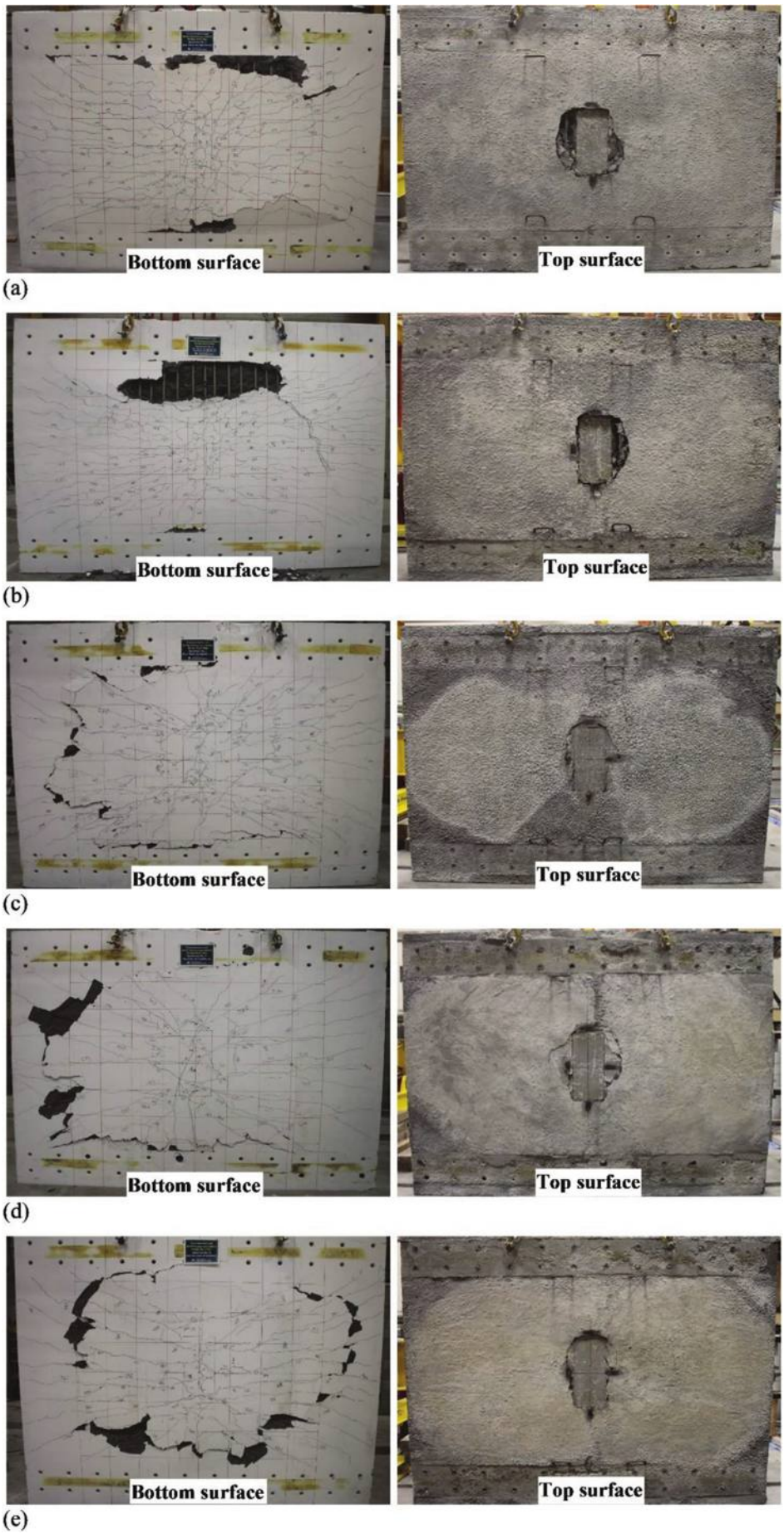

Fig. 6—Cracking patterns at failure: (a) G1-100; (b) G1-150; (c) G1-300; (d) G2-300; and (e) S1-300.

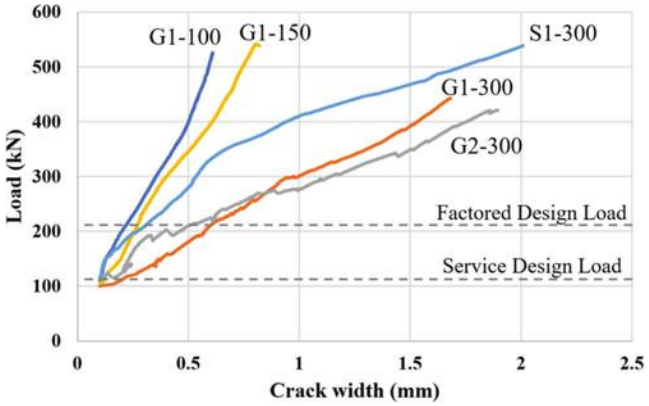

Fig. 7—Load-to-average-crack-width curves. (Note: 1 kN = 0.225 kip; 1 mm = 0.0394 in.)

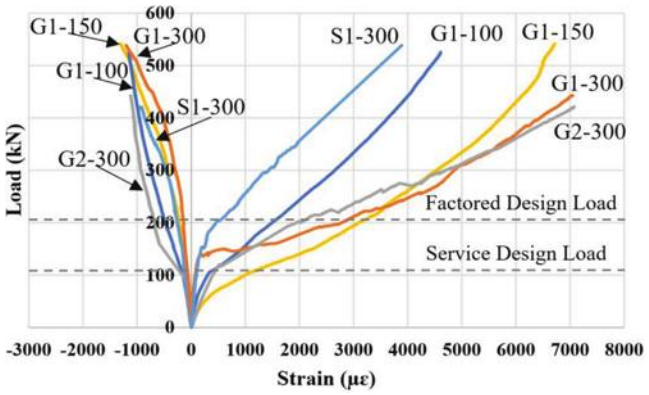

Fig. 8—Strains on bottom reinforcement and surface of concrete. (Note: 1 kN = 0.225 kip.)

The ranges of recorded strains at the service load level (110.25 kN [24.8 kips]) for the top concrete surface and middle reinforcing bars varied from –180 to –70 με and from 90 to 1250 με, respectively. At the factored design load level (208.25 kN [46.8 kip]), these values were from –700 to –150 με and from 580 to 3260 με, respectively. The large difference in the axial-reinforcement stiffness of the specimens produced a large difference in the recorded strains in the top concrete surface and middle reinforcing bars. The maximum strains recorded at service load were 15.8% and 18.4% of that recorded at ultimate load for the top concrete surface and middle reinforcing bar, respectively. These values for the factored design load were 62.4% and 48.5% of the ultimate load, respectively. The safety factor values ranged from 1.6 to 5.5 for the GFRP-reinforced slabs. The recorded tensile strain values at the ultimate load for the Type I GFRP bars ranged from 20 to 32% of the ultimate tensile strain, and for Type II GFRP bars, the recorded tensile strain value was 30% of the ultimate tensile strain. Furthermore, the recorded compressive strains ranged from 27 to 37% of the maximum allowable concrete compressive strain (3500 με) (CSA S806-12 [R2017]). This proves that the mode of failure for all specimens was punching shear, where no concrete crushing or bar rapture was observed.

Figure 9 gives the distribution of the reinforcement strains from strain gauges installed on the middle bar in the bottom reinforcement of the slab. Higher values of the strains were recorded in the middle of the specimens and, conversely, the lowest values were recorded toward the supports. Eventually, these values dropped to zero due to slab edge restraint. The fact that a similar trend can be seen in the graph for all the tested specimens proves that no debonding of reinforcement occurred during the test.

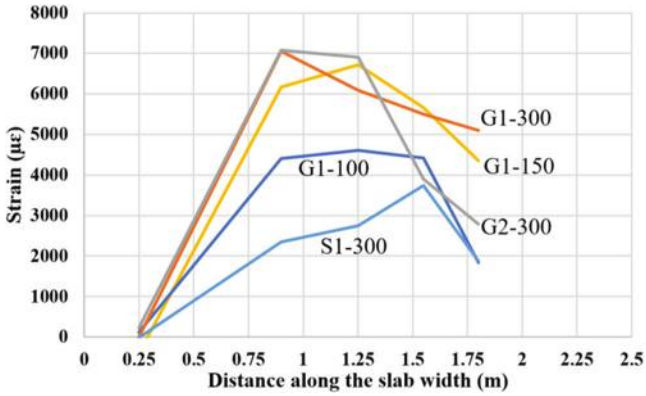

Fig. 9—Distribution of reinforcement strains at middle section of slabs. (Note: Units in m; 1 m = 3.28 ft.)

Load-deflection behavior and effect of test parameters

This section presents the load-deflection curves in three groups to show the effect of the test parameters on the load-deflection behavior of the LWSCC deck slabs, as shown in Fig. 10. It should be noted that the self-weight of the deck slabs was not included in the values of the deflection and the applied load. All the specimens exhibited similar linear load-deflection behavior from initial loading up to the initiation of the first crack. The uncracked response for all the deck slabs showed insignificant deflection, reflecting gross-section stiffness. The post-cracking stiffness was considerably reduced. This change in stiffness represents the transition from gross to effective section properties. After cracking, the LWSCC deck slabs reinforced with GFRP bars behaved nearly linearly with reduced stiffness up to failure. This can be attributed to the linear-elastic characteristics of the GFRP reinforcement. After cracking occurred, however, the load-deflection curve of the slab reinforced with steel was initially linear and then exhibited reduced stiffness after yielding.

The influence of the reinforcement ratio on the punching-shear strength of the LWSCC deck slabs reinforced with GFRP was assessed. Number 5 (16 mm) GFRP bars spaced at 300 mm were used to reinforce G1-300 in the transverse direction of the bottom assembly at a reinforcement ratio of 0.44%. The reinforcement ratio in G1-150 and G1-100 was 0.83% and 1.15%, respectively. Figure 10(a) provides a comparison of the moment-deflection curves for the three LWSCC slabs reinforced with GFRP bars (Type I, sand-coated). The figure indicates that increasing the reinforcement ratio enhanced the post-cracking stiffness of the LWSCC slabs.

Specimens G1-150 and G1-100 experienced lower deflection and higher punching-shear strength than G1-300. Increasing the reinforcement ratio from 0.44% to 0.83%

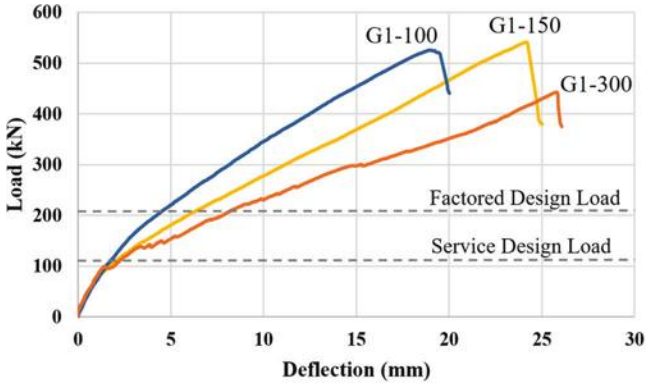

(a)

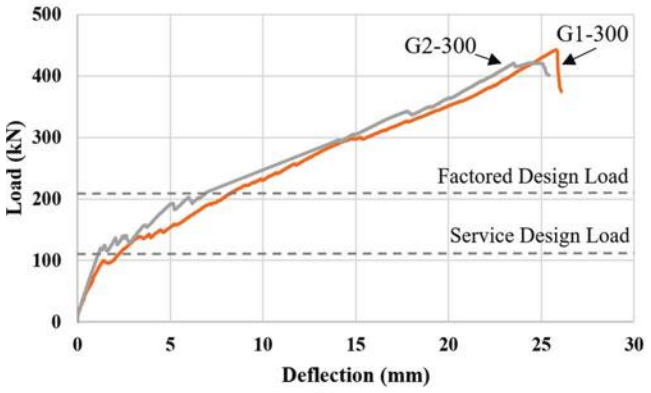

(b)

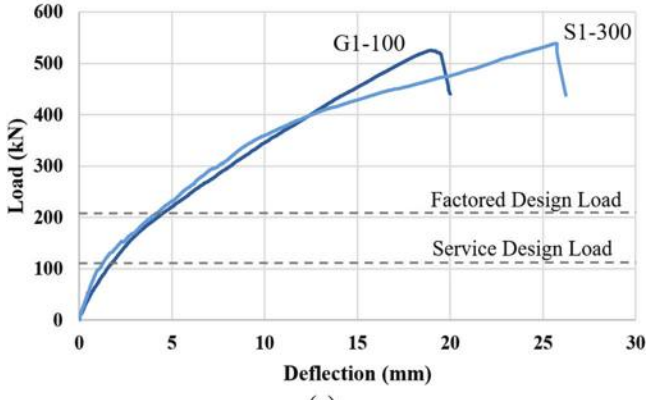

(c)

Fig. 10—Effect of test parameters on load-maximum deflection curves: (a) reinforcement ratio; (b) surface conditioning; and (c) reinforcement type. (Note: 1 kN = 0.225 kip; 1 mm = 0.0394 in.)

and 1.15% decreased the measured deflections by 8.0% and 22.0% at the service load level (110.25 kN [24.8 kip]), respectively, and at the same time, the punching-shear strength enhanced by 22.3% and 18.7%. Indeed, the punching-shear strength and behavior of the LWSCC slabs depended significantly on the GFRP reinforcement ratio.

Specimens G1-300 and G2-300 were reinforced with GFRP bars with different conditioning (sand coated and helically wrapped, respectively). Figure 10(b) shows the load-deflection behavior of G1-300 and G2-300, as well as the comparable punching-shear strength of 442 and 421 kN (99.4 and 94.6 kip), respectively. It can be concluded that the LWSCC slabs with similar reinforcement ratios behaved similarly with respect to deflection, stiffness, and punching-shear strength, regardless of the reinforcing bar surface conditioning.

The GFRP- and steel-reinforced LWSCC slabs (G-100 and S-300) were designed to have similar levels of axial-reinforcement stiffness. As depicted in Fig. 10(c), G1-100 and S1-300 had comparable load-deflection responses up to the yielding of the steel reinforcement in S1-300. After the reinforcement yielded, S1-300 experienced severe deformation, resulting in higher deflection at ultimate load compared to G1-100. The two slabs exhibited almost similar punching-shear strength: 525 and 538 kN (118 and 121 kip), respectively. The GFRP-reinforced slab needed three times as much reinforcement to achieve the same behavior as the steel-reinforced slab; however, the use of LWSCC compensated for the constructability and congestion issues. This proves that the combination of LWSCC and GFRP reinforcement is the great alternative to conventional steel-RC.

COMPARISON OF EXPERIMENTAL PUNCHING-SHEAR CAPACITIES AND THEORETICAL PREDICTIONS

The equations in CSA S806-12 (R2017), ACI 440.1R-15, and AASHTO (2018) for predicting the punching-shear strength of GFRP-reinforced deck slabs can be compared with the experimental results of this study. CSA S806-12 (R2017) provides three design equations (Eq. (1), (2), and (3)) for estimating the punching-shear capacity; the smallest estimated value should be considered as the design value

$$V_c = \left(1 + \frac{2}{\beta_c}\right)\left[0.028\lambda\varphi_c(E_f\rho_f f_c')^{\frac{1}{3}}\right]b_0 d \quad (1)$$

$$V_c = \left(\frac{\alpha_s d}{b_0} + 0.19\right)\left[0.147\lambda\varphi_c(E_f\rho_f f_c')^{\frac{1}{3}}\right]b_0 d \quad (2)$$

$$V_c = \left[0.056\lambda\varphi_c(E_f\rho_f f_c')^{\frac{1}{3}}\right]b_0 d \quad (3)$$

where β_c is the ratio of the long side to the short side of the loading plate; λ is a factor to consider concrete density; f_c' is the concrete compressive strength; b_0 is the perimeter of the critical area underneath the applied load at a distance of $d/2$ from the loading-plate edges; d is the distance from the top surface of the concrete to the center of the bottom reinforcing bars; and α_s is a factor to consider column location. CSA S806-12 (R2017) considers the reduction factor λ for normal-density concrete, structural semi-low-density concrete in which all the fine aggregate is natural sand, and structural low-density concrete in which none of the fine aggregate is natural sand to be values of 1.0, 0.85, and 0.75, respectively. Considering the weight of the LW and NW sand used in the LWSCC mixture, the value of λ for calculating the punching-shear capacity of the tested slabs, using interpolation, was considered to be 0.794.

According to ACI 440.1R-15, the punching-shear capacity of two-way slabs reinforced with GFRP bars is calculated with Eq. (4) and (5), which consider the stiffness of reinforcement as an influential factor in the punching-shear strength of concrete slabs.

$$V_c = \frac{4}{5}\sqrt{f_c'}b_0c \quad (4)$$

$$k = \sqrt{2\rho_f n_f + (\rho_f n_f)^2} - \rho_f n_f \quad (5)$$

where c is the neutral axis depth (mm) of the cracked transformed section; c is kd; and n_f is the modular ratio, $n_f = E_f/E_c$. ACI 440.1R-15 does not provide a specific factor for calculating the punching-shear capacity of different types of LWC. ACI 318-19 (ACI Committee 318 2019), however, provides a modification factor λ based on equilibrium density to compensate for the reduction of mechanical properties of LWC compared to NWC with the same compressive strength. Given a value of 1906 kg/m^3 (119 lb/ft^3) for the equilibrium density of LWC, the value of λ for calculating the punching-shear capacity of the deck slabs was considered to be 0.9.

According to AASHTO (2018), the shear resistance of two-way slabs can be computed in Eq. (6), where V_c is the nominal shear resistance of the concrete

$$V_c = 0.316k\sqrt{f_c'}b_0d_v \quad (6)$$

where k is the ratio of the depth of the neutral axis to the depth of the flexural reinforcement; f_c' is the specified compressive strength of concrete (ksi); b_0 is the perimeter of the critical section calculated at a distance of $d/2$ from the concentrated load (in.); and d_v is the effective shear depth (in.). Although AASHTO (2018) does not cover the use of LWC, with regard to the AASHTO (2020) design specifications, when the splitting tensile strength (f_{ct}) is provided, a modification factor (λ) for concrete density is determined with Eq. (7)

$$\lambda = 4.7\frac{f_{ct}}{\sqrt{f_c'}} \leq 1.0 \quad (7)$$

Table 4 presents the experimental-to-predicted ratio of the punching-shear strength. According to the equations in CSA S806-12 (R2017), the experimental-to-predicted strength ratio was 1.18, 1.01, 1.22, and 1.11 for G1-100, G1-150, G1-300, and G2-300, respectively. The corresponding values using the ACI 440.1R-15 design equation were 1.37, 1.14, 1.48, and 1.37, respectively. Moreover, the calculated ratios obtained with the equations in AASHTO (2018) were 1.40, 1.15, 1.59, and 1.41, respectively. According to the concrete density reduction factor in AASHTO (2020), these values would be 1.40, 1.15, 1.78, and 1.47, respectively. It can be concluded that CSA S806-12 (R2017) provided accurate predictions compared to the experimental results. ACI 440.1R-15 and AASHTO (2018) conservatively underestimated the punching-shear capacity of the tested GFRP-reinforced LWSCC slabs. Moreover, all the predicted concrete punching-shear capacities were estimated without considering the reduction factor (strength reduction factor, concrete and GFRP material reduction factors). Taking into account the reduction factor in the design will provide a conservative prediction of the shear capacity to avoid the brittle failure. Furthermore, according to the equations provided in CSA S6:19 and "AASHTO LRFD Bridge Design Specifications" (2020), the experimental-to-predicted strength ratios for the steel-reinforced slab (S1-300) were 1.22 and 1.33, respectively. This showed that CSA S6:19 predicted more accurate shear strength than AASHTO (2020). Past findings revealed that ACI 440.1R-15 predicted the punching-shear strength of GFRP-reinforced LWC panels more accurately than that of GFRP-reinforced NWC panels (Pantelides et al. 2012a; Liu and Pantelides 2013). ACI 440.1R-15 and AASHTO (2009), however, conservatively predicted the punching-shear capacity of GFRP-reinforced NWC deck slabs (Bouguerra et al. 2011), BFRP-reinforced NWC deck slabs (Elgabbas et al. 2016), and two-way slabs, as well as the shear resistance of GFRP-reinforced ultra-high-performance fiber-reinforced concrete (UHPFRC) closure joints between one-way bridge-deck slabs (Youssef et al. 2019).

SUMMARY AND CONCLUSIONS

In this study, a new mixture design for lightweight self-consolidating concrete (LWSCC) was developed. A comprehensive experimental program was designed and conducted to investigate the behavior of edge-restrained glass fiber-reinforced polymer (GFRP)-reinforced LWSCC bridge-deck slabs. The following conclusions were drawn based on the results of this study.

1. All the specimens experienced punching-shear failure; the recorded ultimate capacities were higher than the predictions and factored design load specified in CSA S6:19.

2. The behavior of the LWSCC deck slabs was significantly affected by the reinforcement ratio as the main parameter. The cracking performance, reinforcement strains, and deflection of the GFRP-reinforced tested specimens were reduced by increasing the reinforcement ratio of the bottom assembly.

3. Comparing LWSCC deck slabs with the same axial-reinforcement stiffness ($\rho \times E$) leads to the conclusion that these slabs have similar behavior and punching-shear strength. Increasing the axial-reinforcement stiffness in the GFRP-reinforced slabs significantly increased the ultimate capacity and reduced maximum crack width, reinforcement strains, and midspan deflection at ultimate load.

4. The surface conditions of the GFRP bars (sand coated or helically wrapped) had a minor effect on the cracking, deflection, and behavior of the tested LWSCC deck slabs.

5. A comparison of the concrete punching-shear capacities of the LWSCC deck slabs to their capacities predicted with the CSA S806-12 (R2017) equations based on a concrete density reduction factor revealed that these equations yielded more accurate predictions of GFRP-reinforced LWSCC deck slabs than did the ACI 440.1R-15 and AASHTO (2018) equations.

6. The experimental evidence from this investigation provides some experimental backbone for including design provisions in bridge design specifications for the use of GFRP bars as internal reinforcement in LWSCC bridge-deck slabs.

Based on the results and conclusions of this study, the integration of GFRP bars with LWSCC can be used effectively in Accelerated Bridge Construction (ABC) with

longer spans and less shipping cost to build durable bridges with smaller cross sections and extended service lives. Further investigations into the behavior of GFRP-reinforced LWSCC bridge-deck slabs with different types of microfibers under static and fatigue loading should be conducted to generate more confidence and encourage wider acceptance of this new material.

AUTHOR BIOS

Mahdi Aflakisamani *is a Doctoral Candidate in the Department of Civil and Building Engineering at the University of Sherbrooke, Sherbrooke, QC, Canada. He received his BSc from the Department of Civil Engineering, Shahrekord University, Shahrekord, Iran, and his MSc from the Department of Civil Engineering, Islamic Azad University, Najafabad Branch, Najafabad, Iran. His research interests include the use of fiber-reinforced polymers (FRPs) in reinforced concrete structures.*

Salaheldin Mousa *is an FRQNT Postdoctoral Fellow in the Department of Civil and Building Engineering at the University of Sherbrooke, where he received his PhD. He received his BSc and MSc from the Faculty of Engineering at Shoubra, Benha University, Benha, Egypt. His research interests include the use of FRPs in reinforced concrete structures.*

Hamdy M. Mohamed *is a Lecturer and Research Associate in the Department of Civil and Building Engineering at the University of Sherbrooke, where he received his PhD. He received his BSc and MSc from the Faculty of Engineering at Helwan University, Cairo, Egypt. His research interests include the use and field applications of FRPs in reinforced concrete structures.*

Ehab A. Ahmed *is an Instructor at Concordia University, Montreal, QC, Canada. He received his BSc and MSc from the Faculty of Engineering, Menoufia University, Menoufia, Egypt, and his PhD from the University of Sherbrooke. His research interests include the use and field applications of FRPs in reinforced concrete structures.*

Brahim Benmokrane, *FACI, is a Professor in the Department of Civil and Building Engineering at the University of Sherbrooke, Tier 1 Canada Research Chair Professor in Advanced Composite Materials for Civil Structures, Industrial Research Chair Professor in FRP Reinforcement for Concrete Infrastructure, and Director of the University of Sherbrooke Research Center on Structural FRP Composite Materials for Concrete Structures (CRUSMAC). He is past Co-Chair and a member of ACI Subcommittee 440-K, FRP-Material Characteristics; a member of ACI Committees 435, Deflection of Concrete Building Structures, and 440, Fiber-Reinforced Polymer Reinforcement; and a member of ACI Subcommittees 440-E, FRP-Professional Education; 440-F, FRP-Repair-Strengthening; 440-H, FRP-Reinforced Concrete; 440-I, FRP-Prestressed Concrete; and 440-L, FRP-Durability. He received the ACI Foundation Arthur J. Boase Award in 2022. His research interests include the development of FRP reinforcement for concrete structures and their durability, structural performance, and field applications.*

ACKNOWLEDGMENTS

This research was conducted with funding from the Tier 1 Canada Research Chair in Advanced Composite Materials for Civil Structures, the Natural Sciences and Engineering Research Council of Canada (NSERC), the Fonds de recherche du Québec – Nature et technologies (FRQNT), and the Canada Foundation for Innovation (CFI), and the technical help provided by the staff of the structural lab of the Department of Civil Engineering at the University of Sherbrooke. The authors would like to express their special thanks and gratitude to Northeast Solite Corporation for their generosity. Their donation of Solite® aggregate was instrumental to the success of this research project.

REFERENCES

AASHTO, 2009, "AASHTO LRFD Bridge Design Guide Specifications for GFRP-Reinforced Concrete Bridge Decks and Traffic Railings," first edition, American Association of State Highway and Transportation Officials, Washington, DC, 68 pp.

AASHTO, 2018, "AASHTO LRFD Bridge Design Guide Specifications for GFRP-Reinforced Concrete," second edition, American Association of State Highway and Transportation Officials, Washington, DC.

AASHTO, 2020, "AASHTO LRFD Bridge Design Specifications," ninth edition, American Association of State Highway and Transportation Officials, Washington, DC.

ACI Committee 318, 2019, "Building Code Requirements for Structural Concrete (ACI 318-19) and Commentary (ACI 318R-19) (Reapproved 2022)," American Concrete Institute, Farmington Hills, MI, 624 pp.

ACI Committee 440, 2006, "Guide for the Design and Construction of Structural Concrete Reinforced with FRP Bars (ACI 440.1R-06)," American Concrete Institute, Farmington Hills, MI, 44 pp.

ACI Committee 440, 2015, "Guide for the Design and Construction of Structural Concrete Reinforced with Fiber-Reinforced Polymer (FRP) Bars (ACI 440.1R-15)," American Concrete Institute, Farmington Hills, MI, 88 pp.

Ahmad, S. H.; Zia, P.; Yu, T. J.; and Xie, Y., 1994, "Punching Shear Tests of Slabs Reinforced with 3-D Carbon Fiber Fabric," *Concrete International*, V. 16, No. 6, June, pp. 36-41.

Arafa, A.; Farghaly, A. S.; Ahmed, E. A.; and Benmokrane, B., 2016, "Laboratory Testing of GFRP-RC Panels with UHPFRC Joints of the Nipigon River Cable-Stayed Bridge in Northwest Ontario, Canada," *Journal of Bridge Engineering*, ASCE, V. 21, No. 11, p. 05016006. doi: 10.1061/(ASCE)BE.1943-5592.0000943

ASTM C150/C150M-18, 2018, "Specification for Portland Cement," ASTM International, West Conshohocken, PA, 9 pp.

ASTM C330/C330M-17a, 2017, "Standard Specification for Lightweight Aggregates for Structural Concrete," ASTM International, West Conshohocken, PA, 4 pp.

ASTM C567/C567M-19, 2019, "Standard Test Method for Determining Density of Structural Lightweight Concrete," ASTM International, West Conshohocken, PA, 4 pp.

ASTM D7205/D7205M-06(2016), 2016, "Standard Test Method for Tensile Properties of Fiber Reinforced Polymer Matrix Composite Bars," ASTM International, West Conshohocken, PA, 13 pp.

Benmokrane, B.; El-Salakawy, E.; El-Gamal, S.; and Goulet, S., 2007, "Construction and Testing of an Innovative Concrete Bridge Deck Totally Reinforced with Glass FRP Bars: Val-Alain Bridge on Highway 20 East," *Journal of Bridge Engineering*, ASCE, V. 12, No. 5, pp. 632-645. doi: 10.1061/(ASCE)1084-0702(2007)12:5(632)

Benmokrane, B.; Mohamed, H. M.; Mohamed, K.; and Mousa, S., 2021a, "Recent Canadian Developments Related to Unconventional Reinforcing for Concrete Structures, Design Codes, and Applications in Buildings and Bridges," *Field Applications of Non-Conventional Reinforcing and Strengthening Methods for Bridges and Structures*, SP-346, Y. J. Kim, S. Nolan, and A. Nanni, eds., American Concrete Institute, Farmington Hills, MI, pp. 93-112.

Benmokrane, B.; Mohamed, H. M.; Mousa, S.; Elsafty, A.; and Nolan, S., 2021b, "Design, Construction, Testing, and Behavior of Driven Precast Concrete Piles Reinforced with GFRP Bars and Spirals," *Journal of Bridge Engineering*, ASCE, V. 26, No. 8, p. 04021050. doi: 10.1061/(ASCE)BE.1943-5592.0001755

Billington, P. N.; Shirley-Smith, H.; and Billington, D. P., 2020, "Bridge," *Encyclopedia Britannica*, https://www.britannica.com/technology/bridge-engineering. (last accessed Apr. 11, 2023)

Bouguerra, K.; Ahmed, E. A.; El-Gamal, S.; and Benmokrane, B., 2011, "Testing of Full-Scale Concrete Bridge Deck Slabs Reinforced with Fiber-Reinforced Polymer (FRP) Bars," *Construction and Building Materials*, V. 25, No. 10, pp. 3956-3965. doi: 10.1016/j.conbuildmat.2011.04.028

CAN/CSA S6-10, 2010, "Canadian Highway Bridge Design Code," CSA Group, Toronto, ON, Canada.

CAN/CSA S806-02, 2002, "Design and Construction of Building Components with Fibre-Reinforced Polymers," CSA Group, Toronto, ON, Canada.

CSA S6:19, 2019, "Canadian Highway Bridge Design Code," CSA Group, Toronto, ON, Canada.

CSA S806-12, 2012, "Design and Construction of Building Components with Fibre-Reinforced Polymers," CSA Group, Toronto, ON, Canada.

CSA S806-12 (R2017), 2017, "Design and Construction of Building Components with Fibre-Reinforced Polymers," CSA Group, Toronto, ON, Canada.

CSA S807:19, 2019, "Specification for Fibre-Reinforced Polymers," CSA Group, Toronto, ON, Canada.

El-Gamal, S.; El-Salakawy, E.; and Benmokrane, B., 2005, "Behavior of Concrete Bridge Deck Slabs Reinforced with Fiber-Reinforced Polymer Bars Under Concentrated Loads," *ACI Structural Journal*, V. 102, No. 5, Sept.-Oct., pp. 727-735.

El-Gamal, S.; El-Salakawy, E.; and Benmokrane, B., 2007, "Influence of Reinforcement on the Behavior of Concrete Bridge Deck Slabs Reinforced with FRP Bars," *Journal of Composites for Construction*, ASCE, V. 11, No. 5, pp. 449-458. doi: 10.1061/(ASCE)1090-0268(2007)11:5(449)

Elgabbas, F.; Ahmed, E. A.; and Benmokrane, B., 2016, "Experimental Testing of Concrete Bridge-Deck Slabs Reinforced with Basalt-FRP Reinforcing Bars under Concentrated Loads," *Journal of Bridge Engineering*, ASCE, V. 21, No. 7, p. 04016029. doi: 10.1061/(ASCE)BE.1943-5592.0000892

Gooranorimi, O.; Gremel, D.; Myers, J. J.; and Nanni, A., 2019, "Long-Term Durability of GFRP Internal Reinforcement in Concrete Structures," *Durability of Concrete Structures Incorporating Conventional and Advanced Materials*, SP-331, Y. J. Kim, I. Yoshitake, and M. F. Green, eds., American Concrete Institute, Farmington Hills, MI, pp. 69-79.

Harmon, K. S., 2007, "Engineering Properties of Structural Lightweight Concrete," Carolina Stalite Company, Salisbury, NC.

Hewitt, B. E., and Batchelor, B., 1975, "Punching Shear Strength of Restrained Slabs," *Journal of the Structural Division*, ASCE, V. 101, No. 9, pp. 1837-1853. doi: 10.1061/JSDEAG.0004158

Hussein, A. H., and El-Salakawy, E. F., 2018, "Punching Shear Behavior of Glass Fiber-Reinforced Polymer-Reinforced Concrete Slab-Column Interior Connections," *ACI Structural Journal*, V. 115, No. 4, July, pp. 1075-1088. doi: 10.14359/51702134

JSCE, 1997, "Recommendation for Design and Construction of Concrete Structures Using Continuous Fiber Reinforcing Materials," Concrete Engineering Series 23, Japan Society of Civil Engineers, Tokyo, Japan.

Liu, R., and Pantelides, C. P., 2013, "Shear Strength of GFRP Reinforced Precast Lightweight Concrete Panels," *Construction and Building Materials*, V. 48, pp. 51-58. doi: 10.1016/j.conbuildmat.2013.06.057

Mehany, S.; Mohamed, H. M.; and Benmokrane, B., 2021, "Contribution of Lightweight Self-Consolidated Concrete (LWSCC) to Shear Strength of Beams Reinforced with Basalt FRP Bars," *Engineering Structures*, V. 231, Article No. 111758. doi: 10.1016/j.engstruct.2020.111758

Mousa, S.; Mohamed, H. M.; and Benmokrane, B., 2018, "Flexural Strength and Design Analysis of Circular Reinforced Concrete Members with Glass Fiber-Reinforced Polymer Bars and Spirals," *ACI Structural Journal*, V. 115, No. 5, Sept., pp. 1353-1364. doi: 10.14359/51702282

Pantelides, C. P.; Besser, B. T.; and Liu, R., 2012a, "One-Way Shear Behavior of Lightweight Concrete Panels Reinforced with GFRP Bars," *Journal of Composites for Construction*, ASCE, V. 16, No. 1, pp. 2-9. doi: 10.1061/(ASCE)CC.1943-5614.0000240

Pantelides, C. P.; Liu, R.; and Reaveley, L. D., 2012b, "Lightweight Concrete Precast Bridge Deck Panels Reinforced with Glass Fiber-Reinforced Polymer Bars," *ACI Structural Journal*, V. 109, No. 6, Nov.-Dec., pp. 879-888.

Perdikaris, P. C., and Beim, S., 1988, "RC Bridge Decks Under Pulsating and Moving Load," *Journal of Structural Engineering*, ASCE, V. 114, No. 3, pp. 591-607. doi: 10.1061/(ASCE)0733-9445(1988)114:3(591)

Youssef, M. H.; Ahmed, E. A.; and Benmokrane, B., 2019, "Structural Behavior of GFRP-RC Bridge Deck Slabs Connected with UHPFRC Joints under Flexure and Shear," *Journal of Bridge Engineering*, ASCE, V. 24, No. 9, p. 04019092. doi: 10.1061/(ASCE)BE.1943-5592.0001475

JOIN AN ACI Chapter!

The American Concrete Institute has Chapters and Student Chapters located throughout the world. Participation in a local chapter can be extremely rewarding in terms of gaining greater technical knowledge and networking with leaders in the concrete community.

Because chapters are distinct and independent legal entities, membership includes both ACI members and non-ACI members and is made up of a diverse blend of architects, engineers, consultants, contractors, educators, material suppliers, equipment suppliers, owners, and students—basically anyone interested in concrete. Many active ACI members initially became involved in ACI through their local chapter. In addition to technical programs and publications, many chapters sponsor ACI Certification programs, ACI educational seminars, project award recognition programs, and social events with the goal of advancing concrete knowledge.

Check out the Chapters Special Section from the November 2020 *Concrete International*: www.concrete.org/publications/concreteinternational.aspx

---

Student Chapters

Join or form an ACI Student Chapter to maximize your influence, knowledge sharing, and camaraderie! ACI has 240+ student chapters located throughout the world, each providing opportunities for students to:

- Connect with their peers and participate in concrete-related activities such as: student competitions, ACI Conventions, ACI Certification Programs, ACI Educational Seminars, local chapter meetings, social events, and community service projects;
- Network with members of local chapters, many of whom have been in the industry for decades and can help to develop professional relationships and offer career advice;
- Win recognition for their universities through the University Award; and
- Learn about the many scholarships and fellowships offered by the ACI Foundation and by ACI's local chapters.

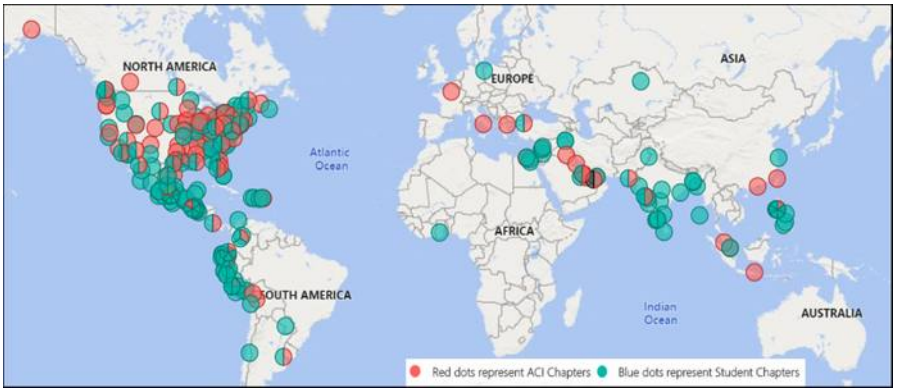

American Concrete Institute

www.concrete.org/chapters

ACI STRUCTURAL JOURNAL TECHNICAL PAPER

Title No. 120-S64

Progressive Collapse Response of Reinforced Concrete Assembly with Realistic Boundary Conditions

by Kai Qian, Guang-Tao Li, Dong-Qiu Lan, and Liu Jin

Previous studies on reinforced concrete (RC) beam-column subassemblies under a column removal scenario are helpful to understand the load-resisting mechanisms of RC structures against progressive collapse, but most of these studies failed to simulate actual boundary conditions, which were simplified as fixed boundaries to allow sufficient development of the load-resisting mechanisms. These studies were unable to reflect the response of joints and side columns under progressive collapse. To fill this gap, an experimental program on six half-scale beam-column subassemblies with joints and side columns was designed and tested to fully understand the effects of boundary conditions on the structural behavior of RC planar frames against progressive collapse. Three subassemblies were specially designed, while the other three were ordinarily designed to quantify the benefits of special detailing. The test results show that the effects of boundary conditions on the development of load-resisting mechanisms are marginal, whereas the effects of special detailing are significant. Specifically, specimens under a middle-column removal scenario and a penultimate-column removal scenario develop similar compressive arch action (CAA) capacities and catenary action (CA) capacities. The CAA capacity dominates the load resistance of specimens with ordinary detailing. In contrast, the CA capacity governs the load resistance of specimens with special detailing mainly due to the larger areas of longitudinal reinforcing bars and the greater rotation capacities of beam ends. However, boundary conditions can greatly affect the failure mode of specimens with ordinary detailing. Finally, an analytical study was performed to demonstrate the contributions of axial force and shear force to load resistance. According to test results and analytical analyses, RC frames with special detailing have sufficient rotational capacity to develop adequate tie forces to resist progressive collapse.

Keywords: boundary condition; progressive collapse; reinforced concrete (RC); special detailing.

INTRODUCTION

The structural engineering community first observed a new failure type due to the collapse of the Ronan Point apartment tower in 1968. Historically, progressive collapse of buildings mainly occurred in two types: the first collapse type is due to excessive lateral displacement induced by major earthquakes; and the second collapse type is due to the failure of vertical structural members caused by extreme loads, such as blasts, impacts, and fires. This study focused on the second collapse type. In practical design, it is impossible to accurately estimate the intensity of such extreme loads. Thus, in this study, the authors notionally removed one or more structural members and allowed for redistribution of the initial load suffered by the lost structural members to the surrounding structural components. Such a method—namely, the alternate load path method—is incorporated in the main design guidelines[1-3] for progressive collapse design and evaluation.

Relying on the alternative load path method, the behavior of a reinforced concrete (RC) frame under loss of column scenarios was investigated extensively. Lew et al.[4] tested two full-scale RC beam-column assemblies designed for Seismic Design Category C or D. The test results showed that changing the Seismic Design Category from C to D could substantially increase the load-carrying capacity of the RC beam-column assemblies due to the greater amount of longitudinal reinforcement and larger sectional dimensions. Yu and Tan[5] tested two half-scale RC beam-column assemblies with or without seismic detailing to study the effects of continuity of beam reinforcement on progressive collapse resistance. They found that Class A splice, as required by ACI 318-05,[6] can provide sufficient continuity under an edge-middle-column removal scenario. Qian and Li[7] tested a series of RC beam-column assemblies under a corner-column removal scenario. The test results indicate that specimens designed with seismic detailing are able to develop a greater flexural capacity to resist progressive collapse. Similarly, Choi and Kim[8] tested four small-scale beam-column assemblies under a near-edge-column removal scenario to quantify the benefits of seismic detailing for the progressive collapse resistance. They found that the assembly with seismic detailing can develop greater catenary action (CA).

Unfortunately, the aforementioned tests failed to demonstrate the behavior of joints and side columns because they were replaced by enlarged side columns to easily investigate the load-resisting mechanism and apply boundary conditions. Similar simplifications were adopted by many studies.[7,9-14] The effects of size and detailing of side columns on the behavior of RC beam-column assemblies to resist progressive collapse have not been investigated sufficiently. Thus, in this study, a series of six RC beam-column assemblies with ordinary or special detailing are tested under different column removal scenarios.

RESEARCH SIGNIFICANCE

The primary objective of this paper is to evaluate the effects of special detailing and side-column size on the

ACI Structural Journal, V. 120, No. 4, July 2023.

MS No. S-2021-489.R1, doi: 10.14359/51738718, received June 1, 2022, and reviewed under Institute publication policies.

Table 1—Specimen details

Test ID	Column size, mm (in.)		Beam reinforcement				Position of removed column	Details
			Ends		Middle			
	Depth	Width	Top	Bottom	Top	Bottom		
OM	250 (9.8)	250 (9.8)	3T10	2T10	2T10	2T10	Middle	Ordinary
OP	250 (9.8)	250 (9.8)	3T10	2T10	2T10	2T10	Penultimate	Ordinary
SM	250 (9.8)	250 (9.8)	3T12	2T12	2T12	2T12	Middle	Special
SP	250 (9.8)	250 (9.8)	3T12	2T12	2T12	2T12	Penultimate	Special
OM-S	220 (8.7)	220 (8.7)	3T10	2T10	2T10	2T10	Middle	Ordinary
OP-S	220 (8.7)	220 (8.7)	3T10	2T10	2T10	2T10	Penultimate	Ordinary

structural behavior and resistance of RC frames to resist progressive collapse. The test results may help structural researchers and engineers understand the behavior of beam-column assemblies with more realistic boundary conditions than those used in prior studies. The test results could help to refine existing design codes or guidelines for progressive collapse design.

EXPERIMENTAL PROGRAM

Specimen design

In this study, the prototype buildings were designed as ordinary moment frames and special moment frames in accordance with ACI 318-14.[15] The design dead load and live load are 5.5 and 2.0 kPa, respectively. A total of six half-scale beam-column assemblies were tested, as listed in Table 1. The specimens can be categorized into two groups: 1) M-series, presenting the frames losing the middle column (OM, SM, and OM-S); and 2) P-series, presenting the frames losing the penultimate column (OP, SP, and OP-S). As tabulated in Table 1, Specimens SM and SP are specially designed, whereas OM, OP, OM-S, and OP-S are ordinarily designed. The second letter represents the location of the removed column. For instance, "M" and "P" represent the loss of a middle column and a penultimate column, respectively. The ordinarily designed specimens are further classified; among them, OM-S and OP-S have identical beam sizes and detailing as OM and OP, but smaller side columns.

Figure 1 shows the dimensions and reinforcement details of the specimens subject to a penultimate-column removal scenario. These specimens include two beams, one removed column stub, and two side columns. One of the side columns has an overhanging beam to simulate horizontal restraints from interior bays. For Specimens OP and SP, the cross section of the column is 250 x 250 mm (9.8 x 9.8 in.), while for OP-S, the column is smaller, with a size of 220 x 220 mm (8.7 x 8.7 in.). The stable axial compressive force was applied on the top of the side columns to simulate the load transmitted from the superstructure, and the designed axial compression ratio was 0.31. The beam cross section is 250 x 150 mm (9.8 x 5.9 in.). As shown in the figure, Specimens OP-S and OP have identical reinforcement detailing. The top and bottom reinforcing bars of the beams are 3T10 and 2T10, respectively. The beam bottom longitudinal reinforcing bars were continuous. However, the curtailment is simulated for top reinforcing bars. The beam transverse reinforcing bars are R6 with a spacing of 150 mm (5.9 in.) throughout the whole beam span, and no transverse reinforcing bar is installed in the joints. In the exterior side joints, the beam longitudinal reinforcing bars are terminated with a 90-degree hook, which has a length of 150 mm (5.9 in.—that is, 15 times the reinforcing bar diameter). However, the beams of SP are reinforced by 3T12 at the top and 2T12 at the bottom. The transverse reinforcing bars are R6 at 50 mm (2.0 in.) and R6 at 100 mm (3.9 in.) in the beam ends and midspan, respectively. The length of the 90-degree hook in the exterior joint was 180 mm (7.1 in. and 15d, where d is the reinforcing bar diameter). Stirrups with a spacing of 50 mm (2.0 in.) are applied in the column, and three stirrups are applied in the joint zone. T12 and T10 herein denote deformed reinforcing bars with diameters of 12 mm (0.5 in.) and 10 mm (0.4 in.), respectively, while R6 represents plain reinforcing bars with a diameter of 6 mm (0.2 in.). Notably, the details of the M-series specimens have similar reinforcement detailing and dimensions as their counterparts, except that both side columns have overhanging beams, which are symmetric.

Based on cylinder tests, the average compressive strength of concrete used in OM-S, OP-S, OM, and OP is 36 MPa (5.2 ksi) as they are cast in the same batch. However, the average compressive strength of concrete of SM and SP is 39 MPa (5.7 ksi). Moreover, the reinforcement properties are measured and listed in Table 2.

Test setup and instrumentation

A typical test setup for the six specimens is illustrated in Fig. 2. A series of horizontal chain poles were connected to the top of the side column and the overhanging beam to simulate horizontal restraints from interior bays. The bottom of each side column was connected to the ground by a pin support. Notably, the pin support and the horizontal restraints for the side column were deliberately designed to simulate the contraflexural points of the side column. A hydraulic jack (Item 1 in Fig. 2(a)) was used to apply a vertical displacement on the top of the removed column stub. Moreover, a stable axial compressive force was applied at the top of the side columns by a hydraulic jack (Item 7 in Fig. 2(a)). A steel assembly (Item 3 in Fig. 2(a)) was installed to prevent undesired out-of-plane failure of the specimens. The applied vertical load was measured by a load cell (Item 2 in Fig. 2(a)). The horizontal reaction force was measured by tension/compression load cells (Item 6 in Fig. 2(a)), which were installed in the chain poles. The vertical and

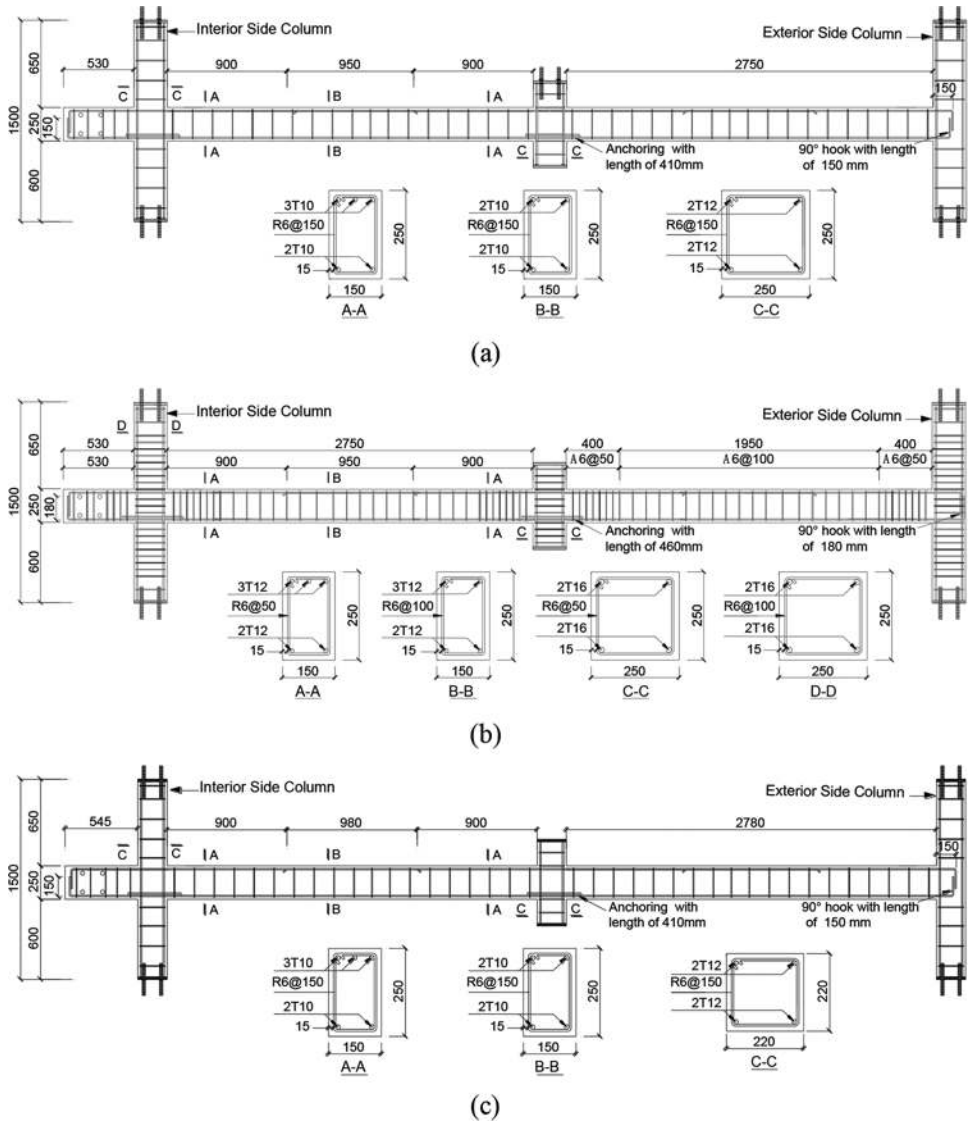

Fig. 1—Details of P-series frames: (a) OP; (b) SP; and (c) OP-S. (Note: Units in mm; 1 mm = 0.039 in.)

Table 2—Material properties of reinforcing bars

Item	Yield load capacity, MPa (ksi)	Ultimate strength, MPa (ksi)	Elastic modulus, MPa (ksi)	Elongation, %
R6	368 (53.4)	485 (70.3)	162,000 (23,496.1)	20.1
T10	532 (77.2)	663 (96.2)	200,241 (29,042.5)	12.7
T12	462 (67.0)	596 (86.4)	171,000 (24,801.5)	14.7
T16	466 (67.6)	604 (87.6)	182,000 (26,396.9)	17.0

Note: R6 represents plain bar with diameter of 6 mm (0.24 in.); T10, T12, and T16 represent deformed reinforcing bars with diameters of 10, 12, and 16 mm (0.39, 0.47, and 0.63 in.), respectively.

horizontal reaction forces at the bottom of the side column were measured by the load pin for each pin support. The deflection of the specimens was measured by a series of linear variable displacement transducers (LVDTs) (Items 5 and 6 in Fig. 2(a)).

TEST RESULTS

To evaluate the behavior of RC assemblies with more realistic boundary conditions and the effects of special design, six assemblies were tested by a pushdown loading regime. The main results are summarized in Table 3 and described as follows.

Global behavior

OM—The measured vertical load-displacement curves of the specimens are shown in Fig. 3(a). For OM, a yield load (YL) of 35 kN (7.9 kip) was reached at a displacement of 22 mm (0.9 in.). At this stage, several flexural cracks formed in the beam ends. The first peak load (FPL) of 45 kN (10.1 in.) was measured at a displacement of 73 mm (2.9 in.). Beyond this point, the further extension of cracks and crushing of concrete led to a drop in load capacity. At displacements of 150, 200, and 250 mm (5.9, 7.9, and 9.8 in.), reinforcing bar fracture occurred at the bottom of the beam end near the removed column in sequence, which led to a sharp drop in load capacity. When the displacement was increased to 275 mm (10.8 in.), reinforcing bar fracture occurred at the top of the beam end near the side columns. After that, two top reinforcing bars at the beam end near the removed column fractured at displacements of 360 and 410 mm (14.2 and 16.1 in.), respectively. At a displacement

Table 3—Critical test results

Test ID	Critical displacements, mm (in.)			Critical loads, kN (kip)			MCHF in interior/ exterior, kN (kip)	MTHF in interior/ exterior, kN (kip)	F_p, kN (kip)
	YL	FPL	UL	YL	FPL	UL			
OM	22 (0.9)	73 (2.9)	532 (20.9)	35 (7.9)	45 (10.1)	40 (9.0)	–82 (–18.4)	102 (22.9)	N/A
OP	30 (1.2)	70 (2.8)	552 (21.7)	33 (7.4)	42 (9.4)	33 (7.4)	–76/–61 (–17.1/–13.7)	90/73 (20.2/16.4)	63 (14.2)
SM	30 (1.2)	70 (2.8)	659 (25.9)	42 (9.4)	53 (11.9)	79 (17.8)	–99 (–22.3)	167 (37.5)	63 (14.2)
SP	27 (1.1)	76 (3.0)	665 (26.2)	40 (9.0)	51 (11.5)	74 (16.6)	–81/–69 (–18.2/–15.5)	153/143 (34.4/32.1)	63 (14.2)
OM-S	20 (0.8)	79 (3.1)	590 (23.2)	29 (6.5)	42 (9.4)	33 (7.4)	–82 (–18.4)	89 (20)	63 (14.2)
OP-S	25 (1.0)	90 (3.5)	438 (17.2)	32 (7.2)	40 (9.0)	28 (6.3)	–72/–52 (–16.2/–11.7)	77/62 (17.3/13.9)	N/A

Note: YL is yield load capacity; FPL is first peak load capacity; UL is ultimate load capacity; MCHF is maximum compressive horizontal reaction force; MTHF is maximum tensile horizontal reaction force; F_p is required peripheral tie force; N/A is not available.

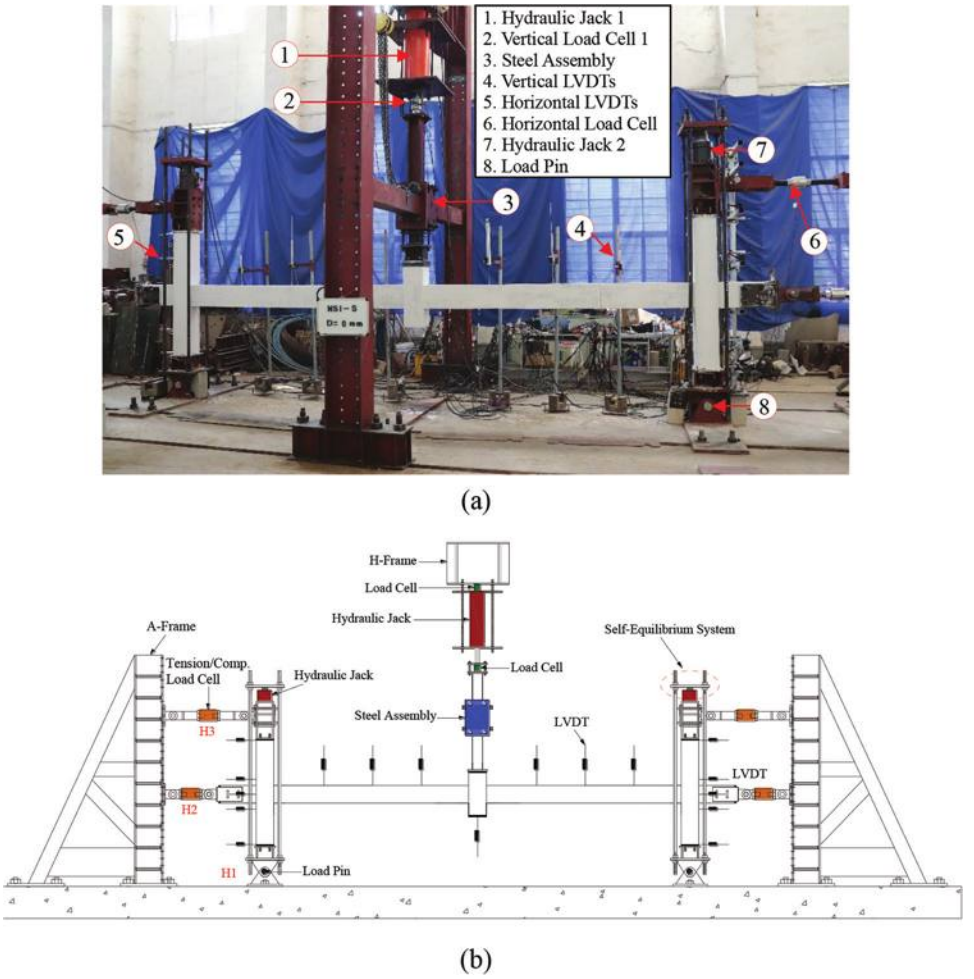

Fig. 2—Test setup and instrumentation: (a) photo; and (b) schematic view.

of 361 mm (14.2 in.), the load capacity reascended because of the onset of CA that developed in the remaining longitudinal reinforcing bars. Further increasing the displacement to 532 mm (20.9 in.), the ultimate load (UL) of 40 kN (9.0 kip) was measured. Subsequently, the concrete was severely crushed, and the reinforcing bars at the top of the beam end near the side columns fractured one by one. Particularly, the reinforcing bar fracture that occurred at the bottom of the beam near the right-side column caused a drop in the load capacity from 30 to 12 kN (6.7 to 2.7 kip). Finally, OM failed because all the reinforcing bars at the top of the beam end near the side columns fractured at a displacement of 590 mm (23.2 in.). The failure mode of OM is shown in Fig. 4. Wide cracks and reinforcing bar fracture occurred at the bottom of the beam end near the removed column and at the top of the beam end near the side column. Severe concrete crushing occurred in the compressive zones of the beam ends, while slight damage occurred in the side columns. Many cracks occurred along the beam span, which indicates that the beam is under tension.

OP—For OP, a YL of 33 kN (7.4 kip) was measured at a displacement of 30 mm (1.2 in.). At a displacement of 70 mm (2.8 in.), an FPL of 42 kN (9.4 kip) was measured, which was 7% lower than that of OM. After this point, the

load capacity began to drop due to the formation and extension of cracks in the beam ends as well as the crushing of concrete. When the displacement reached 125 mm (4.9 in.), the first fracture of the reinforcing bar occurred at the bottom of the beam end near the removed column. Severe concrete crushing occurred at a displacement of 160 mm (6.3 in.). Moreover, at displacements of 163 and 250 mm (6.4 and 9.8 in.), reinforcing bar fracture occurred at the bottom of the beam end near the removed column in sequence. Reinforcing bar fracture occurred at the top of the beam near the exterior side column and the interior side column at displacements of 255 and 356 mm (10.0 and 14.0 in.), respectively. At a displacement of 331 mm (13.0 in.), the load capacity reascended because of the kicked-in CA, while the CA capacity of 33 kN (7.4 kip), also known as UL, was measured at a displacement of 552 mm (21.7 in.). Three flexural cracks extending from the exterior side to the interior side of the side column occurred at displacements of 50, 65, and 90 mm (2.0, 2.6, and 3.5 in.), respectively. A vertical crack occurred at the center of the exterior side column at a displacement of 480 mm (18.9 in.) and extended rapidly with increasing displacement due to the considerable tensile force in the longitudinal reinforcing bars. The failure mode of OP is illustrated in Fig. 5. Reinforcing bar fracture and severe concrete crushing occurred at the bottom and top of the beam end near the removed column, respectively. A large number of penetrating cracks were distributed along the beams. Wide cracks and reinforcing bar fractures occurred at the top of the beam end near the side columns. Long flexural cracks formed at the exterior side column, the damage of which was more severe than that of the side column of OM.

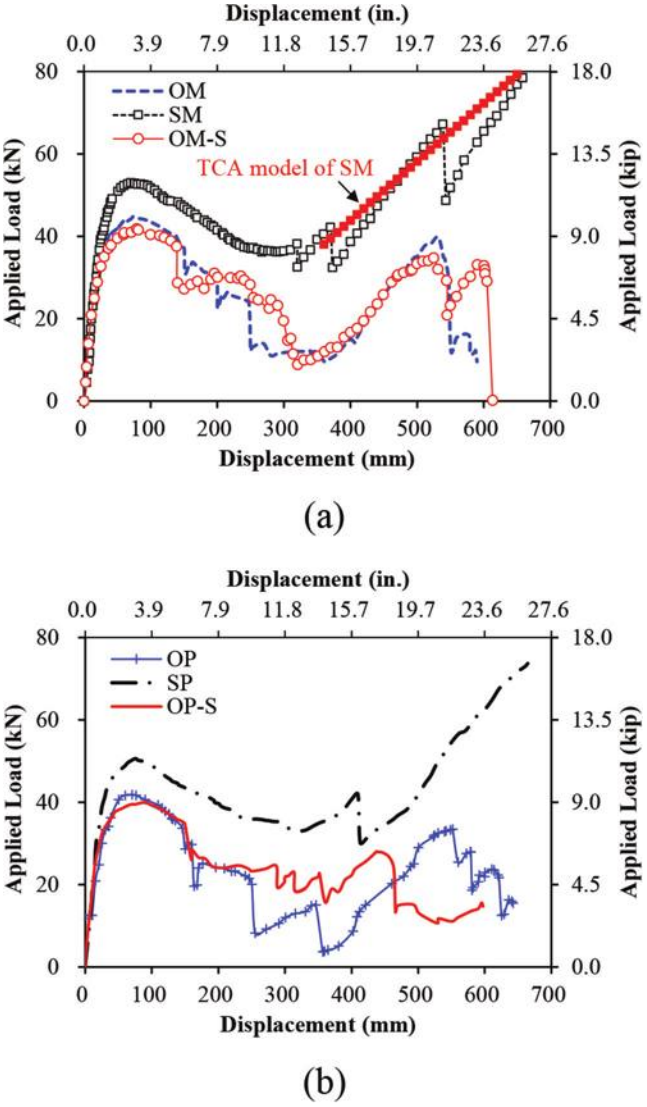

Fig. 3—Comparison of load-displacement curves: (a) M-series; and (b) P-series.

SM—Specimen SM has identical geometric dimensions to those of OM but includes special detailing. The YL and FPL of SM were 42 kN (9.4 kip) and 53 kN (11.9 kip), respectively. As a result of special detailing, the YL and FPL of SM were 120% and 118% of those of OM, respectively. Compared with OM, the CA of SM mobilized at an earlier displacement of 300 mm (11.8 in.) because of no premature fracture of the reinforcing bar. Two reinforcing bars at the bottom of the beam end near the removed column fractured at displacements of 320 and 370 mm (12.6 and 14.6 in.), respectively. When the displacement was further increased to 538 mm (21.2 in.), another two reinforcing bars at the bottom of the beam end near the removed column fractured. After that, the load capacity continued to rise because of the development of CA. This indicates that the special

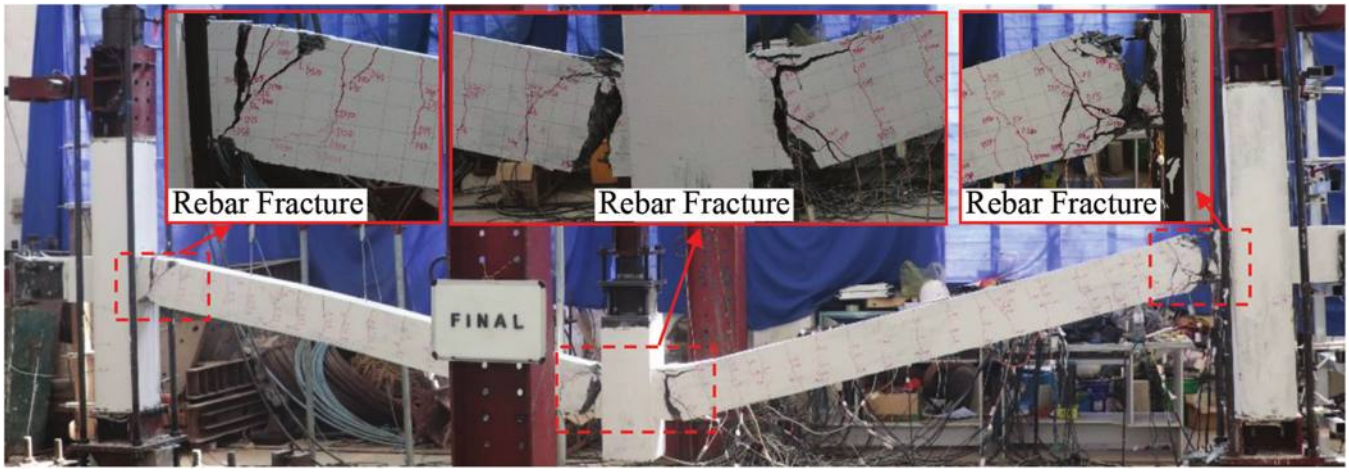

Fig. 4—Failure mode of OM.

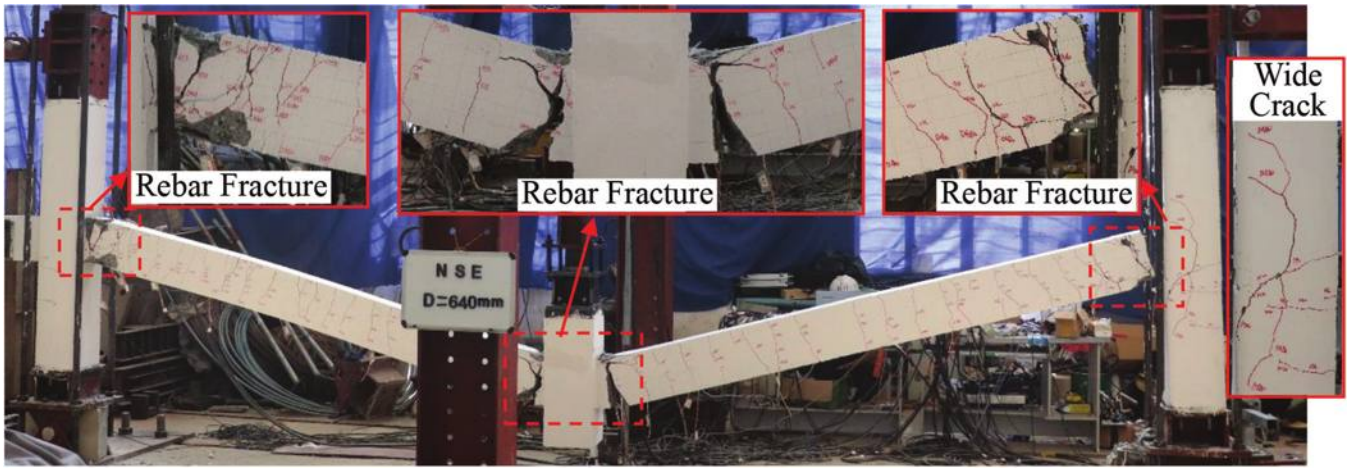

Fig. 5—Failure mode of OP.

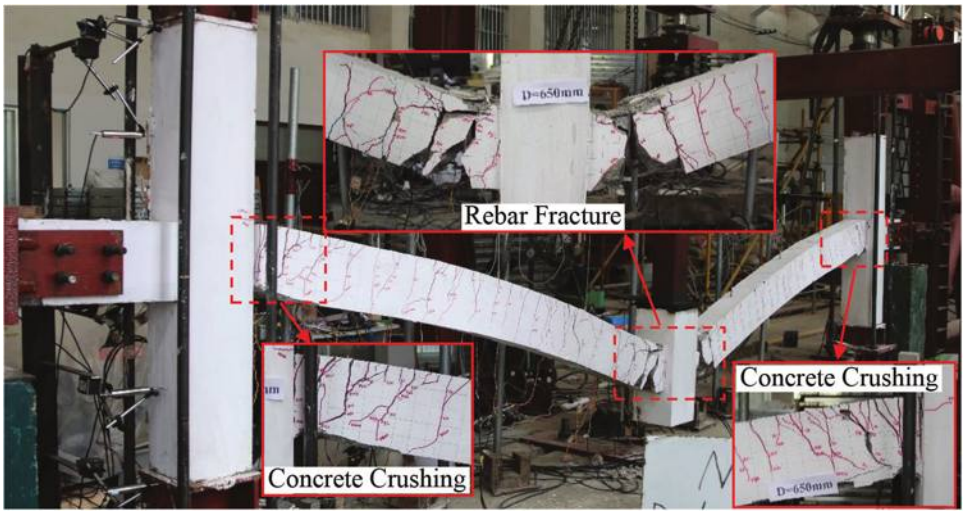

Fig. 6—Failure mode of SM.

design specimen could effectively develop CA even though partial longitudinal reinforcing bars fractured. As a result of the limitation of stroke capacity, the test was stopped at a displacement of 659 mm (25.9 in.). At this point, the UL of 79 kN (17.8 kip) was measured, which was 198% of that of OM. The failure mode of SM is shown in Fig. 6. Several wide penetrating cracks formed along the beams, and fracture of the bottom reinforcing bar and concrete crushing occurred at the beam end near the removed column, which was more severe than that of OM. However, damage at the beam end near the side columns was milder than that of OM.

SP—As shown in Fig. 3(b), the YL and FPL of SP were measured as 40 and 51 kN (9.0 and 11.5 kip), respectively. Thus, the YL and FPL of SP were 21% and 21% higher than those of OP, respectively. The test was stopped at a displacement of 665 mm (26.2 in.) due to the limitation of stroke capacity, and a load capacity of 74 kN (16.6 kip) was measured. Thus, the UL was 124% higher than that of OP. Different from OP, the first flexural crack in the side column occurred at a large displacement of 380 mm (15.0 in.), then the number of cracks continued to increase during the remaining loading steps. Two reinforcing bars at the top of the beam end near the removed column fractured at a displacement of 409 mm (16.1 in.), which resulted in a drop in the load capacity from 42 to 30 kN (9.4 to 6.7 kip). The failure of SP is shown in Fig. 7, and the damage in the right-side beam was more severe than that in the left-side beam. Reinforcing bar fractures and severe concrete crushing occurred in the beam end near the right side of the removed column, while no reinforcing bar fracture was observed at the left-side beam. Moreover, many flexural cracks occurred at the side columns.

OM-S—For OM-S, the YL of 29 kN (6.5 kip) was measured at a displacement of 20 mm (0.8 in.). When the displacement was increased to 79 mm (3.1 in.), the FPL of 42 kN (9.4 kip) was measured, which was 7% lower than that of OM. After this point, the load capacity was reduced due to concrete crushing at the beam end near the removed column. When the displacement was further increased to 140 mm (5.5 in.), reinforcing bar fracture was first observed at the bottom of the beam end near the removed column, while the second reinforcing bar fracture occurred at the bottom of the beam end near the removed column at a displacement of 300 mm (11.8 in.). When the displacement reached 320 mm (12.6 in.), the load-carrying capacity reascended because of the development of CA. With increasing displacement, more

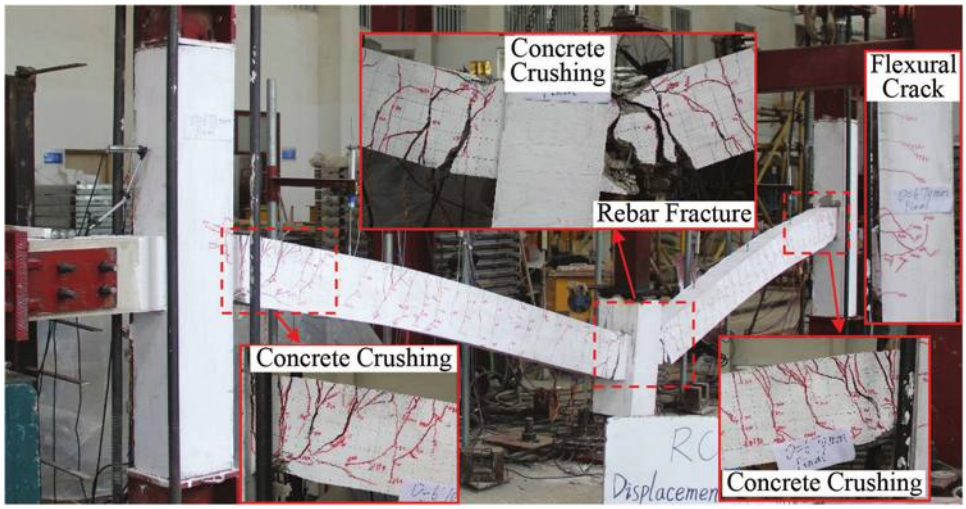

Fig. 7—Failure mode of SP.

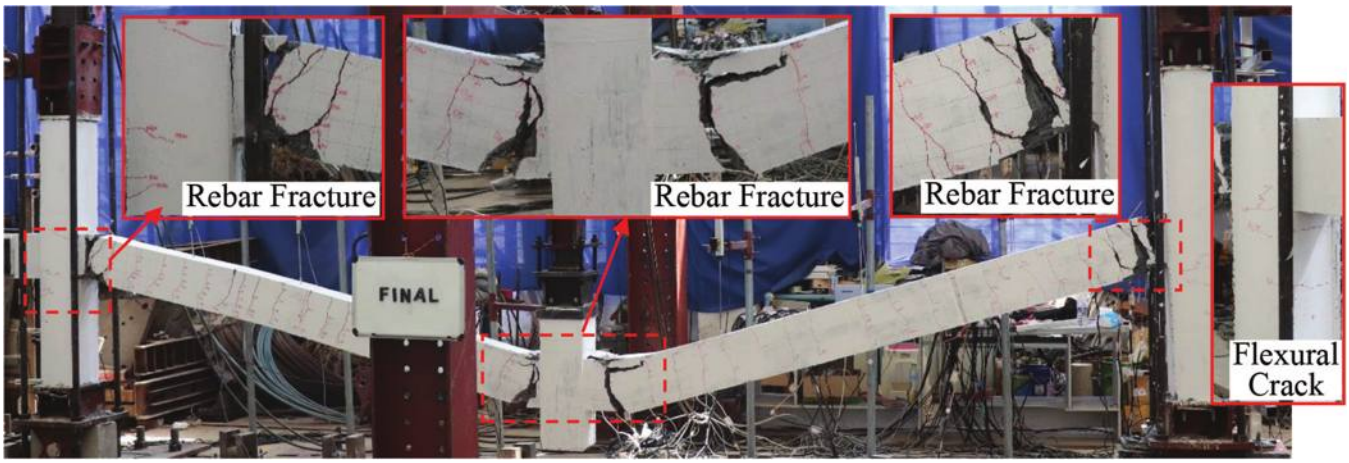

Fig. 8—Failure mode of OM-S.

cracks were generated at the top of the beam end near the side columns, and reinforcing bar fracture first occurred at the top of the beam end near the side column at a displacement of 516 mm (20.3 in.). Then, the second reinforcing bar fracture occurred at the top of the beam end-left side column interface at a displacement of 545 mm (21.5 in.). The UL of 33 kN (7.4 kip) was measured at a displacement of 590 mm (23.2 in.). Thus, the UL of OM-S was 18% lower than that of OM. As shown in Fig. 8, the damage of OM-S was mainly concentrated in the beams, including the fracture of reinforcing bars, the occurrence of wide penetrating cracks, and severe concrete crushing. However, the maximum width of the flexural cracks in the side column is only 0.5 mm.

OP-S—For OP-S, a YL of 32 kN (7.2 kip) was measured at a displacement of 25 mm (1.0 in.). At a displacement of 90 mm (3.5 in.), an FPL of 40 kN (9.0 kip) was measured, which was 5% lower than that of OP. When the displacement reached 125 mm (4.9 in.), a wide penetrating crack and the first reinforcing bar fracture occurred at the bottom of the beam end near the removed column. The second reinforcing bar fracture occurred at this zone at a displacement of 190 mm (7.5 in.). Upon further increasing the displacement, three reinforcing bars fractured successively at the beam near the exterior side column. However, reinforcing bar fracture occurred at the top of the beam end near the interior side column at a displacement of 466 mm (18.3 in.). The UL of 28 kN (6.3 kip) was measured at a displacement of 438 mm (17.2 in.). The first crack on the exterior side column occurred at a displacement of 220 mm (8.7 in.), which expanded from exterior to interior. The second crack from the exterior to the interior occurred on the exterior side column at a displacement of 420 mm (16.5 in.) and expanded rapidly at displacements of approximately between 460 and 480 mm (18.1 and 18.9 in.). As shown in Fig. 9, unlike OM-S, the asymmetric failure mode was observed in OP-S due to insufficient horizontal restraints at the exterior side column. All the tensile reinforcing bars in the bottom of the beam near the right side of the removed column fractured, and severe concrete crushing was observed at the top of this beam end. However, for the left-side beam, only one reinforcing bar fractured at the top of the beam end near the interior column. Asymmetric boundary restraints led to welding failure and further damage to the removed column stub. Due to the tension in the reinforcing bars, wide cracks occurred in the exterior side column, and the damage was much more severe than that in the interior side column of OM-S.

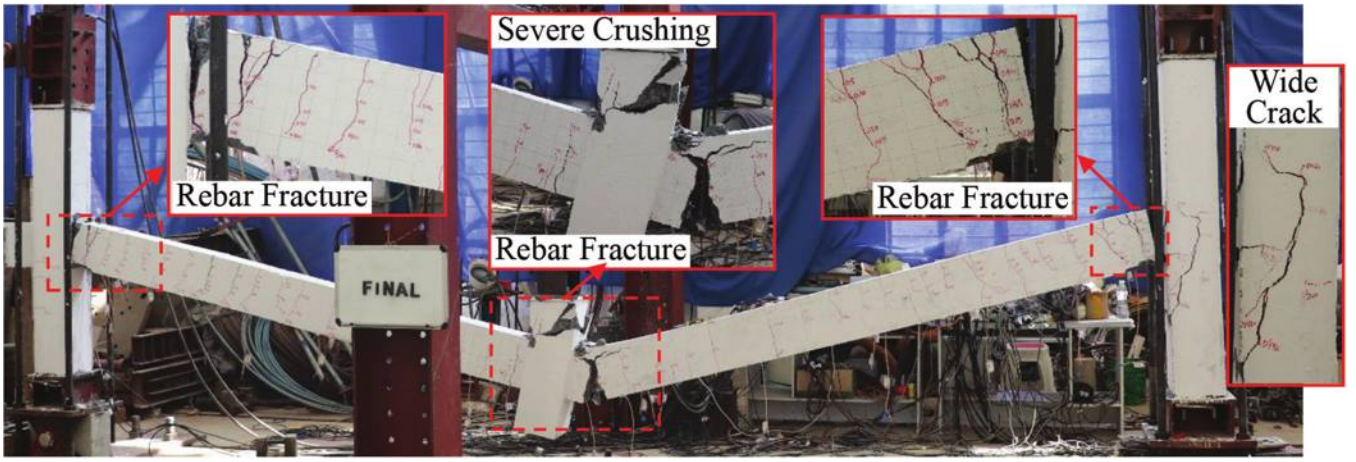

Fig. 9—Failure mode of OP-S.

Horizontal reaction force

Figures 10(a) to (c) show the total horizontal reaction force-vertical displacement curves of the specimens. As shown in the figures, the compressive horizontal reaction force was measured first due to the mobilization of compressive arch action (CAA) at the small deformation stage. The compressive horizontal reaction force was decreased to zero and began to transfer to the tensile horizontal reaction force when CA was mobilized. As a result of sufficient restraints, the peak value of compressive/tensile horizontal reaction forces of specimens under the removal of a middle column was higher than that of specimens under the removal of a penultimate column. For the specimens under penultimate-column removal, the total horizontal reaction forces at both ends were not exactly equal because of the horizontal restraints provided by the steel assembly above the column stub, while the total horizontal reaction force on the interior side was slightly greater than that on the exterior side. Figure 10(d) shows the reaction force of each horizontal restraint of OM. At the small deformation stage, the largest compressive horizontal reaction force was transferred from the bottom of the side column, while the majority of the tensile horizontal reaction force was provided by the restraint of the overhanging beam at the CA stage. Moreover, the horizontal reaction force in the overhanging beam was most sensitive to reinforcing bar fracture.

Deformation measurements

Figure 11 shows the beam deformation shape of SP at different stages. At the small deformation stage, the deformation of the beam was almost straight and symmetrical. However, asymmetric deformation was observed after the fracture of the reinforcing bar, while the slope of the beam near the middle column was larger than that near the side column. Figure 12 shows the horizontal movement of the side columns of SP. Because of the mobilization of CAA, the outward movement was measured at the small deformation stage. The outward movement began to transfer to inward movement at a displacement of approximately 300 mm (11.8 in.). Due to the absence of the overhanging beam, the exterior side column experienced larger inward movement than the interior side column. Moreover, the largest movement occurred at the height of the axis of the beams. Figure 13 shows the rotation of the beam end of OP and the schematic diagram, which includes the method used to calculate it. The rotation can be calculated by Eq. (1)

$$\theta = \arctan\left|\frac{\Delta_{top} - \Delta_{bot}}{d}\right| \approx \left|\frac{\Delta_{top} - \Delta_{bot}}{d}\right| \quad (1)$$

where θ is the rotation of the beam end; Δ_{top} and Δ_{bot} are readings of LVDTs installed horizontally on the top and bottom of beam ends, respectively; and d is the distance between the two horizontal LVDTs. As shown in the figure, the rotation of the beam ends of the exterior beam was close to chord rotation, which indicates that the exterior beam showed linear deformation during the loading process, in good agreement with the failure mode in Fig. 5. The largest rotation was observed in the beam end near the left of the removed column, which was larger than the chord rotation, while the smallest rotation occurred in the beam end near the interior side column. At a displacement of 500 mm (19.7 in.), significant rotation growth was observed in the beam end near the interior side column due to fracture of the reinforcing bar.

ANALYTICAL STUDY AND DISCUSSION

Effects of boundary condition

As tabulated in Table 3, the FPLs of OM, SM, and OM-S were 7, 4, and 5% higher than those of OP, SP, and OP-S, respectively. Thus, the boundary condition had little effect on the CAA capacity. However, the ULs of OM, SM, and OM-S were 21, 7, and 18% higher than those of OP, SP, and OP-S, indicating that boundary conditions have a significant effect on the CA capacity of specimens without special detailing but have a marginal effect on the CA capacity of specimens with special detailing. Moreover, the ULs of OM, OP, SM, SP OM-S, and OP-S were obtained at placements of 532, 552, 659, 665, 590, and 438 mm (20.9, 21.7, 25.9, 26.2, 23.2, and 17.2 in.), respectively. Thus, the deformation capacities of OM and SM were similar to that of OP and SP, respectively, while for the specimens with smaller side columns, the deformation of OM-S was 35% higher than that of OP-S because the exterior side column of OP-S suffered severe damage. Comparing OM and OM-S

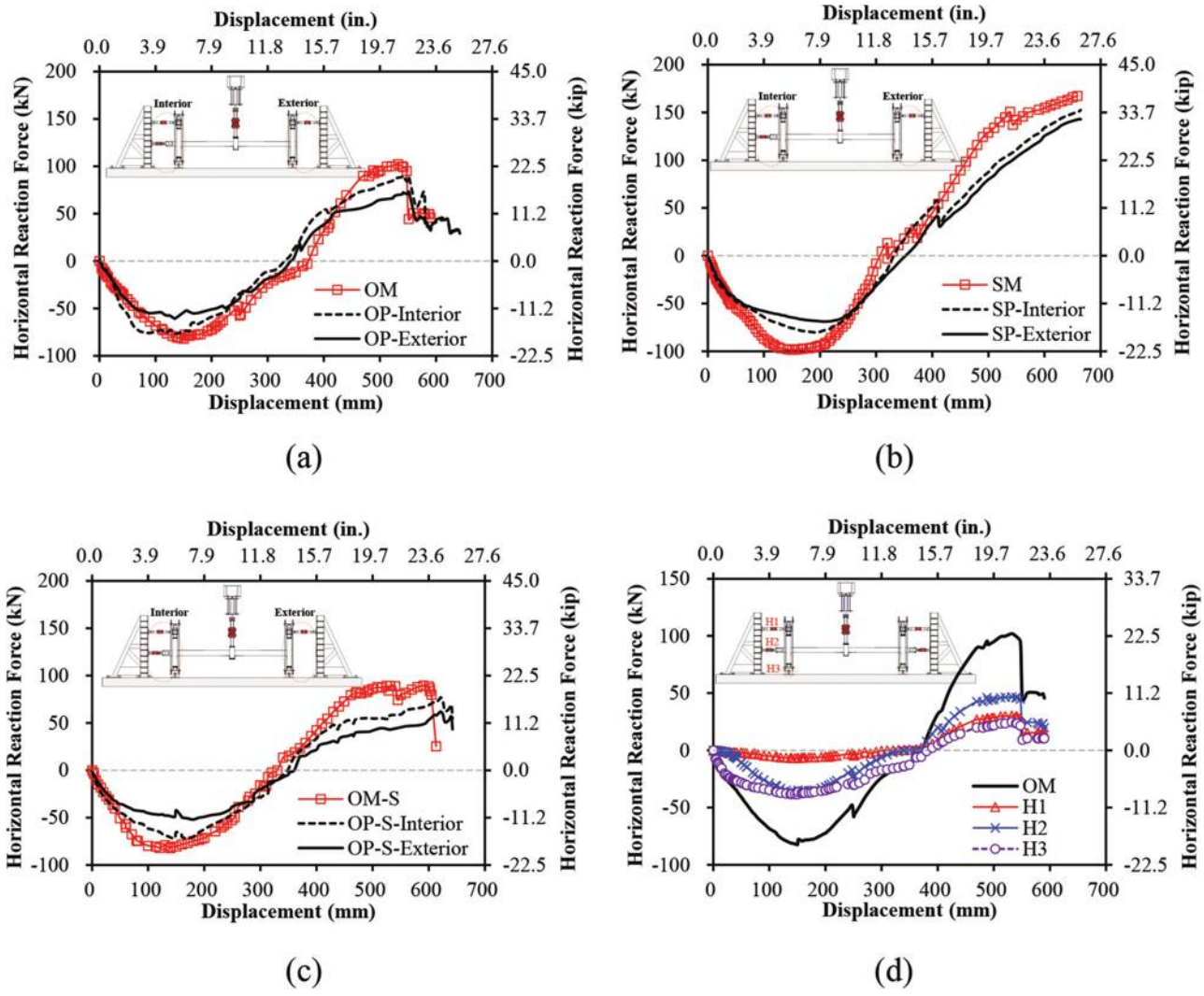

Fig. 10—Horizontal reaction force-displacement curves: (a) OM and OP; (b) SM and SP; (c) OM-S and OP-S; and (d) OM.

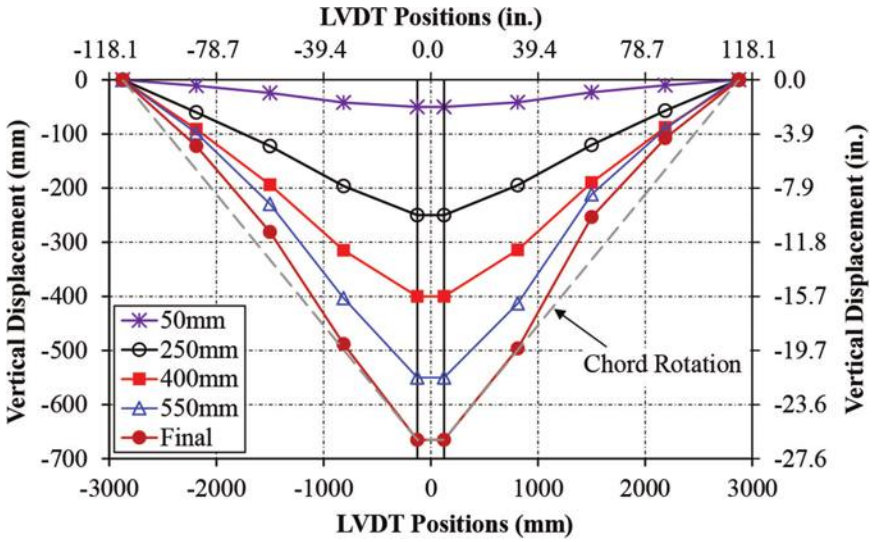

Fig. 11—Deflection shape of beams of SP at various stages.

demonstrates that enlarging the width of columns from 220 to 250 mm (from 8.7 to 9.8 in.) could increase the FPL and UL by 7% and 21%, respectively. Similarly, the FPL and UL of OP were 5 and 18% higher than those of OP-S. As seen in Fig. 4 to 9, the failure modes of specimens under a middle-column removal scenario were symmetric. In comparison, the specimens under a penultimate-column removal scenario had an asymmetric failure mode. The exterior side joints

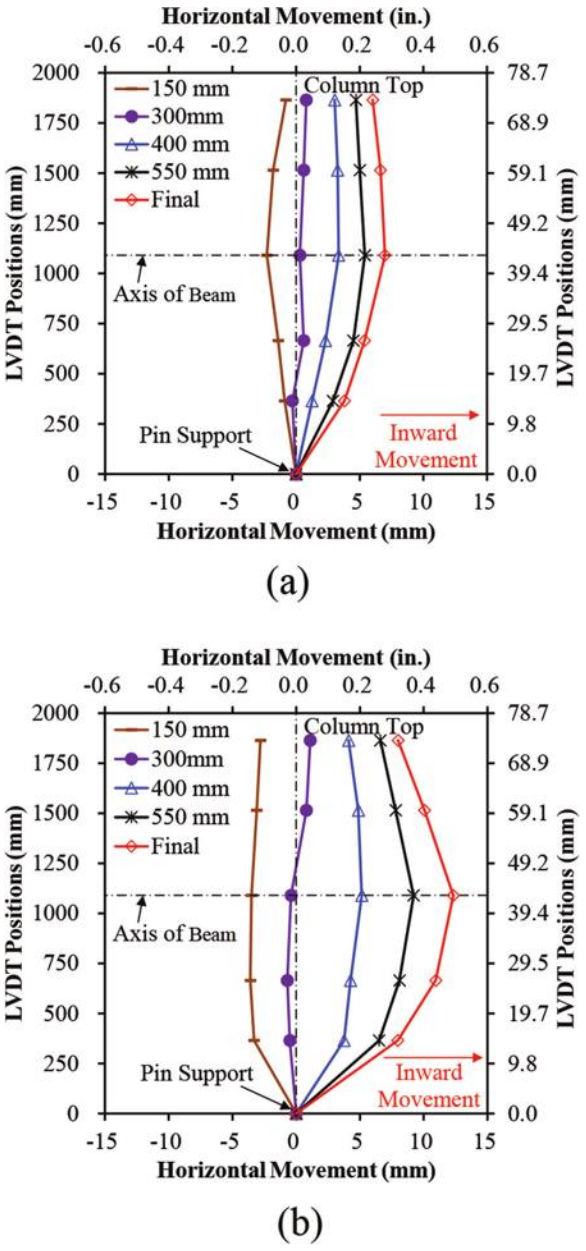

Fig. 12—Horizontal drift in columns of SP: (a) interior side column; and (b) exterior side column.

and columns experienced much more severe damage than the interior joints and columns. This is because the tension developed in the reinforcing bars tended to pull the side columns inward, but the exterior side column had neither adequate horizontal restraints nor transverse reinforcing bars in the joints to confine damage.

Effects of special detailing

Compared with OM and OP, the FPLs of SM and SP were 18% and 21% higher, respectively, mainly because of the greater reinforcement ratio. The ULs of OM, OP, SM, and SP were 40, 33, 79, and 74 kN (9.0, 7.4, 17.8, and 16.6 in.), respectively, which were obtained at displacements of 532, 552, 659, and 665 mm (20.9, 21.7, 25.9, and 26.2 kip), respectively. The UL of SM and SP was obtained when the stroke capacity reached its stroke capacity. It was believed that SM and SP could achieve higher ULs and deformation

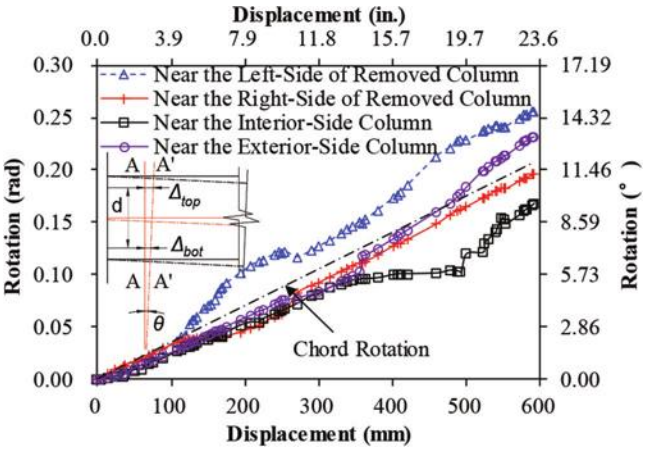

Fig. 13—Rotation of beam end of OP.

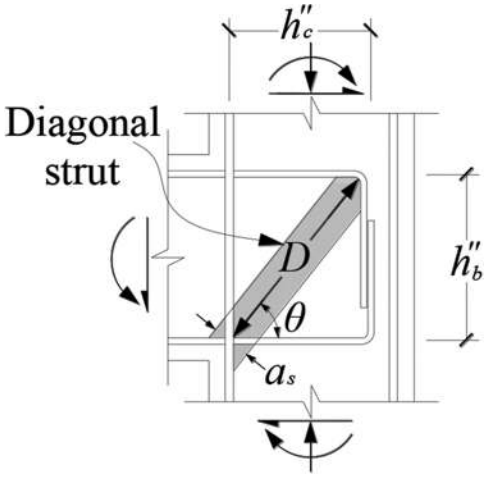

Fig. 14—Strut-and-tie model.

capacities if the jack with a higher stroke capacity was used for the tests. Therefore, the ULs of SM and SP were 98% and 121% higher than those of OM and OP, respectively. Moreover, special detailing increased the deformation capacity of OM and OP by over 24% and 20%, respectively.

During the tests, no pullout occurred in the beam reinforcing bars, and thus it was concluded that the development length of the 90-degree hook can meet the anchorage requirement of the beam longitudinal reinforcing bar. Figure 14 illustrates the strut-and-tie model of the exterior side column in typical P-series specimens. Based on the strut-and-tie model proposed by Hwang and Lee,[16] the shear strength of the exterior joint of Specimens OP, SP, and OP-S was 304, 504, and 235 kN (68.3, 113.3, and 79.1 kip), respectively. However, the shear force of the exterior joint of Specimens OP, SP, and OP-S was 112, 141, and 112 kN (25.2, 31.7, and 25.2 kip), respectively. Thus, the exterior joints had sufficient shear strength to prevent shear failure in a relatively small deformation stage, which agrees with the test results well (refer to Fig. 15). Figure 16 shows the load-transfer path of the exterior side column at the CA stage by truss model. Based on the truss model, the wide crack in the exterior joint of Specimens OP and OP-S was mainly attributed to the tension developed in the beam. In comparison, the exterior joint of the specimen with special detailing

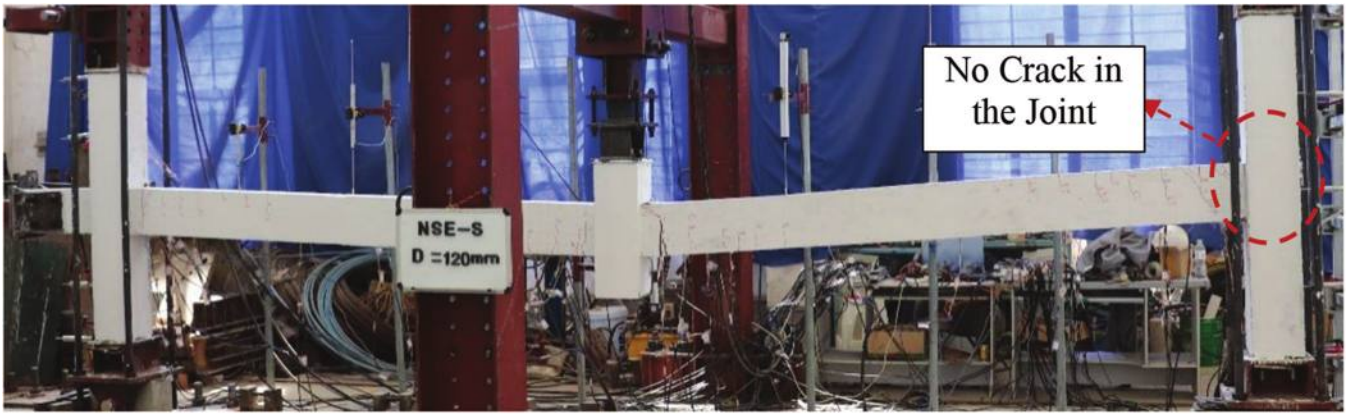

Fig. 15—Crack pattern of OP-S at displacement of 120 mm (4.7 in.).

experienced slight damage due to considerable confinement from the transverse reinforcement.

The ultimate chord rotations of specimens OM, OP, SM, SP, OM-S, and OP-S, which were defined as the ratio of middle joint displacement to beam clear span, were 0.19, 0.20, 0.24, 0.24, 0.21, and 0.16 rad, respectively. The plastic rotational capacities of beams in specially designed specimens SM and SP were greater than that of ordinarily designed specimens, indicating the benefits of special design detailing. The beams of specially designed specimens were capable of providing a 0.2 rad rotation, and thus the CA could be regarded as the second line against progressive collapse, as suggested by the U.S. Department of Defense (DoD).[2] However, the beams of ordinarily designed specimens OM and OP-S showed that the plastic rotational capacities are less than 0.2 rad. In addition, the CA capacity of ordinarily designed specimens is lower than their CAA capacities. Thus, the CA could not be considered the second defense line in resisting progressive collapse for the ordinarily designed specimens.

In summary, special detailing had a significant effect on the load resistance and deformation capacity of the specimens to resist progressive collapse. This is because higher reinforcing bar ratios were used in the special design, which can develop more tensile axial force and improve the rotational capacity of the beam ends. In conclusion, the load capacities of the specimens with special detailing are controlled by CA capacity, whereas those of the specimens without special detailing are controlled by CAA capacity.

Decomposition of load resistance

Figure 17 shows the static equilibrium of a section of the beam under loading. As given in the figure, the vertical applied load can be decomposed into the vertical projection of shear force and axial force, and the static equilibrium in the middle joint is mathematically expressed as

$$P = \sum_{j=1}^{2}(N_j \sin\theta_j + V_j \cos\theta_j) \quad (2)$$

where P is the applied load; N_j and V_j are the axial force and shear force transferred from the beams to the beam-column interfaces, respectively; and θ_j is the rotation of the beam section.

As shown in Fig. 18, the load-resisting mechanism was generally composed of beam action and CA, while the beam

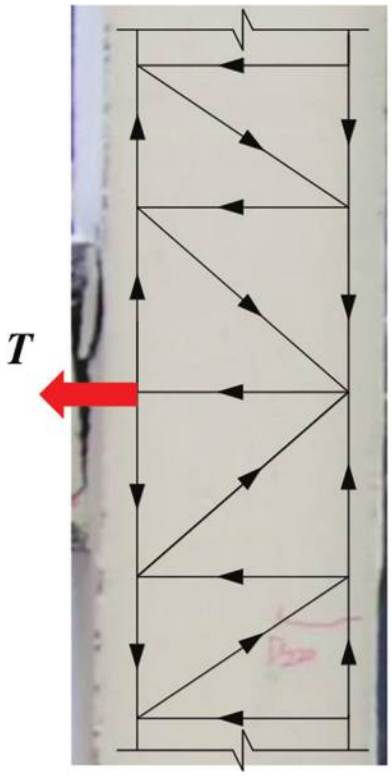

Fig. 16—Load-transfer path in exterior side column at CA stage.

action was further divided into flexural action and CAA. At the small deformation stage, shear force (bending moment) contributed the majority of the load resistance. At this stage, axial compression made a positive contribution by developing an additional plastic bending moment at the beam ends through axial force-bending moment interaction (namely, CAA). Subsequently, the axial force made a negative contribution because the negative contribution of the second-order effect induced by the axial compression surpassed the positive contribution (corresponding to load capacity softening) at the large deformation stage, and the negative contribution became positive, indicating the mobilization of CA. After this point, the contribution of the axial force increased while that of the shear force decreased when the displacement was further increased. The shear force dropped sharply when the fracture of the reinforcing

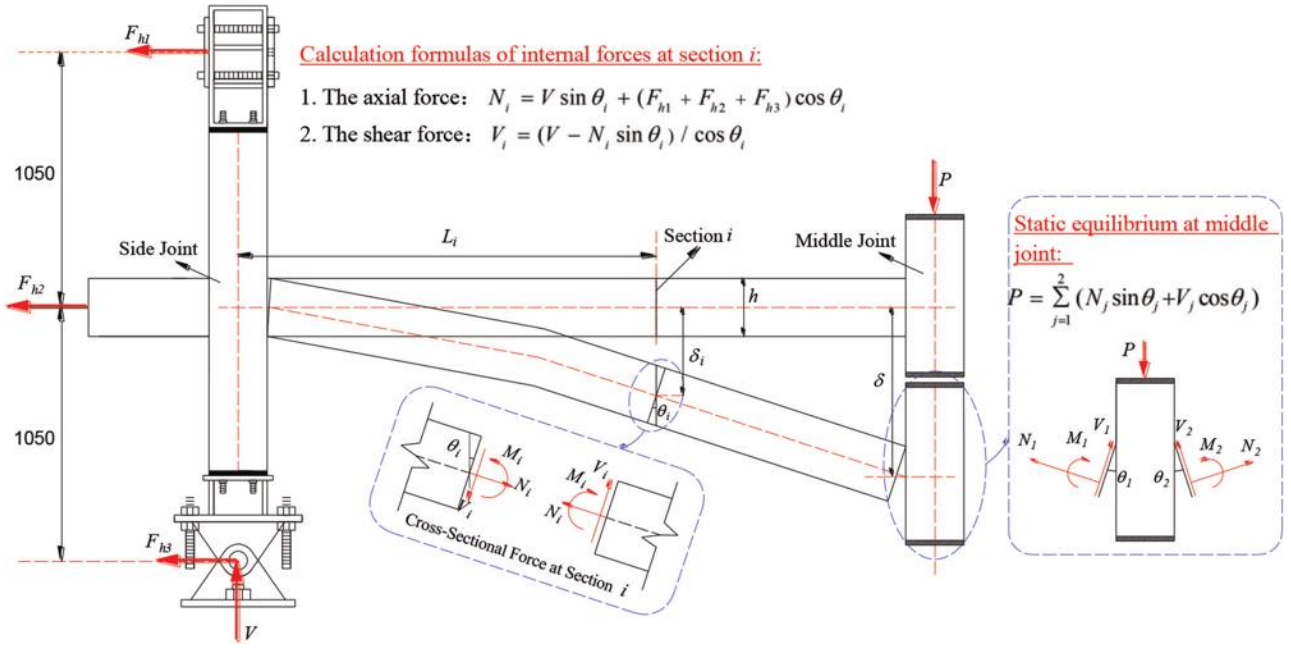

Fig. 17—Determination of internal forces.

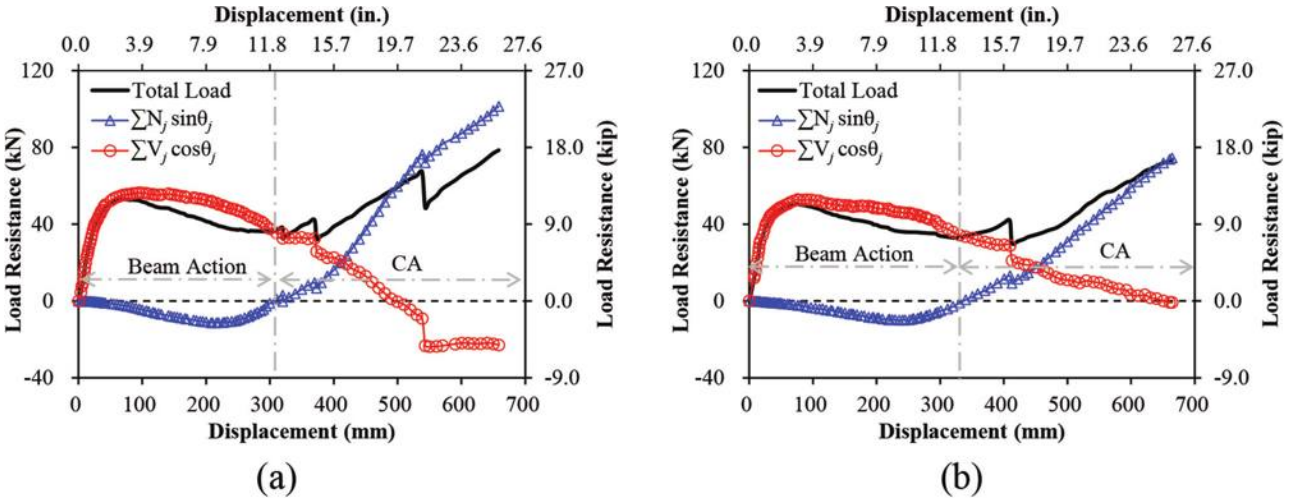

Fig. 18—Variation in internal forces at beam ends: (a) SM; and (b) SP.

bars occurred at the beam end near the removed column. Compared with SP, the shear force of SM was much lower at the large deformation stage due to multiple reinforcing bar fractures.

Dynamic progressive collapse resistance

Sudden column removal due to blast or vehicular impact is a dynamic event. Although quasi-static analysis has been proven to be a good method for progressive collapse investigation, it is still necessary to determine the dynamic response of the test specimens to accurately evaluate their progressive collapse resistance. Based on the work of Izzuddin et al.,[17] the quasi-static vertical load-displacement curve can be transferred to dynamic resistance by energy equilibrium. The energy equilibrium method is mathematically expressed as

$$P_d(u_d) = \frac{1}{u_d}\int_0^{u_d} P_{qs}(u)du \quad (3)$$

where $P_d(u)$ and $P_{qs}(u)$ are the dynamic load resistance and quasi-static load resistance at a specific displacement demand u, respectively.

As shown in Fig. 19, the dynamic resistances of OM, OP, SM, SP, OM-S, and OP-S were 39, 35, 48, 44, 36, and 35 kN (8.8, 7.9, 10.8, 9.9, 8.1, and 7.9 in.), respectively. Similar to the measurement in quasi-static tests, the dynamic resistance of the specimens with special detailing is obtained at the CA stage, whereas that of the specimens without special detailing is obtained at the CAA stage.

Tie force

The ultimate chord rotation, which was defined as the ratio of the ultimate displacement to the beam clear span, of OM, OP, SM, SP, OM-S, and OP-S was 0.19, 0.20, 0.24, 0.24, 0.21, and 0.16, respectively. According to the DoD,[2] CA can be considered a defense line against progressive collapse when a beam has the ability to show a rotational capacity

of 0.2 rad. The tie force requirements of DoD[2] are discussed herein, which are mathematically expressed as

$$F_p = 6W_F L_1 L_P \quad (4)$$

where W_F is the floor load (7.6 kN/m^2 [1.1 psi] as a result of the load combination of (1.2 DL + 0.5 LL)); L_1 is the distance between the centers of two adjacent columns; and L_P is the allowed floor width (0.91 m [35.8 in.] in DoD[2] and 0.46 m [18.1 in.] herein as half-scale frames).

The tie force requirements are listed in Table 3. The measured tie forces (UL herein) of ordinarily designed assemblies were lower than the required tie forces. Thus, it is unreliable to resist progressive collapse by the tie force method. However, assemblies with special detailing could provide sufficient tie force to resist progressive collapse.

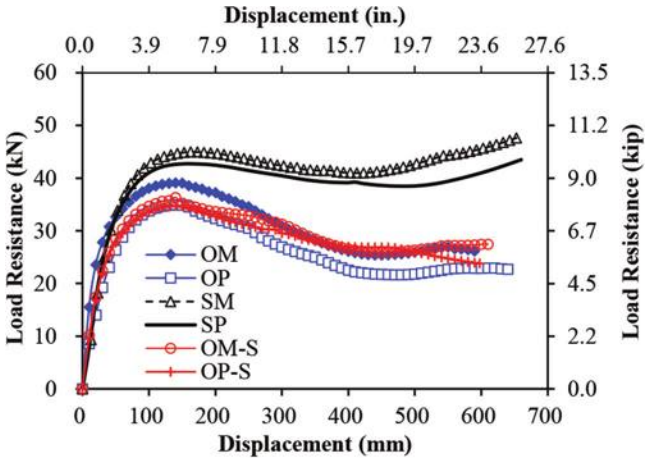

Fig. 19—Dynamic load resistance of specimens.

Assessment of reliability of existing CAA and CA models

As the first defense mechanism to prevent structural collapse, the development of CAA is the primary concern. To assess CAA capacity, analytical models were proposed by Yu and Tan[18] and Lu et al.[19] For the models, please refer to corresponding papers because of space limitations. To quantify the reliability of these models, the theoretical CAA capacity was compared with the measured capacity herein. As shown in Fig. 20(a) to (f), both analytical models reasonably predicted the CAA capacity of the specimens. However, Yu and Tan's model[18] was recommended because of its higher accuracy.

To facilitate practical applications of CA, a simplified model to predict the CA capacity was proposed in a previous work[14] and can be expressed as follows

$$P_{TCA} = 2f_u A_{st} \sin\theta \quad (5)$$

where f_u and A_{st} are the ultimate strength and area of the top reinforcement of the section near the removed column, respectively; and θ is the angle of the tensile force in the beam.

Because only the specially designed specimens showed a sufficient ability to develop a tie force, they were used to evaluate the reliability of the CA model. As shown in Fig. 3(a), the calculated results agreed well with the test

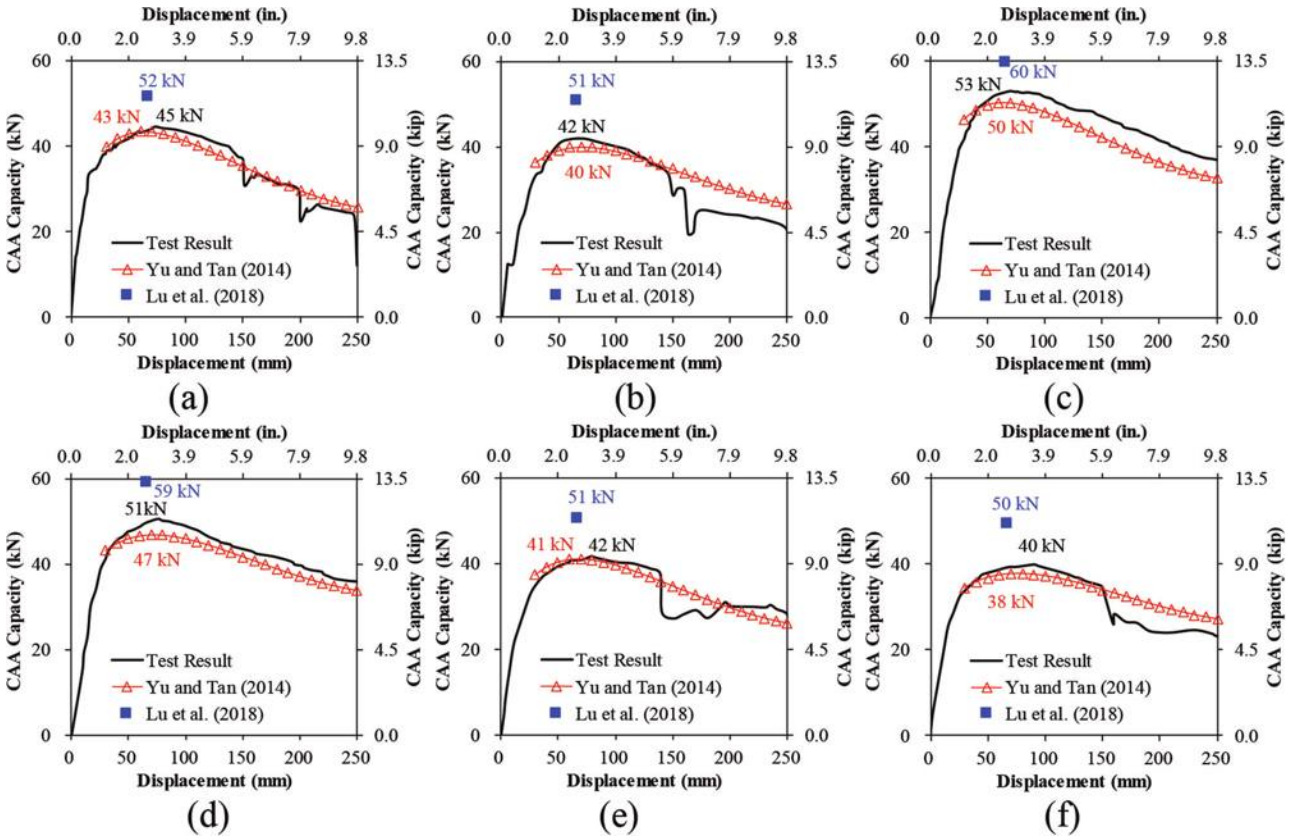

Fig. 20—Comparison of theoretical CAA capacities with test results: (a) OM; (b) OP; (c) SM; (d) SP; (e) OM-S; and (f) OP-S.

results. This indicates that the predicted model is reliable for calculating the CA capacity of the RC frame.

CONCLUSIONS

Based on the experimental and analytical results, the findings of this study are as follows:

1. The test results show that the effects of boundary conditions on the development of load-resisting mechanisms are marginal, whereas the effects of special detailing are significant. Specimens under a middle-column removal scenario and a penultimate-removal scenario are able to develop similar compressive arch action (CAA) capacities and catenary action (CA) capacities.

2. In this study, CAA capacity dominates the load resistance of specimens with ordinary designs. In contrast, CA capacity dominates the load resistance of specimens adopting a special design mainly due to the larger areas of longitudinal reinforcing bars and the greater rotation capacities of beam ends. However, boundary conditions can greatly affect the failure mode of specimens with ordinary designs.

3. Although the exterior side joints and columns of the specimens with ordinary detailing experienced severe damage, the failure of the specimens was controlled by fracture of the beam reinforcing bars, which was similar to those with special detailing, indicating the anchorage capacity of beam reinforcing bars was sufficient. Thus, beam ends rather than joints play the most critical roles in resisting progressive collapse regardless of the adopted detailing.

4. Reinforced concrete (RC) frames with the special design could provide sufficient tie force, as required by the U.S. Department of Defense (DoD).[2] Both existing CAA and CA models were reasonable for predicting the CAA and CA capacity, respectively. For the CAA models, the model proposed by Yu and Tan[18] was recommended because of its higher accuracy.

FUTURE WORKS

The findings in this paper were limited to single-story specimens, which could not fully reflect the structural behavior of a real building subjected to progressive collapse. In the future, it is suggested to conduct more multi-story test models to resist progressive collapse.

AUTHOR BIOS

ACI member **Kai Qian** *is a Professor in the Guangxi Key Laboratory of New Energy and Building Energy Saving at Guilin University of Technology, Guilin, Guangxi, China. He received his MSc and PhD from Nanyang Technological University, Singapore. His research interests include reinforced concrete and prestressed concrete structures design, particularly in the area of progressive collapse and blast resistance.*

Guang-Tao Li *is a Research Student in the Guangxi Key Laboratory of New Energy and Building Energy Saving at Guilin University of Technology. His research interests include reinforced concrete design in the area of progressive collapse.*

Dong-Qiu Lan *is a PhD Student in the Key Laboratory of Urban Security and Disaster Engineering of Ministry of Education at Beijing University of Technology, Beijing, China. Her research interests include reinforced concrete and prestressed concrete structures design, particularly in the area of progressive collapse.*

Liu Jin *is a Professor in the Key Laboratory of Urban Security and Disaster Engineering of Ministry of Education at Beijing University of Technology. His research interests include the mechanical performances of engineering structures under multiple hazards and the size effect in concrete materials and components.*

REFERENCES

1. ASCE/SEI 7-05, "Minimum Design Loads for Buildings and Other Structures," Structural Engineering Institute, American Society of Civil Engineers, Reston, VA, 2005, 424 pp.

2. UFC 4-023-03, "Design of Buildings to Resist Progressive Collapse," Unified Facilities Criteria, U.S. Department of Defense, Washington, DC, 2013.

3. GSA, "Progressive Collapse Analysis and Design Guidelines for New Federal Office Buildings and Major Modernization Projects," U.S. General Services Administration, Washington, DC, 2009.

4. Lew, H. S.; Bao, Y.; Pujol, S.; and Sozen, M. A., "Experimental Study of Reinforced Concrete Assemblies under Column Removal Scenario," *ACI Structural Journal*, V. 111, No. 4, July-Aug. 2014, pp. 881-892. doi: 10.14359/51686739

5. Yu, J., and Tan, K.-H., "Experimental and Numerical Investigation on Progressive Collapse Resistance of Reinforced Concrete Beam Column Sub-Assemblages," *Engineering Structures*, V. 55, Oct. 2013, pp. 90-106. doi: 10.1016/j.engstruct.2011.08.040

6. ACI Committee 318, "Building Code Requirements for Structural Concrete (ACI 318-05) and Commentary (ACI 318R-05)," American Concrete Institute, Farmington Hills, MI, 2005, 430 pp.

7. Qian, K., and Li, B., "Performance of Three-Dimensional Reinforced Concrete Beam-Column Substructures under Loss of a Corner Column Scenario," *Journal of Structural Engineering*, ASCE, V. 139, No. 4, Apr. 2013, pp. 584-594. doi: 10.1061/(ASCE)ST.1943-541X.0000630

8. Choi, H., and Kim, J., "Progressive Collapse-Resisting Capacity of RC Beam–Column Sub-Assemblage," *Magazine of Concrete Research*, V. 63, No. 4, Apr. 2011, pp. 297-310.

9. Sadek, F.; Main, J. A.; Lew, H. S.; and Bao, Y., "Testing and Analysis of Steel and Concrete Beam-Column Assemblies under a Column Removal Scenario," *Journal of Structural Engineering*, ASCE, V. 137, No. 9, Sept. 2011, pp. 881-892. doi: 10.1061/(ASCE)ST.1943-541X.0000422

10. Qian, K., and Li, B., "Dynamic Performance of RC Beam-Column Substructures under the Scenario of the Loss of a Corner Column—Experimental Results," *Engineering Structures*, V. 42, Sept. 2012, pp. 154-167.

11. Li, Y.; Lu, X.; Guan, H.; and Ye, L., "Progressive Collapse Resistance Demand of Reinforced Concrete Frames under Catenary Mechanism," *ACI Structural Journal*, V. 111, No. 5, Sept.-Oct. 2014, pp. 1225-1234. doi: 10.14359/51687029

12. Yu, J., and Tan, K. H., "Structural Behavior of RC Beam-Column Subassemblages under a Middle Column Removal Scenario," *Journal of Structural Engineering*, ASCE, V. 139, No. 2, Feb. 2013, pp. 233-250. doi: 10.1061/(ASCE)ST.1943-541X.0000658

13. Deng, X.-F.; Liang, S.-L.; Fu, F.; and Qian, K., "Effects of High-Strength Concrete on Progressive Collapse Resistance of Reinforced Concrete Frame," *Journal of Structural Engineering*, ASCE, V. 146, No. 6, June 2020, p. 04020078. doi: 10.1061/(ASCE)ST.1943-541X.0002628

14. Qian, K.; Liang, S.-L.; Fu, F.; and Li, Y., "Progressive Collapse Resistance of Emulative Precast Concrete Frames with Various Reinforcing Details," *Journal of Structural Engineering*, ASCE, V. 147, No. 8, Aug. 2021, p. 04021107. doi: 10.1061/(ASCE)ST.1943-541X.0003065

15. ACI Committee 318, "Building Code Requirements for Structural Concrete (ACI 318-14) and Commentary (318R-14)," American Concrete Institute, Farmington Hills, MI, 2014, 520 pp.

16. Hwang, S.-J., and Lee, H.-J., "Strength Prediction for Discontinuity Regions by Softened Strut-and-Tie Model," *Journal of Structural Engineering*, ASCE, V. 128, No. 12, Dec. 2002, pp. 1519-1526. doi: 10.1061/(ASCE)0733-9445(2002)128:12(1519)

17. Izzuddin, B. A.; Vlassis, A. G.; Elghazouli, A. Y.; and Nethercot, D. A., "Progressive Collapse of Multi-Storey Buildings due to Sudden Column Loss—Part I: Simplified Assessment Framework," *Engineering Structures*, V. 30, No. 5, May 2008, pp. 1308-1318. doi: 10.1016/j.engstruct.2007.07.011

18. Yu, J., and Tan, K. H., "Analytical Model for the Capacity of Compressive Arch Action of Reinforced Concrete Sub-Assemblages," *Magazine of Concrete Research*, V. 66, No. 3, Feb. 2014, pp. 109-126. doi: 10.1680/macr.13.00217

19. Lu, X.; Lin, K.; Li, C.; and Li, Y., "New Analytical Calculation Models for Compressive Arch Action in Reinforced Concrete Structures," *Engineering Structures*, V. 168, Aug. 2018, pp. 721-735. doi: 10.1016/j.engstruct.2018.04.097

ACI STRUCTURAL JOURNAL TECHNICAL PAPER

Title No. 120-S65

Crack-Spacing-Based Flexural Capacity of Polymer Cement Mortar-Overlay Reinforced Concrete Beams at High Environmental Temperature

by Khuram Rashid, Minkwan Ju, Tamon Ueda, and Dawei Zhang

Overlaying a reinforced concrete beam (RCB) with polymer cement mortar (PCM) is a strengthening method that improves flexural stiffness by the increasing sectional force. However, the reduction between bond strength and the reinforcement in PCM overlay at high temperatures results in an increase in flexural crack spacing. Therefore, the pullout force must be taken into account when estimating the flexural capacity of PCM-overlay RCBs. The experimental study aims to assess the flexural performance of PCM-overlay RCBs under three different environmental temperature conditions: 20, 40, and 60°C. Seventeen beams with varying reinforcement ratios in PCM are tested at the mentioned temperature levels. Experimental results indicate a decrease of approximately 6 to 13% in strength at elevated temperatures, which can be attributed to the reduction in bond strength of the reinforcement caused by the degradation of the PCM. Analytically, the strength reduction is calculated by determining the average crack spacing in the flexural zone. Therefore, the proposed average crack spacing method (CSM) predicts that the flexural strength is within ±10% limits of experimental observations. This method is more conservative than the conventional sectional analysis method (SAM). The average CSM can contribute to a safer design of PCM-overlay RCBs by preventing overestimated prediction of the ultimate strength at high environmental temperatures.

Keywords: average crack spacing; environmental temperature; flexural strength prediction; polymer cement mortar (PCM)-overlay reinforced concrete beam (RCB); pullout force; strengthening.

INTRODUCTION

Overlaying of reinforced concrete beams (RCBs) for flexural strengthening is considered one of the most appropriate techniques for strengthening and repairing, simultaneously, with cementitious material. This technique is essential for a specific damage condition such as spalling or delaminated sections that cannot normally use the externally bonded strengthening method using fiber-reinforced polymer (FRP) materials. Moreover, this technique can easily be applied by spraying the repairing material, such as grouting/shotcreting. It can easily be applied in all directions of structural members: the vertical for retaining walls or jacketing of columns and overlaying beams, and the horizontal under and over the slab bridge decks. After spraying suitable cementitious materials for the overlaying section, it is important to have the guaranteed bond strength between the overlay materials and reinforcements. Thus, the bond degradation issue can govern the strengthening capacity, resulting in the failure or collapse of the structures when the service load is applied. It is required that the bond degradation of overlay materials under different environmental conditions is investigated while designing such members.

Researchers have developed several types of engineered cementitious materials with excellent properties that can be used for repairing or strengthening purposes.[1] One of them is polymer cement mortar (PCM), which was developed by incorporating polymers in the mortar. For overlaying, PCM is considered a promising material due to its adhesive properties and good compatibility with the substrate concrete. It outperforms conventional cementitious materials due to the adhesive polymer film configuration, and it was found that its material properties were suitable for repairing and strengthening concrete.[2] Thus, PCM better resists, compared with conventional cement mortar, deterioration mechanisms such as freezing and thawing, carbonation, drying shrinkage, and chloride-ion penetration.[2-4] Hence, it has been widely accepted for the purpose of maintenance of reinforced concrete (RC) members. Although PCM performs well at ambient temperature, the authors of this study have pointed out that PCM can be weak for mechanical and flexural performance under elevated temperatures.[5-7] Therefore, it must predict the residual flexural strength of the overlay RC members accounting for the PCM-reinforcement bond degradation at elevated temperatures.

If the high environmental temperature under ambient conditions is sustained around the RC structures in service, the material properties or composite behavior (concrete-steel, PCM-steel, and concrete-PCM) may be yielded. Thus, a relative expansion can degrade the structural integrity. According to the design guideline (ASTM C666/C666M-15),[8] the influence that occurred by the low temperatures significantly explained the design construction consideration. In the case of high temperature conditions in service, there is little specific information even in such guidelines. There are many regions under high environmental temperatures; it is a fact that the environmental temperature exceeds more than 50°C and even reaches up to 60°C in the United Arab Emirates. Recently, North America has suffered from a serious heat-dome phenomenon; over a couple of weeks recorded temperatures of approximately 50°C and higher.

ACI Structural Journal, V. 120, No. 4, July 2023.

MS No. S-2022-021.R2, doi: 10.14359/51738749, received October 5, 2022, and reviewed under Institute publication policies.

In India, it has been reported that such a strong heat wave leads to serious deformation or melting of roads. Therefore, assessment of the structural capacity of RC members under high environmental temperatures is important, especially for strengthening members, particularly at the bonded interface.

RCBs resist tensile stresses through embedded steel reinforcement, which has a strong bond with concrete due to the chemical adhesion and mechanical interlocking at ambient temperature, whereas the decrease in bond strength is accelerated under severe degradation conditions such as elevated temperatures, corrosion of steel bar, and carbonation of concrete.[9-11] In RC members, the bond between concrete and reinforcement is assumed as a perfect bond condition; therefore, the cross-sectional theory has been enough for structural analysis even without considering the bond mechanism. For the overlay strengthening method, however, the chemical adhesion is also governed between the hardened concrete and new overlay materials. Thus, the vertically penetrated cracks may significantly influence the development of the lateral microcracks by the shear stress in the overlay interface before the crack is further propagated to the concrete section.[12] This cracking mechanism can determine the structural performance of the overlay-strengthened RC members under flexure. Therefore, the average crack spacing of overlay-strengthened RC members is important in transferring the shear stress along the overlay interface due to the possibility of premature debonding failure. The analytical average crack spacing is introduced in structural design codes for typical RC members and has been summarized by Zhang et al.[13]; it was concluded that for overlay beams, conventional design codes are not applicable. A different approach has been proposed for evaluating the average flexural crack spacing of overlay RC beams.[13] The approach was further modified by the author's group by incorporating the influence of the type of bar (plain or deformed).[14] Moreover, it was used for predicting the crack width[14] and crack spacing of FRP-reinforced beams.[15] The analytical average crack spacing, however, has not been employed for predicting the flexural capacity of PCM-overlay RCBs considering bond strength of reinforcement in PCM under high environmental temperatures.

This study proposes a modified prediction formula for the flexural strength of PCM-overlay RCBs by considering the development of cracking in PCM and the expected loss of the PCM-reinforcement bond with sustained high environmental temperatures. Analytical parameters are incorporated to predict the flexural crack spacing, and the pullout force is calculated. Thus, it is essential to evaluate the residual flexural capacity of PCM-overlay RCBs by incorporating pullout force and simple equations of equilibrium. The temperature levels are 20°C (ambient), 40°C, and 60°C, including high environmental temperatures. The sustained temperatures were maintained by a specially designed environmental chamber, and all testing setups are installed within that chamber. Based on the test results, it has been investigated that the proposed method, which is based on the crack spacing approach, can predict the flexural strength that incorporates the material strength degradation as well as the bond performance under high temperatures. Moreover, the average crack spacing method (CSM) is also applied to the database of PCM-overlay RCBs at ambient conditions. Hence, the prediction of the flexural strength of PCM-overlay RCBs under environmental temperatures is discussed.

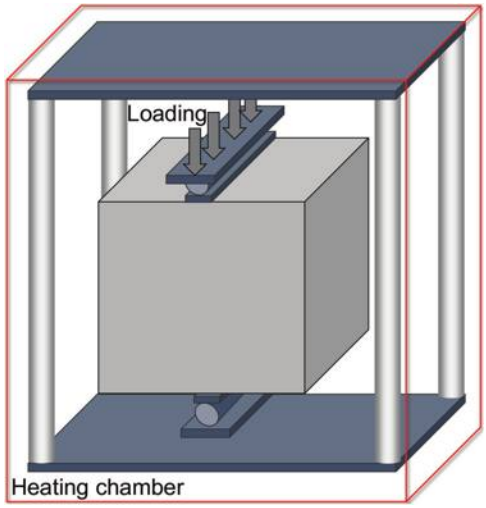

Fig. 1—Test setup of splitting tensile strength test using cubic specimens at elevated temperatures.

RESEARCH SIGNIFICANCE

Cracking in overlay RC structures significantly influences flexural structural performance because of the interaction with the substrate material. This study employs the average crack spacing in the flexural zone to suggest a modified prediction formula for the flexural strength of PCM-overlay-strengthened RCBs. Besides, high environmental temperatures degrade the flexural resistance due to a reduction in the bond strength of the reinforcement in PCM. Therefore, to prevent the overestimation of the flexural strength, a bond coefficient is additionally applied in the modified prediction formula. The proposed model can provide a conservative and reasonably accurate prediction compared to conventional sectional analysis, which tends to overestimate.

EXPERIMENTAL PROGRAM

Material properties at elevated temperatures

The materials used for the casting of PCM-overlay RCBs are concrete, PCM, reinforcements, and primer. Ready mixed concrete with a design compressive strength of 30 MPa is used. For the material properties, three cubic specimens of concrete (150 mm) and PCM (100 mm) are fabricated for each temperature (20, 40, and 60°C) as environmental temperatures, and after curing, specimens were exposed to elevated temperatures for 24 hours in an oven. Eighteen cubes are cast; half of the cubic specimens were used for the compressive strength test, while the others were for the splitting tensile strength test. They were exposed under the same temperature until the compressive and splitting tensile strength tests (Fig. 1) are conducted according to ASTM C39/C39M-20[16] and ASTM C496/C496M-17,[17] respectively. However, cubical specimens were used instead of cylindrical specimens; such provisions are provided in other codes and recommended by previous research.[7]

Table 1—Proportions of PCM mixture of this study

Type of polymer	Portland cement, %	Sand, %	Latex solid to cement, %	Unit volume, kg/L
Ethylene-vinyl acetate	38.0	62.0	1 to 5	2.90

Table 2—Compressive and splitting tensile strengths of concrete and PCM at elevated temperatures

	Compressive strength, MPa			Splitting tensile strength, MPa			Elastic modulus, GPa		
Materials	20°C	40°C	60°C	20°C	40°C	60°C	20°C	40°C	60°C
Concrete	28.3 (1.3)	29.1 (2.4)	31.4 (1.3)	3.5 (0.3)	3.4 (0.3)	3.4 (0.2)	25.0*	25.3*	26.3*
PCM	59.7 (1.2)	33.7 (2.5)	27.7 (2.0)	6.1 (0.3)	4.5 (0.2)	4.2 (0.5)	22.0†	16.5†	15.0†

*$E_c = 4700\sqrt{f'_c}$ (ACI 318-19).

†Measured by manufacturer.

Note: Standard deviation in parentheses. 1 MPa = 145 psi.

Table 3—Properties of reinforcements

Diameter, mm	Type	Yield strength, MPa	Ultimate strength, MPa	Elastic modulus, GPa	Elongation, %	Reinforced section
10	Deformed	470	614	200	25	RC
6	Plain	430	617	200	35	PCM

In this study, a commercial product of PCM is used. The prescribed ratios of the constituents of PCM and the physicochemical properties of PCM[5] and primer are given by the manufacturer and shown in Table 1. The mechanical properties of both the compressive and tensile strength tests of concrete and PCM are obtained by cube specimen test and are summarized in Table 2. The temperature variation influences the strength of the concrete and PCM. Concrete strength slightly increases due to acceleration in hydration at elevated temperatures; however, there are no significant changes due to short exposure to temperature (24 hours only). The compressive and splitting tensile strengths of PCM are largely affected by temperature. The reduction in mechanical strength was due to the sensitivity of PCM to temperature, as it may degrade the polymer film and increase the porosity of the PCM.[7] The compressive strength decreases up to 43.6 and 53.6% corresponding to 40 and 60°C, while the tensile strength reduction is approximately 30% compared to the control specimen at the ambient temperature. It is noted that the reduction of tensile strength of concrete is reasonable at the high temperature level; however, PCM strength degrades as the temperature goes up. Therefore, the resistance to crack initiation decreases with the drop in the tensile strength. Moreover, the elastic modulus of concrete was obtained from ACI 318-19[18] using the compressive strength of concrete under the temperatures, while the values of PCM were provided by the manufacturer. It is found that the strength of PCM is higher than the concrete; however, the elastic modulus is lower. Primer was applied at the interface between the concrete and PCM to avoid moisture ingress. The main ingredient of the primer was a polymer named styrene-acrylic ester latex. Deformed steel bars of 10 mm diameter for RCBs were used, and a plain steel bar of 6 mm, which is the smallest standard bar diameter in the PCM-overlay section, was employed considering the small overlay height of 25 mm. The properties of steel reinforcing bars are mentioned in Table 3.

Specimen preparation

The length of the RCB is 1800 mm with a span of 1380 mm. The width and height of the cross section are 200 and 150 mm, respectively. The top and bottom reinforcements are installed with a diameter of 10 mm (RC section), while the plain bar of diameter 6 mm is used in the PCM-overlay strengthened section, as introduced in Table 3. Before concrete casting, a retarder is spread inside the bottom of the wooden mold to avoid hardening of the bottom surface of the concrete beam. This is to easily form the rough surface for better composite action between the concrete and the PCM overlay.

After 36 hours of curing time, the wooden form at the bottom of the RCB is removed, and the overlay surface is roughened using a steel wire brush and a strong water jet to meet the criterion of CSP 7 (concrete surface profile) provided by the International Concrete Repair Institute.[19] Then, the RCBs are cured in wet conditions using water sprinklers for 28 days until the overlay strengthening process using PCM. There are two ways to treat the PCM-overlay surface: applying the primer (with primer [WP]) or no primer (NP). One of the PCM-overlay RCBs used the primer application, while the other did not. Generally, applying primer enhances the adhesive properties of the externally bonded strengthening surface. This experimental test investigates the flexural capacity of the RCB strengthened by PCM overlay under high temperatures, according to the application of the primer. The PCM-overlay strengthening procedures are as follows. First, the formwork with a 25 mm thickness at the perimeter of the strengthening surface is completed, and primer is applied to the treated surface of the concrete and cured for 3 hours. Next, different numbers of plain reinforcements with diameters of 6 mm are installed in the longitudinal direction and separated by tie bars. The bars were placed on the treated substrate surface, as shown in Fig. 2. The sectional details and specimen ID of this work are defined in Table 4. Lastly, PCM is uniformly sprayed inside the formwork. The specimen fabrication is described

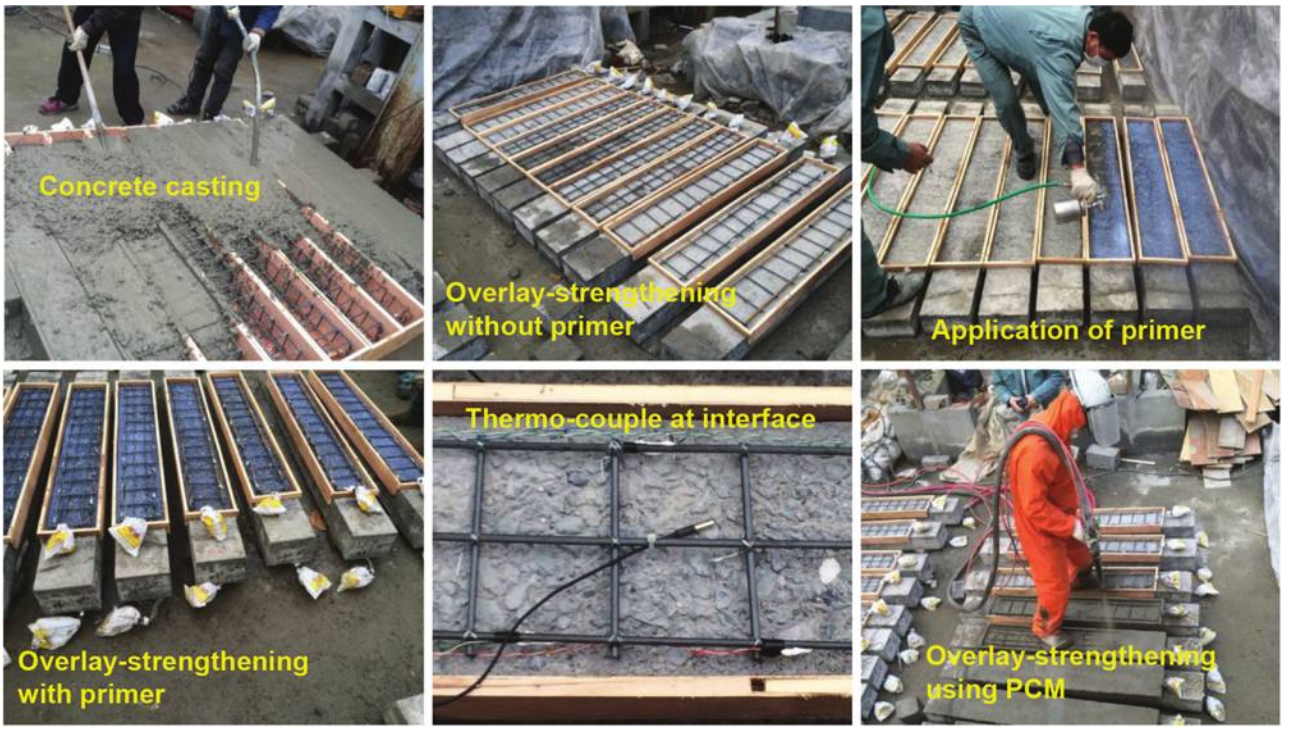

Fig. 2—Fabrication of PCM-overlay RCBs.

Table 4—Sectional details and specimen summary of PCM-overlay RCBs

Specimen ID	Area, mm^2	Reinforcement ratio, %	Temperature, °C		
			20	40	60
2Ø6	56.1	0.7	2*	2	2
3Ø6	84.2	0.8	2	2	2
4Ø6	112.2	0.9	2	2	1

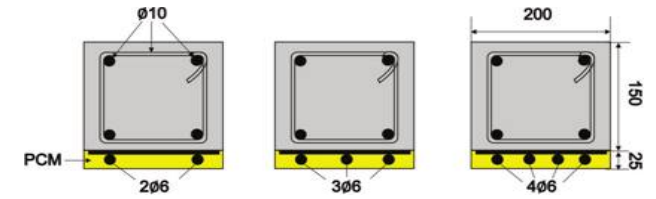

*Two specimens tested at 20°C: one specimen with primer at the interface (WP) and the other without any primer (NP) at the interface between PCM-concrete.

Note: 1 mm = 0.0394 in.

in Fig. 2. After the complete fabrication of the test specimens, they are covered with polyethylene sheets to avoid drying shrinkage due to the excessive evaporation of water. The curing condition is applied with 7 days of wet curing, and a further 21 days of dry curing.

Testing at elevated temperatures

All types of beams are exposed to a temperature of 20, 40, and 60°C and a relative humidity of 60% in an environmental chamber during the test, as shown in Fig. 3, and the testing setup within the chamber is schematically presented in Fig. 4. Before the experimental test for each temperature variable, the environmental chamber, including the test specimens, is kept for 24 hours at the specific temperature before and during the test. The temperature at the interface is measured by inserting a thermocouple during casting (Fig. 2) and its value is confirmed before loading (Fig. 3). The temperature duration is comparable to the real application when temperature shoots more than 50°C in peak summer, and its duration will be approximately 18 hours. To counter that situation, the authors put the specimens in a well-established environmental chamber. A four-point bending test is applied using a hydraulic jack with a capacity of more than 200 kN, and the shear span is 460 mm. Four numbers of linear variable displacement transducers (LVDTs) are installed at the mid and the supports. To measure the applied load, a load cell was installed between the hydraulic jack and the loading jig on the specimen. After finishing the test, the environmental chamber is turned off and then the tested specimens are removed from the chamber.

EXPERIMENTAL TEST RESULTS AND DISCUSSION

Flexural failure mode

All types of PCM-overlay RCBs are tested under four-point loading up to failure. In all cases, the failure mode was flexural failure instead of debonding. However, based on previous experimental observations, it was found that premature debonding failures for overlay-strengthened RCBs are one of the common modes of failure.[12,20] This mode of failure can be explained on the basis of the elastic modulus difference between the concrete and PCM, as introduced in Table 2. High-performance concrete is usually selected as the overlay material for strengthening RCBs, which has an obviously higher mechanical performance than substrate concrete.[12,20-22] But, a high modulus

of elasticity of overlay material leads to the initiation of cracks in concrete substrate before the overlay material.[12] The PCM in this study, however, has a higher compressive strength than substrate concrete, while its modulus of elasticity is less than concrete. Accordingly, the crack initiated in the PCM and then propagated toward the concrete substrate. It is the mechanical advantage for the delamination of the PCM-overlay not to occur under the flexure failure regardless of the difference in curvature of the test RCBs. It is observed that the PCM-overlay method can provide sufficient composite performance under flexural failure with or without using the primer. The crack orientation, length, and number are monitored at the front and back of the beams visually during testing at 20 and 40°C; however, it is noted after the test for specimens tested at 60°C. The measured number of cracks is used to calculate the average crack spacing ($S_{cr,exp}$). It was observed that the first crack of the beam was initiated at the PCM-overlay section within the constant moment zone (L_e) and then it propagated vertically toward the compressive zone around the loading points. The representative crack patterns measured are shown in Fig. 5.

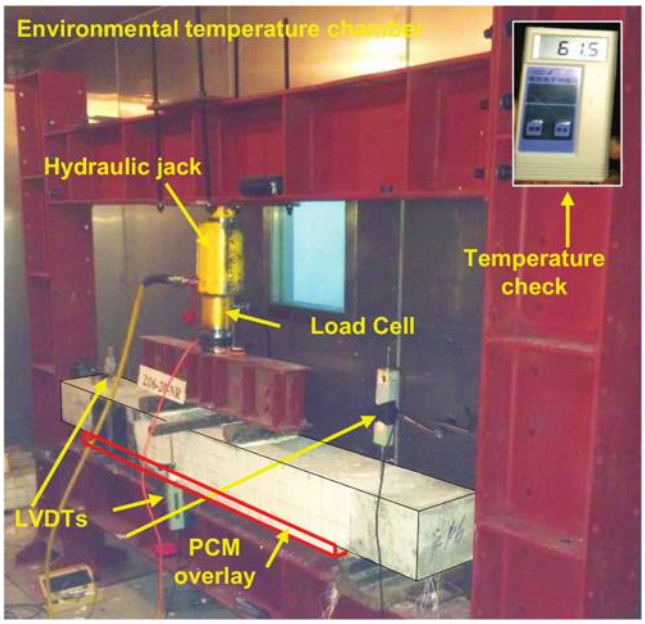

Fig. 3—Test setup of PCM-overlay RCB in environmental chamber.

Load-displacement behavior

The midspan deflection of all types of PCM-overlay and unstrengthened RCBs was continuously recorded, and the load-displacement curves are presented in Fig. 6. It was observed that, in almost all cases, trilinear parts were observed. The first part indicates the initial stiffness, the second part indicates the crack initiation load on the yield point of steel bars, and the third part is the displacement hardening up to the failure. The ultimate loads of all PCM-overlay RCBs were obviously more than unstrengthened RCBs at all temperature levels (Fig. 6). The comparison was also made with respect to temperature level, the influence of primer, and the influence of the PCM-overlay reinforcement ratio. From Fig. 6(a), it was observed that the 2Ø6-20°C specimen has the highest load compared with the same specimen tested at 40 and 60°C. A similar trend was observed in all cases (Fig. 6(b) and (c)). The initial stiffness reduces with the increase in temperature level, and the crack initiation load was extracted and reported in the "Cracking load" section. It is observed that the specimen with the lowest PCM-overlay reinforcement ratio shows better performance with the primer application compared with those not using the primer at elevated temperatures.

The primer application slightly reduces the initial stiffness and flexural strength as the PCM-overlay reinforcement ratio increases. This is because when a large number of stresses are transferred from the soffit toward the loading points, the influence of primer plays a negative role, and at elevated temperatures, the structure of the primer may get damaged, as the polymers are sensitive to temperature; therefore, composite action was slightly degraded. Furthermore,

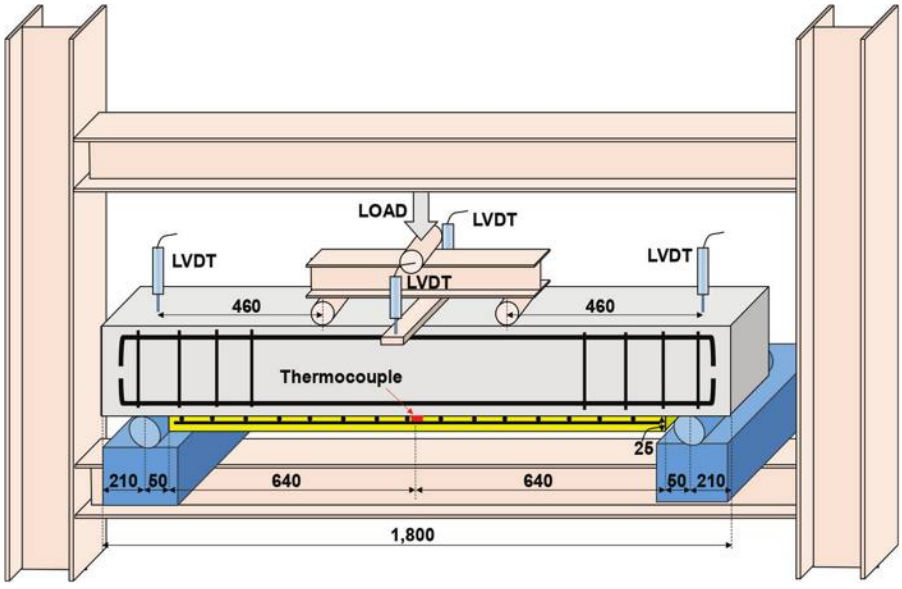

Fig. 4—Schematic appearance of four-point bending test performed on PCM-overlay RCBs. (Note: 1 mm = 0.0394 in.)

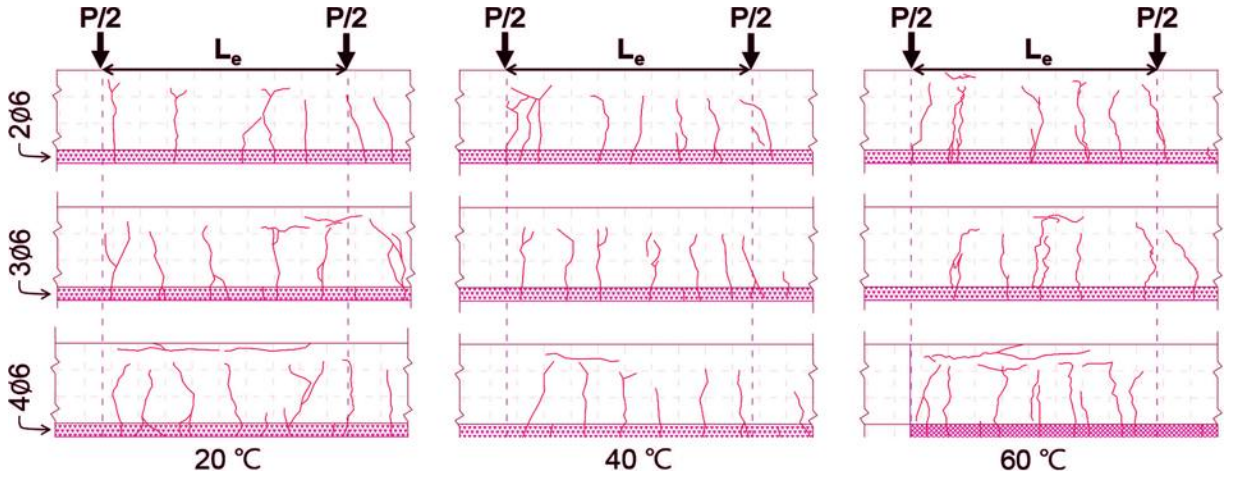

Fig. 5—Crack patterns for PCM-overlay RCBs with primer application at stabilized cracking stage.

it has been reported that the degradation in the interfacial shear strength of the composite (concrete-PCM) with the primer is increased at elevated temperatures compared to the composite without primer,[5] whereas the reduction in the interfacial tensile strength of the composite without primer is more. In the case of PCM-overlay RCBs, the combination of tensile and shear stress generated at the interface and shear stresses is dominant. Therefore, the interface property of the beams applied with primer may be degraded in the flexural capacity.

With the increase in the PCM-overlay reinforcement ratio (Fig. 6(b) and (c)), higher initial stiffness and flexural capacity are shown compared with those of the 2Ø6 specimens under elevated temperatures. Unlike the 2Ø6 specimens, the 3Ø6 specimens with primer application show fewer ultimate loads at elevated temperatures, and the 4Ø6 specimens with the highest PCM-overlay reinforcement ratio showed no significant difference in the ultimate loads according to the primer application.

It is found that the flexural performance at the low PCM-overlay reinforcement ratio is governed by the primer application, while the interface treatment may not be critical to the flexural performance at the higher PCM-overlay reinforcement ratio. At the low PCM-overlay reinforcement ratio, the tensile stress reaches the yield stress earlier than those of the high reinforcement ratio; then, the PCM-overlay section gets stressed hard so that the overlay interface property is critical for the flexural performance. At the high PCM-overlay reinforcement ratio, the steel bar stress is developed enough up to the ultimate loading condition; hence, the stress acceleration at the PCM-overlay section can be sufficiently delayed until the overlay interface gets critical shear stress. For the flexural capacity development at high temperatures, the PCM-overlay reinforcement ratio is the key factor, even though the primer interface performance is degraded under the temperature. The rise in ultimate load was obvious with the increase in the tensile reinforcement area. The flexural capacity was also improved with added reinforcement in the overlay section, as explained in the discussion of Fig. 6. Moreover, the average of the ultimate loads (with and without the application of primer) was taken, and normalized values are plotted in Fig. 7. It was observed that the ultimate load drop with the increase in temperature, a 6 to 13% decline, was observed at 60°C when compared with beams tested at 20°C.

The reduction in the ultimate load with elevated temperatures was induced by the slippage of plain bar in the overlay section due to the decrease in PCM strength evidenced in Table 2. A previous study investigated the reinforcement slippage with temperature,[9] where many beams were tested under temperature loading, and a 44% reduction in the bond strength was reported. Moreover, more than a 10% reduction in the ultimate load was observed even at 100°C.

Stiffness at cracking and yielding

The flexural behavior of RCBs up to failure is mainly defined by two significant moments in the trilinear curve: initial cracking and initial yielding, respectively.[23] Table 5 summarizes the stiffness calculation of the two types at the initial cracking and initial yielding. Note that the initial cracking occurs at the PCM overlay. RCBs have no significant change in stiffness due to elevated environmental temperatures; thus, RCBs with PCM overlay can maintain their structural performance regardless of temperature increase. Compared to RCBs, PCM strengthening gives a large increase in cracking and yielding stiffness, and the strengthening effect is demonstrated at elevated temperatures. The presence of primer at the strengthening interface is largely sensitive for PCM-overlay beams with a lower reinforcement ratio rather than that of a higher ratio of 4Ø6. This is because the higher reinforcement ratio can greatly resist the curvature increase under bending, as demonstrated by the increasing results of both stiffnesses. Figure 8 presents the initial cracking stiffness with respect to the serviceable cracking behavior. Note that the 2Ø6 specimens are excluded due to the lower flexural strength as well as the initial yielding stiffness than those of 3Ø6 and 4Ø6 under high environmental temperatures. Therefore, the higher strengthening effect of PCM overlay is being investigated. At 20°C, the initial cracking stiffness shows no significant change regardless of the use of primer. At the elevated temperatures, however, it is found that there is no apparent trend of stiffness reduction, whereas the stiffness is higher than that at 20°C without primer. The use of primer may

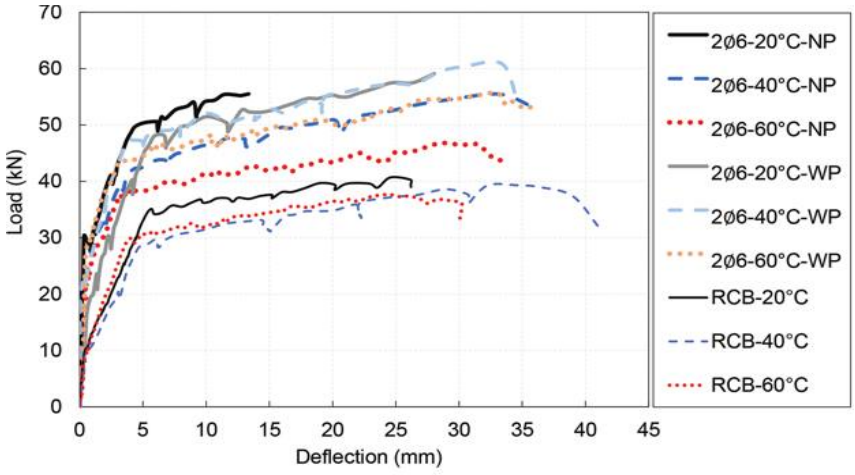

(a)

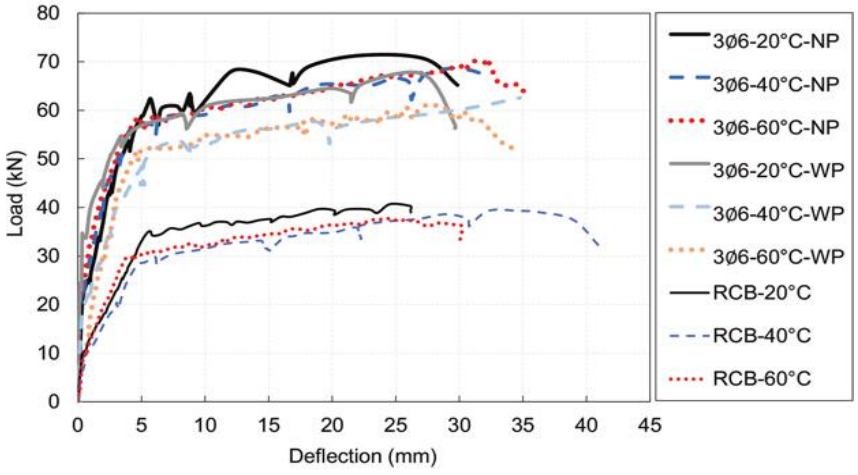

(b)

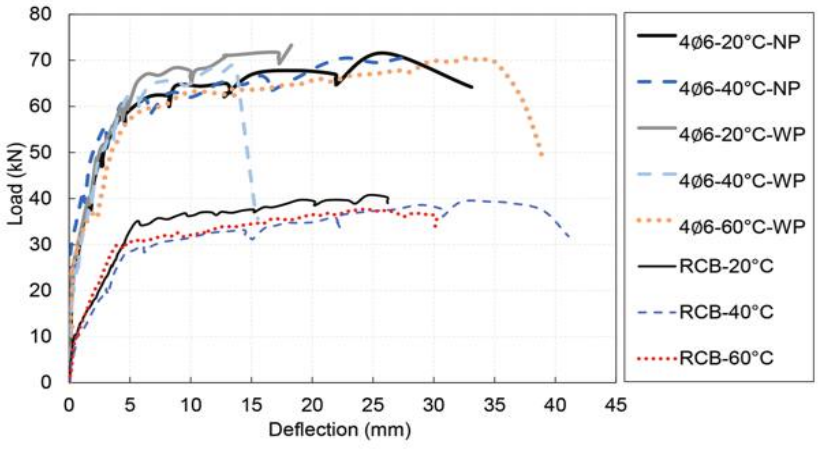

(c)

Fig. 6—Load-deflection relationships of PCM-overlay RCBs exposed to different temperature levels: (a) 2Ø6 specimens; (b) 3Ø6 specimens; and (c) 4Ø6 specimens. (Note: 1 kN = 0.225 kip; 1 mm = 0.0394 in.)

have an adverse effect at elevated temperatures for PCM overlay.

Cracking load

Cracking load investigation under flexural behavior is an important observation to assess the structural stiffness. It is a more critical issue for PCM-overlay RCBs that PCM overlay can give the effective stress transfer as a good composite action. They are completed to give the sufficient strengthening effect. To analytically estimate the cracking load, a cracking moment is calculated from Eq. (1), which is the function of the compressive strength and geometrical

detail of the specimen. The other notations in Eq. (1) are x_p, the depth of the neutral axis of the transformed section; and I_{un}, the uncracked moment of inertia.[24]

$$M_{cr} = f_{cr} I_{un}/(h - x_p)$$

where x_p =

$$\frac{bh^2/2 + (n_s - 1)A_s' d_s' + (n_s - 1)A_{s,RC} d_{RC} + (n_s - 1)A_{s,OL} d_{OL}}{bh + (n_s - 1)A_s' + (n_s - 1)A_{s,RC} + (n_s - 1)A_{s,OL}} \quad (1)$$

$$I_{un} = (bh^3/12) + bh(x_p - (h/2))^2 + (n_s - 1)A_s'(x_p - d_s')^2 + (n_s - 1)A_s(x_p - d_s)^2 + (n_s - 1)A_{s,OL}(x_p - d_{OL})^2$$

where f_{cr} is the concrete tensile strength under flexure ($0.62\sqrt{f_c'}$); f_c' is the compressive strength (MPa); I_{un} is the moment of inertia of the cracked section (mm^4); b is the beam width (mm); h is the beam height (mm); x_p is the centroid of the transformed section (mm); n_s is the modular ratio; d and d' are the effective depth from the bottom and top surface, respectively (mm); A_s and A_s' are the bar area of the bottom and top section, respectively (mm^2); and $A_{s,RC}$ and $A_{s,OL}$ are the area of reinforcement in the concrete and overlay section, respectively (mm^2).

Based on the experimental cracking load and analytical cracking load based on Eq. (1), a comparison was made between them and plotted in Fig. 9. It is observed that the cracking load increased, obviously, with the increase in the PCM-overlay reinforcement ratio, but they are reduced as the temperature increases.

The experimental cracking load at 60°C was reduced by 29% compared with the load at 20°C. Thus, elevated temperatures sensitively act to degrade the initial stiffness of PCM-overlay RCBs. Analytical prediction of the cracking loads underestimates the experimental test results so that the analytical equation can assess the structural stiffness of PCM-overlay RCBs in a conservative manner. As a result, a safe prediction of the initial stiffness can be achieved.

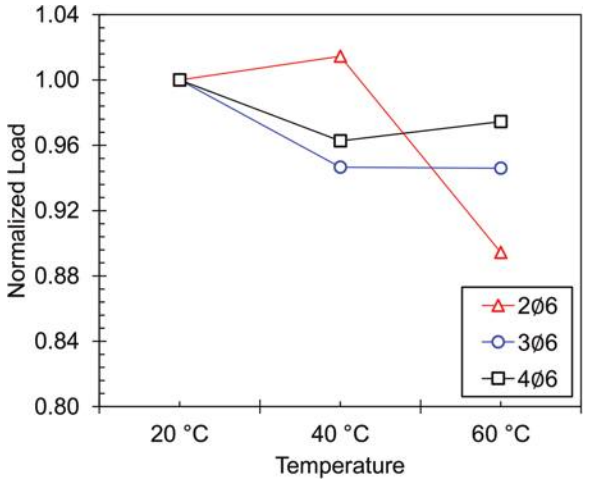

Fig. 7—Influence of temperature on reduction in ultimate load of PCM-overlay RCBs.

Table 5—Calculation of stiffness from load and displacement curves

Specimen ID	Initial cracking		Initial yielding		Stiffness, kN/mm	
	Deflection, mm	Load, kN	Deflection, mm	Load, kN	Initial cracking	Initial yielding
RCB-20°C	0.44	10.2	5.39	34.6	23.18	4.93
RCB-40°C	0.575	9.6	5.27	28.7	16.70	4.07
RCB-60°C	0.34	8.1	3.98	29.8	23.82	5.96
2Ø6-20°C-NP	0.59	29.4	4.38	49.7	49.83	5.36
2Ø6-40°C-NP	0.26	21.7	3.82	41.4	83.46	5.53
2Ø6-60°C-NP	0.455	20.5	3.32	37.6	45.05	5.97
2Ø6-20°C-WP	0.84	19.4	5.92	48.1	23.10	5.65
2Ø6-40°C-WP	0.04	21.3	3.77	47.2	532.50	6.94
2Ø6-60°C-WP	0.46	26.9	3.19	43.7	58.48	6.15
3Ø6-20°C-NP	0.345	20.6	5.51	61.3	59.71	7.88
3Ø6-40°C-NP	0.175	19.8	4.62	57.3	113.14	8.44
3Ø6-60°C-NP	0.085	20.1	5.05	57.7	236.47	7.57
3Ø6-20°C-WP	0.43	33.8	4.28	55.8	78.60	5.71
3Ø6-40°C-WP	0.365	18.4	6.51	52.7	50.41	5.58
3Ø6-60°C-WP	0.52	8.6	4.85	51	16.54	9.79
4Ø6-20°C-NP	0.4	26.2	4.59	58	65.50	7.59
4Ø6-40°C-NP	0.44	24.8	3	55.9	56.36	12.15
4Ø6-20°C-NP	0.34	25.7	4.31	60.2	75.59	8.69
4Ø6-40°C-WP	0.34	19.8	5.04	62.6	58.24	9.11
4Ø6-60°C-WP	0.28	24.6	5.23	57.8	87.86	6.71

Note: 1 mm = 0.394 in.; 1 kN = 0.225 kip.

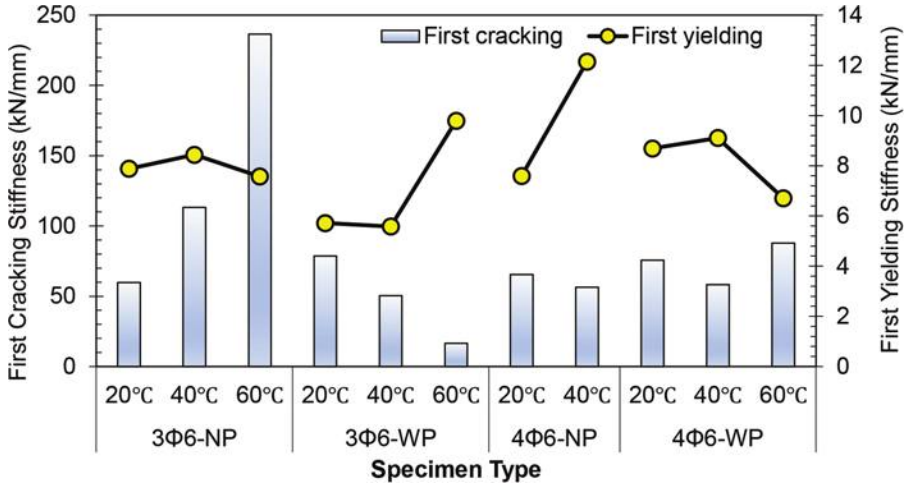

Fig. 8—Serviceable cracking stiffness according to elevated temperatures. (Note: 1 kN = 0.225 kip; 1 mm = 0.0394 in.)

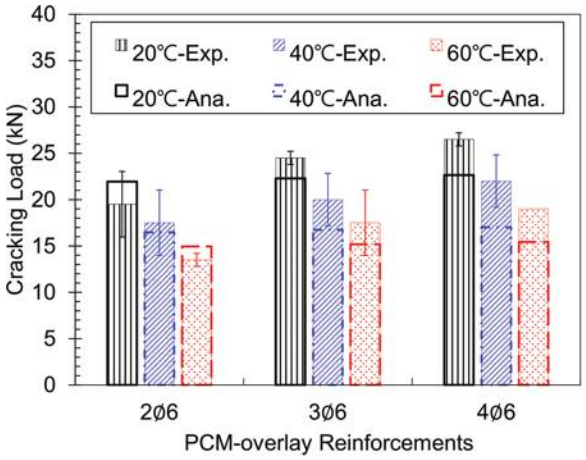

Fig. 9—Measured cracking loads in average and analytical predictions. (Note: 1 kN = 0.225 kip.)

Flexural crack spacing

When the initiation of flexural cracks occurs within the constant moment zone, it gets propagated vertically toward the loading points, and additional flexural cracks are observed and stabilized having a crack spacing as the load approaches the ultimate state (Fig. 5). In the stabilized cracking stage, where the crack pattern has already been completed and no new cracks occur, the flexural crack spacing is measured by taking the average number of cracks at the bottom and front of the beam (Fig. 10). Mathematically, it is described in Eq. (2)

$$S_{cr,exp} = \frac{1}{2}\left[\frac{L_e}{(n_{c,F}-1)} + \frac{L_e}{(n_{c,B}-1)}\right] \quad (2)$$

where $S_{cr,exp}$ is the experimental flexural crack spacing (mm); L_e is the effective length (constant moment zone or pure flexural zone) (mm); and $n_{c,F}$ and $n_{c,B}$ are the number of cracks at the front and bottom of the beam, respectively.

After testing, all the beams were observed for the measurement of flexural crack spacing. The cracking patterns of all the beams were reproduced using Autodesk software by inserting the raster image of a beam. The cracking pattern and crack spacing of all the beams are shown in Fig. 5. The crack spacing was quantitatively measured from Eq. (2) and

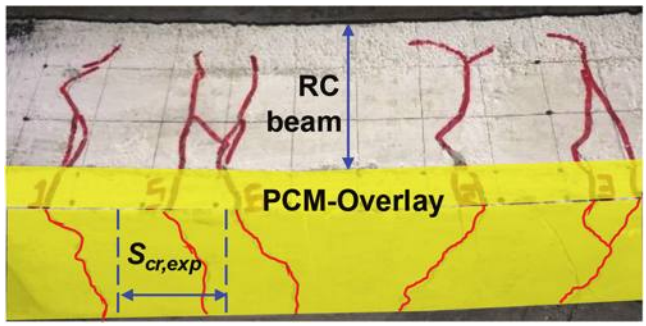

Fig. 10—Average crack spacing from measured crack spacing within constant moment zone.

is presented in Table 6. It can be observed that the crack spacing was reduced by increasing the PCM-overlay reinforcement ratio. The increase in the perimeter of the bars is obvious with the increase in area, thus reducing the crack spacing due to adequate bonding between concrete and reinforcement or PCM and reinforcement.

It is also observed from Fig. 11 that there is an increase in crack spacing due to an increase in temperature, even though the reinforcement ratio is the same. Up to a 25% increase in crack spacing was observed with temperature, which was due to the significant reduction in the tensile strength of the PCM with temperature.[6] Moreover, as indicated in the "Cracking load" section, the cracking load decreases with the increase in temperature. Therefore, early initiation of cracking load resulted in relatively less bond performance between the PCM and reinforcement, thus resulting in an increase in crack spacing. This is demonstrated by the incorporation of the influence of plain and deformed bars using the bond coefficient β introduced in the following section.

PREDICTION OF FLEXURAL STRENGTH INCORPORATING PULLOUT STRENGTH OF REINFORCEMENT UNDER TEMPERATURES

The flexural capacity of RC members is predicted by conventional strain compatibility analysis by considering force equilibrium conditions, and can be analyzed by drawing a Whitney block.[25] The same approach has also been successfully applied to the strengthened RCBs overlaid

Table 6—Comparison between experimental and analytical crack spacing in mm

	Experiment			Without β			With β		
				Eq. (6) and (7)			Eq. (8) and (9)		
Specimen ID	20°C	40°C	60°C	20°C	40°C	60°C	20°C	40°C	60°C
2Ø6	115	134	123	146	160	162	126	137	132
3Ø6	92	104	115	118	133	136	99	111	108
4Ø6	84	88	90	99	114	118	82	93	92

Note: 1 mm = 0.394 in.

with PCM.[20,21] The higher PCM-overlay reinforcement ratio obviously increases the flexural capacity. Along with that, the tensile stress of concrete and PCM also contributes and results in an increase in the initial stiffness (Fig. 6 and 8) and an increase in the cracking load (Fig. 9). The tensile stress of each material (concrete, PCM, and reinforcement), along with the local pullout after cracking, has been incorporated into the average CSM for predicting the flexural capacity of PCM-overlay RCBs.

For the calculation of the compressive and tensile strengths of concrete and PCM at elevated temperatures, the regression equation is employed. It has been observed that the mechanical properties of PCM degrade significantly with temperature compared to concrete. The authors have investigated the properties of concrete and PCM at various exposure conditions, and from their database (which includes different compressive strengths of normal-strength concrete and different types of PCMs),[5-7] the temperature range varies from 20 to 60°C. Equation (3) and (4) were extracted to obtain the tensile strength of concrete ($f_{t,T(c)}$) and PCM ($f_{t,T(OL)}$) at elevated temperatures, whereas $f_{t,c}$ and $f_{t,OL}$ are the tensile strengths at ambient conditions. Both equations are valid for temperatures (T) from 20 to 60°C.

$$f_{t,T(c)} = 1.07_{ft,c}\exp(-0.004T) \quad (3)$$

$$f_{t,T(OL)} = 1.2f_{t,OL}\exp(-0.0095T) \quad (4)$$

Similarly, Eq. (4) can be modified to follow Eq. (5) by incorporating values of compressive strength ($f'_{c(OL)}$) at a designated temperature ($f'_{c,T(OL)}$). The procedure can be explained in the following five steps.

$$f'_{c,T(OL)} = 1.38f'_{c(OL)}\exp(-0.0038T) \quad (5)$$

Step 1: Evaluation of flexural crack spacing

Several codes are available for evaluating crack spacing, but it is invalid for the PCM-overlay RCBs due to the different or unclear cracking mechanism compared with multilayer reinforced beams.[13] An alternate method had been proposed by considering the equilibrium condition at the stabilized cracking stage for PCM-overlay RCBs (Fig. 12). The effective tensile area of concrete ($A_{t,c}$) and PCM-overlay section ($A_{t,OL}$) were considered along with the maximum bond strength (τ_b) between concrete-steel ($\tau_{bm,c}$) and PCM reinforcement ($\tau_{bm,OL}$). The free-body diagram along with

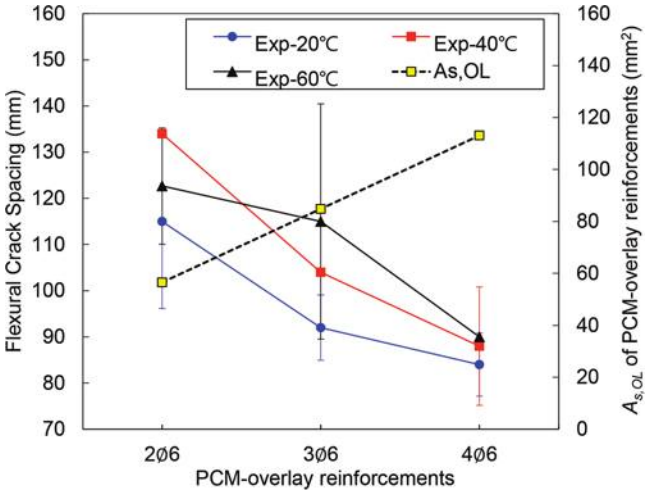

Fig. 11—Influence of temperature and area of strengthening reinforcement on flexural crack spacing. (Note: 1 mm = 0.0394 in.)

the explanation of notations is illustrated in Fig. 12. Finally, the flexural crack spacing (S_{cr}) of the PCM-overlay beam was calculated from Eq. (6) and (7), for the RC part (SRC) and overlay section (S_{OL}), respectively. The details of the derivation of equations and explanation of notations have been described.[13]

$$S_{RC} = \frac{3f_{ct}\left(A_{t,c} + A_{t,OL}\frac{E_{OL}}{E_c}\right)}{(\sum O_{RC}\tau_{bm,c} + \sum O_{OL}\tau_{bm,OL})} \quad (6)$$

$$S_{OL} = \frac{3f_{t,OL}\left(A_{t,c}\frac{E_c}{E_{OL}} + A_{t,OL}\right)}{(\sum O_{RC}\tau_{bm,c} + \sum O_{OL}\tau_{bm,OL})} \quad (7)$$

where f_{ct} and $f_{t,OL}$ are the splitting tensile strength of concrete and PCM, respectively; E is the modulus of elasticity; O is the perimeter of steel bars; and $\tau_{bm,c(OL)} = 5(f'_{c,(OL)}/20)^{1/4}$.

Step 2: Incorporation of influence of plain and deformed bars

The bond strength influenced the flexural crack spacing, and the bond strength of plain and deformed bars will obviously be different; therefore, it was incorporated into the authors' previous work.[14] It was incorporated by following β according to the recommendations of the JSCE code.[26] For a plain bar, β is 1.3, and for a deformed bar, β is 1.0. The modified equations are as follows (Eq. (8) and (9))

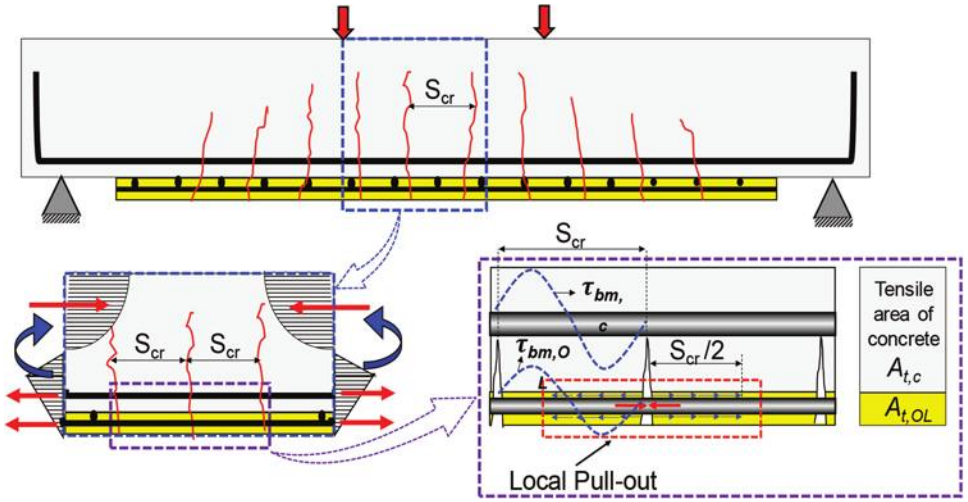

Fig. 12—Schematic and free-body diagram of various forces incorporated in average crack spacing method.

$$S_{RC} = \frac{3f_{t,c}\left(A_{t,c} + A_{t,OL}\frac{E_{OL}}{E_c}\right)}{(\beta_{RC}\sum O_{rc}\tau_{bm,c} + \beta_{OL}\sum O_{OL}\tau_{bm,OL})} \quad (8)$$

$$S_{OL} = \frac{3f_{t,OL}\left(A_{t,c}\frac{E_c}{E_{OL}} + A_{t,OL}\right)}{(\beta_{RC}\sum O_{RC}\tau_{bm,c} + \beta_{OL}\sum O_{OL}\tau_{bm,OL})} \quad (9)$$

Finally, analytical flexural crack spacing ($S_{cr,ana}$) was selected for a strengthened RCB by following Eq. (10), where k_1 is the strain gradient coefficient and is calculated based on CSA S474:04 (R2019).[27] Its value ranges from 0.5 to 1.0, and 0.5 was selected in this work.

$$S_{cr,ana} = k_1 \cdot \min(S_{RC}, S_{OL}) \quad (10)$$

The comparison was made between experimental and analytical flexural crack spacing, and is presented in Table 6. Experimental values were the average of beams with and without applying primer at the interface between concrete and PCM, whereas two types of analytical values, to see the influence of β, are described in Table 6 and plotted in Fig. 13. Moreover, the influence of temperature was incorporated in Eq. (8) and (9) by using the corresponding value of tensile strength of concrete (Eq. (3)) and PCM (Eq. (4)) at respective temperature levels. The comparison was made between analytical flexural crack spacing predicted from Eq. (6) and (7), and from Eq. (8) and (9). The overestimation observed from Eq. (6) and (7) was from 17.9 to 31.7%, whereas the difference between experimental and analytical values (Eq. (8) and (9)) varied from 6.1 to 9.6%. This difference can easily be visualized from Fig. 13. The close prediction from Eq. (8) and (9), even at ambient conditions, was due to the incorporation of the influence of the type of bar, either plain or deformed, and their corresponding β value.

Step 3: Incorporating pullout force

The next step is the calculation of the pullout force (F_{po}) of the reinforcement in PCM overlay. To calculate the pullout force, the crack spacing (S_{cr}) and the bond strength were incorporated according to *fib* Model Code 2010,[28] given in Eq. (11) and (12)

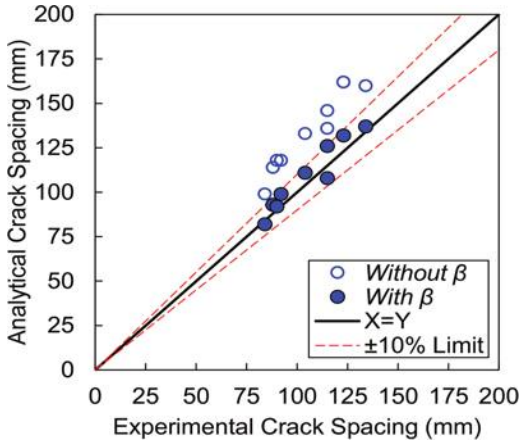

Fig. 13—Comparison results between predicted and experimental crack spacing with effect of bond coefficient β. (Note: 1 mm = 0.0394 in.)

$$F_{po} = S_{cr}\sum O_{OL}\tau_{bm,OL} \quad (11)$$

$$\tau_{bm,OL} = 5.0\left(\frac{f'_{c,OL}}{20}\right)^{1/4} \quad (12)$$

Step 4: Analytical model for flexural moment

The types and number of forces are mentioned in the Whitney stress block diagram (Fig. 14), and the tensile strength of concrete and PCM is also incorporated. The concrete tension force ($F_{t,c}$) and PCM-overlay tension force ($F_{t,OL}$) are expressed in Eq. (13) and (14)

$$F_{t,c} = A_{t,c} \cdot f_{t,T(c)} \quad (13)$$

$$F_{t,OL} = A_{t,OL} \cdot f_{t,T(OL)} \quad (14)$$

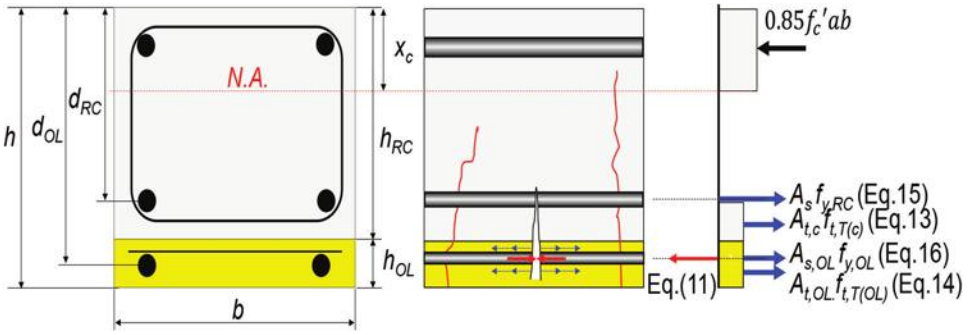

Fig. 14—Force equilibrium of PCM-overlay RCBs.

For the reinforcements, the tensile force of the deformed steel bar (F_s) and the plain bar ($F_{s,OL}$) are adopted from Eq. (15) and (16)

$$F_s = A_s \cdot f_y \tag{15}$$

$$F_{s,OL} = A_{s,OL} \cdot f_{y,OL} \tag{16}$$

In contrast to the perfect bond assumption for deformed steel bar in concrete, the plain bar in the PCM overlay is experienced by the slippage of bars due to its smooth outer surface under high temperatures. Therefore, the bond force property from Eq. (11) is employed, and the force equilibrium is illustrated in Eq. (17). It is worth noting that pullout force is a result of the bond strength and corresponding crack spacing. The slippage of steel bars resulted in crack spacing and slippage; therefore, there must be a reduction in the flexural strength, and this force is in compression in the tensile region, as shown in Fig. 14. By using the same equilibrium condition, the corresponding flexural moment can easily be computed by using the analytical expression described in Eq. (18).

$$F_s + F_{t,c} + F_{s,OL} + F_{t,OL} - F_{po} - F_c = 0 \tag{17}$$

$$M = F_s\left(d_{RC} - \frac{a}{2}\right) + F_{t,c}\left(h_{RC} - \frac{a}{2}\right) + F_{s,OL}\left(d_{OL} - \frac{a}{2}\right) + F_{t,OL}\left(h - \frac{a}{2}\right) - F_{po}\left(d_{OL} - \frac{a}{2}\right) \tag{18}$$

VALIDATIONS OF EXPERIMENTAL TESTS

At ambient temperature

The average CSM was validated using the PCM-overlay test results in previous studies.[12,20] From the previous test results, only ambient condition was selected because the test data at such a sustained temperature was not available. Hence, 11 beam data from the previous studies and six beams tested in this study were employed for the verification. The details of the beams are presented in the Appendix, and the experimental and analytical crack spacing of beams used in the database were provided in a previous study.[12] Analytical crack spacing was incorporated to calculate the pullout force (Eq. (11)) and the flexural capacity (Eq. (18)).

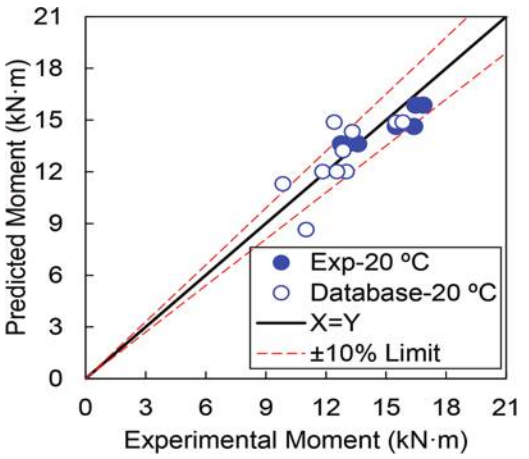

Fig. 15—Comparison between experimental database and analytical moments estimated by proposed methodology at ambient condition. (Note: 1 kN = 0.225 kip; 1 mm = 0.0394 in.)

The comparison is mentioned in Fig. 15. It can be observed that most of the data lie within ±10% limits of the X = Y line and verify the proposed methodology of average crack spacing at ambient conditions.

At elevated temperatures

All types of PCM-overlay RCBs were loaded until failure, and flexural crack spacing was measured. The load was noted until failure, as explained in the section "Experimental Test Results and Discussion." The flexural crack spacing was also measured analytically, as explained in Steps 1 and 2. Then, the pullout force was calculated (Eq. (11)) according to Step 3. The influence of temperature was incorporated to calculate the flexural crack spacing analytically (Table 6) and the bond strength. Finally, the flexural capacity was calculated at an elevated temperature by following Step 4.

The comparison of experimental and analytical moment capacity at three temperature levels is provided in Fig. 16. The comparison was also made by the sectional analysis method (SAM), and it can be observed that most of the data lie above the line of equality. This means that the authors' predicted value is greater than the experimental observation. However, it can also be observed from Fig. 16 that the data lie below the X = Y line, which indicates the right estimation of the predicted value. It can confidently explain the safer side. Moreover, all data lie within ±10% limits of the X = Y line, which reconfirms the applicability

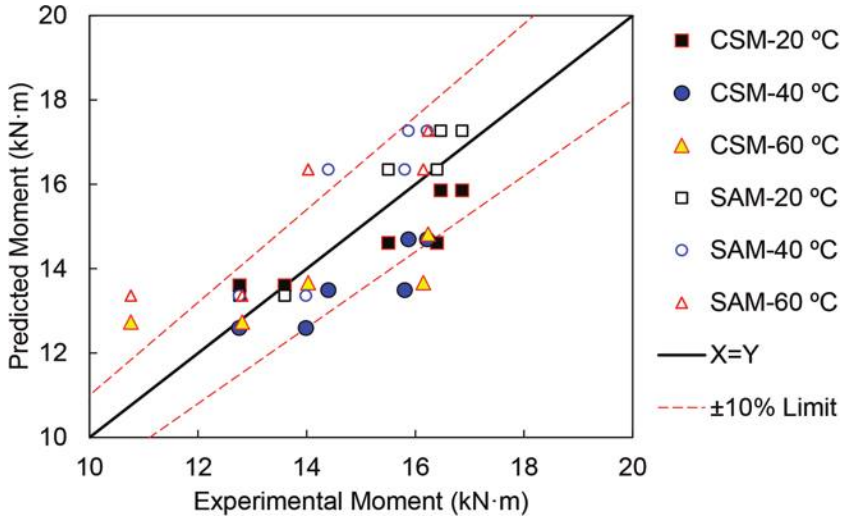

Fig. 16—Comparison between experimental moment and analytical moment, predicted by average crack spacing method (CSM) and sectional analysis method (SAM). (Note: 1 kN = 0.225 kip; 1 mm = 0.0394 in.)

of the proposed methodology. Therefore, it can be observed that due to cracking, the reduction in the flexural strength is obvious and may be extended to evaluate the service state of structures. Therefore, the first step was the in-depth study of flexural crack spacing with different reinforcement ratios and at different temperature levels. The analytical flexural crack spacing was used by the authors to predict the crack width of such beams.[14]

The proposed methodology can be employed for flexural strength analysis without any experimentation. It requires basic material properties such as compressive and tensile strengths of concrete and PCM and tensile strength of reinforcement. The flexural crack spacing and bond strength of the reinforcement are analytically obtained using the aforementioned material properties. Consequently, by using the Whitney block and considering the pullout force (Fig. 14), the flexural moment can be accurately predicted.

CONCLUSIONS

In this study, the flexural capacity of reinforced concrete beams (RCBs) with polymer cement mortar (PCM) overlays is predicted by incorporating the average crack spacing. This approach accounts for the degradation of bond performance in the PCM. To validate the experiment, 17 beams were tested under four-point bending in a temperature-controlled chamber specifically designed for this purpose. Three different high environmental temperatures—20, 40, and 60°C—were maintained for 24 hours during the test. The following conclusions have been drawn from the experimental and analytical study:

1. The crack initiation load decreases with an increase in sustained temperature level due to degradation in the compressive strength of PCM. It is observed that the cracking loads at 60°C decreased by approximately 29% compared with that of 20°C. The analytical cracking load represented a 31% reduction at 60°C, so it can properly estimate the cracking load under high environmental temperatures with respect to the serviceability.

2. Stiffness at the initial cracking and initial yielding increases with PCM-overlay strengthening at high environmental temperatures when compared to RCBs. The increase corresponds to the increase in the reinforcement ratio in PCM overlay, and the primer effect may not be significant.

3. The bar effect (β) for the plain and deformed bars has a significant effect on accurately estimating flexural crack spacing. Analytical results demonstrate that the variation from the experimental observation is 9.6% with the bar effect, while it shows 31.7% without the bar effect on flexural crack spacing.

4. Flexural crack spacing and bond strength are incorporated to calculate the pullout force. Finally, one additional compressive force in the tensile zone is considered in the Whitney block. The feasibility of the average crack spacing method (CSM) has been confirmed and validated by 28 beams, including those tested in this study. The validation results are within ±10% limits of the line of equality.

5. Compared with the sectional analysis method (SAM), the proposed methodology of CSM underestimates the flexural strength of PCM-overlay RCBs under elevated temperatures. This is due to the consideration of the bond strength degradation at elevated temperatures; therefore, it can bring a safer and more precise prediction.

AUTHOR BIOS

Khuram Rashid *is a Professor in the Department of Architectural Engineering and Design at the University of Engineering and Technology, Lahore, Lahore, Pakistan. He received his PhD from Hokkaido University, Sapporo, Japan. His research interests include strengthening of reinforced concrete structures with cementitious and non-cementitious materials, the development of sustainable materials, and the development of geopolymer-based construction materials (aggregates, concrete, and brick).*

Minkwan Ju *is a Research Professor in the Department of Civil and Environmental Engineering at Yonsei University, Seoul, South Korea. He received his PhD from Hanyang University, Seoul, South Korea. His research interests include fiber-reinforced polymer concrete structures and carbon-sequestrated recycled concrete.*

Tamon Ueda *is a Distinguished Professor in the Provincial Key Laboratory of Durability for Marine Civil Engineering, College of Civil and Transportation Engineering at Shenzhen University, Shenzhen, Guangdong, China. He received his Doctor of Engineering from The University of Tokyo, Tokyo,*

Japan. His research interests include structural intervention and service life prediction of concrete and hybrid structures with both the experimental approach and numerical simulation.

Dawei Zhang *is a Professor in the Institute of Structural Engineering, College of Civil Engineering and Architecture at Zhejiang University, Hangzhou, Zhejiang, China. He received his Doctor of Engineering from Hokkaido University. His research interests include the durability and safety improvement needs during the design, assessment, repair, and strengthening stages of the life cycle of concrete structures under combined environment and load impacts.*

ACKNOWLEDGMENTS

This research was performed by the Basic Science Research Program through the National Research Foundation of Korea (NRF) funded by the Ministry of Science and ICT (NRF-2020R1A2C1013043). The authors appreciate the support.

REFERENCES

1. Li, V. C., "On Engineered Cementitious Composites (ECC)," *Journal of Advanced Concrete Technology*, V. 1, No. 3, 2003, pp. 215-230. doi: 10.3151/jact.1.215

2. Ohama, Y., "Recent Progress in Concrete-Polymer Composites," *Advanced Cement Based Materials*, V. 5, No. 2, 1997, pp. 31-40. doi: 10.1016/S1065-7355(96)00005-3

3. Fowler, D. W., "Polymers in Concrete: A Vision for the 21st Century," *Cement and Concrete Composites*, V. 21, No. 5-6, 1999, pp. 449-452. doi: 10.1016/S0958-9465(99)00032-3

4. Ganesh, R., and Ravikumar, P., "Polymer Modified Mortar and Concrete Present Status a Review," *IOSR Journal of Mechanical and Civil Engineering (IOSR-JMCE)*, V. 13, No. 3, Version 7, 2016, pp. 89-100.

5. Rashid, K.; Zhang, D.; Ueda, T.; and Jin, W., "Investigation on Concrete-PCM Interface under Elevated Temperature: At Material Level and Member Level," *Construction and Building Materials*, V. 125, 2016, pp. 465-478. doi: 10.1016/j.conbuildmat.2016.08.067

6. Rashid, K.; Wang, Y.; and Ueda, T., "Influence of Continuous and Cyclic Temperature Durations on the Performance of Polymer Cement Mortar and Its Composite with Concrete," *Composite Structures*, V. 215, 2019, pp. 214-225. doi: 10.1016/j.compstruct.2019.02.057

7. Rashid, K.; Ueda, T.; Zhang, D.; Miyaguchi, K.; and Nakai, H., "Experimental and Analytical Investigations on the Behavior of Interface between Concrete and Polymer Cement Mortar under Hygrothermal Conditions," *Construction and Building Materials*, V. 94, 2015, pp. 414-425. doi: 10.1016/j.conbuildmat.2015.07.035

8. ASTM C666/C666M-15, "Standard Test Method for Resistance of Concrete to Rapid Freezing and Thawing," ASTM International, West Conshohocken, PA, 2015, 7 pp.

9. Khan, M. S.; Prasad, J.; and Abbas, H., "Bond Strength of RC Beams Subjected to Cyclic Thermal Loading," *Construction and Building Materials*, V. 38, 2013, pp. 644-657. doi: 10.1016/j.conbuildmat.2012.09.018

10. Wang, L.; Zhang, X.; Zhang, J.; Dai, L.; and Liu, Y., "Failure Analysis of Corroded PC Beams under Flexural Load Considering Bond Degradation," *Engineering Failure Analysis*, V. 73, 2017, pp. 11-24. doi: 10.1016/j.engfailanal.2016.12.004

11. Zhang, X.; Wang, L.; Zhang, J.; and Liu, Y., "Model for Flexural Strength Calculation of Corroded RC Beams Considering Bond–Slip Behavior," *Journal of Engineering Mechanics*, ASCE, V. 142, No. 7, 2016, p. 04016038. doi: 10.1061/(ASCE)EM.1943-7889.0001079

12. Zhang, D.; Ueda, T.; and Furuuchi, H., "Intermediate Crack Debonding of Polymer Cement Mortar Overlay-Strengthened RC Beam," *Journal of Materials in Civil Engineering*, ASCE, V. 23, No. 6, 2011, pp. 857-865. doi: 10.1061/(ASCE)MT.1943-5533.0000240

13. Zhang, D.; Ueda, T.; and Furuuchi, H., "Average Crack Spacing of Overlay-Strengthened RC Beams," *Journal of Materials in Civil Engineering*, ASCE, V. 23, No. 10, 2011, pp. 1460-1472. doi: 10.1061/(ASCE)MT.1943-5533.0000316

14. Zhang, D.; Rashid, K.; Wang, B.; and Ueda, T., "Experimental and Analytical Investigation of Crack Spacing and Width for Overlaid RC Beams at Elevated Temperatures," *Journal of Structural Engineering*, ASCE, V. 143, No. 12, 2017, p. 04017168. doi: 10.1061/(ASCE)ST.1943-541X.0001910

15. Rashid, K.; Li, X.; Xie, Y.; Deng, J.; and Zhang, F., "Cracking Behavior of Geopolymer Concrete Beams Reinforced with Steel and Fiber Reinforced Polymer Bars under Flexural Load," *Composites Part B: Engineering*, V. 186, 2020, Article No. 107777. doi: 10.1016/j.compositesb.2020.107777

16. ASTM C39/C39M-20, "Standard Test Method for Compressive Strength of Cylindrical Concrete Specimens," ASTM International, West Conshohocken, PA, 2020, 8 pp.

17. ASTM C496/C496M-17, "Standard Test Method for Splitting Tensile Strength of Cylindrical Concrete Specimens," ASTM International, West Conshohocken, PA, 2017, 5 pp.

18. ACI Committee 318, "Building Code Requirements for Structural Concrete (ACI 318-19) and Commentary (ACI 318R-19) (Reapproved 2022)," American Concrete Institute, Farmington Hills, MI, 2019, 624 pp.

19. ICRI, "Selecting and Specifying Concrete Surface Preparation for Sealers, Coatings and Polymer Overlays," International Concrete Repair Institute, Inc., St. Paul, MN, 1997.

20. Satoh, K., and Kodama, K., "Central Peeling Failure Behavior of Polymer Cement Mortar Retrofitting of Reinforced Concrete Beams," *Journal of Materials in Civil Engineering*, ASCE, V. 17, No. 2, 2005, pp. 126-136. doi: 10.1061/(ASCE)0899-1561(2005)17:2(126)

21. Zhang, D.; Ueda, T.; and Furuuchi, H., "Concrete Cover Separation Failure of Overlay-Strengthened Reinforced Concrete Beams," *Construction and Building Materials*, V. 26, No. 1, 2012, pp. 735-745. doi: 10.1016/j.conbuildmat.2011.06.082

22. Safdar, M.; Matsumoto, T.; and Kakuma, K., "Flexural Behavior of Reinforced Concrete Beams Repaired with Ultra-High Performance Fiber Reinforced Concrete (UHPFRC)," *Composite Structures*, V. 157, 2016, pp. 448-460. doi: 10.1016/j.compstruct.2016.09.010

23. Park, R., and Paulay, T., *Reinforced Concrete Structures*, John Wiley & Sons, Inc., Hoboken, NJ, 1975.

24. Rashid, K.; Li, X.; Deng, J.; Xie, Y.; Wang, Y.; and Chen, S., "Experimental and Analytical Study on the Flexural Performance of CFRP-Strengthened RC Beams at Various Pre-Stressing Levels," *Composite Structures*, V. 227, 2019, Article No. 111323. doi: 10.1016/j.compstruct.2019.111323

25. Nilson, A. H.; Darwin, D.; and Dolan, C. W., *Design of Concrete Structures*, 14th edition, McGraw-Hill, New York, NY, 2010.

26. JSCE, "Concrete," Japan Society of Civil Engineers, Tokyo, Japan, 2007.

27. CSA S474:04 (R2019), "Concrete Structures," CSA Group, Toronto, ON, Canada, 2004, 70 pp.

28. *fib*, "*fib* Model Code for Concrete Structures 2010," International Federation for Structural Concrete, Lausanne, Switzerland, 2013, 434 pp.

APPENDIX

Table A1—Experimental test data for validation[13,22]

No.	Beam ID	S_{cr}, mm		Overlay reinforcement			d_{OL}, mm	Perimeter, mm	Overlay thickness, mm
		Analytical	Experimental	No. of bars	Diameter, mm	Area, mm^2			
1	R6-2-10	93.42	128.91	2	10	71.33	155	62.83	30
2	R6-2-10	118.38	120.31	2	10	71.33	155	62.83	30
3	R6-3-10	93.42	100.78	3	10	71.33	155	94.25	30
4	R8-3-6	124.11	122.19	3	6	31.67	153	56.55	22
5	R8-2-10	118.38	102.5	2	10	71.33	155	62.83	30
6	R8-3-10	93.42	96.25	3	10	71.33	155	94.25	30
7	R8-3-6	124.11	114	3	6	31.67	153	56.55	22
8	R8-2-10	118.38	96	2	10	71.33	155	62.83	30
9	R8-3-10	93.42	96	3	10	71.33	155	94.25	30
10	R4-2-10	140.53	151.6	2	10	71.33	170	62.83	30
11	R4-3-10	110.01	126.6	3	10	71.33	170	94.25	30

TECHNOLOGY FORUM

29 - 31 AUGUST 2023

PORTLAND, OR

THE BENSON PORTLAND, CURIO COLLECTIONS BY HILTON

SAVE THE DATE

The **Technology Forum** is an industry-exclusive educational and networking event for concrete professionals **powered by ACI Foundation's Concrete Innovation Council**.

Whether you are an emerging professional or a seasoned veteran, the ACI Foundation Technology Forum is the place to learn about **current trends, emerging technologies, and discoveries within the concrete industry**.

Join us for an exciting and insightful event featuring thought leaders and technology innovators to discuss the future of the concrete industry.

acifoundation.org

aci Foundation
Building the Future

ACI STRUCTURAL JOURNAL TECHNICAL PAPER

Title No. 120-S66

Quasi-Static Cyclic Flexural Loading Behavior of Precast Reinforced Concrete Tunnel Segments with Glass Fiber-Reinforced Polymer Bars

by Basil Ibrahim, Salaheldin Mousa, Hamdy M. Mohamed, and Brahim Benmokrane

The strength and behavior of segments of precast concrete tunnel linings (PCTLs) reinforced internally with fiber-reinforced polymer (FRP) bars under quasi-static cyclic flexural loading is one area in which no experimental research results are available. This research investigated the cyclic behavior of glass FRP (GFRP)-reinforced PCTL segments, both experimentally and theoretically. Full-scale specimens with a total length, width, and thickness of 3100 mm (122 in.), 1500 mm (59 in.), and 250 mm (9.8 in.), respectively, were constructed and tested under quasi-static cyclic flexural loading. Two cycles of loading and unloading were applied at 1.25%, 2.5%, 5%, 10%, 25%, 50%, and 75% of the estimated maximum displacement, followed by a single cycle up to failure. The test parameters included reinforcement flexural stiffness (GFRP versus steel) and GFRP longitudinal reinforcement ratio. The hysteresis response, cracking pattern, residual deformation, dissipated energy, deformability, and secant stiffness damage index of the tested specimens were defined, estimated, and evaluated. The experimental results of this study show that the hysteresis cycles of the GFRP-reinforced specimens reflected stable cyclic behavior with no or limited strength degradation. Moreover, the test results show that the GFRP-reinforced specimens demonstrated adequate ductility index and deformability limits. A theoretical prediction according to the various current design provisions—including the flexural and shear capacities of the PCTL segments—was carried out and compared to the experimental results. The results of this study show the feasibility and efficiency of using GFRP bars instead of steel bars for PCTL segments under quasi-static cyclic flexural loading.

Keywords: deformability; design codes; energy dissipation; flexural and shear strength; glass fiber-reinforced polymer (GFRP) bars; hysteretic behavior; precast concrete tunnel lining (PCTL) segments; quasi-static cyclic load.

INTRODUCTION

The use of precast concrete tunnel lining (PCTL) systems in tunneling construction projects has been gaining ground over conventional on-site lining technique because of its economic efficiency. PCTL speeds the construction process and ensures the highest quality due to enhanced control during the fabrication of precast segments in precast plants (Cheong et al. 2005). The structural performance of PCTL segments significantly depends on their durability performance. Tunnel structures built with steel-reinforced concrete are designed for service lives exceeding 100 years. The ingress of chloride ions into PCTL segments can induce reinforcement corrosion, which has been the primary cause threatening the structural safety of PCTLs and shortening their designed service lives. Corrosion of embedded reinforcement bars is considered the most prevalent mode of deterioration affecting the serviceability, safety, and structural integrity of tunnel structures (Gulikers 2003). In fact, many reinforced concrete (RC) tunnels around the world are deteriorating as they age (Zhiqiang and Mansoor 2013). Steel-reinforced PCTLs often experience premature degradation mainly due to corrosion of the reinforcement bars, requiring expensive repairs and maintenance. Because concrete is not perfectly impermeable, groundwater—often high in chlorine—gradually saturates the concrete, ultimately permeating the cover and producing an electrolytic reaction with the steel, which accelerates corrosion of the reinforcement (Rancourt 2016). This corrosion can lead to oxide jacking (also known as rust burst) and loss of structural integrity. Corrosion of steel reinforcement is the most expensive and problematic deterioration mechanism in concrete structures (ACI 440.1R-15 [ACI Committee 440 2015]). In Canada, the annual cost of repairing corrosion damage in reinforced concrete structures has been estimated at more than $10 billion per year (Davis 2000). In the United States, the problem of corrosion of reinforced concrete structures costs the economy approximately $100 billion each year, or nearly 1% of the country's gross domestic product (Whitmore and Ball 2004). One effective solution to this corrosion problem is to replace steel reinforcement with noncorroding fiber-reinforced polymer (FRP) reinforcing bars. These lightweight, high-strength FRP bars are characterized by high corrosion resistance, long service life, and reduced maintenance costs (Manalo et al. 2020).

Recently, a few studies investigated the possibility of using glass FRP (GFRP) reinforcement in PCTL segments (Caratelli et al. 2017; Spagnuolo et al. 2017; Meda et al. 2019; Hosseini et al. 2022). All these studies proved the suitability of using GFRP bars as reinforcement for PCTL segments. The experimental evidence from these investigations showed that the GFRP-reinforced PCTL segments exhibited better cracking control behavior compared to traditional reinforced concrete segments. The load related to the first crack was higher and the crack openings were

ACI Structural Journal, V. 120, No. 4, July 2023.

MS No. S-2022-029.R1, doi: 10.14359/51738719, received June 16, 2022, and reviewed under Institute publication policies.

narrower. Moreover, these studies revealed no significant difference in the flexural behavior of the GFRP-reinforced PCTL segments compared to the steel-reinforced ones. Substantively, increasing of the strength of the GFRP bars compensated for the lack of ductility compared to the steel-reinforced PCTL segments. Past studies, however, have focused mainly on the static flexural resistance of PCTLs to evaluate their structural properties. During its service life, a tunnel structure can be subjected to permanent loads (dead loads, earth pressure, surcharge loads), live loads (vehicular loads, live-load surcharges, and so on), or transient loads (water loads, earthquake, superimposed deformations, blasts, fire, construction loads). According to ACI 544.7R-16 (ACI Committee 544 2016), the loads acting on PCTLs from the time of segment casting up to the time of segment erection within the tunnel-boring machine (TBM) shield fall into three stages. They are termed the production and transient stage, the construction stage, and the service stage. The internal forces and stresses in the production and transient stages are included in the design of PCTL segments. The construction stage includes the TBM jacking thrust loads on the circumferential ring joints and the pressures during the grouting operation exerted against the exterior of the completed rings. PCTL segments are designed to resist significant bursting and spalling tensile stresses that develop along the circumferential joints due to advancement of the TBM. The final service stages are represented by the long-term loads imposed on the lining from the ground, groundwater, surcharges, and other loads (such as seismic loads). The flexural behavior of steel-fiber reinforced concrete and conventionally steel-reinforced PCTL segments under quasi-static cyclic flexural loading was experimentally studied by Abbas (2014). It was revealed that both steel-fiber reinforced concrete and conventionally steel-reinforced PCTL segments exhibited reasonable levels of ductility and energy dissipation capacities and satisfied the flexural requirement under quasi-static cyclic flexural loading. Basically, there are no research results in the literature on the cyclic behavior of GFRP-reinforced PCTLs. Accordingly, the performance of full-scale PCTL segments under quasi-static cyclic flexural loading needs to be investigated.

This study is part of an ongoing comprehensive research program carried out in the Department of Civil Engineering at the University of Sherbrooke to improve current practices and develop more efficient design and construction approaches for using curvilinear GFRP bars and stirrups in precast concrete tunnel lining segments. Full-scale GFRP-reinforced PCTL segments are tested under different loading conditions—static flexural loading (Hosseini et al. 2022), quasi-static cyclic flexural loading, and punching shear and settlement—to investigate different variables and design parameters. This paper presents the structural behavior of full-scale GFRP-reinforced PCTL segments under quasi-static cyclic flexural loading, according to ACI 374.2R-13 (ACI Committee 374 2013). The effect of reinforcement type and ratio on the behavior of GFRP-reinforced precast concrete tunnel lining segments under quasi-static cyclic flexural loading was investigated. This paper is the first study to investigate the cyclic behavior of PCTL segments reinforced with GFRP bars. It also aimed at determining the feasibility and efficiency of using GFRP instead of steel reinforcement.

RESEARCH SIGNIFICANCE

The design of the PCTL segments reinforced with FRP bars is not defined or discussed in the current design provisions such as in ACI 440.1R-15, ACI 544.7R-16, and ACI 533.5-20 (ACI Committee 533 2020). The strength and behavior of such members reinforced with FRP bars is one area in which limited research results are available for implementing this noncorroding composite reinforcement. So far, this research is the first experimental work aimed at providing experimental data involving the laboratory testing of the performance of PCTL segments reinforced with GFRP reinforcement under quasi-static cyclic flexural loading. Full-scale PCTL specimens were tested to determine the effects of reinforcement flexural stiffness (GFRP versus steel) and GFRP longitudinal reinforcement ratio. A theoretical study was also conducted to calculate the flexural and shear capacities of PCTL segments reinforced with GFRP bars according to the various current design provisions (ACI 440.1R-15; CSA S806-12(R2017) 2017; *fib* TG-9.3 2007; CNR-DT 203 2006; AFGC 2021). As this study presents the first results of their kind on the applicability of using GFRP as internal reinforcement for PCTLs under quasi-static cyclic flexural loading, the results reported in this manuscript represent a significant contribution to the relevant literature and provide end users, engineers, and code committees with much-needed data and recommendations to advance the use of GFRP reinforcement in PCTL segments. The study also is expected to be a step toward further research to assess the possibility of developing new applications for GFRP bars and ties, resulting in more durable, economic, and competitive PCTL segments for tunnel applications.

EXPERIMENTS

Materials

Table 1 provides the mechanical properties of the GFRP and steel bars used to reinforce the PCTL segments in this study. The GFRP bars were manufactured by pultruding boron-free glass fibers impregnated in a thermosetting vinylester resin. The ultimate tensile strength f_{fu} and modulus of elasticity E_f of the GFRP bars were determined according to ASTM D7205 (2021). The GFRP bars had a sand-coated surface to enhance bonding and force transfer between the bars and concrete. Number 6 (20 mm), No. 5 (15 mm), and No. 4 (13 mm) GFRP bars were used for both longitudinal and transverse reinforcement in the segments, as shown in Figure 1(a). Moreover, No. 6 (20 mm) and No. 5 (15 mm) closed U-shaped GFRP bars were used as anchorage for the longitudinal reinforcement bars. For the control specimen, deformed 15M (16 mm) steel bars were used as longitudinal reinforcement and deformed 10M (11 mm) steel bars as transverse reinforcement. Deformed 15M (16 mm) U-shaped steel bars were used to anchor the longitudinal reinforcement bars.

All PCTL segments were cast with normalweight concrete by a local precast company. The average actual compressive

Table 1—Mechanical properties of reinforcement bars

Reinforcement type	Bar size	Bar diameter, mm	Nominal cross-sectional area, mm^2	Modulus of elasticity, GPa	Tensile strength, MPa	Tensile strain, %
Curvilinear GFRP bars	No. 5	15.0	199	55.1	1115	2.0
	No. 6	20.0	284	52.9	1068	2.0
U-shaped GFRP bars	No. 5	15.0	199	53.5	1283	2.4
	No. 6	20.0	284	53.2	1131	2.1
Closed GFRP ties	No. 4	13.0	129	55.6	1248	2.2
Steel bars	10M	11.3	100	200.0	480*	0.24†
	15M	16.0	200	200.0	460*	0.23†

*Yield strength of steel bars.

†Yield strain of steel bars.

Note: 1 mm = 0.0394 in.; 1 MPa = 145 psi; 1 GPa = 145 ksi.

Table 2—Test matrix

Specimen ID	Reinforcement type	Concrete compressive strength f_c', MPa	Longitudinal reinforcement		Transverse reinforcement
			ρ_f, %	Number of bars	
7S15	Steel	53	0.5	Seven 15M bars	10M bars @ 200 mm
7G15	GFRP	52	0.5	Seven No. 5 bars	No. 4 bars @ 200 mm
13G15	GFRP	52	0.9	Thirteen No. 5 bars	No. 4 bars @ 200 mm
13G20	GFRP	50	1.2	Thirteen No. 6 bars	No. 4 bars @ 200 mm

Note: 1 mm = 0.0394 in.; 1 MPa = 145 psi.

Fig. 1—Overview of: (a) GFRP bars and ties; (b) assembled GFRP cage for specimens with seven top and bottom longitudinal bars; and (c) assembled GFRP cage for the specimens with 13 top and bottom longitudinal bars.

strength based on the average test results of 100 x 200 mm (3.94 x 7.89 in.) concrete cylinders tested on the first day of the start of testing of the specimens was 52.2 MPa (7.6 ksi).

Specimen details

The experimental program was designed to provide data on the cyclic behavior of PCTL segments reinforced with GFRP bars. Four full-scale PCTL segments (three reinforced with GFRP bars and one with conventional steel reinforcement) were tested under quasi-static cyclic flexural loading. The inner and outer radii of the four PCTL segments were designed to be 3250 and 3500 mm (128 and 138 in.), respectively. The test specimens measured 3100 mm (122 in.) in length, 1500 mm (59 in.) in width, and 250 mm (9.8 in.) in thickness. The segments were skewed at their ends rather than straight. Figures 1(b) and (c) show assembled GFRP cages for the test specimens. The test matrix was arranged to assess the influence of the flexural reinforcement type (GFRP versus steel) and the GFRP flexural reinforcement ratio. Longitudinal reinforcement ratios of 0.5%, 0.9%, and 1.2% were chosen as the minimum reinforcement ratio for concrete crushing controlled by flexural failure, an intermediate reinforcement ratio, and the maximum reinforcement ratio practically possible. Table 2 provides the test matrix and reinforcement details of the test specimens. The test specimens are identified as follows. The first number indicates the number of longitudinal bars. The letters G and S stand for GFRP and steel reinforcement, respectively. The second number indicates the nominal diameter of the longitudinal bars. Specimen 7G15 had top and bottom longitudinal reinforcement consisting of seven No. 5 GFRP bars with a longitudinal reinforcement ratio of 0.5%. Seven

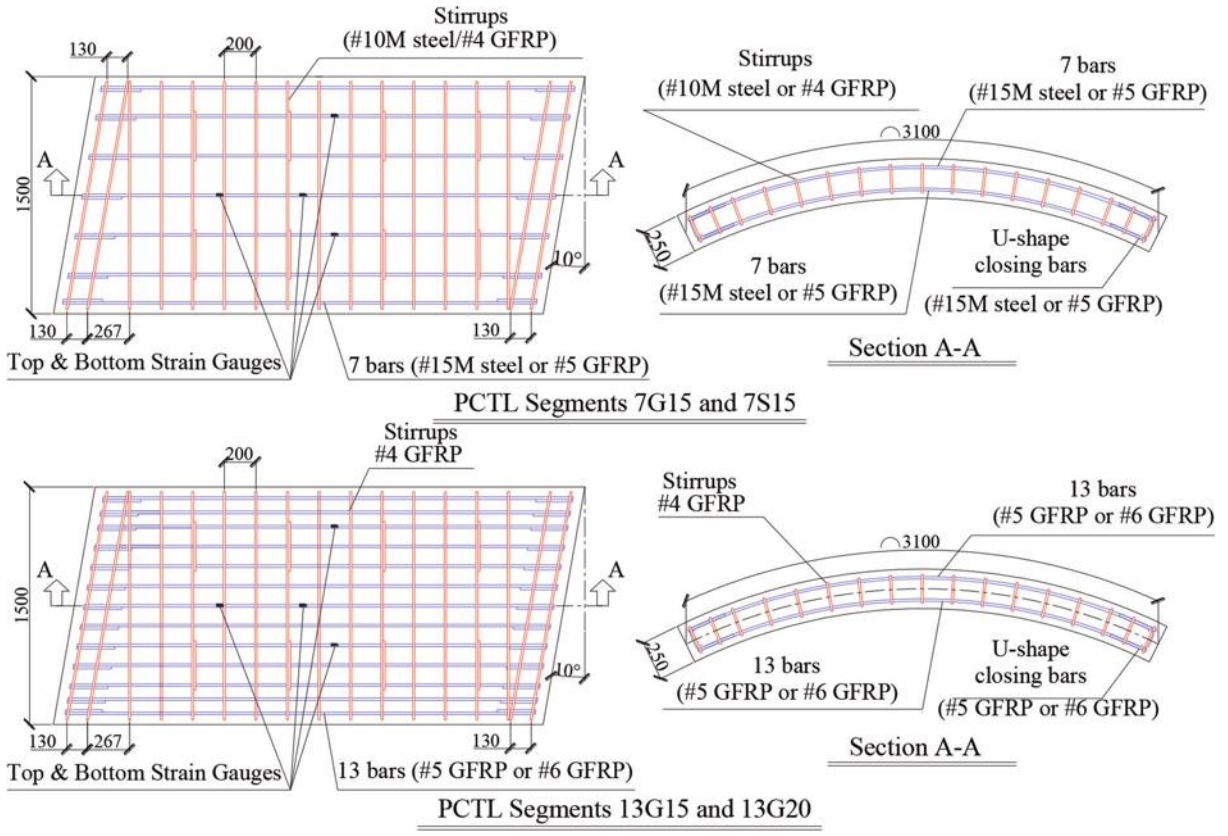

Fig. 2—Reinforcement details for test specimens. (Note: All dimensions in mm; 1 mm = 0.0394 in.)

No. 5 U-shaped GFRP anchorage bars were installed on each side of the specimen. Specimens 13G15 and 13G20 had top and bottom longitudinal reinforcement consisting of 13 No. 5 GFRP bars and 13 No. 6 GFRP bars with longitudinal reinforcement ratios of 0.9% and 1.25%, respectively. Thirteen No. 5 U-shaped GFRP anchorage bars and 13 No. 6 U-shaped GFRP anchorage bars were installed on each side of Specimens 13G15 and 13G20, respectively. All the GFRP specimens were reinforced transversally with No. 4 GFRP ties at a spacing of 200 mm (7.87 in.). The control steel specimen (7S15) had top and bottom longitudinal reinforcement consisting of seven M15 deformed steel bars with a reinforcement ratio of 0.5% and transverse reinforcement consisting of M10 ties at a spacing of 200 mm (7.87 in.). Seven deformed 15M U-shaped anchorage steel bars were installed on each side of the specimen. Figure 2 shows the reinforcement details for all the test specimens. The clear cover was kept constant at 40 mm (1.57 in.) for all specimens.

Instrumentation and test setup

Strains in the longitudinal and transverse reinforcing bars were measured with electrical resistance strain gauges with a gauge length of 10 mm (0.39 in.) (Fig. 2). In addition, five strain gauges with a gauge length of 60 mm (2.36 in.) were mounted on the concrete surface at the mid- and quarter span to measure the concrete compressive strain. Specimen deflections were measured with five linear potentiometers (LPOTs) placed at the mid- and quarter span. The test setup was designed and fabricated at the University of Sherbrooke's CFI structural laboratory.

The specimens were loaded under three-point bending load, as shown in Fig. 3(a), using an 11,000 kN (247.3 kip) capacity universal testing machine attached to a spreader beam. The span for the test specimens was 2400 mm (94.5 in.). The load was applied at a displacement-controlled rate of 0.8 mm/min. An automatic data-acquisition system monitored by a computer was used to record the readings of the LPOTs, load cells, and strain gauges.

Quasi-static cyclic loading procedure

The test protocol followed is that in ACI 374.2R-13: tests of structural components under slowly applied quasi-static loading, either as monotonically increasing or reversed cyclic loading. Quasi-static cyclic flexural loading was applied in terms of the percentage of the maximum displacement (Δ_{max}) obtained from the static testing results in the literature (Hosseini et al. 2022). Two cycles of loading and unloading were conducted for 1.25, 2.5, 5, 10, 25, 50, and 75% of Δ_{max}, followed by one cycle up to failure. In all cycles, the unloading phase was finished with a minimum load of 5 kN (1.12 kip) to keep the test jack engaged. Figure 3(b) shows the loading scheme for the tested specimens.

TEST RESULTS AND DISCUSSION

This section summarizes the experimental results, including the general behavior of the test specimens in terms of hysteresis response, crack patterns and failure modes, strain in reinforcement and concrete, neutral-axis depth, deformability, dissipated energy, and ductility and secant-stiffness damage index. Table 3 summarizes the

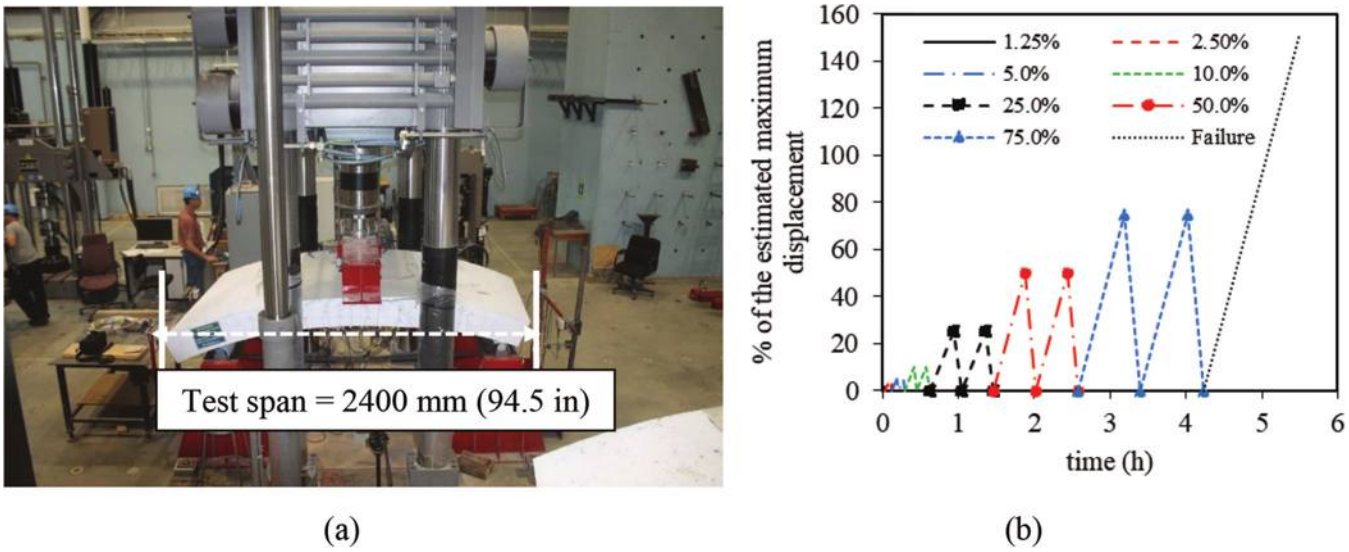

Fig. 3—(a) Test setup; and (b) loading scheme for tested specimens.

Table 3—Summary of experimental and theoretical results

Specimen ID	Cracking moment, kN·m	Failure moment, kN·m	M_{exp}/M_{pred}					V_{exp}/V_{pred}				
			ACI 440.1R-15	CSA S806-12	*fib* TG-9.3-2007	AFGC 2021	CNR-DT 203-2006	ACI 440.1R-15	CSA S806-12	*fib* TG-9.3-2007	AFGC 2021	CNR-DT 203-2006
7G15	48	206	0.97	0.86	0.96	0.96	1.29	1.63	1.11	1.26	1.19	0.81
13G15	49	243*	0.87	0.78	0.81	0.87	0.88	1.44	1.09	1.11	1.14	0.85
13G20	55	238†	0.76	0.68	0.68	0.77	0.67	1.28	0.97	0.99	1.01	0.76

*Shear load failure = 178 kN (40.02 kip).

†Shear load failure = 174 kN (39.12 kip).

Note: 1 mm = 0.0394 in.; 1 kN·m = 0.738 kip·ft.

flexural moment and shear load-carrying capacities of the test specimens.

Hysteresis response

The hysteresis behavior is shown in the form of the moment versus midspan deflection of specimens, as presented in Fig. 4. Initially, all the specimens exhibited identical linear load-deflection behavior. After cracking, the stiffness of the GFRP specimens reduced with almost linear load-deflection behavior. The steel-reinforced specimen also had initial linear load-deflection behavior corresponding to the uncracked condition of the specimen. Its stiffness decreased due to yielding of the longitudinal reinforcement in the tension zone, followed by a gradual decrease in overall stiffness. Figure 5 shows the cracking pattern in the test specimens. The first vertical flexural crack initiated in the tension zone under the loading point. The corresponding cracking moment was recorded during testing and verified from the moment-strain and moment-deflection relationships. The cracking moment M_{cr} ranged from 48 to 55 kN·m (35.40 to 40.57 kip·ft), occurring in the first cycle at 5% of the maximum displacement. At this stage, there were no significant strain-gauge readings for the GFRP or steel reinforcing bars before initiation of the first flexural crack. In addition, the concrete strains were insignificant in all specimens, ranging from –60 to –130 με at the top location of the midspan, as shown in Fig. 6(a). Beyond the first cracking load, additional flexural cracks developed within the shear span of the 7G15 specimen, in the 10% and 25% maximum displacement cycles. With further loading, in the first 75% of the maximum displacement cycle, the flexural cracks became wider and propagated upward towards the loading point, while some new cracks started to develop in the shear span (Fig. 5). Before failure occurred, the cracks along the shear span started to incline towards the loading points. The concrete crushing moment M_n for the 7G15 specimen was 206 kN·m (151.9 kip·ft), with a maximum recorded midspan concrete compressive strain of –3840 με on concrete crushing, as shown in Fig. 6(a). Specimens 13G15 and 13G20 behaved similarly before 75% of the maximum displacement cycle. Beyond this stage, a main shear crack started to develop and propagated until shear failure occurred at a shear load V_n of 178 and 174 kN (40.02 and 39.12 kip), respectively. The failure of Specimens 13G15 and 13G20 occurred by shear compression failure and diagonal tension failure, respectively. The maximum recorded midspan concrete compressive strain in specimen 13G15 was –3285 με, indicating shear compression failure. In contrast, the diagonal tension failure in Specimen 13G20 resulted in a maximum midspan concrete compressive strain of –2051 με, as shown in Fig. 6(a). The hysteretic response for the GFRP-reinforced specimens, in all second excursion

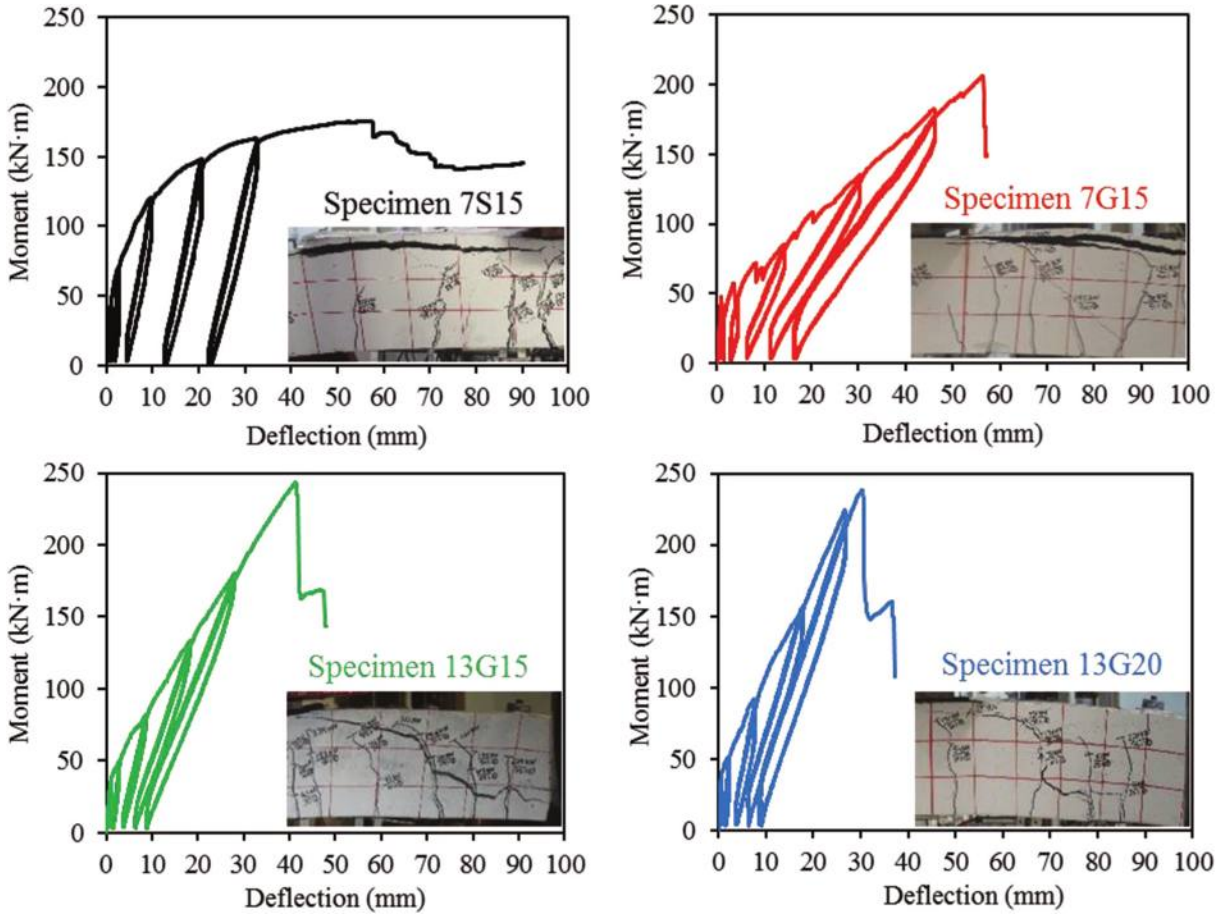

Fig. 4—Hysteresis response and failure mode of test specimens.

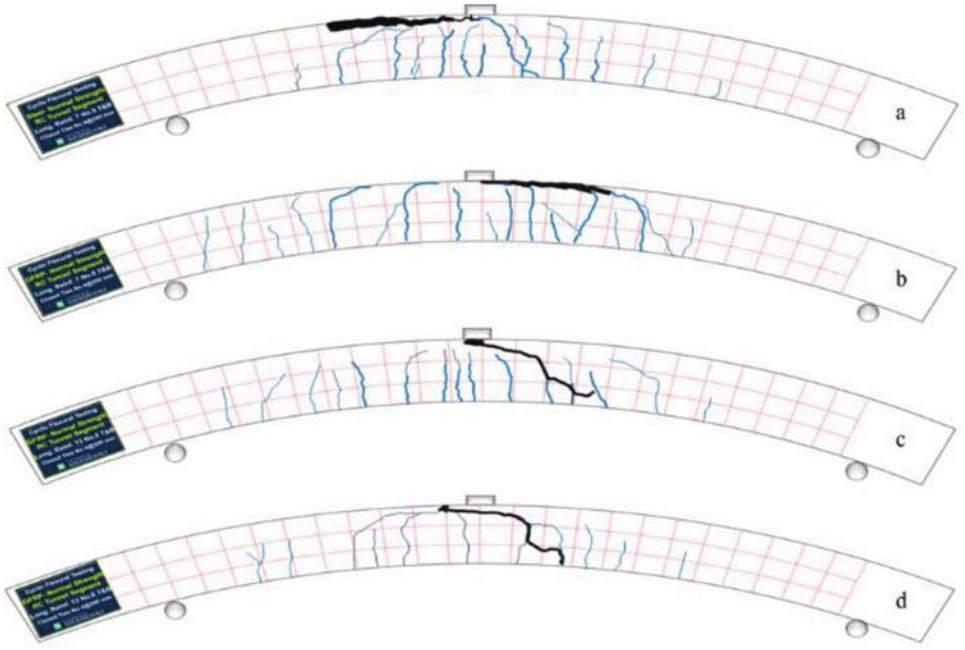

Fig. 5—Cracking pattern in: (a) Specimen 7S15; (b) Specimen 7G15; (c) Specimen 13G15; and (d) Specimen 13G20.

loading cycles, reflected stable cyclic behavior with no or limited strength degradation until failure. In contrast, the early yielding of the steel bars in specimen 7S15 resulted in wider concentrated cracks compared to the GFRP-reinforced specimens. Specimen 7S15 yielded (at a corresponding strain of approximately 2300 με) in the first 25% of the maximum displacement cycle at an applied moment of 114 kN·m (84.1 kip·ft) (approximately at 64% of the specimen's peak moment). The midspan concrete compressive strain reading in Specimen 7S15 when the steel yielded was

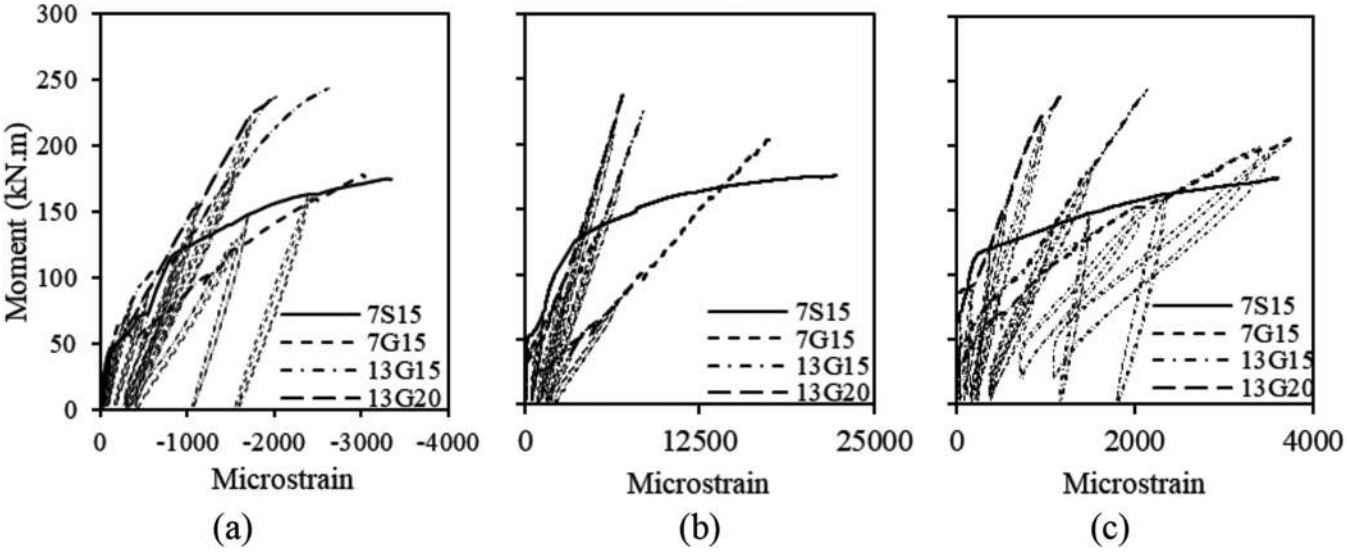

Fig. 6—Moment-strain relationship at midspan at: (a) concrete surface; (b) bottom reinforcement bars; and (c) top reinforcement bars.

–795 με, as shown in Fig. 6(a). The concrete strain gauge continued recording after this point until the ultimate applied moment of 176 kN·m (129.8 kip·ft) (concrete crushing) at 3336 με. The strain in the GFRP bars on the tension side gradually increased up to specimen failure at 17,695, 8508, and 7023 με (88%, 43%, and 35% of the ultimate tensile strain of the GFRP bars) for Specimens 7G15, 13G15 and 13G20, respectively, as shown in Fig. 6(b). In addition, the strain-gauge readings show that the top reinforcement bars in all the specimens were under tension, which enhanced specimen strength. The recorded strains in Specimens 7S15, 7G15, 13G15, and 13G20 in the top reinforcement (GFRP or steel bars) at failure were 3761, 2163, 1164, and 3603 με, respectively, as shown in Fig. 6(c). The test results indicate that the recorded strains at the quarter span for both the reinforcement bars and the concrete surface were less than that at midspan.

Unloading stiffness and residual deformation

Unloading stiffness is an important parameter because it determines the value of the residual deformation, thus determining the recoverability of the structure (Fahmy et al. 2009). As shown in Fig. 4, the unloading stiffness for the GFRP-reinforced specimens in all cycles was nearly equal to the reloading stiffness. In contrast, the yielding of the steel bars in Specimen 7S15 at 25% of the maximum displacement cycle resulted in higher residual deformation compared to the GFRP-reinforced Specimen 7G15. The average unloading stiffness of Specimen 7S15 at 25%, 50%, and 75% of the estimated maximum displacement cycles was 95%, 85%, and 89%, respectively, of the reloading stiffness. Residual deformation is often used as a key measure of the required recoverability of RC structures (Dong et al. 2016). Figure 7 compares the cumulative residual deformation of Specimens 7G15 and 7S15. The residual deformation of the GFRP-reinforced specimen during unloading at 50% and 75% of the maximum displacement cycles was less than that of the steel-reinforced specimen due to the yielding

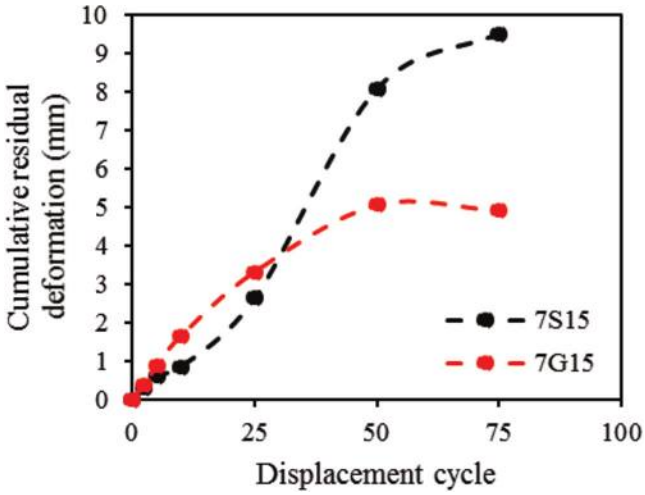

Fig. 7—Cumulative residual deformation for GFRP-reinforced (7G15) versus steel-reinforced (7S15) specimens with similar reinforcement ratios.

of the steel bars in the tension zone. In general, the GFRP specimens recovered most of their deflection during the unloading at 50% and 75% of the maximum displacement cycles. When 50% of the maximum displacement cycles in Specimen 7S15 was exceeded, a permanent deflection occurred in the unloading cycles due to the yielding of the steel bars.

Effect of parameters

This section presents the envelope moment-deflection curves at the midspan of the test specimens in two groups to show the effect of test parameters on specimen behavior, as depicted in Fig. 8. Before cracking occurred, identical linear moment-deflection behavior was observed in all the test specimens, regardless of reinforcement ratio and type, representing the uncracked condition governed by the properties of the concrete section. After cracking occurred, the response of the GFRP-reinforced specimens was almost linear up to failure. The moment-deflection curve of the

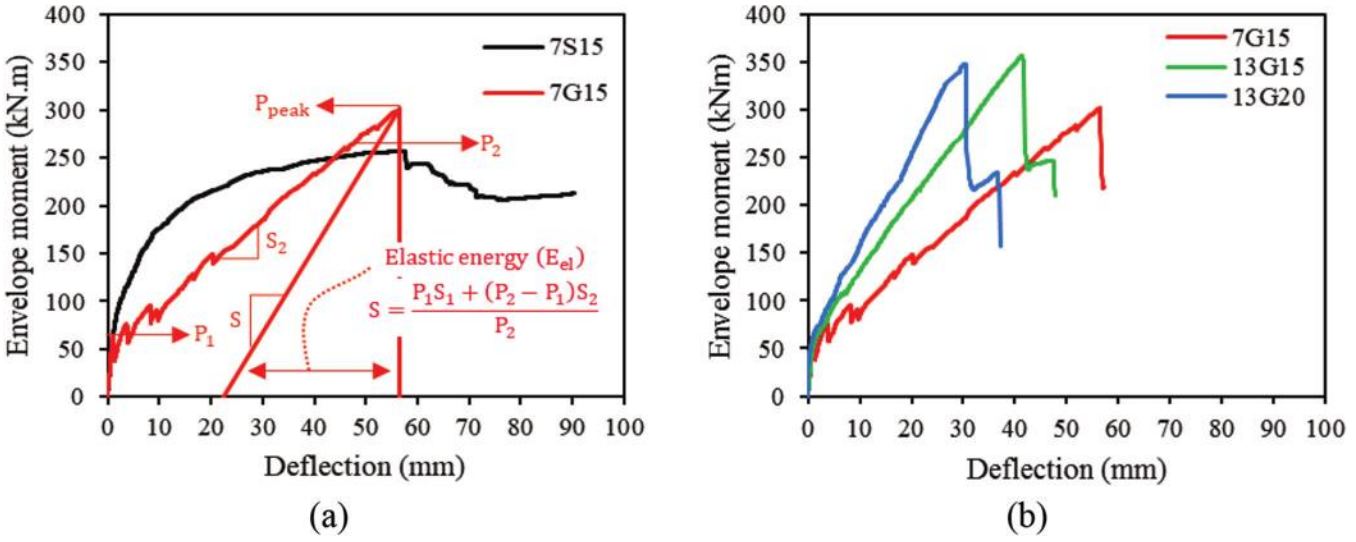

Fig. 8—Effect of test parameters on envelope moment-deflection relationship: (a) stiffness of longitudinal reinforcement; and (b) longitudinal reinforcement ratio.

steel-reinforced specimen shows a typical yielding plateau, followed by concrete crushing in the compression zone. Afterward, a sudden load drop occurred, followed by total loss of flexural stiffness.

Effect of axial stiffness of longitudinal reinforcement

Specimens 7G15 and 7S15 were designed to have the same flexural longitudinal reinforcement ratio. Before Specimen 7G15 cracked, its stiffness was similar to that of 7S15, as shown in Fig. 8(a). Specimen 7G15 had lower post-cracking flexural stiffness—calculated as the average slope of the curve—than its steel-reinforced counterpart (Specimen 7S15). The ratio between the post-cracking flexural stiffness of Specimens 7S15 to 7G15 was approximately 4.28. This ratio is approximately the same as the 4.35 ratio of the axial stiffness (EA) of the steel to that of the GFRP bars. This is in good agreement with the results of Mousa et al. (2018). It can be seen, however, that the GFRP-reinforced specimen had a longer ascending branch with higher stiffness compared to the post-yielding flexural stiffness of the steel-reinforced specimen. This is mainly due to the fact that, after the steel bars yielded, their tangent modulus was lower than that of the GFRP bars, which maintained their modulus of elasticity throughout the entire duration of loading. In addition, the test results indicate that Specimen 7G15 had 1.5 times the flexural strength of Specimen 7S15 at yielding, as shown in Table 3. The higher strength gain of the GFRP specimen provided sufficient deformability according to the CSA S6-19 (2019) code limit of 4 for rectangular sections, so that warning of failure in the form of excessive deflection and cracking would be expected before reaching the GFRP bars reached their rupture tensile strain.

Effect of longitudinal reinforcement ratio

The three GFRP-reinforced specimens (7G15, 13G15, and 13G20) were designed to have reinforcement ratios of 0.50%, 0.90%, and 1.20%, respectively. Figure 8(b) provides a comparison of the envelope moment-deflection curves for the three specimens, indicating that Specimen 13G15 had ultimate strength 18% higher than Specimen 7G15, as shown in Table 3. Moreover, Table 3 shows that the percentage was lower when comparing Specimen 13G20 to 13G15. This could be attributed to the fact that the failures of Specimens 13G15 and 13G20 were shear compression failure and diagonal tension failure, respectively. The post-cracking flexural stiffness of Specimen 13G15 (reinforcement ratio of 0.90%) was 72% higher than that of Specimen 7G15 (reinforcement ratio of 0.50%). Similarly, the post-cracking flexural stiffness of Specimen 13G20 (reinforcement ratio of 1.20%) was 140% higher than that of Specimen 7G15 (reinforcement ratio of 0.50%) and 39% higher than that of Specimen 13G15 (reinforcement ratio of 0.90%). These percentages were approximately similar to the percentage increases in the reinforcement ratios (80% from 0.50 to 0.90%, 33% from 0.90 to 1.2%, and 140% from 0.50 to 1.2%).

Strain distribution over cross section

An analysis of strains along the cross section was carried out using the results from the concrete and bar strain gauges at the midspan of the specimens; the experimental neutral-axis depth was deduced. Figure 9 presents the strain profile along the depth of the section at different moment levels. The figure shows a linear strain profile with some deviation. It is worth mentioning, however, that the strain gauges in Specimen 13G15 were damaged before failure because several cracks occurred in the instrumented region. The Bernoulli hypothesis (a plane section remains plane after deformation up to failure), however, could be considered an acceptable simplification of this behavior. Figure 10 illustrates the relation between neutral-axis depth at midspan with the applied moment for the test specimens. In all test specimens, the position of the neutral axis in a section prior to cracking remained unchanged at the geometrical centroid of the specimen cross section. After cracking occurred, the neutral axis depth decreased rapidly at first and then tended to stabilize. In the GFRP-reinforced specimens, the stabilizing behavior continued up to concrete crushing. In contrast, the yielding

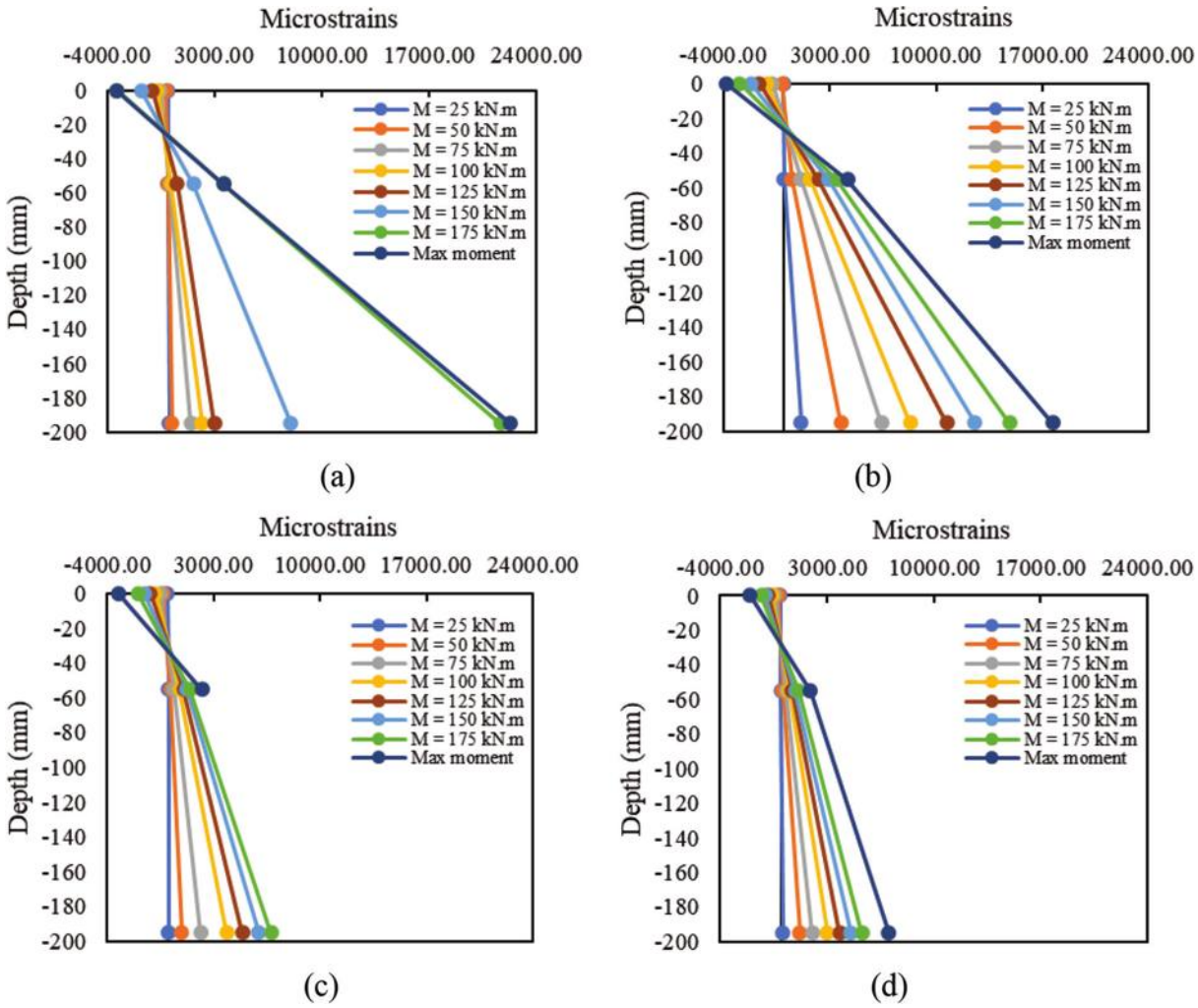

Fig. 9—Strain along midspan section for Specimens: (a) 7S15; (b) 7G15; (c) 13G15; and (d) 13G20.

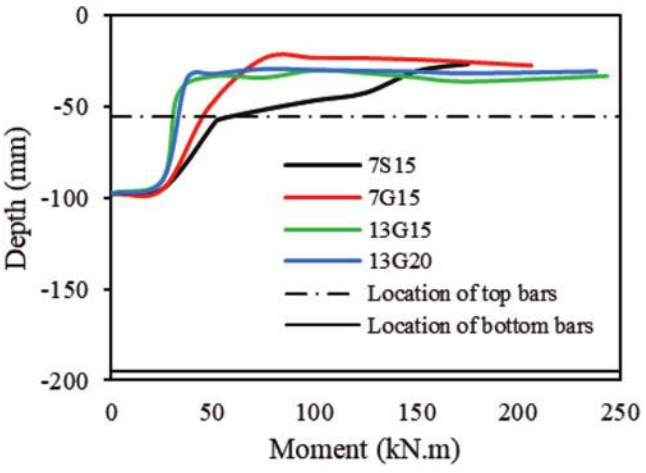

Fig. 10—Neutral-axis depth.

of tensile steel in the reinforced-steel specimen resulted in a rapid decrease in the neutral axis depth. Figure 10 also shows that the neutral-axis depth for Specimen 7G15 was less than that of Specimen 7S15 despite them having similar reinforcement ratios. This could be attributed to the difference in the modulus of elasticity of the GFRP and steel bars.

Cumulative dissipated energy

Earthquakes transfer energy into structures that must then be dissipated for safety reasons. The measurement of dissipated energy could thus become a good efficiency index independently of structural ductility considerations. During cyclic tests on structures, dissipative mechanisms are frequently encountered and must be distinguished to determine the action of reinforcement on the dissipated energy (Eq. (1)). In fact, a principal energy E_T is transferred to the structure and supports. One component of this energy is redistributed into the soil E_s, while the other is used by the structure over the elastic E_e and inelastic E_a domains. The first component E_e represents the energy necessary both for specimen displacement (kinematic energy E_c) and for elastic strain E_{es}. The component E_a includes the damping energy E_d and hysteretic energy E_h (Daniel and Loukili 2002).

$$E_T - E_S = E_e + E_a \quad (1)$$

$$E_e = E_c + E_{es} \quad (2)$$

$$E_a = E_d + E_h \quad (3)$$

To avoid structural collapse from occurring, it is important to increase the energy storage capability in the elastic

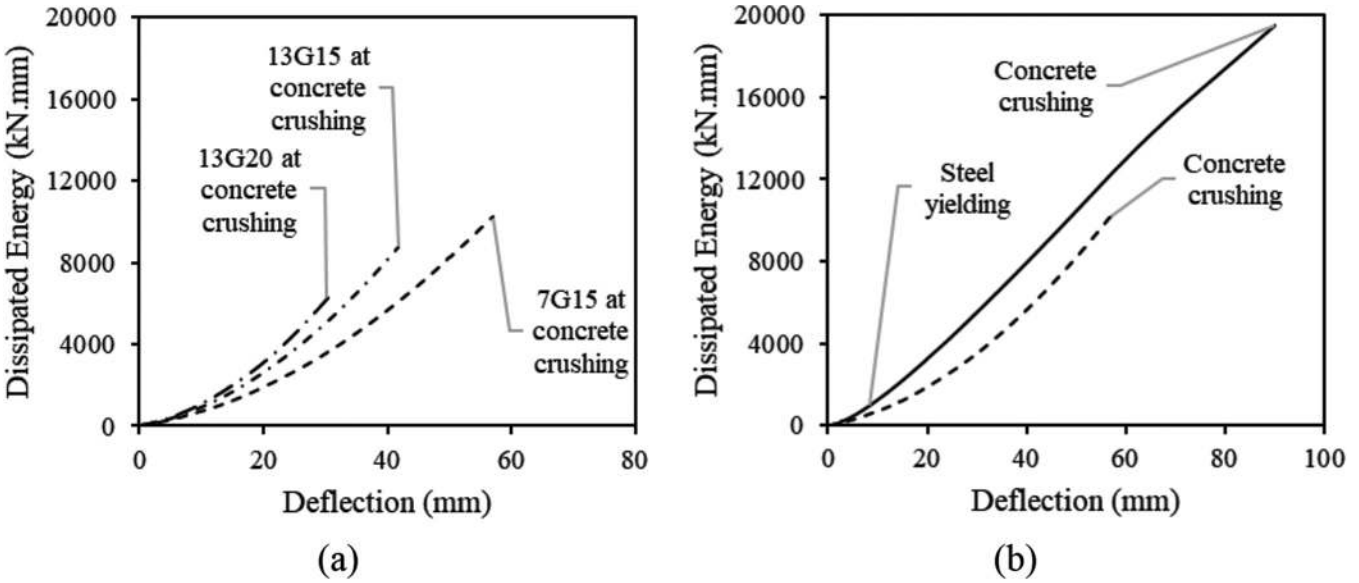

Fig. 11—Dissipated energy versus normalized deflection for: (a) specimens with different longitudinal reinforcement ratios; and (b) specimens with different reinforcement type.

domain and energy dissipation in the inelastic domain. For the former, increasing the longitudinal reinforcement ratio increases structural stiffness. Therefore, having higher reinforcement ratio prevents increasing energy storage in the inelastic domain, as shown in Fig. 11(a). The computation of primary dissipated energy was carried out up until concrete crushing. The energy dissipated during a loading cycle was determined by computing the hysteretic area of the loop. The overall dissipated energy of Specimen 7G15 was 16% and 63% higher than that of Specimens 13G15 and 13G20, respectively. Similarly, the overall dissipated energy of Specimen 13G15 was 40% higher than that of Specimen 13G20. Considering the type of reinforcement, Fig. 11(b) shows that Specimen 7G15, at concrete crushing failure, showed approximately 10 times the cumulative dissipated energy than its steel-reinforced counterpart Specimen 7S15, at steel yielding. The steel specimen's cumulative dissipated energy, however, was approximately twice the cumulative dissipated energy of GFRP-reinforced Specimen 7G15 at concrete crushing.

Energy-based ductility index

Ductility is a structural-design requirement in most design codes. The traditional definition of ductility for steel-reinforced concrete members, which considers the yielding of steel bars as a reference point, cannot be directly applied to members reinforced with FRP reinforcement due to the linear elastic behavior of FRP bars up to failure. Several methods have been proposed to calculate the ductility of FRP-RC structures. Naaman and Jeong (1995) defined ductility as the ratio of the total energy to the elastic energy and proposed Eq. (4) to compute the ductility index μ_e, which can be applied to steel- and FRP-reinforced concrete members

$$\mu_e = 0.5((E_{tot}/E_{el}) + 1) \quad (4)$$

where E_{tot} is the total energy computed as the area under the load-deflection curve; and E_{el} is the elastic energy released upon failure, computed as the area of the triangle formed at failure load by the line having the weighted average slope of the two initial straight lines of the load-deflection curve, as illustrated in Fig. 8(a). The computed energy-based ductility index μ_e for Specimens 7G15, 13G15, 13G20, and 7S15 were 1.5, 1.3, 1.3, and 1.9, respectively. Considering the type of reinforcement, Specimen 7G15 had a ductility index equal to 78% of the ductility of Specimen 7S15, its steel-reinforced counterpart. This difference in ductility was compensated for by the high strength reserve of Specimen 7G15, which had flexural strength 150% higher than Specimen 7S15 at yielding. Moreover, the computed μ_e was slightly lower when the reinforcement ratio was increased. In the case of Specimen 13G15, increasing its reinforcement ratio resulted in a computed μ_e slightly lower than that of Specimen 7G15 (from 1.5 to 1.3). Further increasing the reinforcement ratio did not lower the computed μ_e for Specimen 13G20 further.

Deformability factor

ACI 440.1R-15 defines the deformability factor as the ratio of the energy absorption at ultimate strength of the section to the energy absorption at the service level. The Canadian Highway Bridge Design Code (CSA S6-19) adopted the Jaeger et al. (1997) (J-factor) approach to evaluate the deformability index of FRP-RC members. The J-factor takes into account the strength effect as well as the curvature effect at service and ultimate conditions. Equation (5) can be used to calculate the deformability J-factor

$$J = \frac{M_{ultimate}}{M_s} \times \frac{\psi_{ultimate}}{\psi_s} = \frac{M_{ultimate} \cdot \psi_{ultimate}}{M_s \cdot \psi_s} \quad (5)$$

where ψ_s is the curvature at service condition (concrete strain equal to 0.001); ψ_u is the curvature at ultimate; M_s is the moment at service condition; and M_u is the ultimate moment. CSA S6-19 requires a J-factor greater than 4 for

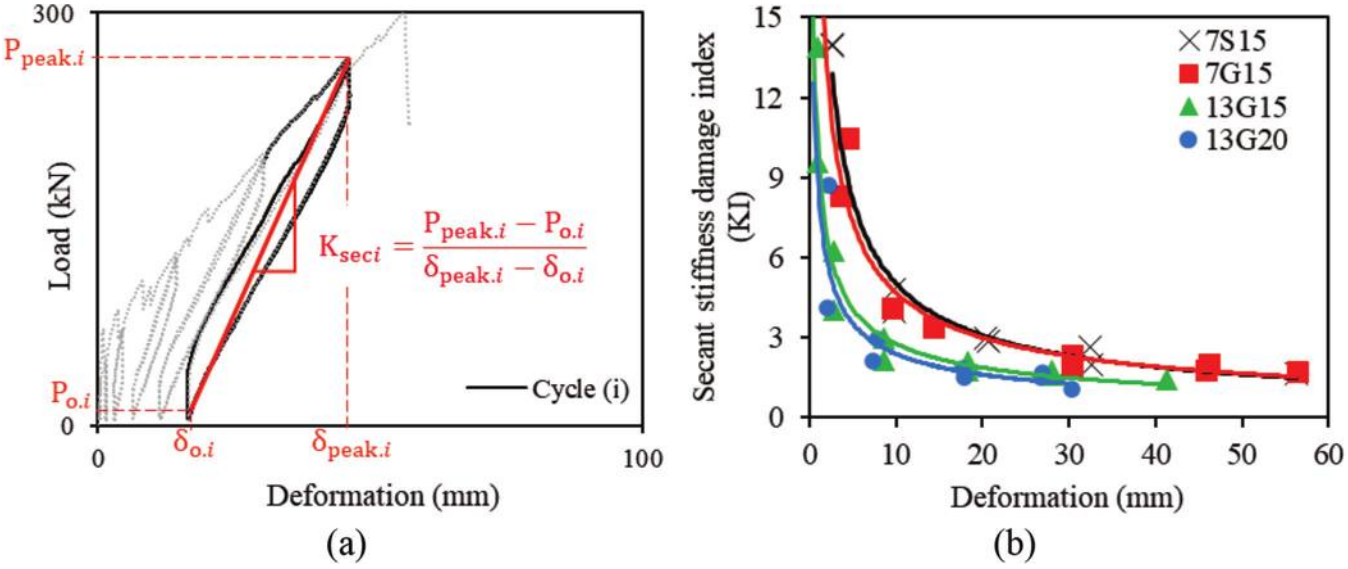

Fig. 12—(a) Secant stiffness; and (b) secant stiffness damage index versus deflection.

rectangular sections: the higher the J-factor values, the more sufficient warning given by the FRP-RC specimen before failure. In other words, the J-factor indicates the amount of cracking and deflection that the FRP-RC member will exhibit throughout the load history from service to ultimate condition. The computed deformability J-factor shows that all the GFRP-reinforced specimens demonstrated adequate deformability when compared to the CSA S6-19 code limit of 4 for rectangular sections. The deformability J-factors for Specimens 7G15, 13G15, and 13G20 were 7.1, 6.1, and 4.1, respectively.

Secant-stiffness damage index

Several researchers have established a set of damage indexes to ascertain the residual capacity of structures (Daniel and Loukili 2002; Ranjbaran et al. 2018). A wide array of parameters may be used, such as number of cycles, stiffness, and ductility. This section discusses the effect of the longitudinal reinforcement ratio on the secant stiffness index (KI) in loading and unloading. The parameter's values and changes are the index of damage in the specimens. This stiffness index is described as the cycle's secant stiffness K_{seci} to the after-cracking stiffness ratio of the specimens. For each loading cycle, the cycle's secant stiffness damage index K_{seci} was computed using Eq. (6), as illustrated in Fig. 12(a).

$$K_{seci} = \frac{P_{peak.i} - P_{o.i}}{\delta_{peak.i} - \delta_{o.i}} \quad (6)$$

Figure 12(b) illustrates the effect of the GFRP longitudinal reinforcement ratio on the secant stiffness damage index (KI). As shown, GFRP-reinforced PCLT Specimen 7G15 had a decrease in stiffness comparable to that of its counterpart Specimen 7S15. Moreover, increasing the longitudinal reinforcement ratio did not significantly affect the rate of decrease in stiffness. The residual stiffness at ultimate deflection of Specimen 13G15 (reinforcement ratio of 0.90%) was 18.8% lower than that of Specimen 7G15 (reinforcement ratio of 0.50%). Similarly, the residual stiffness at ultimate deflection of Specimen 13G20 (reinforcement ratio of 1.20%) was 34.9% lower than that of Specimen 13G15 (reinforcement ratio of 0.90%).

THEORETICAL STUDY

This section presents a theoretical study to calculate the flexural and shear capacities of PCTL segments reinforced with GFRP bars. It provides the calculations of the flexural and shear capacities of the PCTL tunnel segments reinforced with GFRP bars considering the requirements in ACI 440.1R-15, CSA S806-12(R2017), *fib* TG-9.3, CNR-DT 203, and AFGC.

Flexural capacity

The flexural design of FRP-reinforced concrete members is analogous to the design of steel-reinforced concrete members. Experimental data on concrete members reinforced with FRP bars show that the flexural capacity can be calculated based on assumptions similar to those made for members reinforced with steel bars (Ruan et al. 2020). The flexural strength of the FRP-reinforced cross section is calculated based on the following assumptions:

(a) Strain in the concrete and the FRP reinforcement is proportional to the distance from the neutral axis (a plane section before loading remains plane after loading).

(b) The tensile strength of the concrete is ignored.

(c) The tensile behavior of the FRP reinforcement is linearly elastic until failure.

(d) A perfect bond exists between the concrete and FRP reinforcement.

(e) The maximum usable compressive strain in the concrete is assumed to be 0.003 in ACI 440.15 and 0.0035 in CSA S806-12, *fib* TG-9.3, CNR-DT 203, and AFGC.

ACI 440.1R (2015)—The FRP reinforcement ratio is computed according to ACI 440.1R-15 with Eq. (7), and the balanced FRP reinforcement ratio can be computed with Eq. (8)

$$\rho_f = A_f/bd \quad (7)$$

where A_f is the area of the FRP reinforcement; b is the width of the rectangular cross section; and d is the distance from the extreme compression fiber to the centroid of the tension reinforcement

$$\rho_{fb} = 0.85\beta_1 \frac{f_c'}{f_{fu}} \frac{E_f \varepsilon_{cu}}{E_f \varepsilon_{cu} + f_{fu}} \quad (8)$$

where f_c' is the specified compressive strength of the concrete; f_{fu} is the design tensile strength of the FRP, defined as the guaranteed tensile strength multiplied by the environmental reduction factor; E_f is the design or guaranteed modulus of elasticity of FRP, defined as the mean modulus of a sample from the test specimens; and ε_{cu} is the ultimate strain in the concrete.

According to ACI 440.1R-15, when $\rho_f > \rho_{fb}$, the controlling limit state is crushing of the concrete, and the stress distribution in the concrete can be approximated with the ACI rectangular stress block. Based on the equilibrium of forces and strain compatibility, the following can be derived

$$M_n = A_f f_f (d - (a/2)) \quad (9)$$

$$a = \frac{A_f f_f}{0.85 f_c' b} \quad (10)$$

$$f_f = E_f \varepsilon_{cu} \frac{\beta_1 d - a}{a} \quad (11)$$

In ACI 440.1R-15, the nominal flexural strength is determined from Eq. (9) through (11).

The FRP reinforcement is linearly elastic at the concrete crushing limit state, so the stress level in the FRP can be found from Eq. (11), as it is less than f_{fu}.

Alternatively, the nominal flexural strength at a section can be expressed, according to ACI 440.1R-15, in terms of the FRP reinforcement ratio, as given in Eq. (12).

$$M_n = \rho_f f_f \left(1 - 0.59 \frac{\rho_f f_f}{f_c'}\right) b d^2 \quad (12)$$

CAN/CSA S806-12(R2017)—According to CAN/CSA S806-12(R2017), the concrete crushing mode of failure occurs in the FRP-reinforced section when the extreme compressive strain in the concrete reaches its ultimate strain, provided that

$$(c/d) \geq 7 / (7 + 2000\varepsilon_{Fu}) \quad (13)$$

where c is the distance from the extreme compression fiber to the neutral axis; d is the distance from the extreme compression fiber to the centroid of the longitudinal tension force; and ε_{Fu} is the ultimate strain in the FRP reinforcement.

When c/d satisfies the requirements of Eq. (13), the nominal flexural strength in a section can be determined, similar to as in ACI 440.1R-15, based on the equilibrium of forces and strain compatibility.

fib *TG-9.3 (2007)*—According to *fib* TG-9.3, the ultimate flexural moment resistance of an FRP RC section can be evaluated by adopting the framework of Eurocode 2 (CEN 2004). Similar to as in ACI 440.1R-15, when $\rho_f > \rho_{fb}$, flexural failure is expected to occur due to concrete crushing, and the ultimate moment resistance can be calculated based on the equilibrium of forces and strain compatibility with Eq. (14)

$$M_u = \eta f_{cd} b d^2 (\lambda\zeta)(1 - (\lambda\zeta/2)) \quad (14)$$

where η is a factor defining the effective strength of the concrete; f_{cd} is the design value of the concrete compressive strength; b is the width of the rectangular cross section; d is the effective depth of a cross section; λ is a factor defining the effective height of the compression zone; and ζ is a reduction factor coefficient.

AFGC (2021)—As in *fib* TG-9.3, the ultimate flexural moment resistance of an FRP-RC section can be evaluated according to AFGC by adopting the framework of Eurocode 2 (CEN 2004). According to AFGC (2021), the FRP reinforcement ratio can be computed with Eq. (15), and the balanced FRP reinforcement ratio can be computed with Eq. (16)

$$\rho_{PRF} = A_{PRF}/A_{c,red} \quad (15)$$

where A_{PRF} is the area of the longitudinal reinforcement composite bars; and $A_{c,red}$ is the reduced area of the concrete section

$$\rho_{PRF,b} = \frac{\eta f_{cd} \lambda x_u}{\varepsilon_{PRF,u,d} E_{PRF} d} = \frac{\eta f_{cd} \lambda}{f_{PRF,d}} = \frac{\varepsilon_{cu2}}{\varepsilon_{PRF,u,d} + \varepsilon_{cu2}} \quad (16)$$

where η is a factor defining the effective strength of the concrete; f_{cd} is the design value of the concrete compressive strength; λ is a factor defining the effective height of the compression zone; x_u is the position of the neutral axis corresponding to the concrete balanced section; $\varepsilon_{PRF,u,d}$ is the limit strain of the FRP reinforcement; E_{PRF} is the FRP modulus of elasticity; d is the effective depth of a cross section; $f_{PRF,d}$ is the design FRP stress; and ε_{cu2} is the ultimate concrete strain.

Similar to *fib* TG-9.3, when $\rho_f > \rho_{fb}$, flexural failure is expected to occur due to concrete crushing, and the ultimate moment resistance M_{Rd} in AFGC can be calculated, based on the equilibrium of forces and strain compatibility, with Eq. (17)

$$M_{Rd} = A_{PRF} E_{PRF} \varepsilon_{PRF} \left(d - \frac{\lambda x}{2}\right) = \lambda x \eta f_{cd} b \left(d - \frac{\lambda x}{2}\right) \quad (17)$$

where A_{PRF} is the area of the longitudinal reinforcement composite bars; E_{PRF} is the FRP modulus of elasticity; ε_{PRF} is the strain in the FRP reinforcement; d is the effective depth of a cross section; λ is a factor defining the effective height of the compression zone; x is the position of the neutral axis; and f_{cd} is the design value of the concrete compressive strength.

CNR-DT 203 (2006)—CNR-DT 203 assumes that flexural failure takes place when one of the following conditions is met:

(a) The maximum concrete compressive strain, as defined by the current building code, is reached.

(b) The maximum FRP tensile strain ε_{fd} is reached. This value is computed from the characteristic tensile strength ε_{fk} with Eq. (18)

$$\varepsilon_{fd} = 0.9\eta_a(\varepsilon_{fk}/\gamma_f) \tag{18}$$

where η_a is an environmental conversion factor; and γ_f is a material partial factor.

For both failure modes, the nominal flexural strength in a section can be determined based on the equilibrium of forces and strain compatibility.

Shear capacity

The shear design of FRP-reinforced concrete is similar to that of steel-reinforced concrete members. The different mechanical properties of FRP bars, however, affect shear strength and should be considered. GFRP bars have a relatively low modulus of elasticity compared to steel, low transverse shear resistance, and high tensile strength with no yielding point. In addition, the tensile strength of the bent portion of an FRP bar is significantly lower than that of the straight portion.

ACI 440.1R-15—The concrete shear capacity V_c of flexural members using FRP as the main reinforcement can be evaluated according to ACI 440.1R-15 based on Eq. (19)

$$V_c = \frac{2}{5}\sqrt{f_c'}b_w(kd) \tag{19}$$

where b_w is the width of the web; k is the ratio of the neutral-axis depth to the reinforcement depth; and d is the distance from the extreme compression fiber to the centroid of the tension reinforcement.

CAN/CSA S806—In CSA S806-12 (R2017), the concrete shear capacity V_c for sections having an effective depth not exceeding 300 mm (12 in.) and with no axial load action on them can be calculated using Eq. (20)

$$V_c = 0.05\lambda\phi_c k_m k_r (f_c')^{1/3} b_w d_v \tag{20}$$

where λ is a factor to account the concrete density; ϕ_c is the resistance factor for concrete; k_m is a coefficient taking into account the effect of moment in the section on the shear strength; k_r is coefficient taking into account the effect of reinforcement rigidity on its shear strength; f_c' is the specified concrete compressive strength; b_w is the minimum effective web width; and d_v is the effective shear depth.

According to CSA S806-12 (R2017), however, V_c shall not be taken as greater than $0.22\phi_c\sqrt{f_c'}b_w d_v$ or less than $0.11\phi_c\sqrt{f_c'}b_w d_v$

fib *TG-9.3 (2007)—fib* TG-9.3 presents and discusses various shear design recommendations to allow for the use of FRP reinforcement for the various design specifications available. Moreover, the modification in Eq. (21) has been proposed for the ACI shear equation to compensate for the unnecessary conservative shear prediction

$$V_{c,proposed} = V_{c,ACI}\left(\frac{E_{FRP}}{E_s}\phi_s\right)^{1/3} \tag{21}$$

where $\phi_s = \varepsilon_f/\varepsilon_y$ represents the ratio between the maximum strain allowed in the FRP reinforcement ε_f and the yield strain of the steel ε_y.

AFGC (2021)—The concrete shear capacity $V_{Rd,c}$ of flexural members with FRP as the main reinforcement is determined according to the Eurocode 2 (CEN 2004) equation, as shown in Eq. (22)

$$V_{Rd,PFR} = C_{Rd,c}k\left(100\frac{E_{PRF}}{E_S}\cdot\frac{A_{PFR}}{b_w d}f_{ck}\right)^{1/3} b_w d \tag{22}$$

where $C_{Rd,c} = 0.18/\gamma_c$; $k = \min\{2.0;\ 1 + \sqrt{200/d}\}$; E_{PRF} is the FRP modulus of elasticity; E_S is the steel modulus of elasticity; A_{PRF} is the area of the longitudinal reinforcement composite bars; b_w is the width of the web; d is the distance from the extreme compression fiber to the centroid of the tension reinforcement; and f_{ck} is the concrete compressive strength.

CNR-DT 203 (2006)—In CNR-TD 203, the concrete shear capacity $V_{Rd,ct}$ of flexural members with FRP as the main reinforcement can be evaluated with Eq. (23)

$$V_{Rd,ct} = 1.3\left(\frac{E_f}{E_s}\right)^{1/2}\tau_{Rd}k(1.2 + 40\rho_1)bd \tag{23}$$

where E_f and E_s are the Young's modulus of elasticity of the FRP and steel bars; τ_{Rd} is the design shear stress; k is a coefficient to be set as equal to 1 for members if more than 50% of the bottom reinforcement is interrupted, and $(1.6 - d) \geq 1$ if that is not the case; ρ_1 is the FRP reinforcement ratio; b is the width of rectangular cross section; and d is the effective depth of the cross section.

Comparison of theoretical to experimental results

The nominal flexural-moment and shear-load capacities of the test segments were compared to the theoretical predictions according to ACI 440.1R-15, CAN/CSA S806-12(R2017), *fib* TG-9.3, AFGC, and CNR-DT 203. In all the theoretical analyses, the concrete density factor, material resistance factor, and member safety factor were taken as equal to unity. Table 3 presents the experimental-to-predicted ratios for the flexural and shear capacities of the segments. As shown in Table 3, ACI 440.1R-15 yielded accurate predictions for the segments' moment carrying capacity, where the experimental-to-predicted ratio for the moment capacity of Specimen 7G15 was 0.97. The ACI 440.1R-15 shear predictions were, however, conservative with experimental-to-predicted ratios of 1.44 and 1.28 for 13G15 and 13G20, respectively. The ACI shear modification model proposed in *fib* TG-9.3 compensated for the unnecessary conservativism in the ACI shear predictions. The *fib* TG-9.3 shear predictions were in good agreement with the experimental shear results with experimental-to-predicted ratios of 1.11 and 0.99 for 13G15 and 13G20, respectively. Moreover, both *fib* TG-9.3 and AFGC (2021) produced accurate predictions for the segments' moment-carrying capacity, where the experimental-to-predicted ratio for the moment capacity of Specimen 7G15 was 0.96 according to both. Moreover, the AFGC shear predictions were in good

agreement with the experimental shear results with experimental-to-predicted ratios of 1.14 and 1.01 for 13G15 and 13G20, respectively.

Furthermore, Table 3 illustrates that CAN/CSA S806-12(R2017) accurately predicted the shear capacity of the test segments with experimental-to-predicted ratios of 1.09 and 0.97 for 13G15 and 13G20, respectively. CAN/CSA S806-12(R2017), however, overestimated the moment carrying capacity of 7G15, with an experimental-to-predicted ratio of 0.86. On the other hand, considering the maximum FRP strain limit ε_{fd} in CNR-DT 203 resulted in conservative predictions of the moment capacities of the test segments. CNR-DT 203 underestimated the moment-carrying capacity of 7G15 with an experimental-to-predicted ratio of 1.29. Conversely, CNR-DT 203 overestimated the shear capacity of the test segments with experimental-to-predicted ratios of 0.85 and 0.76 for 13G15 and 13G20, respectively. Table 3 illustrates that all the design codes properly predicted the shear failure over the flexural failure for Specimens 13G15 and 13G20 with experimental-to-predicted flexural moment capacities less than 1 and experimental-to-predicted shear load capacities greater than 1. In contrast, all the design codes, except CNR-DT 203, failed to correctly predict the flexural failure of Specimen 7G15. However, it predicted that the concrete flexural crushing failure would occur before the shear failure at an experimental-to-predicted flexural moment and shear load ratios of 1.29 and 0.81, respectively.

CONCLUSIONS

This paper reports on an experimental and theoretical investigation of the behavior of precast concrete tunnel lining (PCTL) segments reinforced with glass fiber-reinforced polymer (GFRP) bars under quasi-static cyclic flexural loading. Based on the experimental results and the theoretical study presented in this paper, the following conclusions can be drawn:

1. The failure of Specimen 7G15 occurred by concrete crushing, while Specimens 13G15 and 13G20 failed due to shear compression and diagonal shear, respectively. Specimen 7S15, which was reinforced with steel, failed due to steel yielding, followed by concrete crushing.

2. The hysteresis cycles of the GFRP-reinforced specimens reflected stable cyclic behavior with no or limited strength degradation that was less than that experienced by the steel-reinforced specimen.

3. The unloading stiffness for the GFRP-reinforced specimens in all cycles was nearly equal to the reloading stiffness. The yielding of the steel bars in the steel-reinforced specimen resulted in degradation of the specimen's unloading stiffness.

4. The residual deformation of the GFRP-reinforced specimens during unloading at 50 and 75% of the maximum displacement cycles was less than in the steel-reinforced specimen due to the steel bars yielding.

5. The GFRP-reinforced specimens' ductility index was 78% of the steel-reinforced specimens' ductility at a similar reinforcement ratio. This difference in ductility was compensated for by the high strength reserve of Specimen 7G15. Specimen 7G15 achieved a flexural strength 1.5 times that of Specimen 7S15 at yielding.

6. The test results show that all the GFRP-reinforced specimens demonstrated adequate deformability when compared to the CSA S6-19 (2019) code limit of 4 for rectangular sections.

7. The experimental results indicate that the hysteresis cycles of the GFRP-reinforced specimens had stable cyclic behavior with no or limited strength degradation. In addition, these specimens demonstrated adequate strength, ductility index, and deformability limits.

8. The experimental-to-predicted ratio of the flexural-moment capacity of Specimen 7G15 indicates good predictions for ACI 440.1R-15, *fib* TG-9.3 (2007), and AFGC (2021), while CAN/CSA S806-12(R2017) overestimated its flexural-moment capacity. On the other hand, CNR-DT 203 (2006) yielded conservative predictions of its flexural-moment capacity.

9. ACI 440.1R-15 produced conservative shear-load predictions for the test specimens. Conversely, CNR-DT 203 (2006) overestimated the shear-load capacities for the test segments. The ACI shear modification model proposed in *fib* TG-9.3, AFGC, and CAN/CSA S806-12(R2017) yielded accurate predictions of the shear-load capacities for the test specimens.

10. The experimental results were the first of their kind on the applicability of using GFRP as internal reinforcement for PCTLs under quasi-static cyclic flexural loading. These experimental results can be considered in the forthcoming provisions of ACI codes for the use of GFRP as internal reinforcement for PCTL applications.

AUTHOR BIOS

Basil Ibrahim *is a Doctoral Candidate in the Department of Civil and Building Engineering at the University of Sherbrooke, Sherbrooke, QC, Canada. He received his BSc and MSc in civil engineering from the Faculty of Engineering, University of Sharjah, Sharjah, UAE. His research interests include the use of fiber-reinforced polymers (FRPs) in reinforced concrete structures.*

Salaheldin Mousa *is a Postdoctoral Fellow in the Department of Civil and Building Engineering at the University of Sherbrooke, where he also received his PhD. He received his BSc and MSc from and is a Lecturer at the Faculty of Engineering at Shoubra, Benha University, Cairo, Egypt. His research interests include the use of FRPs in reinforced concrete structures.*

Hamdy M. Mohamed *is a Lecturer and Research Associate in the Department of Civil and Building Engineering at the University of Sherbrooke, where he received his PhD. He received his BSc and MSc from the Faculty of Engineering at Helwan University, Cairo, Egypt. His research interests include the use and field applications of FRPs in reinforced concrete structures.*

Brahim Benmokrane, *FACI, is Professor in the Department of Civil and Building Engineering at the University of Sherbrooke, Tier-1 Canada Research Chair Professor in Advanced Composite Materials for Civil Structures and Industrial Research Chair Professor in FRP Reinforcement for Concrete Infrastructure, and Director of the University of Sherbrooke Research Center on Structural FRP Composite Materials for Concrete Structures (CRUSMAC). He is a member of ACI Committees 435, Deflection of Building Concrete Structures, and 440, Fiber-Reinforced Polymer Reinforcement; member and past Co-Chair of ACI Subcommittee 440-K, FRP-Material Characteristics; and member of ACI Subcommittees 440-E, Professional Education; 440-F, FRP-Repair-Strengthening; 440-H, FRP-Reinforced Concrete; 440-I, FRP-Prestressed Concrete; and 440-L, FRP-Durability. His research interests include the development of FRP reinforcement for concrete structures and their durability, structural performance, and field applications.*

ACKNOWLEDGMENTS

This research was conducted with funding from the Natural Sciences and Engineering Research Council of Canada (NSERC), Mathematics of Information Technology and Complex Systems (MITACS), the Fonds de recherche du Québec en nature et technologies (FRQ-NT), The Pole de Recherche et d'Innovation en Matériaux Avancés au Quebec (PRIMA Quebec), and the Tier-1 Canada Research Chair in Advanced Composite Materials for Civil Structures. The authors are grateful to the precast company (Sym-Tech Béton Préfabriqué, Sainte-Hyacinthe, QC, Canada) and to the GFRP bar manufacturer (Pultrall Inc., Thetford Mines, QC, Canada) for their effective involvement in this project, and to the technical staff of the structural lab in the Department of Civil Engineering at the University of Sherbrooke.

REFERENCES

Abbas, S., 2014, "Structural and Durability Performance of Precast Segmental Tunnel Linings," doctoral dissertation, Western University, London, ON, Canada.

ACI Committee 374, 2013, "Guide for Testing Reinforced Concrete Structural Elements under Slowly Applied Simulated Seismic Loads (ACI 374.2R-13)," American Concrete Institute, Farmington Hills, MI, 18 pp.

ACI Committee 440, 2015, "Guide for the Design and Construction of Structural Concrete Reinforced with Fiber-Reinforced Polymer (FRP) Bars (ACI 440.1R-15)," American Concrete Institute, Farmington Hills, MI, 88 pp.

ACI Committee 533, 2020, "Guide for Precast Concrete Tunnel Segments (ACI 533.5R-20)," American Concrete Institute, Farmington Hills, MI, 80 pp.

ACI Committee 544, 2016, "Report on Design and Construction of Fiber-Reinforced Precast Concrete Tunnel Segments (ACI 544.7R-16)," American Concrete Institute, Farmington Hills, MI, 36 pp.

AFGC, 2021, "Réparation et renforcement des structures en béton au moyen des matériaux composites," Bulletin scientifique et technique de l'Association Française de Génie Civil, Paris, France. (in French)

ASTM D7205-21, 2021, "Standard Test Method for Tensile Properties of Fiber Reinforced Polymer Matrix Composite Bars," ASTM International, West Conshohocken, PA.

CAN/CSA-S6-19, 2019, "Canadian Highway Bridge Design Code," CSA Group, Toronto, ON, Canada.

CAN/CSA S806-12(R2017), 2017, "Design and Construction of Building Components with Fiber-Reinforced Polymers," CSA Group, Toronto, ON, Canada.

Caratelli, A.; Meda, A.; Rinaldi, Z.; Spagnuolo, S.; and Maddaluno, G., 2017, "Optimization of GFRP Reinforcement in Precast Segments for Metro Tunnel Lining," *Composite Structures*, V. 181, pp. 336-346. doi: 10.1016/j.compstruct.2017.08.083

CEN, 2004, "Eurocode 2, Design of Concrete Structures—Part 1-1: General Rules and Rules for Buildings." European Committee for Standardization, Brussels, Belgium.

Cheong, Y. W.; Kwan, H. P.; and Hariyanto, A. D., 2005, "Quality Control in Precast Production: A Case Study on Tunnel Segment Manufacture," *Journal of Architecture and Built Environment*, V. 33, No. 2.

CNR-DT 203, 2006, "Guide for the Design and Construction of Concrete Structures Reinforced with Fiber-Reinforced Polymer Bars," National Research Council, Rome, Italy.

Daniel, L., and Loukili, A., 2002, "Behavior of High Strength Fiber-Reinforced Concrete Beams under Cyclic Loading," *ACI Structural Journal*, V. 99, No. 3, May-June, pp. 248-256.

Davis, J. R., ed., 2000, *Corrosion: Understanding the Basics*, ASM International, The Materials Information Society, Materials Park, OH, 571 pp.

Dong, Z.; Zhang, P.; Zhu, H.; Wu, G.; and Wu, Z., 2016, "Study on Stiffness and Recoverability of Fiber Reinforced Polymers-Reinforced Concrete (FRP-RC) Composite T-Beams with Prefabricated Basalt Fiber-Reinforced Polymers Shell," *Journal of Reinforced Plastics and Composites*, V. 35, No. 6, pp. 516-529. doi: 10.1177/0731684415618019

Fahmy, M.; Wu, Z. S.; and Wu, G., 2009, "Seismic Performance Assessment of Damage-Controlled FRP-Retrofitted RC Bridge Columns Using Residual Deformations," *Journal of Composites for Construction*, ASCE, V. 13, No. 6, pp. 498-513. doi: 10.1061/(ASCE)CC.1943-5614.0000046

fib Task Group 9.3, 2007, "FRP Reinforcement in RC Structures," Fédération Internationale de Béton, Lausanne, Switzerland, 157 pp.

Gulikers, J., 2003, "Problems Encountered in the Detection of Reinforcement Corrosion in Concrete Tunnel Linings–Theoretical Considerations," *Materials and Corrosion*, V. 54, No. 6, pp. 454-459. doi: 10.1002/maco.200390097

Hosseini, S. M.; Mousa, S.; Mohamed, H. M.; and Benmokrane, B., 2022, "Structural Behavior of Precast RC Tunnel Segments with GFRP Bars and Ties Under Bending Load," *ACI Structural Journal*, V. 119, No. 1, Jan., pp. 307-319.

Jaeger, L. G.; Mufti, A. A.; and Tadros, G., 1997, "The Concept of the Overall Performance Factor in Rectangular-Section Reinforced Concrete Members," *Proceedings, 3rd International Symposium on Non-Metallic (FRP) Reinforcement for Concrete Structures, FRPRCS-3*, V. 2, Japan Concrete Institute, Tokyo, Japan, pp. 551-559.

Manalo, A.; Maranan, G.; Benmokrane, B.; Cousin, P.; Alajarmeh, O.; Ferdous, W.; and Hota, G., 2020, "Comparative Durability of GFRP Composite Reinforcing Bars in Concrete and in Simulated Concrete Environments," *Cement and Concrete Composites*, V. 109, p. 103564. doi: 10.1016/j.cemconcomp.2020.103564

Meda, A.; Rinaldi, Z.; Spagnuolo, S.; De Rivaz, B.; and Giamundo, N., 2019, "Hybrid Precast Tunnel Segments in Fiber Reinforced Concrete with Glass Fiber Reinforced Bars," *Tunnelling and Underground Space Technology*, V. 86, pp. 100-112. doi: 10.1016/j.tust.2019.01.016

Mousa, S.; Mohamed, H. M.; and Benmokrane, B., 2018, "Flexural Strength and Design Analysis of Circular Reinforced Concrete Members with Glass Fiber-Reinforced Polymer Bars and Spirals," *ACI Structural Journal*, V. 115, No. 5, Sept., pp. 1353-1364. doi: 10.14359/51702282

Naaman, A. E., and Jeong, S. M., 1995, "Structural Ductility of Concrete Beams Prestressed with FRP Tendons," *Proceedings, 2nd International RILEM Symposium on Non-Metallic (FRP) Reinforcement for Concrete Structures*, RILEM, Bagneux, France, pp. 379-386.

Rancourt, A., 2016, "Analysis of the Costs of a Tunnel Drilled between Beauport and Lévis," Report, Géosys, 35 pp.

Ranjbaran, F.; Rezayfar, O.; and Mirzababai, R., 2018, "Experimental Investigation of Steel Fiber-Reinforced Concrete Beams under Cyclic Loading," *International Journal of Advanced Structural Engineering*, V. 10, No. 1, pp. 49-60. doi: 10.1007/s40091-018-0177-1

Ruan, X.; Lu, C.; Xu, K.; Xuan, G.; and Ni, M., 2020, "Flexural Behavior and Serviceability of Concrete Beams Hybrid-Reinforced with GFRP Bars and Steel Bars," *Composite Structures*, V. 235, p. 111772. doi: 10.1016/j.compstruct.2019.111772

Spagnuolo, S.; Meda, A.; Rinaldi, Z.; and Nanni, A., 2017, "Precast Concrete Tunnel Segments with GFRP Reinforcement," *Journal of Composites for Construction*, ASCE, V. 21, No. 5, p. 04017020. doi: 10.1061/(ASCE)CC.1943-5614.0000803

Whitmore, D. W., and Ball, J. C., 2004, "Corrosion Management," *Concrete International*, V. 26, No. 12, Dec., pp. 82-85.

Zhiqiang, Z., and Mansoor, Y. A., 2013, "Evaluating the Strength of Corroded Tunnel Lining Under Limiting Corrosion Conditions," *Tunnelling and Underground Space Technology*, V. 38, pp. 464-475. doi: 10.1016/j.tust.2013.08.003

ACI in Your Classroom

Integrate ACI into your classroom!

To support future leaders, ACI has launched several initiatives to engage students in the Institute's activities and programs – select programs that may be of interest to Educators are:

- **Free student membership –** encourage students to sign up
- **Special student discounts on *ACI 318 Building Code Requirements for Structural Concrete*, *ACI 530 Building Code Requirements and Specification for Masonry Structure*, & *Formwork for Concrete* manual.**
- **Access to *Concrete International* –** free to all ACI student members
- **Access to *ACI Structural Journal* and *ACI Materials Journal* –** free to all ACI student members
- **Free sustainability resources –** free copies of Sustainable Concrete Guides provided to universities for use in the classroom
- **Student competitions –** participate in ACI's written and/or team-based competitions
- **Scholarships and fellowships –** students who win awards are provided up to $15,000 and may be offered internships and paid travel to attend ACI's conventions
- **ACI Award for University Student Activities –** receive local and international recognition for your University's participation in concrete-related activities
- **Free access to the *ACI Collection of Concrete Codes, Specifications, and Practices* –** in conjunction with ACI's chapters, students are provided free access to the online ACI Collection
- **ACI online recorded web sessions and continuing education programs –** online learning tools ideal for use as quizzes or in-class study material

https://www.concrete.org/educatorsandresearchers/aciinyourclassroom.aspx

ACI STRUCTURAL JOURNAL TECHNICAL PAPER

Title No. 120-S67

Variable Cylindrical Concrete Confined by Carbon Fiber-Reinforced Polymer under Axial Compression

by Yail J. Kim and Aliasghar Hassani

This paper presents the axial behavior of cylindrical concrete with variable cross sections confined by carbon fiber-reinforced polymer (CFRP) sheets. The test specimens are classified into three conformational categories: right angles (Type 1), truncated cones (Types 2 and 3), and barrels (Types 4 and 5), which are subjected to a preload level of 0%f_c', 30%f_c', and 60%f_c' (f_c' is the compressive strength of plain concrete) for the representation of existing damage in core concrete prior to wrapping with CFRP. The average capacity of the confined concrete in Type 1 is 106% higher than that of its unconfined counterpart. With an increase in the taper angle, the axial resistance of Types 2 and 3 is improved due to the enlarged base areas; however, the expanded bellies along the height of Types 4 and 5 lower the capacity by reducing the confining pressure of the CFRP sheets. Although the adverse effects of the preloading are evident in the context of reserved reliability and damage evolution, the validity of the confinement system is preserved from a strengthening standpoint. The geometric attributes dominate the load-displacement relationships, post-peak deformations, energy dissipation, and failure characteristics of the specimens. Analytical modeling clarifies that, compared with other parameters, the thickness of CFRP is the salient factor influencing the confining pressure of the system. According to the principle of energy conservation, a simplified design proposal is suggested to calculate the strength of the confined nonprismatic concrete.

Keywords: carbon fiber-reinforced polymer (CFRP); confinement; rehabilitation; strengthening; variable cross sections.

INTRODUCTION

For aesthetic reasons, vertical load-bearing components may be designed with nonconstant cross sections. Tapered and barrel-shaped (or bellied) profiles constitute the archetypical forms of nonprismatic columns. In view of variable cross sections, the behavior of these columns is controlled by longitudinal distance from supporting boundaries,[1] where the moment of inertia and axial rigidity affect the deformation of solid planes at a certain elevation. Most provisions in established standards are dedicated to prismatic sections[2,3] and, thus, the continuum geometry of nonprismatic columns is often decomposed into multiple segments for the convenience of analysis[4]: both analytical and computational methods are usable, depending on the degree of spatial complexity.[5] As is the case for ordinary columns, routine inspections are essential for nonprismatic ones. If major faults are detected, a diagnosis is made to determine the level of technical actions that can reinstate the condition of the members. Structural rehabilitation is a viable solution to resolve safety issues at an affordable expense. From a traditional perspective, column sections are enlarged by supplementary concrete[6] or jacketed by steel shells.[7] Those prevalent techniques are, however, effective for a limited period because the nondurable constituents deteriorate over time. Owners and engineering consultants are eager to find sustainable approaches that will markedly extend the longevity of degraded structures.

Since carbon fiber-reinforced polymer (CFRP) sheets opened a new era of rehabilitation in the 1990s, numerous research projects and field applications have been performed.[8-10] The composite sheets are adhesively bonded to the designated surface of a member (frequently called "wet layup") for the sake of restoring or improving its ability to continuously carry external loads without compromising the intended use. As far as axial strengthening is concerned, concrete columns are wrapped with hoop-directional CFRP so that the transverse expansion of the core is restricted and a triaxial stress state is accomplished, thereby increasing the strength and ductility of the concrete.[11] In addition, the confining pressure precludes the buckling of principal reinforcing bars until the rehabilitation system fails.[12] A plethora of scientific findings were reported with a focus on capacity enhancement,[13] failure,[14] reliability,[15] durability,[16] ultimate strains,[17] stress-strain relationships,[18] and design recommendations.[19] State-of-the-art articles deal with a comprehensive review of other areas in regard to CFRP-confined concrete.[20-22]

Although the use of nonprismatic members is commonplace and the need for rehabilitation is continually growing in modern society, there has been little attempt to effectively strengthen deficient nonprismatic load-supporting units. As a prerequisite for assessing the behavior of columns in such a category, element-level investigations should first be conducted. More specific to CFRP-confined concrete, the majority of knowledge was derived from unreinforced bodies with uniform cross sections[23] and was adopted as part of practice guidelines.[2,11] In this paper, an experimental program is conducted to understand the implications of variable cross sections for the response of CFRP-confined cylindrical concrete subjected to axial compression. Two groups of cores are tested with and without pre-damage to examine the functionality of the confinement system when upgrading constructed structures that have suffered excessive service

ACI Structural Journal, V. 120, No. 4, July 2023.

MS No. S-2022-048.R1, doi: 10.14359/51737340, received June 23, 2022, and reviewed under Institute publication policies.

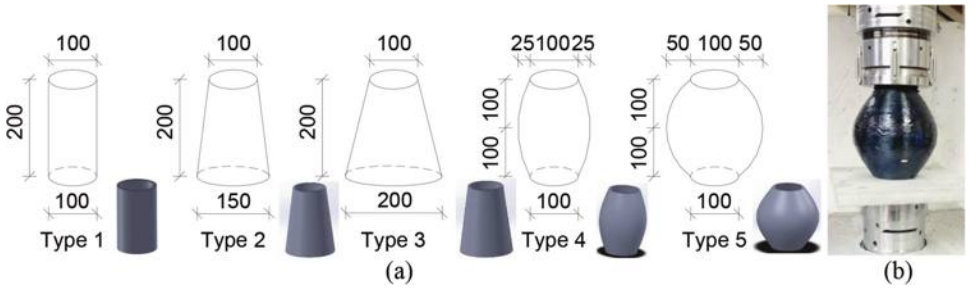

Fig. 1—Specimens: (a) type and dimensions; and (b) loading.

loads. Analytical modeling ascertains how external pressures induced by CFRP wrapping are related to the geometric features and furnishes necessary data for evaluating the relevance of a design proposal.

RESEARCH SIGNIFICANCE

The paucity of relevant acquaintance can lead to inappropriate retrofit strategies; therefore, the expected degree of safety may not be effectuated during the operational life of strengthened structures. Despite the considerable endeavors expended over the last three decades, CFRP-confinement techniques have not been studied for nonprismatic concrete elements. As a result, insufficient information is prescribed in design documents and practitioners encounter difficulties when handling such nonconventional elements. Recognizing that the discretion of professional engineers plays an important role in determining rehabilitation methods owing to a lack of published guidance, research is imperative to comprehend the underlying mechanics of CFRP application and to develop design procedures. The present work aims to address these identified challenges for the advancement of resilient built environments.

EXPERIMENTAL PROGRAM

A test campaign is described to explain constituent materials, cylindrical specimens, confinement schemes, and mechanical loading. Assorted geometric parameters are detailed for investigating the behavior of load-bearing concrete under axial compression.

Materials

The prepared ready mixed concrete cylinders (100 mm [4 in.] in diameter and 200 mm [8 in.] in depth) were tested per ASTM C39/C39M-18,[24] and an average compressive strength of $f_c' = 35.6$ MPa (5163 psi) was recorded. Unidirectional CFRP sheets had a nominal tensile strength of $f_{fu} = 3800$ MPa (551 ksi) and an elastic modulus of $E_f = 227$ GPa (32,900 ksi) alongside an equivalent fiber thickness of $t_f = 0.165$ mm (0.006 in.). A two-part epoxy adhesive was the bonding agent between the concrete cylinders and CFRP, which was composed of a resin and a hardener to be blended at a ratio of 3 to 1 until a homogeneous mixture was obtained. The manufacturer-reported properties of the hardened epoxy were a tensile strength of $f_p = 52$ MPa (7542 psi) with an elastic modulus of $E_p = 2.6$ GPa (377 ksi) after 7 days of curing. For the production of variable cylinder molds, polyethylene terephthalate glycol (PETG) was deposited for three-dimensional (3-D) printing with the succeeding properties: density (γ_{PETG}) = 1.27 g/cm^3 (0.046 lb/in.^{3}), yield strength ($f_{y\text{-}PETG}$) = 50 MPa (7252 psi), elastic modulus (E_{PETG}) = 2.1 GPa (305 ksi), and elongation at break ($\varepsilon_{u\text{-}PETG}$) = 130%.

Specimens

A total of 60 solid cylinders were cast with five types (12 specimens, each), as depicted in Fig. 1. Type 1 possessed parallel bases of 100 mm (4 in.) in diameter at right angles to the circular surface, Types 2 and 3 were truncated cones with top and bottom diameters of 100 to 200 mm (4 to 8 in.), and Types 4 and 5 were barrels with convex diameters of 100 to 200 mm (4 to 8 in.). The height of all cylinders was set to 200 mm (8 in.) for consistency. Additive manufacturing technology was employed to produce custom-made molds through a 3-D printer (Fig. 2). The printing device is equipped with a 0.4 mm (0.016 in.) nozzle for a filament diameter of 1.75 mm (0.069 in.) and operates at a maximum travel speed of 200 mm/s (8 in./s), accompanied by a printing accuracy of 0.05 mm (0.002 in.). Single forms were used to make Types 1 to 3, while a set of two symmetric segments was necessary for Types 4 and 5 for demolding convenience (Fig. 2, inset). Before placing the concrete, the inner surface of the PETG molds was lubricated. The cylinders were stripped in 1 day and moisture-cured for 28 days.

Preloading and confinement

To represent a variety of damage levels in constructed concrete, the cured cylinders were preloaded to 0%f_c', 30%f_c', and 60%f_c'.[25-27] Table 1 enumerates the types and preload intensities of each specimen. For those that were to be tested under confinement, the surfaces were cleaned with an airbrush, washed, and dried for implementing a wet layup process. The mixed two-part epoxy was pasted to the cylinder sides and carbon fabrics were placed; then, a top-coat epoxy layer was added to form a CFRP-confinement system. The overlapped length of 50 mm (2 in.) precluded the premature debonding of the CFRP sheets. Complying with the manufacturer's instructions, the CFRP-wrapped specimens were cured for 7 days at room temperature.

Loading

All cylinders were located on a 25 mm (1 in.) thick steel plate in a universal testing machine (Fig. 1) and monotonically loaded at a rate of 0.5 mm/min (0.02 in./min) until failure. The applied axial load and corresponding displacements were logged by a built-in load cell and a non-contacting

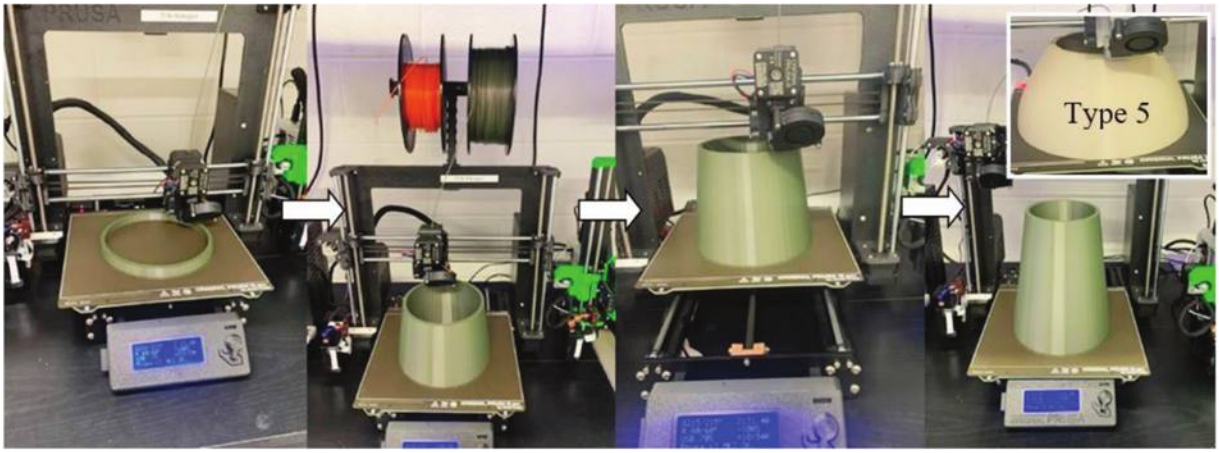

Fig. 2—3-D printing of concrete mold.

laser extensometer. A computerized data acquisition system recorded experimental data.

TEST RESULTS

The behavior of various concrete shapes with and without CFRP confinement is elaborated, including axial capacities, damage evolution, deformation and energy, and a failure process. Also delineated are the repercussions of preexisting damage in core concrete that can reflect the condition of decrepit structural components.

Load-carrying capacity

Figure 3(a) shows the compressive strength of the test specimens without preloading (0%f_c'). The confined cylinders in Type 1 failed at 73.3 MPa (10.6 ksi), on average, which was 106% higher than the capacity of the unconfined right-angle cylinders. As the taper angle increased in Types 2 and 3, the strengths progressively rose due to the enlarged base areas that reduced bearing stresses. When the midheight areas were dilated in Types 4 and 5, the average load-carrying capacities of the confined specimens declined by 14.6% and 34.9% relative to that of Type 1, respectively. On the contrary, the strengths of the unconfined concrete in Types 4 and 5 revealed marginal changes of 7.3% and 1.9%, respectively, compared with the case of Type 1. This fact indicates that the confining pressure of CFRP was a function of the cylinder geometry; further discussion is available in the "Analytical Modeling" section. The effects of preloading on the average strength of the confined concrete are visible in Fig. 3(b). The difference caused by the core damage was apparent (0%f_c' versus 30% and 60%f_c'), whereas the extent of the decreased capacity was dependent upon the specimen shape. According to the normalized capacities of the individual cylinders given in Fig. 3(c), the preload-induced capacity drops of Types 2 and 3 were prominent in relation to the drops of Types 4 and 5; specifically, their average magnitudes were 9.2% (Types 2 and 3) and 5.2% (Types 4 and 5), respectively, which were lower than the drop of 9.5% in Type 1. The efficacy of the CFRP confinement is graphed in Fig. 3(d). Irrespective of the preload level, the ratio between the confined and unconfined strengths (f_{cc}'/f_c') of all cylinder types exceeded unity; in other words, wrapping with CFRP was an effective method for enhancing the axial capacity of the concrete even with significant damage. It is, however, noted that the degraded performance of the confinement system was evident as the irregularity of the shape grew in Types 3 and 5.

Quantified damage

Because the capacities of the confined concrete were reliant on the shape and preloading of the cylinders, refined analysis was carried out in accordance with probability theory. The variation of the concrete strength in each cylinder type subjected to a certain level of preloading ($f_{cc}'(x\%)$) may be expressed as the format of the two-parameter Weibull model

$$\frac{f_{cc}'(x\%)}{f_{cc}'(0\%)} = \exp\left[-\left(\frac{f_{cc}'(x\%)}{\alpha}\right)^{\beta}\right] \quad (1)$$

where $f_{cc}'(0\%)$ is the confined strength without preloading; and α and β are the scale and shape parameters, respectively. Taking the logarithm of Eq. (1) renders

$$\ln\left[-\ln\left(\frac{f_{cc}'(x\%)}{f_{cc}'(0\%)}\right)\right] = \beta\ln(f_{cc}'(x\%)) - \beta\ln\alpha \quad (2)$$

The α and β parameters, solved using the test data, are presented in Fig. 4(a). As per the Weibull model, a damage index (DI) can be defined ($0 \le DI \le 1$)

$$DI = 1 - \exp\left[-\left(\frac{f_{cc}'(x\%)}{\alpha}\right)^{\beta}\right] \quad (3)$$

Built on the fitted Weibull parameters, the distribution of damage indexes is linked with the confined strength in Fig. 4(b). The physical interpretation of the plunging indexes is that the likelihood of damage was remarkably reduced by the activation of the confinement system, which raised the strength of the core concrete; scilicet, the damage indexes of Types 1 to 5 drastically decreased after passing the strength of the unconfined concrete specimens (Fig. 3(a)) spreading between 32.9 and 47.9 MPa (4772 and 6947 psi). The trajectories of Types 2 to 5 were away from the curvation

Table 1—Test specimens

Type	Confinement	Preload	Compressive strength, MPa		Type	Confinement	Preload	Compressive strength, MPa	
			Individual strength	Average				Individual strength	Average
1	None	0%f_c'	35.4	35.6	3	CFRP	30%f_c'	60.0	68.1
1	None	0%f_c'	36.5		3	CFRP	30%f_c'	68.1	
1	None	0%f_c'	34.8		3	CFRP	30%f_c'	76.1	
1	CFRP	0%f_c'	70.9	73.2	3	CFRP	60%f_c'	68.2	67.3
1	CFRP	0%f_c'	72.4		3	CFRP	60%f_c'	78.4	
1	CFRP	0%f_c'	76.4		3	CFRP	60%f_c'	55.4	
1	CFRP	30%f_c'	74.4	67.2	4	None	0%f_c'	31.9	32.9
1	CFRP	30%f_c'	63.7		4	None	0%f_c'	32.4	
1	CFRP	30%f_c'	63.6		4	None	0%f_c'	34.4	
1	CFRP	60%f_c'	63.0	65.4	4	CFRP	0%f_c'	65.8	62.6
1	CFRP	60%f_c'	66.6		4	CFRP	0%f_c'	59.1	
1	CFRP	60%f_c'	66.5		4	CFRP	0%f_c'	62.9	
2	None	0%f_c'	36.7	37.1	4	CFRP	30%f_c'	58.1	59.0
2	None	0%f_c'	36.6		4	CFRP	30%f_c'	60.3	
2	None	0%f_c'	38.1		4	CFRP	30%f_c'	58.6	
2	CFRP	0%f_c'	73.9	73.9	4	CFRP	60%f_c'	62.8	58.8
2	CFRP	0%f_c'	75.7		4	CFRP	60%f_c'	57.6	
2	CFRP	0%f_c'	72.1		4	CFRP	60%f_c'	56.2	
2	CFRP	30%f_c'	71.9	70.5	5	None	0%f_c'	36.6	36.2
2	CFRP	30%f_c'	68.4		5	None	0%f_c'	36.2	
2	CFRP	30%f_c'	71.3		5	None	0%f_c'	35.8	
2	CFRP	60%f_c'	58.3	63.1	5	CFRP	0%f_c'	56.9	52.3
2	CFRP	60%f_c'	58.4		5	CFRP	0%f_c'	49.2	
2	CFRP	60%f_c'	72.6		5	CFRP	0%f_c'	50.9	
3	None	0%f_c'	48.7	47.8	5	CFRP	30%f_c'	43.8	46.1
3	None	0%f_c'	45.6		5	CFRP	30%f_c'	51.6	
3	None	0%f_c'	49.2		5	CFRP	30%f_c'	42.8	
3	CFRP	0%f_c'	79.4	79.2	5	CFRP	60%f_c'	36.4	44.9
3	CFRP	0%f_c'	75.3		5	CFRP	60%f_c'	50.1	
3	CFRP	0%f_c'	82.8		5	CFRP	60%f_c'	48.1	

Note: 1 MPa = 145 psi.

of Type 1, corroborating the geometric significance of the core concrete wrapped with CFRP. On the preload level, the damage indexes of the specimens at 0%f_c' were consistently lower than those at 30%f_c' and 60%f_c' (Fig. 4(c)), and the barrel-shaped cylinders were generally vulnerable to the damage. Given the suddenly ascending indexes from Types 4 to 5, it is conjectured that there would be a transition curvature between these configurations. Figure 4(d) displays the reserved reliability of the cylinder types (R_R), quantified by modifying the definition of a safety index (a distance of the mean safety margin from the failure point of the limit state function)

$$R_R = \frac{(f_{cc}'(x\%) - f_c'(x\%))/\sqrt{\sigma_{cc}^2(x\%) + \sigma_c^2(x\%)}}{(f_{cc}'(0\%) - f_c'(0\%))/\sqrt{\sigma_{cc}^2(0\%) + \sigma_c^2(0\%)}} \quad (4)$$

where σ_{cc} and σ_c are the average standard deviations of the confined and unconfined specimens obtained from the test, respectively. The reliability of the cylinders dwindled with the increased preload level, and the trend was virtually independent of the geometry (Fig. 4(d)). That is, the overall validity of the CFRP system remained unchanged when confining the considerably damaged core concrete.

Load-displacement

The load-displacement relationship of the cylinders is provided in Fig. 5. For the Type 1 specimens without preloading (Fig. 5(a)), the response was linear up to 279 kN (62.7 kip), at which a bifurcation was observed owing to the abrupt crushing of the plain concrete, and the rupture of CFRP prompted the brittle failure of the confined ones at 576 kN

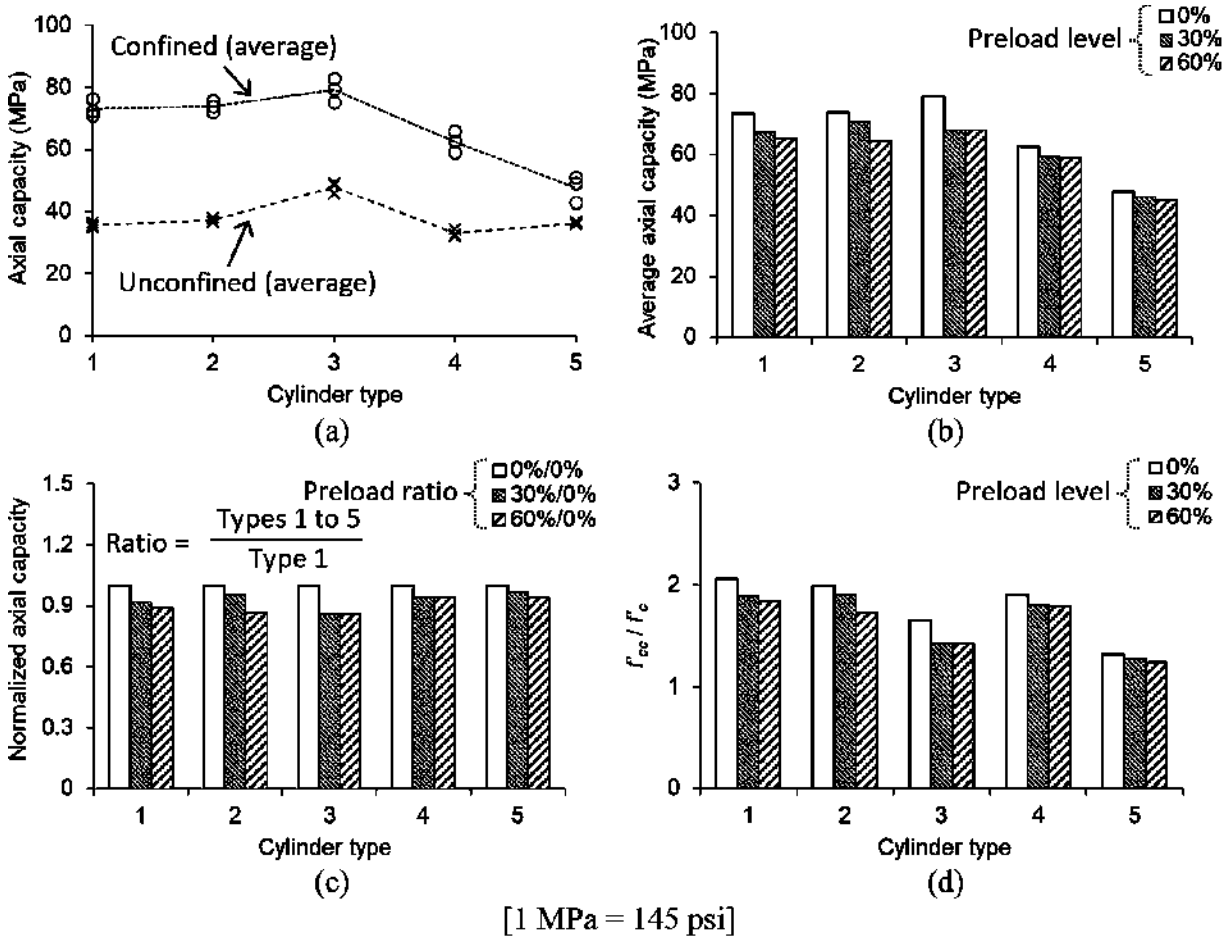

Fig. 3—Load-carrying capacity: (a) confined and unconfined concrete specimens without preloading (0%f_c'); (b) confined concrete with preloading; (c) normalized capacity; and (d) confinement effect.

(129.5 kip), on average. When the preloading was incorporated in Type 3 (Fig. 5(b)), the linearly elevating tendency of the CFRP-wrapped concrete was shortened, followed by the erratic post-peak responses (additional explanations will be given in the "Failure mode" section). The behavior of the confined cylinders in Type 5 was approximately bilinear until the peak loads were achieved (Fig. 5(c)): the first slope was akin to that of Type 3 in Fig. 5(b); on the other hand, the second slope differed because the convex zone of the concrete dispersed internal stresses so that the progression of the CFRP rupture was relatively stable. A comprehensive comparison is made to clarify dissimilarities among the concrete types in Fig. 5(d). As the shape of the cylinders deviated from the right-angle one in Type 1, their responses became nonlinear in conjunction with the fluctuant post-peak deformations stemming from the nonuniform rupture of the CFRP sheets. The obvious difference between the slopes of Type 1 and the others is ascribed to the fact that the axial rigidity of the cylinders was correlated with the cross-sectional area.

Energy dissipation

Figure 6(a) charts the average energy dissipation of the cylindrical concrete at 0%f_c', which was gained by numerically integrating the area under the load-displacement curves of the experimental specimens up to their peak loads. The unconfined plain cylinders in Types 1 to 3 showed an analogous amount of energy at approximately 330 kN·mm (2920 lb·in.); contrarily, those in Types 4 and 5 demonstrated lower values of 136 and 174 kN·mm (1204 and 1540 lb·in.), respectively. When the concrete was confined, the energy of Type 1 was greater than that of the others, particularly discernable from Types 4 and 5. To better elucidate the implications of morphology, the energy density (energy per unit volume) of the respective types was figured out and summarized in Fig. 6(b). Even with contemplating the preload levels, Type 1 was still the highest, reaffirming that the cylinder geometry was a crucial factor for controlling the effectiveness of CFRP in terms of energy dissipation, whether the core concrete was deficient or not.

Failure mode

Pictured in Fig. 7(a) are the failure modes of the plain cylinders. Unlike the right-angle specimen associated with an archetypal shear plane, the truncated cones in Types 2 and 3 involved several cracks initiating from the top of the cylinders where the smallest cross-sectional area carried the applied load. The barrel-shaped concrete in Types 4 and 5 was split into two parts with a concentrated crack, implying that the internal stresses were transferred to the larger sections before the top portion of the cylinders was fragmented. The confined specimens in Types 1 and 3 failed by

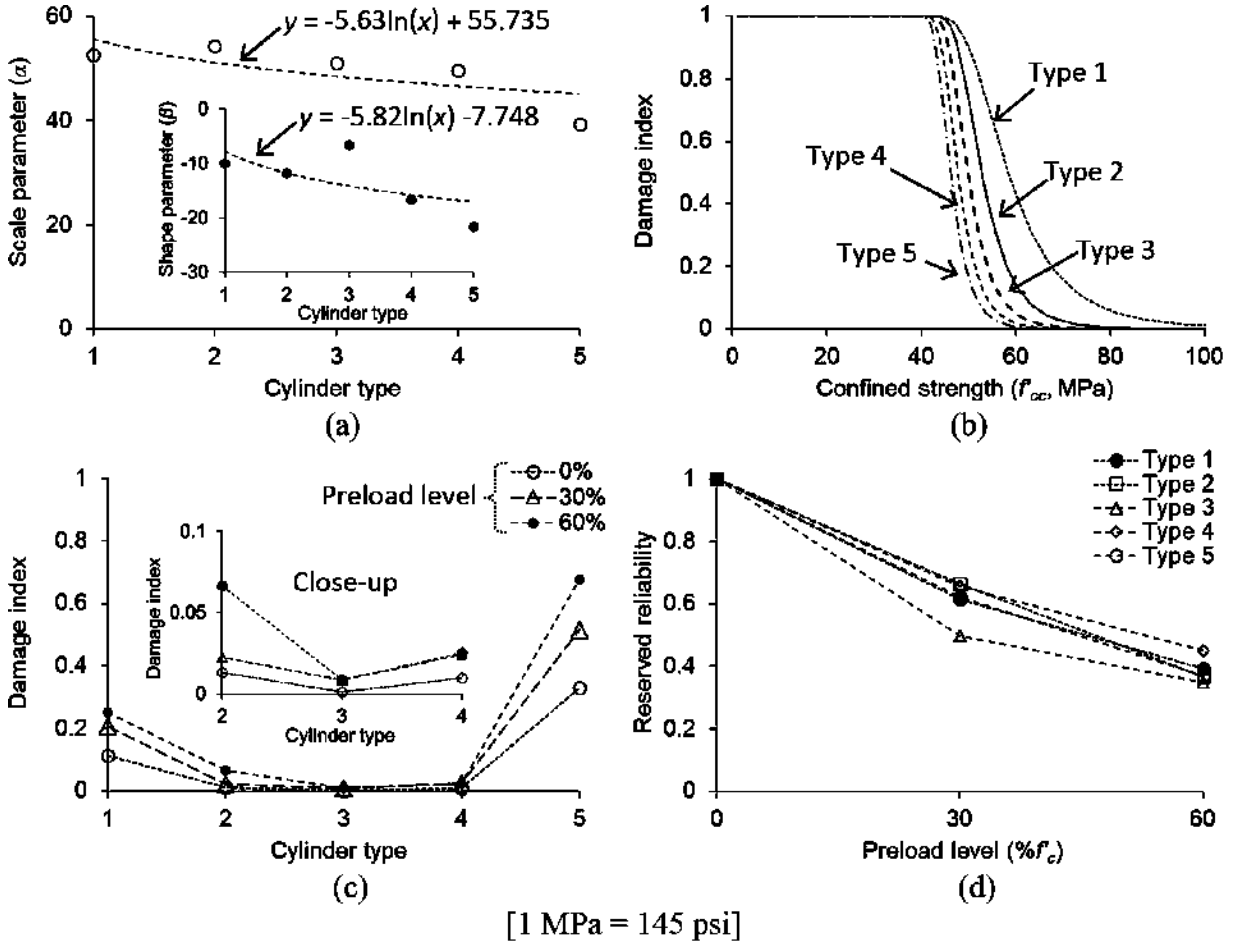

Fig. 4—Damage evolution: (a) determination of Weibull parameters; (b) distribution of damage index; (c) damage index with preload level; and (d) reserved reliability.

the rupture of CFRP (Fig. 7(b) and (c), respectively), and the disintegrated region was above the midheight of the cylinders. The appreciably spalled concrete substantiates that the cores were severely damaged prior to the activation of the CFRP jacket (known as passive confinement[11]), and no conspicuous difference was discovered between the intact and preloaded cores. With regard to the case of Types 4 and 5 (Fig. 7(d) and (e), respectively), a distinct propensity was found: the CFRP sheets were ruptured along the vertical direction of the specimens, especially near the midheight. The succeeding section accounts for the mechanism of these failure observations.

ANALYTICAL MODELING

To complement experimental findings, a theoretical study is undertaken in compliance with ACI 440.2R-17.[11] The variable geometry of confined concrete is allowed for, and the applicability of existing design provisions is appraised. Through parametric investigations, data are generated to propose design recommendations.

Description

The cross-sectional areas ($A(x)$) of the truncated cone and barrel shapes are calculated by Eq. (5) and (6) and shown in Fig. 8(a) and (b), respectively

$$A(x) = \frac{\pi}{4}\left(d_1 - \frac{(h-x)(d_1-d_3)}{h}\right)^2 \quad (5)$$

$$A(x) = \frac{\pi}{4}\left(d_2 - \frac{2}{h}\left(\frac{h}{2}-x\right)(d_2-d_3)\right)^2 \text{ if } 0 \le x \le h/2 \quad (6a)$$

$$A(x) = \frac{\pi}{4}\left(\frac{2}{h}\left(\frac{h}{2}-x\right)(d_2-d_1)+d_2\right)^2 \text{ if } h/2 < x \le h \quad (6b)$$

where d_i is the characteristic diameters (i = 1, 2, and 3); h is the height of the cylinder; and x is the axial distance from the cylinder bottom. The axial capacity (f_{cc}') and confining pressure (f_l) of the CFRP-strengthened concrete are expressed as (Fig. 8(c)[11])

$$f_{cc}' = f_c' + \psi_f 3.3 \kappa_a f_l \quad (7)$$

$$f_l = \frac{2E_f n t_f (\kappa_\varepsilon \varepsilon_{fu})}{D(x)} \quad (8)$$

where ψ_f and κ_a are the reduction and shape factors, respectively (ψ_f = 1 for the test results and κ_a = 1 for circular sections); κ_ε is the strain efficiency factor (κ_ε = 0.55 for design); and $D(x)$ is the variable diameter of the cylinder. Combining Eq. (7) and (8) to solve for experimental strain efficiency factors yields

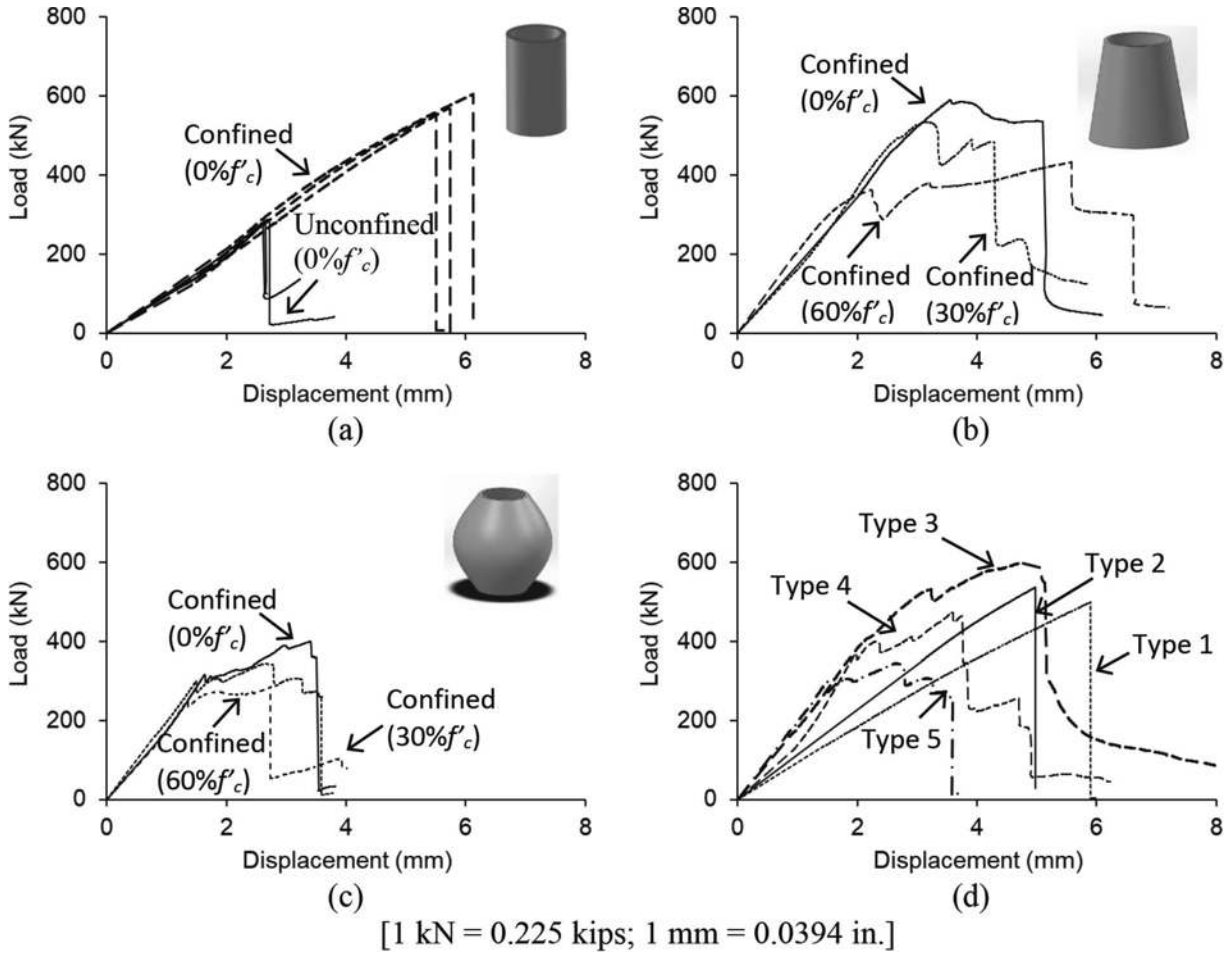

Fig. 5—Load-displacement relationship: (a) Type 1 without preloading (0%f_c'); (b) Type 3 with variable preload levels; (c) Type 5 with variable preload levels; and (d) confined concrete at 30%f_c'.

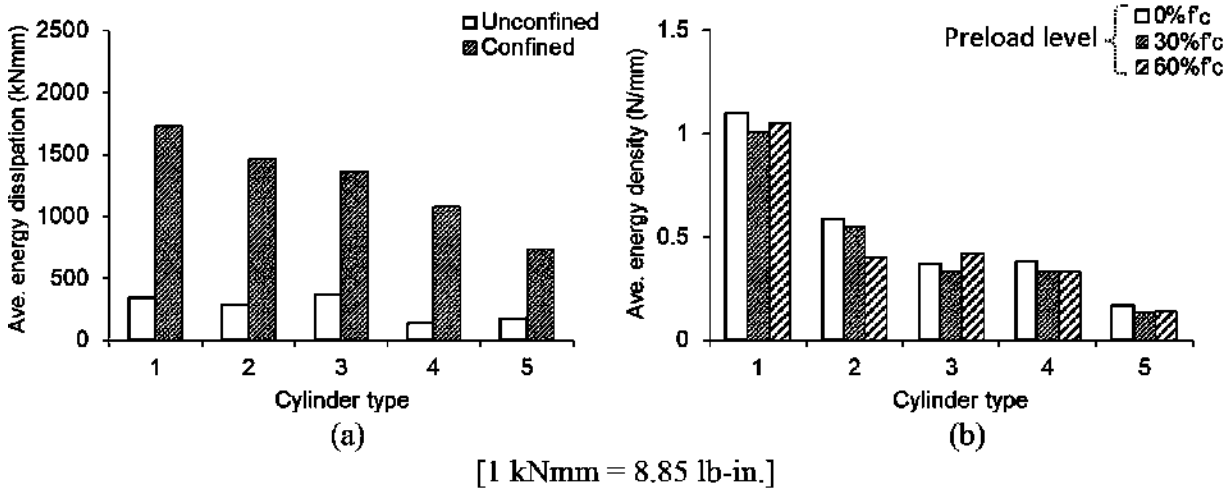

Fig. 6—Energy dissipation: (a) confined and unconfined specimens at 0%f_c'; and (b) average energy density of confined specimens at variable preload levels.

$$\kappa_\varepsilon = \frac{(f_{cc}' - f_c')D(x)}{6.6E_f n t_f \varepsilon_{fu}} \leq 1.0 \quad (9)$$

Confinement system

Efficiency of CFRP—Figures 9(a) and (b) exhibit the strain efficiency factors of selected cylinders to illustrate the ramifications of the variable cross sections (the average test values of f_{cc}' and f_c' were put into Eq. (9)). For comparison, a normalized height ratio was used (x/h). The efficiency factor of the Type 1 cylinder was constant along the height ratio (Fig. 9(a)), while the degree of efficiency diminished with the increased preload level: 16.1% and 20.9% drops were noticed in the 30%f_c' and 60%f_c' cases from the control cylinder with 0%f_c', respectively, due to the damaged core.

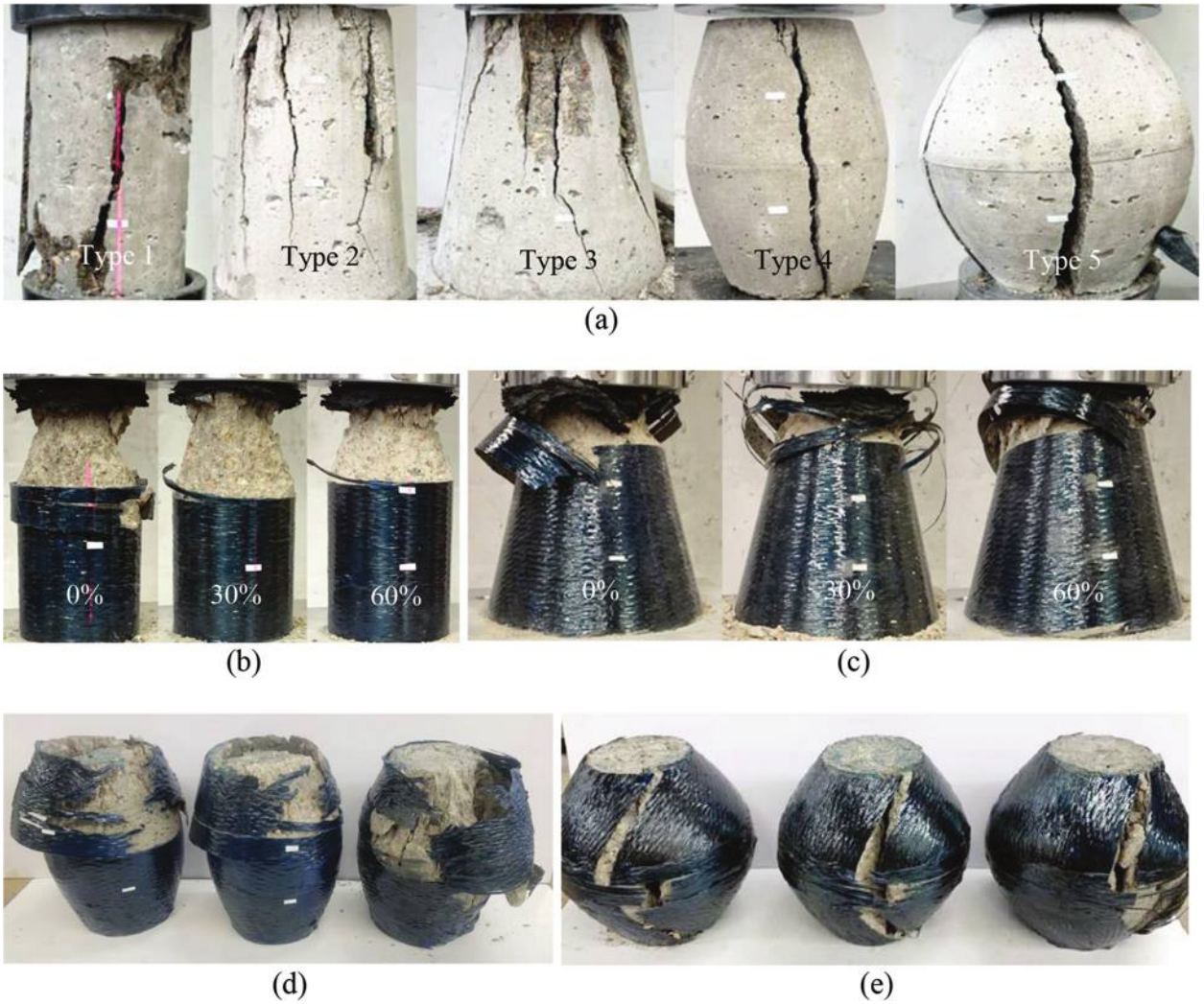

Fig. 7—Failure mode: (a) unconfined concrete; (b) Type 1; (c) Type 3; (d) Type 4 at 0%; and (e) Type 5 at 60%.

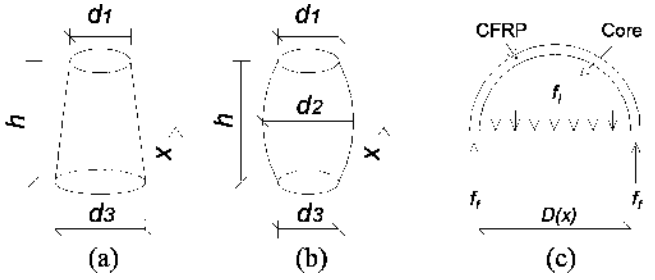

Fig. 8—Analytical model: (a) truncated cone; (b) barrel; and (c) confining pressure across section.

The design factor of $\kappa_\varepsilon = 0.55$ specified in ACI 440.2R-17[11] was sufficiently conservative and enveloped the experimentally determined factors. As the height ratio of the barrel-shaped cylinders in Type 5 went up (Fig. 9(b)), the efficiency factor ascended to the midheight of the specimens and symmetrically descended. Although the influence of the preload load was similar to the Type 1 specimens (14.0% and 24.2% drops in the 30%f_c' and 60%f_c' cases at x/h = 0.5, respectively), the magnitudes of the efficiency factors in Type 5 were lower than that of ACI 440.2R-17.[11] This observation implies that an alternative design approach is necessary for cylindrical concrete possessing variable cross sections.

Figure 9(c) shows the κ_ε factors of the individual shapes divided by the invariable factor of Type 1 with 0%f_c'. The truncated-cone cylinders in Types 2 and 3 maintained a uniform ratio of 1.09 until the x/h ratios of 0.77 and 0.69 were reached, respectively; afterward, these factors declined below the reference value of 1.0 in Type 1. Speaking of the barrel shapes, the radius of concave curvature on the flank dominated the efficiency of the CFRP sheets. For example, the ratios of Types 4 and 5 were 1.09 and 0.61 at x/h = 0.5, respectively. When the impaired core concrete was retrofitted (Fig. 9(d)), the ratio profiles of Types 2 and 3 altered substantially and the ratios of Types 4 and 5 changed as well, which were obvious signs of manifesting redistributed internal stresses within the confinement system. It is, thus, stated that both geometric configurations and soundness of the core influenced the use of CFRP.

Confining pressure—By substituting the aforementioned strain efficiency factors into Eq. (8), the confining pressure of each type with 0%f_c' was calculated and is plotted at three locations (top, middle, and bottom) in Fig. 10(a). The right-angle cylinder in Type 1 demonstrated a single value of 11.4 MPa (1653 psi), while the truncated-cone cylinders in

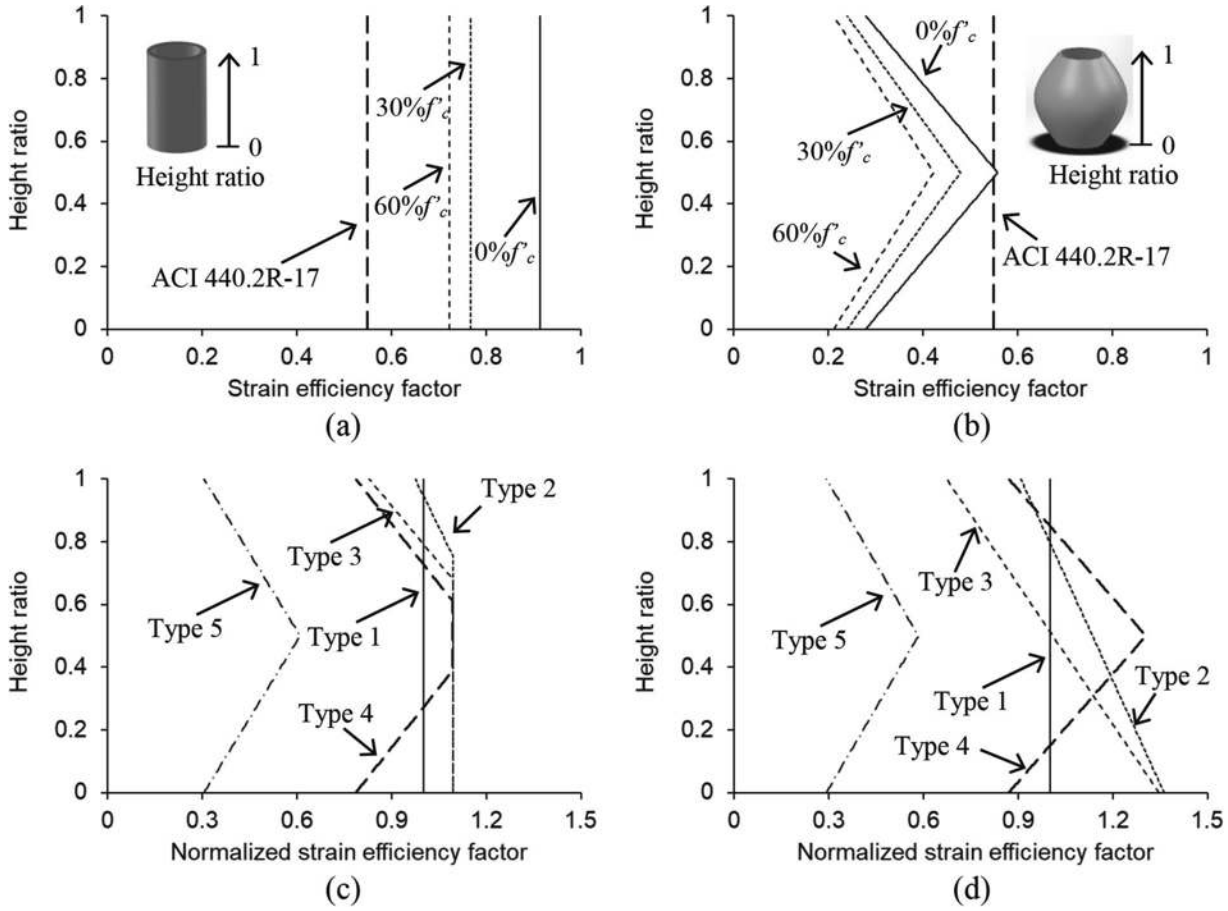

Fig. 9—Strain efficiency factor: (a) Type 1; (b) Type 5; (c) normalized strain efficiency factor at 0%f_c'; and (d) normalized strain efficiency factor at 60%f_c'.

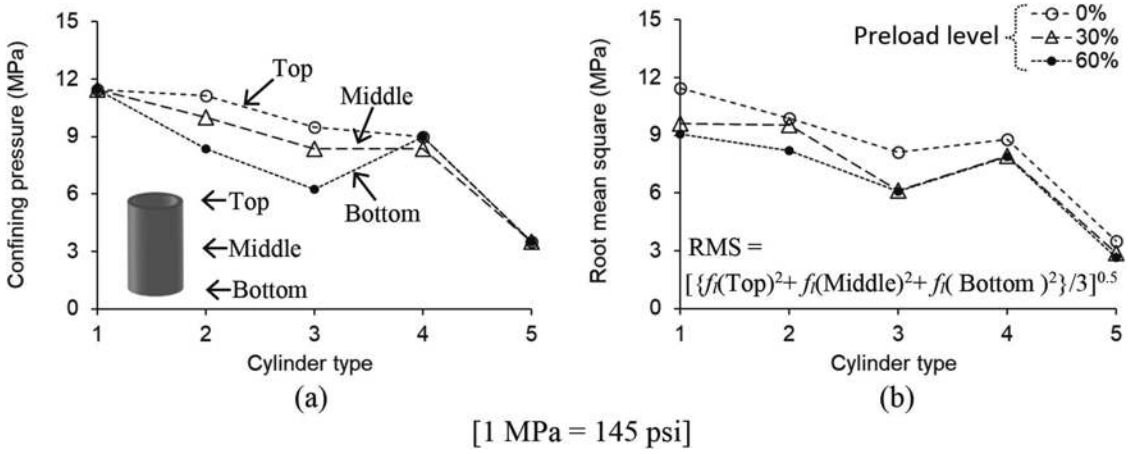

Fig. 10—Confining pressure: (a) selected locations at preload level of 0%f_c'; and (b) root-mean-square confining pressure.

Types 2 and 3 revealed distinguishable pressures along the axial direction. With an increase in the inclined angle from 7 degrees (Type 2) to 14 degrees (Type 3), the confining pressures of the cone cylinders decreased. The noticeable reduction at the bottom of the cylinders (8.3 and 6.3 MPa [1204 and 914 psi] for Types 2 and 3, respectively) is explained by the fact that, from a mechanics point of view, the radial stresses of the cross sections were inversely proportional to the distance from the origin of the polar coordinate space[28]; hence, the enlarged bottom sections resulted in the lower pressures. Regarding the barrel-shaped cylinders in Types 4 and 5, the confining pressures were insensitive to the axial locations because the contribution of the bulged portion ($D(x)$ in Eq. (8)) was offset by the lessened strain efficiency factors (κ_ε in Fig. 9(b)). To approximate the vertically varying confining pressures, the root mean square (RMS) of all types was taken alongside the preload levels (Fig. 10(b)). The cylinders with the inclined and curvilinear topography showed less pressure owing to the previously described geometric reason and, albeit locally irregular, the RMS pattern of the core-damaged specimens resembled that of the control ones (0%f_c').

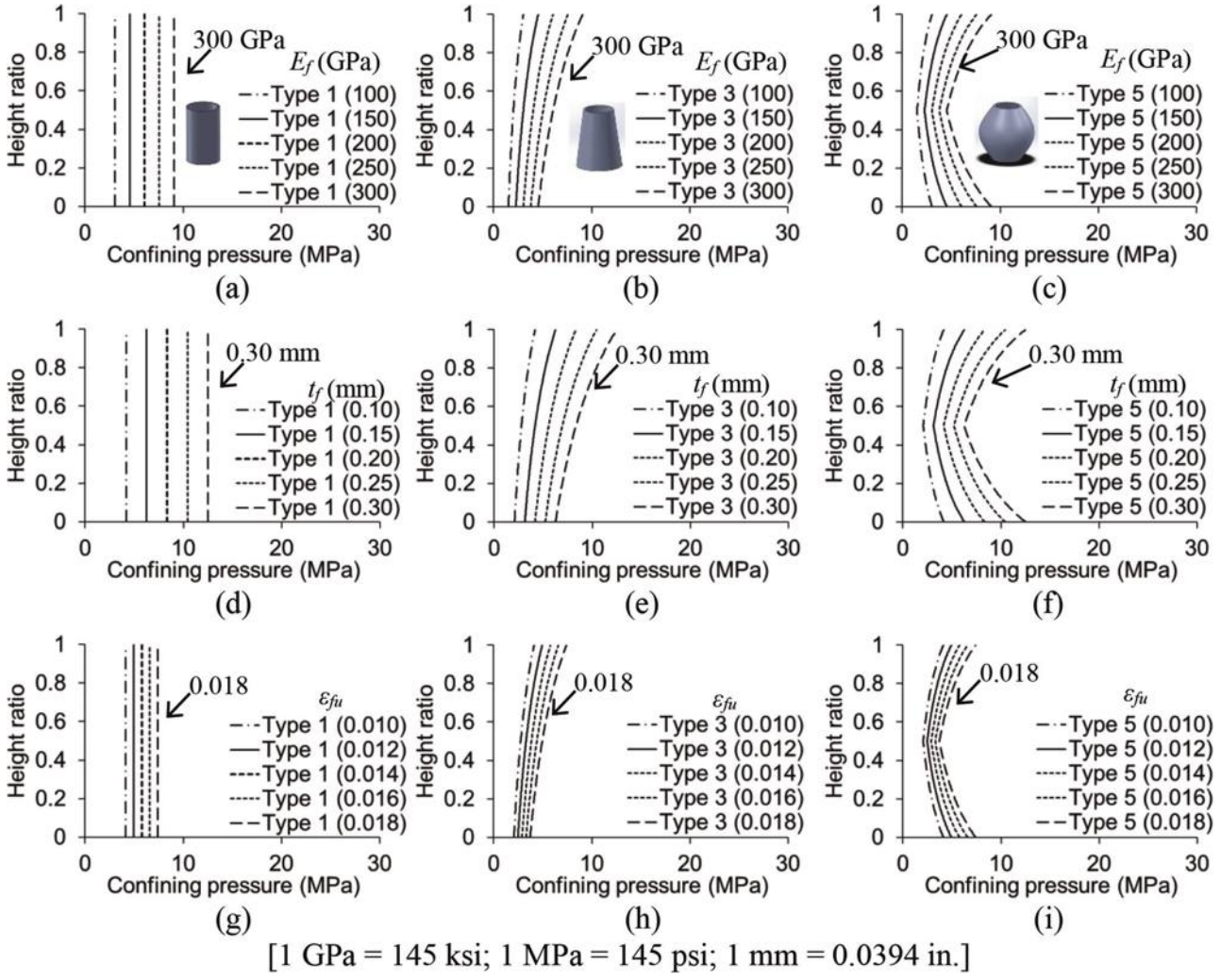

Fig. 11—Effects of CFRP properties: (a) modulus for Type 1; (b) modulus for Type 3; (c) modulus for Type 5; (d) ply thickness for Type 1; (e) ply thickness for Type 3; (f) ply thickness for Type 5; (g) failure strain for Type 1; (h) failure strain for Type 3; and (i) failure strain for Type 5.

Parametric study

Figure 11 exhibits the effects of CFRP properties on the confining pressure of the strengthened concrete. Unless otherwise stated, the attributes of the experimental specimens were taken as the default. Graphed in Fig. 11(a) to (c) are the consequences of CFRP moduli ranging from E_f = 100 to 300 GPa (14,504 to 43,511 ksi), encompassing most commercial products available in the market.[11] The use of high-modulus CFRP uniformly incremented the confining pressure in Type 1 (Fig. 11(a)), whereas the pressure intervals became narrow: for instance, the pressures were raised by 50.2% and 20.1% associated with E_f = 100 to 150 GPa (14,504 to 21,756 ksi) and E_f = 250 to 300 GPa (36,260 to 43,511 ksi), respectively. When the moduli were changed for the truncated-cone cylinders in Type 3 (Fig. 11(b)), the almost-straight profile with E_f = 100 GPa (14,504 ksi) was gradually transformed to nonlinear layouts; accordingly, the top region of the cylinder (x/h = 1) was more responsive than the bottom (x/h = 0). The conformation of pressure distributions was bowed in Type 5 (Fig. 11(c)), and the extent of warping was contingent upon the modulus. The midheight of the barrel-shaped cylinder at x/h = 0.5 was the least sensitive, and the pressure difference between E_f = 100 and 300 GPa (14,504 and 43,511 ksi) was broadened near the top and bottom. The outcomes of adjusting the thickness and failure strain of the CFRP sheets (0.1 mm [0.0039 in.] ≤ t_f ≤ 0.3 mm [0.012 in.] in Fig. 11(d) to (f) and 0.010 ≤ ε_{fu} ≤ 0.018 in Fig. 11(g) to (i), respectively) brought about the confining-pressure development similar to the case of the modulus. Nonetheless, the response range of the pressures belonging to the thickness variation was wider than its failure-strain counterpart. Overall, the response sensitivity of the confining pressure was preponderated by the thickness, modulus, and rupture strain of CFRP in order.

DESIGN RECOMMENDATIONS

A practical approach is conceptualized to assist engineering professionals in performing the rehabilitation of concrete members under axial compression. Based on the assumption that the total energy of CFRP-confined elements is conserved in line with the notion of fundamental physics, succinct expressions are suggested, and their applicability is evaluated.

Formulation

For design convenience, the geometry of the truncated cone (Types 2 and 3) and barrel (Types 4 and 5) cylinders may be converted to the shape of the right-angle cylinder (Type 1). Pursuant to the principle of energy conservation, the actual strain energy of the test cylinders (U_{act}) equals the equivalent strain energy (U_{eq})

$$U_{act} = U_{eq} \tag{10}$$

$$U_{act} = \int_0^h \frac{P^2}{2EA(x)}dx \tag{11}$$

$$U_{eq} = P^2h/2EA_{eq} \tag{12}$$

where P is the applied axial load; E is the elastic modulus of the confined cylinder; $A(x)$ is the variable cross-sectional area of the test cylinder; and A_{eq} is the equivalent cross-sectional area of the right-angle cylinder. Solving Eq. (10) to (12) for A_{eq} yields

$$A_{eq} = \frac{h}{\int_0^h \frac{1}{A(x)}dx} \tag{13}$$

The variable cross-sectional areas of the nonconventional cylinders (Eq. (5) and (6)) are plugged in and simplified to offer

$$\int_0^h \frac{1}{A(x)}dx = \int_0^h \frac{4}{\pi}\left\{\frac{(d_1 - d_3)}{h}x + d_3\right\}^{-2}dx \text{ for Types 2 and 3} \tag{14}$$

$$\int_0^h \frac{1}{A(x)}dx = \int_0^h \frac{4}{\pi}\left\{\frac{2(d_2 - d_3)}{h}x + d_3\right\}^{-2}dx \text{ for Types 4 and 5 } (0 \le x \le h/2) \tag{15a}$$

$$\int_0^h \frac{1}{A(x)}dx = \int_0^h \frac{4}{\pi}\left\{\frac{2(d_1 - d_2)}{h}x + (2d_2 - d_1)\right\}^{-2}dx \text{ for Types 4 and 5 } (h/2 < x \le h) \tag{15b}$$

These manipulated formulas are used to determine the equivalent cross-sectional areas of the specimens in tandem with Eq. (13)

$$A_{eq} = (\pi/4)d_1d_3 \text{ for Types 2 and 3} \tag{16}$$

$$A_{eq} = \frac{\pi}{4}d_3(2d_2 - d_3) \text{ for Types 4 and 5 } (0 \le x \le h/2) \tag{17a}$$

$$A_{eq} = \frac{\pi}{4}d_1(2d_2 - d_1) \text{ for Types 4 and 5 } (h/2 < x \le h) \tag{17b}$$

Finally, the equivalent diameters of the truncated-cone and barrel cylinders are attained for calculating the confining pressure in Eq. (8)

$$D_{eq} = \sqrt{d_1d_3} \text{ for Types 2 and 3} \tag{18}$$

$$D_{eq} = \sqrt{d_3(2d_2 - d_3)} \text{ for Types 4 and 5 } (0 \le x \le h/2) \tag{19a}$$

$$D_{eq} = \sqrt{d_1(2d_2 - d_1)} \text{ for Types 4 and 5 } (h/2 < x \le h) \tag{19b}$$

Considering that the confining pressure of CFRP tended to show a parallel shift for the preloaded cores without reshaping the RMS pattern (Fig. 10(b)), Eq. (18) and (19) can be applicable regardless of core condition.

Implementation

Figures 12(a) and (b) compare the cross-sectional areas of the actual and equivalent cylinders. The constant area of $A(x)$ = 7850 mm^2 (12.6 in.^{2}) in Type 1 steadily increased up to $A(x)$ = 31,400 mm^2 (50.2 in.^{2}) in Types 3 and 5; by contrast, the equivalent areas of Types 3 and 5 were A_{eq} = 17,500 and 23,550 mm^2 (28 and 37.7 in.^{2}), respectively. The confining pressures of the actual Type-3 and -5 cylinders without preloading spanned from 3.4 to 6.9 MPa (493 to 1001 psi); however, their equivalent pressures were 4.9 and 4.0 MPa (711 and 580 psi) in Fig. 12(c) and (d), respectively. It should be noted that the efficiency factor of κ_ε = 0.55 prescribed in ACI 440.2R-17[11] was employed to generate conservative design outcomes. For the assessment of the equivalent cross-sectional area, the strengths of the confined cylinders (f_{cc}') collected from the parametric study were adopted and are displayed in Fig. 13(a). The 12,060 data points relating the strengths calculated with the actual and equivalent diameters in Types 2 to 5 revealed an average absolute error of 4.6%. Figure 13(b) shows the coefficient of variation (COV) of the ratios between f_{cc}' (actual) and f_{cc}' (equivalent) in Types 1 to 5, containing 15,075 data points. The degree of scatter was found to be less than COV = 0.063 for the proposed design method, which was lower than a typical COV range of 0.12 to 0.17 for the compressive strength of ordinary concrete.[29]

SUMMARY AND CONCLUSIONS

This paper explored the consequences of variable geometry on the behavior of carbon fiber-reinforced polymer (CFRP)-confined concrete subjected to monotonic compression. A total of 60 cylinders were tested with the succeeding configurations: right angles (Type 1), truncated cones (Types 2 and 3), and barrels (Types 4 and 5). For the representation of existing damage in constructed structures, the specimens were preloaded to 0%f_c', 30%f_c', and 60%f_c' before applying CFRP sheets. The axial responses of the confined cylinders were examined against those of plain cylinders to characterize their load-bearing capacities, damage growth, vertical deformations, and failure mechanisms. The theoretical models, formulated per the principle of energy conservation, expatiated on a relationship between the spatial arrangement of the concrete and the performance of the CFRP system. The results of a sensitivity analysis

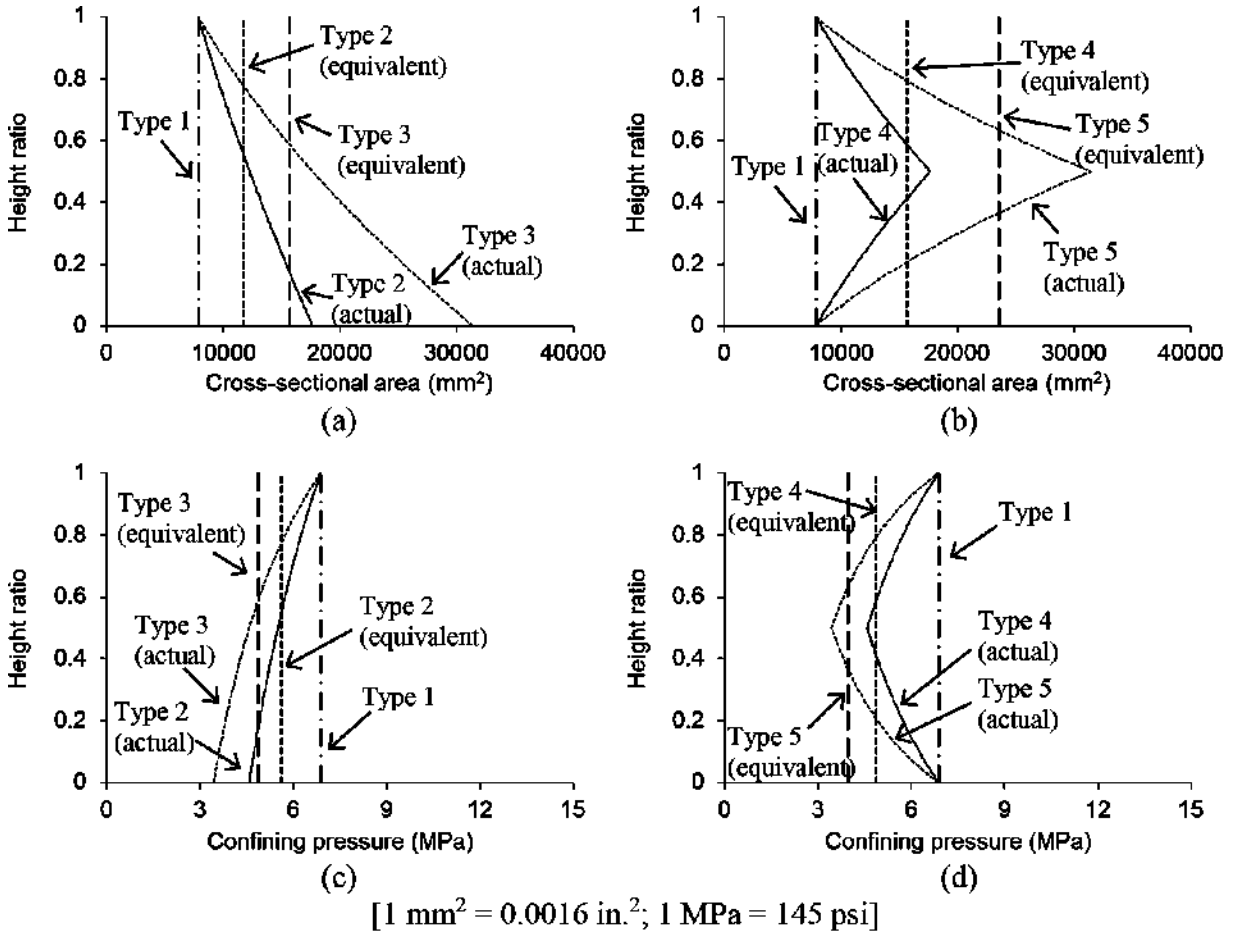

Fig. 12—Equivalent properties of variable cylindrical specimens with 0%f_c': (a) cross-sectional area of truncated cone shape; (b) cross-sectional area of barrel shape; (c) confining pressure of truncated cone shape; and (d) confining pressure of barrel shape.

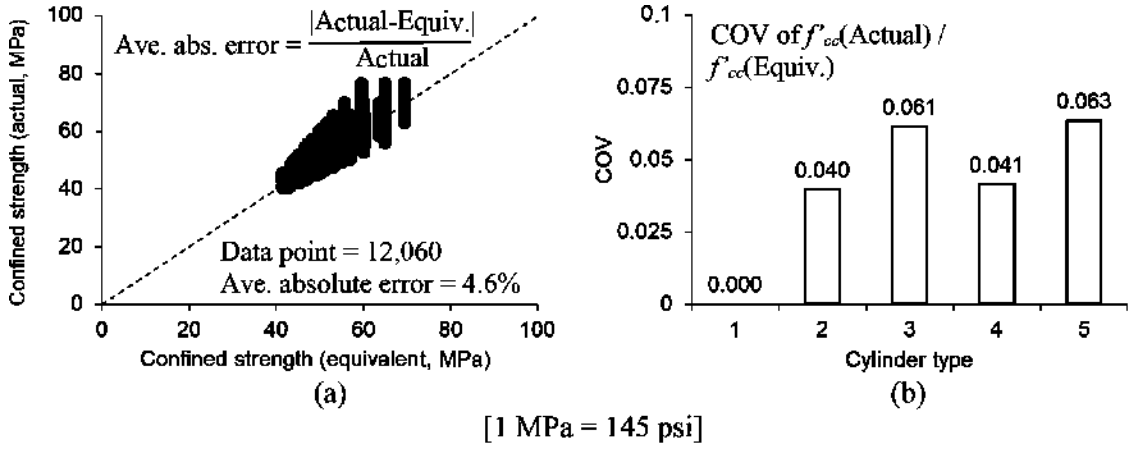

Fig. 13—Assessment for implementation: (a) comparison of strength between actual and equivalent diameters of Types 2 to 5; and (b) variation range of individual cylinder types.

were employed to impart technical information for the sake of practicing engineers. The following are concluded.

- For Type 1, the average capacity of the confined concrete was 106% higher than that of the plain concrete. The increased taper angles in Types 2 and 3, incorporating reduced bearing stresses, raised the compressive strength of the confined specimens; however, the bulged portion of Types 4 and 5 with CFRP lowered the ability to take the applied load by up to 35%. Even if the preexisting core damage was detrimental, the confinement system was still effective in terms of upgrading the load-bearing capacity.
- The probability-based Weibull model supported that the activation of the CFRP jackets drastically alleviated the evolution of damage in the confined concrete and also articulated the vulnerability of the barrel-shaped

cylinders to the axial loading. Without regard for the geometry, the reserved reliability of the confined specimens consistently decreased when the initial condition of the cores was degraded.

- The linear load-displacement behavior of Type 1 was transformed to a combination of diverse responses in other types, comprising unstable post-peak deformations coupled with the preloading effects and the uneven rupture of CFRP. Concerning energy dissipation, the cylinders in Types 1 to 3 were clustered with comparable magnitudes, which were greater than those of Types 4 and 5 by over 59%, and the confined ones indicated a resemblant trend. The conventional shear-plane failure of Type 1 differed from the radially cracked truncated cones (Types 2 and 3) and the localized cracking of the barrels (Types 4 and 5).
- The strain efficiency factor of CFRP (κ_ε) was governed by the soundness of the core concrete and the conformation of the cylinders. In comparison with the constant κ_ε factor of Type 1, the presence of the taper angle and concave curvature in Types 2 to 5 lowered the factors along the cylinder height and redistributed internal stresses; accordingly, the confining pressures of the CFRP system were adjusted.
- The sensitivity analysis disclosed that, among other material properties, the thickness of CFRP was the most influential parameter in quantifying the confining pressure of the system. The strength of the confined concrete involving the variable cross sections was reasonably approximated using the suggested design method at an average absolute error of 4.6% and the coefficient of variation (COV) of 0.063.

AUTHOR BIOS

Yail J. Kim, *FACI, is President of the Bridge Engineering Institute, An International Technical Society, and a Professor in the Department of Civil Engineering at the University of Colorado Denver, Denver, CO. He is Chair of ACI Subcommittee 440-I, FRP-Prestressed Concrete, past Chair of ACI Committee 345, Bridge Construction and Preservation, and a member of ACI Committees 342, Evaluation of Concrete Bridges and Bridge Elements; 377, Performance-Based Structural Integrity & Resilience of Concrete Structures; and 440, Fiber-Reinforced Polymer Reinforcement; and Joint ACI-ASCE Committee 343, Concrete Bridge Design. He received the Chester Paul Siess Award for Excellence in Structural Research in 2019. His research interests include advanced composite materials for rehabilitation; structural informatics; complex systems; and science-based structural engineering, including statistical, interfacial, and quantum physics.*

Aliasghar Hassani *is a Master's Student in the Department of Civil Engineering at the University of Colorado Denver. He received his BS in civil engineering from Islamic Azad University, Tehran, Iran, in 2016. His research interests include emerging materials and concrete structures.*

ACKNOWLEDGMENTS

The authors would like to gratefully acknowledge support from the U.S. Department of Transportation through the Mountain-Plains Consortium program. Technical contents presented in this paper are based on the opinion of the authors and do not necessarily represent that of others.

REFERENCES

1. Groper, M., and Kenig, M. J., "Inelastic Buckling of Nonprismatic Columns," *Journal of Engineering Mechanics*, ASCE, V. 113, No. 8, Aug. 1987, pp. 1233-1239. doi: 10.1061/(ASCE)0733-9399(1987)113:8(1233)

2. AASHTO, "Guide Specifications for Design of Bonded FRP Systems for Repair and Strengthening of Concrete Bridge Elements," American Association of State Highway and Transportation Officials, Washington, DC, 2012.

3. ACI Committee 318, "Building Code Requirements for Structural Concrete (ACI 318-19) and Commentary (ACI 318R-19) (Reapproved 2022)," American Concrete Institute, Farmington Hills, MI, 2019, 624 pp.

4. Manzelli, A. A., and Harik, I. E., "Prismatic and Nonprismatic Slender Columns and Bridge Piers," *Journal of Structural Engineering*, ASCE, V. 119, No. 4, Apr. 1993, pp. 1133-1149. doi: 10.1061/(ASCE)0733-9445(1993)119:4(1133)

5. Goel, M. D.; Bedon, C.; Singh, A.; Khatri, A. P.; and Gupta, L. M., "An Abridged Review of Buckling Analysis of Compression Members in Construction," *Buildings*, V. 11, No. 5, May 2021, Article No. 211. doi: 10.3390/buildings11050211

6. Sayed, A. M.; Rashwan, M. M.; and Helmy, M. E., "Experimental Behavior of Cracked Reinforced Concrete Columns Strengthened with Reinforced Concrete Jacketing," *Materials*, V. 13, No. 12, June 2020, Article No. 2832. doi: 10.3390/ma13122832

7. Villar-Salinas, S.; Guzmán, A.; and Carrillo, J., "Performance Evaluation of Structures with Reinforced Concrete Columns Retrofitted with Steel Jacketing," *Journal of Building Engineering*, V. 33, Jan. 2021, Article No. 101510. doi: 10.1016/j.jobe.2020.101510

8. ACI Committee 440, "Report on Fiber-Reinforced Polymer (FRP) Reinforcement for Concrete Structures (ACI 440R-07)," American Concrete Institute, Farmington Hills, MI, 2007, 100 pp.

9. Al-Saadi, N. T. K.; Mohammed, A.; Al-Mahaidi, R.; and Sanjayan, J., "A State-of-the-Art Review: Near-Surface Mounted FRP Composites for Reinforced Concrete Structures," *Construction and Building Materials*, V. 209, June 2019, pp. 748-769. doi: 10.1016/j.conbuildmat.2019.03.121

10. Gkournelos, P. D.; Triantafillou, T. C.; and Bournas, D. A., "Seismic Upgrading of Existing Reinforced Concrete Buildings: A State-of-the-Art Review," *Engineering Structures*, V. 240, Aug. 2021, Article No. 112273. doi: 10.1016/j.engstruct.2021.112273

11. ACI Committee 440, "Guide for the Design and Construction of Externally Bonded FRP Systems for Strengthening Concrete Structures (ACI 440.2R-17)," American Concrete Institute, Farmington Hills, MI, 2017, 112 pp.

12. Si Youcef, Y.; Amziane, S.; and Chemrouk, M., "CFRP Confinement Effectiveness on the Behavior of Reinforced Concrete Columns with Respect to Buckling Instability," *Construction and Building Materials*, V. 81, Apr. 2015, pp. 81-92. doi: 10.1016/j.conbuildmat.2015.02.006

13. Zhou, J.; Tian, Y.; Bi, F.; and Zhao, X., "Size Effect on Strength of Reinforced Concrete Cylinders Confined by Carbon Fiber-Reinforced Polymer and Transverse Stirrup Reinforcement," *ACI Structural Journal*, V. 118, No. 2, Mar. 2021, pp. 263-272.

14. Karam, G. N., and Tabbara, M. R., "Localization and Confinement Efficiency in Carbon Fiber-Reinforced Plastic-Confined Materials," *ACI Structural Journal*, V. 117, No. 6, Nov. 2020, pp. 7-15.

15. Ahmad, A.; Khan, Q. U. Z.; and Raza, A., "Reliability Analysis of Strength Models for CFRP-Confined Concrete Cylinders," *Composite Structures*, V. 244, July 2020, Article No. 112312. doi: 10.1016/j.compstruct.2020.112312

16. Kashi, A.; Ramezanianpour, A. A.; Moodi, F.; and Malekitabar, H., "Effect of Aggressive Marine Environment on Strain Efficiency Factor of FRP-Confined Concrete," *Construction and Building Materials*, V. 222, Oct. 2019, pp. 882-891. doi: 10.1016/j.conbuildmat.2019.07.055

17. Wu, Y.-F., and Cao, Y., "Energy Balance Method for Modeling Ultimate Strain of Confined Concrete," *ACI Structural Journal*, V. 114, No. 2, Mar.-Apr. 2017, pp. 373-381. doi: 10.14359/51689429

18. Jiang, K.; Han, Q.; Bai, Y.; and Du, X., "Data-Driven Ultimate Conditions Prediction and Stress-Strain Model for FRP-Confined Concrete," *Composite Structures*, V. 242, June 2020, Article No. 112094. doi: 10.1016/j.compstruct.2020.112094

19. Teng, J. G.; Jiang, T.; Lam, L.; and Luo, Y. Z., "Refinement of a Design-Oriented Stress–Strain Model for FRP-Confined Concrete," *Journal of Composites for Construction*, ASCE, V. 13, No. 4, Aug. 2009, pp. 269-278. doi: 10.1061/(ASCE)CC.1943-5614.0000012

20. Rocca, S.; Galati, N.; and Nanni, A., "Review of Design Guidelines for FRP Confinement of Reinforced Concrete Columns of Noncircular Cross Sections," *Journal of Composites for Construction*, ASCE, V. 12, No. 1, Feb. 2008, pp. 80-92. doi: 10.1061/(ASCE)1090-0268(2008)12:1(80)

21. Guler, S., and Ashour, A., "Review of Current Design Guidelines for Circular FRP-Wrapped Plain Concrete Cylinders," *Journal of Composites for Construction*, ASCE, V. 20, No. 2, Apr. 2016, p. 04015057. doi: 10.1061/(ASCE)CC.1943-5614.0000619

22. Raza, S.; Khan, M. K. I.; Menegon, S. J.; Tsang, H.-H.; and Wilson, J. L., "Strengthening and Repair of Reinforced Concrete Columns by Jacketing: State-of-the-Art Review," *Sustainability*, V. 11, No. 11, June 2019, Article No. 3208. doi: 10.3390/su11113208

23. Teng, J. G., and Lam, L., "Behavior and Modeling of FRP-Confined Concrete: A State-of-the-Art Review," *International Symposium on Confined Concrete*, SP-238, Y. Xiao, S. Kunnath, and W. Yi, eds., American Concrete Institute, Farmington Hills, MI, 2006, pp. 327-346.

24. ASTM C39/C39M-18, "Standard Test Method for Compressive Strength of Cylindrical Concrete Specimens," ASTM International, West Conshohocken, PA, 2018, 8 pp.

25. Ramaswamy, A.; Chachithanantham, S.; and Arumugam, S., "Performance of BFRP Retrofitted RCC Piles Subjected to Axial Loads," *Advances in Materials Science and Engineering*, V. 2014, 2014, Article No. 323909. doi: 10.1155/2014/323909

26. Wang, H.; Li, C.; Tu, J.; and Li, D., "Dynamic Tensile Test of Mass Concrete with Shapai Dam Cores," *Materials and Structures*, V. 50, No. 1, Feb. 2017, Article No. 44. doi: 10.1617/s11527-016-0901-x

27. Wang, J.; Lu, S.; and Yang, J., "Behavior of Eccentrically Loaded Rectangular RC Columns Wrapped with CFRP Jackets under Different Preloading Levels," *Journal of Building Engineering*, V. 34, Feb. 2021, Article No. 101943. doi: 10.1016/j.jobe.2020.101943

28. Ugural, A. C., and Fenster, S. K., *Advanced Strength and Applied Elasticity*, third edition, Prentice Hall, Hoboken, NJ, 1995.

29. Nowak, A. S., and Collins, K. R., *Reliability of Structures*, second edition, CRC Press, Boca Raton, FL, 2013.

ACI STRUCTURAL JOURNAL TECHNICAL PAPER

Title No. 120-S68

Generation of Optimal Load Paths for Corroded Reinforced Concrete Beams—Part I: Automatic Stiffness Adjustment Technique

by Ping Yuan, Lei Wang, and Royce W. Floyd

The conversion of material density during nonlinear topology optimization (NTO) results in the excessive distortion of minimum-density elements. An automatic stiffness adjustment technique is first proposed to overcome numerical instability. A multi-proportional growth strategy of the minimum-density element stiffness is given according to the change of maximum strain. On this basis, a generation method of optimal load paths for corroded reinforced concrete (CRC) beams is presented by considering material properties loss and bond degradation. The design sensitivity in the form of corrosion-damaged strain energy is then derived based on the adjoint variable method. Finally, the effectiveness of the proposed method is illustrated by numerical examples. The load paths of CRC beams under various corrosion levels are studied. Results show that the proposed method can reasonably generate the load paths of CRC beams without the numerical instability.

Keywords: automatic stiffness adjustment; corroded reinforced concrete (RC) beams; nonlinear topology optimization; optimal load paths.

INTRODUCTION

Reinforcement corrosion is recognized as one of the dominant destructive factors of reinforced concrete (RC) structures[1,2] and affects structural capacity mainly through material properties loss, bond degradation, and spalling of concrete cover.[3-5] When RC structures undergo these damages, the trajectory patterns of internal forces will be changed. The trajectory patterns of internal forces (that is, load paths) are of primary importance for describing the force transfer mechanisms and guiding structural reinforcement, especially for RC beams under corrosion damage.

Some topology optimization methods[6-9] have been successfully applied in RC structures to generate the load paths. Early contributions[8,10,11] mainly focused on capturing the load paths of elastic RC structures. These studies overlook the effects of embedded reinforcement and the tension-compression asymmetric response of concrete on the load paths of RC structures. Several nonlinear optimization methods,[6,7,9,12] considering the elastoplastic mechanical properties of concrete and reinforcement, have been proposed to seek the optimal layouts of the two materials within RC structures. However, the stress constraints were imposed in these methods,[12] leading to incomplete nonlinear response during nonlinear topology optimization (NTO) process. It is difficult to capture the actual trajectory of load paths of corroded reinforced concrete (CRC) beams with these methods due to the neglect of bond behavior between reinforcement and concrete.

Corrosion damage can affect structural nonlinear response and change the trajectory of load paths within CRC beams. The load paths of CRC beams are not only related to the elastoplastic mechanical behavior of corroded reinforcement and concrete, but also the bond behavior between them. The embedded reinforcement has stiffness contribution to RC structures through the bond behavior. The material properties loss and bond degradation caused by corrosion decrease the stiffness contribution of reinforcement and further affect the trajectory of load paths within CRC beams. Until now, there are few studies on generating the load paths of RC beams considering corrosion damage.

Numerical instability can be observed during the generation of load path for CRC beams. The minimum-density elements in the bidirectional evolutionary structural optimization (BESO) method are simulated as elastic material with infinitesimal stiffness by using the material interpolation schemes.[13-15] The minimum-density elements with the infinitesimal stiffness can cause excessive distortion and numerical instability during NTO process.[16,17] Some methods have been proposed to overcome the numerical instability, including the element removal method,[18] the convergence criterion relaxation method,[19-21] the energy interpolation scheme,[22] the element connectivity parameterization method,[23] and the additive hyperelasticity technique.[17] These methods mainly focus on the geometrically nonlinear topological configurations of elastic structures. However, these methods are difficult to use for generating the load paths of CRC beams due to their complexity.

This paper aims to propose a generation method of optimal load paths for CRC beams based on the automatic stiffness adjustment technique. The remaining context is arranged as follows: First, an automatic stiffness adjustment technique is presented to overcome the numerical instability. Then, the proposed method gives the nonlinear optimization formulation and the design sensitivity. The material properties loss and bond degeneration caused by corrosion are also considered. Subsequently, the optimization procedure for the generation of load paths of CRC beams is given. Finally, the effectiveness of the proposed method is illustrated. The

ACI Structural Journal, V. 120, No. 4, July 2023.

MS No. S-2022-095.R, doi: 10.14359/51738750, received October 22, 2022, and reviewed under Institute publication policies.

load paths of CRC beams under various corrosion levels are studied.

RESEARCH SIGNIFICANCE

The load paths of RC structures are of primary importance for describing the force transfer mechanism and aiding structural design and repair. Some topology optimization methods have been successfully applied in elastic RC structures for generating the load paths. However, these methods are difficult to capture the actual trajectory of load paths for CRC structures. The force transfer mechanism of CRC structures is still difficult to understand. It is time-consuming and difficult for structural designers to find the appropriate strut-and-tie models of CRC structures by using conventional methods. No study has been conducted to search the load paths of CRC structures. Therefore, this study aims to propose a generation method of load paths for CRC beams by considering material property loss and bond degradation.

AUTOMATIC STIFFNESS ADJUSTMENT TECHNIQUE OF MINIMUM-DENSITY ELEMENTS

In this section, an automatic stiffness adjustment technique is proposed to overcome numerical instability during the generation of load paths for CRC beams. A multi-proportional growth strategy of minimum-density element stiffness is given according to the change of maximal strain. The minimum-density element stiffness can be automatically adjusted in different proportions according to the change of maximum strain until the threshold value is reached.

The removal of elements in the BESO method[24] is realized by switching the fictitious density from maximum density 1.0 to minimum density $\tilde{x}_m$. The stiffness matrix of each element k_i is related to density $\tilde{x}_i$, which is defined as

$$k_i = \tilde{x}_i^P \int_{v_{co}} B^T D_c B d v_{c0} = \tilde{x}_i^P k_c,\ \tilde{x}_i = \tilde{x}_m, \text{ or } 1 \qquad (1)$$

where B is the strain-displacement matrix; k_c is the stiffness matrix of concrete element; v_{co} is the volume of concrete element; D_c is the elastoplastic constitutive matrix; and P is the penalty factor, which should be greater than 1 to make sure the existence of 0/1 solution.[25] The penalty factor is usually taken as $P = 3$. The elemental density $\tilde{x}_i = x_m$ indicates that the i-th element is void status (that is, minimum-density elements) and its elemental stiffness is $\tilde{x}_m^P k_c$. The minimum density is usually taken as $\tilde{x}_m = 0.001$. The elemental stiffness is artificially reduced by a factor of 10^{-9}. The infinitesimal stiffness can cause the excessive distortion of minimum-density elements and lead to the numerical instability during NTO process.

A simple method is to increase the minimum-density element stiffness to alleviate its excessive distortion. The minimum-density elements with the infinitesimal stiffness have little effect on the nonlinear response of original structures. However, the increasing stiffness of the minimum-density elements can affect the nonlinear response of remodeled structures and cause computation errors during the NTO process.[17] Hence, an automatic stiffness adjustment technique is proposed to overcome the numerical instability and restrain the errors caused by the increasing stiffness.

The minimum-density elements with the increasing stiffness can be regarded as a weakly elastic material. The element stiffness of the weakly elastic material can be formulated as

$$k_e = \int_{v_i} B^T D_e B d v_i,\ D_e = \frac{E_{min}}{1 - v_e^2} \begin{bmatrix} 1 & v_e & 0 \\ v_e & 1 & 0 \\ 0 & 0 & \frac{1 - v_e}{2} \end{bmatrix} \qquad (2)$$

where k_e is the stiffness matrix of the weakly elastic material; D_e is the elastic constitutive matrix; v_i the volume of the i-th element; and v_e and E_{min} are the Poisson's ratio and elastic modulus of the weakly-elastic material, respectively.

The minimum-density element stiffness can be adjusted by changing the elastic modulus, E_{min}. The elastic modulus E_{min} in the k-th optimization step can be automatically adjusted by tracking the maximal strain of minimum-density elements. The maximum strain increment of the minimum-density elements is different in each optimization step. If the maximum strain increment is large, the minimum-density element stiffness should be adjusted by a large amplitude. On the contrary, a small strain increment corresponds to a small adjustment amplitude of the minimum density element stiffness. Therefore, a multi-proportional growth strategy is given to adjust the minimum-density element stiffness in different proportions.

The minimum-density element stiffness can be automatically adjusted according to the maximal strain. The initial elastic modulus E_{min}^0 should be set as a relatively high value to avoid the numerical instability. In the k+1 optimization step, E_{min}^{k+1} can be automatically adjusted by using the multi-proportional growth strategy. When the maximal strain ε_{max}^k is greater than the strain threshold ε^*, the multi-proportional growth strategy can be expressed as

$$E_{min}^{k+1} = \begin{cases} \left(\alpha_2 + f(x)\right) \cdot E_{min}^k & \text{if } f(x) < f(\alpha_1) \\ \left(\alpha_3 + f(x)\right) \cdot E_{min}^k & \text{if } f(\alpha_1) \le f(x) < f(e) \\ \ln(x) \cdot E_{min}^k & \text{if } f(e) \le f(x) < 0.999 \\ x \cdot E_{min}^k & \text{if } 0.999 \le f(x) \end{cases} \qquad (3)$$

When $\varepsilon_{max}^k \le \varepsilon^*$, the multi-proportional growth strategy can be expressed as

$$E_{min}^{k+1} = \max(f(x) + 1 - f(1), \alpha_4) \cdot E_{min}^k \text{ (MPa)} \qquad (4)$$

where E_{min}^k and E_{min}^{k+1} are the elastic modulus of minimum-density elements in the k-th and k+1 optimization step, respectively; ε_{max}^k is the maximal strain of minimum-density elements; α_1, α_2, α_3, and α_4 are the coefficients to control the growth rate of element stiffness; and ε^* is the strain threshold of minimum-density elements. The initial threshold value ε^* is equal to the maximal strain of concrete elements in the original numerical model. The strain threshold value ε^* is then updated to $\varepsilon^* = (\varepsilon_{max}^k + \varepsilon^*)/2$ in each optimization step. $f(x)$ is the sigmoid function, which can be expressed as

$$f(x) = 1/(1 + e^{-x}\, x) > 0 \qquad (5)$$

where the independent variable x is defined as $x = \varepsilon_{max}^k/\varepsilon^*$, which represents the deformation degree of the

minimum-density elements. The sigmoid function is adopted to adjust the elastic modulus E_{min}^{k}, as illustrated in Fig. 1.

According to the difference of the strain increment of the minimum-density elements, the range of the variable x can be divided into multiple intervals. In different intervals, the element stiffness can be automatically adjusted in different proportions according to the change of maximum strain until the threshold value is reached. Therefore, the coefficient α_1 should be greater than 1 and less than the constant e. The coefficient α_2 should be greater than 0 and less than α_3, and the coefficient α_3 should be less than the constant e. The coefficient α_4 should be greater than 0 and less than 1.

When $\varepsilon_{max}^{k} > \varepsilon^*$, it means that some portions of the minimum-density elements will be excessive distortion in the next optimization step. The elastic modulus, E_{min}^{k}, should be increased to alleviate the excessive distortion. Then, the minimum-density element stiffness can be increased based on the multi-proportional growth strategy according to the maximal strain. If $\varepsilon_{max}^{k} \le \varepsilon^*$, E_{min}^{k} should be reduced to restrain the errors caused by the increasing stiffness. The maximum elastic modulus of minimum-density elements, E_{min}^{k}, eventually approaches the threshold value E_{max} during NTO process.

NONLINEAR OPTIMIZATION FORMULATION AND SENSITIVITY ANALYSIS OF CRC BEAMS

A classical formulation of NTO for minimum-compliance problems can be written in terms of the scalar product of load vector F and displacements vector U. The bond degradation and material property loss induced by corrosion can affect the structural displacement U and then change the load paths within CRC beams. A generation method of load paths for CRC beams is proposed based on the automatic stiffness adjustment technique. The design sensitivity in the forms of the corrosion-damaged element strain energy is derived based on the adjoint variable method.

Material property loss and bond degeneration

The concrete damaged plasticity (CDP) model[26] in ABAQUS is employed to simulate the asymmetric responses in tension and compression of concrete. More details on the CDP model and corresponding parameters can be found elsewhere.[26,27] Corrosion damage can decrease the compressive strength of concrete. It is assumed that the longitudinal reinforcement is subjected to uniform corrosion. The compressive strength of corrosion-damaged concrete f_{cm}' can be expressed as[28,29]

$$f_{cm}' = \frac{f_{cm}}{1 + k_r \cdot \varepsilon_1 / \varepsilon_{cu}} \text{ (MPa)} \tag{6}$$

where f_{cm} is the compressive strength of uncorroded concrete; $k_r = 0.1$ is the empirical coefficient; ε_{cu} is the maximal compressive strain; and ε_1 is the average tensile strain of cracked concrete, which can be expressed as[28,29]

$$\varepsilon_1 = n_{bs} \cdot w_{cr} / b_w \tag{7}$$

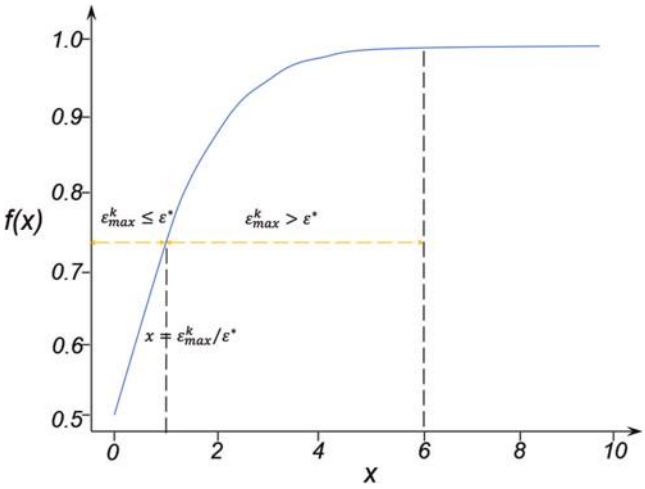

Fig. 1—Schematic of sigmoid function.

where b_w is the width of uncorroded RC beam; n_{bs} is the number of steel bars under compression; and w_{cr} is the total crack width of CRC beam, which can be calculated as[28,30]

$$w_{cr} = 2\pi X(u_{rs} - 1) \text{ (mm)} \tag{8}$$

where $u_{rs} = 2$ is the volumetric expansion rate; and X is the corrosion depth that can be expressed as[31]

$$X = \left(1 - \sqrt{1 - \eta_l}\right) r_l \text{ (mm)} \tag{9}$$

where r_l is the radius of longitudinal reinforcement; and η_l is the corrosion level of longitudinal reinforcement, which is defined as the ratio of the mass loss of corroded reinforcement to the mass of uncorroded reinforcement[32]

$$\eta_l = \Delta m_{l,\eta} / m_l = \Delta A_{l,\eta} / A_l \cdot 100\% \text{ (\%)} \tag{10}$$

where $\Delta m_{l,n}$ is the mass loss of corroded reinforcement; m_l is the mass of uncorroded reinforcement; $\Delta A_{l,n}$ is the loss of sectional area of corroded reinforcement; and A_l is the sectional area of uncorroded reinforcement.

The bilinear constitutive law proposed by Cairns et al.[33] is employed to character the tensile strength of corroded reinforcement. The yield and ultimate strength of corroded reinforcement are given as

$$f_{ly,\eta} = (1 - \alpha_y \eta_l) f_{ly} \text{ (MPa)} \tag{11}$$

$$f_{lu,\eta} = (1 - \alpha_u \eta_l) f_{lu} \text{ (MPa)} \tag{12}$$

where $f_{ly,\eta}$ and f_{ly} are the yield strength for corroded and uncorroded reinforcement, respectively; $f_{lu,\eta}$ and f_{lu} are the ultimate strength for corroded and uncorroded reinforcement, respectively; and $\alpha_y = 0.012$ and $\alpha_u = 0.011$ are the empirical coefficients.[33]

Bond degradation caused by corrosion can decrease the stiffness contribution of corroded reinforcement to structures. Bond behavior between corroded reinforcement and concrete is simulated by spring elements. The transverse stirrups and upper longitudinal reinforcement in test specimens

are usually epoxy coated to keep them free from corrosion.[34] Therefore, it is assumed that the transverse stirrup and upper longitudinal reinforcement are fully bonded to surrounding concrete. The bond strength $\tau_{a,\eta}$ of corroded longitudinal reinforcement can be expressed as[29,35]

$$\tau_{a,\eta} = 0.6\left(0.5+\frac{C_c}{D_l}\right)f_{ct}(1-\lambda X^{\zeta})+\frac{kA_{s,\eta}f_{sy,\eta}}{sD_l}\text{(MPa)} \quad (13)$$

where $\tau_{a,\eta}$ is the bond strength of corroded reinforcement; C_c is the depth of concrete cover; D_l is the diameter of longitudinal reinforcement; $A_{s,\eta} = (1 - \eta_s)A_s$, where $A_{s,\eta}$ and A_s are the sectional areas of corroded and uncorroded stirrups, respectively; η_s is the corrosion levels of corroded stirrups (units in %); $\lambda = 0.4$, $\zeta = 0.1$, and $k = 0.16$ are the empirical coefficients[35,36]; and s is the stirrup spacing. The tensile strength of concrete f_{ct} relates to the corresponding compressive strength f_{cm}, as $f_{ct} = 0.56\sqrt{f_{cm}}$[37]; $f_{sy,\eta}$ is the yield strength of corroded stirrups, which can be expressed as[38]

$$f_{sy,\eta} = (1 - 1.1 \cdot \eta_s)/(1 - \eta_s)\text{ (MPa)} \quad (14)$$

where f_{sy} is the yield strength of uncorroded stirrups.

The stiffness of the spring elements can be defined by the bond strength and corresponding slip between corroded reinforcement and concrete.[39] The stiffness of the spring elements can be expressed as

$$k_{sp} = \pi \cdot D_l \cdot l_r \cdot \tau_{a,\eta}/S_1 \quad (15)$$

where l_r is the length of concrete element; and S_1 is the slip at the maximum bond stress.

Optimization formulation of CRC beams

The goal of the optimization problem is to generate the load paths of CRC beams with minimum compliance. The nonlinear optimization problem of CRC beams is formulated as

$$\text{Minimize: } C(\tilde{x},U_{\eta l}) = f_{ext}{}^{T}U_{\eta l} \quad (16)$$

$$\text{Subject to:}\begin{cases} R\left(\tilde{x},U_{\eta_l}\right) = 0 \\ \sum_{i=1}^{n}\tilde{x}_i v_i \le V^* \\ \tilde{x} = \left[\tilde{x}_1\ \tilde{x}_2 \cdots \tilde{x}_n\right]^T \\ \tilde{x}_i \in \left(\tilde{x}_m, 1\right)(i = 1, 2, \cdots n) \end{cases} \quad (17)$$

where $C(\tilde{x},U_{\eta l})$ is the objective function (that is, compliance of CRC beams); $\tilde{x}$ is the element density vector; $\tilde{x}_i$ is the density variable of the i-th element; f_{ext} is the external force vector; $U_{\eta l}$ is the displacement vector under the corrosion levels η_l; v_i and V^* are the volume of the i-th element and the target volume fraction, respectively; n is the total number of concrete elements in the design domain; and $R(\tilde{x},U_{\eta l})$ is the residual force vector of CRC beams.

Newton's method[26] is adopted to solve the nonlinear equilibrium equations of CRC beams. The residual force of CRC beams can be expressed as

$$R(\tilde{x},U_{\eta l}) = f_{ext} - f_{int}(\tilde{x},U_{\eta l}) \quad (18)$$

where $f_{int}(\tilde{x},U_{\eta l})$ is the internal load vector. When the residual force $R(\tilde{x},U_{\eta l})$ is less than the tolerance (that is, 0.5%), the structure is in equilibrium state under the external load f_{ext}. A converged solution is obtained when the increment converges is less than 15 iterations.

Sensitivity analysis considering corrosion damage

The sensitivity is the derivative of the objective function $C(\tilde{x},U_{\eta l})$ with respect to the design variable, $\tilde{x}_i$, which can be given as[16,17,22]

$$\frac{\partial C\left(\tilde{x},U_{\eta_l}\right)}{\partial \tilde{x}_i} = -(f_{ext}K_{t,\eta_l}^{-1})^{T}\frac{\partial f_{int}\left(\tilde{x},U_{\eta_l}\right)}{\partial \tilde{x}_i} \quad (19)$$

where $K_{t,\eta l}$ is the tangent stiffness matrix of CRC beams. During the finite element analysis (FEA), the equilibrium equations in the m-th and m+1 iteration steps are respectively expressed as

$$f_{ext}{}^{m} - f_{int}{}^{m}(\tilde{x},U_{\eta l}{}^{m}) = 0 \quad (20)$$

$$f_{ext}^{m} + \delta f_{ext}^{m+1} - f_{int}^{m+1}\left(\tilde{x},U_{\eta_l}^{m+1}\right) = 0 \quad (21)$$

where δf_{ext}^{m+1} is the increment of external force. The Taylor series of the internal load $f_{int}^{m+1}\left(\tilde{x},U_{\eta_l}^{m+1}\right)$ can be expressed as[16]

$$f_{int}^{m+1}\left(\tilde{x},U_{\eta_l}^{m+1}\right) = f_{int}^{m}\left(\tilde{x},U_{\eta_l}^{m}\right) + K_{t,\eta_l}^{m}\delta U_{\eta_l}^{m+1} + o\left(\delta U_{\eta_l}^{m+1}\right) \quad (22)$$

where $o\left(\delta U_{\eta_l}^{m+1}\right)$ is the higher-order infinitesimal, which can be neglected.[16] Substituting Eq. (20) and (22) into Eq. (21), the term $f_{ext}K_{t,\eta l}{}^{-1}$ in the m+1 iteration step can be expressed as

$$\delta f_{ext}^{m+1}K_{t,\eta_l}^{m\ -1} \approx \delta U_{\eta_l}^{m+1} \quad (23)$$

Hence, the structural compliance can be approximated expressed as

$$C(\tilde{x},U_{\eta l}) \approx -U_{\eta l}{}^{T}f_{int}(\tilde{x},U_{\eta l}) \quad (24)$$

The term $U_{\eta l}{}^{T}f_{int}(\tilde{x},U_{\eta l})$ can be regarded as the work of external forces (that is, strain energy). The sensitivity function $\partial C(\tilde{x},U_{\eta l})/\partial \tilde{x}_i$ can be approximately rewritten as

$$\frac{\partial C\left(\tilde{x},U_{\eta_l}\right)}{\partial \tilde{x}_i} \approx -\frac{w_{i,\eta_l}}{\partial \tilde{x}_i} \quad (25)$$

where $w_{i,\eta l}$ is the elemental strain energy.

The CRC beam consists of concrete material, weakly elastic material, and corroded reinforcement. The internal load $f_{int}(\tilde{x},U_{\eta l})$ can be written as

$$f_{int}(\tilde{x},U_{\eta l}) = f_{co,\eta l} + f_{we} + f_{cr,\eta l} \quad (26)$$

where $f_{co,\eta l}$, f_{we}, and $f_{cr,\eta l}$ are the internal load of concrete, weakly elastic material, and corroded reinforcement, respectively. The internal load of corroded reinforcement is independent of the design variable. Therefore, the term $\partial f_{cr,\eta l}/\partial \tilde{x}_i$

is equal to 0. The strain energy of the CRC beam at the equilibrium state is convenient to operate during the NTO process. The strain energy of each element can be directly obtained from the numerical result. The strain energy, $w_{i,\eta l}$, of the element i is given as

$$w_{i,\eta l} = \tilde{x}_i^p w_{co,\eta l} + (1 - \tilde{x}_i^p) w_{we} \tag{27}$$

where $w_{co,\eta l}$ and w_{we} are the strain energy of concrete and weakly elastic elements, respectively.

The sensitivity function based on the proposed method can be expressed as

$$\frac{\partial C(\tilde{x}, U_{\eta_l})}{\partial \tilde{x}_i} = \frac{p}{\tilde{x}_i} \tilde{x}_i^p w_{co,\eta_l} - \frac{p \tilde{x}_i^{p-1}}{1 - \tilde{x}_i^p + \lambda_o} \left(1 - \tilde{x}_i^p\right) w_{we} \tag{28}$$

where λ_o is a small constant,[17] which can be set as $\lambda_o = 10^{-10}$.

OPTIMIZATION PROCEDURE OF CRC BEAMS

The optimization procedure of the generation of load paths for CRC beams is given based on the automatic stiffness adjustment technique. The filtering scheme and the convergence criterion are introduced in the proposed method. The optimization procedure of CRC beams consists of three stages: including pretreatment stage, optimization stage and stiffness adjustment stage. Figure 2 shows the flowchart of the optimization procedure of the generation of load paths for CRC beams. It can be outlined as follows.

In the pretreatment stage, the material parameters (that is, f_{cm}', $f_{ly,\eta}$, $f_{lu,\eta}$, and $\tau_{a,\eta}$) are calculated, and then the constitutive model of concrete and corroded reinforcement are defined. The FE model of CRC beam is established, and the FEA outputs are defined (that is, element strain energy).

In the optimization stage, the iteration process is similar to that of the BESO method.

Step 1: Define the optimization parameters (that is, r_{min}, V^*, ER, ε^*, E_{max}, and E_{min}^0).

Step 2: Carry out the FEA based on ABAQUS and retrieve elastic and plastic strain energy of each element. The strain energy, w_i, of element i can be expressed as[40]

$$w_i = w_i^e + w_i^p \tag{29}$$

where w_i^e and w_i^p are the elastic and plastic strain energy of i-th element, respectively.

Step 3: Calculate the elemental sensitivity by using Eq. (28).

Step 4: Update the elemental sensitivity by filtering and averaging with historical information. A blurring filtering scheme proposed by Huang and Xie[25] is employed to obtain a mesh-independent solution. The filtering scheme can be written as

$$\hat{\alpha}_i = \frac{\partial C(\tilde{x}, U_{\eta_l})}{\partial \tilde{x}_i} = \frac{\sum_j w(r_{ij}) \alpha_j}{\sum_j w(r_{ij})} = \sum_J \left(\frac{w(r_{ij})}{\sum_j w(r_{ij})} \alpha_j \right) = \sum_J \eta_j \alpha_j \tag{30}$$

$$w(r_{ij}) = \max(0, r_{min} - r_{ij}) \tag{31}$$

where r_{ij} is the distance between the centers of elements i and j; η_j is the weight factor; w is a weight function for averaging the raw sensitivities; and r_{min} is the filter radius, which is usually used to identify the nodes that influence the sensitivity of the i-th element.[25] The filter radius r_{min} should be larger than half of the element size. It is recommended that r_{min} is selected to be about one to three times of the element size.[25]

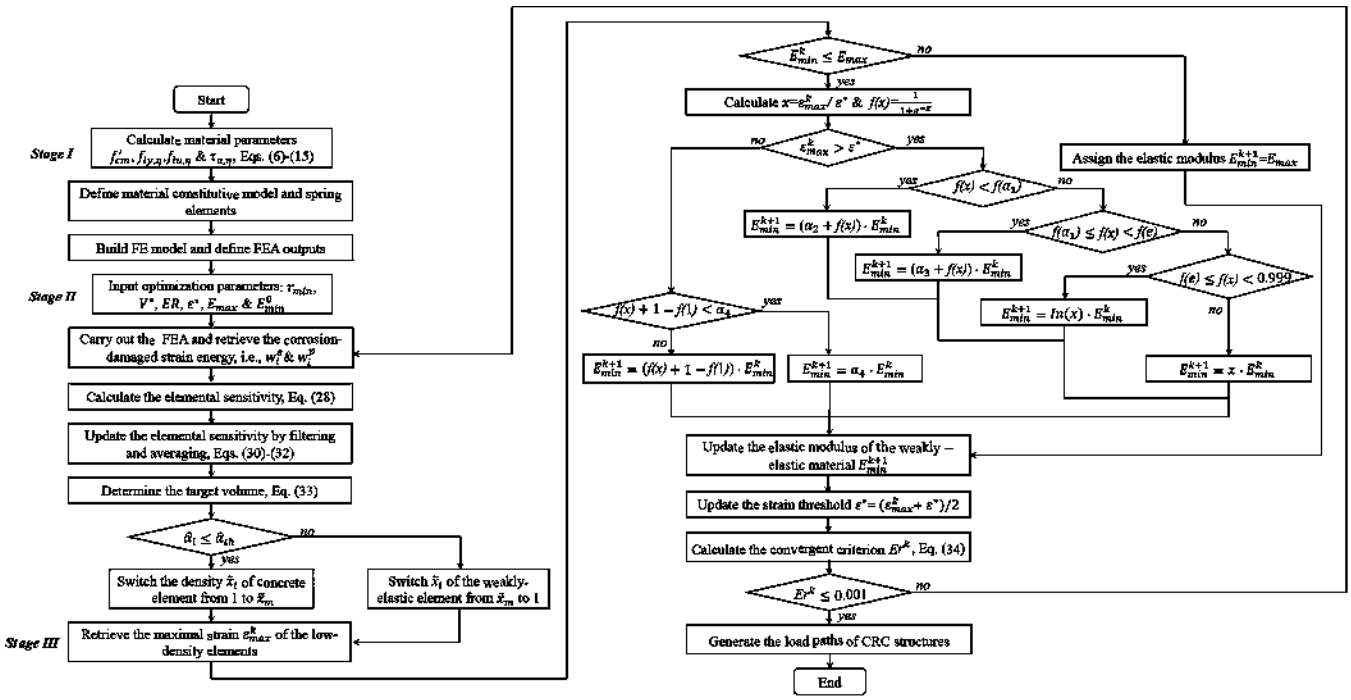

Fig. 2—Flowchart of optimization procedure of load paths of CRC beams.

The sensitivity $\hat{\alpha}_i^k$ in current iteration need to be further averaged with that in the previous iteration.[25] The sensitivity $\hat{\alpha}_i^k$ can be expressed as

$$\hat{\alpha}_i^k = \frac{\hat{\alpha}_i^k + \hat{\alpha}_i^{k-1}}{2} \tag{32}$$

where $\hat{\alpha}_i^k$ and $\hat{\alpha}_i^{k-1}$ are the sensitivity in the k and k–1 optimization step, respectively.

Step 5: Determine the target volume. The target volume in next iteration[41] V^{k+1} can be expressed as

$$V^{k+1} = V^k(1 \pm ER) \tag{33}$$

where V^k and V^{k+1} are the target volume in the k-th and k+1 optimization step, respectively; and ER is the evolutionary ratio, which is usually taken as $ER = 0.02$.

Step 6: Update the design variables. The sensitivity threshold $\hat{\alpha}_{th}$ is determined by using the bisection algorithm. If the sensitivity of concrete element $\hat{\alpha}_i$ is less than the sensitivity threshold $\hat{\alpha}_{th}$, the elemental density $\tilde{x}_i$ is switched from 1 to $\tilde{x}_m$. For the weakly elastic elements, if $\hat{\alpha}_i > \hat{\alpha}_{th}$, the elemental density $\tilde{x}_i$ is switched from $\tilde{x}_m$ to 1.

In the stiffness adjustment stage, the maximal strain ε_{max}^k of minimum-density elements is first retrieved. If $\varepsilon_{max}^k > \varepsilon^*$, the elastic modulus E_{min}^k should be increased in the next optimization step using Eq. (3). If $\varepsilon_{max}^k \le \varepsilon^*$, E_{min}^k should be reduced to restrain the errors caused by the increasing stiffness using Eq. (4). Finally, the NTO process is iteratively repeated until the convergent criterion and the objective volume are satisfied. The convergence criterion can be expressed as[41]

$$Er^k = \frac{\left|\sum_{i=1}^{N}(C_{k-i+1} - C_{k-N-i+1})\right|}{\sum_{i=1}^{N} C_{k-i+1}} \le \epsilon \tag{34}$$

where Er^k is the convergence error; N is the optimization step, which is set as $N = 5$; and ϵ is the allowable convergence error, which is set as $\epsilon = 0.01\%$. The NTO process is terminated when the structural compliance is stable at least in successive 10 iterations.

VERIFICATION AND DISCUSSION

In this section, the effectiveness and applicability of the proposed method are first illustrated by the numerical examples of cantilever beams and uncorroded RC beams. Then, the load paths of CRC beams with various corrosion levels are studied. Finally, the effects of the tensile strength loss and bond degradation of corroded reinforcement on the load paths are discussed, respectively.

VERIFICATION

Topology optimization of cantilever beam —A classical cantilever beam is first introduced to illustrate the effectiveness of the proposed automatic stiffness adjustment technique, as depicted in Fig. 3. The geometrical nonlinearity is considered in the optimization model. To compare the accuracy of the proposed technique, the same material of cantilever beam in other literatures[16,18] is used. The elastic modulus and Poisson's ratio of the elastic material are E_n = 3.0 GPa (435 ksi) and v_n = 0.4, respectively. The design domain of the cantilever beam has the dimension of 120 x 30 x 1 mm (4.68 x 1.17 x 0.039 in.), which is discretized by a 120 × 30 quadrilateral element mesh. The concentrated forces are uniformly distributed over nine nodes and are applied downward at the midpoint of the right side of the cantilever beam.

In this example, the penalty factor is taken as $P = 3$. The filter radius r_{min}, the target volume fraction V^*, and the evolutionary ratio ER are set as 1.5 mm (0.0585 in.), 50%, and 0.02, respectively. The initial elastic modulus and Poisson's ratio of the weakly elastic material are set as $E_{min}^0 = 10^{-4}E_n$ and $v_n = 0.4$, respectively. The initial threshold value ε^* is determined based on the numerical results under the different load cases. The threshold values of elastic modulus E_{max} are set as 5, 50, 100, and 200 MPa (0.725, 7.25, 14.5, and 29 ksi) for the different load cases, respectively. The coefficient α_1, α_2, α_3, and α_4 can be taken as 1.2, 0.5, 1, and 0.9, respectively.

Figure 4 shows the optimal topologies considering the geometrical nonlinearity based on the BESO method.[15] Figure 4(a) shows the up-down symmetric and elastic topology of the cantilever beam. The optimal topology becomes asymmetric by considering the geometrical nonlinearity, as shown in Fig. 4(b). The numerical instability occurs when the applied load increases to 0.01 kN (0.00225 kip). The final optimization step is 32 and then the NTO process is suddenly broken down, as shown in Fig. 4(c). Figure 4(d) shows that the excessive distortion occurs in the minimum-density region. It is indicated that the BESO method considering geometric nonlinearity can lead to the numerical instability.

Figure 5 shows the optimal topologies based on the proposed method under the different magnitudes of F = 0.01, 0.1, 0.25, and 0.5 kN (0.00225, 0.0225, 0.0563, and 0.1125 kip). The optimal topologies based on the proposed method are almost consistent with the results in existing studies.[17,19] The optimal topology under the applied load F = 0.01 kN in Fig. 5(a) is asymmetric, which is different

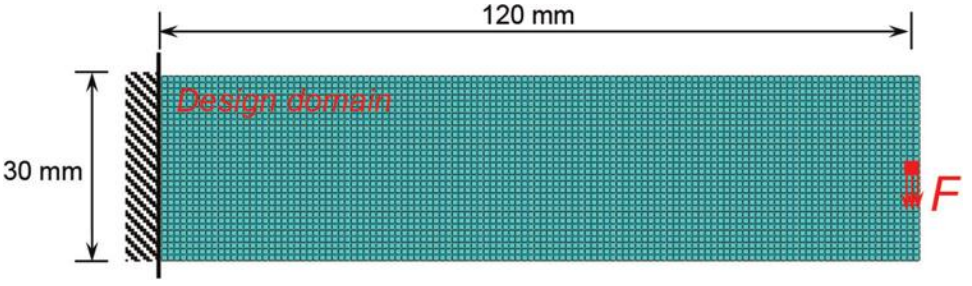

Fig. 3—Schematic diagram of optimization model for cantilever beam. (Note: 1 mm = 0.0394 in.)

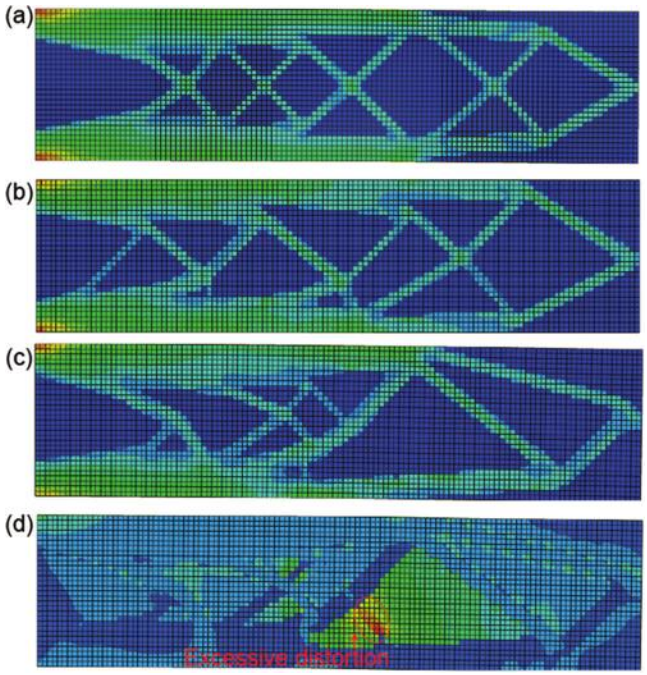

Fig. 4—Optimal topologies of cantilever beam based on BESO method: (a) elastic topology under load F = *0.0001 kN; (b)* F = *0.001 kN; (c)* F = *0.01 kN; and (d) strain distribution under load* F = *0.01 kN. (Note: 1 kN = 0.225 kip.)*

from the symmetric result in existing result.[17] The optimal topology under the same load in Fig. 4(c) is also asymmetric by considering the geometrical nonlinearity. It is indicated that the BESO method can generate the asymmetric topology when the geometrical nonlinearity of structures is considered.

When the applied load increases to $F = 0.25$ kN, the topological configurations in Fig. 5(b) to (c) are similar to the existing results[17] except for some redundant members at local locations. When the applied load further increases, it is easily checked that the optimal topology in Fig. 5(d) is consistent with the existing result.[17] The length and width of the tensile member increase with the applied load. The tensile member on the right side provides a direct load path in Fig. 5(d) when the geometrical nonlinearity becomes dominant.

Figure 6 shows the evolutionary histories of the elastic modulus $E_{min}{}^{k}$ and the mean compliance by using the proposed method. The elastic modulus $E_{min}{}^{k}$ of minimum-density elements initially increases and then approaches a constant value. Figures 6(a) to (c) show a stable convergence of the mean compliance during NTO process. The local numerical instability in Fig. 6(d) can be attributed to the small elastic modulus E^{k}_{min} in this optimization step. The proposed method allows local non-convergence. E^{k}_{min} will be increased in the next optimization step to overcome the local numerical instability.

Load paths of uncorroded RC beam—The generation of the load path for an RC beam is used to illustrate the applicability of the proposed method, as depicted in Fig. 7. The design domain of RC beam has the dimension of 600 x 100 x 1 mm (23.4 x 3.9 x 0.039 in.), which is discretized by a 120 × 20 quadrilateral element mesh. The concentrated forces are uniformly distributed over five nodes and are applied downward at the upper center of the design domain. The concentrated forces and constraints are applied on the rigid steel plate to relax the element distortion. The contact surfaces between the rigid steel plates and the design domain are tied using the mesh tie constraint. Steel reinforcement is simulated by the linear truss element. The upper longitudinal reinforcement and stirrups are embedded within concrete by using the embedded equation.

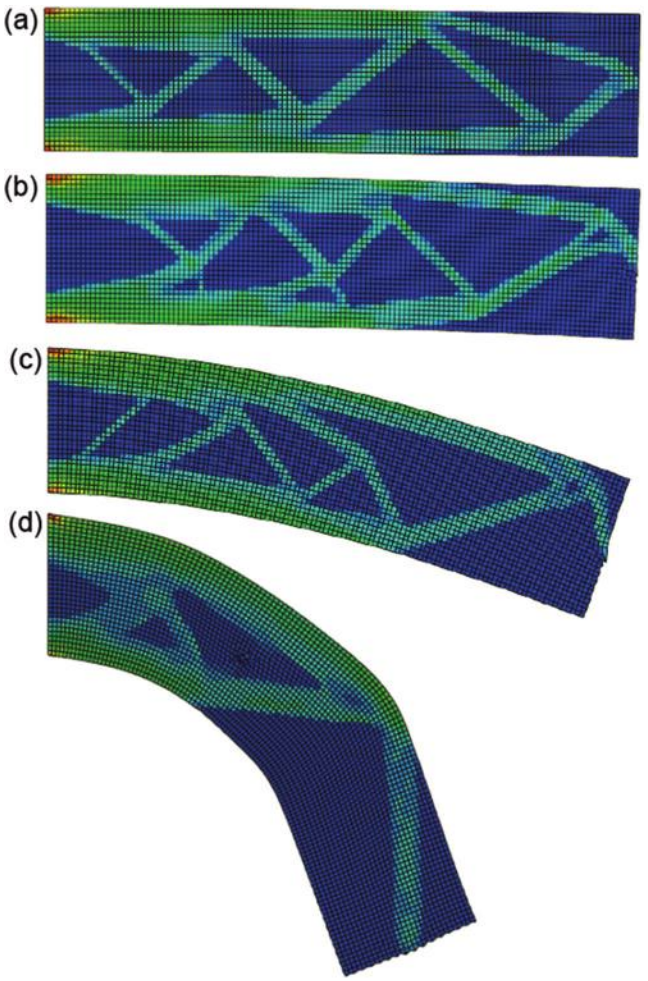

Fig. 5—Optimized topologies under different magnitudes of loads: F = *0.01 kN; (b)* F = *0.1 kN; (c)* F = *0.25 kN; and (d)* F = *0.5 kN. (Note: 1 kN = 0.225 kip.)*

In this example, the penalty factor P and the evolutionary ratio ER are taken as 3 and 0.02, respectively. The filter radius r_{min} and the target volume fraction V^* can be set as a relatively large value for RC beam under the limit state. In this case, the filter radius r_{min} and the target volume fraction V^* are set as 20 mm (0.78 in.) and 50%, respectively. The initial elastic modulus and Poisson's ratio of the weakly elastic material are set as $E_{min}{}^{0} = 10^{-4}E_c$ and $\nu_0 = 0.3$, respectively. The initial threshold value ε^* is determined based on the numerical results under the different load cases. The threshold values of elastic modulus E_{max} are set as 1, 5, 10, 25, 50, 80, and 100 MPa (0.145, 0.725, 1.45, 3.625, 7.25, 11.6, and 14.5 ksi) for the different load cases, respectively. The coefficients α_1, α_2, α_3, and α_4 can be taken as 1.2,

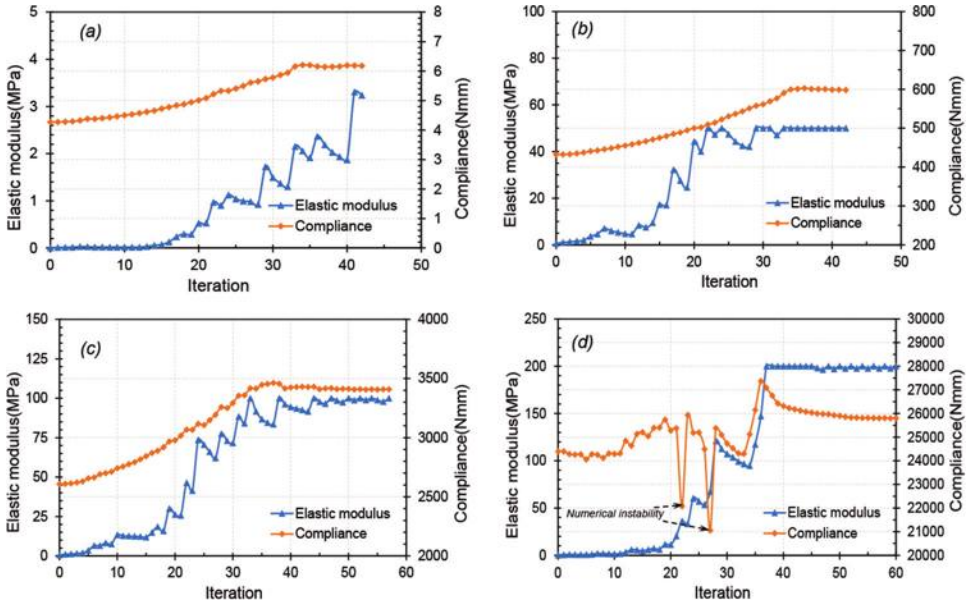

Fig. 6—Evolutionary histories of elastic modulus and mean compliance under different magnitudes of loads: (a) F = *0.01 kN; (b)* F = *0.1 kN; (c)* F = *0.25 kN; and (d)* F = *0.5 kN. (Note: 1 kN = 0.225 kip; 1 MPa = 0.145 ksi; 1 Nmm = 0.00885 lbf-in.)*

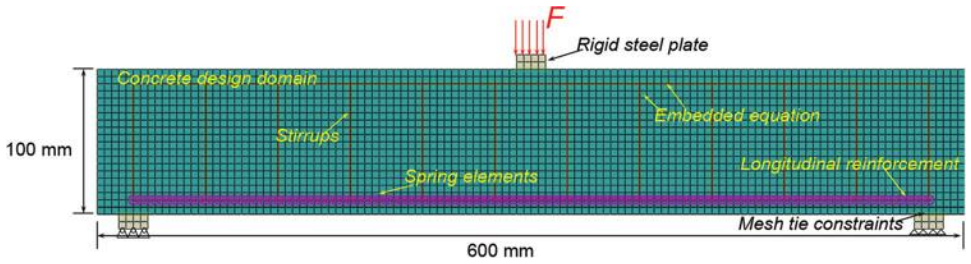

Fig. 7—Schematic diagram of optimization model for uncorroded RC beams. (Note: 1 mm = 0.0394 in.)

0.5, 1, and 0.9, respectively. The mechanical properties of concrete and reinforcement are depicted in Tables 1 and 2, respectively.

Figure 8 shows the load paths of RC beam under the different load cases (that is, F = 0.005, 0.05, 0.1, 0.15, 0.2, 0.25, and 0.3 kN [0.00113, 0.0113, 0.0225, 0.0338, 0.045, 0.056, and 0.0675 kip]). The load path under the smallest load F = 0.005 kN (0.00113 kip) in Fig. 8(b) is similar to the elastic solution in Fig. 8(a). When the applied load F increases to 0.05 kN (0.0113 kip), the load path in Fig. 8(c) starts to change. The load paths of the RC beam extend directly from the loading point to the support point. The tensile concrete member in the elastic solution disappears due to the different strengths in tension and compression of concrete.

With the further increase of the applied load, the end of load paths near the support point gradually moves to the midspan of RC beam, as shown in Fig. 8(c) to (f). Simultaneously, the width and inclination angle β of the inclination compression strut increase with the applied load. The internal force extends directly from the loading point to the middle of the shear span, and then is further transferred to the support point due to the bond behavior. The effective bond region increases with the applied load to balance the bottom tensile forces of beam.

When the applied load approaches the ultimate load, the load paths in Fig. 8(g) to (h) have distinct differences from that in Fig. 8(c) to (f) due to the shear action. Two compressive inclination compression struts are almost parallel to reflect the shear action in the shear span. The load paths can reasonably describe the force transmission mechanism of uncorroded RC beam.

Load paths of CRC beams—Figure 9 shows the load paths under the corrosion levels η_l from 0 to 20% for CRC beams subjected to F = 0.1 kN (0.0225 kip). The load paths of CRC beams change with the increase of corrosion levels. It is indicated that corrosion damage can accelerate the transition of load paths from the non-limit state to the limit state. The variation of load paths with various corrosion levels is consistent with that under the different applied forces. This phenomenon can be attributed that the ultimate bearing capacity of CRC beam decreases with the increase of corrosion levels. The applied load F = 0.1 kN (0.0225 kip) will gradually become the ultimate load of CRC beams with the increase of corrosion levels.

Discussion

Figure 10 shows the load paths of CRC beams under different bond strengths. The corrosion levels of 0, 1.5, 3, 5, 10, 15, and 20% are adopted to investigate the effects of bond degradation on the load paths of CRC beams. The

Table 1—Details of mechanical properties for concrete

Parameter	Elastic modulus E_c, MPa	Poisson's ratio v_c	Compressive strength f_{cm}, MPa	Ultimate strain ε_{cu}	Slip S_1, mm
Value	32,000	0.2	40	0.0033	1

Note: 1 mm = 0.0394 in.; 1 MPa = 0.145 ksi.

Table 2—Details of mechanical properties for reinforcement

Parameter	Elastic modulus E_s, GPa	Poisson's ratio v_s	Bar diameter D_l, mm	Yield strength f_{py}, MPa	Ultimate strength f_{pu}, MPa
Value	190	0.3	24	400	580

Note: 1 mm = 0.0394 in.; 1 MPa = 0.145 ksi.

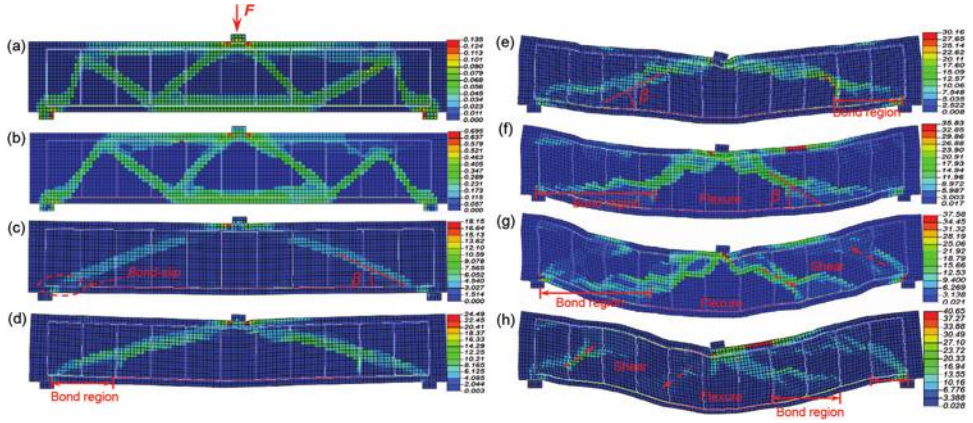

Fig. 8—Optimized topologies of uncorroded RC beams under different load cases: (a) elastic solution; (b) F *= 0.005 kN; (c)* F *= 0.05 kN; (d)* F *= 0.1 kN; (e)* F *= 0.15 kN; (f)* F *= 0.2 kN; (g)* F *= 0.25 kN; and (h)* F *= 0.3 kN. (Note: 1 kN = 0.225 kip.)*

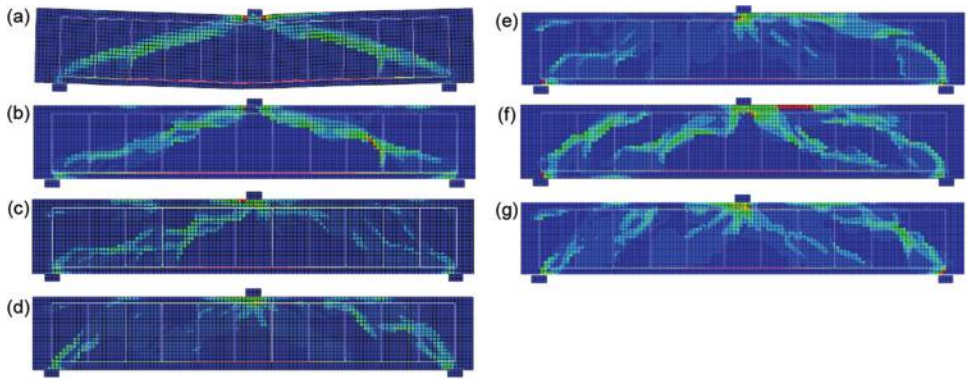

Fig. 9—Load paths with various corrosion levels for CRC beams under F *= 0.1 kN: (a) η_1 = 0%; (b) η_1 = 1.5%; (c) η_1 = 3%; (d) η_1 = 5%; (e) η_1 = 10%; (f) η_1 = 15%; and (g) η_1 = 20%. (Note: 1 kN = 0.225 kip.)*

corresponding bond strengths of CRC beams can be determined based on Eq. (13). The load paths of CRC beams change with bond degradation. The load paths under the initial load F = 0.2 kN (0.045 kip) are gradually transformed to that under the ultimate load due to the bond degradation. This is because that the bond degradation decreases the ultimate bearing capacity of CRC beam.

Figure 11 shows the load paths of CRC beams under different tensile strengths of corroded reinforcement. The same corrosion levels (that is, 0, 1.5, 3, 5, 10, 15, and 20%) are used to investigate the effects of tensile strengths of corroded reinforcement on the load paths of CRC beams. The corresponding tensile strengths of corroded reinforcement can be determined based on Eq. (11) and (12). The load paths under different tensile strengths of corroded reinforcement are almost same except for the last load path. This is because the CRC beams have not reached the limit state under the tensile strength loss of corroded reinforcement. It is indicated that the load paths are more sensitive to the bond degradation than the tensile strength loss of corroded reinforcement under the same corrosion level.

As mentioned previously, the proposed method can reasonably generate the load paths of CRC beams and effectively overcome the numerical instability. In the proposed method, the increasing stiffness of minimum-density elements can still affect the nonlinear response of the remodeled structures. Although the nonlinear response of the remodeled structure approximates to that of the original structure, there are still some errors between them. The errors are difficult to be quantified by an index. The previously mentioned numerical examples indicated that the proposed method could obtain meaningful solutions.

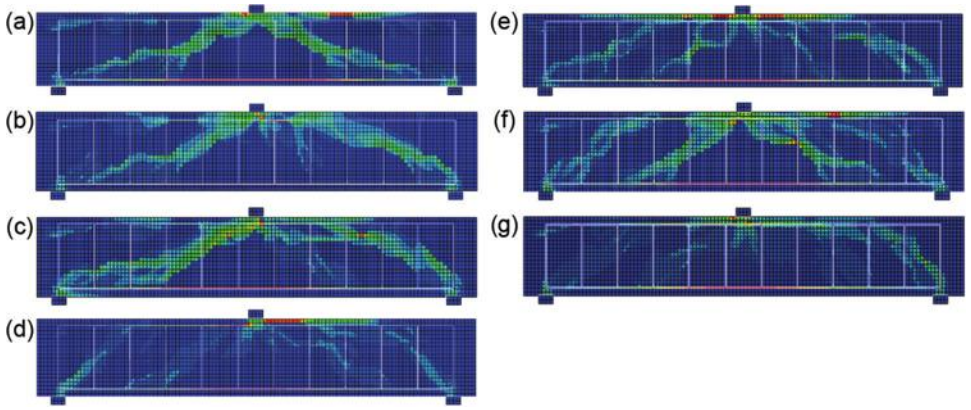

Fig. 10—Load paths of CRC beams under different bond strengths: (a) $\tau_{a,\eta}$ = 4.85 MPa; (b) $\tau_{a,\eta}$ = 3.95 MPa; (c) $\tau_{a,\eta}$ = 3.88 MPa; (d) $\tau_{a,\eta}$ = 3.82 MPa; (e) $\tau_{a,\eta}$ = 3.76 MPa; (f) $\tau_{a,\eta}$ = 3.71 MPa; and (g) $\tau_{a,\eta}$ = 3.68 MPa. (Note: 1 MPa = 0.145 ksi.)

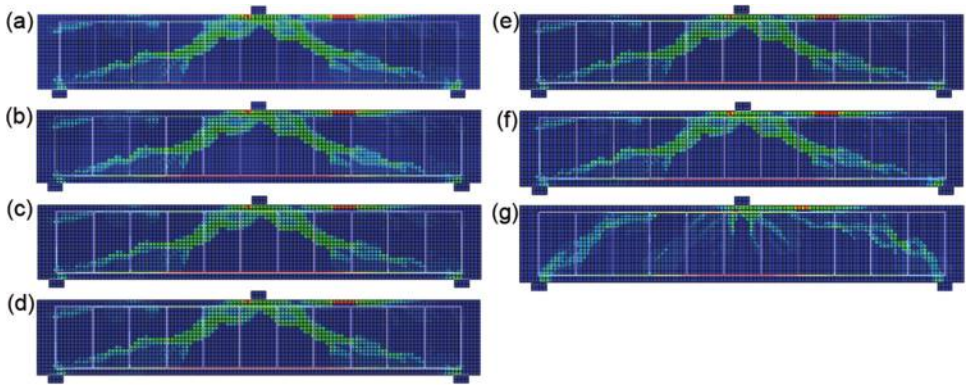

Fig. 11—Load paths of CRC beams under different tensile strengths of corroded reinforcement: (a) $f_{ly,\eta}$ = 400 MPa; (b) $f_{ly,\eta}$ = 392.8 MPa; (c) $f_{ly,\eta}$ = 385.6 MPa; (d) $f_{ly,\eta}$ = 376 MPa; (e) $f_{ly,\eta}$ = 352 MPa; (f) $f_{ly,\eta}$ = 328 MPa; and (g) $f_{ly,\eta}$ = 304 MPa. (Note: 1 MPa = 0.145 ksi.)

Topology optimization method requires high computational resources, especially for the large scale and fine numerical model of CRC structures. Hundreds of expensive optimization iterations and nonlinear FEA are required during the NTO process of CRC structures. In the traditional topology optimization methods, the small-scale problems and simplified numerical model are usually considered to save the computational resources. Therefore, some reasonable simplifications and assumptions on the numerical models of CRC beams are used in this study to improve the computational efficiency. The proposed method is not only helpful for the structural designers to understand the force transfer mechanism, but also provides a valuable design tool to find the appropriate strut-and-tie models for aiding structural design and repair.

CONCLUSIONS

A generation method of load paths for corroded reinforced concrete (CRC) beams is proposed by considering material properties loss and bond degradation. An automatic stiffness adjustment technique is presented to overcome the numerical instability during the generation of load path of CRC beams. The effectiveness of the proposed method is illustrated by the numerical examples. The effects of the tensile strength loss and bond degradation of corroded reinforcement on the load paths are discussed, respectively. The conclusions are as follows:

- The proposed method can reasonably generate the load paths of CRC beams. The load paths of reinforced concrete (RC) beams change with the increase of applied forces and corrosion levels, respectively. Corrosion damage accelerates the transition of load paths from the non-limit state to the limit state of CRC beams.
- The proposed stiffness adjustment technique is simple but effective to overcome the numerical instability caused by the excessive distortion of minimum-density elements. The errors caused by the increased stiffness can also be effectively alleviated based on the proposed technique.
- The load paths of CRC beams change with the tensile strength loss and bond degradation of corroded reinforcement, respectively. The load paths are more sensitive to the bond degradation than the tensile strength loss of corroded reinforcement under the same corrosion level.

AUTHOR BIOS

Ping Yuan *is a Postdoctoral Researcher in the College of Civil and Transportation Engineering at Shenzhen University, Shenzhen, China. He received his PhD from the School of Civil Engineering at Changsha University of Science and Technology, Changsha, China. His research interests include durability evaluation and topology optimization of concrete structures.*

Lei Wang *is the corresponding author and a Professor in the School of Civil Engineering at Changsha University of Science and Technology, where he received his BSc, MSc, and PhD. His research interests include reliability and durability evaluation of bridge engineering, maintenance, and strengthening of service bridges.*

ACI member **Royce W. Floyd** *is an Assistant Professor at the University of Oklahoma, Norman, OK. He received his PhD from the University of Arkansas, Fayetteville, AR. He is a member of ACI Committees 213, Lightweight Aggregate and Concrete, and 363, High-Strength Concrete. His research interests include concrete materials, mixture proportioning, and prestressed concrete.*

ACKNOWLEDGMENTS

This study is supported by the key field research plan project (Grant No. 2021YFB2600900), the Hunan province key field research plan project (Grant No. 2019SK2171), and Open Fund of Key Laboratory of Mechanical Behavior and Intelligent Control of Advanced Engineering Materials and Structures at Universities of Hunan Province (Grant No. 18KA04). The authors are grateful for the support.

NOTATION

A_l = sectional area of uncorroded reinforcement
$A_{s,\eta}$, A_s = sectional areas of corroded and uncorroded stirrups, respectively
B = strain-displacement matrix
b_w = width of uncorroded RC beam
C_cA_s = depth of concrete cover
$C(\tilde{x},U_{\eta l})$ = objective function
D_c = elastoplastic constitutive matrix
D_e = elastic constitutive matrix
D_l = diameter of longitudinal reinforcement
E_{min} = elastic modulus of weakly-elastic material
E_{min}^k, E_{min}^{k+1} = elastic modulus of minimum-density elements in k and k+1 optimization step, respectively
E_{min}^0 = initial elastic modulus
E_n = elastic modulus of elastic material in cantilever beam
ER = evolutionary ratio
Er^k = convergence error
f_{cm} = compressive strength of uncorroded concrete
f_{cm}' = compressive strength of corrosion-damaged concrete
$f_{co,\eta l}$, f_{we}, $f_{cr,\eta l}$ = internal load of concrete, weakly elastic material, and corroded reinforcement, respectively
f_{ct} = tensile strength of concrete
f_{ext} = external force vector
$f_{int}(\tilde{x},U_{\eta l})$ = internal load vector
$f_{lu,\eta}$, f_{lu} = ultimate strength for corroded and uncorroded reinforcement, respectively
$f_{ly,\eta}$, f_{ly} = yield strength for corroded and uncorroded reinforcement, respectively
$f_{sy,\eta}$, f_{sy} = yield strength for uncorroded and uncorroded stirrups, respectively
$f(x)$ = sigmoid function
$K_{t,\eta l}$ = tangent stiffness matrix of CRC beam
k_c = stiffness matrix of concrete element
k_e = stiffness matrix of weakly elastic material
k_r = empirical coefficient
k_{sp} = stiffness of spring elements
l_r = length of concrete element
m_l = mass of uncorroded reinforcement
N = optimization step
n = total number of concrete elements in design domain
n_{bs} = number of steel bars under compression
$o(\delta U_{\eta l}^{m+1})$ = higher-order infinitesimal
P = penalty factor
$R(\tilde{x},U_{\eta l})$ = residual force vector of CRC beams
r_{ij} = distance between centers of elements i and j
r_l = radius of longitudinal reinforcement
r_{min} = filter radius
S_1 = slip at maximum bond stress
s = stirrup spacing
$U_{\eta l}$ = displacement vector under corrosion levels η_l
u_{rs} = volumetric expansion rate
V^k, V^{k+1} = target volume in k and k+1 optimization step, respectively
V^* = target volume fraction
v_{co} = volume of concrete element
v_e = Poisson's ratio of weakly elastic material
v_i = volume of i-th element
v_n = Poisson's ratio of elastic material in cantilever beam
w = weight function for averaging raw sensitivities
$w_{co,\eta l}$, w_{we} = strain energy of concrete and weakly elastic elements, respectively
w_{cr} = total crack width of CRC beam
$w_{i,\eta l}$ = strain energy of i-th element
w_i^e, w_i^p = elastic and plastic strain energy of i-th element, respectively
X = corrosion depth
$\tilde{x}$ = element density vector
$\tilde{x}_i$ = density variable of i-th element
$\tilde{x}_m$ = minimum density
α_1, α_2, α_3, α_4 = coefficients to control growth rate of element stiffness
α_y, α_u = empirical coefficients
$\dot{\alpha}_{th}$ = sensitivity threshold
β = inclination angle of inclination compression strut
$\Delta A_{l,\eta}$ = loss of sectional area of corroded reinforcement
$\Delta m_{l,\eta}$ = mass loss of corroded reinforcement
ε^* = strain threshold of minimum-density elements
ε_{cu} = maximal compressive strain of concrete
ε_{max}^k = maximal strain of minimum-density elements
ε_1 = average tensile strain of cracked concrete
η_j = weight factor
η_l = corrosion level of longitudinal reinforcement
η_s = corrosion levels of corroded stirrups
$\tau_{a,\eta}$ = bond strength of corroded reinforcement
λ, ζ, k = empirical coefficient
λ_o = small constant
ϵ = allowable convergence error

REFERENCES

1. Soltani, M.; Safiey, A.; and Brennan, A., "A State-of-the-Art Review of Bending and Shear Behaviors of Corrosion-Damaged Reinforced Concrete Beams," *ACI Structural Journal*, V. 116, No. 3, May 2019, pp. 55-64. doi: 10.14359/51706919

2. Wang, L.; Ma, Y.; Ding, W.; Zhang, J.; and Liu, Y., "Comparative Study of Flexural Behavior of Corroded Beams With Different Types of Steel Bars," *Journal of Performance of Constructed Facilities*, ASCE, V. 29, No. 6, 2015, pp. 26-37. doi: 10.1061/(ASCE)CF.1943-5509.0000661

3. Zhang, X.; Wang, L.; Zhang, J.; and Liu, Y., "Model for Flexural Strength Calculation of Corroded RC Beams Considering Bond-Slip Behavior," *Journal of Engineering Mechanics*, ASCE, V. 142, No. 7, 2016, p. 04016038. doi: 10.1061/(ASCE)EM.1943-7889.0001079

4. Ye, Z.; Zhang, W.; and Gu, X., "Deterioration of Shear Behavior of Corroded Reinforced Concrete Beams," *Engineering Structures*, V. 168, Aug. 2018, pp. 708-720. doi: 10.1016/j.engstruct.2018.05.023

5. Yang, Y.; Liu, Z.; Tang, H.; and Peng, J., "Deflection-Based Failure Probability Analysis of Low Shrinkage-Creep Concrete Structures in Presence of Non-Stationary Evolution of Shrinkage and Creep Uncertainties," *Construction and Building Materials*, V. 376, May 2023, p. 131077.

6. Bruggi, M., "A Numerical Method to Generate Optimal Load Paths in Plain and Reinforced Concrete Structures," *Computers & Structures*, V. 170, No. 2016, pp. 26-36.

7. Bogomolny, M., and Amir, O., "Conceptual Design of Reinforced Concrete Structures Using Topology Optimization With Elastoplastic Material Modeling," *International Journal for Numerical Methods in Engineering*, V. 90, No. 13, 2012, pp. 1578-1597. doi: 10.1002/nme.4253

8. Bruggi, M., "Generating Strut-and-Tie Patterns for Reinforced Concrete Structures Using Topology Optimization," *Computers & Structures*, V. 87, No. 23-24, 2009, pp. 1483-1495. doi: 10.1016/j.compstruc.2009.06.003

9. Luo, Y., and Kang, Z., "Layout Design of Reinforced Concrete Structures Using Two-Material Topology Optimization With Drucker-Prager Yield Constraints," *Structural and Multidisciplinary Optimization*, V. 47, No. 1, 2013, pp. 95-110. doi: 10.1007/s00158-012-0809-1

10. Leu, L.-J.; Huang, C.-W.; Chen, C.-S.; and Liao, Y.-P., "Strut-and-Tie Design Methodology for Three-Dimensional Reinforced Concrete Structures," *Journal of Structural Engineering*, ASCE, V. 132, No. 6, 2006, pp. 929-938. doi: 10.1061/(ASCE)0733-9445(2006)132:6(929)

11. Liang, Q.; Xie, Y.; and Steven, G. P., "Topology Optimization of Strut-and-Tie Models in Reinforced Concrete Structures Using an Evolutionary Procedure," *ACI Structural Journal*, V. 97, No. 2, Mar.-Apr. 2000, pp. 322-332.

12. Amir, O., "A Topology Optimization Procedure for Reinforced Concrete Structures," *Computers & Structures*, V. 114-115, Jan. 2013, pp. 46-58. doi: 10.1016/j.compstruc.2012.10.011

13. Bendsøe, M. P., "Optimal Shape Design as a Material Distribution Problem," *Structural and Multidisciplinary Optimization*, V. 1, No. 4, 1989, pp. 193-202. doi: 10.1007/BF01650949

14. Zhou, M., and Rozvany, G. I. N., "The COC Algorithm, Part II: Topological, Geometrical and Generalized Shape Optimization," *Computer Methods in Applied Mechanics and Engineering*, V. 89, No. 1-3, 1991, pp. 309-336. doi: 10.1016/0045-7825(91)90046-9

15. Xie, Y., and Steven, G. P., "A Simple Evolutionary Procedure for Structural Optimization," *Computers & Structures*, V. 49, No. 5, 1993, pp. 885-896. doi: 10.1016/0045-7949(93)90035-C

16. Chen, Q.; Zhang, X.; and Zhu, B., "A 213-Line Topology Optimization Code for Geometrically Nonlinear Structures," *Structural and Multidisciplinary Optimization*, V. 59, No. 5, 2019, pp. 1863-1879. doi: 10.1007/s00158-018-2138-5

17. Luo, Y.; Wang, M.; and Kang, Z., "Topology Optimization of Geometrically Nonlinear Structures Based on an Additive Hyperelasticity Technique," *Computer Methods in Applied Mechanics and Engineering*, V. 286, Dec. 2015, pp. 422-441. doi: 10.1016/j.cma.2014.12.023

18. Bruns, T. E., and Tortorelli, D. A., "An Element Removal and Reintroduction Strategy for the Topology Optimization of Structures and Compliant Mechanisms," *International Journal for Numerical Methods in Engineering*, V. 57, No. 10, 2003, pp. 1413-1430. doi: 10.1002/nme.783

19. Buhl, T.; Pedersen, C. B.; and Sigmund, O., "Stiffness Design of Geometrically Nonlinear Structures Using Topology Optimization," *Structural and Multidisciplinary Optimization*, V. 19, No. 2, 2000, pp. 93-104. doi: 10.1007/s001580050089

20. Pedersen, C. B. W.; Buhl, T.; and Sigmund, O., "Topology Synthesis of Large-Displacement Compliant Mechanisms," *International Journal for Numerical Methods in Engineering*, V. 50, No. 12, 2001, pp. 2683-2705. doi: 10.1002/nme.148

21. Sigmund, O., "Design of Multiphysics Actuators Using Topology Optimization-Part I: One-Material Structures," *Computer Methods in Applied Mechanics and Engineering*, V. 190, No. 49-50, 2001, pp. 6577-6604. doi: 10.1016/S0045-7825(01)00251-1

22. Wang, F.; Lazarov, B. S.; Sigmund, O.; and Jensen, J. S., "Interpolation Scheme for Fictitious Domain Techniques and Topology Optimization of Finite Strain Elastic Problems," *Computer Methods in Applied Mechanics and Engineering*, V. 276, July 2014, pp. 453-472. doi: 10.1016/j.cma.2014.03.021

23. Yoon, G. H., and Kim, Y. Y., "Element Connectivity Parameterization for Topology Optimization of Geometrically Nonlinear Structures," *International Journal of Solids and Structures*, V. 42, No. 7, 2005, pp. 1983-2009. doi: 10.1016/j.ijsolstr.2004.09.005

24. Yang, X.; Xie, Y.; Steven, G. P.; and Querin, O. M., "Bidirectional Evolutionary Method for Stiffness Optimization," *AIAA Journal*, V. 37, No. 11, 1999, pp. 1483-1488. doi: 10.2514/2.626

25. Huang, X., and Xie, Y., "Convergent and Mesh-Independent Solutions for the Bi-Directional Evolutionary Structural Optimization Method," *Finite Elements in Analysis and Design*, V. 43, No. 14, 2007, pp. 1039-1049. doi: 10.1016/j.finel.2007.06.006

26. ABAQUS, Abaqus Analysis User's Manual, Version 6.9. Dassault Systèmes. 2010.

27. Kmiecik, P., and Kamiński, M., "Modelling of Reinforced Concrete Structures and Composite Structures With Concrete Strength Degradation Taken Into Consideration," *Archives of Civil and Mechanical Engineering*, V. 11, No. 3, 2011, pp. 623-636. doi: 10.1016/S1644-9665(12)60105-8

28. Recupero, A.; Spinella, N.; and Tondolo, F., "Failure Analysis of Corroded RC Beams Subjected to Shear-Flexural Actions," *Engineering Failure Analysis*, V. 93, November, 2018, pp. 26-37. doi: 10.1016/j.engfailanal.2018.06.025

29. Coronelli, D., and Gambarova, P., "Structural Assessment of Corroded Reinforced Concrete Beams: Modeling Guidelines," *Journal of Structural Engineering*, ASCE, V. 130, No. 8, 2004, pp. 1214-1224. doi: 10.1061/(ASCE)0733-9445(2004)130:8(1214)

30. Molina, F. J.; Alonso, C.; and Andrade, C., "Cover Cracking as a Function of Rebar Corrosion: Part 2-Numerical Model," *Materials and Structures*, V. 26, No. 9, 1993, pp. 532-548. doi: 10.1007/BF02472864

31. Dekoster, M.; Buyle-Bodin, F.; Maurel, O.; and Delmas, Y., "Modelling of the Flexural Behaviour of RC Beams Subjected to Localised and Uniform Corrosion," *Engineering Structures*, V. 25, No. 10, 2003, pp. 1333-1341. doi: 10.1016/S0141-0296(03)00108-1

32. Chen, H., and Nepal, J., "Analytical Model for Residual Bond Strength of Corroded Reinforcement in Concrete Structures," *Journal of Engineering Mechanics*, ASCE, V. 142, No. 2, 2016, p. 04015079. doi: 10.1061/(ASCE)EM.1943-7889.0000997

33. Cairns, J.; Plizzari, G. A.; Du, Y.; Law, D. W.; and Franzoni, C., "Mechanical Properties of Corrosion-Damaged Reinforcement," *ACI Materials Journal*, V. 102, No. 4, July-Aug. 2005, pp. 256-264.

34. Wang, L.; Yi, J.; Zhang, J.; Floyd, R. W.; and Ma, Y., "Bond Behavior of Corroded Strand in Pretensioned Prestressed Concrete Beams," *ACI Structural Journal*, V. 115, No. 6, Nov. 2018, pp. 1803-1812. doi: 10.14359/51706892

35. Campione, G.; Cannella, F.; and Cavaleri, L., "Shear and Flexural Strength Prediction of Corroded RC Beams," *Construction and Building Materials*, V. 149, Sept. 2017, pp. 395-405. doi: 10.1016/j.conbuildmat.2017.05.125

36. Rodriguez, J.; Ortega, L.; and Garcia, A., "Corrosion of Reinforcing Bars and Service Life of RC Structures: Corrosion and Bond Deterioration," *Concrete Across Borders, Odense, Denmark*, V. 2, 1994, pp.315-26.

37. ACI Committee 318, "Building Code Requirements for Structural Concrete (ACI 318-11) and Commentary (ACI 318R-11)," American Concrete Institute, Farmington Hills, MI, 2011, 503 pp.

38. Zhang, W.; Zhou, B.; Gu, X.; and Dai, H., "Probability Distribution Model for Cross-Sectional Area of Corroded Reinforcing Steel Bars," *Journal of Materials in Civil Engineering*, ASCE, V. 26, No. 5, 2014, pp. 822-832. doi: 10.1061/(ASCE)MT.1943-5533.0000888

39. Khalaf, J., and Huang, Z., "Analysis of the Bond Behaviour Between Prestressed Strands and Concrete In Fire," *Construction and Building Materials*, V. 128, Oct. 2016, pp. 12-23. doi: 10.1016/j.conbuildmat.2016.10.016

40. Huang, X., and Xie, Y., "Bidirectional Evolutionary Topology Optimization for Structures with Geometrical and Material Nonlinearities," *AIAA Journal*, V. 45, No. 1, 2007, pp. 308-313. doi: 10.2514/1.25046

41. Huang, X., and Xie, Y., "Bi-Directional Evolutionary Topology Optimization of Continuum Structures With One or Multiple Materials," *Computational Mechanics*, V. 43, No. 3, 2009, pp. 393-401. doi: 10.1007/s00466-008-0312-0

ACI STRUCTURAL JOURNAL TECHNICAL PAPER

Title No. 120-S69

Generation of Optimal Load Paths for Corroded Reinforced Concrete Beams Part II: Multi-Angle Truss Model

by Lei Wang, Ping Yuan, and Royce W. Floyd

A multi-angle truss model is proposed based on the optimal load paths of corroded reinforced concrete (CRC) beams. The load paths of CRC beams at the ultimate limit state, considering various corrosion levels, shear span-depth ratios, stirrup ratios, and loading methods are first studied. The load paths incorporating multiple variable-inclination struts can realistically describe the force-transfer mechanisms of CRC beams under flexure-shear interaction. The limiting failure criteria of the proposed truss model are then presented to estimate the shear capacity of CRC beams. Finally, the proposed model is verified by comparing with the experimental results of uncorroded and corroded reinforced concrete (RC) beams. Results show that the proposed model can reasonably predict the shear capacity and failure mode of CRC beams. For CRC beams at the ultimate limit state, corrosion damage has a negligible influence on the trajectory of load paths. The load paths change with the increase of the shear span-depth ratios of CRC beams.

Keywords: corroded reinforced concrete (CRC) beams; multi-angle truss model; multiple variable-inclination struts; optimal load paths; shear capacity.

INTRODUCTION

Truss models[1-3] have been widely used to describe the trajectory of internal forces of reinforced concrete (RC) beams. The internal forces in the truss models are transmitted by the inclined compression struts and tension ties. The configurations of truss models and the inclination angles of compression struts are two key factors to estimate the structural shear capacity. These two factors, which are related to various factors including corrosion levels, concrete strength, reinforcement ratios, and shear span-depth ratios (l_s/h_0), are very complicated for corroded reinforced concrete (CRC) beams.

Numerous truss models with a single inclination strut have been proposed to predict the shear capacity of RC beams. The original 45-degree truss models[4,5] are conservative because the inclination angle of the concrete stress field is a fixed 45 degrees.[6,7] In the variable-angle truss models,[8,9] the inclination angle is limited to 21.8 degrees $\leq \beta \leq$ 45 degrees. The Modified Compression Field Theory[10-12] was then proposed to predict the variable inclination angle through the deformation compatibility conditions. In addition, Eurocode 2[13] adopted the lower-bound theorem of plasticity[14] to determine the inclination angle. However, these truss models contain only a single inclination strut, which is difficult to describe the actual trajectory of internal forces for RC beams subjected to shear-flexure interaction.

Some studies attempted to describe the concrete stress fields using the truss models incorporating multiple compression struts. Wang et al.[15] proposed a multi-angle truss model, where the configuration of this truss model relates to the diagonal crack angles. DeDomenico and Ricciardi[16] adopted two variable inclination struts to improve the Eurocode 2 truss model. An optimized truss model with various struts[17] was derived from the minimum total strain energy theorem. A statically indeterminate truss model[18] was established by considering concrete contribution. However, the configurations of these truss models were developed based on some hypotheses, which are different from the actual load paths of CRC beams.

Many experimental investigations[19-21] have been conducted to study the shear capacity of CRC beams. Several analytical methods,[22,23] considering the influence of corrosion damage on the reliability of CRC beams under shear failure, were presented. Finite element analysis[24,25] was also employed to predict the shear capacity. These methods are complicated and are not suitable for a fast evaluation of the shear capacity. Some theoretical models on evaluating the shear capacity of CRC beams[26-29] were established based on the truss models in shear codes. However, these models incorporating a single strut are empirical, which can limit their prediction accuracy and applicability. Beyond that, the evaluation of shear capacity for CRC beams is limited and further study is necessary to aid structural design and repair.

This paper aims to propose a multi-angle truss model of CRC beams based on the optimal load paths. The remaining context is arranged as follows: first, the optimal load paths of CRC beams are studied and then are transformed into the corresponding truss models. Then, the limiting failure criteria of the proposed truss model are presented. Finally, the proposed model is verified by comparing the predicted shear capacity with the experimental results of uncorroded and corroded RC beams.

RESEARCH SIGNIFICANCE

Numerous truss models have been presented to predict the shear capacity of RC beams. However, it is still difficult to determine the configuration of truss models of CRC beams due to their complex stress state. The material property loss and bond degradation induced by corrosion can change the load paths and affect the configurations of truss models for CRC beams. This study proposes a multi-angle truss model of CRC beams based on the optimal load paths. The

ACI Structural Journal, V. 120, No. 4, July 2023.

MS No. S-2022-097.R1, doi: 10.14359/51738751, received October 22, 2022, and reviewed under Institute publication policies.

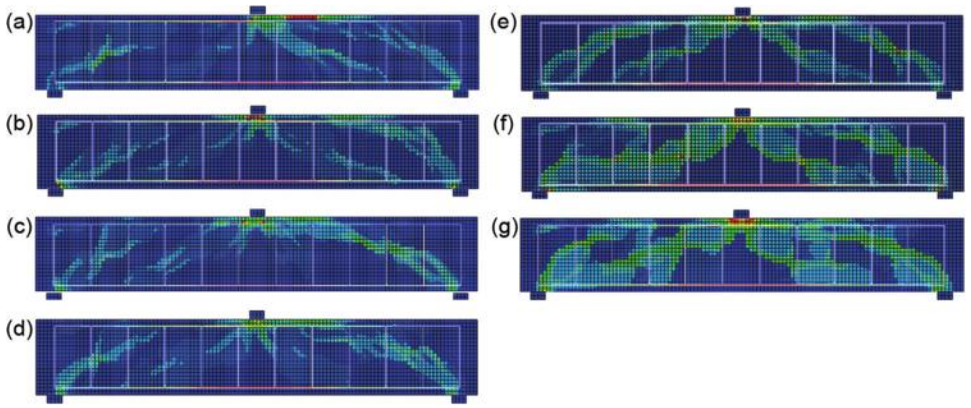

Fig. 1—Load paths with various corrosion levels for CRC beams at ultimate limit state: (a) η = 0%; (b) η = 1.5%; (c) η = 3%; (d) η = 5%; (e) η = 10%; (f) η = 15%; and (g) η = 20%.

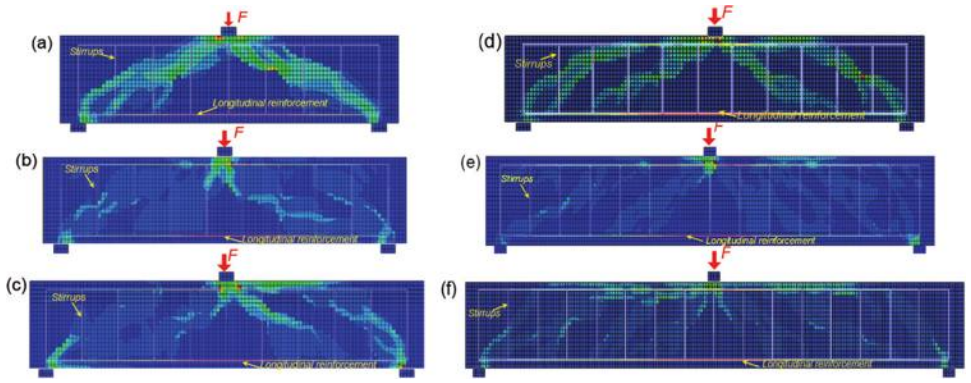

Fig. 2—Optimal load paths of CRC beams with different l_s/h_0*: (a)* $l_s/h_0 = 2.22$*; (b)* $l_s/h_0 = 2.5$*; (c)* $l_s/h_0 = 2.78$*; (d)* $l_s/h_0 = 3.05$*; (e)* $l_s/h_0 = 3.89$*; and (f)* $l_s/h_0 = 4.44$*.*

proposed method is helpful to accurately evaluate the shear capacity of CRC beams.

MULTI-ANGLE TRUSS MODEL BASED ON OPTIMAL LOAD PATHS

In this section, a multi-angle truss model of CRC beams is proposed based on the optimal load paths. The optimal load paths of CRC beams at the ultimate limit state, considering various corrosion levels, l_s/h_0, stirrup ratios, and loading methods, are studied based on the proposed method in the first part. Three types of truss models incorporating multiple variable-inclination struts are developed based on the load paths of CRC beams.

Optimal load path of CRC beams

The CRC beam described in the first part is further employed to study the influence of corrosion damage on the trajectory of load paths. In this section, the CRC beams are subjected to the ultimate load F = 0.3 kN (0.0675 kip). It is assumed that the transverse and longitudinal reinforcements are subjected to uniform corrosion.

Figure 1 shows the load paths with various corrosion levels for CRC beams at the ultimate limit state. The trajectory of load paths for CRC beams under various corrosion levels are almost consistent. The width of compression strut increases with the corrosion levels. This is because the sectional area of corroded reinforcement decreases with the increase of corrosion levels. The corroded reinforcement is actually simulated by the uncorroded reinforcement with a smaller diameter. In this case, it is equivalent to reducing the reinforcement ratio, so the applied load carried by the corroded reinforcement will be reduced. The applied load transferred to the compression strut increases, leading to an increase in the compression strut width. It is indicated that corrosion damage has little influence on the trajectory of load paths for CRC beams at the ultimate limit state. Therefore, a random corrosion level η = 10% is chosen to further study the effects of l_s/h_0, stirrup ratios, and loading methods on the trajectory of load paths of CRC beams. The corrosion levels of the stirrup η_s and longitudinal reinforcement η_l are equal to 10%.

Figure 2 presents the optimal load paths of CRC beams with various l_s/h_0. Figure 2(a) shows the load path of the CRC beam with l_s/h_0 = 2.22, which consists of inclined compression struts and bottom steel ties. No tensile concrete member is found in the bottom load path in Fig. 2(a). The external force is transmitted directly from the loading point to the support point through the inclined concrete blocks. The bottom tensile force of CRC beams is carried by the longitudinal reinforcement. The load path with l_s/h_0 = 2.22 is consistent with the configuration of the classical strut-and-tie model (STM). When the l_s/h_0 increases to 2.5, the load paths of CRC beam change, as depicted in Fig. 2(b). It is indicated

that the load paths for CRC deep beams ($1 \le l_s/h_0 < 2.5$) are consistent with the configuration of the classical STM.

Figures 2(b) through (e) show the similar load paths for slender CRC beams with $2.5 \le l_s/h_0 \le 4$. The load paths of slender beams consist of the inclined and vaulted compression struts as well as the transverse and longitudinal reinforcement. The load paths of slender beams are different from those of deep beams due to the increased l_s/h_0. Figure 2(f) shows the optimal load path of the CRC beam with l_s/h_0 = 4.44. The trajectory of the load path is similar with that of the CRC beam ($2.5 \le l_s/h_0 \le 4$), except for the number of inclination struts. The number of inclination struts in the load paths increases with the increase of the l_s/h_0. The multiple inclination struts and the vaulted struts are more consistent with the actual concrete stress field of the CRC beam under flexure-shear interaction.

The load paths can reasonably describe the shear-transfer mechanisms of slender beams, which are also corroborated by the typical crack patterns, as depicted in Fig. 3. The critical diagonal crack divides the RC beam into a large vaulted concrete block and a number of inclined concrete blocks.

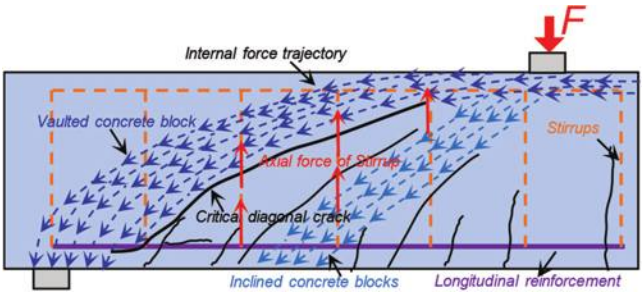

Fig. 3—Typical crack patterns of slender beams under shear failure.

The transverse stirrups are responsible for holding together the vaulted and inclined concrete blocks. A portion of the external force is directly transmitted from the loading point to the support point through the vaulted concrete block. Another part of external force is transferred to the bottom reinforcement by the inclined concrete blocks, and then is further transferred to the large vaulted block through the transverse stirrups. The force-transfer mechanisms based on the crack patterns are consistent with that of the load paths for CRC beams.

Figure 4 shows the optimal load paths of CRC beams with different stirrup ratios and loading methods. Figures 4(a) through (c) show that the stirrup ratio has a negligible effect on the trajectory of load paths. However, the stirrup ratios can affect the width of concrete struts within the load paths. This is because the reduction of stirrup ratios of the CRC beam will lead to the decrease in the applied load carried by the transverse stirrup. The other part of the applied load requires a wider compression strut to bear. Figure 4(d) shows that the trajectory of the load path of the CRC beam subjected to the symmetrical two-point load is consistent with that under the single concentrated load. That is because the length of the shear span is the same under the different loading methods. The load paths of the CRC beam with various l_s/h_0 can describe the concrete stress field with imprecise direction.

Multi-angle truss model with multi-inclination struts

As discussed previously, the load path of the CRC deep beam is consistent with the configuration of the classical STM. This load path can be explicitly transformed into the corresponding truss model I, as depicted in Fig. 5. The concrete strut $\overline{KL}$ and the inclination stirrup are inclined by angles β_1 and θ to the longitudinal axis, respectively.

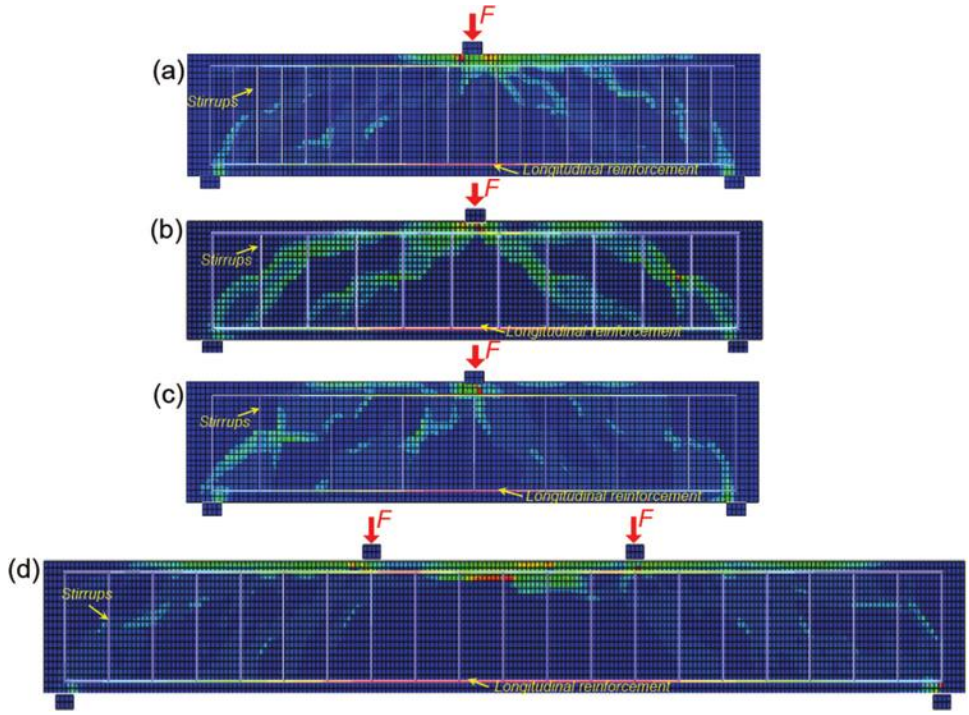

Fig. 4—Optimal load paths of RC beams with different stirrup ratios and loading methods: (a) Φ8@25mm; (b) Φ8@50mm; (c) Φ8@75mm; and (d) symmetrical two-point load. (Note: Units in mm; 1 mm = 0.0394 in.)

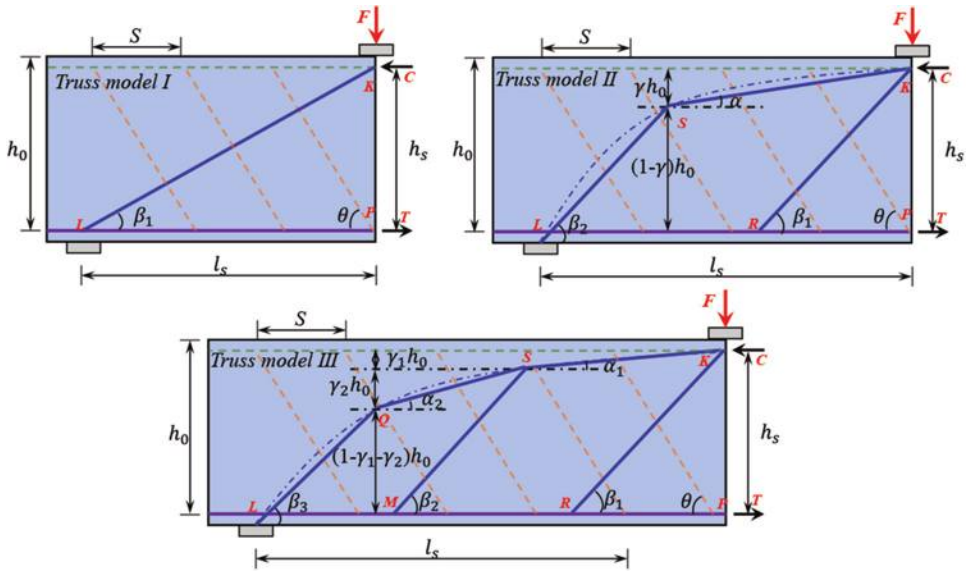

Fig. 5—Three types of truss models of CRC beams with various l_s/h_0: (a) truss model I; (b) truss model II; and (c) truss model III.

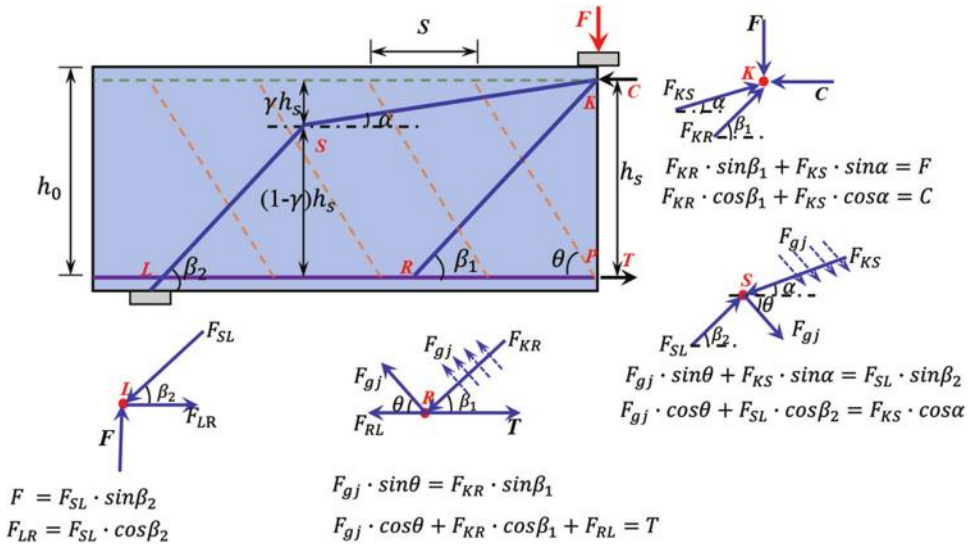

Fig. 6—Mechanical analysis of each member in truss model II.

For the CRC slender beams with $2.5 \le l_s/h_0 \le 4$, the directions of concrete stress field in the vaulted struts vary gradually along the beam height. Two inclination struts are introduced to describe the variability of the stress direction of the vaulted struts, as depicted in Fig. 5(b). The load paths of the CRC beam with $2.5 \le l_s/h_0 \le 4$ can be transformed into the truss model II. The inclination angles of the concrete struts $\overline{KS}$, $\overline{KR}$, and $\overline{SL}$ are α, β_1, and β_2, respectively. The transition depths between the two inclination struts are controlled by a parameter γ.

For the CRC slender beams with $4 \le l_s/h_0 \le 5$, as depicted in Fig. 5(c), three inclination struts are introduced into the truss model III to reflect the concrete stress fields of the vaulted struts. The inclination angles of the concrete struts $\overline{KS}$, $\overline{SQ}$, $\overline{KR}$, $\overline{SM}$, and $\overline{SL}$ are inclined by the angles α_1, α_1, β_1, β_2, and β_3 to the longitudinal axis, respectively. The parameters γ_1 and γ_2 control the transition depths between two inclination struts.

SHEAR CAPACITY EVALUATION OF MULTI-ANGLE TRUSS MODEL

In this section, the limiting failure criteria of the multi-angle truss model are proposed to evaluate the shear capacity of CRC beams. The proposed model gives the criteria to determine the dimension and inclination angles of inclination concrete struts. The analytical expressions of the shear capacity are presented based on the equilibrium conditions and the static analysis.

Failure of individual truss model members

For any given external load, the stress state of each member in the proposed model can be determined based on the equilibrium conditions and the static analysis. On the contrary, if one member in the truss model fails first, the corresponding bearing capacity can be determined. According to the lower-bound theorem, the ultimate bearing capacity is related to the ultimate strength of the weakest member. Generally, there are four types of failure modes, including the crushing failure of concrete struts, the yield

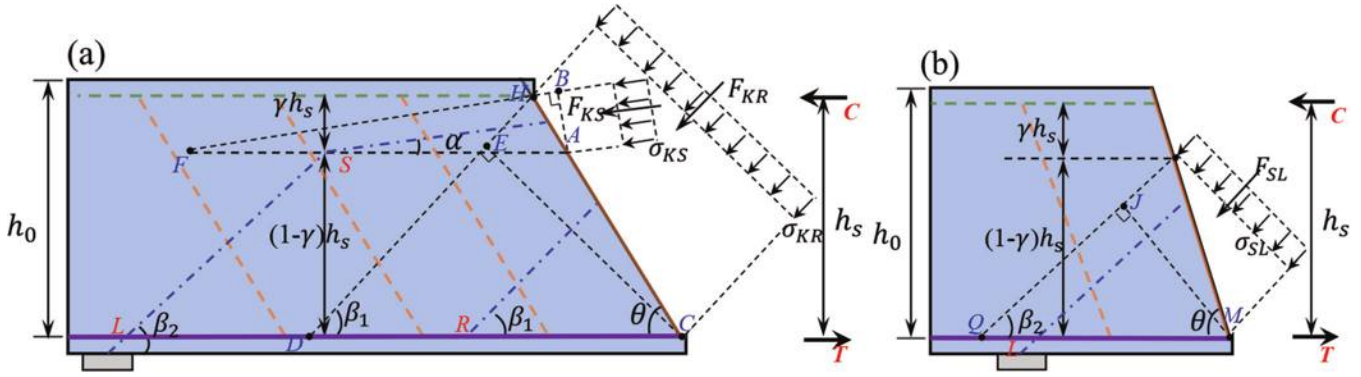

Fig. 7—Concrete compression stress field with different beam segments in truss model II.

failure of transverse and longitudinal reinforcement, as well as bond failure. The truss model II is taken as the representative to predict shear capacity and failure modes of CRC beams, as shown in Fig. 6.

Crushing failure of concrete struts—Two different beam segments parallel to the diagonal stirrups are taken and analyzed to determine the compressive forces of concrete struts, as shown in Fig. 7. The resultants of the concrete struts can be expressed as

$$F_{KR} = \sigma_{KR} b_w \overline{EC} = \sigma_{KR} b_{wef} [h_s \cdot \sin\beta 1 \cdot (\cot\beta_1 + \cot\theta)] \text{ (kN)} \quad (1)$$

$$F_{KS} = \sigma_{KS} b_w \overline{AB} = \sigma_{KS} b_{wef} [\gamma h_s \cdot \sin\alpha \cdot (\cot\alpha + \cot\theta)] \text{ (kN)} \quad (2)$$

$$F_{SL} = \sigma_{SL} b_w \overline{MJ} = \sigma_{SL} b_{wef} [(1-\gamma) h_s \cdot \sin\beta_2 \cdot (\cot\beta_2 + \cot\theta)] \text{ (kN)} \quad (3)$$

where F_{KR}, F_{KS}, and F_{SL} are the resultants of the concrete struts $\overline{KR}$, $\overline{KS}$, and $\overline{SL}$, respectively; $\overline{EC}$, $\overline{AB}$, and $\overline{MJ}$ are the dimensions of the sectional width of concrete struts (refer to Fig. 7); $h_s h_0$ is the inner lever arm that can be set as $0.9h_0$; h_0 is the effective depth of RC beams; b_w is the width of uncorroded RC beam; θ is the inclination angle between inclination stirrups and longitudinal axis; γ is the control parameter of the transition depths between two inclination struts; b_{wef} is the effective width of RC beams under stirrups corrosion; α, β_1, and β_2 are the inclination angles of the concrete struts; and σ_{KR}, σ_{KS}, and σ_{SL} are the uniform stresses of the concrete struts $\overline{KR}$, $\overline{KS}$, and $\overline{SL}$, respectively. In the limit condition, the uniform stress of concrete struts is equal to the allowable stress, $\sigma_{a,st}$, which can be expressed as

$$\sigma_{a,st} = v_c f_{cm} \text{ (MPa)} \quad (4)$$

where $\sigma_{a,st}$ is the allowable stress of concrete struts; v_c is the strength reduction factor for cracked concrete, which can be taken as $v_c = 0.6\left(1 - \frac{f_{cm}}{250}\right)$[13,30]; and f_{cm} is the compressive strength of uncorroded concrete.

Stirrups corrosion will cause the spalling of concrete cover, which will decrease the effective width of CRC beams for resisting shear force. The effective width of CRC beams under stirrups corrosion can be given as[31]

$$b_{wef} = \begin{cases} b_w - 2(C_c + D_s) + \frac{s}{5.5} & s \le 5.5(C_c + D_s) \\ b_w - \frac{5.5}{s(C_c + D_s)^2} & s > 5.5(C_c + D_s) \end{cases} \text{ (mm)} \quad (5)$$

where D_s is the diameter of diagonal stirrups; C_c is the depth of concrete cover; and s is the stirrups spacing.

Stirrups corrosion has little influence on the effective width of CRC beams when the crack width does not exceed the critical crack width w_{cc}.[31] Otherwise, it is assumed that the concrete cover has been spalled without the shear resistance. The crack width caused by stirrups corrosion can be calculated as[32]

$$w_c = k_{cr}(\Delta_{as,\eta} - \Delta A_{so}) \text{ (mm)} \quad (6)$$

where w_c is the crack width; k_{cr} is the parameter for crack width, which can be taken as 0.0575; $\Delta_{as,\eta}$ is the loss of sectional area of corroded stirrups; and ΔA_{so} is the loss of sectional area at cracking initiation, which can be expressed as[32]

$$\Delta A_{so} = A_s \left[1 - \left(1 - \frac{\alpha_p}{d_s}\left(7.53 + 9.32\frac{C_c}{d_s}\right)10^{-3}\right)^2\right] \text{ (mm}^2\text{)} \quad (7)$$

where A_s is the sectional area of uncorroded stirrups; α_p is the pit penetration factor, which can be taken as 2 for uniform corrosion[33]; and w_{cc} is the critical crack width, which can be taken as 0.1 mm (0.039 in.).[31]

Assuming that the concrete struts $\overline{KR}$, $\overline{KS}$, and $\overline{SL}$ fail, the corresponding bearing capacity $F_{U,KR}$, $F_{U,KS}$, and $F_{U,SL}$ of the truss model II can be calculated based on the static analysis (refer to Fig. 6).

$$F_{U,KR} = F_{KR}\frac{(1 + \cot\theta \cdot \tan\alpha)\sin\beta_1}{1 - \cot\beta_2 \tan\alpha} \text{ (kN)} \quad (8)$$

$$F_{U,KS} = F_{KS}\frac{\cos\alpha(1 + \tan\alpha \cdot \cot\theta)}{\cot\theta + \cot\beta_2} \text{ (kN)} \quad (9)$$

$$F_{U,SL} = F_{SL}\sin\beta_2 \text{ (kN)} \quad (10)$$

where $F_{U,KR}$, $F_{U,KS}$, and $F_{U,SL}$ are the corresponding bearing capacity when the concrete struts $\overline{KR}$, $\overline{KS}$, and $\overline{SL}$ fail.

Yield failure of corroded stirrups—The tensile forces of diagonal stirrups can be calculated as

$$F_{gj} = \sigma_{ds} A_{s,\eta} N_{cs} \text{ (kN)} \tag{11}$$

where σ_{ds} and F_{gj} are the tensile stress and resultant force of corroded stirrups, respectively; $A_{s,\eta}$ is the sectional area of corroded stirrups; and N_{cs} is the number of stirrups crossing concrete struts. In the limit condition, the tensile stress of the corroded stirrup, σ_{ds}, is equal to the yield strength of corroded stirrup $f_{sy,\eta}$. The number of stirrups crossing concrete struts can be expressed as

$$N_{KR} = \frac{h_0(\cot\beta_1 + \cot\theta)}{s} \tag{12}$$

$$N_{KS} = \frac{\gamma h_0(\cot\alpha + \cot\theta)}{s} \tag{13}$$

$$N_{SL} = \frac{(1-\gamma) h_0(\cot\beta_2 + \cot\theta)}{s} \tag{14}$$

where N_{KR}, N_{KS}, and N_{SL} are the number of stirrups crossing the concrete struts $\overline{KR}$, $\overline{KS}$, and $\overline{SL}$, respectively. When the diagonal stirrups fail, the ultimate bearing capacity $F_{U,gj}$ can be expressed as

$$F_{U,gj} = F_{gj} \frac{\sin\theta(1 + \tan\alpha \cdot \cot\theta)}{1 - \tan\alpha \cdot \cot\beta_2} \text{ (kN)} \tag{15}$$

where $F_{U,gj}$ is the bearing capacity corresponding to the yield failure of corroded stirrups.

Bond behavior between corroded stirrups and concrete is slightly enhanced before the concrete cover cracks. With the further increase of corrosion levels, the concrete cover cracks and the bond behavior deteriorates.[31] Bond deterioration between corroded stirrups and concrete leads to a slight reduction in shear resistance, and ignoring bond deterioration is acceptable.[31,34] Therefore, the effects of the bond deterioration caused by stirrups corrosion on the shear resistance are ignored for predicting the shear capacity.

Yield and bond failure of corroded reinforcement—In the limit condition, the tensile stress of the bottom tensile chord is provided by the bond stress or the tensile force of corroded longitudinal reinforcement. If the bond stress is sufficient, the corroded longitudinal reinforcement can reach its ultimate strength. If the bond stress is insufficient, the corroded reinforcement cannot develop its full tensile capacity and the limited bond force should be applied to calculate the bearing capacity. Bond stress is assumed to uniformly distribute along the transfer length of corroded longitudinal reinforcement. The effective bond forces of corroded reinforcement are estimated as

$$F_{eb} = \pi D_l l_{eb} \tau_{a,\eta} \text{ (kN)} \tag{16}$$

where F_{eb} is the effective bond force; $\tau_{a,\eta}$ is the average bond stress of corroded longitudinal reinforcement; D_l is the diameter of longitudinal reinforcement; and l_{eb} is the effective bond length, which can be expressed as[6]

$$l_{eb} = 0.48 \frac{f_{ly,\eta}}{\sqrt{f_{cm}}} D_l \text{ (mm)} \tag{17}$$

where $f_{ly,\eta}$ is the yield strength of corroded longitudinal reinforcement. The tensile forces of corroded longitudinal reinforcement can be expressed as

$$F_{RP} = A_{l,\eta} f_{ly,\eta} \text{ (kN)} \tag{18}$$

where F_{RP} is the tensile force of corroded longitudinal reinforcement; and $A_{l,\eta}$ is the sectional area of corroded longitudinal reinforcement. The maximum tensile forces of the bottom tensile chord, $F_{b,tie}$, can be estimated as

$$F_{b,tie} = F_{eb} \ (F_{eb} \le F_{RP}) \text{ (kN)} \tag{19}$$

$$F_{b,tie} = F_{RP} \ (F_{eb} > F_{RP}) \text{ (kN)} \tag{20}$$

where $F_{b,tie}$ is the maximum tensile forces of the bottom tensile chord.

When the tensile chord $\overline{RP}$ fails, the bearing capacity $F_{U,RP}$ of the truss model II can be expressed as

$$F_{U,RP} = F_{b,tie} \frac{1 + \tan\alpha \cdot \cot\theta}{\cot\theta + \cot\beta_1 - \cot\beta_2 \cdot \tan\alpha \cdot \cot\beta_1 + \cot\beta_2} \text{ (kN)} \tag{21}$$

where $F_{U,RP}$ is the bearing capacity corresponding to the yield or bond failure of corroded longitudinal reinforcement.

According to the lower-bound theorem, the ultimate bearing capacity of the truss model II is the minimum value of these bearing capacities. The ultimate bearing capacity $F_{p,uc}$ can be expressed as

$$F_{p,uc} = \min[F_{U,KR}, F_{U,KS}, F_{U,SL}, F_{U,gj}, F_{U,RP}] \text{ (kN)} \tag{22}$$

where $F_{p,uc}$ is the ultimate bearing capacity of the truss model II. The truss models I and III follow the same theoretical principles.

Determination of multi-inclination angles

The inclination angles of concrete struts α and β are crucial to estimate the structural shear capacity. For the CRC deep beams ($1 \le l_s/h_0 < 2.5$), the inclination angle β_1 can be determined by the geometric relationship between the shear span l_s and the inner lever arm h_s (that is, $\cot\beta_1 = l_s/h_s$). The inclination angle β_1 in the truss model I meets the requirements of Eurocode 2, which recommends that the inclination angle β_1 ranges from 21.8 to 45 degrees.

The truss model II includes three compression struts for CRC slender beams. An improved Eurocode 2 truss model[16] incorporating two variable-inclination compression struts is proposed to predict the shear capacity of RC beams with stirrups. In this model, the upper compression strut has lower inclination than the lower compression strut. The analytical

Table 1—Analytical expressions of inclination angles

w_w limitations	$\cot\beta_1$	$\cot\alpha$
$0 \le w_w \le 0.0716$	$(\cot\beta_1)_{max} = 2.5$	$(\cot\alpha)_{max} = 5$
$0.0716 \le w_w \le 0.1136$	$\cot\beta_1 = \dfrac{5 + \sqrt{25 + 104w_w - 2704w_w^2}}{52w_w}$	$(\cot\alpha)_{max} = 5$
$0.1136 \le w_w \le 0.25$	$\cot\beta_1 = \dfrac{\eta(w_w)}{2\sqrt{2}w_w}$	$\cot\alpha = \dfrac{4w_w\sqrt{1+8w_w} + \sqrt{2}\eta(w_w)}{1 + 4w_w - k(w_w)}$
$0.25 \le w_w \le 0.5$	$\cot\beta_1 = \sqrt{\dfrac{1-w_w}{w_w}}$	$\cot\alpha = \sqrt{\dfrac{1-w_w}{w_w}}$
$0.5 < w_w$	$\cot\beta_1 = 1$	$\cot\alpha = 1$

Note: $k(w_w) = \sqrt{1 + 8w_w - 16w_w^2 - 128w_w^3}$; $\eta(w_w) = \sqrt{1 + 4w_w - 8w_w^2 - k(w_w)}$.

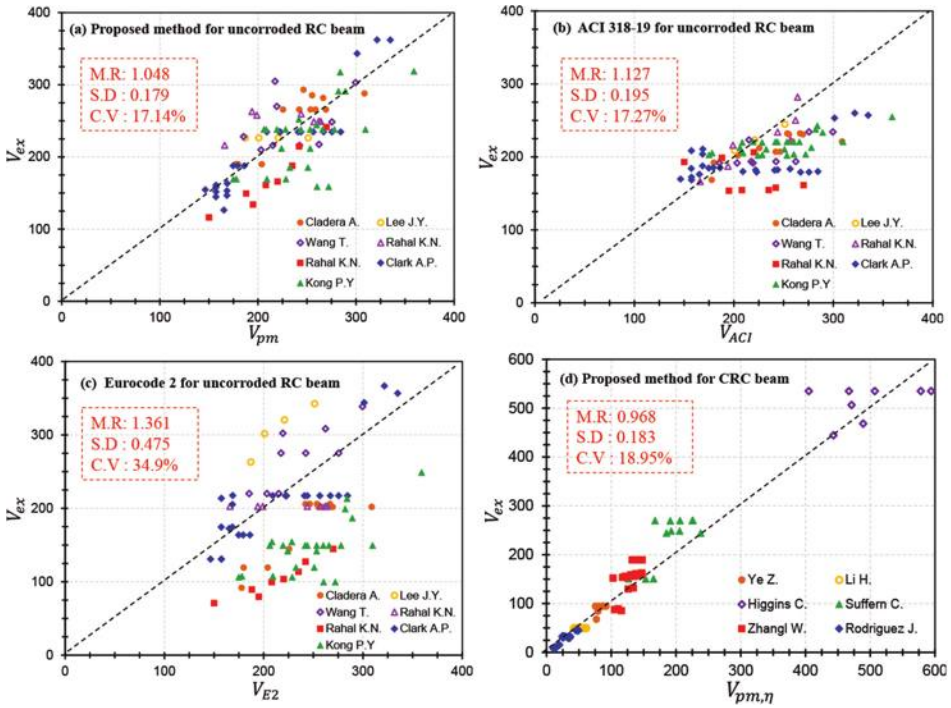

Fig. 8—Comparison of experimental versus predicted shear capacity for uncorroded and corroded RC beams: (a) proposed model for uncorroded RC beams; (b) ACI 318-19 for uncorroded RC beams; (c) Eurocode 2 for uncorroded RC beams; and (d) proposed model for CRC beams.

expressions of inclination angles in the improved Eurocode 2 truss model are derived based on the plasticity theory and equilibrium conditions. The multi-inclination angles are determined based on the assumption that the yield of steel stirrups and crushing of concrete struts are achieved simultaneously. The analytical expressions of inclination angles in the improved Eurocode 2 truss model[16] are employed to predict the inclination angles α_1 and β_1 in the truss model II. The inclination angles relate to the mechanical ratio of stirrups w_w, which can be expressed as

$$w_w = \rho_s \frac{f_{sy}}{v_c f_{cm}} \tag{23}$$

where w_w is the mechanical ratio of stirrups; $\rho_s = A_s/(sb_w\sin\theta)$ is the stirrup ratio; and f_{sy} is the yield strength of uncorroded stirrups. Table 1 shows the analytical expressions of the inclination angles α and β_1. The parameter γ is assumed to be equal to 0.5.[16]

The inclination angle β_2 is assumed to be equal to the angle of the critical diagonal crack of slender beams,[2,34,35] which is closely related to the l_s/h_0 of RC beams. The inclination angle β_2 can be expressed as

$$\beta_2 = -15l_s/h_0 + 89.7 \quad l_s/h_0 \le 3.14 \tag{24}$$

$$\beta_2 = 42.6 \quad l_s/h_0 > 3.14 \tag{25}$$

The truss model III includes five compression struts. To simplify the shear capacity evaluation, the inclination angles α_2 and β_1 can be determined based on the analytical expressions of inclination angles in the improved EC-2 truss model. The inclination angles α_1 and β_2 are assumed to be

Table 2—Significant parameters and corresponding results of uncorroded RC beams

References	Series	No. of beams	ρ_s, %	ρ_l, %	l_s/h_0	Truss model	Inclination angles			FM_{ex}	FM_p	V_{aex}/V_{apm}	SD	CV, %
							α	β_1	β_2					
Lee et al.[36]	S20	4	0.3	2.7	2.5	II	11.31 to 17.13	39.99 to 41.79	52.2	*SF*	*CF*	0.951	0.123	13
Cladera and Mari[37]	H50	3	0.11 to 0.23	2.24	3.08	II	11.31	21.80	43.5	*SF*	*JF*/*EF*/*BF*	0.951	0.075	7.9
	H60	3	0.24 to 0.25	2.24	3.08	II	11.31	21.80	43.5	*SF*	*JF*/*EF*/*BF*			
	H75	3	0.24 to 0.25	2.24	3.08	II	11.31	21.80	43.5	*SF*	*JF*/*EF*/*BF*			
	H100	3	0.24 to 0.25	2.24	3.08	II	11.31	21.80	43.5	*SF*	*JF*/*EF*/*BF*			
Rahal[38]	S1-4	7	0.16 to 0.28	1.89 to 3.15	3	II	11.31	21.80 to 31.04	44.7	*SF*	*JF*/*CF*/*BF*	0.909	0.146	16
Wang et al.[15]	B1,4,5	3	0.25 to 0.38	2.06 to 2.32	1.75	I	—	27.01	—	*SF*	*JF*	0.970	0.164	16.9
	B2,6,7	3	0.25 to 0.38	2.06 to 2.72	2.25	I	—	21.69	—	*SF*	*JF*/*EF*			
	B3,8,9	3	0.25 to 0.38	2.32 to 2.72	2.60	II	11.31 to 14.98	21.8 to 41.15	50.7	*SF*	*CF*/*EF*			
Rahal and Al-Shaleh[39]	A65	3	0.2 to 0.29	2.2	2.8	II	11.31	21.80	44.7	*SF*	*JF*	1.265	0.108	8.5
	B65	5	0.14 to 0.25	4.0	2.8	II	11.31	21.80	44.7	*SF*	*JF*			
Clark[40]	A1	4	0.38	0.31	2.34	I	—	21.05	—	*SF*	*JF*	1.028	0.111	10.8
	B1	5	0.37	0.31	1.95	I	—	24.79	—	*SF*	*JF*			
	B2	3	0.73	0.31	1.95	I	—	24.79	—	*SF*	*CF*/*JF*			
	D1	3	0.46	0.34	1.93	I	—	24.92	—	*SF*	*JF*			
	D2	3	0.61	0.34	2.42	I	—	21.60	—	*SF*	*CF*			
	D4	3	0.49	0.34	2.42	I	—	21.60	—	*SF*	*CF*			
	D5	3	0.37	0.34	2.42	I	—	21.60	—	*SF*	*CF*			
41	S1	6	0.157	0.294	2.5	II	11.31	21.80	52.2	*SF*	*JF*	1.128	0.218	19.3
	S2	6	0.10 to 0.26	0.304	2.5	II	11.31	21.80	52.2	*SF*	*JF*			
	S3	4	0.101	0.19 to 0.3	2.49	II	11.31	21.80	52.2	*SF*	*JF*			
	S5	3	0.157	0.294	3.01 to 2.5	II	11.31	21.80	44.55 to 52.2	*SF*	*JF*			
	S8	6	0.105 to 0.224	0.3	2.5	II	11.31	21.80	52.2	*SF*	*JF*			

Note: FM_{ex} is experimental failure modes; FM_p is predicted failure modes; *SF* is shear failure; *EF* is yield failure of longitudinal reinforcement; *JF* is yield failure of stirrups; *BF* is bond failure; *CF* is crushing failure of concrete struts; V_{aex}/V_{apm} is mean ratio of V_{ex}/V_{pm}.

equal to half of the inclination angles α_2 and β_1, respectively. The parameters γ_1 and γ_2 in Fig. 5 are assumed to be equal to 0.25. The inclination angle β_3 can be determined based on Eq. (25).

VERIFICATION AND DISCUSSION

In this section, the proposed model is first verified by comparing the predicted shear capacity with the experimental results of uncorroded RC beams. A comparison of prediction accuracy between the proposed model and the existing shear provisions is then discussed to investigate the effectiveness of the proposed model. The failure modes of RC beams are also verified. Finally, the proposed model is further verified by comparing the experimental and predicted results of CRC beams under stirrups corrosion.

Verification and discussion of shear capacity for uncorroded RC beams

A total of 89 uncorroded RC beams[15,36-41] were collected to verify the validness of the proposed model by comparing it with the experimental results. All the selected specimens with vertical stirrups (θ = 90 degrees) were subjected to

Table 3—Significant parameters and corresponding results of CRC beams

References	Series	No. of beams	η_s, %	ρ_s, %	ρ_l, %	l_s/h_0	Truss models	Inclination angles			FM_{ex}	FM_p	V_{aex}/V_{apm}	SD	CV, %
								α	β_1	β_2					
Zhang et al.[31]	L0-7,16	9	0 to 30	0.179	0.926	2.16	I	—	22.54	—	*FF*/*SF*	*JF*	0.900	0.170	0.189
	L8,9,17	3	20 to 40	0.101	0.926	2.16	I	—	22.54	—	*SF*	*JF*			
	L10,11,18	3	20 to 40	0.280	0.926	2.16	I	—	22.54	—	*FF*/*SF*	*EF*			
	L12-13	2	20 to 30	0.179	0.926	1.63	I	—	28.96	—	*SF*	*JF*			
	L14-15	2	20 to 30	0.179	0.926	2.71	II	11.31	21.80	49.05	*SF*	*CF*			
	L19-21	3	5 to 20	0.179	0.926	2.16	I	—	22.54	—	*SF*	*JF*			
Li et al.[42]	B0-7	8	0 to 51.42	0.24	2.12	2.42	I	—	21.60	—	*SF*	*JF*	1.012	0.153	0.151
Ye et al.[43]	L1-4LS	5	0 to 20	0.258	1.256	2.22	I	—	22.05	—	*FF*/*SF*	*EF*	0.933	0.106	0.114
	L3LS	2	14 to 16	0.258	1.256	2.22	I	—	22.05	—	*FF*/*SF*	*EF*			
Higgins and Farrow[20]	8RA/D	2	0 to 28.91	0.257	1.21	2.04	I	—	23.72	—	*SF*	*CF*	0.967	0.116	0.120
	10RA/D	4	0 to 25.8	0.206	1.21	2.04	I	—	23.72	—	*SF*	*EF*			
	12RA/D	2	0 to 33.75	0.171	1.21	2.04	I	—	23.72	—	*SF*	*JF*			
Suffern et al.[44]	10M-UR	3	9.87 to 17.2	0.251	2.79	3	II	11.31	21.80	44.7	*SF*	*CF*	0.838	0.134	0.160
	D12-UR	3	7.97 to 16.1	0.317	2.79	3	II	11.31	21.80	44.7	*SF*	*CF*			
	D6-UR	3	1.17 to 4.25	0.079	2.79	3	II	11.31	21.80	44.7	*SF*	*JF*			
	D6-UR-100	3	0.96 to 4.25	0.158	2.79	3	II	11.31	21.80	44.7	*SF*	*CF*			
Rodriguez et al.[45]	11	6	0 to 66	0.111	0.859	4.73	III	11.31 (5.65)	21.8 (10.9)	42.6	*FF*	*EF*	1.092	0.193	0.177
	12	6	0 to 53	0.111	1.843	4.73	III	11.31 (5.65)	21.8 (10.9)	42.6	*SF*	*EF*			
	21	6	0 to 63	0.111	2.178	4.73	III	11.31 (5.65)	21.8 (10.9)	42.6	*SF*	*EF*/*CF*			
	31	6	0 to 63	0.221	1.843	4.73	III	11.31 (5.65)	21.8 (10.9)	42.6	*FF*	*EF*/*CF*			

Note: FM_{ex} is experimental failure modes; FM_p is predicted failure modes; *SF* is shear failure; *FF* is flexural failure; *EF* is yield failure of corroded reinforcement; *JF* is yield failure of corroded stirrups; *BF* is bond failure; *CF* is crushing failure of concrete struts; V_{aex}/V_{apm}= mean ratio of $V_{ex}/V_{pm,\eta}$.

single concentrated load or symmetrical two-point load. The significant parameters, including the number of different types of RC beams, the longitudinal and transverse reinforcement ratios (ρ_l and ρ_s), the shear span-depth ratios l_s/h_0, the inclination angles (α and β), and the truss types are listed in Table 2. For overall comparisons, the mean ratios between experimental and predicted results of the shear capacity (V_{aex}/V_{apm}), the standard deviation (SD), the coefficient of variation (CV), and the failure modes for the different studies are also shown in Table 2.

Figure 8 shows the trend of experimental versus predicted shear capacity for uncorroded and corroded RC beams based on the proposed model, the shear provisions of ACI 318-19,[6] and Eurocode 2,[13] respectively. The majority of the data points in Fig. 8(a) are located close to the diagonal line, which means that the average deviation is small based on the proposed model. The ratios of experimental to predicted shear capacity (V_{ex}/V_{pm}) range from 0.71 to 1.71. The mean ratio of V_{ex}/V_{pm} is 1.048, accompanied by the SD of 0.179 and the CV of 17.14%. The comparison of results provided in Fig. 8(a) and Table 3 show that the proposed model can reasonably predict the shear capacity and failure modes of RC beams.

Most of the data points in Fig. 8(b) are located below the diagonal line. The mean ratio of V_{ex}/V_{pm} is 1.127 based on ACI 318-19, accompanied by the SD of 0.195 and the CV of 17.27%. It is indicated that the shear capacity based on ACI 318-19 is conservative. The data points based on Eurocode 2 are too scattered in Fig. 8(c). Eurocode 2 has a mean ratio equal to 1.361, accompanying the SD of 0.475 and the CV of 34.9%. The shear expressions of ACI 318-19 and Eurocode 2 present different levels of conservatism. This is because

the simple shear expressions are used in the design codes, which are expected to provide conservative estimates of shear capacity.

The proposed model with the lowest mean ratio V_{ex}/V_{pm} and SD is more consistent with the experimental results. The purpose of this comparison is not to demonstrate that the proposed model is more accurate than the codes of ACI 318-19 and Eurocode 2, but to show that the proposed model can predict the shear capacity of uncorroded RC beams with enough accuracy. It is also indicated that the proposed truss model is more in line with the actual load path of RC beams.

Verification of shear capacity of CRC beams

A total of 81 sets of experimental data of RC beams under stirrups corrosion[20,31,42-45] were collected to examine the effectiveness of the proposed model. The experimental specimens are subjected to accelerated corrosion using the electrochemical corrosion method. The transverse stirrups and longitudinal reinforcement in the selected specimens were subjected to uniform corrosion. Most of the longitudinal reinforcements in the test specimens[20,31,42,44] are epoxy coated to keep them free from corrosion. A small part of the longitudinal reinforcements in the test beams[43,45] are subjected to corrosion damage. The corrosion levels of the selected specimens ranged from 0 to 63%. Table 3 shows the significant parameters, failure modes, and shear capacity of CRC beams.

Figure 8(d) shows a good prediction between the predicted and experimental shear capacity of CRC beams. The majority of the data points in Fig. 8(d) are located close to the diagonal line. The ratios $V_{ex}/V_{pm,\eta}$ of CRC beams range from 0.62 to 1.49. The mean ratio $V_{ex}/V_{pm,\eta}$ is 0.968, with the SD of 0.183 and CV of 18.95%. The proposed model can provide an effective and time-saving method to reasonably estimate the shear capacity of uncorroded and corroded RC beams.

CONCLUSIONS

A multi-angle truss model of corroded reinforced concrete (CRC) beams is proposed based on the optimal load paths. The optimal load paths of CRC beams at the ultimate limit state are studied. The load paths incorporate multiple variable-inclination struts that can realistically describe the force-transfer mechanisms. The limiting failure criteria of the proposed model are presented. The proposed model is verified by comparing with the experimental results of uncorroded and corroded reinforced concrete (RC) beams. The conclusions are as follows:

- The proposed model can reasonably predict the failure modes and the shear capacity of CRC beams. The ratios $V_{ex}/V_{pm,\eta}$ range from 0.62 to 1.49. The mean ratio $V_{ex}/V_{pm,\eta}$ is 0.968, associated with the standard deviation (SD) of 0.183 and the coefficient of variation (CV) of 18.95%.
- For CRC beams at the ultimate limit state, corrosion damage has a negligible influence on the trajectory of load paths that are almost consistent under various corrosion levels. The load paths change with the increase of the shear span-depth ratios. The load paths for deep beams are consistent with the classical strut-and-tie model (STM). The load paths for slender beams incorporate multiple variable-inclination struts.
- The proposed model can provide the accurate evaluation of the shear capacity of uncorroded RC beams. The mean ratio of V_{ex}/V_{pm} is 1.048 based on the proposed model, accompanying the SD of 0.179, while ACI 318-19 and Eurocode 2 have a mean ratio of 1.395 and 1.361 with an SD of 0.203 and 0.475, respectively.

AUTHOR BIOS

Lei Wang *is a Professor in the School of Civil Engineering at Changsha University of Science and Technology, Changsha, China, where he received his BSc, MSc, and PhD. His research interests include reliability and durability evaluation of bridge engineering, maintenance, and strengthening of service bridges.*

Ping Yuan *is the corresponding author and a Postdoctoral Researcher in the College of Civil and Transportation Engineering at Shenzhen University, Shenzhen, China. He received his PhD from the School of Civil Engineering at Changsha University of Science and Technology, and conducted this research in the Key Laboratory of Mechanical Behavior and Intelligent Control of Advanced Engineering Materials and Structures. His research interests include durability evaluation and topology optimization of concrete structures.*

Royce W. Floyd *is an Assistant Professor at The University of Oklahoma, Norman, OK. He received his PhD from the University of Arkansas, Fayetteville, AR. He is a member of ACI Committees 213, Lightweight Aggregate and Concrete, and 363, High-Strength Concrete. His research interests include concrete materials, mixture proportioning, and prestressed concrete.*

ACKNOWLEDGMENTS

This study is supported by the key field research plan project (Grant No. 2021YFB2600900), the Hunan province key field research plan project (Grant No. 2019SK2171), and Open Fund of Key Laboratory of Mechanical Behavior and Intelligent Control of Advanced Engineering Materials and Structures at Universities of Hunan Province (Grant No. 18KA04). The authors are grateful for the support.

NOTATION

$A_{l,\eta}$ = sectional area of corroded longitudinal reinforcement
A_s = sectional area of uncorroded stirrups
$A_{s,\eta}$ = sectional area of corroded stirrups
$\Delta A_{s,\eta}$ = loss of sectional area of corroded stirrups
$\Delta A_{s,o}$ = loss of sectional area at cracking initiation
b_w = width of uncorroded RC beam
b_{wef} = effective width of RC beams under stirrups corrosion
C_c = depth of concrete cover
D_l = diameter of longitudinal reinforcement
D_s = diameter of diagonal stirrups
$\underline{EC}$, $\overline{AB}$, $\overline{MJ}$ = dimensions of section width of concrete struts
$F_{b,tie}$ = maximum tensile forces of bottom tensile chord
F_{eb} = effective bond force
F_{gj} = resultant force of corroded stirrups
F_{KR}, F_{KS}, F_{SL} = resultants of concrete struts $\underline{KR}$, $\overline{KS}$, and $\overline{SL}$, respectively
$F_{p,uc}$ = ultimate bearing capacity of truss model II
F_{RP} = tensile force of corroded longitudinal reinforcement
$F_{U,gj}$ = bearing capacity corresponding to yield failure of corroded stirrups
$F_{U,KR}$, $F_{U,KS}$, $F_{U,SL}$ = corresponding bearing capacity when concrete struts $\underline{KR}$, $\overline{KS}$, and $\overline{SL}$ fail, respectively
$F_{U,RP}$ = bearing capacity corresponding to yield or bond failure of corroded longitudinal reinforcement
f_{cm} = compressive strength of uncorroded concrete
$f_{ly,\eta}$ = yield strength of corroded longitudinal reinforcement
$f_{sy,\eta}$, f_{sy} = yield strength of corroded and uncorroded stirrups, respectively
h_0 = effective depth of RC beams
h_s = inner lever arm
k_{cr} = parameter for crack width
l_{eb} = effective bond length
l_s = shear span of RC beams
l_s/h_0 = shear span-depth ratios

N_{cs}	=	number of stirrups crossing concrete struts
N_{KR}, N_{KS}, N_{SL}	=	number of stirrups crossing concrete struts $\overline{KR}$, $\overline{KS}$, and $\overline{SL}$, respectively
s	=	stirrups spacing
v_c	=	strength reduction factor for cracked concrete
w_c	=	crack width of concrete
w_{cc}	=	critical crack width of concrete
w_w	=	mechanical ratio of stirrups
α_1, α_2, β_1, β_2, β_3	=	inclination angles of concrete struts
α_p	=	pit penetration factor
γ, γ_1, γ_2	=	control parameter of transition depths between two inclination struts
η	=	corrosion levels of CRC beams
η_l	=	corrosion levels of longitudinal reinforcement
η_s	=	corrosion levels of stirrups
θ	=	inclination angles between inclination stirrups and longitudinal axis
ρ_s	=	stirrup ratio
$\sigma_{a,st}$	=	allowable stress of concrete struts
σ_{ds}	=	tensile stress of corroded stirrup
σ_{KR}, σ_{KS}, σ_{SL}	=	uniform stress of concrete struts $\overline{KR}$, $\overline{KS}$, and $\overline{SL}$, respectively
$\tau_{a,\eta}$	=	average bond stress of corroded longitudinal reinforcement

REFERENCES

1. He, Z.; Liu, Z.; and John Ma, Z., "Simplified Shear Design of Slender Reinforced Concrete Beams with Stirrups," *Journal of Structural Engineering*, ASCE, V. 142, No. 2, 2016, p. 06015003. doi: 10.1061/(ASCE)ST.1943-541X.0001394

2. Zhang, T.; Visintin, P.; and Oehlers, D. J., "Shear Strength of RC Beams with Steel Stirrups," *Journal of Structural Engineering*, ASCE, V. 142, No. 2, 2016, p. 04015135. doi: 10.1061/(ASCE)ST.1943-541X.0001404

3. Li, B., and Tran, C., "Determination of Inclination of Strut and Shear Strength Using Variable Angle Truss Model for Shear-Critical RC Beams," *Structural Engineering and Mechanics*, V. 41, No. 4, 2012, pp. 459-477. doi: 10.12989/sem.2012.41.4.459

4. Ritter, W., "Die Bauweise Hennebique (Construction Techniques of Hennebique)," *Schweizerische Bauzeitung,* V. 33, No. 7, 1899, pp. 59-66. (in German)

5. Mörsch, E., *Der Eisenbetonbau—Seine Theorie und Anwendung*, Wittwer, Stuttgart, Germany, 1908.

6. ACI Committee 318, "Building Code Requirements for Structural Concrete (ACI 318-19) and Commentary (ACI 318R-19)," American Concrete Institute, Farmington Hills, MI, 2019, 623 pp.

7. ENV 1992-1-1: "Eurocode 2 - Design of Concrete Structures - Part 1-1: General Rules and Rules for Buildings," European Committee for Standardization, Brussels, Belgium, 1991.

8. Bernardo, L.; Andrade, J.; and Lopes, S., "Modified Variable Angle Truss-Model for Torsion in Reinforced Concrete Beams," *Materials and Structures*, V. 45, No. 12, 2012, pp. 1877-1902. doi: 10.1617/s11527-012-9876-4

9. Tran, N. C., and Vu, S. N., "Shear Deformations Based on Variable Angle Truss Model for Concrete Beams Reinforced with FRP Bars," *Structural Engineering and Mechanics*, V. 79, No. 3, 2021, pp. 337-345.

10. Vecchio, F. J., and Collins, M. P., "The Modified Compression-Field Theory for Reinforced Concrete Elements Subjected to Shear," *ACI Structural Journal*, V. 83, No. 2, July-Aug. 1986, pp. 219-231.

11. Collins M. P.; Mitchell, D.; Adebar, P.; and Vecchio, F. J., "A General Shear Design Method," *ACI Structural Journal*, V. 93, No. 1, Jan.-Feb. 1996, pp. 36-45.

12. Bentz, E. C.; Vecchio, F. J.; and Collins, M. P., "Simplified Modified Compression Field Theory for Calculating Shear Strength of Reinforced Concrete Elements," *ACI Materials Journal*, V. 103, No. 4, July-Aug. 2006, pp. 614-624.

13. UNI EN 1992-1-1:2005, "Eurocode 2 - Design of Concrete Structures - Part 1-1: General Rules and Rules for Buildings," European Committee for Standardization, Brussels, Belgium, 2005.

14. Nielsen, M. P., and Hoang, L. C., *Limit Analysis and Concrete Plasticity*, second edition, CRC Press, Boca Raton, FL, 1999.

15. Wang, T.; Dai, J. G.; and Zheng, J. J., "Multi-Angle Truss Model for Predicting the Shear Deformation of RC Beams with Low Span-Effective Depth Ratios," *Engineering Structures*, V. 91, Mar. 2015, pp. 85-95. doi: 10.1016/j.engstruct.2015.02.035

16. De Domenico, D., and Ricciardi, G., "Shear Strength of RC Beams with Stirrups Using an Improved Eurocode 2 Truss Model with Two Variable-Inclination Compression Struts," *Engineering Structures*, V. 198, June 2019, p. 109359. doi: 10.1016/j.engstruct.2019.109359

17. Teo, W., and Hor, Y., "Suitability of Optimized Truss Model to Predict the FRP Contribution to Shear Resistance for Externally Bonded FRP Strengthened RC Beams without Internal Stirrups," *Composites. Part B: Engineering*, V. 80, May 2015, pp. 385-398. doi: 10.1016/j.compositesb.2015.05.004

18. Li, B., and Ngoc Tran, C. T., "Reinforced Concrete Beam Analysis Supplementing Concrete Contribution in Truss Models," *Engineering Structures*, V. 30, No. 11, 2008, pp. 3285-3294. doi: 10.1016/j.engstruct.2008.05.002

19. Zhu, W.; François, R.; Cleland, D.; and Coronelli, D., "Failure Mode Transitions of Corroded Deep Beams Exposed to Marine Environment for Long Period," *Engineering Structures*, V. 96, Apr. 2015, pp. 66-77. doi: 10.1016/j.engstruct.2015.04.004

20. Higgins, C., and Farrow, W. C., "Tests of Reinforced Concrete Beams with Corrosion-Damaged Stirrups," *ACI Materials Journal*, V. 103, No. 1, Jan.-Feb. 2006, pp. 133-141.

21. Xia, J.; Jin, W.; and Li, L., "Shear Performance of Reinforced Concrete Beams with Corroded Stirrups in Chloride Environment," *Corrosion Science*, V. 53, No. 5, 2011, pp. 1794-1805. doi: 10.1016/j.corsci.2011.01.058

22. Bhargava, K.; Mori, Y.; and Ghosh, A. K., "Time-Dependent Reliability of Corrosion-Affected RC Beams—Part 1: Estimation of Time-Dependent Strengths and Associated Variability," *Nuclear Engineering and Design*, V. 241, No. 5, 2011, pp. 1371-1384. doi: 10.1016/j.nucengdes.2011.01.005

23. Val, D. V., "Deterioration of Strength of RC Beams Due to Corrosion and Its Influence on Beam Reliability," *Journal of Structural Engineering*, ASCE, V. 133, No. 9, 2007, pp. 1297-1306. doi: 10.1061/(ASCE)0733-9445(2007)133:9(1297)

24. Potisuk, T.; Higgins, C.; Miller, T. H.; and Yim, S. C., "Finite Element Analysis of Reinforced Concrete Beams with Corrosion Subjected to Shear," *Advances in Civil Engineering*, V. 2011, Mar. 2011, pp. 1-14. doi: 10.1155/2011/706803

25. Coronelli, D., and Gambarova, P., "Structural Assessment of Corroded Reinforced Concrete Beams: Modeling Guidelines," *Journal of Structural Engineering*, ASCE, V. 130, No. 8, 2004, pp. 1214-1224. doi: 10.1061/(ASCE)0733-9445(2004)130:8(1214)

26. Lu, Z.; Li, H.; Li, W.; Zhao, Y. G.; and Dong, W., "An Empirical Model for the Shear Strength of Corroded Reinforced Concrete Beam," *Construction and Building Materials*, V. 188, Sept. 2018, pp. 1234-1248. doi: 10.1016/j.conbuildmat.2018.08.123

27. Alaskar, A.; Alqarni, A. S.; Alfalah, G.; El-Sayed, A. K.; Mohammadhosseini, H.; and Alyousef, R., "Performance Evaluation of Reinforced Concrete Beams with Corroded Web Reinforcement: Experimental and Theoretical Study," *Journal of Building Engineering*, V. 35, Nov. 2021, p. 102038. doi: 10.1016/j.jobe.2020.102038

28. Higgins, C.; Farrow, W. C.; and Turan, O. T., "Analysis of Reinforced Concrete Beams with Corrosion Damaged Stirrups for Shear Capacity," *Structure and Infrastructure Engineering*, V. 8, No. 11, Nov. 2012, pp. 1080-1092.

29. El-Sayed, A. K., "Shear Capacity Assessment of Reinforced Concrete Beams with Corroded Stirrups," *Construction and Building Materials*, V. 134, Dec. 2017, pp. 176-84.

30. Yang, Y.; Liu, Z.; Tang, H.; and Peng, J., "Deflection-Based Failure Probability Analysis of Low Shrinkage-Creep Concrete Structures in Presence of Non-Stationary Evolution of Shrinkage and Creep Uncertainties," *Construction and Building Materials*, V. 376, May 2023, p. 131077.

31. Zhang, W.; Ye, Z.; and Gu, X., "Effects of Stirrup Corrosion on Shear Behaviour of Reinforced Concrete Beams," *Structure and Infrastructure Engineering*, V. 13, No. 8, 2017, pp. 1081-1092. doi: 10.1080/15732479.2016.1243563

32. Vidal, T.; Castel, A.; and François, R., "Analyzing Crack Width to Predict Corrosion in Reinforced Concrete," *Cement and Concrete Research*, V. 34, No. 1, 2004, pp. 165-174. doi: 10.1016/S0008-8846(03)00246-1

33. González, J.; Andrade, C.; Alonso, C.; and Feliu, S., "Comparison of Rates of General Corrosion and Maximum Pitting Penetration on Concrete Embedded Steel Reinforcement," *Cement and Concrete Research*, V. 25, No. 2, 1995, pp. 257-264. doi: 10.1016/0008-8846(95)00006-2

34. Zhang, T.; Oehlers, D.; and Visintin, P., "Shear Strength Of FRP RC Beams And One-Way Slabs Without Stirrups," *Journal of Composites for Construction*, ASCE, V. 18, No. 5, 2014, p. 04014007. doi: 10.1061/(ASCE)CC.1943-5614.0000469

35. Chabib, H. E.; Nehdi, M.; and Said, A., "Predicting the Effect of Stirrups on Shear Strength of Reinforced Normal-Strength Concrete (NSC) and High-Strength Concrete (HSC) Slender Beams Using Artificial Intelligence," *Canadian Journal of Civil Engineering*, V. 33, No. 8, 2006, pp. 933-944. doi: 10.1139/l06-033

36. Lee, J. Y.; Choi, I. J.; and Kim, S. W., "Shear Behavior of Reinforced Concrete Beams with High-Strength Stirrups," *ACI Structural Journal*, V. 108, No. 5, Sept.-Oct. 2011, pp. 620-629.

37. Cladera, A., and Mari, A. R., "Experimental Study on High-Strength Concrete Beams Failing in Shear," *Engineering Structures*, V. 27, No. 10, 2005, pp. 1519-1527. doi: 10.1016/j.engstruct.2005.04.010

38. Rahal, K. N., "Shear Behavior of Reinforced Concrete Beams with Variable Thickness of Concrete Side Cover," *ACI Materials Journal*, V. 103, No. 2, Mar.-Apr. 2006, pp. 171-177.

39. Rahal, K. N., and Al-Shaleh, K. S., "Minimum Transverse Reinforcement in 65 MPa Concrete Beams," *ACI Structural Journal*, V. 101, No. 6, Nov.-Dec. 2004, pp. 872-878.

40. Clark, A. P., "Diagonal Tension in Reinforced Concrete Beams," *ACI Journal Proceedings*, V. 48, No. 10, Oct. 1951, pp. 145-156.

41. Kong, P. Y., "Shear Strength of High Performance Concrete Beams," doctoral dissertation, Curtin University, Perth, Australia, 1996.

42. Li, H.; Wu, J.; and Wang, Z., "Shear Performance of Reinforced Concrete Beams with Corroded Stirrups Strengthened with Carbon Fiber-Reinforced Polymer," *ACI Structural Journal*, V. 113, No. 1, Jan.-Feb. 2016, pp. 51-61. doi: 10.14359/51687913

43. Ye, Z.; Zhang, W.; and Gu, X., "Deterioration of Shear Behavior of Corroded Reinforced Concrete Beams," *Engineering Structures*, V. 168, May 2018, pp. 708-720. doi: 10.1016/j.engstruct.2018.05.023

44. Suffern, C.; El-Sayed, A.; and Soudki, K., "Shear Strength of Disturbed Regions with Corroded Stirrups in Reinforced Concrete Beams," *Canadian Journal of Civil Engineering*, V. 37, No. 8, 2010, pp. 1045-1056. doi: 10.1139/L10-031

45. Rodriguez, J.; Ortega, L.; and Casal, J., "Load Carrying Capacity of Concrete Structures with Corroded Reinforcement," *Construction and Building Materials*, V. 11, No. 4, 1997, pp. 239-248. doi: 10.1016/S0950-0618(97)00043-3

ACI STRUCTURAL JOURNAL TECHNICAL PAPER

Title No. 120-S70

Shear Strength of Extruded, Prestressed Steel Fiber-Reinforced Concrete Hollow-Core Slabs

by Gustavo Parra-Montesinos, Luis B. Fargier-Gabaldón, and Mohamed Al-Tameemi

*ACI 318-19 requires that prestressed concrete hollow-core slabs with depths exceeding 12.5 in. (320 mm) and subjected to a factored shear greater than half the design web-cracking shear strength be provided with at least minimum shear reinforcement. Because the use of bar-type shear reinforcement in hollow-core slabs is generally not possible, this requirement limits the use of these members in shear-critical cases. In this research, the use of hooked steel fibers as a means to increase the shear strength of deep hollow-core slabs was evaluated through 14 tests on extruded hollow-core slabs. Slab thickness was 16 in. (406 mm) and the shear span-effective depth ratio (*a*/*d*) was either 3.0 or 3.5. Two types of hooked steel fibers were evaluated at dosages between 40 and 62 lb/yd^3 (24 and 37 kg/m^3). Type 1 fibers had a single hook at each end and Type 2 fibers had double hooks at each end. The fiber-reinforced concrete slabs exhibited peak shear strengths that ranged between 0.94 and 1.29 times the ACI 318-19 calculated web-cracking shear strength V_{cw}, while the two slabs without fibers failed at shear forces corresponding to 0.93 and 0.87V_{cw}. Besides an increase in shear strength, the presence of fibers, particularly Type 2 fibers, led to a more gradual post-peak strength decay. Failure of the hollow-core slabs without fibers occurred as soon as one web exhibited web-shear cracking. In the hollow-core slabs with fibers, on the other hand, fibers bridging the first web-shear crack prevented this web from experiencing a sudden loss of shear capacity, which allowed the slabs to sustain additional shear until multiple webs had cracked in shear.*

Keywords: extrusion; hooked fibers; precast; shear failure; web cracking.

INTRODUCTION

Precast, prestressed concrete hollow-core slabs are commonly used in residential, office, and industrial construction because of their light weight, rapid construction, and large span-depth ratios. Further, the flat top and bottom surfaces of hollow-core slabs require little or no finishing depending on architectural requirements, which add benefits in terms of construction time and cost.

The manufacturing of precast, prestressed concrete hollow-core slabs is typically performed using either an extrusion or a slipform process. In both cases, nearly zero-slump concrete is used. Further, these manufacturing processes prevent the use of bar-type transverse reinforcement (that is, stirrups). The presence of hollow cores and the impossibility of placing stirrups in hollow-core slabs makes these members susceptible to shear failures, particularly near the supports, where the effective prestressing force has not been fully transferred to the concrete. Moreover, results from past research (Hawkins and Ghosh 2006) indicate that hollow-core slabs with overall thickness greater than or equal to 12.5 in. (320 mm) may fail at shear forces substantially lower than the web-cracking shear strength V_{cw}, calculated according to ACI 318-19 (ACI Committee 318 2019). Based on that research, starting with the 2008 ACI Building Code, transverse reinforcement is required in hollow-core slabs with overall depth greater than 12.5 in. (320 mm) where the factored shear force V_u is greater than $0.5\phi V_{cw}$ (strength reduction factor ϕ is equal to 0.75). Given that the use of bar-type transverse steel is not feasible in most hollow-core slabs, this provision effectively reduces the design web-cracking shear strength by 50% compared to other prestressed concrete members and imposes a severe limitation on the use of hollow-core slabs in shear-critical design scenarios. Similar findings regarding the reduced web-cracking shear strength of deep hollow-core slabs have also been reported in Palmer and Schultz (2011) and Dudnik et al. (2017).

The most common alternative to date to increase the shear strength of hollow-core slabs is by filling the cores with grout or concrete at the ends of the member. While effective, this solution is time-consuming and increases the weight of the member, thereby diminishing one of the major advantages of hollow-core slabs, which is their light weight. This has led to the need for alternative solutions to increase the shear strength of deep hollow-core slabs without affecting their manufacturing process.

An alternative that has been investigated in the past few years to increase the shear strength of prestressed concrete hollow-core slabs is the use of discrete, randomly oriented steel fibers in the concrete mixture (Peaston et al. 1999; Cuenca and Serna 2013; Simasathien and Chao 2015; Dudnik et al. 2017). In general, the use of hooked steel fibers in volume fractions between 0.5 and 1.0% (66 and 132 lb/yd^3 [39 and 78 kgf/m^3]) has led to an increase in shear strength and ductility in hollow-core slabs. To the authors' knowledge, however, the only laboratory study conducted on fiber-reinforced concrete hollow-core slabs with overall depths greater than 12.5 in. (320 mm) was that by Dudnik et al. (2017).

As part of the investigation reported in Dudnik et al. (2017), six tests were conducted on extruded 16 in. (405 mm) deep slabs. Two shear span-effective depth ratios (*a*/*d*) were

ACI Structural Journal, V. 120, No. 4, July 2023.

MS No. S-2022-151.R2, doi: 10.14359/51738770, received December 29, 2022, and reviewed under Institute publication policies.

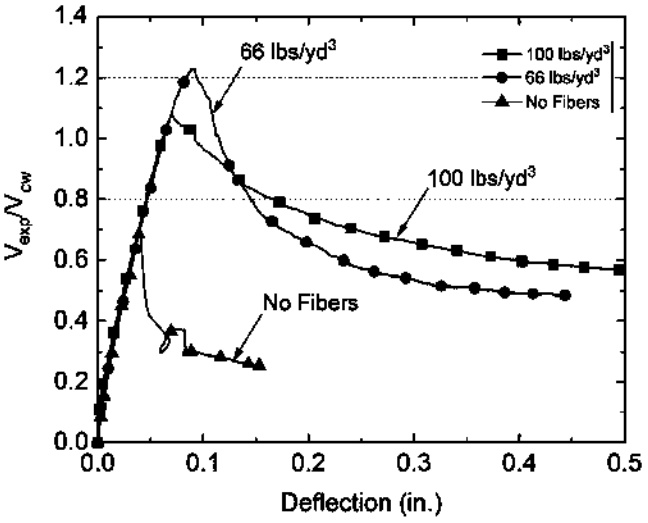

Fig. 1—Load-versus-deflection response for 16 in. (406 mm) deep slabs with a/d *of 3.5 tested by Dudnik et al. (2017). (Note: 1 in. = 25.4 mm; 1 lb/yd³ = 0.591 kgf/m³.)*

evaluated, 3.0 and 3.5. For each *a*/*d*, three shear spans were tested, one without fibers, one with fibers at 66 lb/yd³ (39 kgf/m³) or at a 0.5% fiber volume fraction, and one with fibers at 100 lb/yd³ (59 kgf/m³) or at a 0.76% fiber volume fraction. The steel fibers used had a single hook at each end. The fiber length, diameter, and nominal ultimate strength were, respectively, 1.18 in., 0.022 in., and 160 ksi (30 mm, 0.55 mm, and 1100 MPa). The slabs were simply supported and subjected to a monotonically increased concentrated force.

Figure 1 shows the applied shear, normalized by the calculated web-cracking shear strength according to ACI 318-14 (ACI Committee 318 2014), V_{cw}, versus deflection under the applied load for the tests with *a*/*d* of 3.5. Similar results were obtained for the tests with an *a*/*d* of 3.0. As can be seen, the slab without fibers failed at approximately 70% of the calculated V_{cw}, while the slabs with fibers failed at shear forces greater than V_{cw}. It should be noted that the slab with 66 lb/yd³ (39 kgf/m³) of steel fibers exhibited a greater shear strength than that with steel fibers at 100 lb/yd³ (59 kgf/m³). This was due to difficulties in the mixing of steel fibers for the latter case, which led to some voids at various locations over the shear span.

The substantial increase in shear strength attained through the addition of steel fibers was attributed to the ability of fibers to transfer tension across web diagonal cracks. In the slabs without fibers, diagonal cracking of a single web led to a "zipper" effect, triggering the immediate cracking of the other webs and subsequent failure of the slab. In the case of the slabs with fibers, once one of the webs cracked, the fibers were able to transfer significant tension across the diagonal crack, which allowed the slab to carry additional load. It was only after all webs cracked that a drop in the applied load occurred.

The tests reported in Dudnik et al. (2017) gave clear indication that there is potential for the use of deformed steel fibers to increase the shear strength of deep hollow-core slabs and thus expand their applicability to resist large shear

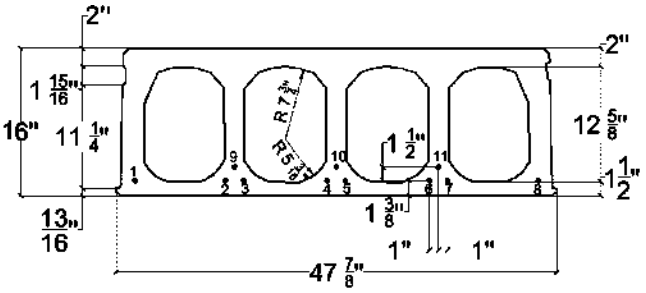

Fig. 2—Cross section for hollow-core slabs tested as part of this investigation. (Note: Strands 1 and 8 had diameter of 0.5 in. [13 mm], while all other strands had diameter of 0.6 in. [15 mm]; 1 in. = 25.4 mm.)

forces. However, only four tests of slabs with steel fibers were conducted, all using the same type of hooked steel fiber. Further, the limited test results indicated that the use of lower fiber dosages may be possible while still leading to an increase in shear strength. Thus, a new experimental research study, reported herein, was undertaken to evaluate the effect of fiber type and dosage on the shear behavior of deep, fiber-reinforced concrete hollow-core slabs.

RESEARCH SIGNIFICANCE

Previous research has shown the potential of using steel fibers in precast, prestressed concrete hollow-core slabs to increase their shear strength. However, experimental data are very limited, particularly for hollow-core slabs thicker than 12.5 in. (320 mm). A literature search indicated data available from only four tests of fiber-reinforced concrete hollow-core slabs thicker than 12.5 in. (320 mm), where the effect on shear strength of a single fiber type at two dosages was evaluated. This research was thus aimed at generating comprehensive experimental information regarding the shear strength of relatively deep (16 in. [405 mm]) hollow-core slabs reinforced with various types of steel fiber-reinforced concretes and constructed using an extrusion process.

EXPERIMENTAL PROGRAM

Overview of test specimens

The shear behavior of prestressed, steel fiber-reinforced concrete hollow-core slabs was evaluated through tests of spans subjected to a monotonically increased concentrated force. The main experimental variables evaluated were fiber type and dosage (two fiber types at up to three dosages; refer to the "Material properties" section), and *a*/*d* (3.0 and 3.5).

A total of seven 16 in. (405 mm) slabs were constructed using an extrusion process and manufactured at a single precast plant. Each slab had a total length of 15 ft (4570 mm). Because the test slabs had to be cast at the same time as other slabs being manufactured by the precast concrete producer, the design of the slabs in terms of number, diameter, and location of the strands was dictated by the design of the slabs being manufactured that day.

All slabs had the same design in terms of cross-section dimensions and prestressing steel (Fig. 2). The slabs were reinforced with 11 seven-wire, 270 ksi (1860 MPa) low-relaxation strands. The two exterior strands were 0.5 in.

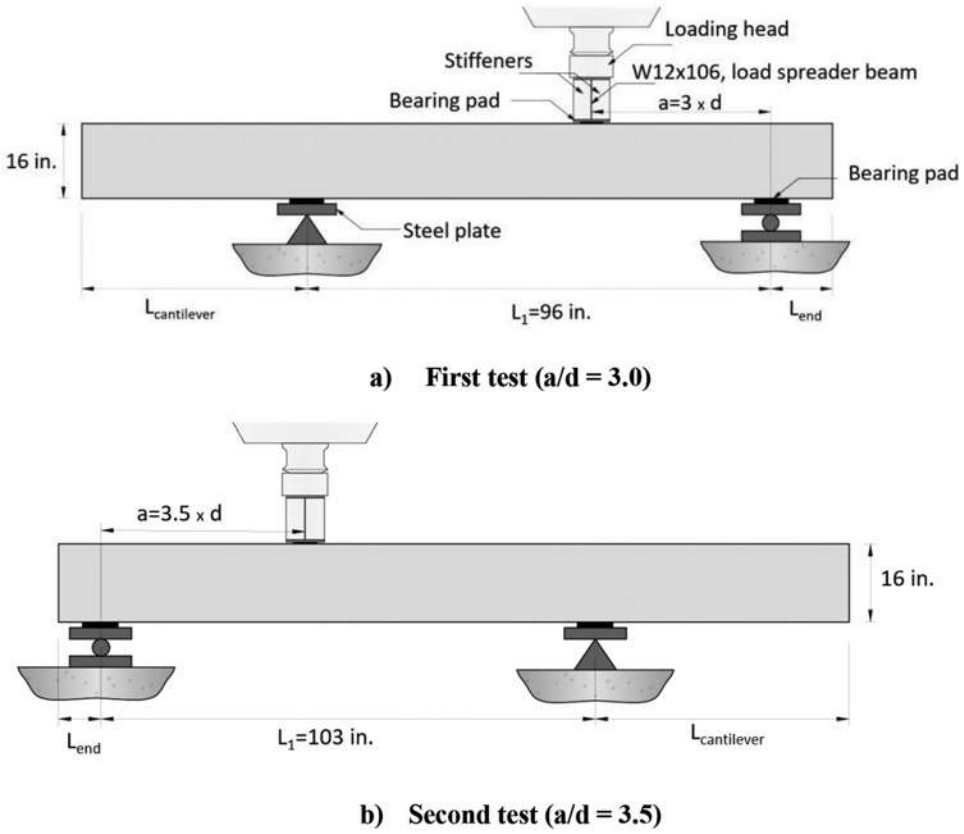

Fig. 3—Sketch of test setup. (Note: 1 in. = 25.4 mm.)

(13 mm) in diameter, while the nine interior strands were 0.6 in. (15 mm) in diameter, for a total area of 2.25 in.^{2} (1452 mm^2). Prior to casting of concrete, these strands were tensioned to a stress of $0.65f_{pu}$ (175.5 ksi [1210 MPa]), where f_{pu} is the nominal ultimate strength of the prestressing steel.

For each slab, the two ends were tested separately (Fig. 3). Thus, a total of 14 tests were conducted. The first test was conducted on a shear span with a length of $3.0d$ (42 in. [1065 mm]). The distance between supports L_1 was 96 in. (2440 mm). The other end of the slab was cantilevered to prevent any damage to this end during the first test (Fig. 3(a)). Once the first test was completed, the supports were relocated and the slab moved for testing of the other end, with a shear span of $3.5d$ (49 in. [1255 mm]) and L_1 = 103 in. (2615 mm) (Fig. 3(b)).

Description of test spans and test method

A summary of the main features of each test span is presented in Table 1. The span designation rules used are as follows. The first letter-number group refers to the fiber type (F1 for fiber type 1, F2 for fiber type 2, and NF for no fibers). The subsequent number refers to the fiber dosage in lb/yd^3, followed by the a/d. If a letter is added at the end, it means that more than one nominally identical shear span was tested, with "a" referring to one test shear span and "b" to the nominally identical shear span tested. Thus, test span F2-40-3.0a refers to one of two spans (letter a at the end) with Type 2 fibers at 40 lb/yd^3 (24 kgf/m^3), and an a/d of 3.0. Twelve tests were performed on shear spans with steel fiber-reinforced concrete, while two tests were conducted on shear spans without fibers. Except for one slab that had the cores at one end accidentally filled (shear span F2-40-3.5a), the distance between the center of the support and the edge of the slab was 1.75 in. (45 mm). For the slab end with filled cores, this distance was 38.0 in. (965 mm) to test the region with hollow cores.

Figure 3 shows a sketch of the setup used for each of the tests. Load was applied through a 1000 kip (4450 kN) testing machine at a constant displacement rate of 0.03 in./min (0.75 mm/min). A steel spreader beam was placed underneath the 12 in. (305 mm) diameter crosshead of the hydraulic actuator to spread the load across the entire width of the slab. A 6 in. (150 mm) wide, 0.5 in. (13 mm) thick, commercial Grade 200 neoprene bearing pad was placed between the spreader beam and the slab to achieve a more uniform distribution of the load. The bearing surface at the test end consisted of a 1.5 in. (38 mm) wide and 0.2 in. (5 mm) thick multi-monomer plastic bearing pad seating on top of a 6 in. (150 mm) wide, 1 in. (25 mm) thick steel plate. This steel plate was in turn placed on top of a 0.75 in. (19 mm) diameter steel roller.

Instrumentation

Applied loads were measured through a load cell connected to the 1000 kip (4450 kN) testing machine. Slab deflections and deformations were calculated using measurements from a noncontact position tracking system (Northern Digital Inc. 2011). This system tracked the position in space of markers attached to the surface of the specimens. Figure 4 shows the marker layout used on the webs of the test slabs. Given the

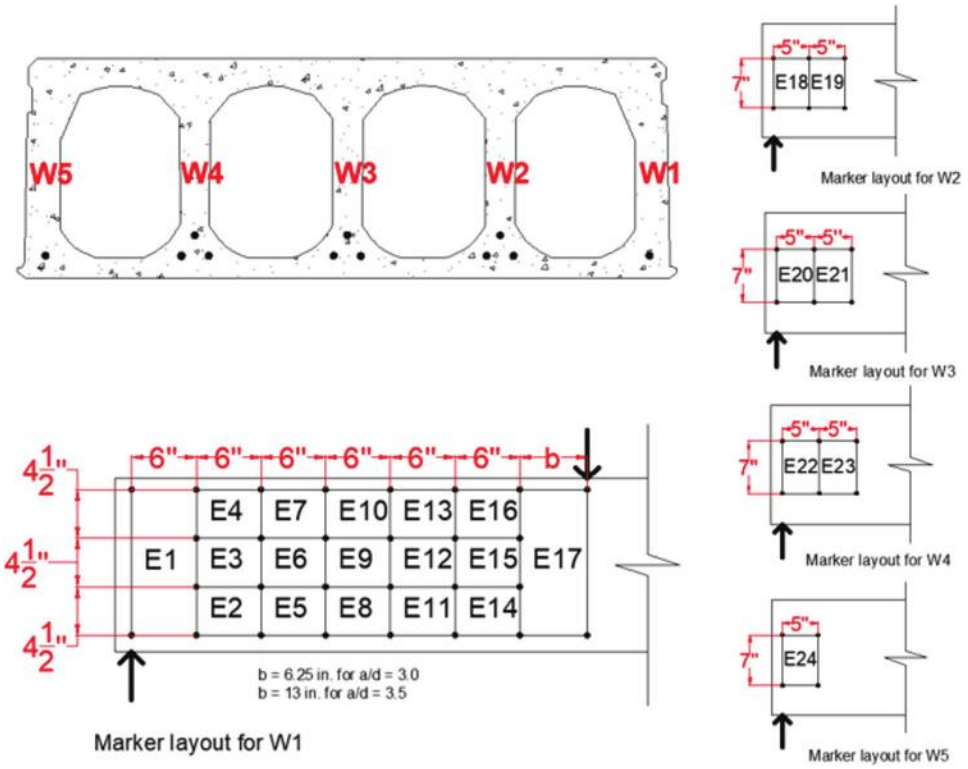

Fig. 4—Typical web marker layout. (Note: 1 in. = 25.4 mm.)

Table 1—Summary of test shear spans and main results

Span ID	V_f, %	α, in.	a/d	L_{end}, in.	L_1, in.	f_c', psi	V_{max}, kip	V_{cw}, kip	V_{pc}, kip	V_{max}/V_{cw}	V_{max}/V_{pc}
NF-3.0	—	42.0	3.0	1.75	96.0	13,100	75.0	80.9	N.A.	0.93	N.A.
NF-3.5	—	49.0	3.5	1.75	103.0		70.1	80.5	N.A.	0.87	N.A.
F1-50-3.0	0.38	42.0	3.0	1.75	96.0	11,390	86.6	76.5	68.7	1.13	1.26
F1-50-3.5	0.38	49.0	3.5	1.75	103.0		95.1	76.2	68.7	1.25	1.38
F2-40-3.0a	0.30	42.0	3.0	1.75	96.0	12,290	93.6	78.9	74.6	1.19	1.26
F2-40-3.5a*	0.30	49.0	3.5	38.0	103.0		121	106	88.8	1.13	1.36
F2-40-3.0b	0.30	42.0	3.0	1.75	96.0		85.0	78.9	74.6	1.08	1.14
F2-40-3.5b	0.30	49.0	3.5	1.75	103.0		94.5	78.5	74.6	1.20	1.27
F2-50-3.0a	0.38	42.0	3.0	1.75	96.0	10,750	71.7	74.8	72.5	0.96	0.99
F2-50-3.5a	0.38	49.0	3.5	1.75	103.0		69.7	74.5	72.5	0.94	0.96
F2-50-3.0b	0.38	42.0	3.0	1.75	96.0		96.5	74.8	72.5	1.29	1.33
F2-50-3.5b	0.38	49.0	3.5	1.75	103.0		84.1	74.5	72.5	1.13	1.16
F2-62-3.0	0.47	42.0	3.0	1.75	96.0	12,570	87.1	79.6	83.9	1.09	1.04
F2-62-3.5	0.47	49.0	3.5	1.75	103.0		100	79.2	83.9	1.26	1.19

*Cores were filled at slab end.

Note: Refer to Fig. 3 for L_{end}, L_1, and α; V_f is fiber volume fraction; a is shear span length; d is effective depth; f_c' is average cylinder compressive strength; V_{max} is peak shear force; V_{cw} is calculated web-cracking shear strength according to ACI 318-19; V_{pc} is calculated post-diagonal cracking shear strength; 1 in. = 25.4 mm; 1 psi = 6895 Pa; 1 kip = 4.45 kN; N.A. is not available.

field of view of the cameras of the position tracking system, most of the markers were attached to one of the exterior webs (W1 in Fig. 4), as well as to the top of the slab. Despite the limited field of view, some markers were attached to the inner face of the opposite exterior web (W5) and to one face of all interior webs (W2 through W4) near the support in an attempt to track the formation of shear cracks in these webs. Reported deflection values correspond to deflections at the loading point relative to the support at the end of the test shear span.

Material properties

Two types of hooked steel fibers were evaluated. Type 1 fibers were 1.18 in. (30 mm) long and 0.022 in. (0.55 mm) in diameter (Fig. 5) for a fiber aspect ratio of approximately 55. The wire used to manufacture the Type 1 fibers had a nominal tensile strength of 160 ksi (1100 MPa). These fibers

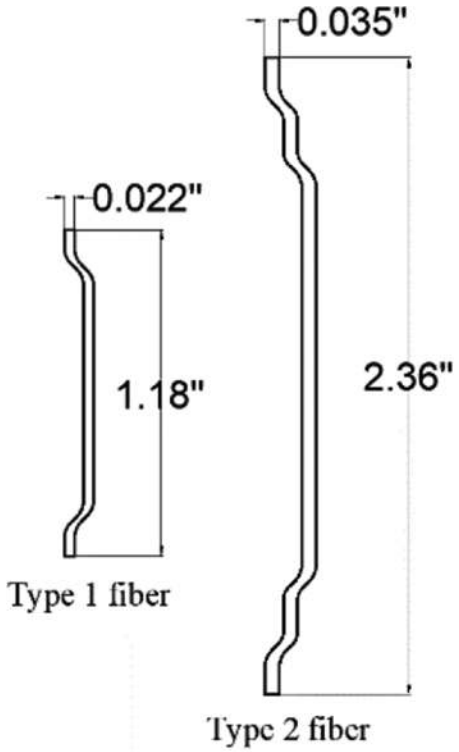

Fig. 5—Geometry of steel fibers used in test specimens. (Note: 1 in. = 25.4 mm.)

had a single hook at each end and were the same as those used in the tests reported in Dudnik et al. (2017). Type 2 fibers, on the other hand, were 2.36 in. (60 mm) long and 0.035 in. (0.9 mm) in diameter (aspect ratio of approximately 65), with double hooks at each end (Fig. 5). The nominal tensile strength for the Type 2 fibers was 335 ksi (2300 MPa).

Type 1 fibers, with a single hook at each end, are expected to slip while remaining elastic (except for the hooked ends) as cracks in the concrete widen. On the other hand, the double hooks in the Type 2 fibers are intended to prevent these fibers from slipping. Thus, fiber yielding is expected for crack widths larger than approximately 0.02 in. (0.5 mm). To prevent early fiber fracture, the minimum tensile strain capacity of these fibers is 5%, which would correspond to a crack width of approximately 0.12 in. (3.0 mm).

As shown in Table 1, Type 1 fibers were evaluated at 50 lb/yd^3 (30 kgf/m^3) (0.38% volume fraction), while Type 2 fibers were evaluated at 40, 50, and 62 lb/yd^3 (24, 30, and 37 kgf/m^3) for fiber volume fractions of 0.30, 0.38, and 0.47%, respectively. Type 1 fibers were evaluated at a single dosage because they had been evaluated in previous research (Dudnik et al. 2017) at 66 and 100 lb/yd^3 (39 and 59 kgf/m^3), or at volume fractions of 0.5 and 0.76%, respectively. Both fiber types were delivered in bundles, with fibers glued to each other by a water-soluble glue that dissolved when in contact with water to improve fiber distribution.

The same concrete mixture was used for all slabs, regardless of the presence of fibers. This concrete had a target compressive strength of 9000 psi (62 MPa) and a water-cement ratio (w/c) of 0.36. Coarse aggregate consisted of crushed limestone with a maximum size of 0.75 in. (19 mm). The same mixing process was used for the concrete used in

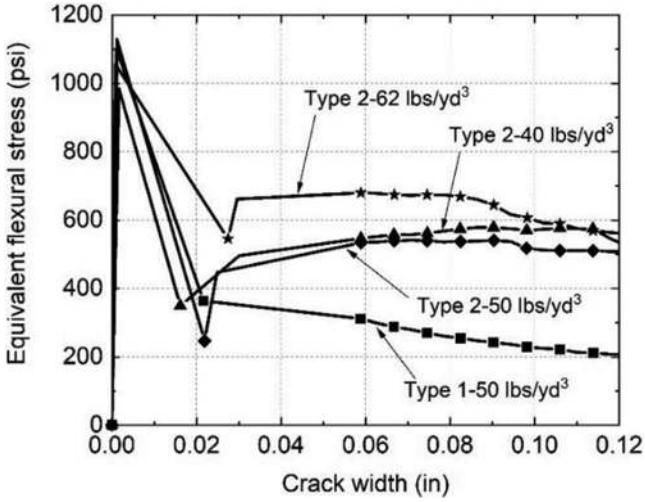

Fig. 6—Average equivalent flexural stress versus crack width response for fiber-reinforced concrete. (Note: 1 psi = 6895 Pa; 1 in. = 25.4 mm; 1 lb/yd^3 = 0.591 kgf/m^3.)

all slabs. In general, a good fiber distribution was observed prior to the concrete being discharged in the extrusion machine and no major issues were encountered during the extrusion process.

As mentioned previously, all slabs were pretensioned using 11 seven-wire, 270 ksi (1860 MPa) low-relaxation strands. These strands were initially tensioned to a stress of 175.5 ksi (1210 MPa), which corresponded to 65% of the nominal ultimate strength of the prestressing steel.

EXPERIMENTAL RESULTS

Concrete cylinder strength and flexural behavior of fiber-reinforced concrete beams

Compressive strength for the concrete used in the test slabs was obtained through testing of at least two 6 x 12 in. (152 x 305 mm) cylinders. The average compressive strengths obtained at or near the day of testing of the shear spans are listed in Table 1. As shown in the table, concrete compressive strength ranged between 10,750 and 13,100 psi (74.1 and 90.3 MPa).

The tensile performance of the various fiber-reinforced concretes used was evaluated indirectly through three- or four-point bending tests of 6 x 6 x 20 in. (150 x 150 x 510 mm) beams. Concrete used in the beam samples was collected after being transported from the mixer using a crane and bucket operation and discharged into the tank of the extrusion machine, but prior to undergoing the extrusion process. The results from these tests, therefore, should be taken with caution given that the process of manufacturing these beams cannot be considered representative of the extrusion process used to cast the concrete in the hollow-core slabs.

Beam tests were conducted using a closed-loop servo-controlled hydraulic machine under displacement control at a rate of 0.005 in./min (0.127 mm/min). Average equivalent bending stress versus crack width responses for the fiber-reinforced concretes used are shown in Fig. 6. Equivalent bending stress was calculated assuming linear-elastic behavior and using uncracked section properties (that is,

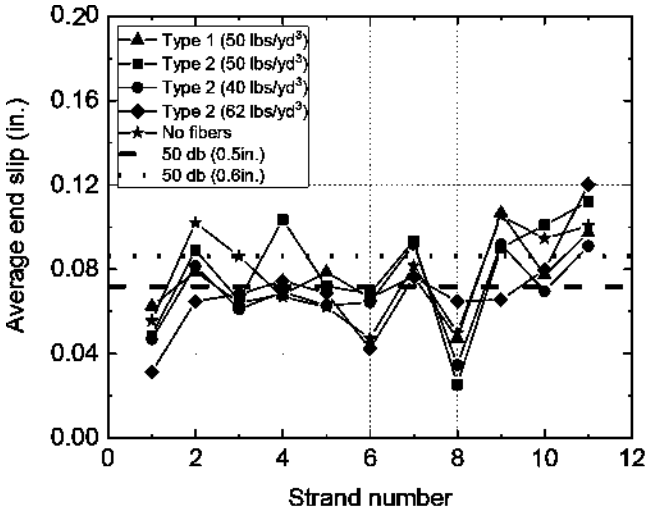

Fig. 7—Average strand end slip. (Note: Strands 1 and 8 had diameter of 0.5 in. [13 mm], while all other strands had diameter of 0.6 in. [15 mm]; 1 in. = 25.4 mm; 1 lb/yd³ = 0.591 kgf/m³.)

applied moment divided by the elastic section modulus). It should be mentioned that the beams with Type 2 fibers at 62 lb/yd³ (37 kgf/m³) were tested under four-point bending, as specified in ASTM C1609/C1609M(2012), while the rest of the beams were erroneously tested under three-point bending. As can be seen in Fig. 6, the behavior of the fiber-reinforced concretes with Type 2 fibers was significantly better than that of the concrete with Type 1 fibers, even when Type 2 fibers were used at a 20% lower dosage. This is attributed to the double hooks at the ends of Type 2 fibers, which leads to an increased average bond stress between the fibers and the surrounding concrete. Increases in the dosage of Type 2 fibers beyond 40 lb/yd³ (24 kgf/m³), however, translated only into a modest improvement in performance, particularly at large crack widths. It should be mentioned that the maximum difference between individual post-cracking strengths and the average strength for the fiber-reinforced concrete beams with Type 1 fibers was 25%, while the maximum difference for the beams with Type 2 fibers was 16%.

Strand end slips

Figure 7 shows the measured end slips for the prestressing steel strands. The slip values reported are lumped into average slips for each concrete material used, which were calculated as the average of the slips measured at both ends of the same strand for all slabs cast using the same material. Also shown in the figure are the calculated slips corresponding to an effective prestress of 95% of the initial prestress (167 ksi [1150 MPa]) and a transfer length of $50d_b$, where d_b is the strand diameter.

As can be seen in Fig. 7, slip values in the slabs did not seem to be affected by the presence of fibers. It should be noted that all strands in these slabs had a diameter of 0.6 in. (15 mm), except for Strands 1 and 8, which were 0.5 in. (13 mm) in diameter. For the same strand diameter, the results were fairly consistent, except for Strand 11 located in one of the webs, for which higher slips were measured regardless of the presence of fibers. In general, $50d_b$ represented an adequate, and often conservative, estimation of the average transfer length for the 0.6 in. (15 mm) diameter strands and was in all cases conservative for estimating transfer length for the 0.5 in. (13 mm) diameter strands.

Web-cracking shear strength

All test specimens failed after the formation of cracks in the webs, near the supports. Thus, it is appropriate to compare the shear strengths exhibited by the test slabs with estimations of web-cracking shear strength of prestressed concrete members. Section 22.5.6.3.2 of ACI 318-19 gives the nominal web-cracking shear strength as follows

$$V_{cw} = (3.5\lambda\sqrt{f_c'} + 0.3f_{pc})b_w d + V_p \quad (1)$$

where λ takes into account the effect of lightweight aggregate (λ = 1.0 in this case); f_{pc} is the compressive stress in the concrete at the centroid of the section due to the effective prestressing force; b_w is the web width; d is the effective depth; and V_p is the vertical component of the effective prestressing force at the section considered (zero for the test slabs). The term in parenthesis in Eq. (1) is a simple and accurate approximation of Eq. (2), which gives the shear stress corresponding to a principal tensile stress at the section centroid equal to the tensile strength of the concrete under biaxial tension-compression stresses

$$v_{cw} = f_{ct}\sqrt{1 + \frac{f_{pc}}{f_{ct}}} = 3.5\lambda\sqrt{f_c'}\sqrt{1 + \frac{f_{pc}}{3.5\lambda\sqrt{f_c'}}} \quad (2)$$

where the concrete tensile strength f_{ct} is taken as $3.5\lambda\sqrt{f_c'}$. It should be noted that in EN 1992-1-1 (2004), web-cracking shear strength is also calculated as the shear stress corresponding to a principal tensile stress equal to f_{ct}.

For the calculation of f_{pc}, the transfer of effective prestress from the strands to the concrete was assumed to occur over 50 strand diameters from the end of the strand. Concrete compressive strength used in the calculations corresponded to the measured average cylinder strength.

Table 1 lists the calculated web-cracking shear strengths for the test spans, which corresponded to the first critical section at $h/2$ from the inner face of the support, where h is the overall slab depth. As can be seen in the table, the two shear spans without fibers exhibited web-cracking shear forces at failure that corresponded to 93% and 87% of the calculated web-cracking shear strength for shear a/d of 3.0 and 3.5, respectively. For these two test spans, failure occurred immediately after one web cracked in shear. It is worth mentioning that two shear spans manufactured at the same facility and tested as part of a previous investigation (Dudnik et al. 2017) failed at approximately 70% of V_{cw}. No explanation could be found for this difference in normalized shear strength, other than the large variabilities that are typical of concrete tensile strength.

The addition of steel fibers to the concrete, given the dosages used, did not lead to a change in the cracking strength of the concrete. The increase in shear strength discussed next

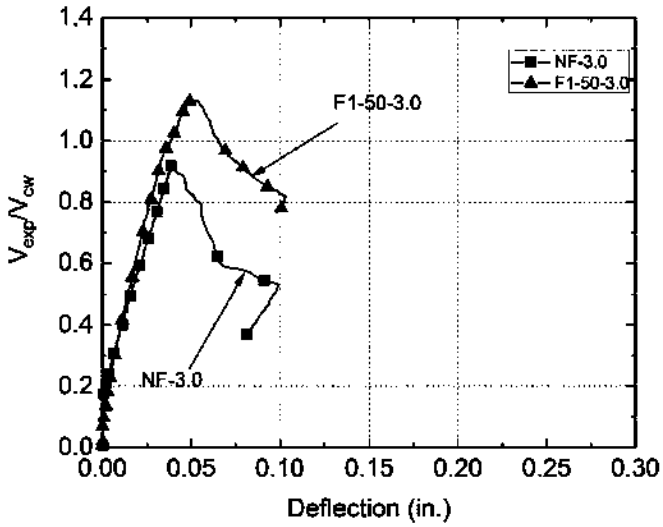

a) Shear span-to-effective depth ratio = 3.0

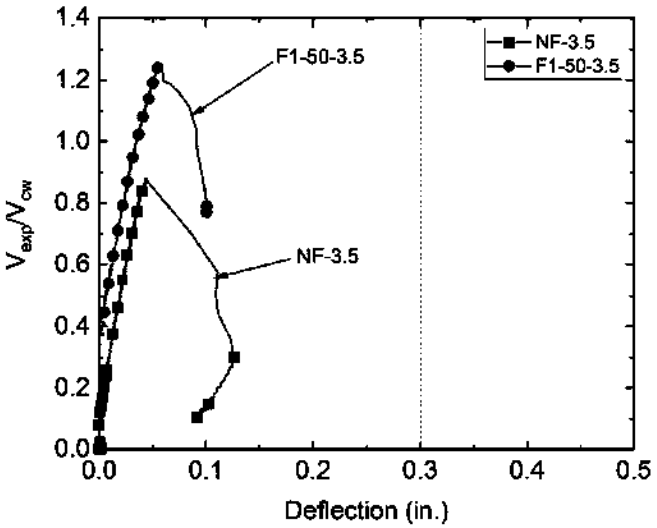

b) Shear span-to-effective depth ratio = 3.5

Fig. 8—Normalized shear strength versus deflection response (slabs with Type 1 fibers and no fibers). (Note: 1 in. = 25.4 mm.)

was thus due to the fact that failure in these slabs occurred only after multiple webs had cracked in shear. Adding Type 1 fibers at 50 lb/yd^3 (30 kgf/m^3) led to a 21 and 44% increase in shear capacity, with shear forces at failure of 1.13 and 1.25 times the calculated web-cracking shear strength for *a*/*d* of 3.0 and 3.5, respectively. The ratio between experimental shear strength and calculated web-cracking shear strength for the slabs reinforced with Type 2 fibers, on the other hand, ranged between 0.94 and 1.29. Two of the shear spans with Type 2 fibers (F2-50-3.0a and F2-50-3.5a), both of the same hollow-core slab, exhibited shear strengths slightly less than the calculated web-cracking shear strength. Shear strengths from two nominally identical shear spans (F2-50-3.0b and F2-50-3.5b), on the other hand, exhibited shear strengths equal to 1.29 and 1.13 times the calculated web-cracking shear strength. It is possible that the lower shear strengths were the results of less than adequate fiber distribution or concrete compaction, particularly because the lower strengths corresponded to the two shear spans tested from the same slab.

Overall, the results from the tests of the shear spans with Type 2 fibers suggest little or no benefit in increasing fiber dosage from 40 lb/yd^3 (24 kgf/m^3) to either 50 lb/yd^3 (30 kgf/m^3) or 62 lb/yd^3 (37 kgf/m^3). This is consistent with the similar equivalent flexural stress versus crack width behavior exhibited by these materials (refer to Fig. 6). A similar observation can be made when comparing the results from the tests with Type 1 fibers with those reported in Dudnik et al. (2017). The two 16 in. (406 mm) deep shear spans tested in that investigation reinforced with Type 1 fibers at 66 lb/yd^3 (39 kgf/m^3) failed at shear forces 1.23 and 1.33 times the calculated web-cracking shear strength for *a*/*d* of 3.0 and 3.5, respectively. This represents a normalized strength increase of only 8.9% and 6.4%, respectively, when compared to the slabs with Type 1 fibers at 50 lb/yd^3 (30 kgf/m^3) despite the use of a 30% higher fiber dosage.

Overall behavior of test shear spans

For convenience, the load versus deflection response of all specimens is presented in terms of the shear force acting on the section where failure occurred, normalized with respect to the calculated web-cracking shear strength in accordance with ACI 318-19 building code. Figures 8(a) and (b) show the normalized shear force versus deflection responses for the test spans with either Type 1 fibers or no fibers for *a*/*d* of 3.0 and 3.5, respectively. Similarly, the normalized shear force versus deflection responses for the test spans with either Type 2 fibers or no fibers are shown in Fig. 9(a) and (b) for *a*/*d* of 3.0 and 3.5, respectively. In these figures, normalized shear force was calculated as the ratio between the applied shear V_{exp} and the calculated web-cracking shear strength V_{cw}, as discussed in the previous section. Deflection, on the other hand, corresponds to the relative downward movement of the slab under the applied load relative to the nearest support. It should be pointed out that due to an instrument malfunction, deflection data for test span F2-40-3.0b in Fig. 9(a) correspond to the movement of the machine crosshead.

All test slabs exhibited a nearly linear response up to web-shear cracking. No flexural cracks were observed in any of the slabs. As mentioned, peak load for the slabs with no fibers corresponded to the formation of a web-shear crack at a single web. The substantial loss of shear-carrying capacity of that web, once it cracked, led to an overload of the other four webs, which triggered the nearly instantaneous formation of shear cracks in the other webs and led to a rapid decrease in applied load.

For the slabs with either Type 1 or Type 2 fibers, some nonlinearity in the load versus deflection response can be observed as the load approached the peak load. This is attributed to the ability of the slabs to resist additional shear once one of the webs experienced web-shear cracking, which led to cracking in multiple webs prior to failure (refer to Fig. 10 for typical web-shear cracking in the test specimens). This was possible because fibers bridging the first web-shear crack prevented this web from experiencing a

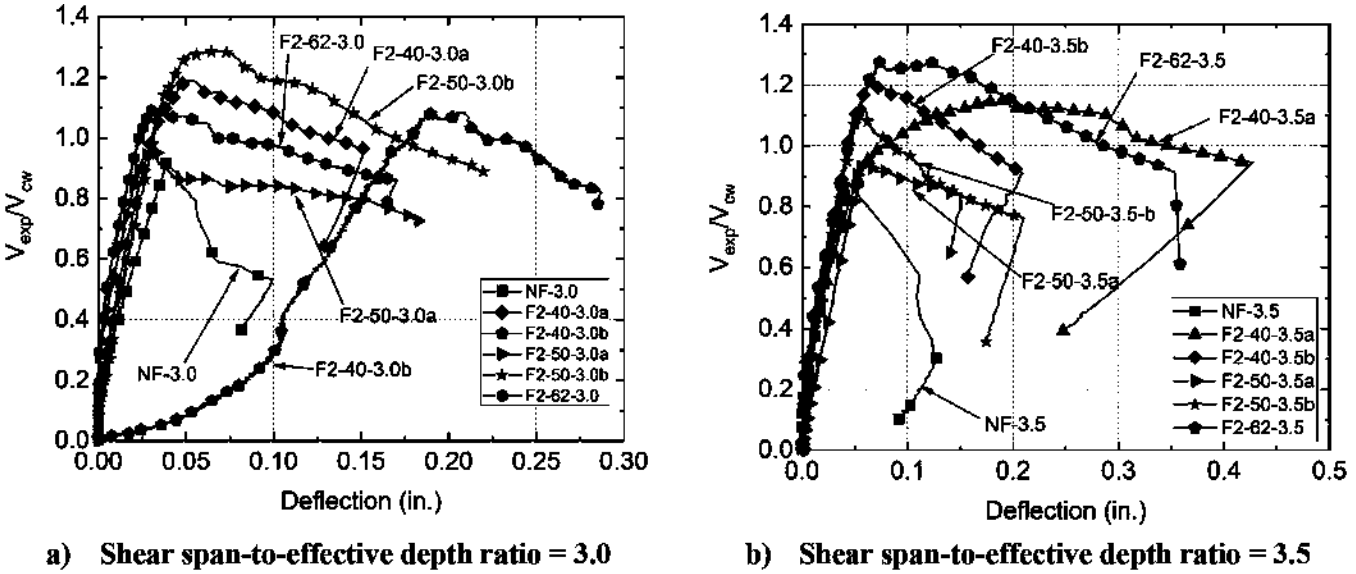

a) Shear span-to-effective depth ratio = 3.0

b) Shear span-to-effective depth ratio = 3.5

Fig. 9—Normalized shear strength versus deflection response (slabs with Type 2 fibers and no fibers). (Note: 1 in. = 25.4 mm.)

Fig. 10—Web-shear cracking in shear span F2-40-3.5b (left: exterior webs; and right: interior web).

sudden loss of shear capacity at cracking and the triggering of a "zipper" effect that would have overloaded the other webs, thus allowing the slab to sustain additional shear. Similar observations were made by Dudnik et. al (2017). This behavior was most evident in shear span F2-40-3.5a, which exhibited a substantial hardening response over a wide range of deflections (Fig. (b)).

The phenomenon discussed previously can be explained using Fig. 11, which shows plots of applied normalized shear versus average principal tensile strains measured either on an exterior and interior web (Fig. 11(a)) or on one exterior web (Fig. 11(b)). Average strains were calculated from measurements of the position in space of sensors attached to the concrete surface during the tests (refer to Fig. 5 for sensor locations and grid numbering). For each sensor quadrant shown in Fig. 5, the average vertical, horizontal, and shear strains were calculated based on the position of the four sensors defining each quadrant, which allowed the calculation of the principal tensile strains shown in Fig. 11. As can be seen in Fig. 11(a), which corresponds to shear span F2-50-3.0b, first cracking on web W4 (Element E23) occurred at approximately $1.04V_{cw}$. This was evident by the sudden increase in average principal tensile strain without an increase in applied load. Despite the formation of a web-shear crack on at least one web, this specimen was capable of sustaining additional load up to $1.29V_{cw}$, at which point web-shear cracking occurred on exterior web W1 and the specimen reached its peak strength. From visual inspection after completion of the test, it was observed that all five webs of this test shear span had cracked in shear. Figure 11(b), on the other hand, illustrates the average strain progression on one exterior web (W1) of shear span F2-40-3.5a. First web-shear cracking on this web occurred at approximately V_{cw}, as indicated by the increase in principal tensile strains in Elements E5 and E16. At approximately $1.1V_{cw}$, a second diagonal crack formed on this web, as indicated by the increase in strain in Element E14. The fact that two diagonal cracks formed on a single web is an indication that the formation of the first web-shear crack did not lead to a loss of shear-carrying capacity of this web.

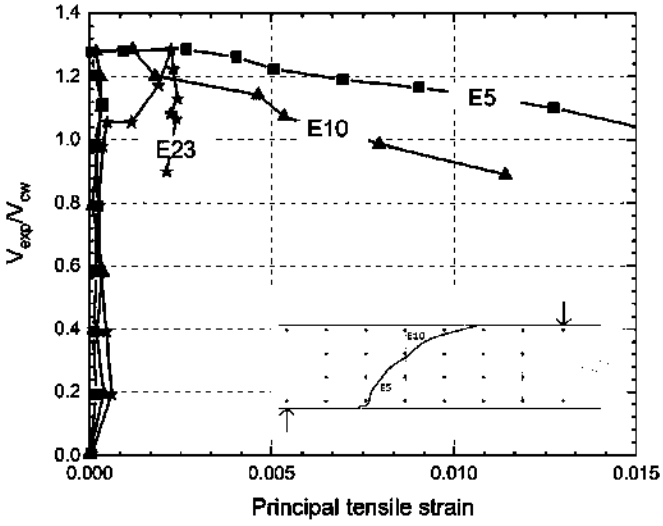

a) Shear span F2-50-3.0b

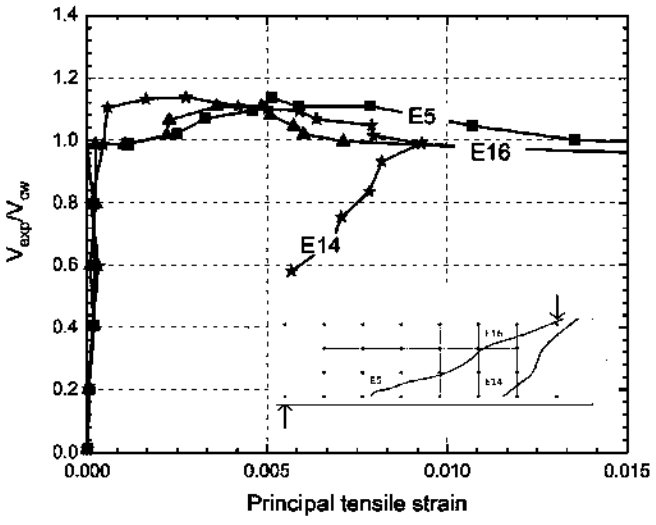

b) Shear span F2-40-3.5a

Fig. 11—Normalized shear force versus average principal tensile strains.

Estimation of post-diagonal cracking shear strength

Steel fibers crossing the diagonal crack are believed to have primarily contributed to maintaining, or even increasing, the post-cracking web-shear strength by: 1) transferring tensile stresses across the diagonal crack; and 2) restraining the opening of the diagonal crack, thereby increasing shear transferred through aggregate interlock. A simple model is proposed to estimate the shear strength of steel fiber-reinforced concrete hollow-core slabs after the occurrence of web-shear cracking (V_{pc}). Referring to the free-body diagram shown in Fig. 12, the web-shear crack is assumed to propagate at 45 degrees downwards to the inner face of the support and upwards toward the compression zone, with a horizontal and vertical projection equal to $0.9h$, where h is the overall height of the slab. The crack is assumed to linearly increase in width from Point O. A uniform equivalent tensile stress $(f_t)_{avg}$ in the fiber-reinforced concrete along the diagonal crack is assumed, which has been shown to be reasonable for fiber-reinforced concrete flexural members (Dinh et al. 2011). The tensile force in the prestressing steel T_{ps} is calculated assuming a uniform bond stress over a transfer length equal to 50 strand diameters. Taking moments about Point O and neglecting the moment caused by the compression force, a relationship can be obtained between the applied shear and the intensity of the diagonal tensile stress block as follows (refer to Fig. 12)

$$V_{pc} = \frac{T_f\left(\frac{L_{cr}}{2}\right) + T_{ps}(d - 0.1h)}{\left(\frac{l_b}{2} + 0.9h\right)} \quad (3)$$

where

$$T_f = (f_t)_{avg} L_{cr} b_w \quad (4)$$

$$L_{cr} = (0.9h)\sqrt{2} \quad (5)$$

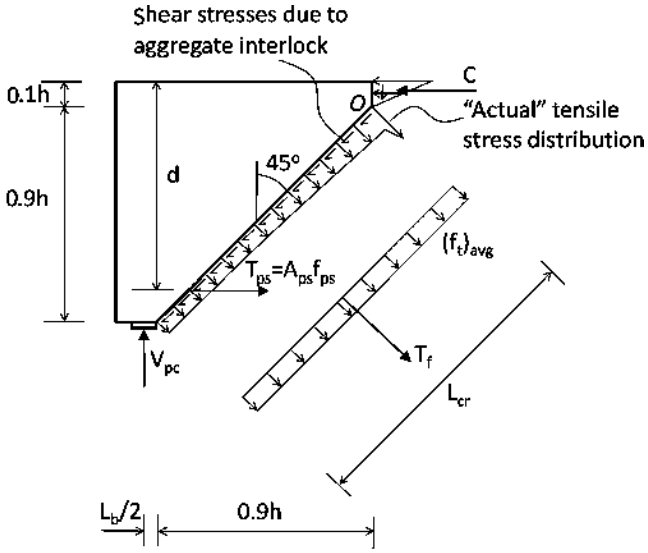

Fig. 12—Assumed stress distribution after diagonal cracking in fiber-reinforced concrete slabs.

and b_w is the summation of all of the web widths.

The average tensile stress $(f_t)_{avg}$ at a given crack width can be obtained from the results of ASTM C1609/C1609M-12 tests following the procedure reported in Dinh et al. (2011). According to this procedure, $(f_t)_{avg}$ can be obtained from Eq. (6)

$$(f_t)_{avg} = 0.37 f_{eq} \quad (6)$$

where f_{eq} is the equivalent flexural stress obtained from ASTM C1609/C1609M tests at a given crack width. Crack widths calculated from the optical sensors attached to the exterior webs indicated that a substantial loss of load-carrying capacity in the slabs with Type 2 fibers occurred at maximum crack widths greater than 0.04 in. (1.0 mm) or 1/60 of the fiber length. A crack width equal to 1/60 of the fiber length (0.02 in.) also seems consistent with the results from the two slabs with Type 1 fibers. Based on these crack

widths, and from Fig. 6 and Eq. (6), an equivalent average tensile stress $(f_t)_{avg}$ equal to 425 psi (2.93 MPa) is obtained for the mixture with Type 1 fibers at 50 lb/yd^3 (30 kgf/m^3). For the mixtures with Type 2 fibers, $(f_t)_{avg}$ is equal to 525, 490, and 680 psi (3.62, 3.38, and 4.69 MPa) for fiber dosages of 40, 50, and 62 lb/yd^3 (24, 30, and 37 kgf/m^3), respectively.

Once $(f_t)_{avg}$ is determined, the post-diagonal cracking shear strength can be calculated from Eq. (3). It should be noted, however, that because Eq. (3) was obtained from moment equilibrium and not from equilibrium of vertical forces, an upper limit is needed for the calculated shear strength. For consistency with the upper limit in Table 22.5.6.2 of ACI 318-19, a maximum shear stress of $5\lambda\sqrt{f_c'}$ is proposed.

The calculated post-diagonal cracking shear strengths for the fiber-reinforced concrete slabs, V_{pc}, are listed in Table 1. As can be seen, the proposed method led to reasonable estimates of post-cracking shear strength, with ratios between experimental and calculated shear strengths ranging between 0.96 and 1.38.

CONCLUSIONS

The following conclusions can be drawn from the results presented in this paper.

- Strand-end slip values in the slabs did not seem to be affected by the presence of fibers. Fifty strand diameters ($50d_b$) represented an adequate, and generally conservative estimation of the average transfer length for the 0.6 in. (15 mm) diameter strands, while being conservative in all cases for estimating transfer length for the 0.5 in. (13 mm) diameter strands.
- The use of steel fibers led to an increase in shear strength and, for the case of Type 2 fibers, to a more gradual post-peak strength decay. Fiber-reinforced concrete shear spans with Type 1 and Type 2 fibers at 50 and 40 lb/yd^3 (30 and 24 kg/m^3), respectively, exhibited peak shear strengths that ranged between 1.08 and 1.20 times the calculated web-cracking shear strength, V_{cw}. The two test spans without fibers, on the other hand, failed at shear forces corresponding to 0.93 and $0.87V_{cw}$. The shear spans with Type 2 fibers at 50 and 62 lb/yd^3 (30 and 37 kg/m^3) showed a greater variability in shear strength, likely due to variations in fiber distribution or concrete compaction. These slabs failed at shear strengths ranging between 0.94 and $1.29V_{cw}$.
- Failure of the hollow-core slabs without fibers occurred as soon as one web exhibited web-shear cracking. The loss of shear-carrying capacity in the cracked web created a "zipper" effect that led to a nearly simultaneous failure of all five webs. In the hollow-core slabs with fibers, on the other hand, fibers bridging the first web-shear crack prevented this web from experiencing a sudden loss of shear capacity that would have caused a "zipper" effect, which allowed the slab to sustain additional shear. Failure of these slabs occurred only after multiple webs cracked in shear.
- The proposed method for calculating the shear strength of the fiber-reinforced concrete slabs after the occurrence of diagonal cracking led to reasonable strength estimations, with ratios between experimental and calculated strengths ranging between 0.96 and 1.38.

AUTHOR BIOS

Gustavo Parra-Montesinos, *FACI, is a Professor of structural engineering at the University of Wisconsin–Madison, Madison, WI. He is Chair of ACI Subcommittee 318-J, Joints and Connections, and a member of ACI Committee 318, Structural Concrete Building Code, and Joint ACI-ASCE Committee 352, Joints and Connections in Monolithic Concrete Structures. His research interests include the behavior and design of reinforced concrete, fiber-reinforced concrete, and hybrid steel-concrete structures.*

ACI member **Luis B. Fargier-Gabaldón** *is the Massman-Beavers Associate Professor of Practice of Heavy Civil Engineering at the University of Notre Dame, Notre Dame, IN. He is a member of ACI Subcommittee 318-F, Foundations, and Joint ACI-ASCE Committee 335, Composite and Hybrid Structures. His research interests include reinforced and prestressed concrete, soil-structure interaction, and bridge engineering.*

ACI member **Mohamed Al-Tameemi** *is a PhD Student in structural engineering at the University of Wisconsin–Madison. He received his BS from the University of Technology, Baghdad, Iraq, and his MS in civil engineering from the University of Wisconsin–Madison. He is a member of ACI Committee 544, Fiber Reinforced Concrete.*

ACKNOWLEDGMENTS

The research reported herein was sponsored by the Concrete Research Council of the ACI Foundation. The support of Mid-States Concrete Industries in the manufacturing of the extruded hollow-core slabs is greatly appreciated. Steel fibers used in this study were kindly donated by N.V. Bekaert S.A. The conclusions presented herein are those of the writers and do not necessarily represent the views of the sponsors.

REFERENCES

ACI Committee 318, 2014, "Building Code Requirements for Structural Concrete (ACI 318-14) and Commentary (ACI 318R-14)," American Concrete Institute, Farmington Hills, MI, 520 pp.

ACI Committee 318, 2019, "Building Code Requirements for Structural Concrete (ACI 318-19) and Commentary (ACI 318R-19)," American Concrete Institute, Farmington Hills, MI, 623 pp.

ASTM C1609/C1609M-12, 2012, Standard Test Method for Flexural Performance of Fiber-Reinforced Concrete (Using Beam With Third-Point Loading), ASTM International, West Conshohocken, PA.

Cuenca, E., and Serna, P., 2013, "Failure Modes and Shear Design of Prestressed Hollow Core Slabs Made of Fiber-Reinforced Concrete," *Composites: Part B*, V. 45, pp. 952-964.

Dinh, H. H.; Parra-Montesinos, G. J.; and Wight, J. K., 2011, "Shear Strength Model for Steel Fiber Reinforced Concrete Beams without Stirrup Reinforcement," *Journal of Structural Engineering*, ASCE, V. 137, No. 10, pp. 1039-1051. doi: 10.1061/(ASCE)ST.1943-541X.0000362

Dudnik, V. S.; Milliman, L. R.; and Parra-Montesinos, G. J., 2017, "Shear Behavior of Prestressed Steel Fiber-Reinforced Concrete Hollow-Core Slabs," *PCI Journal*, V. 62, No. 4, July-Aug., pp. 58-72. doi: 10.15554/pcij62.4-02

EN 1992-1-1:2004, 2004, "Eurocode 2: Design of Concrete Structures—Part 1-1: General Rules and Rules for Buildings," European Committee for Standardization, Brussels, Belgium.

Hawkins, N. M., and Ghosh, S., 2006, "Shear Strength of Hollow-Core Slabs," *PCI Journal*, V. 51, No. 1, Jan.-Feb., pp. 110-115.

Northern Digital Inc., 2011, *OptoTRAK Certus User Guide*, Waterloo, ON, Canada.

Palmer, K. D., and Schultz, A. E., 2010, "Web Shear Strength of Precast, Prestressed Concrete Hollow Core Slab Units," Department of Civil Engineering, University of Minnesota, Minneapolis, MN, 270 pp.

Parra-Montesinos, G. J., 2006, "Shear Strength of Beams with Deformed Steel Fibers," *Concrete International*, V. 28, No. 11, Nov., pp. 61-70.

Peaston, C.; Elliott, K.; and Paine, K., 1999, "Steel Fiber Reinforcement for Extruded Prestressed Hollow Core Slabs," *Structural Applications of Fiber Reinforced Concrete*, SP-182, N. Banthia, C. MacDonald, and P. Tatnall, eds., American Concrete Institute, Farmington Hills, MI, pp. 87-108.

Simasathien, S., and Chao, S.-H., 2015, "Shear Strength of Steel-Fiber-Reinforced Deep Hollow-Core Slabs," *PCI Journal*, V. 60, No. 4, pp. 85-101. doi: 10.15554/pcij.07012015.85.101

ACI STRUCTURAL JOURNAL TECHNICAL PAPER

Title No. 120-S71

Cementitious Resins for Strengthening Reinforced Concrete Beams with Near-Surface-Mounted Carbon Fiber-Reinforced Polymer

by Yail J. Kim and Wajdi Ammar

This paper presents the feasibility and relevance of cementitious resins as bonding agents for near-surface-mounted (NSM) carbon fiber-reinforced polymer (CFRP) strips. Contrary to conventional organic matrixes, such inorganic resins offer promising performance when subjected to aggressive environments, especially under thermal distress. Three emerging resins are employed (polyester-silica, ultra-high-performance concrete [UHPC], and geopolymer) to strengthen reinforced concrete beams alongside NSM CFRP. After stochastically simulating various levels of pitting corrosion for a period of 100 years, the outcomes are represented in the beams by reducing the cross-sectional area of steel reinforcement before applying the rehabilitation system. The emphasis of experimental investigations lies in the workability of those resins and the flexural response of the retrofitted beams. Material-level testing reveals that the rheological properties of the resins are not related to their compressive strength. As far as load-carrying capacity is concerned, the beams bonded with polyester-silica outperform the beams with other resins; however, UHPC enables stable degradation over the years. The interfacial characteristics of the resins dominate the mechanical interaction between the damaged internal reinforcing steel and CFRP, thereby altering the tendency of capacity drops, post-yield plateaus, and crack distributions. Through analytical modeling, the provisions of existing design guidelines are evaluated, and a modification factor is suggested to promote the cementitious resins for NSM CFRP.

Keywords: carbon fiber-reinforced polymer (CFRP); cementitious resins; near-surface-mounted (NSM); rehabilitation; retrofit; strengthening.

INTRODUCTION

Socioeconomic demands are growing for the development of efficient and durable structural members to accomplish sustainable built environments. Multidirectional endeavors, founded upon collaborative synergies between the technical and public sectors, can relieve risk and vulnerability against human-made and natural hazards.[1] In comparison with demolition and reconstruction, rehabilitation is deemed to be a competitive option that satisfies the stringent requirements of modern building codes at an affordable expense.[2] Accordingly, a number of retrofit methodologies have been proposed and executed using concrete jackets,[3] steel plates,[4] prestressing strands,[5] bracings,[6] energy-dissipating dampers,[7] and external frames.[8] Among others, carbon fiber-reinforced polymer (CFRP) composites have become a notable alternative for structural rehabilitation on account of many benefits: light weight, high strength and modulus, noncorrosiveness, tailorability, convenient installation, low maintenance, and longevity.[9] Prevalent CFRP-strengthening techniques are categorized into two groups: 1) the EB method, where CFRP sheets are externally bonded with a polymeric adhesive; and 2) the NSM method, where CFRP strips are inserted into a precut groove and near-surface-mounted with a resin matrix. From an interfacial mechanics perspective, the NSM method is distinct from the EB method in that an integrated system is established between the adhesive and CFRP, which is beneficial in terms of transferring shear stress with the enlarged contact dimensions.[10] Retrofitting concrete members with near-surface-mounted (NSM) CFRP encompasses several advantages over externally bonded (EB) CFRP—namely, reduced labor, minimal surface preparation, debonding resistance, durability, and aesthetics.[11] The two main factors to be considered when choosing an appropriate bonding agent for installing NSM CFRP strips are strength and workability, because premature interfacial failure would lead to the malfunctioning of the strips and improper rheology could give rise to unnecessary impediments to the planned rehabilitation process.

The majority of research projects concerning NSM CFRP have been conducted with organic epoxies; consequently, contemporary design guidelines and specifications do not contain information on other substitutes.[9,12] The need for inorganic resins arises, per contra, when a structure to be strengthened with CFRP is exposed to aggressive environments, which can readily degrade the bond of organic resins. Yang et al.[13] reported the bond of NSM CFRP with an engineered cementitious composite consisting of cement, fly ash, silica fume, sand, a high-range water reducer, and polyvinyl alcohol fibers. The interfacial failure of CFRP with the cementitious resin was not as brittle as the failure with an epoxy resin. Al-Saadi et al.[14] assessed the residual capacity of fatigue-damaged concrete beams strengthened with NSM CFRP incorporating a cementitious adhesive. Until failure occurred, debonding of the CFRP was not observed, and the interfacial transition zone between the strengthening system and the concrete seemed to be uniform. Kuntal et al.[15] carried out a test program on the pullout and shear strengthening of concrete members with NSM CFRP. The bonding agent was a cement grout possessing a 7-day compressive strength

ACI Structural Journal, V. 120, No. 4, July 2023.

MS No. S-2022-152.R1, doi: 10.14359/51738720, received August 23, 2022, and reviewed under Institute publication policies.

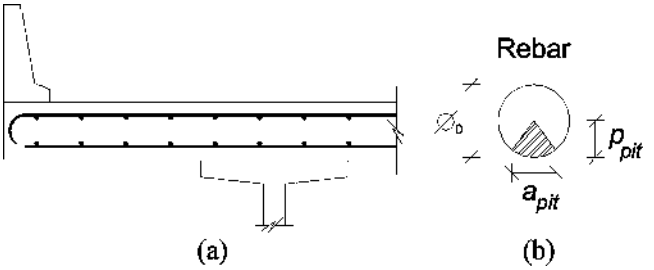

Fig. 1—Corrosion damage: (a) benchmark bridge deck; and (b) pitting corrosion.

of 45 MPa (6526 psi). The installed CFRP strips inhibited the opening of cracks and lowered the evolution of concrete strains. Further details about NSM CFRP coupled with inorganic resins are covered in review articles.[16,17]

Despite their rapid growth and auspicious potential, there is a dearth of knowledge on the application of cementitious resins for adhering NSM CFRP. Especially, the types of usable inorganic resins are still restrictive, and, in most cases, ordinary mortar preponderates in the community. This paper explores the suitability of emerging cementitious resins as part of retrofit technologies, including polyester-silica, ultra-high-performance concrete (UHPC), and geopolymer. Accompanied by the rheological and mechanical characteristics of these resins, the performance of reinforced concrete beams strengthened with NSM CFRP is studied with the aim of elucidating flexural capacities, displacements, and failure modes. To reflect realistic circumstances, the beams are damaged by stochastically simulated corrosion. Analytical modeling accounts for the pertinence of existing design approaches and renders a practice protocol with a modification factor.

RESEARCH SIGNIFICANCE

To advance the state of the art, the relevance of nonconventional bonding agents is examined for the NSM method. The interaction between the cementitious resins and CFRP strips, which is inherent in the fundamental mechanics of the retrofit system, plays an important role in governing the behavior of the strengthened beams. Through the acquaintance gained from the experimental program combined with theoretical modeling, an obscure facet is construed in the discipline of NSM CFRP. The proposed design recommendations allow for a broad range of damage levels paired with a cross-sectional loss in steel reinforcement, equivalent to 100 years of pitting corrosion. Recognizing the propitious opportunity and technical competency of the inorganic resins brings to light the cutting-edge research of structural rehabilitation and will eventually constitute a section in practice guidelines.

SIMULATION OF CORROSION DAMAGE

A benchmark bridge deck was designed to simulate the ramifications of corrosion under an aggressive service environment (Fig. 1(a)). The thickness of the deck was 250 mm (10 in.) with a strip width of 1 m (3.3 ft), which was reinforced by No. 4 bars (12.7 mm [0.5 in.] in diameter) at a cover depth of 63.5 mm (2.5 in.). The following is a description of the initiation and progression of corrosion damage.

Corrosion initiation

Equation (1) predicts the initiation of corrosion (t_i) in years[18]

$$t_i = \frac{C^2}{4D_c}\left[\text{erf}^{-1}\left(\frac{C_{cr} - C_0}{C_i - C_0}\right)\right]^{-2} \quad (1)$$

where C is the concrete cover in cm; D_c is the diffusion coefficient in cm^2/s; erf is the Gauss error function; and C_{cr}, C_0, and C_i are the critical, equilibrium, and initial chloride concentrations, respectively. According to published papers, the following properties were taken: $D_c = 1 \times 10^{-8}$ cm^2/s (1.55×10^{-9} in.^{2}/s) for a bridge member exposed to corrosive environments,[19] $C_{cr} = 0.4\%$ and $C_i = 0\%$ (weight % of the cement),[20] and $C_0 = 1.6\%$.[18]

Pitting corrosion

The pitting depth of the reinforcement (p_{pit} in Fig. 1(b)) may be calculated by

$$p_{pit}(t) = \alpha_p\left(\frac{1}{2}(\phi_0 - \phi_{t_p}(t))\right) \quad (2)$$

where α_p is the pitting factor ($\alpha_p = 4$)[21]; and ϕ_0 and ϕ_{t_p} are the diameters of the initial and damaged reinforcing bars, respectively. The reduced diameter of the steel is estimated using[22,23]

$$\phi_{t_p}(t) = \phi_0 - r_{corr}(t_p) \quad (3)$$

$$r_{corr}(t_p) = C_c\frac{W_a\, i_{corr}(t_p)}{n\rho} \quad (4)$$

$$i_{corr}(t_p) = \frac{37.8(1 - w/c)^{-1.64}}{C}k_1 t_p^{k_2} \quad (5)$$

where t_p is the corrosion time in years ($t_p = t_{current} - t_i$); C_c is a conversion factor ($C_c = 0.00327$ for mm/year); W_a is the atomic weight of iron ($W_a = 55.9$ g/mol [0.12 lb/mol]); $i_{corr}(t_p)$ is the corrosion current density in μA/cm^2; n is the number of electrons in iron ($n = 2$ for Fe → Fe^2 + 2e); ρ is the density (7 g/cm^3 [0.25 lb/in.^{3}]); w/c is the water-cement ratio in concrete; and k_1 and k_2 are constants ($k_1 = 0.85$ and $k_2 = -0.3$ after 1 year of corrosion initiation). The width of the pitted portion ($a_{pit}(t)$ in Fig. 1(b)) is

$$a_{pit}(t) = 2p_{pit}(t)\sqrt{1 - \left(\frac{p_{pit}(t)}{\phi_0}\right)^2} \quad (6)$$

The time-dependent pitting and width ratios of the reinforcing bar ($R_p(t)$ and $R_w(t)$, respectively) are defined as

$$R_p(t) = (p_{pit}(t)/\phi_0) \quad (7)$$

$$R_w(t) = (a_{pit}(t)/\phi_0) \quad (8)$$

Table 1—Statistical properties for stochastic simulation

Variable	Mean	COV	Distribution	Reference
Geometry	Various	0.03	Normal	Okeil et al.[25]
Concrete cover (C)	63.5 mm	0.2	Normal	Li and Melchers[26]
Critical concentration (C_{cr})	0.4%	0.38	Normal	Val and Stewart[27]
Equilibrium concentration (C_0)	1.6%	0.50	Lognormal	Stewart and Rosowsky[28]
Diffusion coefficient (D_c)	1×10^{-8} cm^2/s	0.75	Lognormal	Stewart and Rosowsky[28]
Water-cement ratio (w/c)	0.4	0.10	Normal	Fox et al.[29]
Reinforcing bar diameter (ϕ_0)	12.7 mm	0.015	Normal	Nowak and Collins[30]
Yield strength of steel (f_y)	414 MPa	0.025	Normal	Mirza et al.[31]
Concrete strength (f_c')	27 MPa	0.125	Normal	Nowak and Collins[30]
Concrete crushing strain (ε_{cu})	0.003	0.15	Lognormal	Baji and Ronagh[32]
Cross-sectional area of steel (A_s)	Various	0.015	Normal	Nowak and Collins[30]
Pitting corrosion (a_{pit} and p_{pit})	Various	0.10	Normal	Kim et al.[33]
Elastic modulus of CFRP (E_f)	124 GPa	0.20	Lognormal	Atadero and Karbhari[34]
Cross-sectional area of CFRP (A_f)	32 mm^2	0.05	Lognormal	Atadero and Karbhari[34]

Note: COV is coefficient of variation; 1 mm = 0.0394 in.; 1 cm^2 = 0.16 in.^{2}; 1 MPa = 145 psi; 1 GPa = 145 ksi.

Upon determining $R_p(t)$ and $R_w(t)$, the attributes of pitting corrosion in any reinforcing bar size at time t ($p_{pit}(t)$ and $a_{pit}(t)$) can be attained.

Monte Carlo simulation

Because corrosion characteristics are intrinsically stochastic in a concrete structure, the formulated models were simulated by the Monte Carlo method. This numerical technique generates possible outcomes based on random sampling, which is suitable for solving complex engineering problems with uncertainties.[24] The statistical properties and distribution types enumerated in Table 1 were substituted into Eq. (1) to (5) for the inference of corrosion initiation years and the $R_p(t)$ and $R_w(t)$ ratios up to a service period of 100 years, employing over 50,000 samples.

Pitting corrosion

Figures 2(a) and (b) display the simulated corrosion initiation years and pitting ratios of the benchmark bridge deck, respectively (selected cases are visible for brevity). The density of the data was concentrated within a certain range, albeit scattered, which means that representative values with high occurrence probability can be identified for each parameter. The predicted corrosion initiation time of 20.5 years (Fig. 2(a)), on average, was reasonably close to a reported period of 20 to 30 years.[35,36] As shown in Fig. 2(b), with the increased service year, the extent of deviation was enlarged in the pitting ratio due to accumulated uncertainties. The average pitting and width ratios of the reinforcement after the onset of corrosion are charted in Fig. 2(c) and (d), respectively. The magnitudes of these ratios noticeably went up between 25 and 50 years, pointing out the active progression of corrosion. The literature states that piled rust retards the ingress of oxygen when significant corrosion develops,[37] thereby decelerating electrochemical reactions necessary for the pitting damage.

LABORATORY EXPERIMENT

A test program is delineated to outline material properties, specimen preparation, retrofitting schemes, and instrumentation. For material- and structure-level investigations, mechanical and rheological techniques are used.

Materials

The specified compressive strength of the ready mixed concrete was $f_c' = 25$ MPa (3630 psi). Five cylinders (100 mm [4 in.] in diameter by 200 mm [8 in.] in depth) were tested per ASTM C39/C39M-18,[38] and the average 28-day strength of the cylinders was found to be 27 MPa (3920 psi). The yield strength and elastic modulus of Grade 60 steel reinforcing bars were $f_y = 414$ MPa (60 ksi) and $E_s = 200$ GPa (29,000 ksi), respectively. Prefabricated CFRP strips with dimensions of 2 mm (0.08 in.) in thickness and 16 mm (0.63 in.) in width were the primary strengthening material, comprising high-strength carbon fibers and an epoxy resin. The unidirectional composite strips possessed a tensile strength of $f_{fu} = 2068$ MPa (300 ksi) and a corresponding modulus of $E_f = 124$ GPa (18,000 ksi) with an ultimate strain of $\varepsilon_{fu} = 0.017$. The textured surface of this commercial product enhances the bond against an adhesive. Three types of cementitious resins were employed as bonding agents: polyester-silica, UHPC, and geopolymer. To produce polyester-silica, a catalyst was added to a polyester liquid and the chemically reactive solution was mixed with silica sand at a ratio of 20% and 80% by mass, respectively. The silica had an SiO_2 content of 90.3% with a particle size of 0.45 mm (0.018 in.). The non-shrink UHPC mixture was composed of particle-optimized ingredients along with carbon nanofibers (detailed information is not reported owing to contractual obligations). As guided by the manufacturer's manual, a paste and a deformer were blended with tap water in a mixer for 2 minutes; then, packaged dry powders were added and stirred for an additional 6 minutes until a homogeneous grout was achieved. The geopolymer was an aluminosilicate

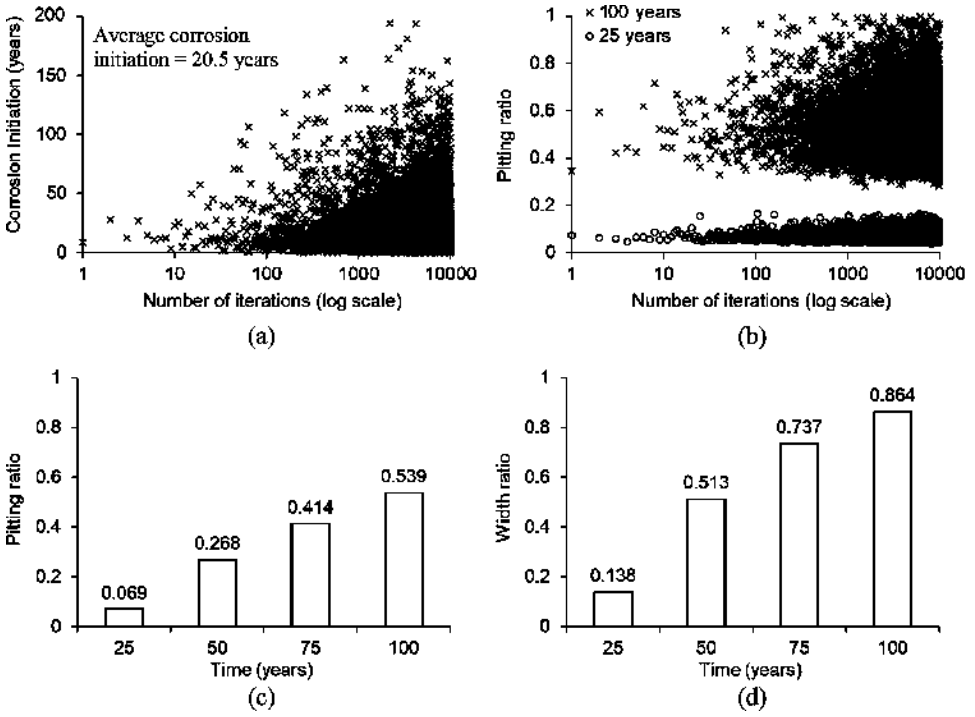

Fig. 2—Corrosion damage of benchmark bridge deck: (a) simulated corrosion initiation years; (b) simulated pitting ratio; (c) average pitting ratio; and (d) width ratio.

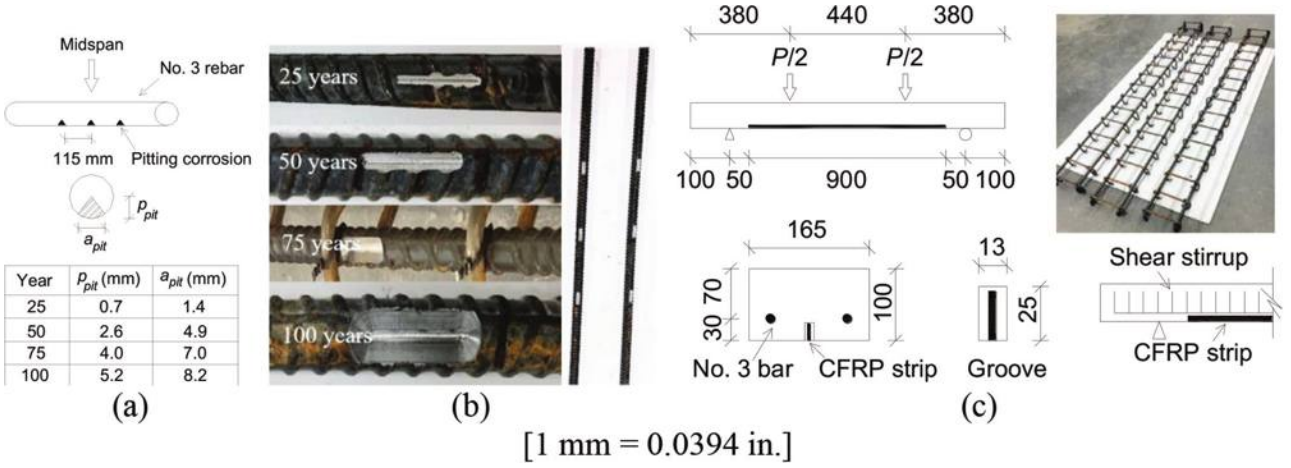

Fig. 3—Beam details (units in mm): (a) pitting corrosion; (b) simulated corrosion damage; and (c) dimensions.

matrix with the succeeding nominal properties: a setting time of 60 minutes,[39] a 28-day shrinkage of 0.07%,[40] a chloride penetration of 60 mm (2.4 in.) at 90-day ponding,[41] and a freezing-and-thawing loss of 0% at 300 cycles.[42]

Specimens

Pitting corrosion—The stochastic model described previously was implemented to replicate pitting corrosion in steel reinforcement (No. 3 bars). Multiplying the diameter of $\phi_0 = 9.53$ mm (0.375 in.) by the simulated pitting and width ratios (Fig. 2), corrosion damage was estimated from 25 to 100 years (Fig. 3(a)). Three spots, targeted near the middle of each reinforcing bar, were cut using a high-precision computer-numerical-control milling machine (Fig. 3(b)).

Cubes and beams—Referring to ASTM C109/C109M-20,[43] 15 cubes (50 mm [2 in.], each side) were cast with the cementitious resins and moisture-cured under a relative humidity of 99% for 14 days. Reinforced concrete beams were prepared with dimensions of 165 mm (6.5 in.) in width by 100 mm (4 in.) in depth by 1200 mm (4 ft.) in length. The machined No. 3 reinforcing bars were located at an effective depth of 70 mm (2.75 in.), as depicted in Fig. 3(c), and No. 2 shear stirrups (6.35 mm [0.25 in.] in diameter) were placed at spacings of 75 mm (3 in.) to ensure flexural failure. A polystyrene strip (900 mm [35 in.] long) was positioned underneath the steel cage for the installation of NSM CFRP and then the concrete was placed.

Strengthening plan

After 28 days of curing in an environmental chamber at 99% relative humidity and 23°C (73°F), all beams were taken out, cleaned with an airbrush, washed, and fully dried.

Table 2—Test matrix

Identification	Resin	Corrosion time, years	Cross-sectional area of steel, mm^2	Ultimate load, kN
P25	Polyester-silica	25	141	47.0
P50	Polyester-silica	50	129	45.2
P75	Polyester-silica	75	114	40.4
P100	Polyester-silica	100	99	38.6
U25	UHPC	25	141	40.5
U50	UHPC	50	129	38.5
U75	UHPC	75	114	37.6
U100	UHPC	100	99	37.3
G25	Geopolymer	25	141	38.5
G50	Geopolymer	50	129	38.3
G75	Geopolymer	75	114	33.8
G100	Geopolymer	100	99	32.3

Note: 1 mm^2 = 0.0016 $in.^2$; 1 kN = 0.225 kip.

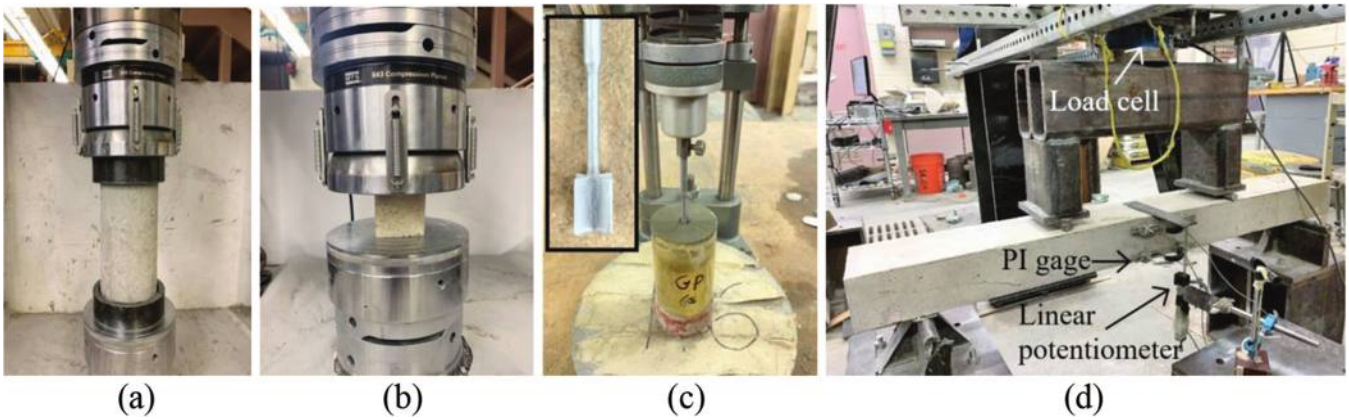

Fig. 4—Test methods: (a) concrete cylinder; (b) resin cube; (c) workability; and (d) beam.

The groove of the beams, created by the polystyrene, was ground using a knotted-wire steel wheel to improve the bond against the cementitious resins. It should be noted that the groove size of 25 mm (1 in.) deep and 13 mm (0.5 in.) wide was in compliance with the provisions of ACI 440.2R-17.[9] The inorganic resins were mixed as explained earlier and applied to approximately 70% of the groove depth; afterward, a single piece of CFRP (900 mm [35 in.] long) was firmly inserted and the remaining portion of the groove was filled. In line with the findings of preliminary testing on the strength of the resins (that is, the strength converged after 14 days), the CFRP-bonded beams were additionally cured for 14 days. Table 2 imparts the identification of the prepared beams, depending upon the type of resin and the simulated time of corrosion. For example, the P75 specimen indicates that a beam suffering 75 years of corrosion was CFRP-strengthened with polyester-silica. It is worth noting that unstrengthened beams were not tested because the focus of the study was on exploring the performance of the cementitious resins.

Test methods

Compressive strength—The previously mentioned cylinders and cubes were monotonically compressed to obtain the strength of the concrete and resins (Fig. 4(a) and (b)).

Workability—Given that the morphological nature of the cementitious resins differs from that of conventional epoxies when filling a narrow groove, workability was regarded to be crucial. A vane shear test was performed to measure the rheology of the three resin types (Fig. 4(c)). Cylindrical containers (45 mm [1.8 in.] in diameter and 100 mm [4 in.] in depth) were filled with the individual resins, and the inserted vane (12.7 mm [0.5 in.] in width and 12.7 mm [0.5 in.] in height) was rotated at 0.1 rpm for 60 minutes. Strain rates were acquired (details will be described) for the appraisal of angular velocities that would quantify the resins' applicability to NSM CFRP.

Flexure—The strengthened beams were loaded under four-point bending at a rate of 1 mm (0.0394 in.)/min (Fig. 4(d)). The simply supported beams were instrumented with a load cell and a linear potentiometer at midspan to record the applied load and the displacement, respectively. Strain transducers, customarily called PI gauges, were mounted at a distance of 25 mm (1 in.) from the top and

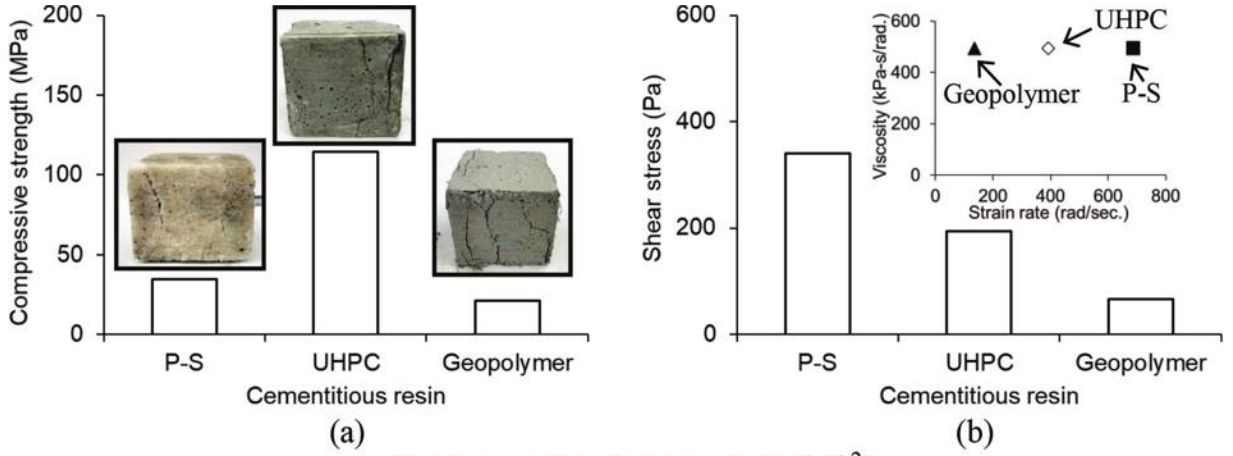

Fig. 5—Properties of cementitious resins: (a) average compressive strength at 14 days of curing; and (b) workability.

bottom of the beams for monitoring compressive and tensile deformations, respectively.

RESULTS AND DISCUSSION

The outcomes of laboratory testing are gleaned and analyzed with an emphasis on the practicality of cementitious resins as bonding agents for NSM CFRP strips. Of interest are the flexural responses of retrofitted beams with pre-damage and the feasibility of the resins.

Properties of cementitious resins

Figure 5(a) summarizes the compressive strength of the cementitious resins. The average 14-day strength of 34.4 MPa (4989 psi) in polyester-silica was higher than the 28-day strength of the concrete (27 MPa [3920 psi]). This illustrates that cross-linked monomers, stemming from the condensation reactions of the resin,[44] were more efficacious compared with the load bearing of the coarse aggregates. It is also known that the strong bond between the polyester and silica was accomplished by mutual engagement through the rough interfacial surfaces.[45] The strength of UHPC reached over 115 MPa (16,679 psi), which was ascribed to the prompt hydration associated with the fine binder particles and tricalcium silicate.[46] From a mechanical standpoint, the carbon nanofibers in the UHPC mixture induced the so-called bridging effect that precluded the formation of microcracks.[47] The strength of the geopolymer resin was 21 MPa (3045 psi): prior research clarifies that the dissolution of aluminum and silicon and the polycondensation with metallic minerals were instrumental in resisting external loadings.[48]

Shown in Fig. 5(b) is an assessment of the resins' workability. The angular change of the vane ($\Delta\theta$) was logged and converted to a shear stress using[49]

$$\tau = \frac{K\Delta\theta}{\pi\left(\frac{D^2H}{2} + \frac{D^3}{6}\right)} \quad (9)$$

where τ is the shear stress of the fresh resin, equivalent to the rotational resistance of the vane; K is the spring constant (1.85 N·mm [0.016 lb·in.] per angular change); and D and H are the width and depth of the vane, respectively. The shear stress of polyester-silica was 340 Pa (6.8 lb/ft^2), which was 175% and 507% higher than those of UHPC and geopolymer, respectively. The inset of Fig. 5(b) reveals the viscosity of the resins with respect to strain rate. In accordance with the theory of Newtonian fluids,[50] the viscosity of an amorphous material is defined as the ratio of shear stress to strain rate ($\Delta\theta$ per unit time). To gain a viscosity of 494 kPa·s/rad (0.07 ksi·s/rad) during the test period of 60 minutes, polyester-silica required a strain rate of 688 rad/s; contrarily, UHPC and geopolymer necessitated 393 rad/s and 135 rad/s, respectively. In other words, the internal friction of polyester-silica was much higher, and thus its workability was concluded to be the least favorable among the three resins.

Capacity

The ultimate load of the test beams is graphed in Fig. 6(a). The flexural capacity of the strengthened beam with polyester-silica at a simulated corrosion period of 25 years (P25 in Table 2) was 47.0 kN (10.6 kip), whereas the capacities of the beams with UHPC (U25) and geopolymer (G25) were 40.5 and 38.5 kN (9.1 and 8.7 kip), respectively. This tendency was maintained irrespective of the corrosion time, leading to the fact that the polyester-silica resin outperformed the other types. Furthermore, it was substantiated that the strength of the cementitious resins (Fig. 5(a)) was not directly proportional to the functionality as a bonding agent for NSM CFRP application. The implications of the corrosion damage are described in Fig. 6(b), where the time-dependent capacities are normalized by the 25-year capacities belonging to the individual resins. The load drop ratio of the beams with UHPC consistently dwindled up to 100 years: 4.96% (25 to 50 years), 2.31% (50 to 75 years), and 0.79% (75 to 100 years). Regarding the beams with polyester-silica and geopolymer, the variation in the load ratios was similar and conspicuous reductions were noticed beyond 50 years. For instance, the drop ratios of the beams with geopolymer were 0.73% (25 to 50 years) and 11.6% (50 to 75 years). It is, hence, stated that the UHPC resin better interacted with the residual cross-sectional area of the corrosion-damaged steel reinforcement and demonstrated reliable long-term

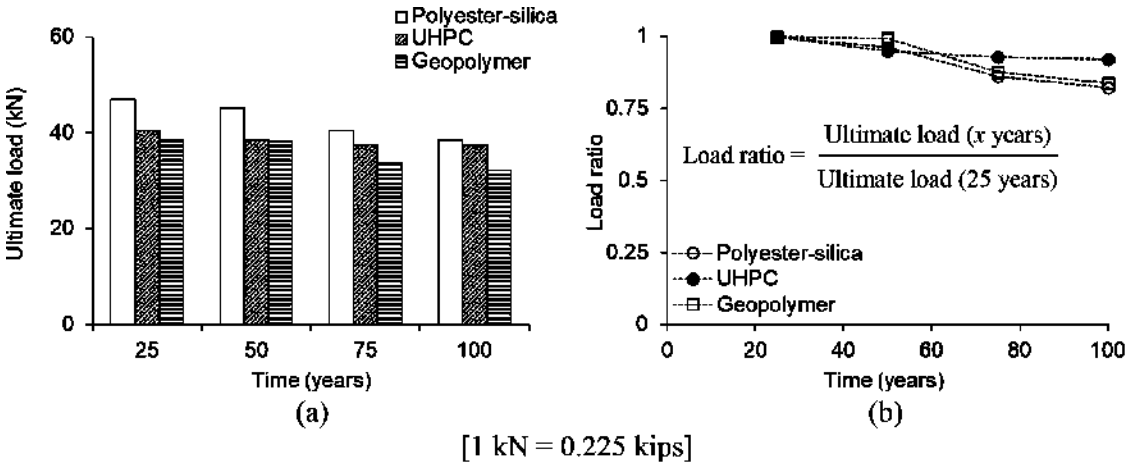

Fig. 6—Flexural capacity of strengthened beams: (a) ultimate load; and (b) load ratio.

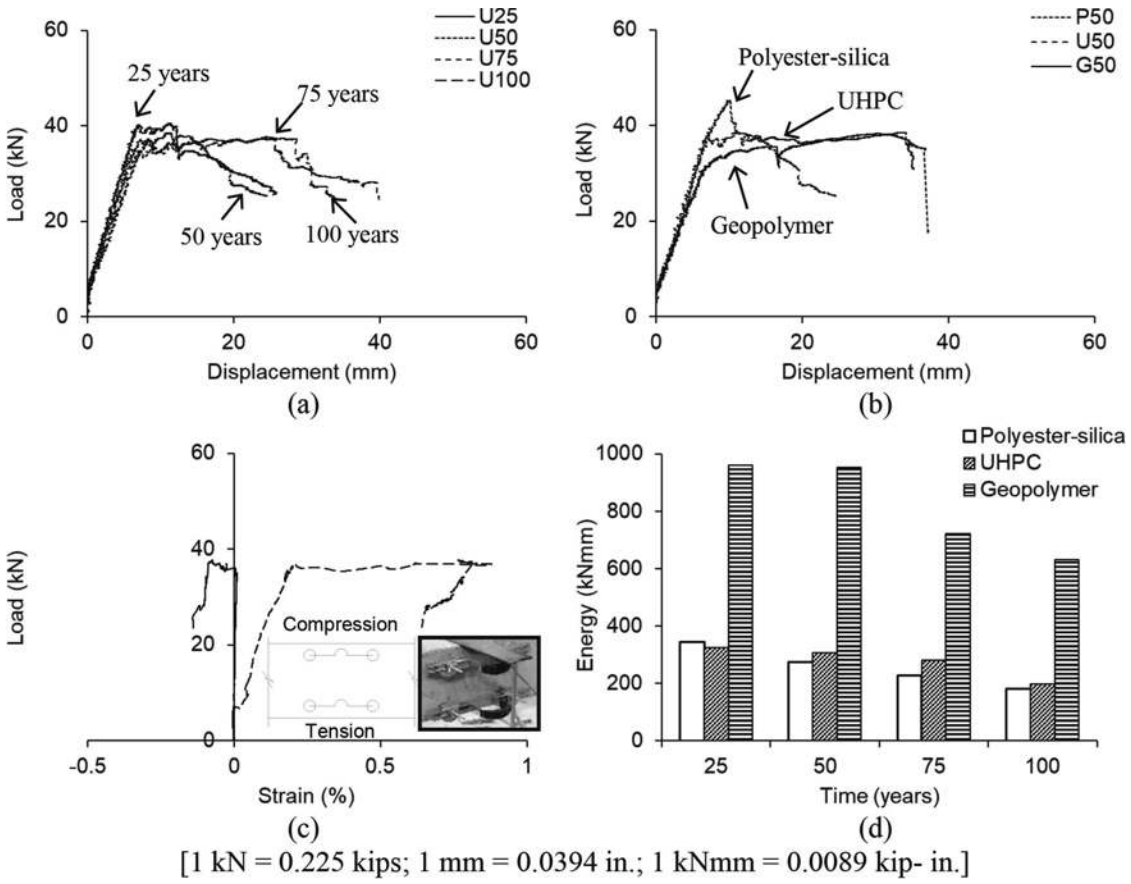

Fig. 7—Flexural behavior: (a) load-displacement for UHPC; (b) comparison of load-displacement at 50 years; (c) strains of U75 beam; and (d) energy dissipation.

performance; specifically, the high-strength UHPC effectively distributed tensile stresses to those reinforcing bars and alleviated strain localizations.

Flexural behavior

Figure 7(a) exhibits the load-displacement relationship of the UHPC-bonded beams. The declined pre-yield slope with an increase in corrosion year signifies that the narrow CFRP strip did not appreciably upgrade the serviceability of the beams. Technically speaking, the transformed CFRP area accounted for 3.6 to 4.0% of the cracked concrete sections with a modular ratio of n_f = 5.05; that is, $n_f A_f$ = 161 mm^2 (0.25 in.^{2}) versus A_{ct} = 4482 and 4020 mm^2 (6.95 and 6.23 in.^{2}) at 25 and 100 years, respectively, where A_f is the cross-sectional area of CFRP; and A_{ct} is the area of the cracked concrete section, respectively. The yield load of the beams was a function of corrosion due to the reduced steel areas, and the fluctuating yield plateaus imply that the UHPC resin fractured periodically (supplementary discussions will be given). As the damage level rose, the breadth of the plateaus enlarged, which is attributable to the lowered steel reinforcement ratio: ρ_s = 1.22% and 0.86% at 25 and

100 years, respectively, in which $\rho_s = A_s/(bd)$, where A_s is the steel area; b is the beam width; and d is the effective depth of the beam. The effects of the resin type are plotted in Fig. 7(b) at a selected period of 50 years. The response of all beams was virtually identical until a load of 23.4 kN (5.3 kip); then, a bifurcation was noted in the beam with geopolymer (G50). Unlike the case of the U50 and G50 beams, the P50 beam showed an abrupt load drop. Care should thus be exercised when adopting polyester-silica for strengthening purposes. The archetypal development of compressive and tensile strains under flexural loading was logged (Fig. 7(c)); however, meaningful comparisons were not available because several readings were corrupted (concrete cracks traversed the installation points of the PI gauges). By numerically integrating the load-displacement curves, the energy of the beams that dissipated up to the peak loads was quantified and is charted in Fig. 7(d). The increased corrosion years lessened the energy levels in all categories. While the use of geopolymer significantly raised the energy dissipation capability, the resin's efficacy plummeted after 50 years. Considering that volume changes and grain friction dominate the inelastic energy dissipation of geopolymer,[51] the decreased steel reinforcement ratios in the G75 and G100 beams appeared to influence the deformational characteristics of the resin.

Failure mode

General pattern—The failure modes of the test beams are pictured in Fig. 8. Although concrete crushing caused the ultimate limit state of all beams in conjunction with flexural and shear cracks, the degree of corrosion and the retrofitting schemes also affected the failure mechanisms. The UHPC-bonded beams at 25 and 50 years (U25 and U50 in Fig. 8(a), respectively) displayed regional failure; on the other hand, those at 75 and 100 years (U75 and U100 in Fig. 8(a), respectively) showed distributed cracks along the loading span. This fact denotes that the applied bending moment spread with a decrease in the beam's reinforcement ratio (ρ_s = 1.22% at 25 years versus ρ_s = 0.86% at 100 years). Such a trend was also observed in the beams with polyester-silica (P25 and P100 in Fig. 8(b)), which was different from the beams with geopolymer (G25 and G100 in Fig. 8(b)) that failed with a few vertical cracks.

Interfacial aspect—The interface between the concrete substrate and CFRP is seen in Fig. 9. Regardless of corrosion time, the integrity of the retrofit system was preserved in the UHPC-bonded beams (U25 and U100 in Fig. 9(a) and (b), respectively). The recurrent crack spacings and the fractured resin were responsible for the oscillating yield plateaus that were articulated in Fig. 7(a). The tensile soffit of the system alongside polyester-silica (P100 in Fig. 9(c)) was analogous to the foregoing cases, except for the several secondary cracks. Contrary to these groups, debonding was spotted in the geopolymer beam after the crushing of the concrete (Fig. 9(d)). The far-right diagonal tension crack near the support (dotted circle) coupled with the relatively weak resin brought about a geometric discontinuity and precipitated the bond failure.

MODELING

Analytical models are formulated to comprehend the degree of stress transfer from a concrete substrate to CFRP strips, dependent upon the type of cementitious resins. Upon examining the adequacy of traditional design approaches, a modification factor is suggested to properly accommodate the repercussions of such resins for an NSM-strengthening system.

Assessment of ACI 440.2R-17

Two possible failure classes are stated in ACI 440.2R-17[9]: 1) concrete crushing at the maximum usable strain of $\varepsilon_{cu} = 0.003$; and 2) CFRP debonding at $\varepsilon_{fd} = 0.7\varepsilon_{fu}$ for an NSM system. Assuming that plane sections remain plane (complete composite action) and force equilibrium is satisfied, a sectional analysis may be conducted to predict the ultimate load of the test beam with the CFRP strip (P_u)

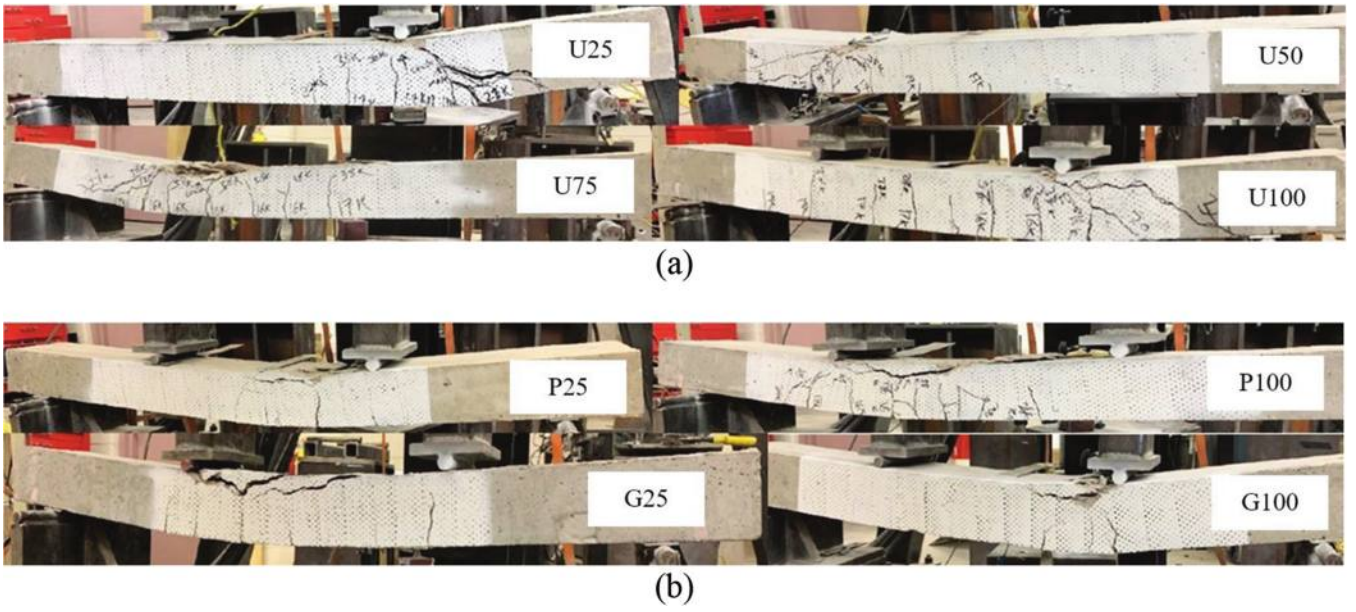

Fig. 8—Failure mode: (a) beams with UHPC; and (b) beams with polyester-silica and geopolymer.

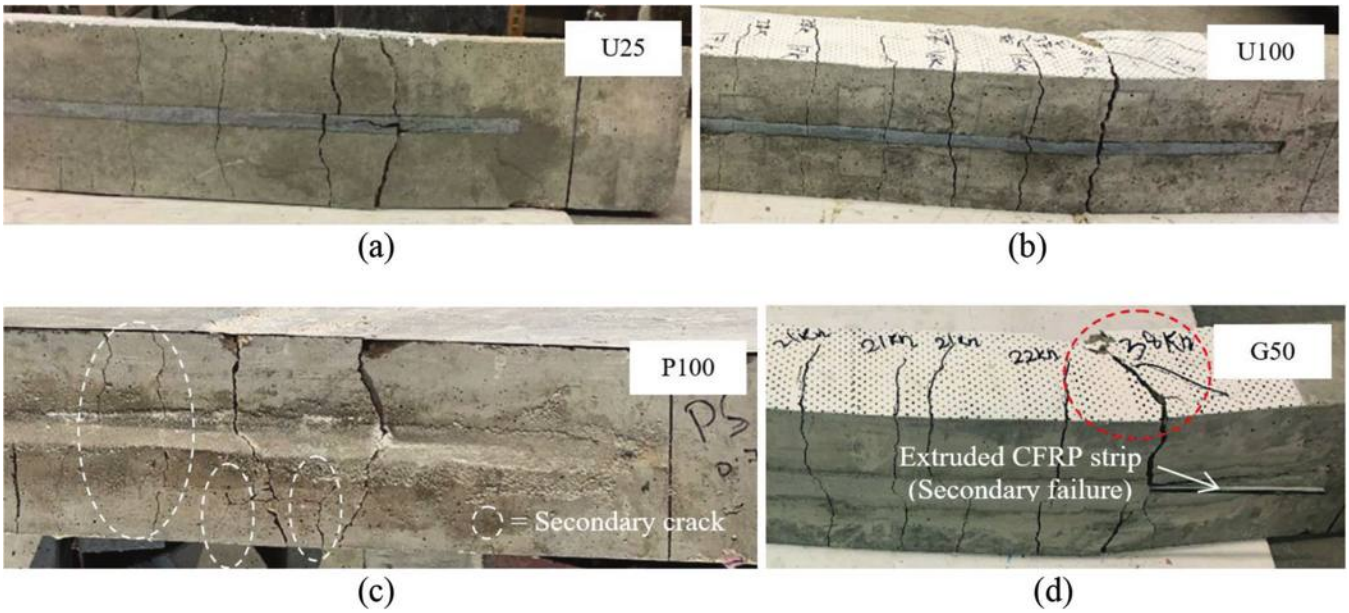

Fig. 9—Interface between CFRP and substrate: (a) beam with UHPC at 25 years; (b) beam with UHPC at 100 years; (c) beam with polyester-silica at 100 years; and (d) beam with geopolymer at 50 years.

subjected to concrete crushing ($\varepsilon_c = \varepsilon_{cu}$, in which ε_c is the concrete strain at the top of the beam)

$$P_u = \frac{2(M_{ns} + M_{nf})}{a} \tag{10}$$

$$M_{ns} = A_s f_y \left(d - \frac{\beta c}{2}\right) \tag{11}$$

$$M_{nf} = A_f f_f \left(d_f - \frac{\beta c}{2}\right) \tag{12}$$

where M_{ns} and M_{nf} are the nominal moment resistance of the steel and CFRP components, respectively; β is the stress block factor; c is the neutral axis depth; f_f is the CFRP stress; and d_f is the distance from the extreme compression fiber of the beam to the centroid of the CFRP strip. In the event of debonding ($\varepsilon_c < \varepsilon_{cu}$), the resultant compressive force of the concrete can be estimated by the equivalent rectangular block with[9]

$$\alpha_1 = \frac{3\varepsilon_c'\varepsilon_c - \varepsilon_c^2}{3\beta_1(\varepsilon_c')^2} \tag{13}$$

$$\beta_1 = \frac{4\varepsilon_c' - \varepsilon_c}{6\varepsilon_c' - 2\varepsilon_c} \tag{14}$$

$$\varepsilon_c' = 1.7 f_c'/E_c \tag{15}$$

where α_1 and β_1 are the empirical factors; and E_c is the elastic modulus of the concrete ($E_c = 57{,}000\sqrt{f_c'}$ psi [$4730\sqrt{f_c'}$ MPa][52]). Provided in Fig. 10(a) are the calculated concrete and CFRP strains pursuant to the provisions of ACI 440.2R-17[9] when the retrofitted section failed. The invariant CFRP strains gradually ascended after the initiation of corrosion, and the strain levels appertaining to the debonding scenario were 22.2% lower than those to the crushing condition, on average. The concrete strains related to the debonding failure were almost constant because the increased steel strains, resulting from the corrosion damage, were offset by the shortened neutral axis depth. As shown in Fig. 10(b), the load-carrying capacity of the retrofitted beam steadily diminished over time, including an average difference of 11.0% between the compression- and tension-controlled sections. Figures 10(c) and (d) evaluate the applicability of the ACI 440.2R-17 method. The flexural capacity of the beam with polyester-silica was 11.3% lower than the full capacity estimated by ACI 440.2R-17 (concrete crushing in Fig. 10(c)), on average, followed by 20.2% and 25.9% for the beams with UHPC and geopolymer, respectively. The discrepancy decreased for the tension-controlled section (Fig. 10(d)): the average load ratios of the crushing and debonding were 0.81 (Fig. 10(c)) and 0.91 (Fig. 10(d)), respectively. Overall, the ACI 440.2R-17 approach needs to be revised for the capacity prediction of NSM CFRP bonded with cementitious resins, particularly when the strengthened beam fails by concrete crushing.

Effective stress factor

Principle—As elaborated earlier, the theoretical capacity of the retrofitted section with full composite action overestimated the ultimate load of the test beams. It is rational to conjecture that the applied tensile stresses were in part transferred to the CFRP strip through the inorganic medium; scilicet, the local deformation of the cementitious resins dissipated interfacial energy[53] and mitigated the development of tensile forces in the strip, which brought down the effectiveness of CFRP strengthening. To handle such inconsistency, an effective stress factor (Ω) was proposed for the execution of the sectional analysis, and Eq. (12) was replaced by Eq. (16)

$$M_{nf} = A_f f_{fe} \left(d_f - \frac{\beta c}{2}\right) \tag{16}$$

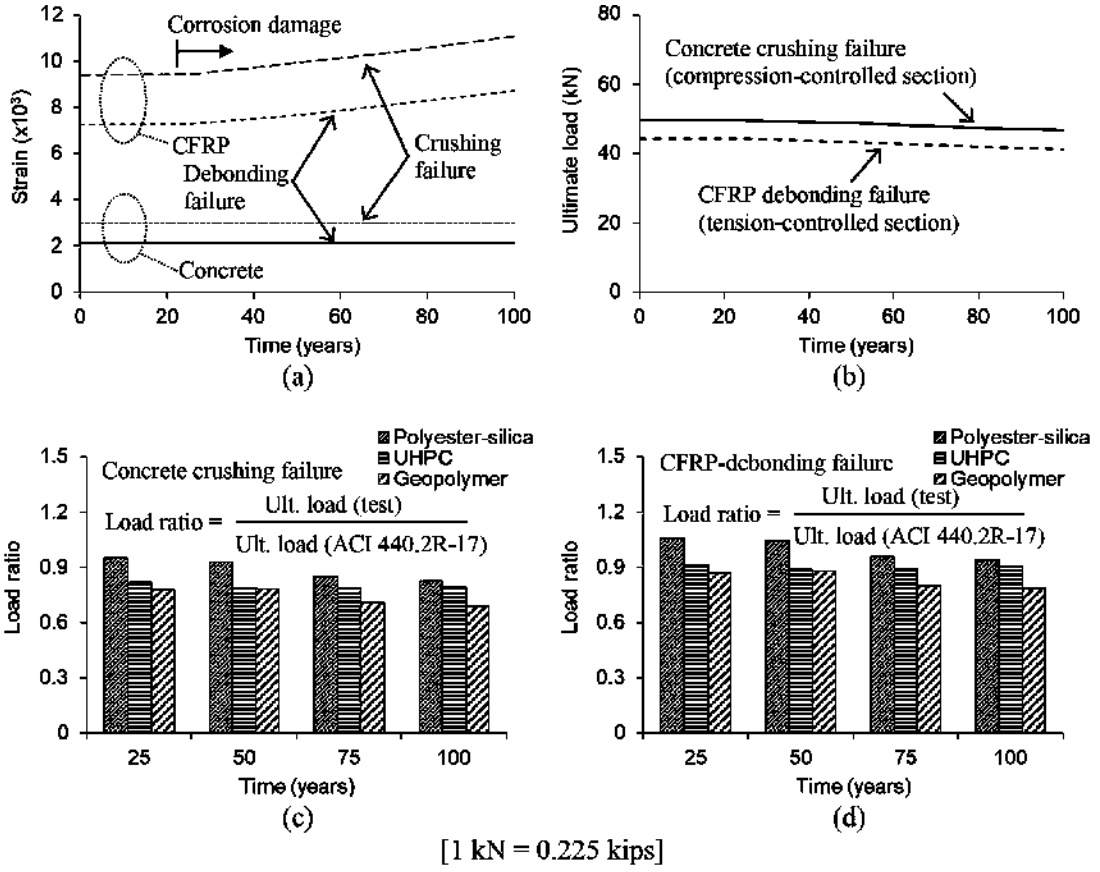

Fig. 10—Assessment of bond performance: (a) calculated strains at failure based on ACI 440.2R-17[9]; (b) capacity based on ACI 440.2R-17[9]; (c) load ratio with compression-controlled section; and (d) load ratio with tension-controlled section.

$$f_{fe} = \Omega f_f = \Omega E_f \varepsilon_f \quad (17)$$

where f_{fe} is the effective stress of CFRP or the fraction of the CFRP stress from the sectional analysis. This concept is similar to the strain reduction factor in prestressed concrete with unbonded tendons.[54] The Ω factor was calibrated by iterating Eq. (10) with assumed c and Ω values until the predicted capacity was equal to its experimental counterpart. Even if CFRP debonding was not considered herein, because concrete crushing was the primary source of failure in all test beams, the same procedure can be adopted with Eq. (13) to (15) when determining the Ω factor for tension-controlled sections.

Implementation—Figure 11(a) compares CFRP strains obtained from the iterative approach (ε_f(cementitious resin)) and the conventional sectional analysis (ε_f(composite action)). On all occasions, the strain ratios were lower than unity, reaffirming the aforementioned partial composite action for the cementitious resins. The strain ratios of the beams with polyester-silica were higher than the ratios of other beams; however, the former was more susceptible to the corrosion damage, with a drop of 16.4% between 50 and 75 years. The collected effective stress factors are given in Fig. 11(b). Aligning with the propensity of the strain ratios, the stress transfer of polyester-silica was superior to that of UHPC and geopolymer (average Ω factor = 0.70 versus 0.47 versus 0.36).

Appraisal—To address potential concerns arising from the limited number of the experimental specimens, Monte Carlo simulations were carried out employing the Ω-based sectional analysis with the statistical properties listed in Table 1. The calibrated effective stress factors were considered to be deterministic, and all other variables were modeled as stochastic parameters. Typical predictions for the beams with polyester-silica at 25 and 100 years are visible in Fig. 11(c). Notwithstanding the scatter of the computed load-carrying capacities, the absolute margin of error was less than 2.0% between the test and simulation (Fig. 11(d)).

Design proposal—In view of the preceding evaluations, the effective stress factors were linked with the corrosion levels, and recommendations are made in Table 3. For practical reasons, the factors were rounded, and three damage categories were defined (Moderate, Significant, and Critical), contingent upon the loss of cross-sectional area in the steel reinforcement. The proposed Ω factors, spanning from 0.30 to 0.80, were intended to be conservative because: 1) the scope of the present research was restrictive; and 2) there would be numerous uncertainties in existing concrete members.

SUMMARY AND CONCLUSIONS

This paper dealt with the relevance of cementitious resins for strengthening reinforced concrete beams with near-surface-mounted (NSM) carbon fiber-reinforced polymer (CFRP) strips. Three types of emerging resins were taken

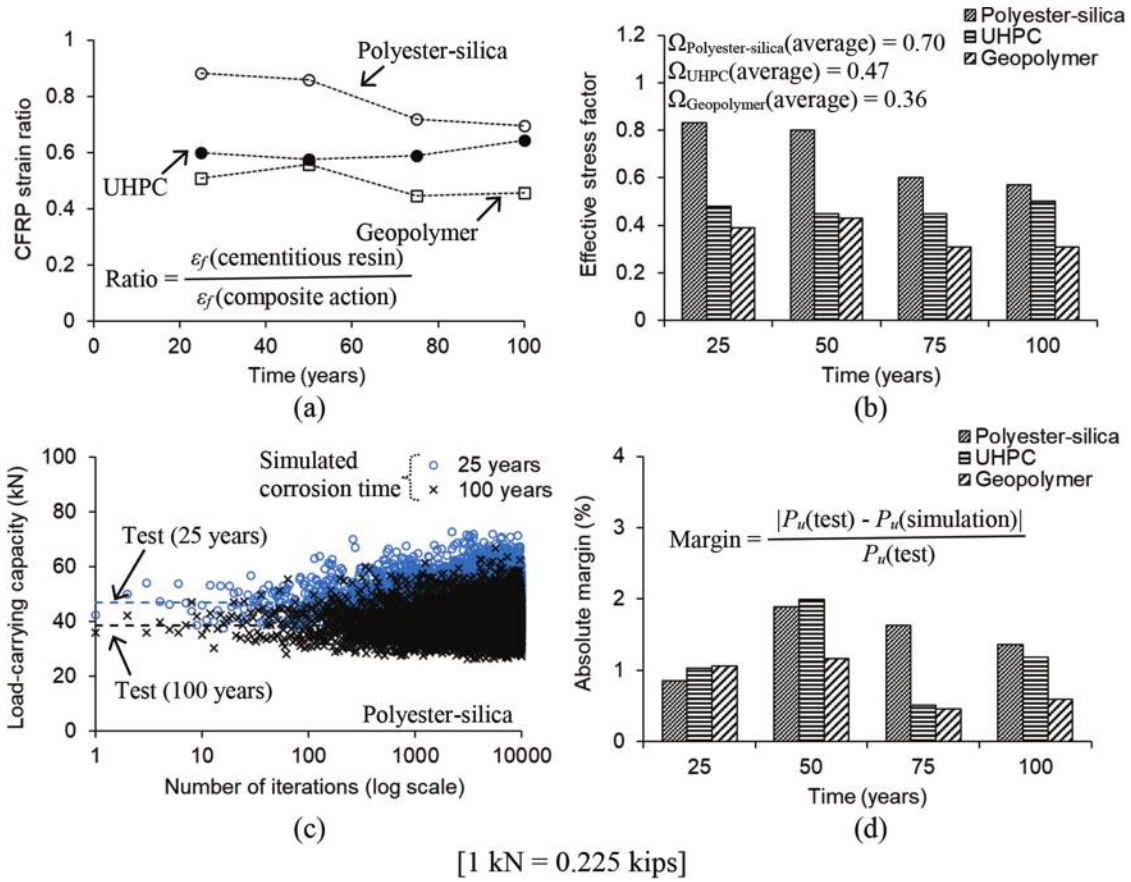

Fig. 11—Bond efficiency of cementitious resins for NSM systems: (a) CFRP strain ratio; (b) effective stress factor; (c) simulated capacity versus test capacity; and (d) average absolute margin between test and simulation.

Table 3—Proposed effective stress factor for cementitious resins

Resin type	Corrosion damage	Expected loss of cross-sectional area of steel reinforcement (ΔA_s)	Effective stress factor (Ω)
Polyester-silica	Moderate	0% ≤ loss < 10%	0.80
	Significant	10% ≤ loss < 20%	0.60
	Critical	30% ≤ loss	0.55
UHPC	Moderate	0% ≤ loss < 10%	0.45
	Significant	10% ≤ loss < 20%	0.45
	Critical	30% ≤ loss	0.45
Geopolymer	Moderate	0% ≤ loss < 10%	0.40
	Significant	10% ≤ loss < 20%	0.30
	Critical	30% ≤ loss	0.30

into consideration: polyester-silica, ultra-high-performance concrete (UHPC), and geopolymer. A wide variety of corrosion intensities were numerically simulated up to 100 years, and representative damage levels were chosen for laboratory testing. A total of 12 strengthened beams were loaded under four-point bending and their load-carrying capacity, displacement, and failure modes were investigated. Additionally, the resins' workability was measured to understand the rheological suitability as a bonding agent for NSM application. As per the findings of the experimental program in tandem with stochastic modeling, design recommendations were suggested. Contemplating that the scope of the research was rather narrow and the number of test specimens was limited, the proposal may be improved by the continuation of a comprehensive study. The following conclusions are drawn:

- There was no correlation between the compressive strength and the rheological resistance of the resins: the workability of polyester-silica showing a strength of 34.4 MPa (4989 psi) was adverse relative to that of UHPC and geopolymer (compressive strength = 115 and 21 MPa [16,679 and 3045 psi], respectively). Nonetheless, all these resins were appropriate bonding agents

that filled the 13 mm (0.5 in.) wide groove of the beams without difficulty.

- Throughout the simulated corrosion period of 100 years, the strengthened beams with polyester-silica demonstrated consistently higher capacities than the beams with other resins. In contrast to the gradually declining capacity of the UHPC-bonded beams with time, the capacity degradation of the polyester-silica- and geopolymer-bonded beams revealed an abrupt transition between 50 and 75 years. Special attention should therefore be paid when retrofitting aged concrete members suffering a substantial loss of steel reinforcement of 10% or more.
- The NSM system did not improve the serviceability of the upgraded beams owing to the marginal influence of the CFRP strip on the transformed concrete section being less than 4.0%. The resin configurations altered the post-yield behavior of the beams. As the level of corrosion rose, the dissipation of flexural energy (up to the peak loads) decreased, in particular for the geopolymer-bonded beams.
- While the cracking pattern of the beams with UHPC and polyester-silica was reliant upon the corrosion year (regional cracking at 25 years versus distributed cracking at 100 years), the beams with geopolymer steadily exhibited localized cracking. The integrity of the CFRP-resin interface was retained until the concrete-crushing failure took place.
- The provisions of ACI 440.2R-17[9] overestimated the capacity of the strengthened beams with the cementitious resins by over 25%. The hypothetical capacities of these beams related to the compression- and tension-controlled sections differed by 12%. With the aim of refining capacity-prediction outcomes, the effective stress factor (Ω) was calibrated and recommended for practice: when deciding the Ω factor ranging from 0.30 to 0.80, the resin type and expected damage level prior to applying the retrofit system should be taken into consideration.

AUTHOR BIOS

Yail J. Kim, *FACI, is President of the Bridge Engineering Institute, An International Technical Society, and a Professor in the Department of Civil Engineering at the University of Colorado Denver, Denver, CO. He is Chair of ACI Subcommittee 440-I, FRP-Prestressed Concrete, past Chair of ACI Committee 345, Bridge Construction and Preservation, and a member of ACI Committees 342, Evaluation of Concrete Bridges and Bridge Elements; 377, Performance-Based Structural Integrity & Resilience of Concrete Structures; and 440, Fiber-Reinforced Polymer Reinforcement; and Joint ACI-ASCE Committee 343, Concrete Bridge Design. He received the Chester Paul Siess Award for Excellence in Structural Research in 2019. His research interests include advanced composite materials for rehabilitation; structural informatics; complex systems; and science-based structural engineering, including statistical, interfacial, and quantum physics.*

Wajdi Ammar *is a PhD Student in the Department of Civil Engineering at the University of Colorado Denver. He received his BS and MS in civil engineering from Sirte University, Sirte, Libya, in 2006, and the University of Colorado Denver in 2021, respectively. His research interests include interface mechanics, advanced composite materials, and structural concrete.*

ACKNOWLEDGMENTS

The authors would like to gratefully acknowledge support from the Libyan Government and the U.S. Department of Transportation through the Mountain-Plains Consortium program. D. Gremel at Owens Corning Infrastructure Solutions and P. Weber at ceEntek donated CFRP and UHPC materials, respectively. Technical contents presented in this paper are based on the opinion of the authors and do not necessarily represent that of others.

REFERENCES

1. Reddy, G. R., "On Structural Rehabilitation and Retrofitting for Risk Reduction," *Civil Engineering for Disaster Risk Reduction*, S. Kolathayar, I. Pal, S. C. Chian, and A. Mondal, eds., Springer, Singapore, 2022, pp. 373-381.

2. Aprile, A., and Monti, G., "Advanced Methods for Structural Rehabilitation," *Buildings*, V. 12, No. 1, Jan. 2022, Article No. 79. doi: 10.3390/buildings12010079

3. Zaiter, A., and Lau, T. L., "Experimental Study of Jacket Height and Reinforcement Effects on Seismic Retrofitting of Concrete Columns," *Structures*, V. 31, June 2021, pp. 1084-1095. doi: 10.1016/j.istruc.2021.02.020

4. Chung, P.-T., and Chou, C.-C., "One-Sided Shear Retrofit of Reinforced Concrete Beams in Existing High-Rise Buildings," *Engineering Structures*, V. 252, Feb. 2022, Article No. 113634. doi: 10.1016/j.engstruct.2021.113634

5. Xue, W.; Tan, Y.; and Peng, F., "Experimental Study on Damaged Prestressed Concrete Beams Using External Post-Tensioned Tendons," *ACI Structural Journal*, V. 117, No. 1, Jan. 2020, pp. 159-168.

6. Labò, S.; Passoni, C.; Marini, A.; and Belleri, A., "Design of Diagrid Exoskeletons for the Retrofit of Existing RC Buildings," *Engineering Structures*, V. 220, Oct. 2020, Article No. 110899. doi: 10.1016/j.engstruct.2020.110899

7. Zhang, C.; Huang, W.; Zhou, Y.; and Luo, W., "Experimental and Numerical Investigation on Seismic Performance of Retrofitted RC Frame with Sector Lead Viscoelastic Damper," *Journal of Building Engineering*, V. 44, Dec. 2021, Article No. 103218. doi: 10.1016/j.jobe.2021.103218

8. Cao, X.-Y.; Wu, G.; and Ju, J.-W. W., "Seismic Performance Improvement of Existing RCFs Using External PT-PBSPC Frame Sub-Structures: Experimental Verification and Numerical Investigation," *Journal of Building Engineering*, V. 46, Apr. 2022, Article No. 103649. doi: 10.1016/j.jobe.2021.103649

9. ACI Committee 440, "Guide for the Design and Construction of Externally Bonded FRP Systems for Strengthening Concrete Structures (ACI 440.2R-17)," American Concrete Institute, Farmington Hills, MI, 2017, 112 pp.

10. Grande, E., and Milani, G., "Numerical Study of the Bond Behavior of DMF Systems," *Structures*, V. 31, June 2021, pp. 921-939. doi: 10.1016/j.istruc.2021.02.013

11. De Lorenzis, L., and Teng, J. G., "Near-Surface Mounted FRP Reinforcement: An Emerging Technique for Strengthening Structures," *Composites Part B: Engineering*, V. 38, No. 2, Mar. 2007, pp. 119-143. doi: 10.1016/j.compositesb.2006.08.003

12. ACI Committee 440, "Guide for the Design and Construction of Externally Bonded Fiber-Reinforced Polymer Systems for Strengthening Unreinforced Masonry Structures (ACI 440.7R-10)," American Concrete Institute, Farmington Hills, MI, 2010, 46 pp.

13. Yang, S.; Wang, S.; Fang, X.; and Tao, Y., "Bond Performance between NSM FRP Rods and Concrete Using ECC as Bonding Materials," *Proceedings of the Second International Conference on Performance-based and Life-cycle Structural Engineering (PLSE 2015)*, D. Fernando, J.-G. Teng, and J. L. Torero, eds., Brisbane, QLD, Australia, 2015, pp. 490-495.

14. Al-Saadi, N. T. K.; Mohammed, A.; and Al-Mahaidi, R., "Assessment of Residual Strength of Concrete Girders Rehabilitated Using NSM CFRP with Cementitious Adhesive Made with Graphene Oxide after Exposure to Fatigue Loading," *Construction and Building Materials*, V. 153, Oct. 2017, pp. 402-422. doi: 10.1016/j.conbuildmat.2017.07.121

15. Kuntal, V. S.; Chellapandian, M.; Prakash, S. S.; and Sharma, A., "Experimental Study on the Effectiveness of Inorganic Bonding Materials for Near-Surface Mounting Shear Strengthening of Prestressed Concrete Beams," *Fibers*, V. 8, No. 6, June 2020, Article No. 40. doi: 10.3390/fib8060040

16. Elsanadedy, H. M.; Abbas, H.; Almusallam, T. H.; and Al-Salloum, Y. A., "Organic versus Inorganic Matrix Composites for Bond-Critical Strengthening Applications of RC Structures – State-of-the-Art Review," *Composites Part B: Engineering*, V. 174, Oct. 2019, Article No. 106947. doi: 10.1016/j.compositesb.2019.106947

17. Yu, J.-G.; Cheng, L.; Liu, S.; Fu, B.; and Li, B., "Inorganic Adhesive Based Near-Surface-Mounted Fibre Reinforced Polymer for Strengthening of Concrete Structures: An Overview," *Structures*, V. 33, Oct. 2021, pp. 2099-2120. doi: 10.1016/j.istruc.2021.04.017

18. Thoft-Christensen, P.; Jensen, F. M.; Middleton, C. R.; and Blackmore, A., "Assessment of the Reliability of Concrete Slab Bridges," *Reliability and Optimization of Structural Systems: Proceedings of the 7th IFIP*

WG 7.5 Working Conference, D. M. Frangopol, R. B. Corotis, and R. Rackwitz, eds., Boulder, CO, 1996, pp. 1-8.

19. Sagüés, A. A., "Modeling the Effects of Corrosion on the Lifetime of Extended Reinforced Concrete Structures," *CORROSION*, V. 59, No. 10, Oct. 2003, pp. 854-866. doi: 10.5006/1.3287706

20. Elsener, B., and Angst, U., "Corrosion Inhibitors for Reinforced Concrete," *Science and Technology of Concrete Admixtures*, P.-C. Aïtcin and R. J. Flatt, eds., Woodhead Publishing, Sawston, UK, 2016, pp. 321-339.

21. Cao, C., and Cheung, M. M. S., "Non-Uniform Rust Expansion for Chloride-Induced Pitting Corrosion in RC Structures," *Construction and Building Materials*, V. 51, Jan. 2014, pp. 75-81. doi: 10.1016/j.conbuildmat.2013.10.042

22. Vu, K. A. T., and Stewart, M. G., "Structural Reliability of Concrete Bridges Including Improved Chloride-Induced Corrosion Models," *Structural Safety*, V. 22, No. 4, 2000, pp. 313-333. doi: 10.1016/S0167-4730(00)00018-7

23. Ahmad, Z., *Principles of Corrosion Engineering and Corrosion Control*, Butterworth-Heinemann, Oxford, UK, 2006.

24. Aslett, L. J. M.; Coolen, F. P. A.; and De Bock, J., eds., *Uncertainty in Engineering: Introduction to Methods and Applications*, Springer, Cham, Switzerland, 2022.

25. Okeil, A. M.; El-Tawil, S.; and Shahawy, M., "Flexural Reliability of Reinforced Concrete Bridge Girders Strengthened with Carbon Fiber-Reinforced Polymer Laminates," *Journal of Bridge Engineering*, ASCE, V. 7, No. 5, Sept. 2002, pp. 290-299. doi: 10.1061/(ASCE)1084-0702(2002)7:5(290)

26. Li, C. Q., and Melchers, R. E., "Time-Dependent Risk Assessment of Structural Deterioration Caused by Reinforcement Corrosion," *ACI Structural Journal*, V. 102, No. 5, Sept.-Oct. 2005, pp. 754-762.

27. Val, D. V., and Stewart, M. G., "Life-Cycle Cost Analysis of Reinforced Concrete Structures in Marine Environments," *Structural Safety*, V. 25, No. 4, Oct. 2003, pp. 343-362. doi: 10.1016/S0167-4730(03)00014-6

28. Stewart, M. G., and Rosowsky, D. V., "Time-Dependent Reliability of Deteriorating Reinforced Concrete Bridge Decks," *Structural Safety*, V. 20, No. 1, 1998, pp. 91-109. doi: 10.1016/S0167-4730(97)00021-0

29. Fox, M.; Trost, S.; and Hellman, S., "Evaluation of Novel Methods to Measure Water-to-Cement Ratio of Fresh Concrete," Final Report for Highway IDEA Project 105, Transportation Research Board, Washington, DC, 2007, 46 pp.

30. Nowak, A. S., and Collins, K. R., *Reliability of Structures*, second edition, CRC Press, Boca Raton, FL, 2013.

31. Mirza, S. A.; Kikuchi, D. K.; and MacGregor, J. G., "Flexural Strength Reduction Factor for Bonded Prestressed Concrete Beams," *ACI Journal Proceedings*, V. 77, No. 4, July-Aug. 1980, pp. 237-246.

32. Baji, H., and Ronagh, H. R., "Reliability-Based Study on Ductility Measures of Reinforced Concrete Beams in ACI 318," *ACI Structural Journal*, V. 113, No. 2, Mar.-Apr. 2016, pp. 373-382. doi: 10.14359/51688201

33. Kim, S.; Frangopol, D. M.; and Zhu, B., "Probabilistic Optimum Inspection/Repair Planning to Extend Lifetime of Deteriorating Structures," *Journal of Performance of Constructed Facilities*, ASCE, V. 25, No. 6, Dec. 2011, pp. 534-544. doi: 10.1061/(ASCE)CF.1943-5509.0000197

34. Atadero, R. A., and Karbhari, V. M., "Calibration of Resistance Factors for Reliability Based Design of Externally-Bonded FRP Composites," *Composites Part B: Engineering*, V. 39, No. 4, June 2008, pp. 665-679. doi: 10.1016/j.compositesb.2007.06.004

35. Stewart, M. G.; Estes, A. C.; and Frangopol, D. M., "Bridge Deck Replacement for Minimum Expected Cost Under Multiple Reliability Constraints," *Journal of Structural Engineering*, ASCE, V. 130, No. 9, Sept. 2004, pp. 1414-1419. doi: 10.1061/(ASCE)0733-9445(2004)130:9(1414)

36. Darwin, D.; Browning, J.; O'Reilly, M.; Locke, C. E. Jr.; and Virmani, Y. P., "Multiple Corrosion-Protection Systems for Reinforced Concrete Bridge Components," Report No. FHWA-HRT-11-060, Federal Highway Administration, Washington, DC, 2011, 260 pp.

37. Yuan, Y.; Jiang, J.; and Peng, T., "Corrosion Process of Steel Bar in Concrete in Full Lifetime," *ACI Materials Journal*, V. 107, No. 6, Nov.-Dec. 2010, pp. 562-567.

38. ASTM C39/C39M-18, "Standard Test Method for Compressive Strength of Cylindrical Concrete Specimens," ASTM International, West Conshohocken, PA, 2018, 8 pp.

39. ASTM C807-20, "Standard Test Method for Time of Setting of Hydraulic Cement Mortar by Modified Vicat Needle," ASTM International, West Conshohocken, PA, 2020, 3 pp.

40. ASTM C1090/C1090M-15, "Standard Test Method for Measuring Changes in Height of Cylindrical Specimens of Hydraulic-Cement Grout," ASTM International, West Conshohocken, PA, 2015, 6 pp.

41. ASTM C1543-10, "Standard Test Method for Determining the Penetration of Chloride Ion into Concrete by Ponding (Withdrawn 2019)," ASTM International, West Conshohocken, PA, 2010.

42. ASTM C666/C666M-15, "Standard Test Method for Resistance of Concrete to Rapid Freezing and Thawing," ASTM International, West Conshohocken, PA, 2015, 7 pp.

43. ASTM C109/C109M-20, "Standard Test Method for Compressive Strength of Hydraulic Cement Mortars (Using 2-in. or [50-mm] Cube Specimens)," ASTM International, West Conshohocken, PA, 2020, 11 pp.

44. Vargas, M. A.; Sachsenheimer, K.; and Guthausen, G., "*In-Situ* Investigations of the Curing of a Polyester Resin," *Polymer Testing*, V. 31, No. 1, Feb. 2012, pp. 127-135. doi: 10.1016/j.polymertesting.2011.10.004

45. Sudirman; Anggaravidya, M.; Budianto, E.; and Gunawan, I., "Synthesis and Characterization of Polyester-Based Nanocomposite," *Procedia Chemistry*, V. 4, 2012, pp. 107-113. doi: 10.1016/j.proche.2012.06.016

46. Neville, A. M., *Properties of Concrete*, fourth edition, Prentice Hall, Essex, UK, 1995.

47. Meng, W., and Khayat, K. H., "Effect of Graphite Nanoplatelets and Carbon Nanofibers on Rheology, Hydration, Shrinkage, Mechanical Properties, and Microstructure of UHPC," *Cement and Concrete Research*, V. 105, Mar. 2018, pp. 64-71. doi: 10.1016/j.cemconres.2018.01.001

48. Xu, H., and Van Deventer, J. S. J., "The Geopolymerisation of Alumino-Silicate Minerals," *International Journal of Mineral Processing*, V. 59, No. 3, June 2000, pp. 247-266. doi: 10.1016/S0301-7516(99)00074-5

49. Bauer, E.; de Sousa, J. G. G.; Guimarães, E. A.; and Silva, F. G. S., "Study of the Laboratory Vane Test on Mortars," *Building and Environment*, V. 42, No. 1, Jan. 2007, pp. 86-92. doi: 10.1016/j.buildenv.2005.08.016

50. Ramsey, M. S., "Rheology, Viscosity, and Fluid Types," *Practical Wellbore Hydraulics and Hole Cleaning: Unlock Faster, More Efficient, and Trouble-Free Drilling Operations*, Gulf Professional Publishing, Cambridge, MA, 2019, pp. 217-237.

51. Akono, A. T.; Koric, S.; and Kriven, W. M., "Influence of Pore Structure on the Strength Behavior of Particle- and Fiber-Reinforced Metakaolin-Based Geopolymer Composites," *Cement and Concrete Composites*, V. 104, Nov. 2019, Article No. 103361. doi: 10.1016/j.cemconcomp.2019.103361

52. ACI Committee 318, "Building Code Requirements for Structural Concrete (ACI 318-19) and Commentary (ACI 318R-19) (Reapproved 2022)," American Concrete Institute, Farmington Hills, MI, 2019, 624 pp.

53. Abrishambaf, A.; Pimentel, M.; and Nunes, S., "Influence of Fibre Orientation on the Tensile Behaviour of Ultra-High Performance Fibre Reinforced Cementitious Composites," *Cement and Concrete Research*, V. 97, July 2017, pp. 28-40. doi: 10.1016/j.cemconres.2017.03.007

54. Naaman, A. E.; Burns, N.; French, C.; Gamble, W. L.; and Mattock, A. H., "Stresses in Unbonded Prestressing Tendons at Ultimate: Recommendation," *ACI Structural Journal*, V. 99, No. 4, July-Aug. 2002, pp. 518-531.

CALL FOR ACTION

ACI Invites You To...

Share your expertise

Do you have EXPERTISE in any of these areas?

- BIM
- Chimneys
- Circular Concrete Structures Prestressed by Wrapping with Wire and Strand
- Circular Concrete Structures Prestressed with Circumferential Tendons
- Concrete Properties
- Demolition
- Deterioration of Concrete in Hydraulic Structures
- Electronic Data Exchange
- Insulating Concrete Forms, Design, and Construction
- Nuclear Reactors, Concrete Components
- Pedestal Water Towers
- Pipe, Cast-in-Place
- Strengthening of Concrete Members
- Sustainability

Then become a REVIEWER for the *ACI Structural Journal* or the *ACI Materials Journal*.

Become a Reviewer for the ACI Journals

How to become a Reviewer:

1. Go to: **http://mc.manuscriptcentral.com/aci**;
2. Click on "Create Account" in the upper right-hand corner; and
3. Enter your E-mail/Name, Address, User ID and Password, and Area(s) of Expertise.

Update your Manuscript Central user account information

Did you know that the database for MANUSCRIPT CENTRAL, our manuscript submission program, is separate from the ACI membership database?

How to update your user account:

1. Go to **http://mc.manuscriptcentral.com/aci**;
2. Log in with your current User ID & Password; and
3. Update your E-mail/Name, Address, User ID and Password, and Area(s) of Expertise.

QUESTIONS?

E-mail any questions to Journals.Manuscripts@concrete.org.

American Concrete Institute

Always advancing

ACI STRUCTURAL JOURNAL TECHNICAL PAPER

Title No. 120-S72

Struts and Ties Realization in Reinforced Concrete Ring Deep Beams

by Khattab Saleem Abdul-Razzaq, Wisam H. Khaleel, and Asala A. Dawood

This study aims to shed light on the inclined direct stress paths of curved struts in deep ring beams by converting them into real members. Five specimens were tested with three loading and three supporting points. Three specimens were conventional rings and two were in the form of a frame that took its cross-sectional dimensions from the strut-and-tie model (STM) in ACI 318-19. The effect of reinforcing struts was studied by reinforcing the rings with both proposed and conventional reinforcements, and the frames with the proposed reinforcement only. The findings show that the proposed reinforcement reduced weight and cost by approximately 18% and 13%, respectively, and provided openings for services by approximately 24%. Additionally, strut curvature was found to reduce load capacity by 3 to 6%, meaning that the STM is safe and can be used efficiently in this type of deep curved member.

Keywords: beam; curvature; deep; proposed strut-and-tie model (STM); reinforced concrete (RC); ring; strut; tie.

INTRODUCTION

The importance of reinforced concrete (RC) ring deep beams is highlighted in their unique ability to support domes, silos, tanks, and foundations, thereby resisting the various stresses that result from applied loads. The significance of these structures has increased in accordance with the adoption of curvatures in facilities for architectural and service purposes. Thus, it became a growing necessity to understand more about their behavior. When loads are applied to horizontally curved members, various types of stresses are produced, including flexural, shear, and torsional stresses.[1-7] Due to their horizontal curvature, the loading and supporting points do not pass within the same main longitudinal axis of the beam, which causes the beam sections to rotate around this axis, resulting in torsional moments. In deep members, shear stresses are dominant due to the low effective span-effective depth ratio (a/d).[8]

The current study took the determinants of deep beams from ACI 318-19: the ratio of the clear distance between the supports to the height (L_n/h) is less than 4, or the ratio of the distance between the loading and supporting points to the height (a/h) is less than 2.[9] The beams that fall within the category of deep members are characterized by the phenomenon of transmission of compressive stresses from the loading to supporting points directly (struts), whose ends meet with the tensile stresses (ties) at specific points (nodes)—that is, they produce what looks like a truss.[10,11] The main assumptions in strut-and-tie modeling (STM) are: 1) there must be equilibrium; 2) all loading lines pass through the center of the components and joints; and 3) when the tie reaches yield or the node or strut is crushed, failure has occurred and, consequently, a mechanism appears (for truss models that are statically determinate). STM requires the designer to define realistic stress paths and ensure that these stresses do not cause any part of these paths to fail. The compressive strength of concrete determines the strength of the struts, a strut coefficient (β_s), and the strut cross-sectional area as detailed in ACI 318-19, Section 23.4.3. Struts are of various types, but the most common is the bottle shape (interior struts) in which the compressive stresses are spread on both sides of the midlength region. Based on ACI 318-19, Table 23.4.3(a), if the interior struts are reinforced by more than 0.25%, β_s is considered equal to 0.75; otherwise, its value is 0.4. The strength of the tie depends on the reinforcement yield strength in which it is contained, considering that the concrete tensile strength is neglected. Note that, in the case of a bottle type, there are perpendicular tensile stresses on the strut itself, whereas the idealized strut (boundary) consists of only compressive stresses parallel to its main axis.[12,13] In ACI 318-14, in the case of a steel reinforcement ratio less than 0.3%, $\beta_s = 0.6\lambda$ instead of 0.4. Kondalraj and Appa Rao[14] studied the strut efficiency factor without reinforcement using 11 experimental specimens, in addition to 607 others from previous studies. They concluded that ACI 318-19 overestimated the capacity of beams with a/d greater than 1.5 and concrete strengths greater than 60 MPa, even after reducing the strut efficiency factor from 0.6 to 0.4. However, ACI 318-19's overestimation is only 5.0%. If the maximum shear strength limit is taken into account, ACI 318-14 estimates the capacity more precisely than ACI 318-19 with a strut efficiency factor of 0.6, with only 6.0% of overestimation. The ACI 318-14 maximum shear strength limit is quite conservative. Estimates are extremely conservative as a result of reducing the strut efficiency factor in ACI 318-19 without changing the maximum shear strength limit.[14]

The shear dominance in deep members leads to the formation of a strut with an angle (ϕ) dependent on the a/d (Fig. 1). As for torsion, it also leads to the formation of a torsional strut according to the space truss analogy, and its angle (θ) is specified by the ACI Code at 45 degrees (Fig. 2). The inclination angle of compression, or tension crack, on the vertical faces depends on L_n/h. It is approximately constant

ACI Structural Journal, V. 120, No. 4, July 2023.
MS No. S-2022-167.R1, doi: 10.14359/51738771, received December 3, 2022, and reviewed under Institute publication policies.

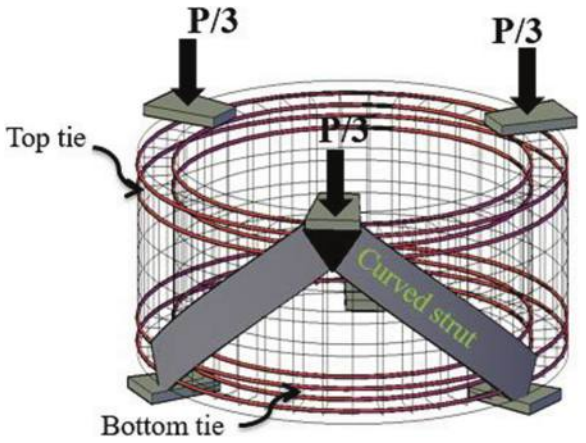

Fig. 1—Ring deep beam.

for L_n/h greater or equal to 3.0, but increases sharply for L_n/h less than 3.0. Thus, in beams with a low L_n/h, the addition of a horizontal secondary reinforcement is more beneficial than the addition of vertical stirrups in torsion resistance.[15] Moreover, torsional capacity regularly increases as L_n/h decreases from 3 to 1. The increase of depth-width or span-depth ratio reduces beam stiffness and increases the twist angle and energy absorption.[16] The topic here is a study of the superiority of shear stresses over torsional stresses, considering that the struts formed between the loading and supporting points—as a result of the low a/d—are the cause of failure, while the struts resulting from torsion at an angle of approximately 45 degrees have less effect. Consequently, in the current study, concrete will only be cast into the STM stress paths to investigate how these two main cracks act in the remaining strut. In addition, the reinforcement of these remaining struts will be studied to precisely determine the role of reinforcement in resisting the combined stresses in horizontally curved deep beams. The current study is an extension of previous studies conducted by the authors, where the STM stress paths were reinforced to investigate the efficacy of the STM in analyzing simple and continuous deep beams,[17,18] deep pile caps,[19] and concrete corbels.[20]

Abdul-Razzaq et al.[21] studied the role of the web and flexural reinforcing steel in six deep ring concrete beams, changing the steel reinforcement ratio. In terms of load capacity, the authors concluded that the role of the vertical web reinforcing steel is 94%, which is more than that of the horizontal web reinforcement (36%), and both of them are more than the role of the flexure one by approximately 42%. They also presented a mathematical model for the development of the STM method, so that they took into account the role of the web reinforcement in more detail, in addition to including the role of torsional moments. This proposed model gave results closer to the experimental (11%) compared to the STM of ACI 318-19 theoretical estimation (29%).[21]

Prakash et al.[22] experimentally studied RC columns under combined loading with different cross-sectional shapes (circle and square), hysteretic torsional and flexural response, damage distribution, and ductility characteristics with respect to various torsion-to-bending moment ratios (T/M). The presence of torsion changed the mode of failure

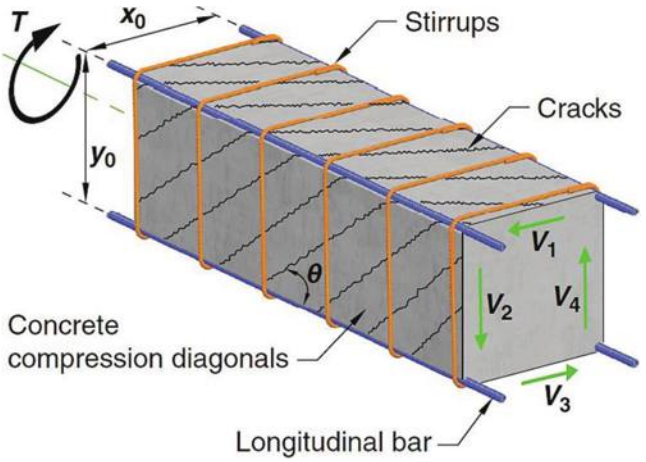

Fig. 2—Space truss analogy under torsion.[9]

to RC columns under load combination. Due to high shear stresses from torsional moments and shear forces under load combination, the inclined cracks propagated considerably, leading to early concrete cover spalling even before reaching the ultimate shear capacity.[22]

In the current study, these strut axial compressive forces are realistically simulated, and a reinforcement proposal is suggested that accentuates the function of the compression member by taking the struts as an independent column. The presence of curvature in struts, in the case of ring deep beams, results in bending moments, so it behaves like the beam column. On the other hand, the torsional moments caused by the horizontal curvature of the beam cause inclined cracks, separation of the concrete cover, and lateral displacement when approaching failure.

RESEARCH SIGNIFICANCE

When testing a conventional ring deep reference beam specimen, it has been observed that failure occurs in the strut region. As for the zones outside these struts, no cracks worth mentioning were apparent, or they did not appear at all. Accordingly, concrete was omitted in these zones and the role of the remaining struts was studied with and without steel reinforcement to ensure the efficacy of the STM from ACI 318-19 in analyzing the deep curved beams. In addition, the horizontal curvature of the beams generates torsional moments that are worthy of study, not to mention the curvature in the strut itself, which generates bending moments. Here, the authors verified the role of the torsional moments and prepared a mathematical model to add the strut bending moments to the STM of ACI 318-19.

EXPERIMENTAL INVESTIGATION

Five reinforced concrete ring deep specimens were cast and tested in the current experimental program (Table 1 and Fig. 3):

1. A conventionally RC reference ring deep beam specimen (RR).
2. A ring deep beam in which only struts and ties are reinforced (RST).
3. A ring deep beam in which only flexural reinforcement for ties is used (ROT).

Table 1—Details of test specimens

Specimen No.	Specimen designation	f_c', MPa cylinders	f_{ct}, MPa cylinders	f_r, MPa prisms	Main reinforcement	Secondary reinforcement	Sketch
1	RR	23.7	3.09	3.33	4Ø10 mm (two layers) for both top and bottom ties	Vertical: Ø4 mm @ 7.35 degrees center-to-center Horizontal: Ø4 mm @ 70 mm center-to-center	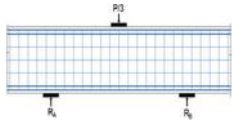
2	RST	22.3	2.79	3.05	4Ø10 mm (two layers) for both top and bottom ties Each strut: 5Ø6 mm	Top and bottom ties: Ø4 mm @ 11.61 degrees center-to-center Struts: Ø4 mm @ 96 mm center-to-center	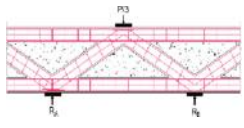
3	ROT	23.3	2.62	2.94	4Ø10 mm (two layers) for both top and bottom ties	—	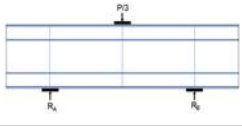
4	FST	20.4	2.86	3.21	4Ø10 mm (two layers) for both top and bottom ties Each strut: 5Ø6 mm	Top and bottom ties: Ø4 mm @ 11.61 degrees center-to-center Struts: Ø4 mm @ 96 mm center-to-center	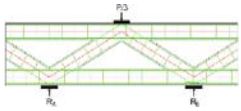
5	FOT	22.4	2.80	3.17	4Ø10 mm (two layers) for both top and bottom ties	Top and bottom ties: Ø4 mm @ 11.61 degrees center-to-center Struts: no reinforcement	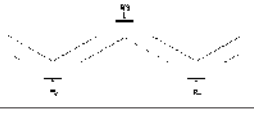

Note: 1 MPa = 145.04 psi; 1 mm = 0.039 in.

4. An RC frame that took its geometry from the stress paths described by STM of ACI 318M-19 (FST).

5. A concrete frame in which only flexural reinforcement for ties is used (FOT).

Each specimen had a diameter of 1000 mm (39.37 in.) center-to-center, a width of 120 mm (4.72 in.), and a height of 400 mm (15.75 in.). Each midspan was loaded by a central single load—that is, a/d was 1.48. All specimens were subjected to three midspan point loads and placed on three equally spaced supports. Resting the ring specimen on three supports is considered the most critical case in terms of the effect of horizontal curvature or strut curvature. The ring specimens were reinforced with different reinforcement details, as shown in Fig. 4—that is, top and bottom flexural reinforcement, horizontal and vertical web reinforcement, and proposed strut reinforcement. All specimens were cast with the same quantities of top and bottom flexural reinforcement of 4Ø10 mm (four No. 3). The adopted web reinforcement was Ø4 (No. 1) at 70 mm (2.76 in.) center-to-center for horizontal web reinforcement, and stirrups of Ø4 (No. 1) at 7.35 degrees for vertical web reinforcement. For the proposed frame specimens FST and FOT, the frame had a tie cross section of 120 x 110 mm (4.72 x 4.33 in.), which was reinforced by four steel bars of 10 mm (No. 3) diameter as flexural reinforcement, in addition to 4 mm (No. 1) diameter steel bars at 11.61 degrees center-to-center as stirrups; the cross section of struts was also 120 x 110 mm (4.72 x 4.33 in.). In proposed specimens RST and FST, struts were reinforced by the minimum requirements of ACI 318-19, Section 10.6.1.1, for longitudinal reinforcement for columns ($\rho_{min} = 0.01$), which is five 6 mm (No. 2) diameter steel bars, in addition to stirrups of 4 mm (No. 1) diameter at 96 mm (3.78 in.). Figure 5 shows the steel molds and reinforcement cages inside them after concrete casting.

Materials

All specimens were cast-in-place. Locally available coarse aggregate, river sand, and ordinary portland cement were used for the concrete preparation. The coarse aggregate maximum size was 10 mm (0.39 in.). The concrete mixture proportion used was 1:1.85:1.94 (cement:fine aggregate:coarse aggregate), with a water-cement ratio (w/c) of 0.625. During each casting campaign, six standard cylinders of 150 mm (5.91 in.) and three prisms of 100 x 100 x 500 mm (3.94 x 3.94 x 19.69 in.) were likewise cast to find the compressive, splitting, and modulus of rupture strength values of the concrete according to ASTM C39/C39M-03,[23] ASTM C496-96,[24] and ASTM C78-02,[25] respectively. All beam specimens, along with control specimens (which were related to the compression, tensile, and flexural tests of the concrete), were cured within 28 days, then tested on the 30th day. Reinforcing bars with a 10 mm (No. 3) diameter were used as flexural reinforcement, in addition to 4 mm (No. 1) diameter bars for secondary web reinforcement and 6 mm (No. 2) diameter bars for strut main reinforcement. From each size, three bars were tested according to ASTM A615/A615M-05[26] and ASTM A496-02[27] to obtain reinforcement tensile properties (Table 2).

Test setup and instrumentation

A three-point load distributer was especially designed and manufactured to conduct testing (Fig. 6). The specimens were tested by applying successive increments of monotonic-static loading until failure. When the total load on the specimen started to drop off, the test was completed. The

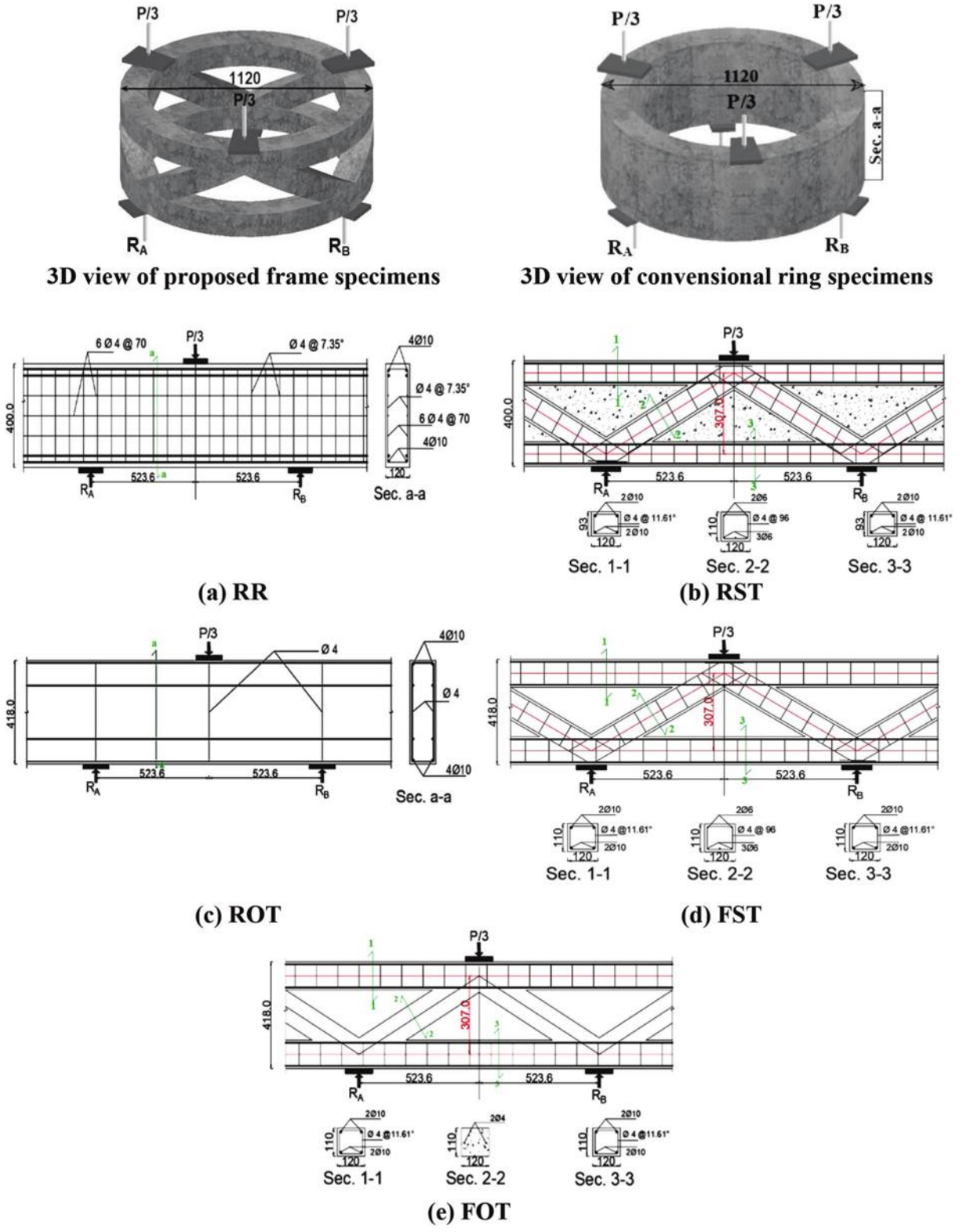

Fig. 3—Geometry and reinforcement details of ring specimens. (Note: All dimensions are in mm; 1 mm = 0.039 in.)

specimens were equipped for testing by setting the load point positions. The loading rate was 2 kN/s. Two linear voltage displacement transducers (LVDTs) were used. The first was used to measure the vertical average deflection by placing it at the load application hydraulic jack, in addition to placing the second horizontally (at the top of the specimen) next to the load application point to measure the lateral displacement of the specimen (Fig. 6). Bearing plates of 20 x 120 x 180 mm (0.79 x 4.72 x 7.09 in.) (thickness x width at center x length) were used at the loading and supporting points to avoid the effect of load concentration on the concrete. Neoprene rubber pads were placed between the bearing plate and the concrete specimen to eliminate any irregularities in the concrete surface. In every specimen, to follow up the strain values of the critical locations, 10 electrical strain gauges of 25 and 6 mm (0.98 and 0.24 in.) length were fixed

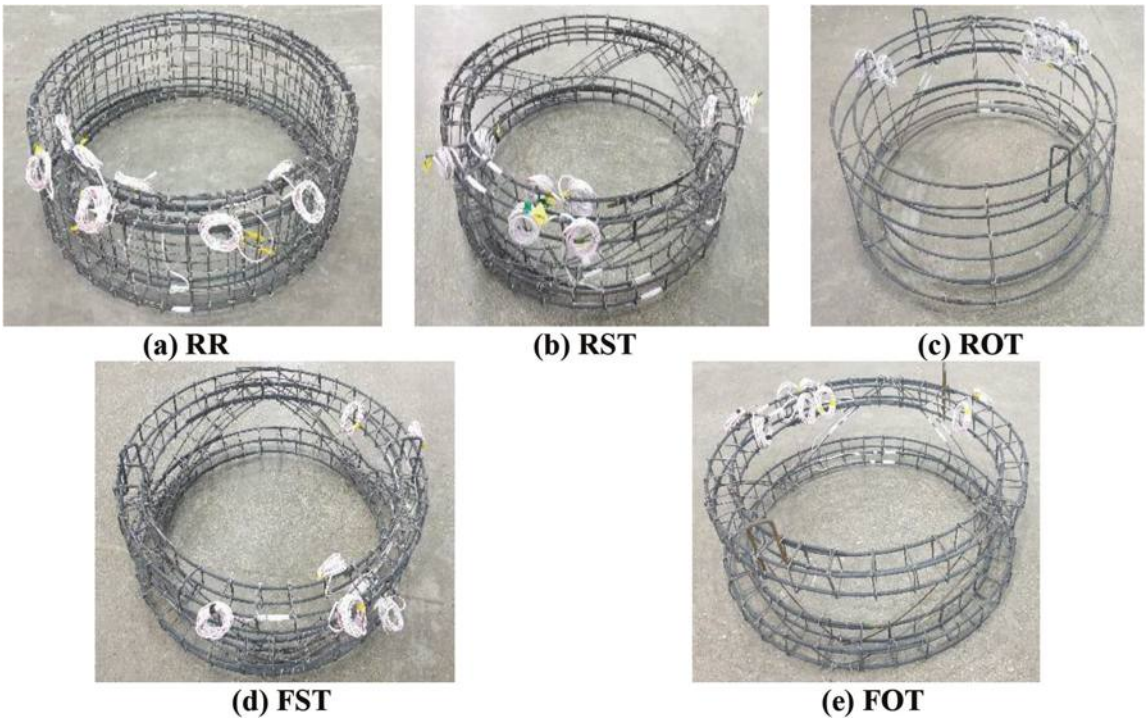

Fig. 4—Steel reinforcement for all specimens.

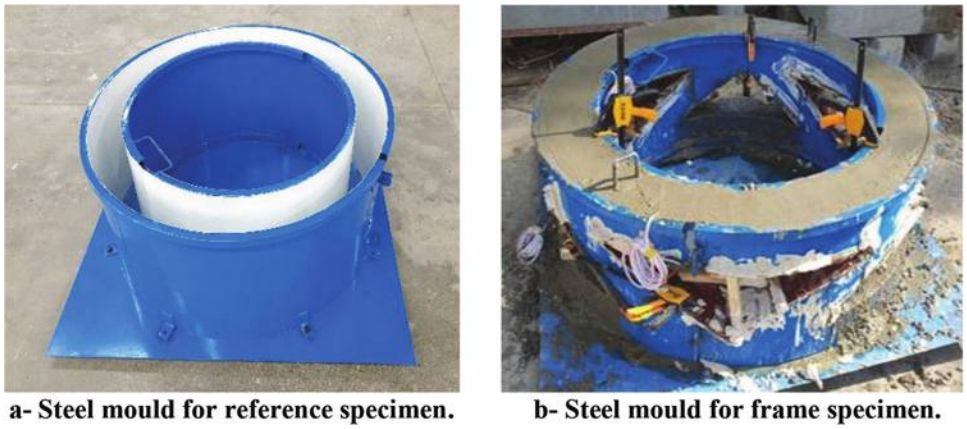

Fig. 5—Casting concrete in steel molds.

Table 2—Mechanical properties of steel bars reinforcement

Type of bar used	Nominal diameter, mm	Yield stress, MPa	Ultimate stress, MPa	E_s, GPa	Yield strain ε_{yield}	Ultimate strain $\varepsilon_{ultimate}$
Flexural reinforcement	10	595	680	200	0.00298	0.034
Compression reinforcement	6	432	520	200	0.00216	0.026
Vertical and horizontal web reinforcement	4	580	657	200	0.0029	0.033

Note: Tests were conducted at the Structural Laboratory of the College of Engineering, University of Diyala. 1 MPa = 145.04 psi; 1 mm = 0.039 in.

on the concrete surface and steel bars, respectively. Two steel strain gauges were fixed parallel to the strut, and the same for the opposite strut within the same span (on both specimen faces: inner and outer). Two concrete strain gauges were fixed perpendicular to the strut and the same number on the opposite strut within the same span (on both specimen faces: inner and outer). One steel strain gauge was fixed on the main reinforcement of the lower tie and the same on the upper tie reinforcement—that is, in the zones of maximum positive and maximum negative moments, respectively.

EXPERIMENTAL RESULTS

The following subsections contain a summary of the behavior of the five specimens in the current study. The results are also summarized in Table 3, while the development of cracks at the failure stage is illustrated in Fig. 7.

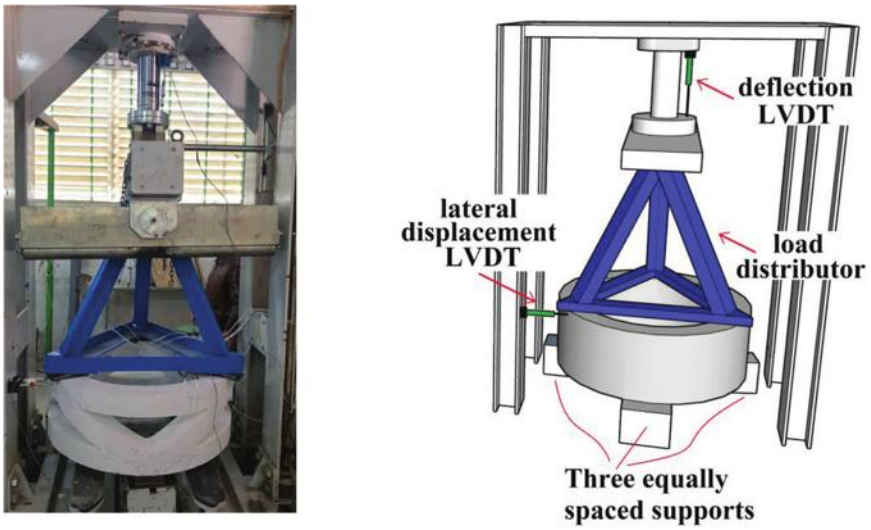

Fig. 6—Test setup.

Table 3—Experimental results for all tested specimens

No.	Specimen designation	$P_{cr\text{-}diag}$, kN	$P_{cr\text{-}flex}$, kN	P_{STM}, kN	P, kN	P/P_{STM}	$P_{cr\text{-}diag}/P$, %	$P_{cr\text{-}flex}/P$, %	$\Delta_{cr\text{-}diag}$, mm	$\Delta_{cr\text{-}flex}$, mm	Δ, mm	Δ_L, mm	Failure mode
1	RR	203	550	608	764	1.26	26.57	71.89	1.74	3.84	6.9	6.19	C
2	RST	200	260	572	682	1.19	29.33	38.12	2.15	2.54	6.97	5.68	C
3	ROT	250	290	319	573	1.80	43.63	50.61	2.34	2.62	6.25	5.29	D
4	FST	150	190	523	526	1.01	28.52	36.12	1.74	1.99	4.45	4.95	C
5	FOT	110	190	307	496	1.62	22.18	38.31	1.43	1.95	4.89	4.37	C

Note: C is compressive strut failure; D is diagonal splitting failure; P_{STM} is theoretical load according to ACI 318 STM; $P_{cr\text{-}flex}$ is first flexural cracking load; $P_{cr\text{-}diag}$ is first diagonal cracking load; P is experimental failure load; $\Delta_{cr\text{-}flex}$ is deflection at first flexural crack; $\Delta_{cr\text{-}diag}$ is deflection at first diagonal crack; Δ is deflection at the experimental failure load; and Δ_L is lateral displacement at the experimental failure load. 1 kN = 0.225 kip; 1 mm = 0.039 in.

Cracking patterns and failure modes

In general, the failure modes in all specimens did not change, even in the case of changing the steel reinforcement details or omitting the concrete outside the paths of the STM. The failure remained within the region of the struts due to the direct transfer of stresses from the loading to the supporting points. The behavior of the specimens can be summarized as follows:

- RR: This specimen is considered a reference for the rest of the specimens because it was cast and reinforced conventionally. When it was subjected to increasing loading, the first diagonal cracks appeared in the outer face, parallel to the lines connecting the loading to the supporting points (struts) at approximately 27% of the experimental failure load (P) (Fig. 7(a)). As for the inner face of the beam, vertical flexural cracks appeared in the middle of the spans. With increasing loading, the development of diagonal cracks was observed on both faces, especially on the outer face. At 62%P, 45-degree diagonal cracks appeared in the out-of-STM paths. Finally, by increasing the loading, the specimen failed with the compressive struts.
- RST: In this specimen, the STM paths were reinforced while keeping the concrete that lies outside the STM (Fig. 7(b)). At 30%P, diagonal cracks appeared in the strut regions and on almost both faces. As for the zones outside the STM, no cracks appeared. At 38%P, the vertical flexural cracks started to appear in the middle of the spans (which bent toward the loading points later). With increasing loading, diagonal cracks developed to connect the supporting to the loading points on both beam faces, noting that the cracks on the inner face were approximately a third thinner. At failure, in the out-of-STM paths, diagonal cracks with an angle of 45 degrees appeared, which were interpreted here as resulting from the torsional stresses because they contacted their counterparts from the neighboring shear spans, forming a curve resembling a bowl. Finally, with increasing loading, strut diagonal cracks that connected loading to supporting points developed in width and number, leading to compressive strut failure.
- ROT: No openings were made in this specimen, but only the ties were reinforced as tensile members (Fig. 7(c)). After applying a gradual load, the inclined cracks appeared on the struts at 44%P. When loading continued, flexural cracks appeared in the middle of the ties at 51%P. After, no new cracks appeared that are worth mentioning. However, the existing cracks increased approximately 86% in width, especially the cracks of the struts linking the loading and supporting points. Close to failure—more specifically, at approximately 85%P—inclined cracks appeared in the upper

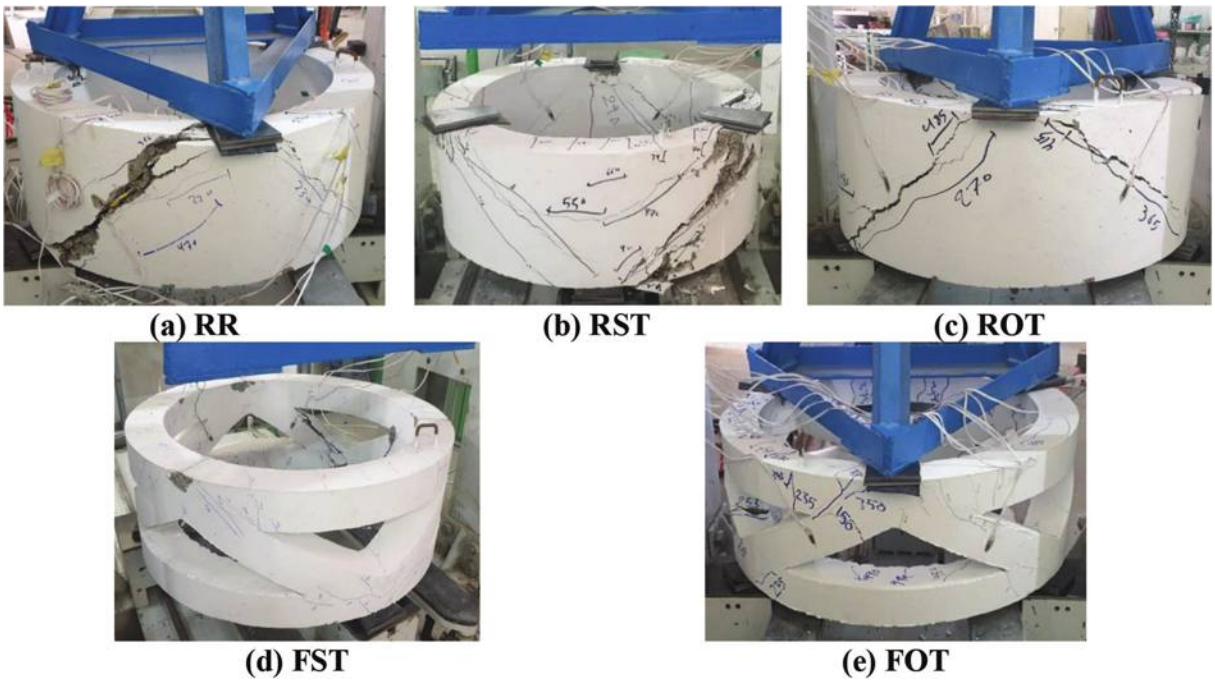

Fig. 7—Crack pattern of test specimens at failure.

nodes due to torsional moments, but they did not lead to failure. Finally, due to the absence of the strut reinforcement that resists perpendicular tensile stresses, the splitting failure occurred at one of the struts.

- FST: This specimen is the proposed frame in which only the STM paths were cast (Fig. 7(d)). The remaining struts were reinforced with the ACI 318-19 minimum reinforcement as compressive members. This proposed frame was gradually loaded until the first cracks appeared in the struts at 29%*P*. At 36%*P*, vertical flexural cracks appeared in the middle of the ties. On the other hand, no cracks were observed for the torsional moments as in the conventional specimen RR, because each of the reinforced struts and ties alone ensured the resistance of the torque. Finally, the struts failed in compressive crushing, with a noticeable concrete cover spalling that was accompanied by an increase in lateral displacement.
- FOT: This specimen was cast in the form of the STM paths; the struts were not reinforced. In other words, the struts in this specimen remained dependent on concrete resistance only (Fig. 7(e)). With increasing loading to 22%*P*, at the outer face of the specimen, the first diagonal cracks appeared in the struts. Then, flexural cracks appeared in the middle of the ties at 38%*P*. With more loading, the diagonal and flexural cracks increased. In general, the unreinforced struts remained with few cracks (Fig. 7(c) and (e)). Then, the crack width increased rapidly before failure. Finally, the specimen exhibited compressive strut brittle failure.

Load-deflection response

In general, the trend of the load-deflection response did not change in all specimens (Fig. 8). The response appeared linear before failure, where there was a bend and a noticeable

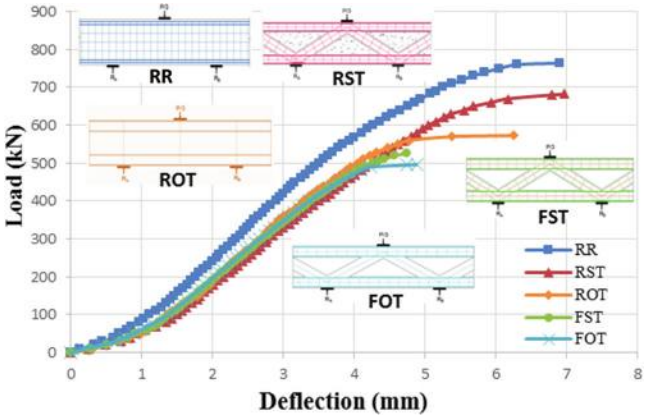

Fig. 8—Load-deflection response. (Note: 1 mm = 0.039 in.; 1 kN = 0.225 kip.)

increase in deflection values compared to load. This increase is a result of the greater development of cracks, an increase in reliance on reinforcement, and a decrease in stiffness. More specifically, this indicates two main points: first, the shear deformation control over the behavior of deep specimens here, and second, the stresses in all specimens were transmitted in one way, which is the strut and tie. For this reason, shear deformation dominance reduced the ductility of the specimens, which reduced the load capacity below the flexural capacity. It should also be noted that, in the first stages of loading, the proposed frame specimens FST and FOT showed more load-deflection straightness than in ring specimens RR, RST, and ROT. This is because the load was transferred through them in a more direct way due to omitting the concrete outside the STM.

Load-lateral displacement

Lateral displacement is one of the important indicators of the role of torsional moments because of their direct

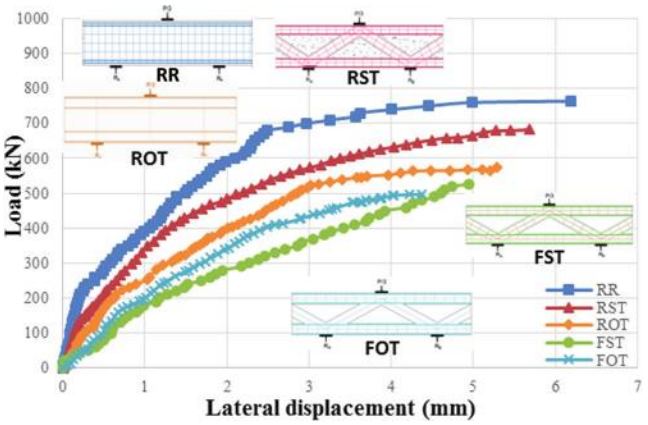

Fig. 9—Load-lateral displacement response. (Note: 1 mm = 0.039 in.; 1 kN = 0.225 kip.)

Table 4—Experimental cracking loads versus that obtained from strain diagrams

Specimen	P, kN	Eye-detected cracks		Measured cracks from strain readings	
		$P_{cr\text{-}diag}$, kN	$P_{cr\text{-}diag}/P$, %	$P_{cr\text{-}diag}$, kN	$P_{cr\text{-}diag}/P$, %
RR	764	203	27	195	26
RST	682	200	29	190	28
ROT	573	250	44	250	44
FST	526	150	29	150	29
FOT	496	110	22	100	20

Note: 1 kN = 0.225 kip.

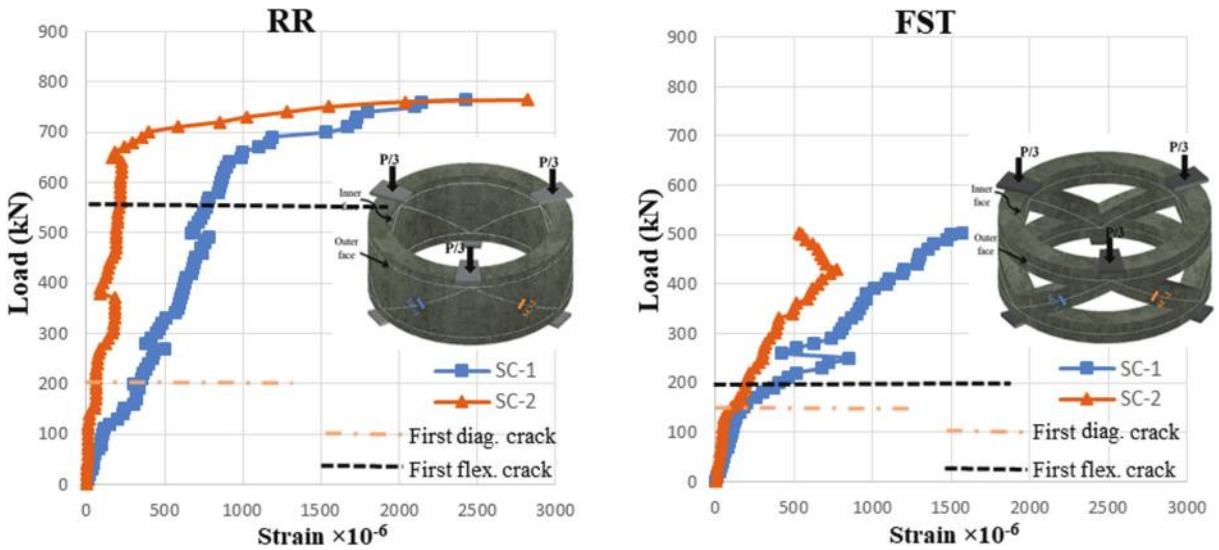

Fig. 10—Load versus average concrete compressive strain. (Note: 1 kN = 0.225 kip.)

relationship. In general, the lateral displacement values are low compared to the beam height, which led to a low rotation angle (0.6 to 0.9 degrees) as the torsional moments were not dominant here (Fig. 9). The load-lateral displacement curves were approximately linear up to 40%P, after which the curves became nonlinear, illustrating a torsional stiffness reduction.

The torsional stiffness in the RST specimen decreased in comparison with the RR specimen when the reinforcement was placed only in the STM regions. This indicates the importance of web reinforcement with resistance to torsional moments. In addition, when the web reinforcement was completely omitted in the ROT specimen, the stiffness decreased more. In the case of frame specimens, stiffness recorded the largest decrease compared to the RR specimen, especially in the FOT specimen, which completely lacked web reinforcement.

When it comes to torsional stiffness, it is necessary to mention the effect of the continuity of the ring specimens due to their annular shape. For this reason, the RR, RST, and FST specimens showed greater torsional stiffness in the case of using reinforcement, and very little torsional stiffness in the case of no reinforcement (ROT and FOT). In other words, steel bars contributed to resisting lateral displacement. The unreinforced frame specimen FOT had less ductility than the proposed reinforced frame specimen FST. However, the specimen FOT resisted lateral displacement even when it was not reinforced.

Concrete and reinforcement strains

Strain values in concrete—The measured strain in the critical zones, which are the strains perpendicular to the struts (in the middle zones of struts), helped more in understanding the specimens' behavior as the strain values were low on the concrete surfaces. To be more precise, all strain gauges recorded linear readings from the beginning of the loading until the appearance of cracks (Fig. 10). The appearance of cracks caused sudden changes in the perpendicular strain reading values that became unsteady. There were differences between the cracks measured by strain gauges and those seen with the naked eye. These differences seem to be logical due to the different accuracy levels of the strain measurements compared to the human eye (Table 4).

Perpendicular strain readings on the strut were greater in the RR specimen than in the proposed frame specimens FST and FOT by approximately 44% and 7%, respectively. This

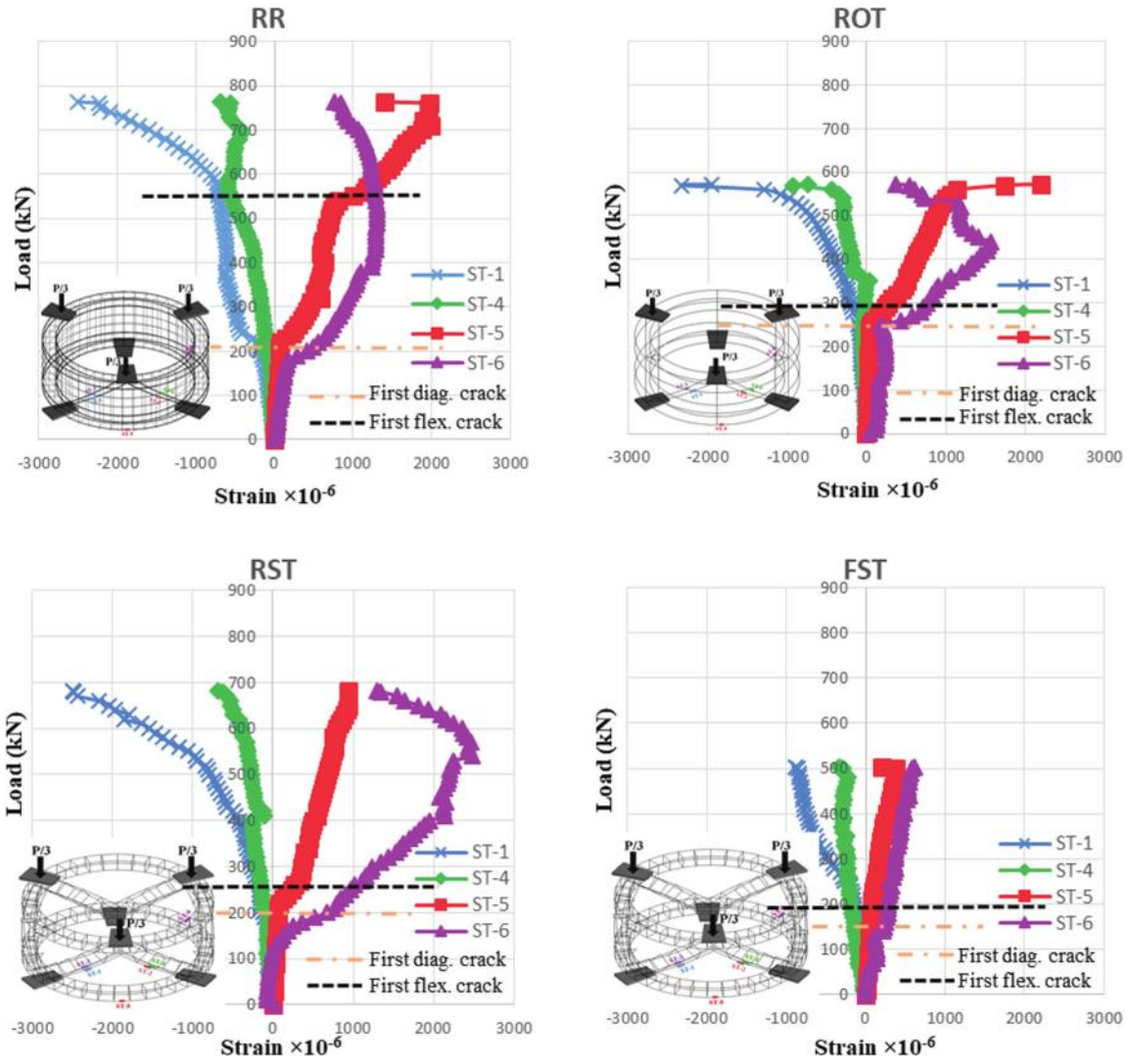

Fig. 11—Load versus steel strain values. (Note: 1 kN = 0.225 kip.)

is because the struts in the frame specimens followed the behavior of the idealized (boundary) strut that ACI 318-19 detailed in Table 23.4.3(a), while the struts in the reference RR were in the form of a bottle.

Strain values in steel bars—Steel reinforcement gauges were placed in points of maximum stresses—more precisely, in the middle of struts and the middle of ties (Fig. 11). The strain readings were low (approximately 0 to 0.000123) at the start of loading and then increased steadily when cracks appeared due to the more explicit contribution of reinforcement. In general, the readings of the strains were greater on the outer face compared to the inner face by approximately 42%. As a result of the convexity of the outer face, the shear stresses resulting from shear and torsion were in the same direction, while they were in the opposite direction on the inner face (Fig. 12). By contemplating the values of strains, the following can be observed:

- Referring to Fig. 11, the reinforcing steel strain values in the ties of the RR specimen were higher than that in the FST specimen by 50 to 81%, while in FOT, the upper tie strain values reached the yield, leading to a clear increase in lateral displacement. In general, tie reinforcement was less affected by applied loads because of the low torsional and flexural stresses due to the small a/d in all specimens.
- The not-omitted concrete in RR, RST, and ROT led to the formation of tensile stresses perpendicular to the struts due to the formation of the strut bottle shape. Nonetheless, in the case of FST and FOT, the struts were an idealized (boundary) strut type.
- The continuity in the successive tension ties, due to the closed annular shape of the ring beam, led to the prominence of the strut compression stresses.

Reinforcement contribution to strength

The steel reinforcement contribution to the struts' and ties' strength in specimens RST and FST was determined using the experimental strain readings and comparing them with those calculated according to ACI 318M-19. The forces $AF_{s\text{-}exp}$, $AF_{c\text{-}code}$, $AF_{s\text{-}code}$, and $AF_{c\text{-}exp}$ are calculated as follows:

1. Calculate $AF_{s\text{-}exp}$ by multiplying the measured strain at the main reinforcement by the steel bars area and elastic modulus.

2. Analyze the STM truss model formed in the specimen subjected to the experimental ultimate failure load. From

Table 5—Reinforcement contribution of struts and ties to strength

Specimen	Member	Experimental			ACI 318-19 equations					Notes
		$AF_{s\text{-}exp}$, kN	$AF_{c\text{-}exp}$, kN	$AF_{s\text{-}exp}/AF_{c\text{-}exp}$	$AF_{s\text{-}code}$, kN	$AF_{c\text{-}code}$, kN	$AF_{s\text{-}code}/AF_{c\text{-}code}$	$AF_{s\text{-}exp}/AF_{s\text{-}code}$	$AF_{s\text{-}exp}/AF_{c\text{-}code}$	
RST	Strut	61	163.8	0.37	48.9	187.7	0.26	1.25	0.87	—
	B. Tie	87.9	—	—	186.9	—	—	0.47	—	Concrete tensile force in tie is neglected by ACI Code
	T. Tie	138.7	—	—	186.9	—	—	0.74	—	
FST	Strut	21.5	151.8	0.14	48.9	171.7	0.28	0.44	0.88	—
	B. Tie	35.4	—	—	186.9	—	—	0.19	—	Concrete tensile force in tie is neglected by ACI Code
	T. Tie	57.4	—	—	186.9	—	—	0.31	—	

Note: 1 kN = 0.225 kip.

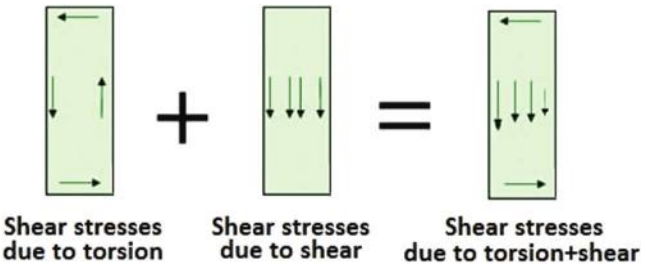

Fig. 12—Shear stresses in curved beams.

this analysis, the total force for each truss member can be found.

3. Calculate the force in concrete $AF_{c\text{-}exp}$ by subtracting the force in steel reinforcement $AF_{s\text{-}exp}$ from the total member force calculated in Step 2.

4. Calculate the force in steel reinforcement $AF_{s\text{-}code}$ using Eq. (23.7.2) of ACI 318M-19.

5. Calculate the force in concrete $AF_{c\text{-}code}$ using Eq. (23.4.1a) of ACI 318M-19.

Table 5 shows the reinforcement contribution to the struts' and ties' strength. It must be noted herein that the symbols B and T refer to bottom and top members, respectively.

The contribution of strut reinforcement in the RST specimen is greater than that in the proposed frame FST specimen by approximately 62%, which indicates a greater investment of concrete in the proposed frame specimen despite the reduction of concrete. The reason for this is that the strut section, in the proposed frame FST, was able to reach the ultimate compressive strength as an idealized (boundary) strut. As for the reference ring specimen RR, the increase in the width of the strut through which the perpendicular tensile stresses spread on the strut (bottle-shaped strut) may lead to the occurrence of splitting. ACI 318 predicted the contribution of concrete in the unreinforced frame specimen FOT because the Code did not include reinforcement in detail within its calculations.

In general, ACI 318-19 predicted the steel reinforcement contribution to strength of the proposed frame specimens more accurately than that of the ring specimens, and this supports the paths of STM validity.

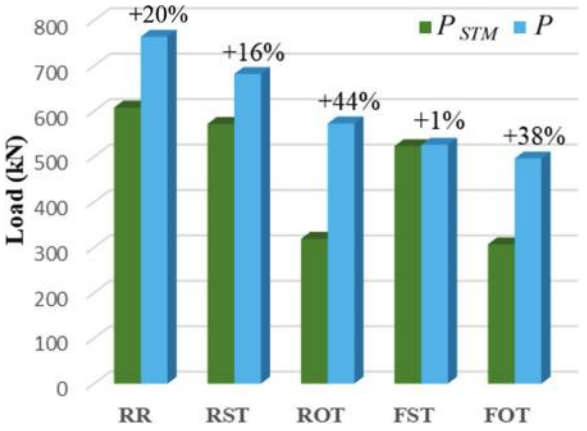

Fig. 13—Comparisons between P_{STM} *and* P. *(Note: 1 kN = 0.225 kip.)*

STM validation

From the failure modes that occurred in all specimens, it was found that the stresses were actually transmitted from the loading to the supporting points by means of compression struts, which met the tensile ties at the nodes. When comparing the theoretical calculations of the STM of ACI 318-19 with the experimental failure loads, it could be seen that the STM preserved its famous conservatism, even with the deep ring beams (Fig. 13). However, this does not take into account the presence of curvature. Because STM has remained safe with this type of structures, the authors here recommend its use as it is. It was also observed that the failure modes in all specimens remained the same (strut failure), which supports the STM philosophy: that is to say, the STM, in its theoretical calculations, takes the coefficient of $\beta_s = 0.75$ for the reinforced members and $\beta_s = 0.4$ for the unreinforced members.

As mentioned previously, ACI 318 does not take the effect of the torsional moments as a result of the horizontal curvature, nor does it take the effect of strut curvature. Accordingly, the effect of torsional moments' role was checked here.

When calculating the torsional moments that led to the appearance of the crack (T_{cr}) in unreinforced specimens, using ACI 318-19 Eq. (22.7.5.1a) and Table 22.7.5.1 and comparing them with the values in which the first experimental crack ($T_{exp\text{-}cr}$) appeared, it was found that $T_{cr} > T_{exp\text{-}cr}$. That is to say, the appearance of the first experimental crack

Table 6—CUSTM validation

No.	Specimen designation	P, kN	% decrease in P	ACI 318-19 P_{STM}, kN	P_{CUSTM}, kN	P/P_{STM}	P/P_{CUSTM}
1	RR	764	—	608	570	1.26	1.34
2	RST	682	11	572	537	1.19	1.27
3	ROT	573	25	319	308	1.80	1.86
4	FST	526	31	523	498	1.01	1.06
5	FOT	496	35	307	296	1.62	1.68

Note: 1 kN = 0.225 kip.

was not due to the torque value generated in the specimen. These calculations are also in line with the experiment, where inclined torque cracks appeared just before the failure of the specimens in the laboratory (Appendix A*).

The effect of the strut bending moments was added to the STM in a proposed mathematical model. The authors note that $\beta_s = 0.4$ is conservative in the unreinforced specimens. The difference between specimens ROT and FOT in the experimental test was 44% and 38%, respectively. Therefore, the authors believe that this topic needs further investigation.

Modifying STM by adding moments

The strut curvature generates bending moments, which are not taken into account by the theoretical STM calculations in ACI 318-19. Therefore, in this subsection, these bending moments were added to STM through considering the strut as a curved column, which led to modifying STM to curved strut-and-tie modeling (CUSTM):

Combined stresses:

$$\sigma = (V/A) \pm (MC/I) \tag{1}$$

Using Eq. (1) to calculate strut stresses:

$$0.85\beta_s f_c' \sin\phi = \frac{V}{w_s \times b} \pm \frac{V \times e \times \frac{b}{2}}{\frac{w_s \times b^3}{12}} \tag{2}$$

Euler equation:

$$V_E = (E_c I \pi)/L^2 \tag{3}$$

Additional strut midheight out of straightness due to V:

$$e = \frac{V/V_E}{1 - V/V_E} \times e_o \tag{4}$$

where e_o is the initial strut midheight out of straightness

$$e_o = r - r\frac{\sqrt{3}}{2} \tag{5}$$

Substituting Eq. (4) in Eq. (2):

$$0.85\beta_s f_c' \sin\phi = \frac{V}{w_s \times b} \pm \frac{6V e_o \frac{V/V_E}{1 - V/V_E}}{w_s \times b^2} \tag{6}$$

*The Appendix is available at **www.concrete.org/publications** in PDF format, appended to the online version of the published paper. It is also available in hard copy from ACI headquarters for a fee equal to the cost of reproduction plus handling at the time of the request.

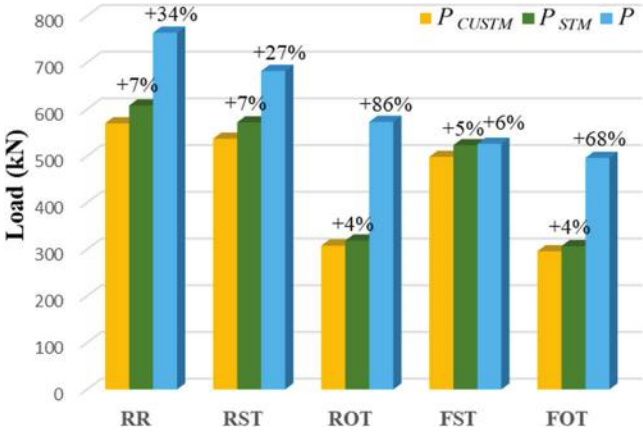

Fig. 14—Comparisons between P_{CUSTM}, P_{STM}, *and* P. *(Note: 1 kN = 0.225 kip.)*

Then

$$V = \frac{0.85\beta_s f_c' w_s b^2}{b_s \pm 6e_o \frac{V}{V_E - V}} \sin\phi \tag{7}$$

Solving Eq. (7) for V, it is possible to include the effect of curvature along the strut. Then, the total theoretical load capacity of CUSTM is

$$P_{CUSTM} = \text{number of struts} \times V = 6V$$

In Table 6, the results of CUSTM were compared with the experimental failure loads. It was found that the STM of ACI 318-19 is conservative enough and that it is safe. Furthermore, there is no need to increase its conservativeness by adding the effect of strut bending moments. Figure 14 shows the efficacy of the CUSTM. What is apparent is that there was an increase in STM conservatism in an exaggerated manner. Therefore, it is recommended here to adopt STM as there is no need for modifications in the horizontally curved deep beams because it is easy and safe.

Reduction in weight and gain in openings

In the conventionally cast ring deep beams, it was observed that there were no cracks worth mentioning in the out-of-STM zones (Fig. 15). For this reason, these zones are omitted in specimens FST and FOT to reduce cost and weight, in addition to providing service passage openings. The savings in weight and cost was approximately 18.12% and 12.85%, respectively, in addition to providing openings for services by approximately 23.5% for specimen FST in comparison with reference RR. Although the RR specimen

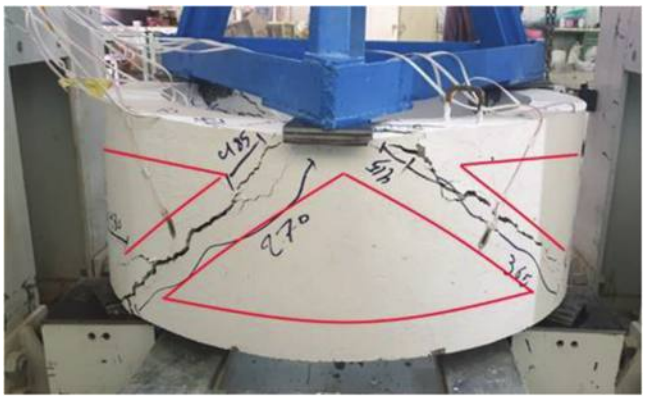

Fig. 15—Zones where struts and ties do not pass through in specimen ROT.

was superior to the FST specimen in terms of load capacity by approximately 31% in the laboratory, the latter remained within the tolerances of 1% that were calculated by the STM from ACI 318-19. Therefore, the authors suggest the FST specimen reinforcement method as an alternative to the conventional method.

DISCUSSION OF TEST RESULTS

In the conventional reference RR specimen, the inclined cracks connecting the loading and supporting points appeared on the outer face first and then penetrated toward the inner face. The reason for this can be attributed to the fact that the stresses resulting from shear and torsion were in the same direction in the outer face, while they were opposite in the inner face (Fig. 12). On the other hand, when reinforcing the struts and ties only, without omitting the concrete in the RST specimen, cracks developed on both sides out of the strut. This indicates that the strut reinforcement increased the number of cracks and prevented them from penetrating. As the zone around the reinforced strut contained concrete only, the tie flexural cracks appeared earlier, but they were not dominant in failure. This means that in reference beam RR, the presence of conventional horizontal web reinforcement effectively resisted the flexural and torsional stresses. For this reason, specimen RST failed with a lesser load capacity by 11%.

In the ROT specimen, the failure mode changed from compressive strut crushing to splitting, accompanied by rapid development of diagonal crack width. Regarding the load capacity, it decreased by 25%, but it remained higher than the STM of ACI 318-19 calculations. The reason for this decrease is due to the absence of web reinforcement, which was supposed to help the strut to resist the parallel compressive and the perpendicular tensile stresses, not to mention the torsional stresses.

In specimen FST, when the concrete outside the STM was omitted, and only the struts and ties were reinforced, a proposed frame containing outwardly curved compression and tension members was formed. Therefore, the strut reinforcement directly prevented the development of strut diagonal cracks. Limiting the stress paths in specific sections (reinforced struts and ties) reduced the effect of tensile stresses perpendicular to the strut, thus reducing the possibility of diagonal splitting failure.

In specimen FOT, load capacity decreased approximately 35% in comparison with RR, which was also higher than the STM calculations. In other words, concrete alone gave sufficient strength to the strut. However, at the same time, the bending moments in the FOT strut caused strut perpendicular cracks to appear at 30 to 51%*P*.

The difference in load capacity due to strut reinforcement between FST and FOT was only 6%. This is due to the well-known resistance of concrete to compression. However, this reinforcement increased ductility and reduced the width of the cracks with a slight increase in their numbers (Fig. 7(d) and (e)). This took place due to the role of both the supportive longitudinal reinforcement and the stirrups that produced concrete confinement. As illustrated earlier, the beam horizontal curvature, in addition to curvature of the strut itself, caused torsional and bending moments, respectively. Although the torsional moments did not cause the failure (because of low a/d), their effect in terms of the separation of the concrete cover and the increase in the lateral displacement before the failure was evident.

The contribution of strut reinforcement in the proposed FST specimen was rather small (14%), while the contribution of concrete in the FOT specimen was 86%. Nonetheless, these varying contribution rates do not diminish the fact that the strut reinforcement guaranteed the occurrence of ductile failure. In the RST, the strut bottle shape was formed, therefore, the role of concrete became 63%.

On the other hand, the load capacity of ROT exceeded that of FOT by 16% due to the non-removed concrete, which generated a side confinement for the ROT struts. Furthermore, the unremoved concrete provided more space for the distribution of the perpendicular stresses on the strut due to the bottle-shape strut formation, in addition to a larger zone for the spread of torsional stresses.

It should be noted that, before the failure, inclined cracks appeared outside the STM in specimens RR, RST, and ROT resulting from torsional shearing stresses, which were at an angle of approximately 45 degrees within the shear span. These cracks developed to meet their counterparts in adjacent spans. When omitting the concrete in the FST and FOT frame specimens, these cracks spread through the struts, considering that they were supposed to pass through the omitted concrete (outside the STM).

With regard to the FST and FOT specimens, omitting the concrete caused the strain readings to be lower in the bottom ties than those of the top ties—that is, the deformation transformation did not take place due to the omitted concrete. This is logical because the transfer of stresses took place directly from the loading to the supporting points. On the other hand, omitting the concrete in these frames led to an increase in lateral displacement compared with the RR, RST, and ROT specimens, meaning that the torque resistance of the frames decreased compared to the ring specimens.

It should also be mentioned here that reinforcing the struts and ties by omitting the concrete located outside the STM was previously studied by the authors. The load capacity of the frame specimens was less than that of the conventional

reference specimens by 7 to 23% and 7 to 26% in the cases of simple and continuous non-curved deep beams, respectively.[17,18] Even with concrete corbels, the difference in terms of load capacity was 15 to 55%.[20] The difference in the current study did not change much, reaching 11 to 31%, despite the presence of a horizontal curvature in the specimens, in addition to the curvature of the struts themselves.

CONCLUSIONS

It is known that strut-and-tie modeling (STM) from ACI 318-19 is conservative, safe, and easy to use in the analysis of deep straight beams, but it does not take horizontal curvature nor strut curvature into account in its theoretical calculations. Accordingly, five deep beams with an effective span-effective depth ratio (a/d) of 1.48 were cast and tested with different reinforcement patterns to study the effectiveness of the STM of ACI 318-19 in analyzing beams on the one hand, and to stand on the role of reinforcement in the behavior and strength of this type of deep beams on the other hand. Based on the laboratory study that was carried out in the current research, the most important conclusions can be summarized as follows:

1. When using STM of ACI 318-19 in the analysis of conventional ring deep beams, it was found that it is conservative by 1 to 80%—that is, enough to be used, even though STM does not take into account the horizontal curvature or the inclined curvature of the struts. Here, the effect of bending moments that were generated due to the curvature of the strut were added to the STM calculations of ACI 318-19, which resulted in a proposed method—named here curved strut-and-tie modeling (CUSTM)—which showed acceptable and conservative results as in the original STM.

2. Omitting the concrete outside the paths of STM and reinforcing these paths produced a frame with a laboratory load capacity less than the conventional specimen capacity by 31%. At the same time, the proposed frame outperformed the theoretical calculations of STM and CUSTM by 1% and 6%, respectively. Nonetheless, this proposed casting and reinforcing technique reduced weight and cost by 18% and 13%, respectively, in addition to providing openings for the passage of services by 24%.

3. A conventional ring and a proposed frame specimen were not reinforced in the strut zones, in comparison with their reinforced counterpart specimens, the role of strut reinforcement appeared to reduce the development of cracks and make failure more ductile. Moreover, in terms of load capacity, the role of web steel reinforcement was 33% in the conventional reference ring beam. From the other side, in the conventional ring beam in which only struts were reinforced, the role of steel was 19%, while it became 6% in the case of proposed frame specimen. That also shows the important role of concrete in the strength of this type of deep beam.

4. In general, there is no significant difference between the conventional and proposed specimens regarding the load-deflection response, because the transmission of stresses is always directly from the loading to the supporting points. On the other hand, in the conventional specimen, the ductility decreases as a result of omitting web steel reinforcement, which leads to a decrease in the deflection by approximately 9%. The ductility also decreases when the concrete is omitted outside the paths of the STM, which leads to a deflection decrease of approximately 36%.

5. The lateral displacement values are relatively low (rotation angle of 0.6 to 0.9 degrees) because the torsional stresses are not dominant in the ring deep beams. On the other hand, the reference conventional specimen showed the higher stiffness because it contained all the secondary web reinforcement and all the concrete that lies outside the STM paths.

6. According to ACI 318-19, Table 23.4.3(a), the value of the strut coefficient β_s is 0.75 in the case of reinforcing ring deep beams; regardless of its quantity and method of distribution, this led to a difference with laboratory load capacity of approximately 20%. On the other hand, in the case of non-reinforcement, the value of β_s is 0.4, which gave the STM of ACI 318-19 theoretical predictions roughly 44% less than the laboratory load capacity. Consequently, the authors believe that the β_s value needs more study.

AUTHOR BIOS

Khattab Saleem Abdul-Razzaq *is a Professor in the Department of Civil Engineering at the University of Diyala, Baqubah, Iraq. He received his BSc in 1997 and MSc in 1999 from the University of Baghdad, Baghdad, Iraq, and his PhD in civil engineering from Moscow State University, Moscow, Russia, in 2005. His research interests include reinforced concrete members.*

Wisam H. Khaleel *is a Researcher in the Department of Civil Engineering at the University of Diyala, where he received his BSc and MSc in 2009 and 2022, respectively. His research interests include strut-and-tie modeling of reinforced concrete deep members.*

Asala A. Dawood *is an Instructor in the Department of Civil Engineering at the University of Diyala, where she received her BSc and MSc in 2016 and 2020, respectively. Her research interests include reinforced concrete deep members.*

ACKNOWLEDGMENTS

The authors wish to express their deep thanks for the support provided by the Department of Civil Engineering, College of Engineering, University of Diyala, Baqubah, Iraq.

NOTATION

a	=	shear span measured from support center to load center, mm
b	=	width of beam, mm
d	=	effective depth of beam, mm
E_c	=	modulus of elasticity of concrete, MPa
E_s	=	modulus of elasticity of steel reinforcement, MPa
e	=	additional strut midheight out of straightness due to applied load, mm
e_o	=	initial strut midheight out of straightness, mm
f'_c	=	specified compressive strength of concrete, MPa
f_{ct}	=	indirect tensile strength (splitting tensile strength), MPa
f_r	=	modulus of rupture of concrete, MPa
f_y	=	yield strength of steel reinforcement, MPa
I	=	moment of inertia of section about centroidal axis, mm^4
L	=	total length of the strut, mm
L_n	=	clear span length, mm
M	=	maximum moment in strut due to e, N·mm
P	=	experimental failure load, kN
$P_{cr\text{-}diag}$	=	first diagonal cracking load, kN
$P_{cr\text{-}flex}$	=	first flexural cracking load, kN
P_{STM}	=	theoretical load according to ACI 318M-19 STM, kN
r	=	ring radius, mm
V	=	nominal strength of strut, kN
V_E	=	Euler load, kN
w_s	=	width of strut perpendicular to axis of strut, mm

β_s = factor used to account for effect of cracking and confining reinforcement on effective compressive strength of concrete in strut
Δ = displacement corresponding to experimental failure load, mm
$\Delta_{cr\text{-}diag}$ = displacement corresponding to first diagonal cracking load, mm
$\Delta_{cr\text{-}flex}$ = displacement corresponding to first flexural cracking load, mm
Δ_L = lateral displacement at experimental failure load, mm
ε_{yield} = steel reinforcement yield strain, MPa
ϕ = angle between strut and tie, degrees

REFERENCES

1. Abdul-Razzaq, K. S.; Jalil, A. M.; and Dawood, A. A., "Ring Deep Beam–A Parametric Study," *AIP Conference Proceedings*, V. 2213, No. 1, 2020, p. 020128. doi: 10.1063/5.0000056

2. Talal, A. A.; Khaleel, W. H.; Hassan, B. N.; Abdul-Razzaq, K. S.; and Dawood, A. A., "A Finite Element Parametric Study of Reinforced Concrete Horizontally Circular Deep Beams," *E3S Web of Conferences*, V. 318, 2021, p. 03013.

3. Mansur, M. A., and Rangan, B. V., "Study of Design Methods for Reinforced Concrete Curved Beams," *ACI Journal Proceedings*, V. 78, No. 3, May-June 1981, pp. 226-254.

4. Hsu, T. T., "Torsion of Structural Concrete-Behavior of Reinforced Concrete Rectangular Members," *Torsion of Structural Concrete*, SP-18, American Concrete Institute, Farmington Hills, MI, 1968, pp. 261-306.

5. Hsu, T. T.; Inan, M.; and Fonticiella, L., "Behavior of Reinforced Concrete Horizontally Curved Beams," *ACI Journal Proceedings*, V. 75, No. 4, Apr. 1978, pp. 112-123.

6. Badawy, H. E. I.; McMullen, A. E.; and Jordaan, I. J., "Experimental Investigation of the Collapse of Reinforced Concrete Curved Beams," *Magazine of Concrete Research*, V. 29, No. 99, 1977, pp. 59-69. doi: 10.1680/macr.1977.29.99.59

7. Tamura, T., and Murata, H., "Experimental Study on the Ultimate Strength of R/C Curved Beam," *Fracture Mechanics of Concrete and Concrete Structures—High Performance, Fiber Reinforced Concrete, Special Loadings and Structural Applications (FraMCos-7)*, Jeju, South Korea, May 2010, pp. 1783-1788.

8. Abdul-Razzaq, K. S., and Dawood, A. A., "Corbel Strut and Tie Modeling–Experimental Verification," *Structures*, V. 26, 2020, pp. 327-339. doi: 10.1016/j.istruc.2020.04.021

9. ACI Committee 318, "Building Code Requirements for Structural Concrete (ACI 318-19) and Commentary (ACI 318R-19)," American Concrete Institute, Farmington Hills, MI, 2019, 623 pp.

10. Schlaich, J.; Schafer, K.; and Jennewein, M., "Toward a Consistent Design of Structural Concrete," *PCI Journal*, V. 32, No. 3, 1987, pp. 74-150. doi: 10.15554/pcij.05011987.74.150

11. Schlaich, J., and Schafer, K., "Design and Detailing of Structural Concrete Using Strut-and-Tie Models," *Structural Engineering*, V. 69, No. 6, 1991, pp. 113-125.

12. Sahoo, D. K.; Singh, B.; and Bhargava, P., "An Appraisal of the ACI Strut Efficiency Factors," *Magazine of Concrete Research*, V. 61, No. 6, 2009, pp. 445-456. doi: 10.1680/macr.2008.00112

13. Sahoo, D. K.; Singh, B.; and Bhargava, P., "Effect of Inclination on the Strength of Struts," *Magazine of Concrete Research*, V. 63, No. 2, 2011, pp. 111-117. doi: 10.1680/macr.9.00178

14. Kondalraj, R., and Appa Rao, G., "Experimental Verification of ACI 318 Strut-and-Tie Method for Design of Deep Beams without Web Reinforcement," *ACI Structural Journal*, V. 118, No. 1, Jan. 2021, pp. 139-152.

15. Akhtaruzzaman, A. A., and Hasnat, A., "Torsion in Concrete Deep Beams with an Opening," *ACI Structural Journal*, V. 86, No. 1, Jan.-Feb. 1989, pp. 20-25.

16. Samman, T. A., and Mesawa, A. A., "Torsional Behavior of High-Strength Concrete Deep Beams with Variable Dimensions," *Engineering and Science*, V. 9, No. 1, 1997, pp. 41-57. doi: 10.4197/Eng.9-1.3

17. Abdul-Razzaq, K. S., and Jebur, S. F., "Suggesting Alternatives for Reinforced Concrete Deep Beams by Reinforcing Struts and Ties," *MATEC Web of Conferences*, V. 120, 2017, p. 01004.

18. Abdul-Razzaq, K. S.; Mustafa Jalil, A.; and Asaad Dawood, A., "Reinforcing Struts and Ties in Concrete Continuous Deep Beams," *Engineering Structures*, V. 240, 2021, p. 112339. doi: 10.1016/j.engstruct.2021.112339

19. Abdul-Razzaq, K. S., and Farhood, M. A., "Design-Oriented Testing and Modeling of Reinforced Concrete Pile Caps," *KSCE Journal of Civil Engineering*, V. 23, No. 8, 2019, pp. 3509-3524. doi: 10.1007/s12205-019-1650-5

20. Abdul-Razzaq, K. S., and Dawood, A. A., "Reinforcing Struts and Ties in Concrete Corbels," *ACI Structural Journal*, V. 118, No. 4, July 2021, pp. 153-162.

21. Abdul-Razzaq, K. S.; Talal, A. A.; and Dawood, A. A., "The Role of Reinforcement in Concrete Ring Deep Beams," *ACI Structural Journal*, V. 120, No. 2, Mar. 2023, pp. 129-141.

22. Prakash, S.; Li, Q.; and Belarbi, A., "Behavior of Circular and Square Reinforced Concrete Bridge Columns under Combined Loading Including Torsion," *ACI Structural Journal*, V. 109, No. 3, May-June 2012, pp. 317-328.

23. ASTM C39/C39M-03, "Standard Specification for Testing Method for Compressive Strength of Cylindrical Concrete Specimens," ASTM International, West Conshohocken, PA, 2003.

24. ASTM C496-96, "Standard Specification for Splitting Tensile Strength of Cylindrical Concrete Specimens," ASTM International, West Conshohocken, PA, 1996.

25. ASTM C78-02, "Standard Test Method for Flexural Strength Of Concrete (Using Simple Beam with Third-Point Loading)," ASTM International, West Conshohocken, PA, 2002.

26. ASTM A615/A615M-05, "Standard Specification for Deformed and Plain Billet-Steel Bars for Concrete Reinforcement," ASTM International, West Conshohocken, PA, 2005, 5 pp.

27. ASTM A496-02, "Standard Specification for Steel Wire, Deformed, for Concrete Reinforcement," ASTM International, West Conshohocken, PA, 2002, 5 pp.

ACI STRUCTURAL JOURNAL TECHNICAL PAPER

Title No. 120-S73

Reinforced Concrete Coupling Beams with Different Layouts under Seismic and Wind Loads

by Tse-An Chou, Seung Heon Lee, Chunho Chang, and Thomas H.-K. Kang

Reinforced concrete (RC) coupling beams can act as an efficient energy-dissipating fuse and force transfer element between RC shear walls in low- to high-rise buildings. To investigate the effect of different reinforcement layouts, amounts of confinement, and loading protocols on RC coupling beams, eight RC coupling beams with a span-depth ratio of 2.5 were tested with three parameters: 1) longitudinal or diagonal reinforcement layout; 2) full, two-thirds, or one-half the amount of confinement relative to ACI 318-19 requirements; and 3) seismic or wind loading protocols. The test results showed that: first, the nominal shear and upper-limit equations for diagonally RC coupling beams in ACI 318-19 may need to be improved, and it is also recommended to consider the contribution of confinement to shear strength; and second, because only minor cracks were observed under the wind with no significant damage, the experiment in this study can act as an example of structural verification for performance-based wind design.

Keywords: confinement; coupling beam; diagonal reinforcement; longitudinal reinforcement; reinforced concrete (RC); seismic loading; wind loading.

INTRODUCTION

With a rapidly growing population, taller and taller buildings are being built in this era. Coupling beams are often used in high-rise buildings due to their advantages of opening windows or doorways on core walls and acting as an efficient energy-dissipating system to resist lateral loads. They are typically designed with a span-depth ratio (l_n/h) of 2.4 for residential and 3.3 for office use in high-rise buildings (Naish et al. 2013).

In the ACI 318-19 (ACI Committee 318 2019) design procedure, intermediate reinforced concrete (RC) coupling beams with a span-depth ratio of 2 to 4 do not have specific regulations of reinforcement layout, whether longitudinally or diagonally. Thus, the nominal shear strength ($V_{n,beam}$) for a longitudinally RC coupling beam is estimated based on the nominal one-way shear strength of a normal beam by Eq. (1)

$$V_{n,beam} = V_c + V_s \tag{1}$$

where V_c is the nominal shear strength provided by concrete; and V_s is the nominal shear strength provided by confinements. The equation of nominal shear strength for a diagonally RC coupling beam can be calculated using Eq. (2)

$$V_{n,beam} = 2A_{vd}f_y\sin\alpha \tag{2}$$

where A_{vd} is the total area of diagonal reinforcing bars in each group in a diagonally RC coupling beam; and α is the angle between the diagonal bars and the longitudinal axis of a coupling beam. However, in ACI 318-19, the nominal shear strength (V_n) shall not be taken greater than the upper limit ($V_{n,upper}$), as Eq. (3)

$$V_{n,upper} = 0.83\sqrt{f_c'\,(\text{MPa})}A_{cw} \tag{3}$$

where A_{cw} is the area of the concrete section of a coupling beam resisting shear.

Diagonally RC coupling beams can provide better shear strength, deformation capacity, and energy dissipation behavior compared to longitudinally RC coupling beams because diagonal reinforcing bars simultaneously function as flexural and shear reinforcements. Their contribution to shear strength typically results in well-rounded hysteresis loops without the pinching effect. However, many previous outcomes (Naish et al. 2013; Lim et al. 2016a,b; Cheng et al. 2019) show that the actual shear strength of a diagonally RC coupling beam is notably larger than the nominal shear strength and upper limit in ACI 318-19. If coupling beams do not sufficiently develop plastic hinges due to overconservative design, this could cause undesirable forces (such as flexural force) or damage to adjacent structural elements. Based on this mechanism, it may be more acceptable to use the nominal flexural strength (M_n) of a coupling beam to estimate the shear strength, as shown in Eq. (4). Park et al. (2020) also proposed an estimation model for diagonally RC coupling beams with l_n/h of 1 to 3, which additionally considered the contribution of longitudinal reinforcing bars and concrete for diagonally RC coupling beams.

$$V_{Mn} = 2M_n/l_n \tag{4}$$

Moreover, the amount of confinement had a significant influence on the cyclic behavior and failure modes of diagonally RC coupling beams (Han et al. 2019), and this effect has also not been incorporated into the equations of nominal shear strength and the upper limit in ACI 318-19. In general, these two aforementioned equations for diagonally RC coupling beams should be updated, preferably also considering the effects of confinement, because excessive conservatism in coupling beams may be detrimental to achieving

ACI Structural Journal, V. 120, No. 4, July 2023.
MS No. S-2022-191.R1, doi: 10.14359/51738743, received October 31, 2022, and reviewed under Institute publication policies.

the desired behavior for performance-based design and evaluation.

For high-rise buildings, wind loads are as critical as seismic loads. In particular, the design of certain structural elements, including coupling beams, is generally controlled by wind demands (Aswegan et al. 2017). In terms of seismic design, structural elements are allowed to reach inelastic behavior, and numerous previous tests (Paulay and Binney 1974; Barney et al. 1980; Tassios et al. 1996; Xiao et al. 1999; Galano and Vignoli 2000; Kwan and Zhao 2002; Naish et al. 2013; Cheng et al. 2019; Park et al. 2020) regarding seismic loading have been performed.

For wind design, compared to the former provision of ASCE/SEI 7-16 (2017), which used equivalent static wind load to keep buildings in the elastic phase, inelastic behavior under 700- to 3000-year mean recurrence interval (MRI) wind loads in ASCE/SEI (2019) is now permitted in the latest ASCE/SEI 7-22 (2022) provision. Among the components of wind load, including along-wind, across-wind, and torsional wind, the response of across-wind is generally larger than along-wind for a taller building due to its large resonant response (Alinejad and Kang 2020). According to analysis results from Jeong et al. (2021), reducing the design wind force (resonant component only) by using wind load reduction factors (R_{WR}) of 2 and 3 to introduce inelastic behavior could significantly decrease the design demand of a coupling beam, while also increasing the ductility of the system.

In terms of structural performance levels for wind hazard scenarios, the damage control (DC) performance level for performance-based wind design is suggested by Alinejad et al. (2020), which is defined as the midpoint between the immediate occupancy (IO) and life safety (LS) performance objectives in ASCE/SEI 41-17 (2017). To satisfy the DC performance level and check the safety margin against low-cycle fatigue and ratcheting failures under extreme wind events, the performance of coupling beams is likely to be confirmed through testing under moderate inelastic deformations with an appropriate number of cycles for wind load. Therefore, Abdullah et al. (2020a) established a wind loading protocol to represent the inelastic response of a tall building by determining the number and amplitude of the cycles from loading histories corresponding to 1700- to 3000-year MRI wind loads. The test results show that the specimens satisfied the IO performance level with relatively negligible damage observed, but testing various specimens with alternative wind protocols was recommended due to a lack of experimental data.

To summarize all the needs stated previously, a total of eight specimens with a span-depth ratio (l_n/h) of 2.5 were tested, and the purposes of this study were to: 1) investigate the behaviors of both longitudinally and diagonally RC coupling beams with three different amounts of confinement (full, two-thirds, and one-half) relative to ACI 318-19 requirements; and 2) develop a wind loading protocol based on the peak factor of across-wind in the Korean Building Code (KBC) (2016) and represent the behavior of RC coupling beams under the wind loading protocol composed of a large number of linear cycles and limited nonlinear cycles.

RESEARCH SIGNIFICANCE

This study aims to provide useful experimental data for the development of future building codes and investigate the feasibility of extending performance-based design to wind engineering. Data from eight large-scale tests of RC coupling beams with a span-depth ratio of 2.5 tested under seismic and wind loading protocols are represented. The key parameters were reinforcement layout (longitudinal or diagonal reinforcement), the amount of confinement, and loading protocol. The findings show that the different layouts and amounts of confinement did have a meaningful influence on the RC coupling beams, and specimens tested under a simulated wind event only had minor cracks with no extensive damage observed.

EXPERIMENTAL PROGRAM

Among a total of eight two-thirds-scale RC coupling beams, there are four series of layouts, and each series was tested under seismic and wind loading protocols. Except for the test parameters, all other conditions were designed the same, with a focus on investigating modeling parameters for the RC coupled wall systems used in regions of moderate-to-high seismicity and/or high wind speed. The following sections describe the design details, material properties, test setup, instrumentation, and loading protocols in this study.

Test specimens

Eight test specimens were designed based on common coupling beams in residential buildings with a span-depth ratio (clear length/depth, l_n/h) of approximately 2.5. Due to the laboratory space and strength constraints, the coupling beams were scaled down to two-thirds-scale of the prototype coupling beams. Thus, the cross-sectional dimensions (width x depth x span, b_w x h x l_n) were 300 x 500 x 1250 mm (11.8 x 19.7 x 49.2 in.). All details were designed according to the design procedure specified in ACI 318-19, except for the reduction of confinements for the purpose of the study. The specified concrete strength (f_c') was 30 MPa (4.4 ksi), and the yield strength (f_y) was 400 MPa (58.0 ksi) for all reinforcing bars. The longitudinal reinforcement ratio (ρ) of all specimens was approximately 1.9%. Detailed information is provided in subsequent paragraphs, and Fig. 1 illustrates the specimen layouts.

For longitudinally RC coupling beams, the specimen L100 series and L67 series were designed using a traditional reinforcement layout with three D32 (No. 10) headed reinforcing bars as tensile and compressive reinforcements with a sufficient development length of 500 mm (19.75 in.), and were confined by the full and two-thirds amount of D13 reinforcing bars (No. 4) with a spacing of 105 mm (4.1 in.) and 165 mm (6.5 in.), respectively. With regard to the diagonally RC coupling beams, four D25 (No. 8) headed reinforcing bars for each group were placed diagonally with an angle (α) of approximately 15 degrees and an anchorage length of 500 mm (19.75 in.) for the specimen D67 series and D50 series. Because diagonal coupling beams have notably higher

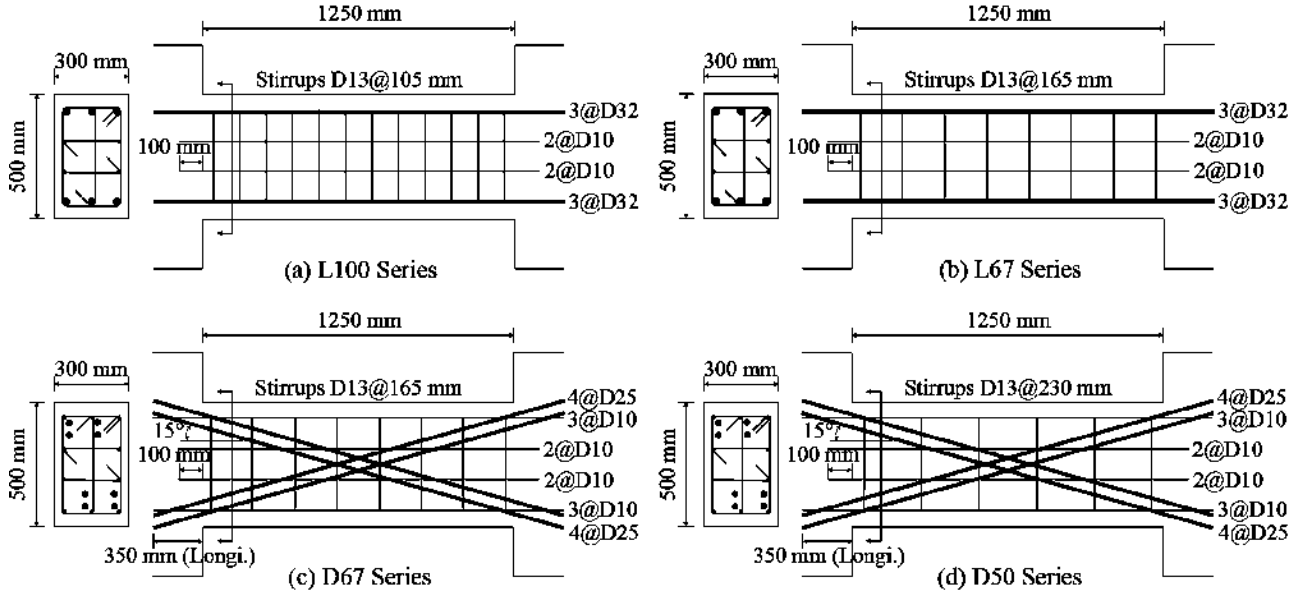

Fig. 1—Specimen layout. (Note: 1 mm = 0.039 in.)

shear strength than longitudinal coupling beams, instead of designating the full amount of confinement, two-thirds amount with a spacing of 165 mm (6.5 in.) for the D67 series and half amount with a spacing of 230 mm (9.1 in.) for the D50 series were arranged. As shown in Fig. 1, four D10 (No. 3) skin reinforcing bars were placed with only 100 mm embedment in the middle of each beam. For the D67 and D50 series, three top and bottom D10 (No. 3) longitudinal bars were provided with a development length of 350 mm (13.75 in.), which is longer than required.

Material properties

A normalweight concrete with a design 28-day concrete compressive strength (f_c') of 30 MPa (4.4 ksi) was specified for all specimens. The maximum aggregate size of 25 mm (1 in.) and a slump of 150 mm (5.9 in.) were requested. Concrete strength was determined based on the average of three standard 100 x 200 mm (4 x 8 in.) cylinders for each series. All cylinders were cast on the same day along with casting specimens from each concrete truck at a local concrete plant. Korean Standard (KS) SD400 deformed bars with a nominal yield strength (f_y) of 400 MPa (58 ksi) were specified for steel reinforcing bars. The average yield strength and ultimate strength (f_u) for each size were determined by submitting three 500 mm (19.7 in.) long specimens to the direct tensile test. Table 1 shows the test results of the concrete and steel reinforcing bars.

Test setup and instrumentation

When a building oscillates, a coupling beam is subject to a slight axial compressive deformation, as well as prominent lateral deformation. To replicate this mechanism, the test setup was arranged as shown in Fig. 2(a), where coupling beams were set in a vertical direction and embedded in two adjacent stiff RC blocks, which were taken as structural wall elements. The bottom block was enlarged to avoid overturning and bolted to the laboratory strong floor, whereas the top block was bolted to the upper steel frame, which was

Table 1—Measured material properties

Specimen series			L100	L67	D67	D50
f_c', MPa			32.2	32.5	32.2	28.9
Steel reinforcement, MPa	D32	f_y	461.7		—	
		f_u	645.1		—	
	D25	f_y	—		427.6	
		f_u	—		668.6	
	D13	f_y	465.3			
		f_u	702.3			
	D10	f_y	433.7			
		f_u	685.6			

Note: 1 MPa = 145 psi.

connected to a 100 ton (220 kip) hydraulic actuator and two steel links including two vertical steel frames and four pin connections. However, if a coupling beam is tested with a consistent height, it will be subjected to axial extension at large drift demands, and the resulting axial force may significantly impact the coupling beam's performance (Lequesne et al. 2013). Thus, two steel links were set to descend slightly while keeping the upper steel frame horizontal, to restrain any end rotation and axial elongation that might occur while the hydraulic actuator applied lateral displacement to the upper steel frame (Fig. 2(b)). Two lower steel frames were set for fixing the steel links to the laboratory's strong floor, and two gusseted angle brackets were inserted between the top block and upper steel frame to prevent sliding.

The external deformation of each specimen was measured by 12 linear variable differential transformers (LVDTs), and four string potentiometers were used to measure global displacements, as shown in Fig. 3. A total of 30 strain gauges were installed to measure strains in longitudinal or diagonal reinforcing bars, confinements, and longitudinal skin reinforcing bars. Crack widths were manually measured at the end of each loading stage.

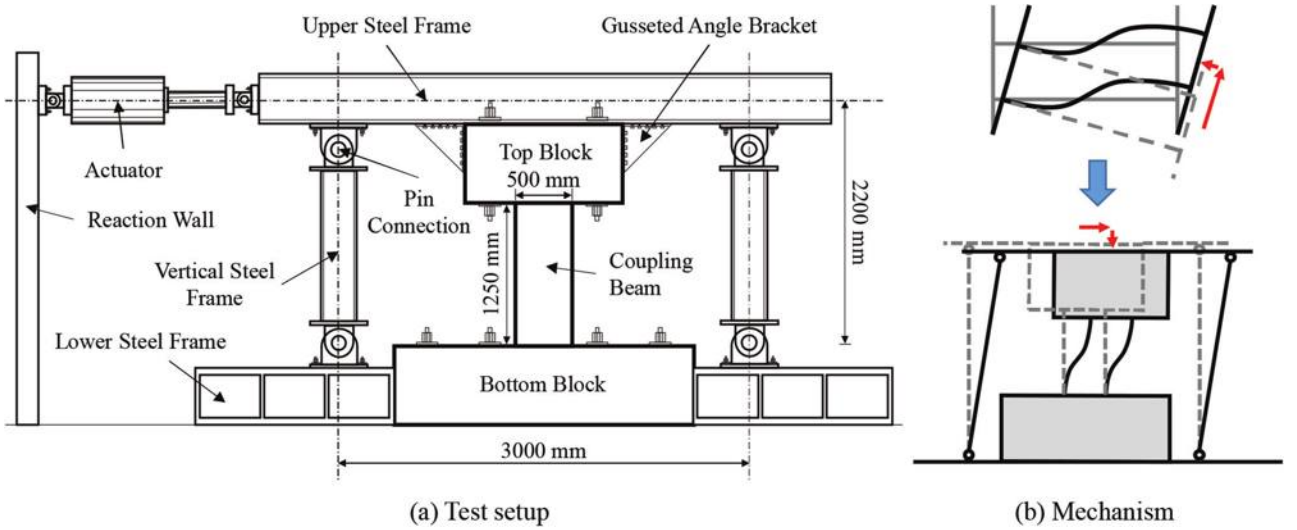

Fig. 2—Test setup.

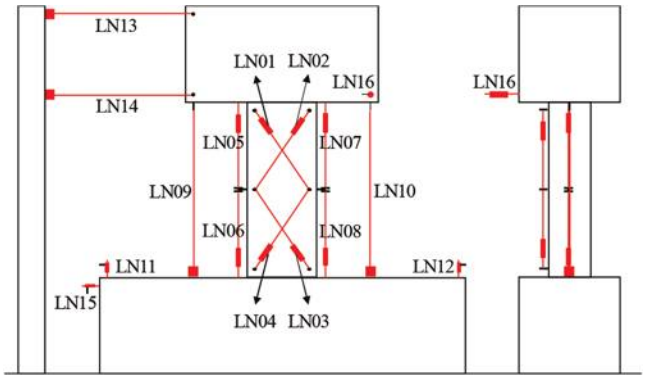

Fig. 3—Instrument layout.

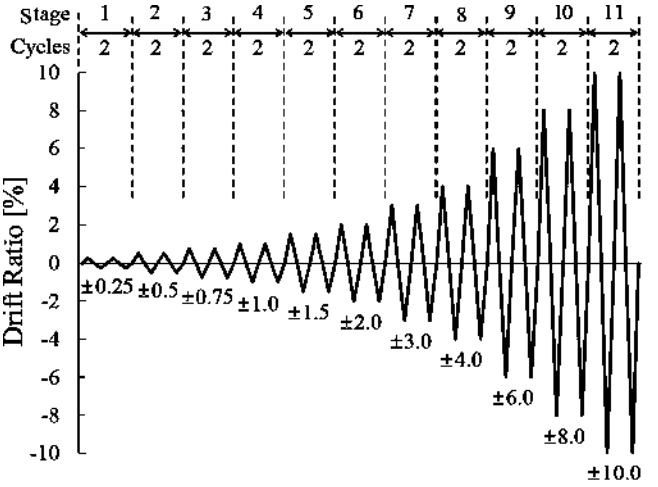

Fig. 4—Seismic loading protocol.

Loading protocols

In this study, each series was tested under both seismic and wind loading protocols. To date, many guidelines have applied performance-based design to earthquake engineering, such as PEER/ATC-72-1 (2010) and the Tall Building Initiative (TBI 2017). ACI 374.2R-13 (ACI Committee 374 2013) recommended a cyclic loading protocol to perform seismic behavior for structural component tests, which was also applied to this study with two displacement-controlled cycles at each stage, as shown in Fig. 4. In terms of wind engineering, the application of performance-based wind design in ASCE/SEI 7-22 is still in its infancy, and a wind loading protocol for testing structural components has not been established so far. Therefore, considering that across-wind is the key factor of wind load for certain structural elements in tall buildings, a displacement-controlled wind loading protocol was developed with a zero-mean process. Buildings of 35 to 70 stories of 150 to 300 m (500 to 1000 ft) height, the general range of the 300 tallest buildings in Korea, with fundamental periods between 3 and 6 seconds were considered, and the following steps describe the procedure in detail:

Amplitude of cycles—The expected maximum ductility demand for coupling beams in an extreme wind event was assumed as 1.5 times the yield ratio (θ_y) in this study, where the yield ratio (θ_y) is the specified yield drift ratio. The ductility factor of 1.5 was considered to be an adequate number, which is the prescribed ductility factor for deformation-controlled elements in the evaluation process in ASCE/SEI (2019), and whose value is much less than the inherent ductility factor of approximately 2.5 to 5 from the seismic response of RC coupling beams. The amplitude set for each stage was increased from 0.25 to 1.5θ_y in increments of 0.25θ_y, and then symmetrically stepped down to 0.25θ_y. The yield ratio was taken from the result of the seismic test, which was performed prior to the wind test for the same series specimen.

Corresponding design force—The maximum design force (F_{max}) was set as $g_L\sigma$, where g_L (Eq. (5)) is the peak factor in the across-wind direction in the KBC (2016), σ is the standard deviation of the equivalent static wind load, and n_L is the natural frequency of the first mode in the across-wind direction. The corresponding design force (F) in the elastic response is equal to the maximum design force × force ratio (F/F_{max}) derived from the equal-energy principle, which resulted in the force reduction factor ($R = F_{max}/F_y$) of 1.41, where F_{max} is the maximum design force for an elastic

system, and F_y (= $0.71F_{max}$) is the specified yield strength, as shown in Fig. 5 and Table 2.

$$g_L = \sqrt{2\ln(600n_L)} + 1.2 \quad (5)$$

Number of cycles—The total amount of cycles was determined by considering tall buildings oscillating under a 1-hour wind event, which is frequently taken in ASCE/SEI 7-16. Consequently, the number of cycles at each stage could be estimated from the cumulative probability density of the corresponding design force based on Gaussian distribution (Fig. 6). Table 2 shows the step-by-step calculation result, and Fig. 7 shows the result of the wind loading protocol that was developed. Based on the fundamental period, it resulted in a total of 915 cycles in the wind loading protocol, which was composed of 900 linear cycles and 15 nonlinear cycles ($1.25\theta_y$ and $1.5\theta_y$). The expected testing time for simulated wind events was approximately 10 hours, whereas seismic events needed only 4 hours.

TEST RESULTS

Cracking progression and hysteretic behavior

Figure 8 presents the crack pattern and maximum crack width at different drift ratios or chord rotations (θ) for all the test specimens, where the drift ratio and θ were defined as the lateral deflection of a specimen measured from the LVDT divided by the beam clear span and adjusted by extra rotations from the top and bottom blocks. Figure 9 presents the lateral load versus chord rotation curves for all specimens, where the ductility demand ($\theta_{test}/\theta_{y,test}$) is also shown in the upper axis, defined as the rotation demand divided by the yield rotation ($\theta_{y,test}$). The $\theta_{y,test}$ was obtained when the first main reinforcing bar reached yield strain from the test result of the seismic event. Initial cracks were observed in the first stage for all specimens except the specimen L100 series (L100-S and L100-W), which were observed in Stage 2 and Stage 3, respectively, due to smaller lateral displacement caused by unexpected out-of-plane displacement. Horizontal cracks first developed at the beam for all specimens, and inclined cracks developed subsequently with a maximum crack width of 0.05 mm (0.002 in.), as shown in the first figures of Fig. 8(a) to (h). All specimens showed similar inclined crack patterns, which mainly appeared on the lower part of beams with an angle of approximately 45 degrees in the final state, as shown in the middle figures of Fig. 8. However, compared to diagonal coupling beams, only longitudinal coupling beams developed vertical cracks along the line of longitudinal reinforcing bars after the inclined cracks occurred. The follow-up progressions of cracking and hysteretic behavior for each specimen are elaborated as follows.

L100 series—In specimen L100-S, a crack with a 2.0 mm (0.079 in.) width occurred at the right-side bottom at a drift ratio of 2.9%, and concrete deteriorated in the lower-right corner at the reverse side of the beam at a drift ratio of 3.5% as its peak shear strength (V_{test}) reached 684.0 kN (153.8 kip), where the test was stopped due to unexpected out-of-plane

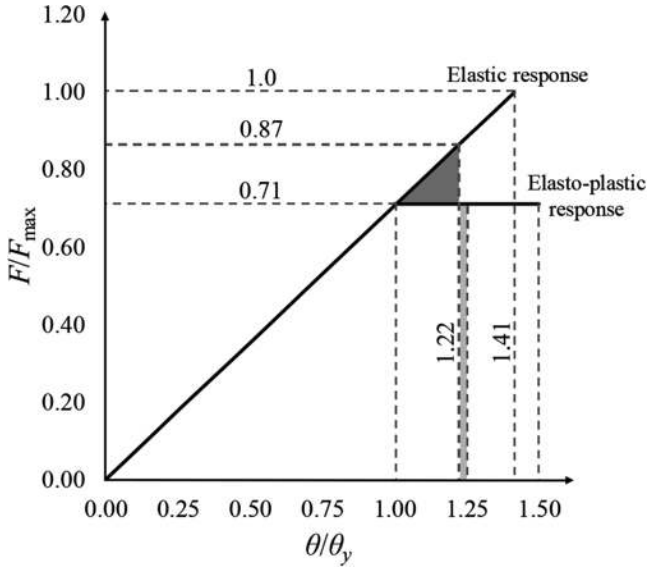

Fig. 5—Equal-energy principle.

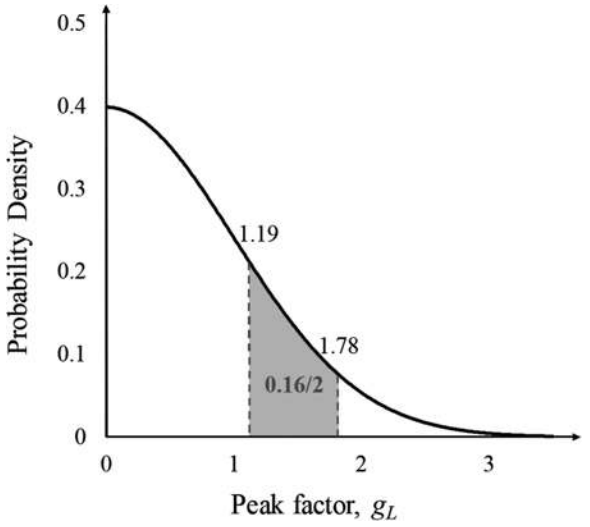

Fig. 6—Gaussian distribution (based on 200 m tall building).

Table 2—Calculation for wind loading protocol

Rotation	Force ratio (F/F_{max})	Design force	Probability	Expected No. of cycles	Design No. of cycles
$1.5\theta_y$	1.00	3.23σ to 3.44σ (= $g_L\sigma$)	0.002 to 0.004	2 to 3	3
$1.25\theta_y$	0.87	2.80σ to 2.98σ	0.012 to 0.017	11 to 15	12
$1.0\theta_y$	0.71	2.28σ to 2.43σ	0.054 to 0.065	39 to 65	50
$0.75\theta_y$	0.53	1.71σ to 1.82σ	0.158 to 0.167	101 to 191	150
$0.5\theta_y$	0.35	1.14σ to 1.22σ	0.314 to 0.322	191 to 391	300
$0.25\theta_y$	0.18	0.57σ to 0.61σ	0.431 to 0.451	261 to 547	400

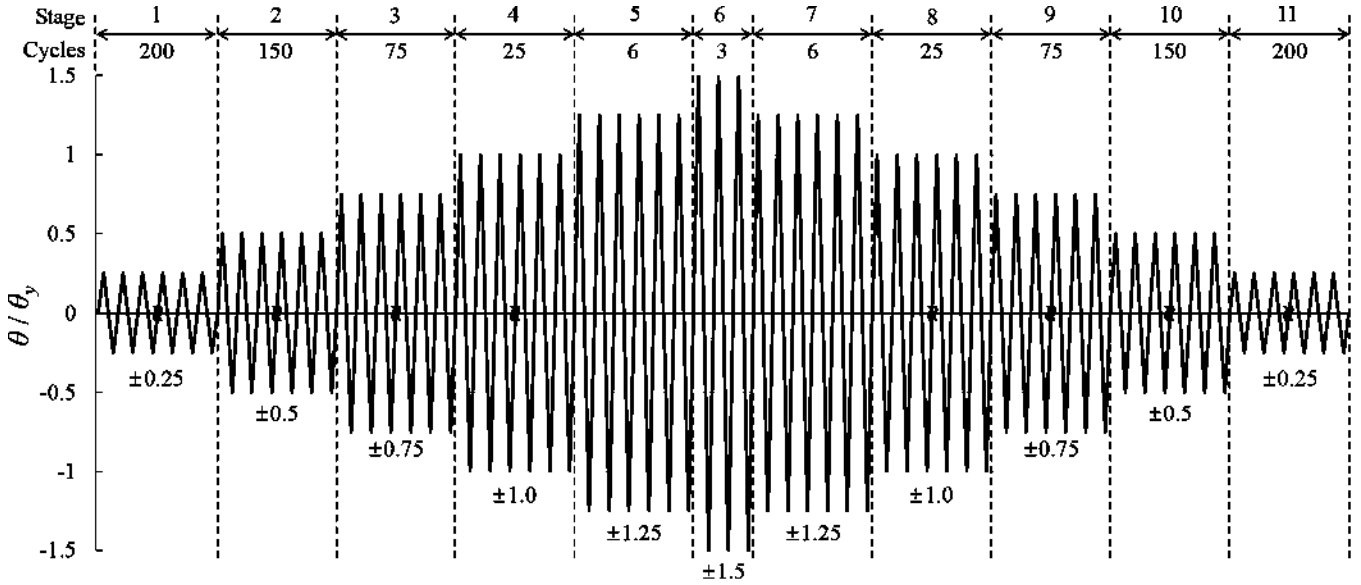

Fig. 7—Wind loading protocol.

displacement occurring. Because the unexpected out-of-plane displacement limited yield rotation ($\theta_{y,test}$) to a small value, specimen L100-W only had a maximum crack width of 0.1 mm (0.004 in.) at Stage 4 (1.0θ_y target drift), and obvious cracks mainly developed until Stage 7 (1.25θ_y target drift). After Stage 7, the specimen only had some extended slight cracks. The problem of unexpected out-of-plane displacement was solved after finishing testing the L100 series.

L67 series—A maximum 3.5 mm (0.14 in.) width vertical crack appeared on specimen L67-S at the first cycle of Stage 7 (3.0% target drift ratio). The peak shear strength (V_{test}) of 632.1 kN (142.1 kip) was reached at a 2.0% drift ratio, and dropped drastically to approximately 60% for the sequential cycle. Concrete significantly spalled out along the line of longitudinal reinforcing bars at the final stage, with roughly 30% of the peak shear load and an ultimate drift ratio θ_u of 3.94%. For specimen L67-W, a vertical 1.6 mm (0.063 in.) width crack developed along the longitudinal reinforcing bars at Stage 6 (1.5θ_y target drift) with a maximum drift ratio of 2.14%, and the crack width got wider to 2.0 mm (0.079 in.) at Stage 7. After that, while the drift ratio decreased progressively, only some slight extended cracks could be observed.

D67 series—The specimen D67-S had a 0.65 mm (0.026 in.) width crack at a drift ratio of 2.97% in the lower right corner at the left side of the beam. The crack continuously widened up to 6.0 mm (0.24 in.) as the peak shear strength V_{test} of 809.0 kN (181.9 kip) was reached at a drift ratio of 6.43%, and then its lateral strength declined by approximately 10% of the peak lateral strength, while concrete spalled off the four corners. This crushing pattern of concrete was most likely caused by flexural compression. The maximum crack width of specimen D67-W developed from 0.15 to 0.45 mm (0.006 to 0.018 in.) from Stages 4 to 6. Except for small sections in lower corners chipping off at Stages 8 and 9 (1.0θ_y and 0.75θ_y target drift) due to flexural compression, the coupling beam did not have any wider cracks.

D50 series—The crack width of D50-S developed to 5 mm (0.197 in.) at a drift ratio of 3.8% (Stage 8), and then the coupling beam reached a maximum lateral strength V_{test} of –761.4 kN (171.2 kip) at Stage 9. However, after concrete in three corners of the beam spalled off at Stage 8 (maximum drift ratio 6.3%), the strength was reduced to approximately 90% of the peak lateral strength at the second cycle. Finally, owing to the presence of reinforcing bars, the test was stopped when the shear strength had dropped to approximately 50% of the peak lateral strength with an ultimate drift ratio θ_u of 8.69%. For specimen D50-W, the maximum crack width increased from 0.2 to 0.35 mm between Stages 4 and 6. A small part of facial concrete in the lower-right corner of the beam fell off at Stage 8 due to flexural compression; however, no new crack or large extended crack was observed.

As can be seen from the test results in Fig. 9, similar to previous findings (Barney et al. 1980; Lim et al. 2016a,b), this study reconfirms that diagonally RC coupling beams do indeed provide higher peak shear strengths (V_{test}) and better capacities of deformation and energy dissipation than longitudinally RC coupling beams, due to the well-rounded curves, which indicate the absence of pinching effects. Therefore, based on the ACI 318-19 design process of coupling beams with a span-depth ratio of 2.5, under a similar ratio of main reinforcements, a diagonally RC coupling beam has superior seismic behavior to a longitudinally RC coupling beam.

The specimens tested under simulated wind events (blue curves) presented more pinching effects due to an increased number of cycles after Stage 6, as shown in Fig. 10, but there was no occurrence of extensive damage and only minor cracks were observed, with widths ranging between 0.35 and 2.0 mm (0.014 and 0.079 in.). The specimens satisfy the DC performance level proposed by Alinejad et al. (2021) for the extreme conditions in the performance-based wind design framework. In this possible scenario of 1700- to 3000-year MRI wind load for the DC performance level, which is also within the applicable range of ASCE/SEI (2019), the drift

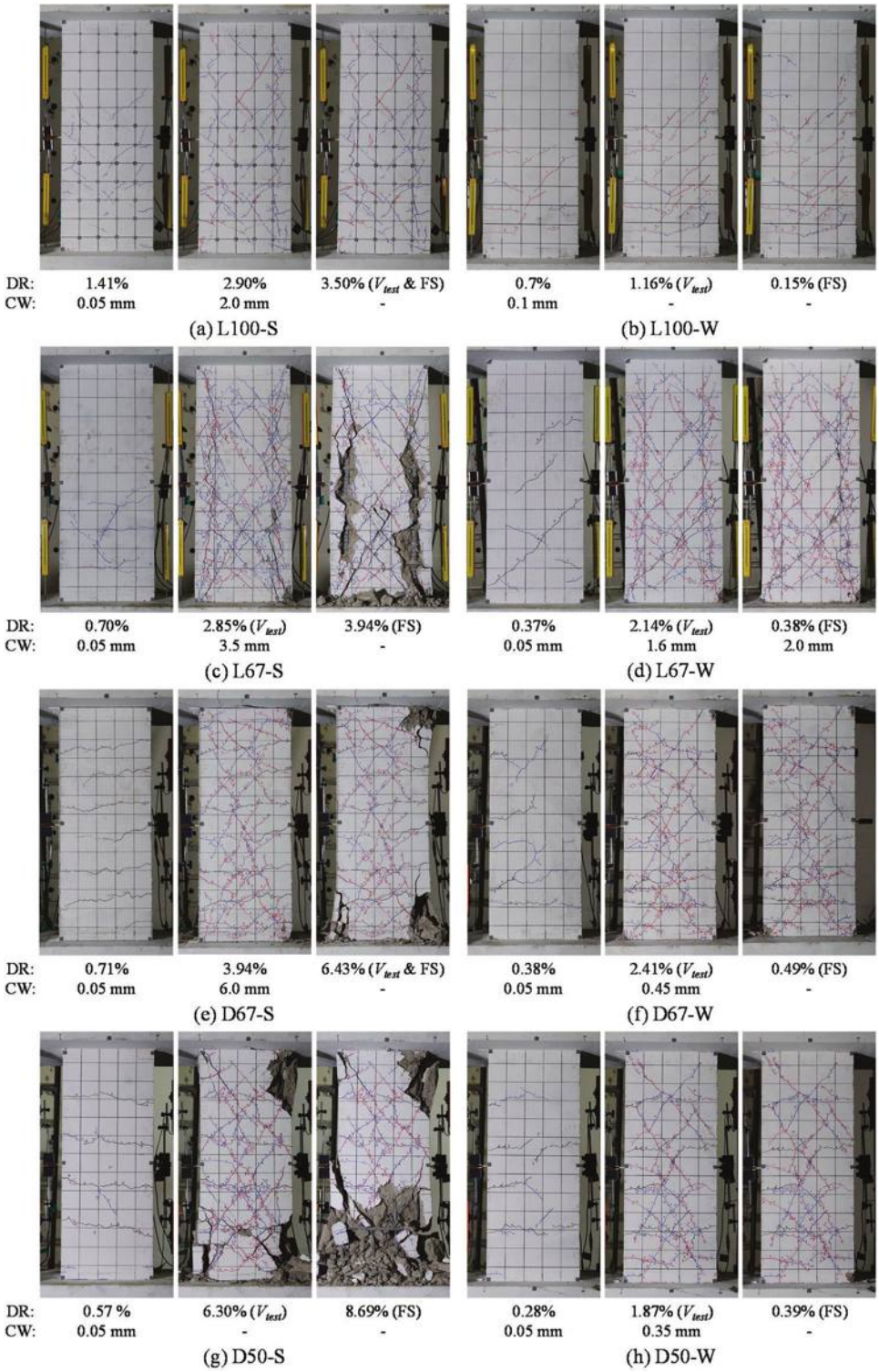

Fig. 8—Cracking progression of specimens. (Note: DR is drift ratio, CW is maximum crack width, and FS is final state of specimen.)

limit is to be set such that a coupling beam will not show severe damage after the applied force exceeds the yield force and corresponding deformation limit.

Overall, the test results of hysteretic behavior signal that diagonally RC beams with half of the required confinement and longitudinally RC beams with two-thirds of the required could be applied to the case of low-to-moderate seismicity and high wind hazard. Moreover, the experiments performed in this study can be seen as an example of the application of the performance-based wind design framework.

Drift contribution

To understand the behavior of coupling beams during the test, the contributions of four components to the total chord rotation were investigated in this study, including shear deformation of the beam, flexure or curvature deformation of

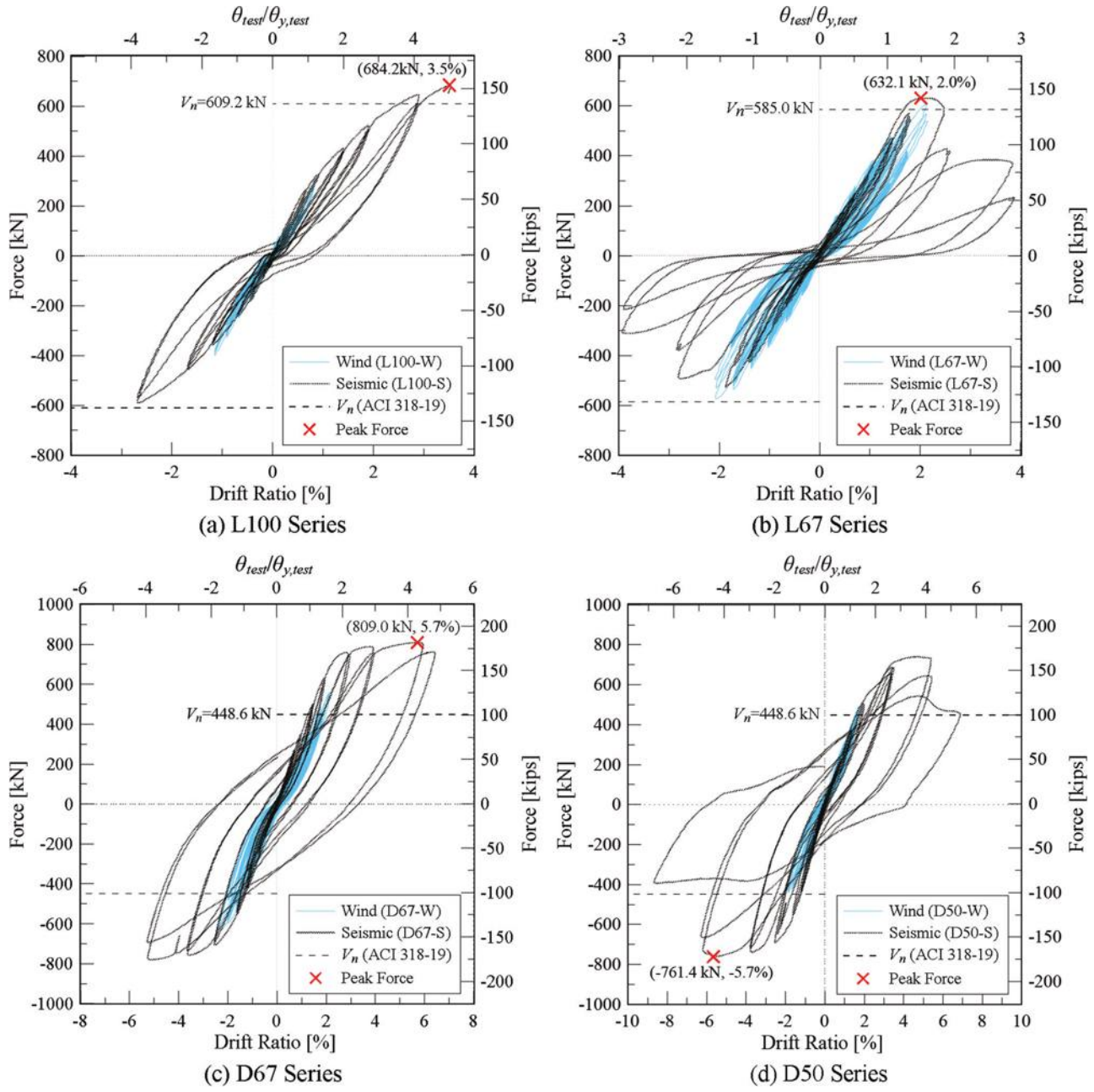

Fig. 9—Lateral load versus chord rotation curves.

the beam, bar slip or extension at the beam ends, and sliding at the beam ends. Each contribution was determined using the measured data and the same approach taken by Cheng et al. (2019) and Abdullah et al. (2020b). As seen in Fig. 11, the vertical axis represents the accumulation of contributions from the four components at peak force in each test stage, and the horizontal axis shows the corresponding drift ratio for the eight test specimens.

The results show that shear and flexural deformations were the main contributors to the initial total chord rotation for all specimens. The most rapid increase among the four components was shear deformation, which followed an increase in drift ratio and accounted for the largest contribution, with more than 70% in the final stage subjected to seismic load, and 60% to wind load in Stage 6. In the meantime, there was a very noticeable trend of the proportion of flexural deformation sharply decreasing to approximately 10% in the final stage. This is because inclined shear cracks grew faster than flexural cracks as deformation demand increased until the coupling beams eventually failed.

However, a different trend emerged for specimens tested under wind load in ramp-down stages (with smaller deformation demands), where the contribution of shear deformation narrowed down again, except for specimen L67-W. The reason for this phenomenon appears to be that specimen L67-W became susceptible to shear distortion after conspicuous cracks occurred along the line of longitudinal reinforcing bars. Specimen L100-W did not have evident cracks due to the small demand of the yield drift ratio taken from L100-S, and the diagonal reinforcing bars in specimens D67-W and D50-W could restrain shear distortion. Therefore, only the shear contribution of L67-W kept rising

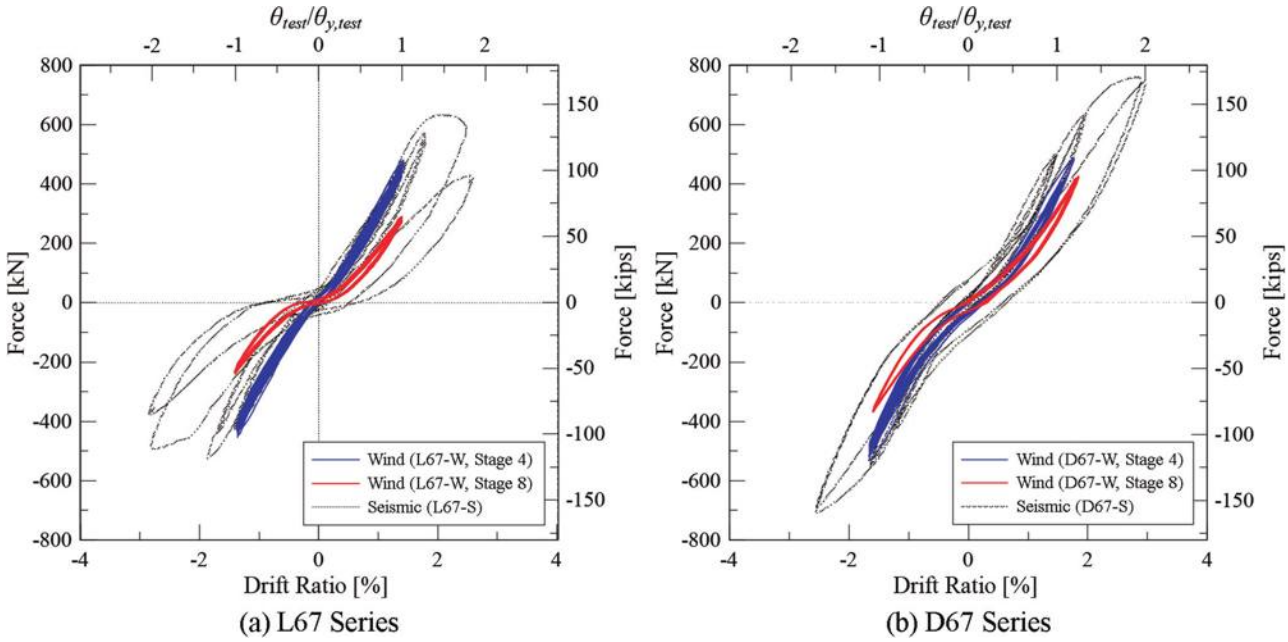

Fig. 10—Lateral load versus chord rotation curves at $1.0\theta_y$.

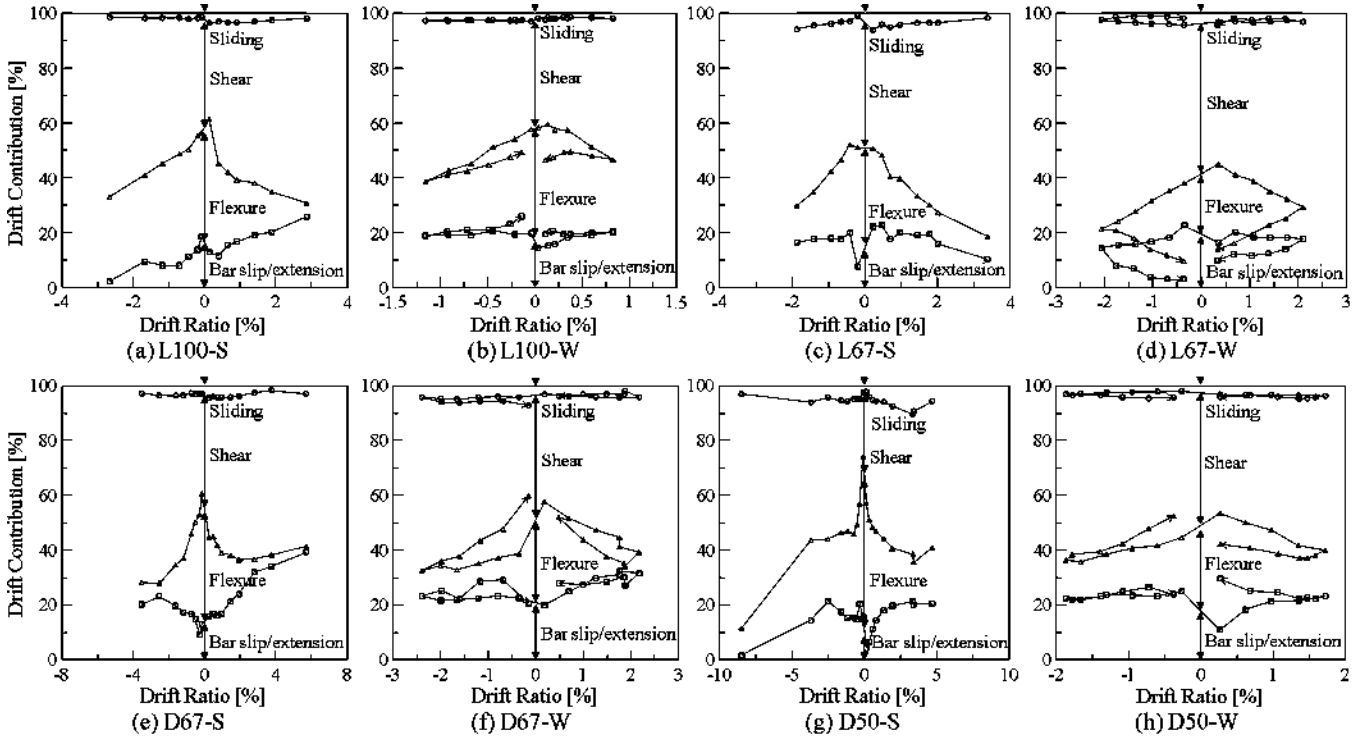

Fig. 11—Drift contribution.

until failure. Although the contribution of bar slip/extension showed a few fluctuations, it generally remained under 25%, except for specimen D67-S. Its bar slip/extension almost reached 40% in the final stage, likely due to the flexural mechanism resulting in the deterioration of corner concrete and the consequent bending of diagonal reinforcing bars. For specimen L100-S, due to unexpected out-of-plane displacement occurring in the pushing direction (positive drift ratio), radial cracks developed in the lower corner and caused the contribution of bar slip/extension to be asymmetric. In terms of sliding contribution, it remained steady at under 10% for all test specimens.

When coupled with the graphic information, a possible conclusion can be derived that the shear contribution increased as deformation increased, but different test mechanisms and reinforcement layouts could cause the different composition of drift contribution to RC coupling beams. Although the bar slip/extension contribution was larger at lower drift ratios under wind load than under seismic load, the general compositions were similar for all the specimens with an l_n/h of 2.5.

DISCUSSION

ACI 318-19 shear design equations

Table 3 shows the test results and evaluated shear strength from ACI 318-19 of four specimens subjected to seismic load. All the notations were defined as follows: the shear strength ($V_{n,beam}$) was estimated by using Eq. (1) for a longitudinally RC coupling beam and Eq. (2) for a diagonally RC coupling beam, while the upper limit ($V_{n,upper}$) was calculated by Eq. (3). As can be seen in column 4 of Table 3, the nominal shear strength (V_n) of specimen L100-S was controlled by the limitation equation, while the others were equal to $V_{n,beam}$. Column 6 of Table 3 shows that all coupling beams in this study had higher normalized shear strength ($V_{test}/\sqrt{f_c'}$ [MPa]A_{cw}) than the parameter 0.83 in Eq. (2). The test results of 20 longitudinal coupling beams and 29 diagonal coupling beams with span-depth ratios between 2 and 4 from previous findings (Barney et al. 1980; Kanakubo et al. 1996; Shimazaki 2004; Breña and Ihtiyar 2011; Fortney et al. 2008; Lim et al. 2016a,b; Han et al. 2019; Naish et al. 2013; Cheng et al. 2019; Park et al. 2020; Abdullah et al. 2020a) were collected and compared with the results of this study in Fig. 12 to 15.

Figure 12 reflects that the limitation equation covered most longitudinally RC coupling beams (Longi.); however, two-thirds of diagonally RC coupling beams (Diag.) exceeded the strength limit of ACI 318-19. Additionally, Fig. 13 reveals that the normalized shear strengths ($V_{test}/A_v f_y \sin\alpha$) of 29 beams mostly ranged from 2.5 to 4.0, which is higher than the parameter of 2.0 in Eq. (2). Those results indicate that the nominal shear strength (V_n) in ACI 318-19 significantly underestimates the shear strength for diagonally RC coupling beams, which may incur damage at the adjacent walls before the diagonally RC coupling beams develop sufficient plastic hinges. Rows 9, 10, and 11 of Table 3 and Fig. 14 compare the ratios of V_n, V_{Mn} (Eq. (4)), and $V_{n,Park}$ to V_{test}. The results in Fig. 14(b) show that V_{Mn}/V_{test} and $V_{n,Park}/V_{test}$ have closer-to-one average values (μ) and smaller standard deviations (σ) than V_n/V_{test}, which indicate that the shear strengths estimated by using the nominal flexural strength (M_n) or Park et al. (2020) model show better prediction than the ACI 318-19 nominal shear strength (V_n) for diagonally RC coupling beams.

Therefore, using the nominal flexural strength or the Park et al. (2020) model may be a relatively efficient and accurate way to evaluate a diagonally RC coupling beam with a span-depth ratio between 2 and 3 and a ratio of confinement of at least 0.35, and it is desirable for the ACI 318-19 nominal shear strength equation (Eq. (2)) and upper limit (Eq. (3)) to be revised to achieve an efficient design. Herein, the ratio of confinement (ρ_t) is defined as the total cross-sectional area of confinement of each layer perpendicular to the beam axis divided by the gross concrete area perpendicular to the

Table 3—Strength of test specimens

Specimen	Row	L100-S	L67-S	D67-S	D50-S
V_{test}, kN	1	684.0	632.1	809.0	–761.4
$V_{n,beam}$, kN	2	848.6	585.0	448.6	448.6
$V_{n,upper}$, kN	3	609.2	612.0	586.9	556.0
V_n, kN	4	609.2	585.0	448.6	448.6
V_{Mn}, kN	5	634.0	635.1	542.3	532.0
$V_{n,Park}$, kN	6	703.5	704.3	666.9	657.9
$V_{test}/\sqrt{f_c'}$ (MPa)A_{cw}	7	0.932	0.857	1.144	1.137
$V_{test}/A_{vd}f_y \sin\alpha$	8	—	—	3.606	3.395
1/4	9	1.123	1.080	1.803	1.697
1/5	10	1.079	0.995	1.492	1.431
1/6	11	0.972	0.897	1.213	1.157

Note: All data were calculated by tested material properties; $\sqrt{f_c'}$ MPa = $12\sqrt{f_c'}$ psi. 1 MPa = 145 psi.

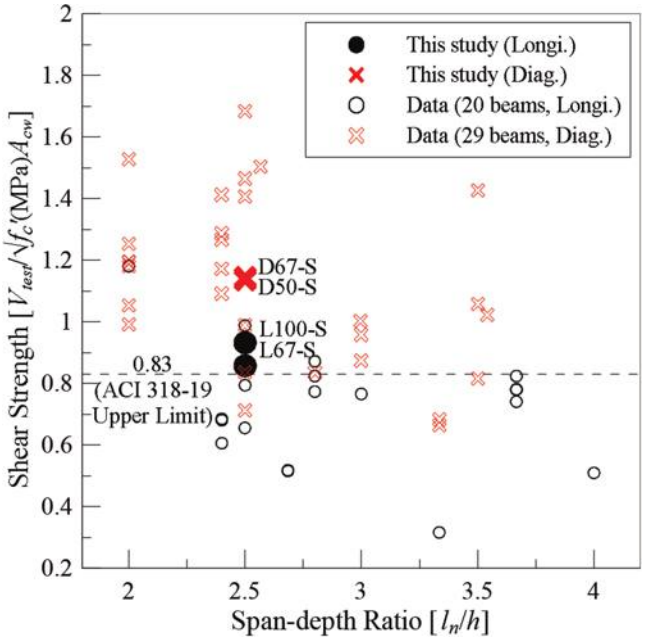

Fig. 12—Shear strength normalized by $\sqrt{f_c'}$ (MPa)A_{cw}.

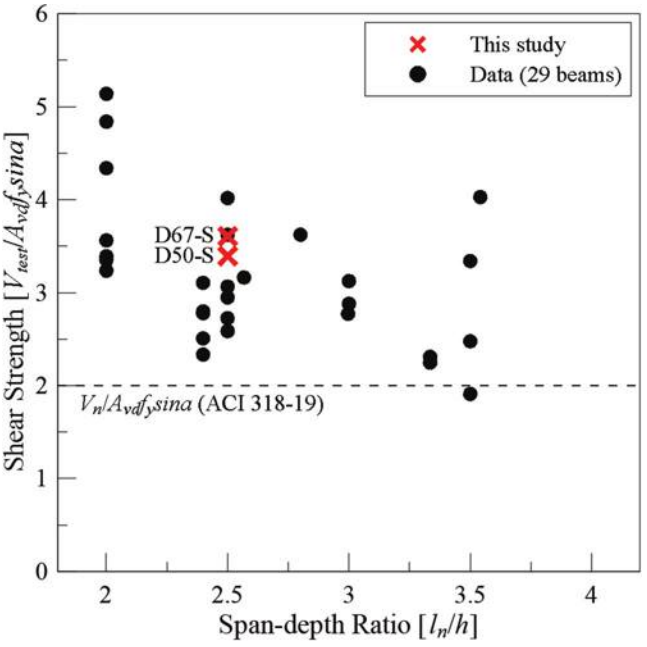

Fig. 13—Shear strength normalized by $A_{vd}f_y sin\alpha$ for diagonally RC coupling beams.

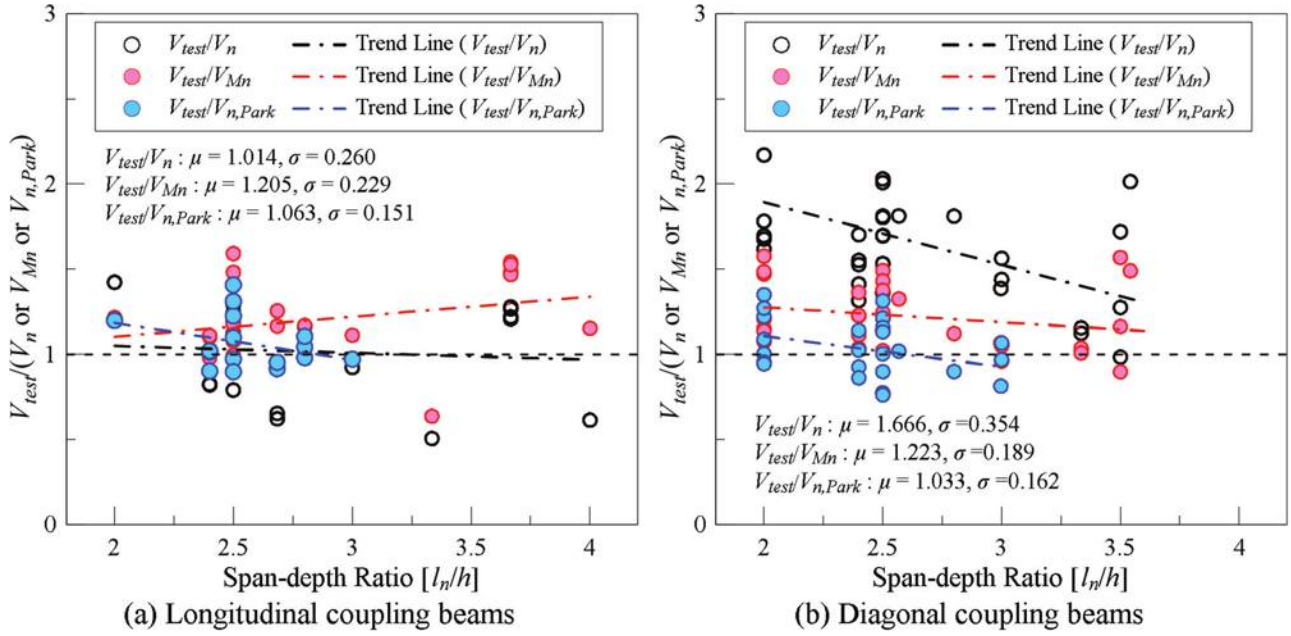

Fig. 14—Comparison of V_{test}/V_n, V_{test}/V_{Mn}, *and* $V_{test}/V_{n,Park}$.

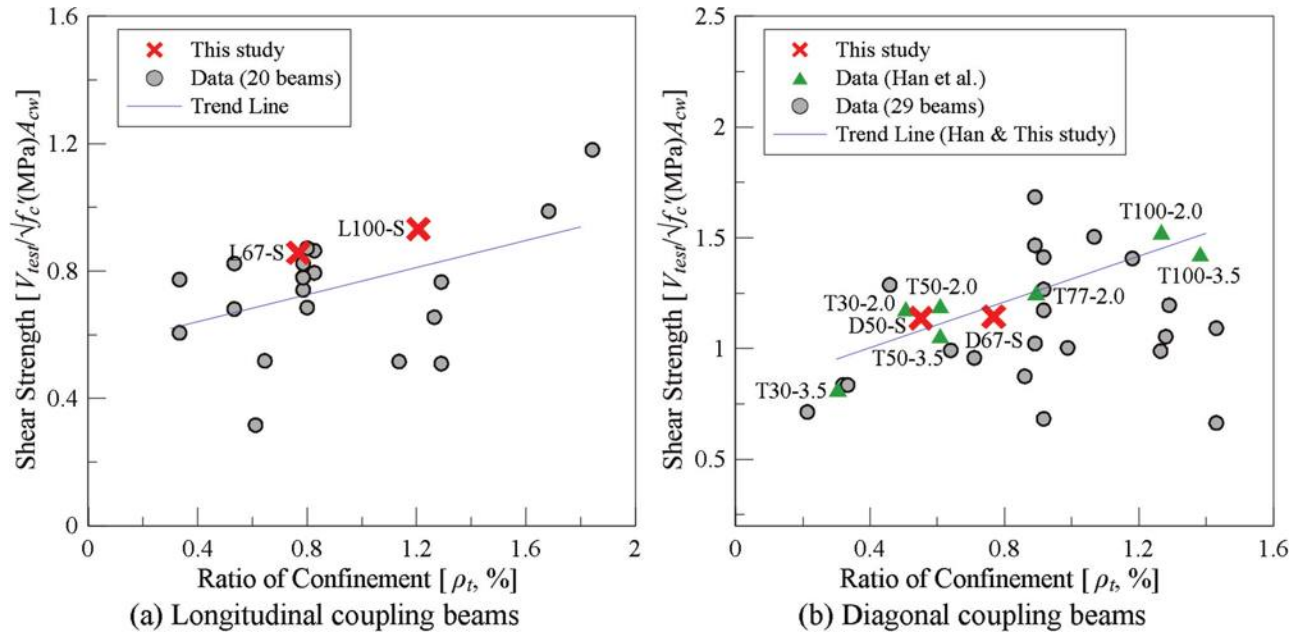

Fig. 15—Shear strength versus ratio of confinement.

confinement ($\rho_t = A_t/b_w s$), where s is the spacing between the layers of confinements.

Impact of confinements

The test results of two longitudinally RC coupling beams with full and two-thirds amounts of confinement and two diagonally RC coupling beams with two-thirds and half amounts of confinement were compared with a total of 62 longitudinally and diagonally RC coupling beams from previous findings in Fig. 15. The coupling beams with more confinement presented higher shear strength for both longitudinally and diagonally RC coupling beams in this study, which is within the trend of test results from previous findings for longitudinally RC coupling beams in Fig. 15(a). In Fig. 15(b), although the relationship between shear strength and the ratio of confinement could not be clearly recognized, the results of this study showed that the maximum shear strength diminished by approximately 32 kN (7.2 kip), while the total number of confinements was reduced from eight to six (D67-S to D50-S).

In addition, Han et al. (2019) reported that the shear strength of diagonal coupling beams was strongly affected by the amount of confinement, and the test results (green triangles in Fig. 15(b)) also show the same trend in this study—shear strength increases as the ratio of confinement rises. Therefore, just as the contribution of transverse reinforcement is considered for estimating nominal shear strength as a conventional beam for longitudinally RC coupling beams, the impact of confinements on diagonally

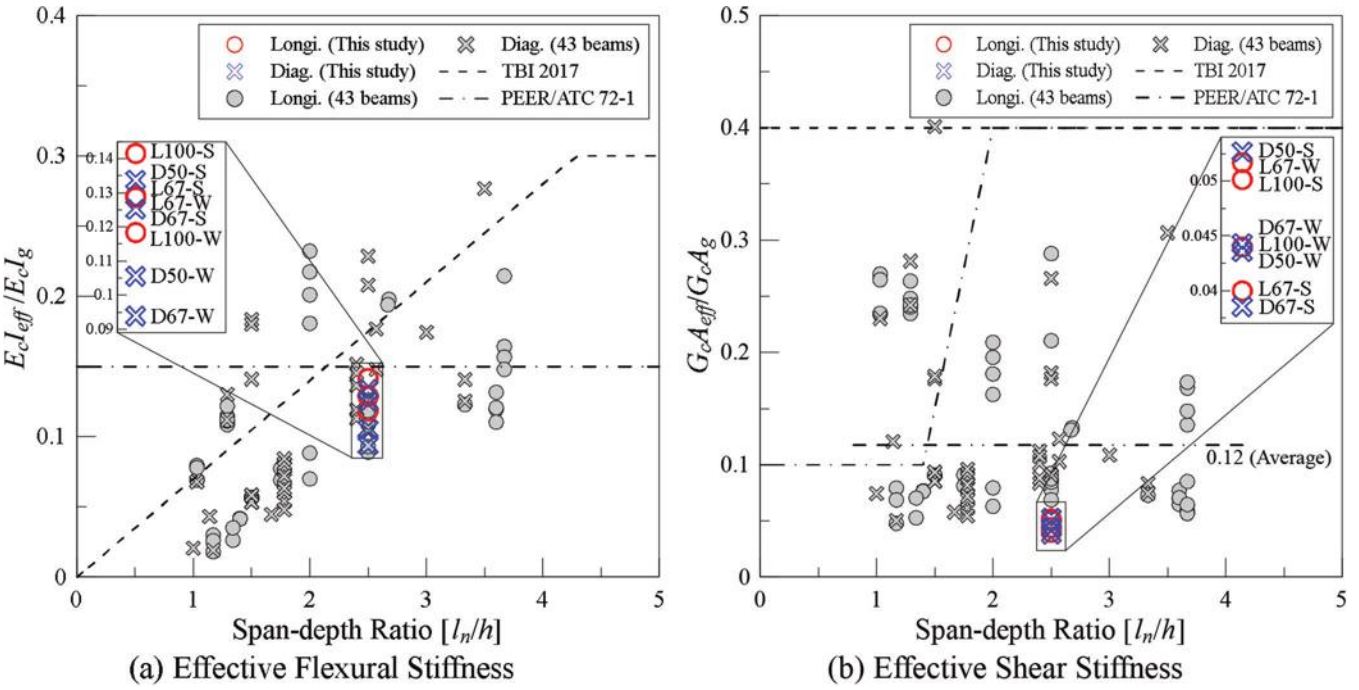

Fig. 16—Effective stiffness.

RC coupling beams may also need to be implemented in their design procedure.

Stiffness

The effective flexural stiffness (K_f) and effective shear stiffness (K_s) of the test specimens were evaluated as follows: 1) the secant stiffness at the value of 0.6 times yield force ($0.6V_{y,test}$) was obtained, where $V_{y,test}$ was obtained when the first main reinforcing bar reached yield strain from the test result; and 2) this value was divided by flexural and shear deformation, respectively, where the flexural deformation including flexure and bar slip/extension was taken as the deformation (corresponding to $0.6V_{y,test}$) times the percentage of the two components, and shear deformation was taken as the corresponding deformation times the percentage of shear and sliding components from drift contribution. The flexural rigidity (E_cI_{eff}) was defined as $K_f \times l_n^3/12$, and the shear rigidity (G_cA_{eff}) was determined by multiplying K_s by l_n, where the modulus of elasticity of concrete was $E_c = 4700\sqrt{f_c'}$ MPa ($57{,}000\sqrt{f_c'}$ psi), and the shear modulus of concrete was $G_c \approx E_c/2.4$. As can be seen in Fig. 16, in this study, the test results of effective flexural stiffness values (E_cI_{eff}/E_cI_g) range from 0.09 to 0.14, and the effective shear stiffness values (G_cA_{eff}/G_cA_g) are approximately 0.05, where I_g and A_g are the moment of inertia and the area of the gross concrete section, respectively. Figure 16 also indicates the test result data of stiffness subjected to seismic protocols collected from Vu et al. (2014), Cheng et al. (2019), and Abdullah et al. (2020b). While coupling beams with span-depth ratios $l_n/h < 2$ are primarily governed by shear behavior, and those with $l_n/h > 4$ could be seen as a flexural beam in the ACI 318-19 design process, the behavior of intermediate coupling beams ($2 \le l_n/h \le 4$) could be indefinite and unpredictable. According to the drift contribution results from Lequesne (2011), Cheng et al. (2019), and Abdullah et al. (2020b), the shear deformation accounted for approximately 40% for deep coupling beams ($l_n/h < 2$) and 20% for coupling beams with a span-depth ratio of approximately 3.5 in the initial state. Conversely, the deformation contributed by flexure was assumed to be 60% for $l_n/h < 2$, $(1 + l_n/h) \times 20\%$ for $2 \le l_n/h \le 4$, and 80% for $l_n/h > 4$ in the calculation process for data of Vu et al. (2014).

It can be observed from Fig. 16(a) that effective flexural stiffness values that consider only the flexural deformation show a similar trend to TBI (2017) ($E_cI_{eff}/E_cI_g = 0.07l_n/h \le 0.3$) for deep coupling beams, while intermediate coupling beams seem more consistent with the constant of 0.15 defined by PEER/ATC-72-1 (2010). In terms of effective shear stiffness values, the average value of the coupling beams is 0.12, and the majority show values between 0.05 and 0.1 in Fig. 16(b), which are significantly less than the values proposed in TBI (2017) and PEER/ATC-72-1 (2010).

Figure 17 shows the secant stiffness (E_cI_{sec}) at each stage divided by the initial secant stiffness ($[E_cI_{sec}]_{initial}$), where the secant stiffness is defined as the ratio of the shear strength to the maximum displacement. Specimens tested under wind loading protocols showed a sharp drop at Stage 2 because of the large number of testing cycles. For ramp-down stages, even though specimens had smaller displacement demands after yielding, the value of $E_cI_{sec}/(E_cI_{sec})_{initial}$ showed a steady decline until the end, where the pinching behavior becomes more prevalent and low-cycle fatigue failure may occur due to cyclic softening. In contrast, for the coupling beams subjected to seismic loading protocol, the secant stiffness dropped sharply after Stage 4 due to larger displacement demands.

CONCLUSIONS

In this study, eight reinforced concrete (RC) coupling beams with a span-depth ratio of 2.5 and four series of

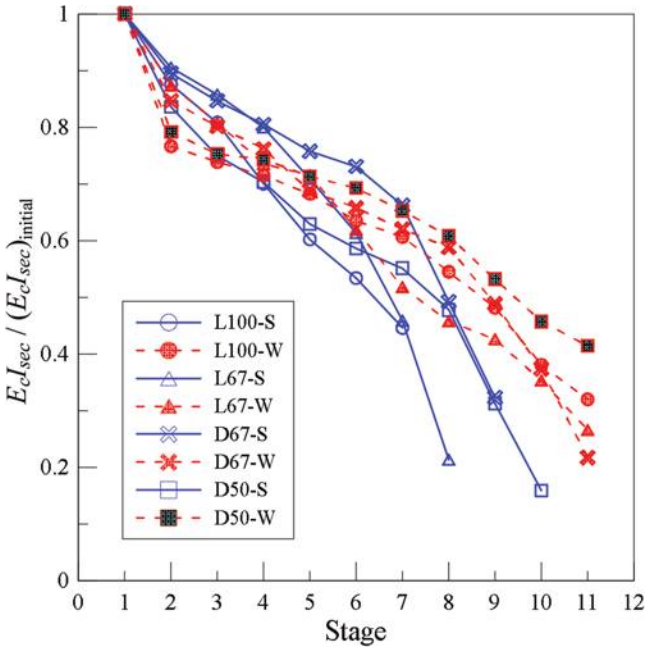

Fig. 17—Secant stiffness at each stage.

layouts were tested under seismic and wind loads. Based on the test results, the following conclusions and recommendations can be drawn:

1. Because the underestimation of the nominal shear strength and upper limit for diagonally RC coupling beams in ACI 318-19 might cause undesirable forces or damage to the wall system, it is advisable to improve the two formulae. Additionally, considering the contribution of confinements for better shear strength prediction is recommended.

2. The test results show that the effective flexural stiffness (E_cI_{eff}/E_cI_g) of approximately 0.12 is more comparable to PEER/ATC-72-1 (2010), and the values of effective shear stiffness (G_cA_{eff}/G_cA_g) of approximately 0.05 are significantly less than both TBI (2017) and PEER/ATC-72-1 (2010).

3. This experiment can act as an example of structural verification for performance-based wind design because specimens subjected to the simulated wind event satisfied the damage control performance objective with no extensive damage, and only minor cracks were observed. However, as the RC coupling beams presented more pinching behavior and less stiffness after yielding, the influence of low-cycle fatigue requires further investigation.

AUTHOR BIOS

ACI member **Tse-An Chou** *is a PhD Student in the Department of Architecture and Architectural Engineering at Seoul National University, Seoul, South Korea. He received his BS and MS in civil and construction engineering from the National Taiwan University of Science and Technology, Taipei, Taiwan. His research interests include seismic behavior and the design of reinforced concrete structures.*

ACI member **Seung Heon Lee** *is a PhD Student in the Department of Architecture and Architectural Engineering at Seoul National University, where he received his BS and MS. His research interests include structural analysis and design of reinforced concrete structures under combined loading conditions.*

Chunho Chang *is a Professor of civil engineering and Director of the Intelligent Construction System Core Center at Keimyung University, Daegu, South Korea, where he received his BS, MS, and PhD. His research interests include the design and behavior of textile-reinforced concrete and composite structures under earthquake loading.*

Thomas H.-K. Kang, *FACI, is a Professor of structural engineering and interdisciplinary artificial intelligence at Seoul National University. He is a member of ACI Subcommittee 318-T, Post-Tensioned Concrete; Joint ACI-PTI Committee 320, Post-Tensioned Structural Concrete Code; Joint ACI-ASCE Committees 352, Joints and Connections in Monolithic Concrete Structures, and 423, Prestressed Concrete; and Joint ACI-ASME Committee 359, Concrete Containments for Nuclear Reactors. His research interests include the design and behavior of reinforced, prestressed, and post-tensioned concrete structures.*

ACKNOWLEDGMENTS

This research was supported by the Korea Basic Science Institute (National Research Facilities and Equipment Center) grant funded by the Ministry of Education (No. 2020R1A6C101B189), and by the Institute of Construction and Environmental Engineering at Seoul National University. The views expressed are those of the authors and do not necessarily represent those of the sponsors or discussants.

REFERENCES

Abdullah, S. A.; Aswegan, K.; Jaberansari, S.; Klemencic, R.; and Wallace, J. W., 2020a, "Performance of Reinforced Concrete Coupling Beams Subjected to Simulated Wind Loading," *ACI Structural Journal*, V. 117, No. 3, May, pp. 283-295.

Abdullah, S. A.; Wallace, J. W.; Aswegan, K.; and Klemencic, R., 2020b, "Experimental Study of Concrete Coupling Beams Subjected to Wind and Seismic Loading Protocols," Final Report, UCLA/SEERL 2020/01, University of California, Los Angeles, Los Angeles, CA, 276 pp.

ACI Committee 318, 2019, "Building Code Requirements for Structural Concrete (ACI 318-19) and Commentary (ACI 318R-19) (Reapproved 2022)," American Concrete Institute, Farmington Hills, MI, 624 pp.

ACI Committee 374, 2013, "Guide for Testing Reinforced Concrete Structural Elements under Slowly Applied Simulated Seismic Loads (ACI 374.2R-13)," American Concrete Institute, Farmington Hills, MI, 18 pp.

Alinejad, H., and Kang, T. H.-K., 2020, "Engineering Review of ASCE 7-16 Wind-Load Provisions and Wind Effect on Tall Concrete-Frame Buildings," *Journal of Structural Engineering*, ASCE, V. 146, No. 6, June, p. 04020100. doi: 10.1061/(ASCE)ST.1943-541X.0002622

Alinejad, H.; Jeong, S. Y.; and Kang, T. H.-K., 2020b, "Performance-Based Design of Tall Buildings for Wind Load and Application of Response Modification Factor," *Wind and Structures*, V. 31, No. 2, pp. 153-164.

Alinejad, H.; Kang, T. H.-K.; and Jeong, S. Y., 2021, "Performance-Based Wind Design Framework Proposal for Tall Buildings," *Wind and Structures*, V. 32, No. 4, Apr., pp. 283-292.

ASCE/SEI, 2019, "Prestandard for Performance-Based Wind Design," American Society of Civil Engineers, Reston, VA.

ASCE/SEI 7-16, 2017, "Minimum Design Loads and Associated Criteria for Buildings and Other Structures," American Society of Civil Engineers, Reston, VA.

ASCE/SEI 7-22, 2022, "Minimum Design Loads and Associated Criteria for Buildings and Other Structures," American Society of Civil Engineers, Reston, VA.

ASCE/SEI 41-17, 2017b, "Seismic Evaluation and Retrofit of Existing Buildings," American Society of Civil Engineers, Reston, VA.

Aswegan, K.; Larsen, R.; Klemencic, R.; Hooper, J.; and Hasselbauer, J., 2017, "Performance-Based Wind and Seismic Engineering: Benefits of Considering Multiple Hazards," *Structures Congress 2017: Buildings and Special Structures*, J. G. Soules, ed., Denver, CO, pp. 473-484.

Barney, G. B.; Shiu, K. N.; Rabbat, B. G.; Fiorato, A. E.; Russell, H. G.; and Corley, W. G., 1980, "Behavior of Coupling Beams under Load Reversals (RD068.01B)," Portland Cement Association, Skokie, IL, 25 pp.

Breña, S. F., and Ihtiyar, O., 2011, "Performance of Conventionally Reinforced Coupling Beams Subjected to Cyclic Loading," *Journal of Structural Engineering*, ASCE, V. 137, No. 6, June, pp. 665-676. doi: 10.1061/(ASCE)ST.1943-541X.0000316

Cheng, M.-Y.; Gitomarsono, J.; and Zeng, H.-Y., 2019, "Cyclic Test of Diagonally Reinforced Concrete Coupling Beam with Different Shear Demand," *ACI Structural Journal*, V. 116, No. 6, Nov., pp. 241-250. doi: 10.14359/51718010

Fortney, P. J.; Rassati, G. A.; and Shahrooz, B. M., 2008, "Investigation on Effect of Transverse Reinforcement on Performance of Diagonally Reinforced Coupling Beams," *ACI Structural Journal*, V. 105, No. 6, Nov.-Dec., pp. 781-788.

Galano, L., and Vignoli, A., 2000, "Seismic Behavior of Short Coupling Beams with Different Reinforcement Layouts," *ACI Structural Journal*, V. 97, No. 6, Nov.-Dec., pp. 876-885.

Han, S. W.; Kim, S. B.; and Kim, T., 2019, "Effect of Transverse Reinforcement on the Seismic Behavior of Diagonally Reinforced Concrete Coupling Beams," *Engineering Structures*, V. 196, Oct., Article No. 109307. doi: 10.1016/j.engstruct.2019.109307

Jeong, S. Y.; Alinejad, H.; and Kang, T. H.-K., 2021, "Performance-Based Wind Design of High-Rise Buildings Using Generated Time-History Wind Loads," *Journal of Structural Engineering*, ASCE, V. 147, No. 9, p. 04021134.

Kanakubo, T.; Fujisawa, M.; Sako, N.; and Sonobe, Y., 1996, "Ductility of Short Span RC Beams," *Proceedings*, Eleventh World Conference on Earthquake Engineering (11 WCEE), Acapulco, Mexico, Paper No. 1369, pp. 1-8.

KBC, 2016, "Korean Building Code (KBC 2016)," Ministry of Land, Infrastructure and Transport, Seoul, South Korea.

Kwan, A. K. H., and Zhao, Z. Z., 2002, "Testing of Coupling Beams with Equal End Rotations Maintained and Local Joint Deformation Allowed," *Structures and Buildings*, V. 152, No. 1, pp. 67-78.

Lequesne, R. D., 2011, "Behavior and Design of High-Performance Fiber-Reinforced Concrete Coupling Beams and Coupled-Wall Systems," PhD dissertation, University of Michigan, Ann Arbor, MI, 298 pp.

Lequesne, R. D.; Parra-Montesinos, G. J.; and Wight, J. K., 2013, "Seismic Behavior and Detailing of High-Performance Fiber-Reinforced Concrete Coupling Beams and Coupled Wall Systems," *Journal of Structural Engineering*, ASCE, V. 139, No. 8, pp. 1362-1370. doi: 10.1061/(ASCE)ST.1943-541X.0000687

Lim, E.; Hwang, S.-J.; Cheng, C.-H.; and Lin, P.-Y., 2016b, "Cyclic Tests of Reinforced Concrete Coupling Beam with Intermediate Span-Depth Ratio," *ACI Structural Journal*, V. 113, No. 3, May-June, pp. 515-524. doi: 10.14359/51688473

Lim, E.; Hwang, S.-J.; Wang, T.-W.; and Chang, Y.-H., 2016a, "An Investigation on the Seismic Behavior of Deep Reinforced Concrete Coupling Beams," *ACI Structural Journal*, V. 113, No. 2, Mar.-Apr., pp. 217-226. doi: 10.14359/51687939

Naish, D.; Fry, A.; Klemencic, R.; and Wallace, J., 2013, "Reinforced Concrete Coupling Beams—Part I: Testing," *ACI Structural Journal*, V. 110, No. 6, Nov.-Dec., pp. 1057-1066.

Park, W.-S.; Kang, T. H.-K.; Kim, S.; and Yun, H.-D., 2020, "Seismic Performance of Moderately Short Concrete Coupling Beams with Various Reinforcements," *ACI Structural Journal*, V. 117, No. 3, May, pp. 141-154.

Paulay, T., and Binney, J. R., 1974, "Diagonally Reinforced Coupling Beams of Shear Walls," *Shear in Reinforced Concrete*, SP-42, American Concrete Institute, Farmington Hills, MI, pp. 579-598.

PEER/ATC-72-1, 2010, "Modeling and Acceptance Criteria for Seismic Design and Analysis of Tall Buildings," Pacific Earthquake Engineering Research Center (PEER)/Applied Technology Council (ATC), Berkeley, CA, 242 pp.

Shimazaki, K., 2004, "De-bonded Diagonally Reinforced Beam for Good Repairability," *Proceedings*, Thirteenth World Conference on Earthquake Engineering (13 WCEE), Vancouver, BC, Canada, Paper No. 3173, pp. 1-14.

Tassios, T. P.; Moretti, M.; and Bezas, A., 1996, "On the Behavior and Ductility of Reinforced Concrete Coupling Beams of Shear Walls," *ACI Structural Journal*, V. 93, No. 6, Nov.-Dec., pp. 711-720.

TBI, 2017, "Guidelines for Performance-Based Seismic Design of Tall Buildings," Tall Buildings Initiative, Pacific Earthquake Engineering Research Center, Berkeley, CA.

Vu, N. S.; Li, B.; and Beyer, K., 2014, "Effective Stiffness of Reinforced Concrete Coupling Beams," *Engineering Structures*, V. 76, Oct., pp. 371-382.

Xiao, Y.; Esmaeily-Ghasemabadi, A.; and Wu, H., 1999, "High-Strength Concrete Short Beams Subjected to Cyclic Shear," *ACI Structural Journal*, V. 96, No. 3, May-June, pp. 392-400.

ACI STRUCTURAL JOURNAL TECHNICAL PAPER

Title No. 120-S74

Design and Detailing of Glass Fiber-Reinforced Polymer-Reinforced Concrete Beams According to ACI CODE-440.11-22

by Zahid Hussain and Antonio Nanni

This paper aims to analyze practical considerations in the design of glass fiber-reinforced polymer-reinforced concrete (GFRP-RC) beams based on the newly adopted ACI CODE-440.11-22, addressing strength, serviceability, and detailing criteria. A beam example was taken from the ACI Reinforced Concrete Design Handbook *and redesigned using GFRP bars and stirrups to analyze the effect of changing the reinforcement type. In the first phase, the beam was designed as an over-reinforced member with high-modulus (*E_f *= 60,000 MPa) and low-modulus (*E_f *= 44,815 MPa) GFRP bars. In the second phase, a parametric study was carried out to analyze the impact of changing key design parameters—namely, bond factor* k_b*, concrete compressive strength* f_c'*, and the maximum deflection limit. GFRP-RC beams require more reinforcement area compared to conventional steel-RC, which may result in bar congestion. Current Code provisions related to detailing in particular are based on conservative assumptions due to a lack of experimentation and greatly penalize the design of GFRP-RC beams. The current Code provisions for development length, bar spacing, skin reinforcement, and stress at service make GFRP-RC design challenging.*

Keywords: building code; detailing; glass fiber-reinforced polymer (GFRP) reinforcement; reinforced concrete (RC) beams; serviceability.

INTRODUCTION

A primary reason for the limited use of glass fiber-reinforced polymer (GFRP) bars in concrete structures has been the lack of engineering design standards. However, with recent developments, owners and practitioners are finding GFRP to be a viable alternative to conventional steel in reinforced concrete (RC) structures for long-term service life.[1] The improvement in material properties, available standards, and new construction strategies allow the exploitation of the full potential of this composite material[2,3] for use in concrete structures.

The Building Code ACI CODE-440.11-22 for GFRP-RC members was recently published, which represents a critical aid to practitioners interested in the use of nonmetallic reinforcement.[4] However, some provisions in ACI CODE-440.11-22[4] may be based on conservative assumptions without validation from experimental programs. These provisions make the design of GFRP-RC members difficult and may require unnecessary reinforcement. Therefore, this study is carried out to show the implications of current Code provisions that may need to be revisited and validated by experimentation.

RESEARCH SIGNIFICANCE

The ACI CODE-440.11-22[4] Building Code for GFRP-RC members is a stepping stone for the full exploitation of composites in concrete construction. However, some Code provisions are possibly unduly conservative and penalize the design. Assumptions for detailing such as development length and bar spacing make implementation difficult. This study analyzes and discusses practical considerations for GFRP-RC beam design and detailing and points out a need for some reconsideration.

METHODOLOGY

In this study, a beam from the *ACI Reinforced Concrete Design Handbook*[5,6] was selected and redesigned using GFRP reinforcement. The selected beam is part of an interior, continuous, six-bay framing, and built integrally with a 178 mm-deep slab, as shown in Fig. 1. The constituent materials selected for beam design are listed in Table 1. The concrete strength f_c' is 35 MPa, while the GFRP type is compliant with material specification ASTM D7957/D7957M-22.[7] Additionally, a new ASTM material specification is under development for a class of GFRP bars with a higher modulus of elasticity and strength; this class of GFRP bars was also considered because it represents the majority of products commercially available in the marketplace today. This study uses M29 nominal bar size for the main reinforcement in both the positive and negative moment regions, whereas for additional hooked bars, M16 and M19 sizes are used as needed. The mechanical properties of GFRP bars affecting design include guaranteed ultimate tensile strength f_{fu}, corresponding ultimate strain ε_{fu}, modulus of elasticity E_f, and modular ratio n_f. A value of 1.35 for the bond coefficient (k_b) and 0.85 for the environmental reduction factor (C_E) are adopted, as indicated in ACI CODE-440.11-22[4] Sections 24.3.2.3 and 20.2.2.3, respectively. It should be noted that the bond factor has changed from 1.35 to 1.20 in the recent publication of ACI CODE-440.11-22,[4] which is used in Phase 2. A concrete cover (c_c) of 38 mm is used, as specified in ACI CODE-440.11-22[4] Section 20.5.1.3.1.

ACI Structural Journal, V. 120, No. 4, July 2023.

MS No. S-2022-199.R1, doi: 10.14359/51738744, received February 16, 2023, and reviewed under Institute publication policies.

Table 1—Properties of GFRP reinforcement and concrete

Designation	Nominal diameter, mm	Nominal area, mm^2	Elastic modulus, MPa	Guaranteed tensile strength, MPa	Ultimate strain, %	Concrete strength, MPa	Concrete clear cover, mm
GFRP-M16*	15.8	200	60,000	907.5	0.015	35.0	38.0
GFRP-M19*	19.0	284		897.7	0.015		
GFRP-M29*	28.6	645		793.0	0.013		
GFRP-M16	15.8	200	44,815	646.7	0.014		
GFRP-M19	19.0	284		640.5	0.014		
GFRP-M29	28.6	645		565.3	0.013		

*New-generation bars with high modulus of elasticity (E_f = 60,000 MPa).

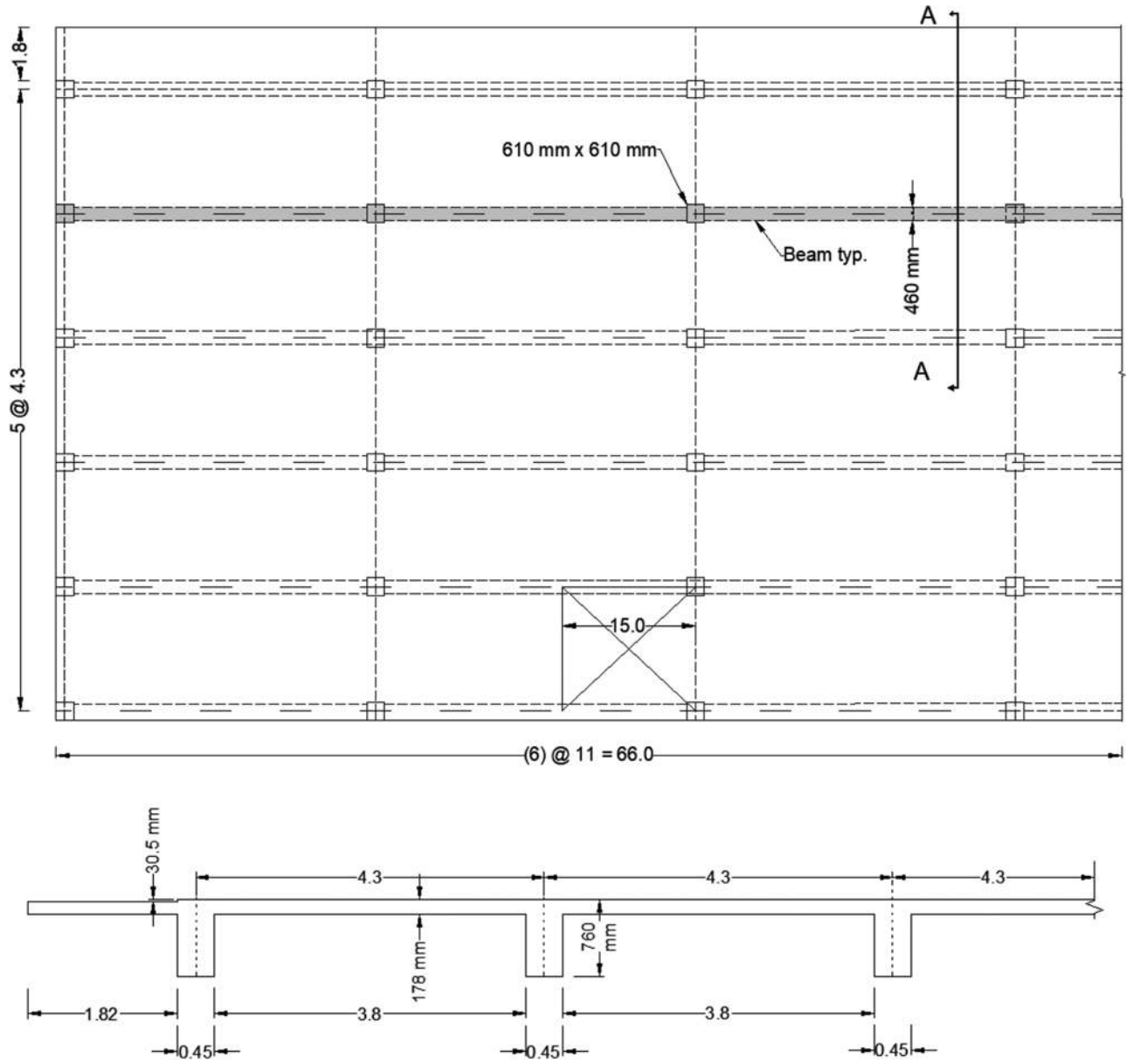

Fig. 1—Framing plan and partial section A-A showing interior beam.[6] (Note: Dimensions in meters unless otherwise indicated.)

The beam is designed as an over-reinforced member (that is, the reinforcement ratio provided exceeds the balanced reinforcement ratio) with both high- and low-modulus GFRP bars. For the former case, a parametric study is carried out by changing parameters such as the bond factor k_b, concrete compressive strength f_c', and the maximum permissible deflection limit.

Table 2—Selected moments and shear values for one-way slabs and beams (ACI CODE-440.11-22[4] Table 6.5.2)

Moment	Location	Condition	M_u	V_u
Positive	Endspan	Discontinuous end integral with support	$\frac{w_u l_n^2}{14}$	—
Negative	Interior face of exterior support	Members built integrally with supporting column	$\frac{w_u l_n^2}{16}$	$w_u l_n/2$
	Exterior face of first interior support	More than two spans	$\frac{w_u l_n^2}{10}$	$1.15(w_u l_n/2)$

ANALYSIS AND DESIGN

The beam carried a superimposed dead load of 718 N/m^2 and a live load of 3112 N/m^2, as given in the design Handbook.[6] These loads were combined as per ASCE/SEI 7-16[8] to compute the maximum factored demand. Maximum factored moments and shear forces were determined using a simplified method of analysis for continuous beams and one-way slabs as per ACI CODE-440.11-22[4] Section 6.5. The specified moment and shear values used in this example are given in Table 2 as taken directly from ACI CODE-440.11-22.[4]

For applicable factored load combinations, design strength at all sections shall satisfy the requirements of ACI CODE-440.11-22[4] Section 9.5.1.1, given as follows

$$\Phi S_n \geq U \tag{1}$$

where S_n is the nominal moment, shear, axial, or torsional strength; U is the strength of a member or cross section required to resist factored loads or related internal moments and forces; and Φ is the strength reduction factor calculated as per ACI CODE-440.11-22,[4] as given in Table 3.

The maximum spacing of GFRP reinforcement is limited, as specified by ACI CODE-440.11-22[4] Eq. (24.3.2a) and (24.3.2b), given as follows

$$S \leq \frac{0.81E_f}{f_{fs}k_b} - 2.5c_c \tag{2}$$

$$S \leq 0.66\frac{E_f}{f_{fs}k_b} - 2.5c_c \tag{3}$$

where f_{fs} is the stress at service loads.

The development length of the GFRP reinforcement is governed by Code Section 25.4.2.1, as the greater of: (a), (b), and (c), given as follows in Eq. (4) to (6)

$$l_d = \frac{d_b\left(\frac{f_{fr}}{0.083\sqrt{f_c}} - 340\right)}{13.6 + \frac{c_b}{d_b}}\omega \tag{4}$$

where f_{fr} is the tensile stress in GFRP reinforcement required to develop the full nominal section capacity, MPa; c_b is the lesser of: a) the distance from the center of a bar to the nearest concrete surface, and b) one-half the center-to-center spacing of bars being developed, mm; d_b is the nominal diameter of the bar, mm; and ω is the bar location modification factor, taken equal to 1.5 if more than 300 mm of fresh concrete is placed below the horizontal reinforcement being developed, and 1.0 for all other cases.

Table 3—Strength reduction factor Φ (ACI CODE-440.11-22[4] Section 21.2.1)

Action or structural element	Φ
Moment, axial force, or combined axial moment and axial force (Section 21.2.2)	0.55 to 0.65*
Shear	0.75

*0.65 is applicable to over-reinforced sections used in this example.

$$20d_b \tag{5}$$

$$300 \text{ mm} \tag{6}$$

There are no provisions for predetermined dimensions of beams in ACI CODE-440.11-22[4] as given in ACI 318-19 Section 9.3.1.1. Therefore, the GFRP-RC beam cross-section dimensions were determined by the trial-and-error method meeting strength and serviceability requirements. The beam cross-section dimensions are identical to those in the design Handbook,[6] and a maximum permissible deflection limit was selected in the first phase of this study as per ACI CODE-440.11-22[4] Section 24.2.2, given as follows

$$\Delta = l/240 \tag{7}$$

This limit is based on the assumption that the beam is not supporting or attached to partitions or other nonstructural elements likely to be damaged by large deflections. The aforementioned deflection limit was taken to make it analogous to the ACI 318-19[5] design taken in this study.

STRENGTH REQUIREMENTS

Flexural strength

The reinforcement area was calculated first as the greater of the area required by the ultimate factored moment demand and the area necessary to ensure that the flexural strength exceeds the cracking strength, indicated in ACI CODE-440.11-22[4] Sections 9.6.1.2(a) and (b), given as follows

$$\frac{0.41\sqrt{f_c}}{f_{fu}}b_w d \tag{8}$$

$$(2.3/f_{fu})b_w d \tag{9}$$

where b_w is the web width or diameter of the circular cross section, mm; and d is the distance from extreme compression fiber to centroid of longitudinal tension reinforcement, mm.

In this example, the factored moment was calculated for the superimposed dead load of 718 N/m^2 and live load of 3112 N/m^2 (that is, larger than the minimum 1915 N/m^2 of a residential load given by ASCE 7-16 Table 4.3-1[8]).

Table 4—Design of GFRP-RC beam using high-modulus bars

Location	Demand, kN·m	Area* for strength only, mm^2	Capacity*, kN·m	Provided area, mm^2, meeting all Code requirements	Provided capacity, kN·m, meeting all Code requirements
Exterior support	362	1935	466	2580	639
Midspan	413	1935	466	3226	885
Interior support	579	2580	639	3870	1064

*Reinforcement area and capacity without meeting Code provisions for strength, detailing, and serviceability.

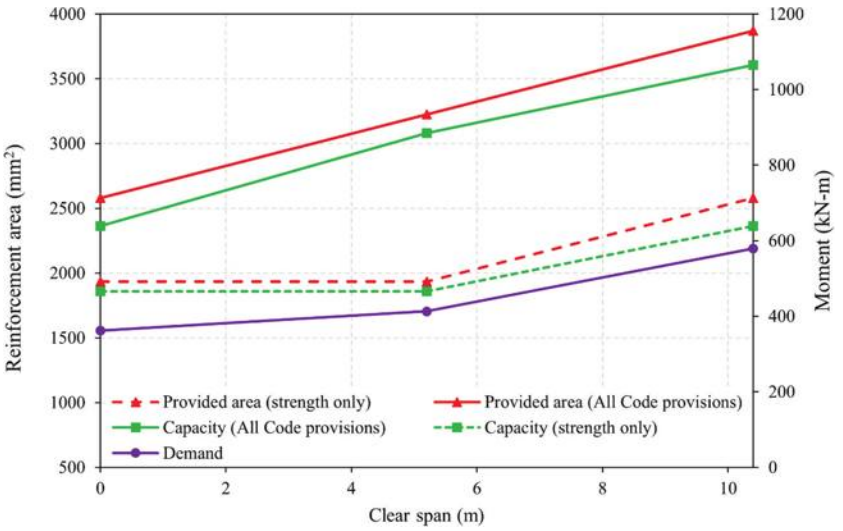

Fig. 2—Reinforcement area, demand, and capacity at three locations, with and without meeting Code provisions.

As shown in Table 4, the required reinforcement area for strength (that is, 1935, 1935, and 2580 mm^2 at exterior support, midspan, and interior support, respectively) produces a capacity large enough to satisfy the factored demand. However, Code provisions for maximum spacing, stress at service, deflection limits, and strength reduction factors penalize the design. As given in Table 4, the provided reinforcement area significantly increased (that is, 2580, 3226, and 3870 mm^2 at exterior support, midspan, and interior support, respectively) after meeting Code provisions for detailing and serviceability. The resulting capacity is 76%, 114%, and 84% higher than demand at the exterior support, midspan, and interior support, respectively. The difference between the required and provided reinforcement areas with and without meeting Code provisions, together with corresponding capacities, can be visualized in Fig. 2. Also, when satisfying Code specifications, the design changed from an under-reinforced to an over-reinforced member.

Shear strength

Separate equations are provided in ACI CODE-440.11-22[4] to avoid diagonal compression failure (Eq. (22.5.1.2), given as follows) and to limit the strain in the GFRP shear reinforcement (Section 20.2.2.6, provided later in this section)

$$V_u \le \Phi 0.2 f_c' bd \tag{10}$$

where V_u is the factored shear force at a section, N.

The nominal shear strength of the beam was calculated as per ACI CODE-440.11-22[4] Eq. (22.5.1.1), given as

$$V_n = V_c + V_f \tag{11}$$

where V_n is the nominal shear strength, N; V_c is the nominal shear strength provided by the concrete, N; and V_f is the nominal shear strength provided by GFRP shear reinforcement, N.

The shear strength provided by concrete was calculated as the greater of two expressions from ACI CODE-440.11-22[4] Sections 22.5.5.1(a) and (b), given as follows

$$V_c = 0.42\lambda k_{cr}\sqrt{f_c'}bd \tag{12}$$

$$V_c = 0.066\lambda\sqrt{f_c'}bd \tag{13}$$

where $\lambda = \sqrt{\frac{2}{1+0.004}}$ is the size effect factor, as given in ACI CODE-440.11-22[4] Section 22.5.1.1; and k_{cr} is the ratio of depth of the elastic cracked section neutral axis to the effective depth given by Commentary Eq. (R22.5.5.1a), shown as follows

$$k_{cr,rect} = \sqrt{2\rho_f n_f + (\rho_f n_f)^2} - \rho_f n_f \tag{14}$$

where $\rho_f = A_f/b_w d$ is the reinforcement ratio; A_f is the area of GFRP longitudinal reinforcement within spacing s, mm^2; $n_f = E_f/E_c$ is the modular ratio; and E_c is the modulus of elasticity of concrete, MPa, calculated as given by Code Eq. (19.2.2.1b), given as follows

Table 5—Properties of high-modulus GFRP shear reinforcement

Designation	Nominal diameter, mm	Nominal area, mm^2	Elastic modulus, MPa	Guaranteed tensile strength, MPa	Design tensile strength, MPa	Quantity
GFRP-M13	12.7	129	60,000	574.3	490	46

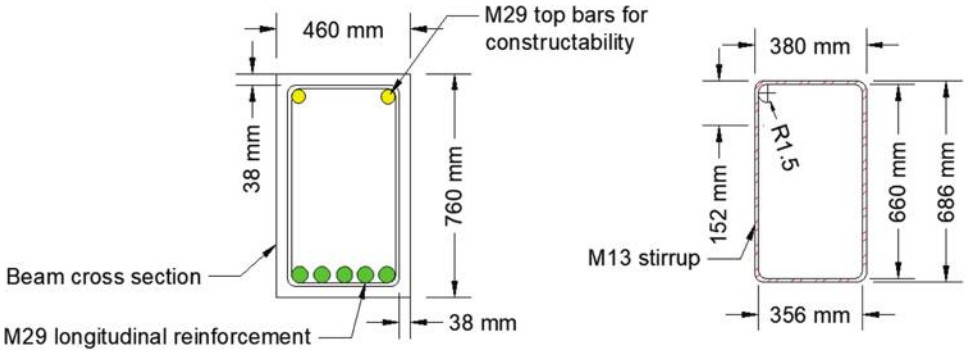

Fig. 3—Beam cross section and stirrup dimensions at midspan.

$$E_c = 4700\sqrt{f_c'} \quad (15)$$

The size effect factor was considered in the beam design because its depth exceeded 254 mm.

The ultimate factored shear force exceeded the concrete strength and the beam required shear reinforcement. Shear strength provided by the GFRP reinforcement was calculated as given in Code Eq. (22.5.8.5.3)

$$V_f = A_{fv} f_{ft} (d/s) \quad (16)$$

where A_{fv} is the area of shear reinforcement calculated as given in the Commentary Eq. (R22.5.8.5), given as follows

$$\frac{A_{fv}}{s} = \frac{V_u - \Phi V_c}{\Phi f_{ft} d} \quad (17)$$

where f_{ft} is the permissible stress in the GFRP shear reinforcement. The design tensile strength of GFRP transverse reinforcement is controlled by the strength of the bent portion of the bar and by a strain limit of 0.005, as given by Code Section 20.2.2.6

$$f_{ft} \le (f_{fb}, 0.005E_f) \quad (18)$$

where $f_{fb} = C_E f_{fb}^*$ is the design tensile strength of the bent portion of GFRP reinforcement; and f_{fb} is the guaranteed ultimate tensile strength of the bent portion of the bar. Its minimum value is taken as specified in ASTM D7957/D7957M[7] by dividing the ultimate guaranteed tensile force of the bent portion of the bar by the nominal cross-sectional area of the bar.

The maximum spacing between legs of shear reinforcement was calculated as the least of the maximum spacing limitations given by the Code and its Commentary in Sections R22.5.8.5.3, 9.6.3.4, and 9.7.6.2.2.

$$S_{max} = \frac{A_{fv} \Phi f_{ft} d}{V_u - \Phi V_c} \quad (19)$$

Following the example in the Design Handbook,[6] torsion effects were not considered; therefore, maximum spacing was limited, as given in Code Sections 9.6.3.4(a) and (b), shown as follows

$$S_{max} = \frac{A_{fv} f_{ft}}{0.062\sqrt{f_c} b} \quad (20)$$

$$S_{max} = A_{fv} f_{ft} / 0.35 b \quad (21)$$

The final limit for the spacing between the legs of shear reinforcement is given in Code Section 9.7.6.2.2, shown as follows

$$S_{max} = \min((d/2), 610 \text{ mm}) \quad (22)$$

A lower value of V_c and a 40% reduction in the strength at the bend of GFRP transverse reinforcement[7] significantly affect shear design, and members using GFRP shear reinforcement require more and larger-diameter stirrups than for the case of steel stirrups. In this example, the beam designed with GFRP required 46 M13 GFRP stirrups, whereas the same beam required 35 M10 steel stirrups. The properties of GFRP shear reinforcement are listed in Table 5. For anchorage, continuous closed stirrups were used as defined in Code Section 25.7.1.3. The radius of the bend for an M13 stirrup used was 38 mm, as per Table 4 in ASTM D7957/D7957M.[7] The stirrup size, its dimensions, and a beam cross section at a typical location are shown in Fig. 3. The shear demand due to factored loads on the beam and shear strength provided by concrete and shear reinforcement can be visualized in shear demand and capacity envelopes given in Fig. 4 together with the stirrup number, size, and spacing varying along the beam length.

DETAILING AND SERVICEABILITY REQUIREMENTS

Design of beam using high-modulus GFRP bars (E_f = 60,000 MPa)

The beam cross section (that is, 460 x 760 mm) was designed as compression-controlled using dimensions identical to the steel-RC beam in the Handbook.[6] The amount of

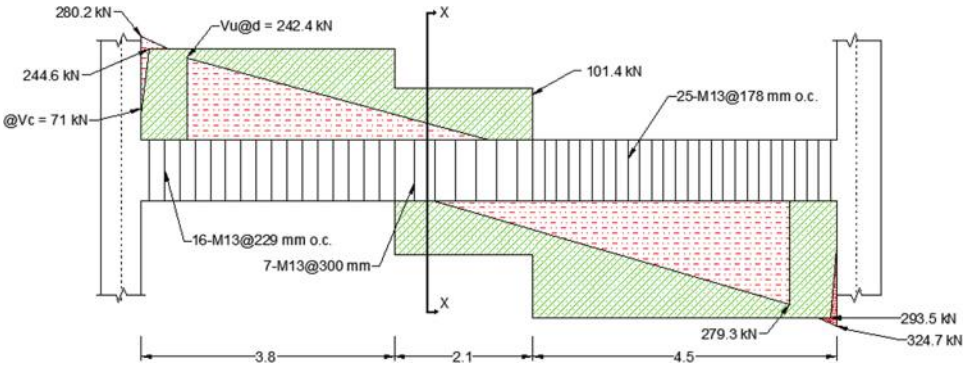

Fig. 4—Shear demand and capacity envelopes.

Table 6—Design of GFRP-RC beam using high-modulus bars (60,000 MPa)

Location	Demand, kN·m	Area for strength only, mm^2	Provided area, mm^2, meeting all Code requirements	Provided capacity, kN·m, meeting all Code requirements	Development length, mm
Exterior support	362	2348	2580	639	2769
Midspan	413	2348	3226	885	1626
Interior support	579	2348	3870	1064	1423

GFRP reinforcement to satisfy strength requirements is indicated as the "required area," whereas the larger amount of GFRP reinforcement needed to satisfy serviceability requirements (that is, deflection control) and detailing requirements (that is, maximum bar spacing) is indicated as the "provided area." The difference between the required and provided areas of reinforcement to meet serviceability and detailing requirements can be observed in Table 6, developed using high-modulus (E_f = 60,000 MPa) GFRP reinforcement.

The required reinforcement area for the negative moment at the exterior support to meet strength requirements is 2348 mm^2, while the provided area increased to 2580 mm^2 to meet the detailing requirements as well. However, the developed capacity at the face of the column is 132 kN·m, lower than the demand of 362 kN·m, as GFRP bars are not fully developed at this location. For full capacity, the GFRP reinforcement needed a development length of 2769 mm, while only 2572 mm is available at the face of the support. Because long M29 bars cannot terminate with a hook, three M19 hooked bars were used to satisfy the demand, thus increasing the provided area to 3420 mm^2 while creating some congestion at this location.

Similarly, at the interior support, the required negative-moment reinforcement area is 2348 mm^2, whereas the provided area is 3870 mm^2, an increase in reinforcement area of 1522 mm^2 over that required for strength. This increase in reinforcement area at the interior support is due to the need of meeting the maximum spacing limitation of the Code, governed by Eq. (24.3.2a) and (24.3.2b).

The required positive-moment reinforcement area at midspan was 2348 mm^2, but the provided area has to increase to 3226 mm^2 to satisfy Code provisions for maximum spacing limits. ACI CODE-440.11-22[4] Section 9.7.3.8.2 requires that one-fourth of the maximum positive-moment reinforcement be extended along the beam bottom into the support. Therefore, two M29 bars were extended into the column. Also, Code Section 9.7.7.4 requires that longitudinal integrity reinforcement at noncontinuous supports be anchored to develop f_{fu} (ultimate guaranteed tensile strength) at the face of the support. To develop a full capacity of 872 kN, GFRP bars required a development length of 2007 mm, with only 572 mm available with a corresponding force of 250 kN. Therefore, three M19 GFRP hooked bars were used to enhance the capacity at the face of the edge column to 898 kN. The required area (one-fourth of positive reinforcement) was 806 mm^2, whereas the provided area at the face of the column increased to 2142 mm^2.

The longitudinal skin reinforcement was provided as required by Code Section 9.7.2.3 (that is, skin reinforcement should be uniformly distributed on both side faces for beams exceeding 458 mm to a distance of h/2 from the tension face). The Code provisions in Section 24.3.2 limit the maximum spacing of skin reinforcement; therefore, four M10 GFRP bars were used in this beam at 114 mm center-to-center spacing on each face.

The required and provided area of reinforcement at the exterior support, midspan, and interior support and corresponding development length values are listed in Table 6. Figure 5(a) shows the detailing of the reinforcement, theoretical cutoff points, and inflection points for three different sections. Demand and capacity along the length of the beam are shown, with the latter being much larger than demand because of the Code provisions for detailing. Figures 5(a) to (e) present the reinforcement details at three locations, the plan view of positive and negative reinforcement, the elevation of the beam showing longitudinal reinforcement details, and the elevation of the beam showing shear reinforcement.

Design of beam using low-modulus GFRP bars (E_f = 44,815 MPa)

By making explicit reference to ASTM D7957/D7957M,[7] ACI CODE-440.11-22[4] is currently based on low-modulus

Table 7—Design of GFRP-RC beam using currently specified low-modulus bars (E_f = 44,815 MPa)

Location	Demand, kN·m	Area for strength only, mm^2	Provided area, mm^2, meeting all Code requirements	Provided capacity, kN·m, meeting all Code requirements	Development length, mm
Exterior support	362	3420	3870	690	1752
Midspan	413	3420	3870	885	1168
Interior support	579	3420	6452	1063	990

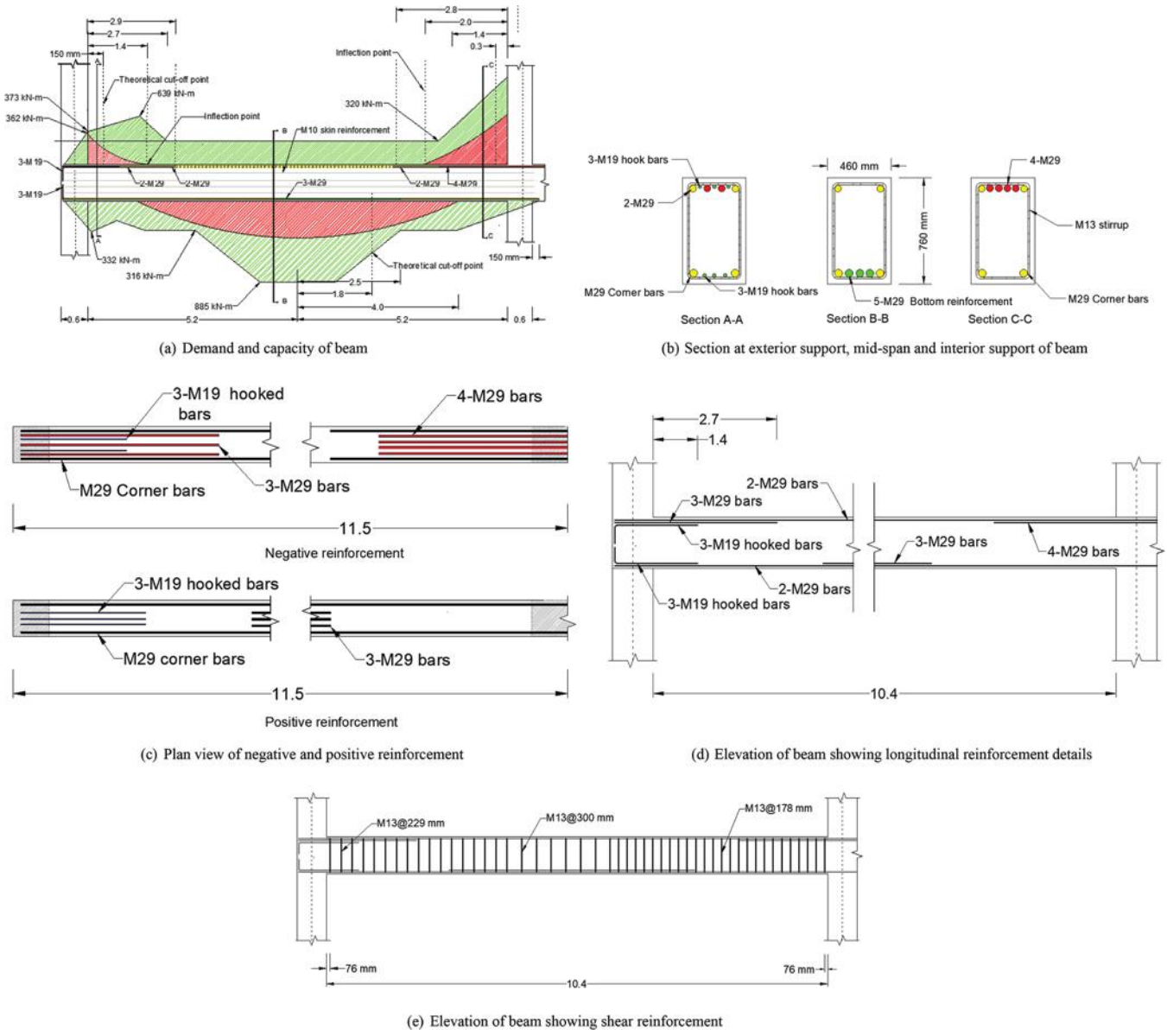

Fig. 5—Demand and capacity envelopes, beam dimensions, and reinforcement details. (Note: Units in meters unless otherwise indicated.)

(E_f = 44,815 MPa) GFRP bars, despite the availability of new-generation high-modulus bars. Therefore, this study also investigated the use of the currently specified bars to evaluate the effect of lower elastic modulus on design and detailing. As old-generation bars have lower strength and stiffness values, the minimum required reinforcement area increased from 2348 mm^2, using high-modulus GFRP bars as shown in Table 6, to 3420 mm^2 with old-generation bars, as given in Table 7. It can be observed that the provided area at the exterior support is 3870 mm^2 greater than the required 3420 mm^2; however, it produced a capacity of 225 kN·m at the face of the column against a demand of 362 kN·m due to higher development length values. To enhance the capacity at the face of the exterior column, three M19 bars were used, increasing the provided area to 4710 mm^2 and the capacity to 398 kN·m at the face of the column.

Similarly, the interior support required reinforcement area for strength was 3420 mm^2. However, the bond stresses were

Table 8—GFRP-RC beam using high-modulus bars with different k_b values

Location	Area for strength only, mm^2	k_b = 1.35		k_b = 1.20		k_b = 1.05	
		Required area, mm^2, without meeting serviceability	Provided area, mm^2, meeting serviceability	Required area, mm^2, without meeting serviceability	Provided area, mm^2, meeting serviceability	Required area, mm^2, without meeting serviceability	Provided area, mm^2, meeting serviceability
Exterior support	1935	2580	2580	2580	2580	2580	2580
Midspan	1935	2580	3226	2580	3226	2580	3226
Interior support	2580	3870	3870	3226	3226	3226	3226

higher than the maximum specified limit in ACI CODE-440.11-22[4] Section 24.3.2.2, calculated as follows.

$$f_{fs} \le 0.36E_f/d_cB_{cr}k_b \quad (23)$$

where d_c is the thickness of concrete cover measured from the extreme tension fiber to the center of the bar location closest thereto, mm; and B_{cr} is the ratio of the distance from the elastic cracked section neutral axis to the extreme tension fiber to the distance from the elastic cracked section neutral axis to the centroid of tensile reinforcement.

To satisfy the maximum allowed stresses at service, the provided area has to increase from 3420 to 6452 mm^2. An increase in the provided area of 3032 mm^2 (beyond the required area) makes detailing difficult. The minimum clear spacing between parallel reinforcement in a horizontal layer is specified in Code Section 25.2.1 as the least of 25.4 mm, the diameter of the bar, and four-thirds the diameter of the aggregate. To avoid violation of this limit, negative reinforcement was placed in two layers at the interior support.

The required reinforcement area at midspan was 3420 mm^2 and the provided area is 3870 mm^2, sufficient to satisfy Code requirements. Additionally, one-fourth of the positive reinforcement should extend into the support (ACI CODE-440.11-22[4] Section 9.7.3.8.2); therefore, two M29 bars were extended to both the exterior and interior supports. Code Section 9.7.7.4 states that this reinforcement should be anchored to generate f_{fu} (that is, a force equal to 618 kN) at the face of the column. To develop f_{fu}, a development length of 1270 mm was required for two M29 bars. However, with the available development length, the developed force was only 276 kN. Therefore, three M19 hooked bars were used to increase the capacity greater than f_{fu}. The required and provided areas of reinforcement and corresponding development length values at three locations are provided in Table 7. It also shows demand and capacity values for the exterior support, midspan, and interior support.

Design of beam with low-modulus GFRP bars (E_f = 44,815 MPa) when h = 660 mm

The current steel-RC beam in the Handbook[6] uses a height of 760 mm based on ACI 318-19 Section 9.3.1.1, thus automatically meeting serviceability requirements. This height value is conservative because the actual height required for deflection control is 660 mm when performing deflection calculations for steel-RC beams.

To maintain the same beam height (that is, 660 mm) when using GFRP reinforcement, 21 M29 bars would be required at midspan, which is obviously not realistic.

PARAMETRIC STUDY

In the second phase of this project, a parametric study was carried out using high-modulus GFRP bars (E_f = 60,000 MPa) by changing the values of bond factor k_b, concrete compressive strength f_c', and deflection limits while maintaining the beam cross-section dimensions equal to 460 x 760 mm.

Design of beam using high-modulus GFRP bars (E_f = 60,000 MPa) with different k_b values

The Code provisions for maximum GFRP bar spacing and stress at service loads were found to be critical design limitations. These provisions are controlled by the bond factor k_b, which was originally 1.35 (as used in Phase 1) and changed to 1.20 in the recent publication of ACI CODE-440.11-22.[4] To better understand its implications, two different k_b values (that is, 1.20 and 1.05) other than 1.35 used in Phase 1 were considered using f_c' = 35 MPa and a deflection limit of l/240, allowing the member to be under-reinforced.

It was found that changing the bond factor from 1.35 to 1.20 had a beneficial effect on the maximum allowable stress limit at service, which increased by 12.5%, and the maximum spacing limit, which also increased by 21.5% at three critical locations in the beam. Though the provided reinforcement area remains the same at the exterior support, the safety margin significantly improved. The effect of a lower bond factor k_b was more apparent at the interior support; here, the required area decreased by 17% while satisfying Code provisions for bond stresses and maximum spacing limitations, as shown in Table 8. It is worth noting that when designing beams using high-modulus GFRP bars, an additional reinforcement area equal to 1522 mm^2 was required to satisfy the maximum service stress limit at the interior support. Because k_b is directly related to the service stress limit, lowering its value showed beneficial effects, as shown in Table 8.

Similarly, reducing k_b to 1.05 increases the maximum allowable stress limit at service by 28.5% and maximum spacing by 49% compared to when using k_b = 1.35. Similar to the case of k_b = 1.20, the reduction in reinforcement areas by 17% was observed at the interior support.

It is worth noting that provided reinforcement areas are similar for three k_b values (1.35, 1.20, and 1.05) at the

Table 9—GFRP-RC beam using high-modulus bars with different concrete strengths

Location	Reinforcement area for strength only, mm²	f_c' = 20 MPa		f_c' = 35 MPa		f_c' = 50 MPa	
		Reinforcement area provided, mm²		Reinforcement area provided, mm²		Reinforcement area provided, mm²	
		Without serviceability	With serviceability	Without serviceability	With serviceability	Without serviceability	With serviceability
Exterior support	1935	2580	2580	2580	2580	2580	2580
Midspan	1935	3226	4516	3226	3226	3226	3226
Interior support	2580	3870	3870	3870	3870	3870	3870

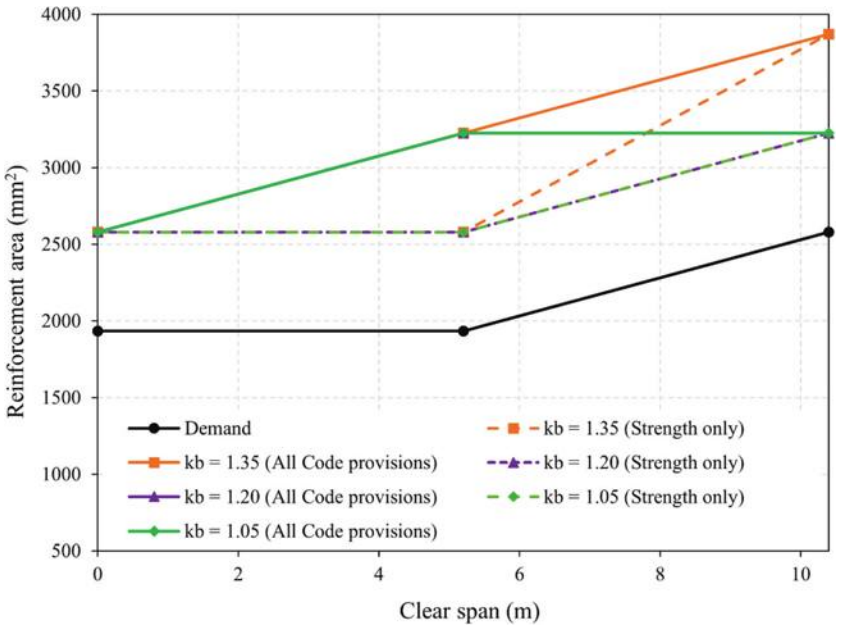

Fig. 6—Reinforcement area with different k_b *values with and without meeting serviceability requirements (lines overlap).*

exterior support and midspan, while reduction is observed at the interior support. This is because lowering k_b increased the maximum allowable spacing and stress at service limits but not enough to reduce the reinforcement area significantly. A lower k_b may not considerably affect the Code provisions for maximum spacing and stress at service. Therefore, the whole equations, especially the value of the coefficients, may need to be revisited with experimentation.

The effect of different k_b values on reinforcement requirements for stress at service and maximum spacing limits with and without meeting Code provisions is depicted in Fig. 6; the difference in the provided area is noticeable at the interior support. It should be noted that reducing the k_b value from 1.35 to 1.20 and 1.05 had some beneficial effects, which were reversed by serviceability requirements. Therefore, the lines in Fig. 6 overlap.

Design of beam using high-modulus GFRP bars (E_f = 60,000 MPa) with different f_c' values

Two different values of concrete strength were used (that is, f_c' = 20 and 50 MPa) to visualize the effects on the design of GFRP-RC members for k_b = 1.35 and a deflection limit of l/240. When the concrete compressive strength becomes 20 MPa, the design is penalized by the maximum spacing provisions of the Code, governed by stresses at service loads and k_b. Hence, as shown in Table 9, the required reinforcement area at the exterior support is 1935 mm², whereas the provided area is 2580 mm². Similarly, at the interior support, to avoid violation of the maximum spacing provisions of the Code, the reinforcement area has to increase to 3870 mm² against the minimum required 2580 mm².

The reduction in concrete strength significantly affects the serviceability requirements. As shown in Table 9, the required reinforcement area at midspan is 1935 mm²; however, to satisfy detailing constraints, it should increase to 3226 mm². Finally, this specification is aggravated by serviceability, requiring a reinforcement area of 4516 mm².

When concrete compressive strength is increased to 50 MPa, serviceability requirements were easily satisfied. As shown in Table 9, there is no difference between provided reinforcement areas with and without serviceability, implying that concrete strength has profound effects on the deflection of GFRP-RC member design, given detailing requirements are satisfied. Additionally, gains achieved by increasing the compressive strength of concrete from 35 to 50 MPa are reversed by Code provisions for maximum spacing and stress at service loads.

As shown in Fig. 7, with a concrete strength of 20 MPa, the reinforcement area at midspan is higher, indicating that GFRP-RC members are prone to more deflection at low

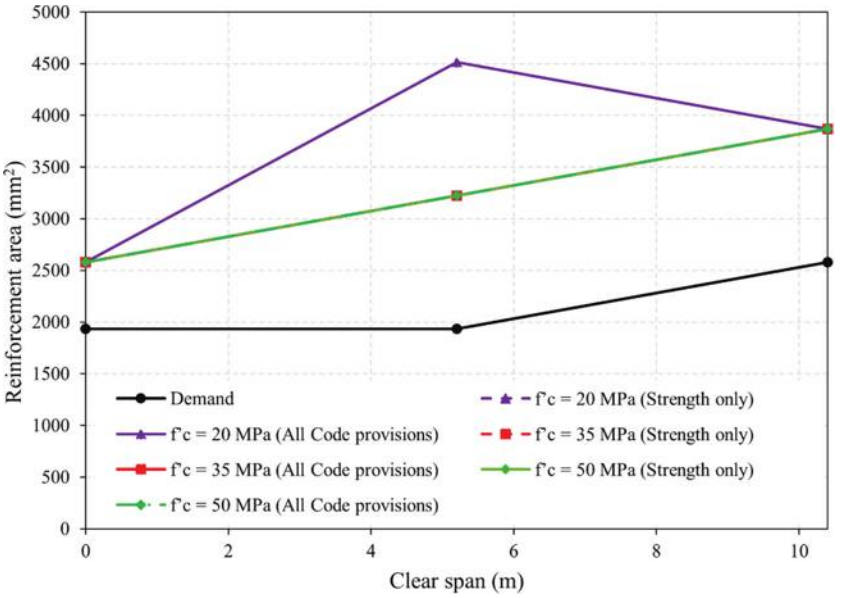

Fig. 7—Reinforcement area with different f_c' *values with and without meeting serviceability requirements (lines overlap).*

Table 10—GFRP-RC beam using high-modulus bars with different deflection limits

Location	Reinforcement area required for strength only, mm²	Reinforcement area provided, mm² Δ = *l*/240	Reinforcement area provided, mm² Δ = *l*/360	Reinforcement area provided, mm² Δ = *l*/480
Exterior support	1935	2580	2580	2580
Midspan	1935	3226	6452	12,258
Interior support	2580	3870	3870	3870

concrete strengths. Increasing concrete strengths significantly decreases the reinforcement area used to meet serviceability requirements. It should be noted that some curves representing identical values in Fig. 7 overlap, hence the difference in using different concrete strengths may not be visible in the figure.

Design of beam using high-modulus GFRP bars (E_f = 60,000 MPa) changing deflection limit

In ACI CODE-440.11-22[4] Section 24.2.2, two more stringent deflection limits (that is, *l*/360 and *l*/480) other than the one used in Phase 1 (*l*/240) are provided. As GFRP-RC members are sensitive to serviceability requirements, a design attempt is made on these two limits using f_c' = 35 MPa and k_b = 1.35.

For the more stringent deflection limits, reinforcement is increased at midspan to satisfy serviceability. As seen in Table 10, provided areas of reinforcement at supports remain the same for any deflection limit. However, the provided area at midspan has to increase to 6451 mm² to satisfy serviceability to meet *l*/360. When the deflection limit was set to *l*/480, the provided reinforcement area increased to 12,258 mm², making it impossible to construct. If the limit of *l*/480 has to be met, the beam cross-section dimensions must change.

OBSERVATIONS

Development length

The development length equation in ACI CODE-440.11-22[4] results in very large values, and this, coupled with the inability to make a hook at the end of long longitudinal bars, makes design challenging and costly. There have been improvements in composite material properties as well as surface deformations since the Code equation was developed. Additionally, the current equation is based on the test data obtained more than two decades ago[9] and the bars used in those tests are no longer available today. Therefore, it is necessary to reassess and update the development length equation for GFRP bars to incorporate the improvements in the material properties and develop a more representative equation for development length.

Maximum spacing limit

The maximum spacing limit is governed by Code Section 24.3.2 to control cracking, developed by Ospina and Bakis in 2007, based on the modifications to the work done by Frosch in 1999 for steel-RC.[10,11] This limit is governed by the bond factor k_b and stress at service loads. Stress at service loads is also dependent on the bond factor. Reinforcement spacing limitations greatly penalize the design, and the resulting capacity becomes typically very large compared to demand. This additional reinforcement not only results in extra cost but in detailing difficulties as well. There have been improvements in GFRP material properties, warranting reconsideration of these provisions.

Skin reinforcement

To control web cracking, provisions for GFRP skin reinforcement are given in Code Section 9.7.2.3.[4] These provisions are based on the physical model developed for steel-RC members for skin reinforcement.[12] Additionally, the provisions for steel-RC are applicable to member depths greater than 760 mm; however, for GFRP-RC members, skin reinforcement needs to be provided for depths greater than

460 mm. Further, Code provisions require skin reinforcement to be placed at a maximum spacing as given in Code Section 24.3.2[4] with an overall outcome that appears unreasonable. Because there has been no experimentation dedicated to GFRP skin reinforcement, the current maximum spacing requirements need to be reassessed.

CONCLUSIONS AND RECOMMENDATIONS

In this study, a beam example was taken from the *ACI Reinforced Concrete Design Handbook*[6] and redesigned with glass fiber-reinforced polymer (GFRP) reinforcement to show the implication of some ACI CODE-440.11-22[4] provisions. This study considered both new-generation (E_f = 60,000 MPa) and old-generation (E_f = 44,815 MPa) bars compliant with ASTM D7957/D7957M-22,[7] as currently specified by the Code. Using the same beam cross section as steel-reinforced concrete (RC), the concrete strength f_c' used was equal to 35 MPa, and the bond coefficient k_b = 1.35. An assumption about the maximum permissible deflection limit of l/240 was also made. Later, a parametric study was carried out to analyze the effects of changing the values of k_b, f_c', and the maximum permissible deflection limit.

Based on the outcomes of this study in the design and detailing, the following conclusions were drawn:

- Design of beams reinforced with GFRP is generally governed by Code serviceability (that is, deflection control) and detailing (that is, maximum reinforcement spacing) requirements.
- Given that the elastic modulus of GFRP bars is lower than that of steel, more reinforcement area is needed to satisfy deflection limits.
- Code provisions for maximum spacing and allowable stress limit at service loads are governed by the bond factor k_b. Changing k_b from the current Code value to lower ones (that is, 1.20 or 1.05) increases the maximum allowable limits for stress at service and bar spacing but does not significantly reduce reinforcement requirements.
- Increasing concrete compressive strength to 50 MPa significantly reduced the deflection of the GFRP-RC member. However, gains achieved by increasing compressive strength are nullified by Code provisions for maximum spacing and stress at service.
- The maximum permissible deflection limits in the Code other than l/240 (that is, l/360 and l/480) are difficult to accomplish with GFRP reinforcement using cross-section dimensions typical of steel-RC.
- The number of skin reinforcement bars is governed by Code maximum spacing provisions, which are found to penalize design.
- The current development length equation results in very large values, causing detailing difficulties and bar congestion, especially at the exterior support.
- Recent developments in the manufacturing of GFRP bars and an increased modulus of elasticity from 44,815 to 60,000 MPa has a positive impact on design.
- Experimental investigations aimed at reassessing Code limits for development length, maximum spacing, and stress at service loads by incorporating the improvements in material properties are needed.
- The shear design of the GFRP-RC beam is affected by a reduction in concrete contribution, V_c, and strength at the bent portion of the GFRP stirrups. Hence, more shear reinforcement than its steel counterpart is required.

AUTHOR BIOS

Zahid Hussain *is a PhD Student in the Civil and Architectural Engineering Department at the University of Miami, Coral Gables, FL. He received his BE and ME in civil engineering from Quaid-e-Awam University of Engineering, Science & Technology, Nawabshah, Sindh, Pakistan, and Universiti Tun Hussein Onn Malaysia, Batu Pahat, Johor, Malaysia, respectively. He is a member of ACI Committee 440, Fiber-Reinforced Polymer Reinforcement. His research interests include sustainable materials, computational methods, design, and behavior of fiber-reinforced polymer (FRP)-reinforced structures.*

Antonio Nanni, *FACI, is an Inaugural Senior Scholar, Professor, and Chair of the Civil and Architectural Engineering Department at the University of Miami. He is a member of ACI Committees 440, Fiber-Reinforced Polymer Reinforcement, and 549, Thin Reinforced Cementitious Products and Ferrocement.*

ACKNOWLEDGMENTS

The authors would like to thank the National Science Foundation (NSF) under Grant No. 1916342, and the Higher Education Commission of Pakistan for their financial support of the lead author.

NOTATION

A_{fv}	=	area of shear reinforcement, mm^2
b_w	=	web width or diameter of circular cross section, mm
c_b	=	lesser of: a) distance from center of bar to nearest concrete surface; and b) one-half center-to-center spacing of bars being developed, mm
c_c	=	concrete cover, mm
d	=	distance from extreme compression fiber to centroid of longitudinal tension reinforcement, mm
d_b	=	nominal diameter of bar, mm
E_c	=	modulus of elasticity of concrete, MPa
E_f	=	modulus of elasticity of GFRP reinforcement, MPa
f_c'	=	compressive strength of concrete at 28 days
f_{fb}	=	guaranteed ultimate tensile strength of bent portion of bar
f_{fr}	=	tensile stress in GFRP reinforcement required to develop full nominal section capacity, MPa
f_{fs}	=	stress at service loads
k_b	=	bond-dependent coefficient
k_{cr}	=	ratio of depth of elastic cracked section neutral axis to effective depth
l_n	=	length of clear span measured between face-to-face of supports, m
M_u	=	ultimate factored moment at section, kN·m
S_{max}	=	maximum allowed spacing, mm
S_n	=	nominal moment, shear, axial or torsional strength
U	=	strength of member or cross section required to resist factored loads or related internal moments and forces
V_c	=	nominal shear strength provided by concrete, N
V_f	=	nominal shear strength provided by GFRP shear reinforcement, N
V_n	=	nominal shear strength, N
V_u	=	factored shear force at section, N
W_u	=	ultimate factored load, kN/m
Δ	=	maximum permissible deflection
ε_f	=	strain in GFRP flexural reinforcement
Φ	=	strength reduction factor
ω	=	bar location modification factor

REFERENCES

1. Bielak, J.; Schönerberg, J.; Classen, M.; and Hegger, J., "Shear Capacity of Continuous Concrete Slabs with CFRP Reinforcement," *Construction and Building Materials*, V. 320, Feb. 2022, Article No. 126117.

2. Hollaway, L. C., "A Review of the Present and Future Utilisation of FRP Composites in the Civil Infrastructure with Reference to Their Important

In-Service Properties," *Construction and Building Materials*, V. 24, No. 12, Dec. 2010, pp. 2419-2445. doi: 10.1016/j.conbuildmat.2010.04.062

3. Mugahed Amran, Y. H.; Alyousef, R.; Rashid, R. S. M.; Alabduljabbar, H.; and Hung, C.-C., "Properties and Applications of FRP in Strengthening RC Structures: A Review," *Structures*, V. 16, Nov. 2018, pp. 208-238. doi: 10.1016/j.istruc.2018.09.008

4. ACI Committee 440, "Building Code Requirements for Structural Concrete Reinforced with Glass Fiber-Reinforced Polymer (GFRP) Bars—Code and Commentary (ACI CODE-440.11-22)," American Concrete Institute, Farmington Hills, MI, 2023, 260 pp.

5. ACI Committee 318, "Building Code Requirements for Structural Concrete (ACI 318-19) and Commentary (ACI 318R-19) (Reapproved 2022)," American Concrete Institute, Farmington Hills, MI, 2019, 624 pp.

6. ACI, *ACI Reinforced Concrete Design Handbook* (ACI MNL-17(21)), American Concrete Institute, Farmington Hills, MI, 2021, pp. 1-568.

7. ASTM D7957/D7957M-22, "Standard Specification for Solid Round Glass Fiber Reinforced Polymer Bars for Concrete Reinforcement," ASTM International, West Conshohocken, PA, 2022, 5 pp.

8. ASCE/SEI 7-16, "Minimum Design Loads and Associated Criteria for Buildings and Other Structures," Structural Engineering Institute, American Society of Civil Engineers, Reston, VA, 2016, 889 pp.

9. Wambeke, B. W., and Shield, C. K., "Development Length of Glass Fiber-Reinforced Polymer Bars in Concrete," *ACI Structural Journal*, V. 103, No. 1, Jan.-Feb. 2006, pp. 11-17.

10. Ospina, C. E., and Bakis, C. E., "Indirect Flexural Crack Control of Concrete Beams and One-Way Slabs Reinforced with FRP Bars," *Proceedings of the 8th International Symposium on Fiber Reinforced Polymer Reinforcement for Reinforced Concrete Structures (FRPRCS-8)*, T. C. Triantafillou, ed., Patras, Greece, 2007.

11. Frosch, R. J., "Another Look at Cracking and Crack Control in Reinforced Concrete," *ACI Structural Journal*, V. 96, No. 3, May-June 1999, pp. 437-442.

12. Frosch, R. J., "Modeling and Control of Side Face Beam Cracking," *ACI Structural Journal*, V. 99, No. 3, May-June 2002, pp. 376-385.

ACI STRUCTURAL JOURNAL TECHNICAL PAPER

Title No. 120-S75

Experimental Study on Column Reinforcing Bar Anchorage in Drilled Shaft Footings

by Y. Yi, H. Kim, R. A. Boehm, Z. D. Webb, J. Choi, J. Murcia-Delso, T. D. Hrynyk, and O. Bayrak

This paper presents an experimental study on the anchorage behavior of column reinforcement subjected to tension in drilled shaft footings loaded under combined axial force and uniaxial bending moment. Large-scale tests were conducted on four footing specimens that were constructed with different column bar anchorage details: straight bars, hooked bars with two different hook orientations, and headed bars. All tension-loaded column reinforcement was shown to yield regardless of anchorage type. Further, all anchorage types developed stresses in the vicinity of the anchorage region except for bars with end hooks that were oriented outwards from the base of the column. Properly oriented hooked bars, considering the internal force flow of the strut-and-tie model, and headed bars developed more uniform stress distributions over their lengths as compared to straight bars. Based on developed stress distributions for the column reinforcement estimated from strain measurements, a critical section was also proposed to establish the anchorage requirement for the column reinforcement in a three-dimensional strut-and-tie model.

Keywords: bar anchorage; bond; critical section; development length; drilled shaft footing; large-scale tests; strut-and-tie method.

INTRODUCTION

A drilled shaft footing is a reinforced concrete member that distributes forces from piers to a group of drilled shafts in deep foundations. Generally, drilled shaft footings have shear span-depth ratios that are less than 2 and are therefore classified as D-regions. Accordingly, these members are good candidates to be designed using the strut-and-tie method (STM). While STM applications for planar D-regions, such as deep beams, are two-dimensional (2-D), drilled shaft footings supported on a grid of drilled shafts require a three-dimensional (3-D) configuration of struts and ties to transmit the forces from the pier to the drilled shafts. The 3-D STM of a drilled shaft footing subjected to combined axial force and moderate uniaxial bending moment, resulting in tension at one face of the column and non-uniform compression in drilled shafts, is presented in Fig. 1.

Tie elements comprising an STM should be properly anchored at nodal regions to ensure full yield strength potential along their lengths. Current STM provisions[1,2] define the critical section for the development of a tie as the point where the centroid of the tie reinforcement intersects the edge of the diagonal strut, as shown in Fig. 2. The nodal region bounded by the edge of the strut is referred to as the extended nodal zone. The anchorage length check based on the critical section defined from this extended nodal zone can be performed only at singular nodes that can define their nodal geometry based on boundary conditions, such as the reaction plate illustrated in Fig. 2. Such is not the case for the bottom end node of the column tie element of drilled shaft footings subjected to combined axial force and moderate uniaxial bending moment (Node A in Fig. 1). This node is classified as a smeared node, for which the nodal geometry cannot be clearly defined. Hence, it is difficult to perform the anchorage check for the column tie element in Fig. 1 based solely on the geometry of the STM.

Several experimental investigations have been conducted on drilled shaft footings subjected to uniaxial compression.[3-8] However, to the authors' knowledge, there are limited experimental studies available in the literature on drilled shaft footings subjected to combined axial force and uniaxial bending moment. Miguel-Tortola et al.[9] tested footings subjected to eccentric loading inducing tension at the column reinforcement. However, they only focused on the behavior of the footing by preventing yielding of the column reinforcement; therefore, the anchorage response of the column reinforcement was not covered in the literature. Although a few studies[10-12] provided STM-based design recommendations and examples for drilled shaft footings subjected to flexure involving vertical column ties, there has been no in-depth research focusing on the anchorage of these ties. Klein[10] proposed a design example with a conservative reinforcement detail consisting of the 90-degree hooked column bar extending beyond the bottom mat reinforcement (Fig. 3(a)). Widianto and Bayrak[11] provided a design example of a drilled shaft footing subjected to large uniaxial bending moments combined with axial force inducing tension in both the column and the reinforcement within the drilled shaft. The column reinforcement in this design example was assumed to be fully developed by way of headed bars that extended beyond the bottom mat reinforcement (Fig. 3(b)). Williams et al.[12] employed 90-degree hooks placed on the bottom mat reinforcement (Fig. 3(c)) based on the successful long-term practice of using 90-degree hooks in column reinforcing bars extending into drilled shaft footings. None of these design examples examined the anchorage length of the column reinforcement.

The lack of clear design guidelines and experimental verification for the anchorage of column reinforcement in drilled shaft footings hinder the practical use of the 3-D STM in

ACI Structural Journal, V. 120, No. 4, July 2023.

MS No. S-2022-220.R1, doi: 10.14359/51738721, received January 6, 2023, and reviewed under Institute publication policies.

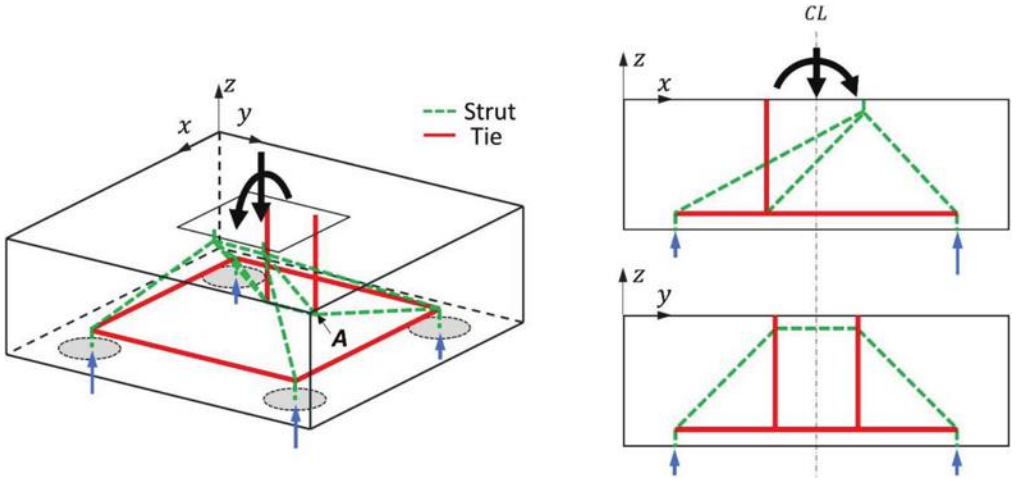

Fig. 1—Three-dimensional STM for drilled shaft footing on four drilled shafts subjected to combined axial force and moderate uniaxial bending moment.

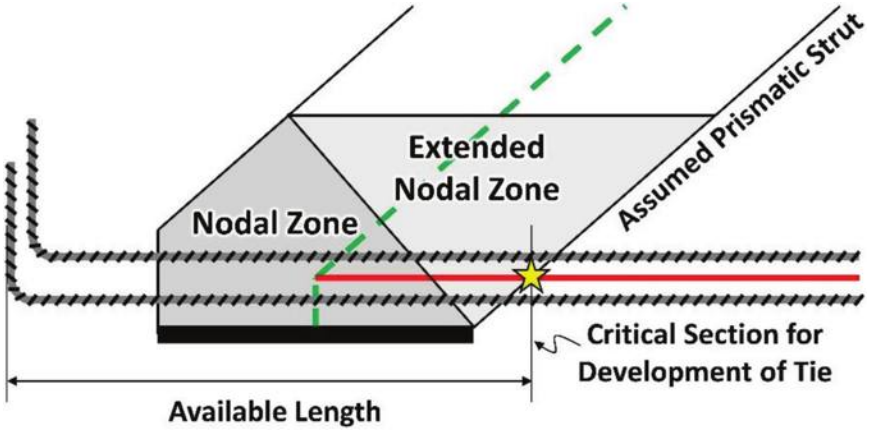

Fig. 2—Definition of extended nodal zone (adapted from AASHTO LRFD[2]).

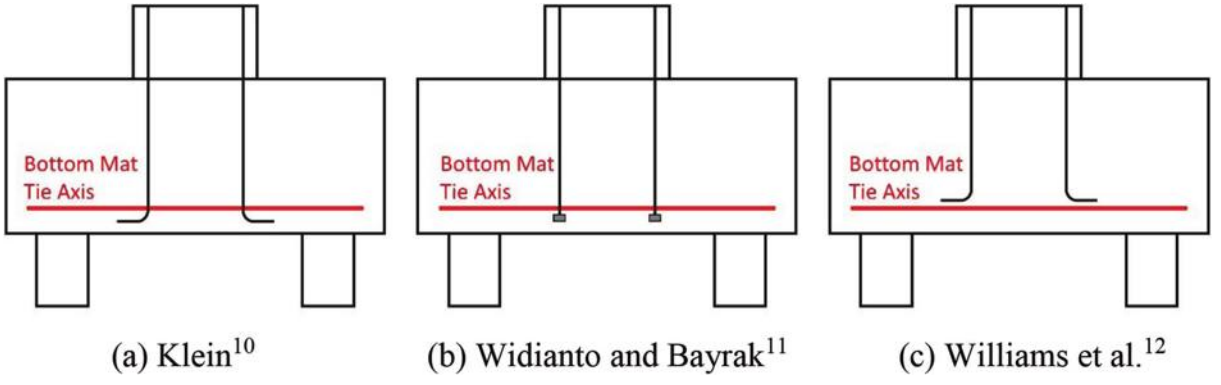

Fig. 3—Detailing of column reinforcement anchorage proposed in literature.

the design of these type of components. To overcome this limitation, a set of large-scale structural tests on four drilled shaft footings, which were designed with different column reinforcement anchorage configurations—straight bars, hooked bars with two different hook orientations, and headed bars—were performed. This paper presents the experimental program and discussion on the behavior of drilled shaft footings, with a primary focus on anchorage performance. Design recommendations regarding anchorage length calculations and design details are also provided.

RESEARCH SIGNIFICANCE

The experimental tests conducted in this study provide much needed data on the behavior of drilled shaft footings under combined axial force and moderate uniaxial bending moment inducing tension in column reinforcement and governed by yielding of the column reinforcement. The large-scale test specimens employed in the experimental program permit the investigation of real-world relevant design details and on the structural behavior of drilled shaft footings used in the field. The test data, insights, and design

Table 1—Test matrix

	Specimen ID	Top/bottom mat of reinforcement		Load eccentricity, in.	Column reinforcement anchorage
		Layout	Anchorage		
1	VI-ST	Grid	Straight (top mat) and hooked (bottom mat)	16.5	Straight
2	VI-HD				Headed
3	VI-HKO				Hooked (Orientation: outward)
4	VI-HKI				Hooked (Orientation: inward)

Note: 1 in. = 25.4 mm.

(a) Tapered bar and threaded fastener (b) Installed fastener

Fig. 4—Detailing of headed bars.

recommendations resulting from this study resolve ambiguities on the anchorage requirements for column reinforcement in 3-D STMs for drilled shaft footings.

EXPERIMENTAL PROGRAM

Test variables

The experimental program presented in this paper is part of a comprehensive research project on drilled shaft footings[13] conducted in the Ferguson Structural Engineering Laboratory at The University of Texas at Austin. The test specimens were designed to investigate the tensile behavior of the vertical column reinforcement embedded in drilled shaft footings with the chief purpose of characterizing the performance of different anchorage details for column reinforcement.

Four test specimens governed by yielding of the column reinforcement were planned with different column reinforcement anchorage types: straight, headed, and two configurations of 90-degree hooked reinforcement with hooks oriented in opposite directions. The test matrix is given in Table 1. Note that a tapered reinforcing bar with a threaded fastener was used for the connection of the headed reinforcement, as shown in Fig. 4. The net bearing area of the provided head was equal to four times the cross-section area of the reinforcing bar. Standard 90-degree hooks employing permissible bend radii were used for the hooked reinforcement.

In practice, the tail end of the hook embedded in the drilled shaft footing is typically oriented in the direction away from the column to facilitate construction. Hooked bar anchorages develop tensile forces by bond stresses on the bar surface and bearing against the concrete in the inner face of the hook. The orientation of the hook has been considered to play an essential role in its bearing action in structural components such as beam-column joints.[14] As illustrated in Fig. 5, the vertical force component of the column tie element of the drilled shaft footing under combined axial force and moderate uniaxial bending moment is equilibrated with the diagonal strut coming from the compression side of the column. Based on the internal force flow, the anchorage mechanism of hooked bars can be properly activated when the hook orientation is placed inward to the column; however, hooked bars with tail ends oriented outward from the column require alternative load resisting mechanisms such as resisting tensile forces by way of reinforcement bond stresses or by engaging foundation mat reinforcement. Therefore, two test specimens of hooked reinforcement were planned with different hook orientations to examine the effect of these orientations on the force transfer mechanisms of the column reinforcement.

Specimen design

The test specimens comprised a drilled shaft footing and attached column corbel to facilitate the application of an eccentric vertical load, as shown in Fig. 6. The geometry of the footings was determined from a database of in-practice drilled shaft footings that was previously established.[13] The database comprises 35 drilled shaft footings constructed between 1994 and 2004 for 16 bridges in the State of Texas. The constructed test specimens are approximately half-scale of the average size of the reviewed footings. The footing specimens consisted of bottom mat, top mat, and side reinforcement to replicate reinforcement details represented in the drilled shaft footing database. The reinforcement details are illustrated in Fig. 7 and summarized in Table 2.

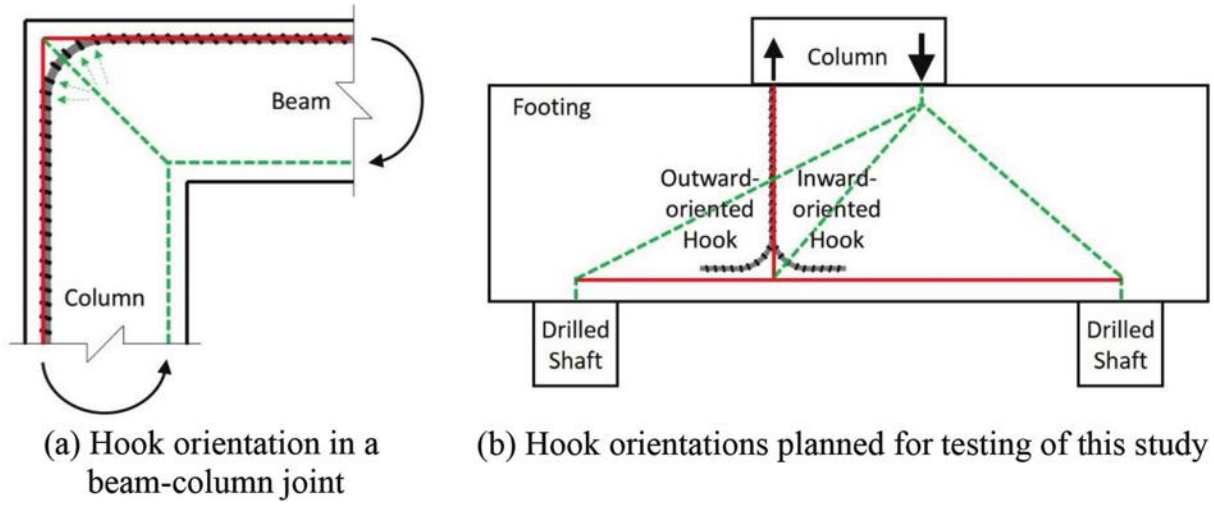

Fig. 5—Hook orientations in structural components designed with STM.

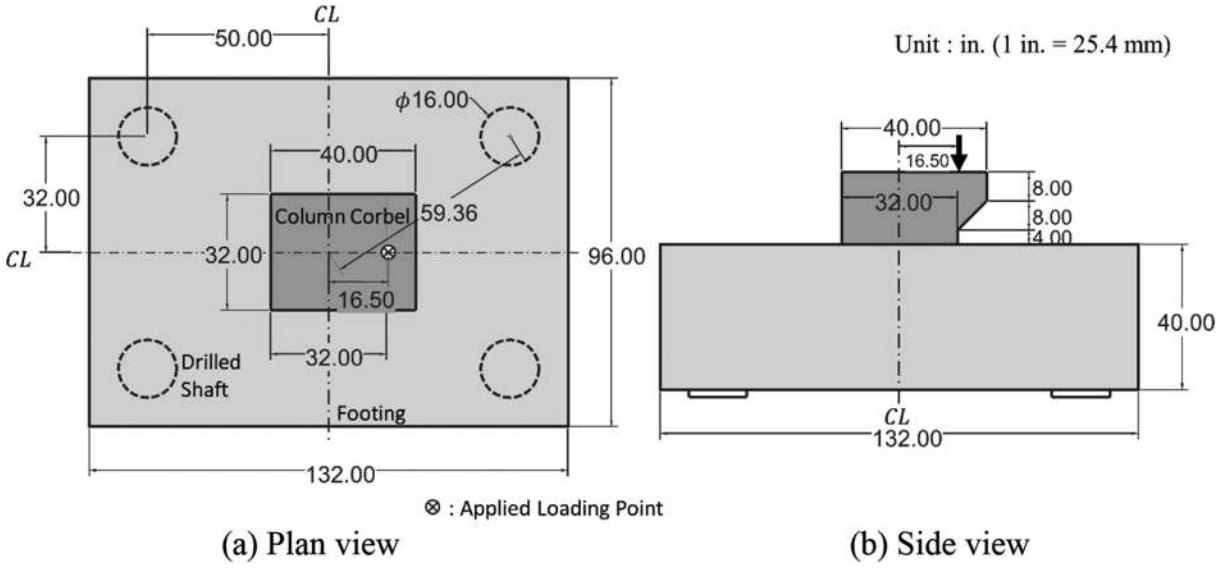

Fig. 6—Geometry of test specimens.

The test specimens were designed so that their capacities would be governed by yielding of the column reinforcement. Therefore, the footings were designed with an increased bottom mat reinforcement ratio (0.96%) than that of the reviewed drilled shaft footings (0.37% on average). A high bottom mat reinforcement ratio was selected to prevent yielding of the bottom mat reinforcement prior to yielding of the column reinforcement, permitting the anchorage of the column reinforcement to be investigated.

The footing specimens had side reinforcement with reinforcement ratios slightly larger than 0.30% in the transverse (0.31%) and longitudinal (0.37%) directions. Shrinkage and temperature reinforcement is generally provided as side reinforcement in footings since crack control reinforcement is not mandated for footings in the STM provisions of ACI 318-19[1] and AASHTO LRFD Bridge Design Specifications (hereafter AASHTO LRFD),[2] respectively. Rather, ACI 318-19[1] recommends using the minimum strut efficiency factor in STMs of drilled shaft footings. However, previous studies[8-13] indicate that the failure of footing specimens exhibits critical cracks on the side surfaces (Fig. 8). To mitigate undesired failures induced by side surface cracks, side reinforcement ratios of 0.37 and 0.31% were provided in the vertical and horizontal directions.

Similarly, a top mat reinforcement ratio of 0.20% was also provided which satisfies the minimum reinforcement ratio specified in AASHTO LRFD[2] (>0.18%) for controlling the shrinkage and temperature cracks on the top surface of the test specimens.

As previously indicated, the test specimens include an integral column corbel for applying an eccentric vertical load to introduce tension in the column reinforcement. This eccentric load results in non-uniform compression at the supports. The eccentricity of the load was carefully determined such that it would yield the column reinforcement in tension while avoiding premature failures of the support regions. To this end, an eccentricity of 16.5 in. (419 mm) was selected. The 20 in. (508 mm) tall column corbel was sized to provide sufficient area for applying the eccentric load and was intentionally over-designed to mitigate premature failures of the corbel. A reinforcement ratio of 0.48% was provided in both longitudinal and transverse directions at side faces of

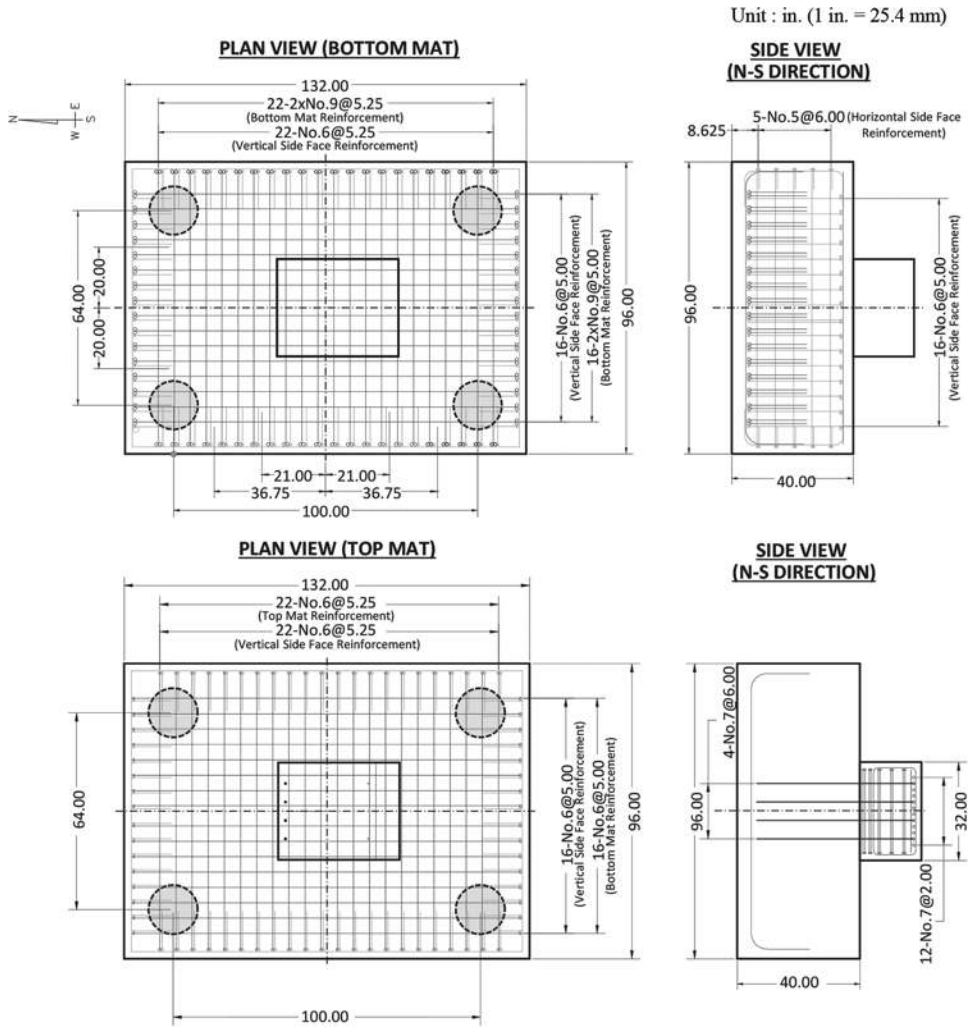

Fig. 7—Reinforcement details of test specimens.

Table 2—Specimen reinforcement details

Footing component					
Bottom mat reinforcement		Side face reinforcement		Top mat reinforcement	
N-S direction	W-E direction	Longitudinal direction	Transverse direction	N-S direction	W-E direction
16-2x No. 9 (No. 29) @ 5.00 in.	22-2x No. 9 (No. 29) @ 5.25 in.	No. 5 (No. 16) @ 5.00 in.	No. 6 (No. 19) @ 5.25 in. No. 6 (No. 19) @ 5.00 in.	No. 6 (No. 19) @ 5.00 in.	No. 6 (No. 19) @ 5.25 in.
Column corbel component					
Vertical column reinforcement		Side face reinforcement		Top reinforcement	
		Longitudinal direction	Transverse direction		
4 No. 7 (No. 22) @ 6.00 in.		No. 5 (No. 16) @ 4.00 in.	No. 5 (No. 16) @ 4.00 in.	12 No. 7 (No. 22) @ 2.00 in.	

Note: 1 in. = 25.4 mm.

the column corbel, which more than satisfied crack control reinforcement requirements specified in AASHTO LRFD[2] for STM and aided in confining the concrete. The corbel was laterally encased with 9/16 in. (14 mm) thick steel plates to preclude any undesired anchorage splitting failure or concrete crushing in the corbel. Furthermore, 3/4 in. (19 mm) diameter threaded rods were inserted through the steel jacket and tightened with nuts to confine the column corbel. A 1/2 in. (13 mm) gap was provided between the steel jacket and the footing to prevent direct contact between those two components during testing.

The sizing of the vertical column reinforcement was determined from the compiled drilled shaft footing database. Identical to in-practice footings and the design example of Williams et al.,[12] all column reinforcing bars were extended to the level of the bottom mat reinforcement for constructability. The embedment lengths of the column reinforcement into the drilled shaft footing ($l_{b,c}$) were determined from the drilled shaft footing database and divided by the diameter of the column reinforcing bars ($d_{b,c}$). To have a similar $l_{b,c}/d_{b,c}$ ratio ($l_{b,c}/d_{b,c}$ = 39.4) in the test specimens, No. 7 (No. 22) reinforcing bars were selected ($l_{b,c}/d_{b,c}$ = 38.6)

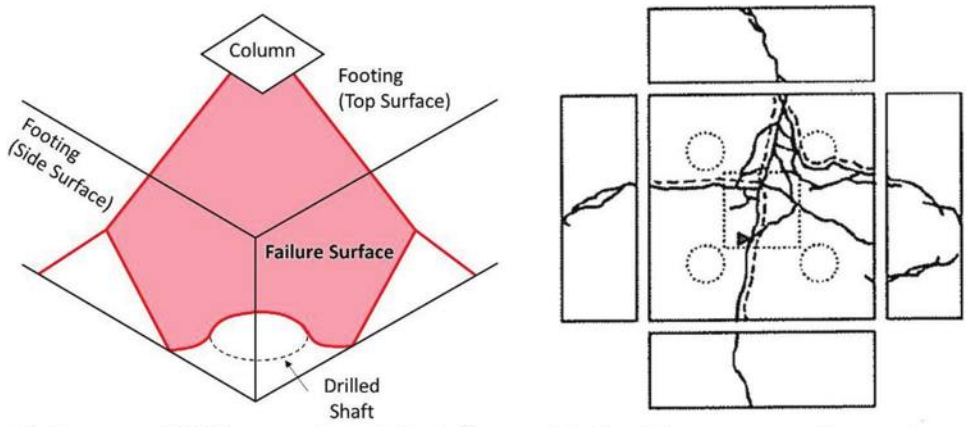

(a) Suggested failure surface (Clarke[8])

(b) Cracking pattern after testing (Specimen No. 23) (Suzuki et al.[6])

Fig. 8—Failure surface of previous drilled shaft footing tests designed with bottom mat reinforcement only.

Table 3—Mechanical properties of materials

Specimen ID			VI-ST	VI-HD	VI-HKO	VI-HKI
Anchorage detail of column reinforcement			Straight	Headed	Hooked (Outward to column)	Hooked (Inward to column)
Concrete	Footing	Compressive strength (f_c'), ksi (day of test)	4.62	5.01	5.00	5.25
	Column	Compressive strength ($f_{c',c}'$), ksi (day of test)	11.97	11.79	10.36	10.02
Reinforcement	Bottom mat	Yield strength ($f_{y,b}$), ksi	67.0			69.9
		Tensile strength ($f_{u,b}$), ksi	109.5			109.6
	Column	Yield strength ($f_{y,c}$), ksi	70.3	72.1	70.3	76.8
		Tensile strength ($f_{u,c}$), ksi	101.3	101.3	101.3	105.0

Note: 1 ksi = 6.9 MPa.

given the available embedment length. To induce reinforcement yielding prior to the failure of the footing, the 1.0% minimum reinforcement ratio for columns as specified in both ACI 318-19[1] and AASHTO LRFD[2] was introduced for designing the column. Therefore, four vertical column reinforcing bars were installed at the tension-side of the corbel, corresponding to a column reinforcement ratio of 0.94% if these column reinforcing bars are equally provided to four sides of the column (16 No. 6 [No. 19] bars).

Material properties

The design concrete strength of the footings was 3.6 ksi (24.8 MPa), and two concrete batches were used to fabricate each footing specimen. Additionally, high-strength concrete with a specified compressive strength of 10 ksi (68.9 MPa) was used for the column corbels. ASTM A706[15] Grade 60 (Grade 420) reinforcing bars were used for the vertical column reinforcement such that the column reinforcement embedded in the corbel could be sufficiently anchored through welding. ASTM A615[16] Grade 60 (Grade 420) reinforcing bars were used for all the other reinforcing bars. The measured mechanical properties of reinforcement are averaged from at least three samples for each reinforcing bar size. Furthermore, two cylindrical concrete strengths obtained from two the concrete batches comprising each footing component of the test specimen are averaged to represent the concrete strength of the footing. The compressive strengths were evaluated at test day using water-cured concrete cylinders fabricated from each concrete batch used in the test specimens. The material properties of the concrete cylinders and reinforcing bars were measured in accordance with ASTM C39[17] and ASTM A370,[18] respectively, and are summarized in Table 3.

Test setup

All test specimens were tested under eccentric vertical loads that were applied to the connected corbels. The vertical load had an eccentricity of 16.5 in. (419 mm) with respect to the centroid of the drilled shaft footing and was applied using a 2000 kip (8.9 MN) capacity hydraulic ram, as shown in Fig. 9(a). The ram was attached to a reaction frame bolted to an elevated strong floor. A loading fixture comprised of a spherical saddle and a series of rollers was placed between the column corbel and the loading ram, as shown in Fig. 9(b), so that the column corbel was allowed to both rotate and translate. Drawings of the test configuration are provided in Fig. 10.

The supports of the specimen were designed to avoid lateral and rotational restraints, and 16 in. (406 mm) diameter circular steel plates representing the drilled shafts supporting the drilled shaft footing were provided at the topmost layer of the support assemblies. All four support fixtures had a spherical saddle layer to allow rotation of the specimen, and three 500 kip (2.2 MN) capacity load cells provided at the

(a) Test setup (b) Loading fixture

Fig. 9—Eccentric loading test setup.

base of each support to measure reaction forces. As illustrated in Fig. 9(a), the lateral restraint conditions were varied among the four supports to provide stability while ensuring that the footing specimens were generally free to develop lateral expansions.

Instrumentation and loading protocol

During testing, support reactions, footing displacements, and reinforcing bar strains were monitored using instrumentation. The vertical (that is, out-of-plane) displacement of the bottom face of the footings was measured using linear potentiometers placed beneath the center of the footing and near the four supports. The relative deformation of the column corbel at the interface was also monitored using linear potentiometers installed vertically at both sides of the column corbel. The tension-side displacement of the column corbel was measured at the level of column reinforcement on the top of the drilled shaft footing, which was subsequently used to measure the relative uplift of the column corbel at its tension face with respect to the drilled shaft footing. Similarly, the compression-side displacement was measured at the symmetric position of the tension-side linear potentiometers.

Strain gauges were installed on the bottom mat reinforcement and the vertical column reinforcement. The vertical column reinforcement was also instrumented with a series of strain gauges along its length so that the measured data could be used to develop stress profiles for the reinforcing bars. Stress profiles of the column reinforcement inside the footings were used to compare the anchorage behaviors of different anchorage details. The gauges were attached on longitudinal ribs of the column reinforcement to minimize grinding of reinforcement ribs, which might adversely affect the bond.

During the tests, vertical loads were applied in 100 kip (445 kN) increments up to the load at which the measured column reinforcement strain reached 75% of its yield strain. Beyond this point, the specimen was continuously loaded up until the end of the test. Between load increments, the condition of the specimens was visually inspected and documented.

EXPERIMENTAL RESULTS

Overall response

The global responses of the test specimens are summarized in Table 4. All specimens exhibited yielding of the vertical column reinforcement. The specimen with straight column reinforcement (VI-ST) failed in the drilled shaft footing at a vertical load of 2025 kip (9.0 MN), whereas the specimen with headed bars (VI-HD) failed by fracture of the column reinforcement at a vertical load of 2080 kip (9.3 MN). These differing failure modes may be attributed to the fact that the concrete strength of the footing component of VI-ST was approximately 10% weaker than that of VI-HD. The reinforcing bar fracture of the column reinforcement led to detachment of the column corbel from the specimen VI-HD. For safety reasons, testing of the remainder test specimens (VI-HKO and VI-HKI) was terminated at 2000 kip (8.9 MN).

First yielding of the column reinforcement was observed at a comparable load level (1150 to 1250 kip [5.1 to 5.6 MN]) in all test specimens. Nevertheless, the bottom mat reinforcement of all test specimens did not experience yielding prior to reaching the 2000 kip (8.9 MN) test termination load level.

To compare load-deflection responses between test specimens designed with different anchorage types, this study also compared the normalized deflection of the footing, and the compression- and tension-side relative displacements of the column corbel. The normalized deflection of the footing was computed from the displacement measured at the center of the footing and that measured at the vicinity of the support. A relative comparison of the load-displacement response progression for all the test specimens is shown in Fig. 11. All specimens behaved with a comparable load-normalized deflection response until 2000 kip (8.9 MN)

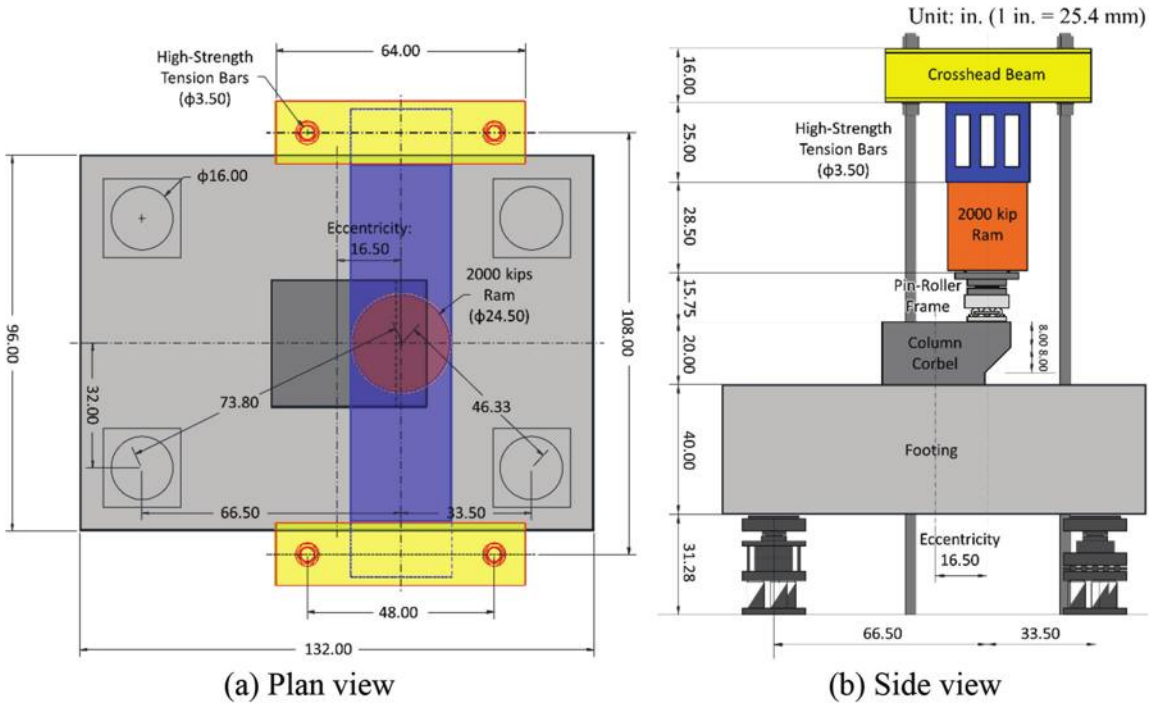

Fig. 10—Detailed drawings of test setup configuration.

Table 4—Summary of test results

Specimen ID	VI-ST	VI-HD	VI-HKO	VI-HKI
Anchorage detail of column reinforcement	Straight	Headed	Hooked (Outward to column)	Hooked (Inward to column)
Measured load at first yielding of column bars* ($P_{fy,c}$), kip	1189	1146	1195	1241
Measured load at yielding of all column bars* ($P_{y,c}$), kip	1564	1540	1416	1422
Measured load at first yielding of bottom mat* ($P_{fy,b}$), kip	2025	2080	N/A†	N/A†
Measured ultimate strength (P_u), kip	2079	2154	N/A†	N/A†
Ultimate failure mode	Failure in footing	Fracture of column reinforcement	No failure†	No failure†

*Strain data analyzed to find yielding on reinforcement.

†Testing stopped prior to failure (at 2000 kip [8.9 MN]).

Note: 1 kip = 4.4 kN; 1 ksi = 6.9 MPa.

loading. Even beyond the yielding load of all column reinforcing bars, the tension-side relative displacement of VI-HKI did not increase significantly compared to that of the compression-side owing to the tensile resistance mechanism acting at the vicinity of the anchorage region, which will be discussed from the stress profiles and cut section of VI-HKI in the next sections. On the other hand, the tension-side relative displacements of the other test specimens increased rapidly after exceeding the yielding load.

Visual observations

The post-failure conditions of VI-ST and VI-HD are depicted in Fig. 12. The ultimate failure of VI-ST occurred in the drilled shaft footing. Multiple arch-shaped cracks extending diagonally to the supports formed on side surfaces of the footing. Diagonal cracking was more severe in the half-span of the footing where supports were subjected to higher reactions (in the vicinity of the south side), as shown in Fig. 12(a). Failure was governed by diagonal tension on this side of the footing. Furthermore, no damage was observed on the column corbel confined by steel plates during testing. Nevertheless, concrete crushing and crack width opening of 3/8 in. (10 mm) could be identified after testing at the compression- and tension-side of the 1/2 in. (13 mm) gap between the steel jacket and the footing, respectively.

Even though the ultimate failure of VI-HD was governed by column bar rupture, the crack pattern of the footing after the test was almost identical to that observed in VI-ST, as shown in Fig. 12(b). This indicates that the footing component of VI-HD was also close to the ultimate state when bar rupture occurred. Because the column corbel was detached from the footing at failure, the interface between the column corbel and the footing could be visually inspected after the test (refer to Fig. 12(b)). On the tension-side of the interface, a small concrete cone formed surrounding the column reinforcement at the top of the footing, and apparent splitting cracks between the column reinforcement could be identified. Crushed concrete debris in the region of the 1/2 in.

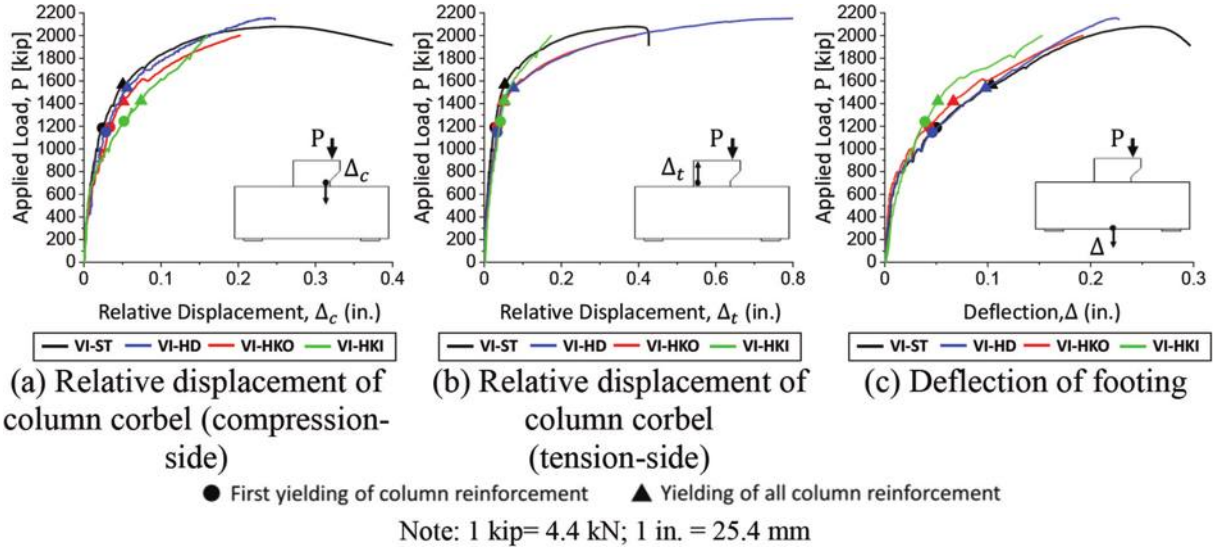

Fig. 11—Load-deflection response of test specimens.

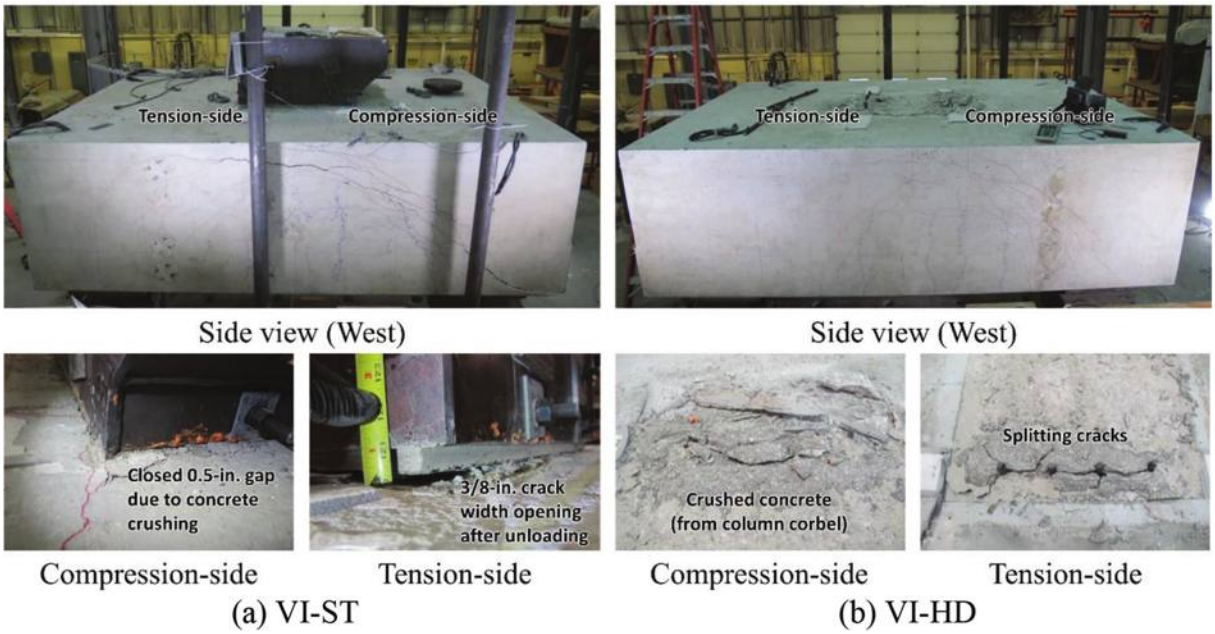

Fig. 12—Post-failure condition of VI-ST and VI-HD.

(13 mm) column gap were found on the compression-side of the interface, but the footing remained largely undamaged.

The test specimens with hooked reinforcement, VI-HKO and VI-HKI, were loaded to 2000 kip (8.9 MN) without failure. The crack patterns developed in the footing components of these specimens were comparable to those formed in VI-ST and VI-HD, as shown in Fig. 13.

All test specimens were dissected orthogonally after testing at a plane crossing the column reinforcement position to inspect interior crack patterns, as shown in Fig. 14. Three crack types were found in the cut sections. The first type (Type I) is a conical crack formed near the top surface of the footing starting from the level of the top mat reinforcement induced by unsustained diagonal struts owing to bond forces. The second and third crack types are splitting cracks formed in the middle region (Type II) and bottom tip of the column reinforcement (Type III) induced by the diagonal struts flowing down from the compression side of the column to the opposed footing support (Struts AC and DF in Fig. 14(a)) and to the bottom end of the column tie element (Struts AB and DE in Fig. 14(b)), respectively. Although the diagonal strut connecting with the footing support (Strut AC and DF in Fig. 14(a)) does not intersect with the column tie element in the 3-D model, the crack induced by the diagonal strut formed over the entire width of the footing (Fig. 15). All noted types of cracking were identified at the cut section of VI-ST and VI-HD. However, the first and second crack types were not identified at the cut sections of VI-HKI and VI-HKO, respectively. Furthermore, the third type of crack passed through the bend radius and the tail of the hook in VI-HKI. In contrast, this type of crack did not cross the column reinforcement in VI-HKO, but passed underneath the bend radius of its hook. This indicates that the hook in VI-HKO was not effective in developing a diagonal strut

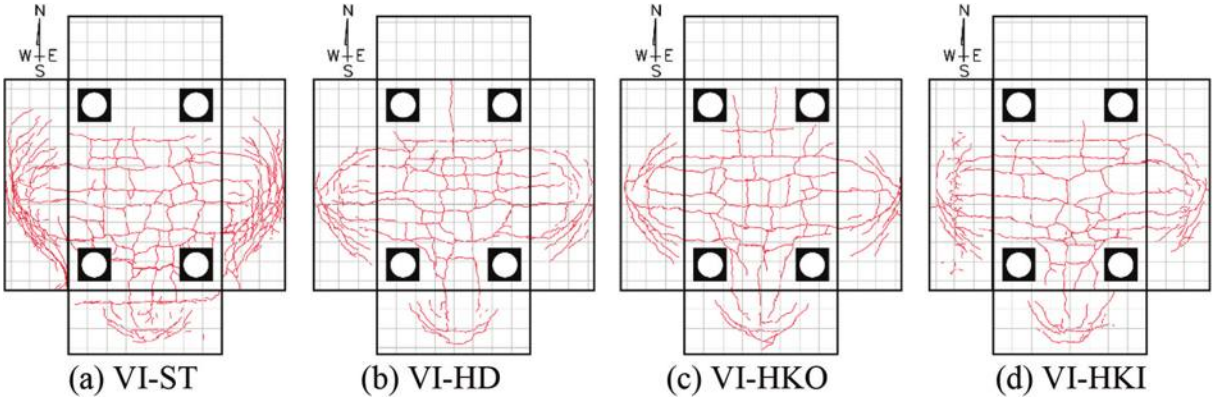

Fig. 13—Crack patterns of test specimens.

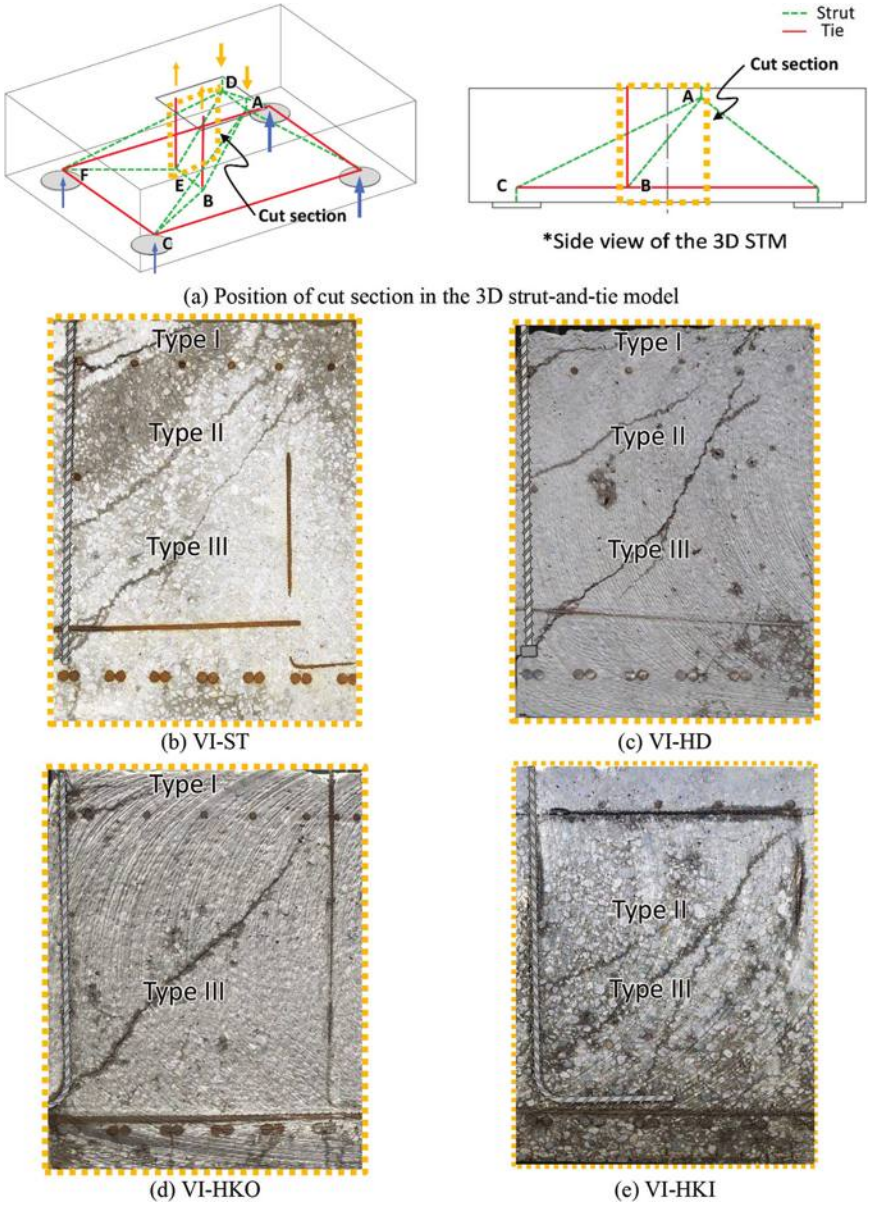

Fig. 14—Cut sections of test specimens.

to anchor the bar, as is further discussed in the "Effects of Anchorage Type" section of this paper.

Stress profiles and bond stress profiles of column reinforcement

The stress profiles of the column reinforcement were derived from strain gauge measurements of the column

Fig. 15—Internal cracks formed across width of specimen VI-ST.

reinforcement combined with stress-strain relationships obtained from steel reinforcing bar tensile tests. Because all vertical column reinforcing bars in the same specimen developed almost identical stress profiles, the stress profile of the column reinforcement positioned at the west-end was selected to compare the anchorage response of the different specimens. The stress profiles are presented in Fig. 16 along with the crack pattern observed in the cut section.

Based on the stress profiles developed, the column reinforcement of VI-ST, VI-HD, and VI-HKI were estimated to develop approximately 85% of their yield strengths within the upper 14 in. (356 mm), or $16d_{b,c}$, of their embedment lengths inside the footing. In contrast, VI-HKO developed its full yield strength within 20 in. (508 mm), or $22.9d_{b,c}$, from the top. The stresses within the lower parts of the anchorage regions increased in all specimens except VI-HKO. Based on the stress profiles presented, the column reinforcement of VI-HKO experienced larger strain levels near the column interface than that of the other specimens. When tensile yielding was identified at the gauge closest to the column interface, the tensile stresses developed at the lowest gauges that were placed immediately above the outer-oriented hook (VI-HKO), the straight bar end (VI-ST), the anchor head (VI-HD), and the inner-oriented hook (VI-HKI) were 0.5 ksi (3 MPa) (0.7% of the yield strength), 5 ksi (34 MPa) (7% of the yield strength), 17 ksi (117 MPa) (24% of the yield strength), and 37 ksi (255 MPa) (48% of the yield strength), respectively. Hence, development of the yield strength was achieved solely by bond along the anchorage length for the straight bar and the outer-oriented hooked bar, while the headed bar and inner-oriented hooked bar developed a significant portion of their resistance from the mechanical bearing action of the head or hook.

Average bond stresses between two consecutive gauges (τ_b) were computed using Eq. (1) and the resulting bond stress profiles are shown in Fig. 16 along with the cracking patterns on the cut section. The computed bond stresses are compared to the maximum local bond strength specified by *fib* Model Code 2010,[19] which corresponds here to the splitting bond strength, $\tau_{bu,split}$

$$\tau_b = \frac{A_s}{d_b \pi}\left(\frac{\Delta f_s}{\Delta l}\right) \quad (1)$$

where A_s is the cross-sectional area of reinforcement to be anchored; d_b is the diameter of reinforcement to be anchored; Δf_s is the change in stress between two consecutive gauges; and Δl is the center-to-center distance between two consecutive gauges.

Apparent from Fig. 16, the peak bond stresses computed near the column interface during the tests were comparable to each other regardless of anchorage type. The maximum computed bond stresses in this region are slightly smaller than the local bond strength, $\tau_{bu,split}$, predicted using *fib* Model Code 2010.[19] Still, it can be argued that the correlation with the analytical estimate of the maximum bond stress is reasonable as the average bond stress profile is not capable of capturing localized peak stresses. The bond stress near the bottom tip of the straight column reinforcement was significantly higher than the other anchorages, resulting from the increased bond resistance provided by confining compressive forces acting on the region. Almost no bond stresses developed near the bottom end of the headed and inner-oriented hooked column reinforcement when the gauge near the column interface exceeded the yield strain (at a load of approximately 1600 kip [7.1 MN]), because the head and hook prevented slip in this region. A slight increase of bond stresses was identified when loading was continued beyond 1600 kip (7.1 MN) for both anchorage types. Lastly, the bond stress near the bottom end of the outer-oriented hook was negligible as no tensile stresses developed in this region.

Strain distribution in bottom mat reinforcement

Figure 17 presents measured strain distributions in the bottom mat reinforcement of the test specimens at the common near-ultimate load level of 2000 kip (8.9 MN). The numbers in the circles of Fig. 17 represent the ratios of measured strains to the yield strain. Regardless of the anchorage type, the bottom mat reinforcement did not yield until 2000 kip (8.9 MN) loading, and the reinforcing bars along the long span (north-south) experienced higher strain than those in the short span (east-west). The strains measured from the bottom mat reinforcing bars placed within the drilled shaft diameter (yellow-shaded region in Fig. 17) were larger than those measured from other reinforcing bars. Overall, the strain measurements presented suggest that the bottom mat reinforcement comprising all test specimens behaved in a similar manner, regardless of anchorage type.

DISCUSSION

Effects of anchorage type

Although all column bars were found to develop their full yield strengths during the tests, different types of anchorage response can be identified from the test results. The diagonal struts flowing down from the interface with the column, towards the drilled shaft support, and the bottom

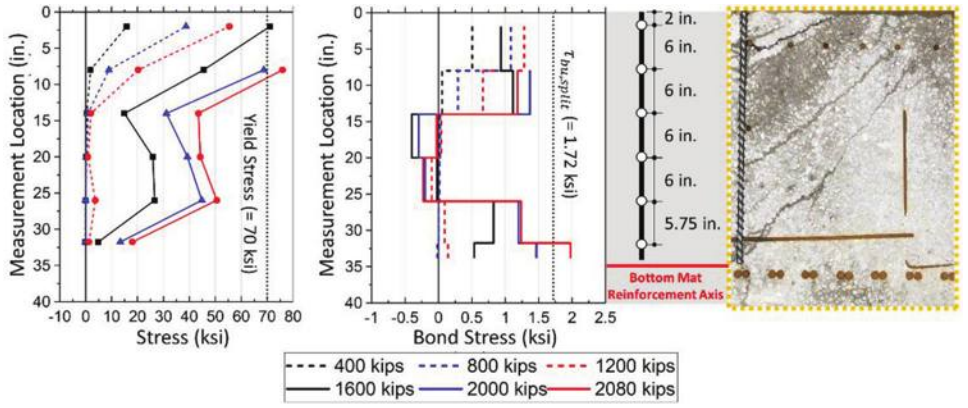

(a) VI-ST

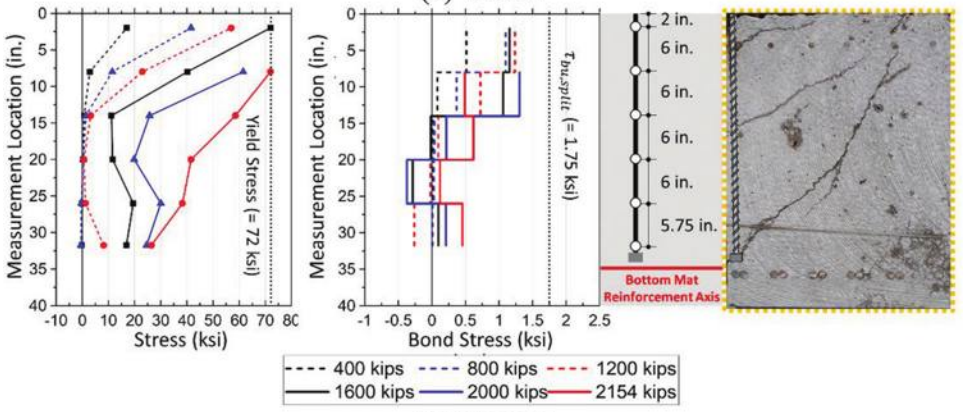

(b) VI-HD

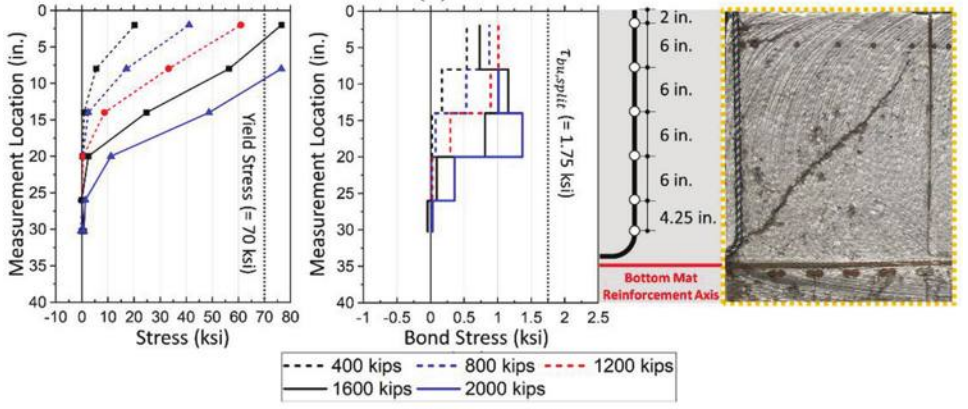

(c) VI-HKO

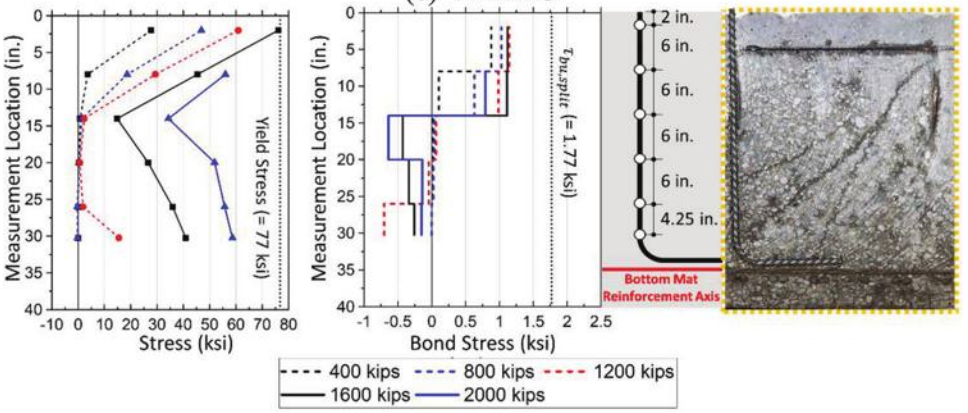

(d) VI-HKI

Note: 1 ksi= 6.9 MPa; 1 in. = 25.4 mm

Fig. 16—Stress and bond stress profiles of column reinforcement.

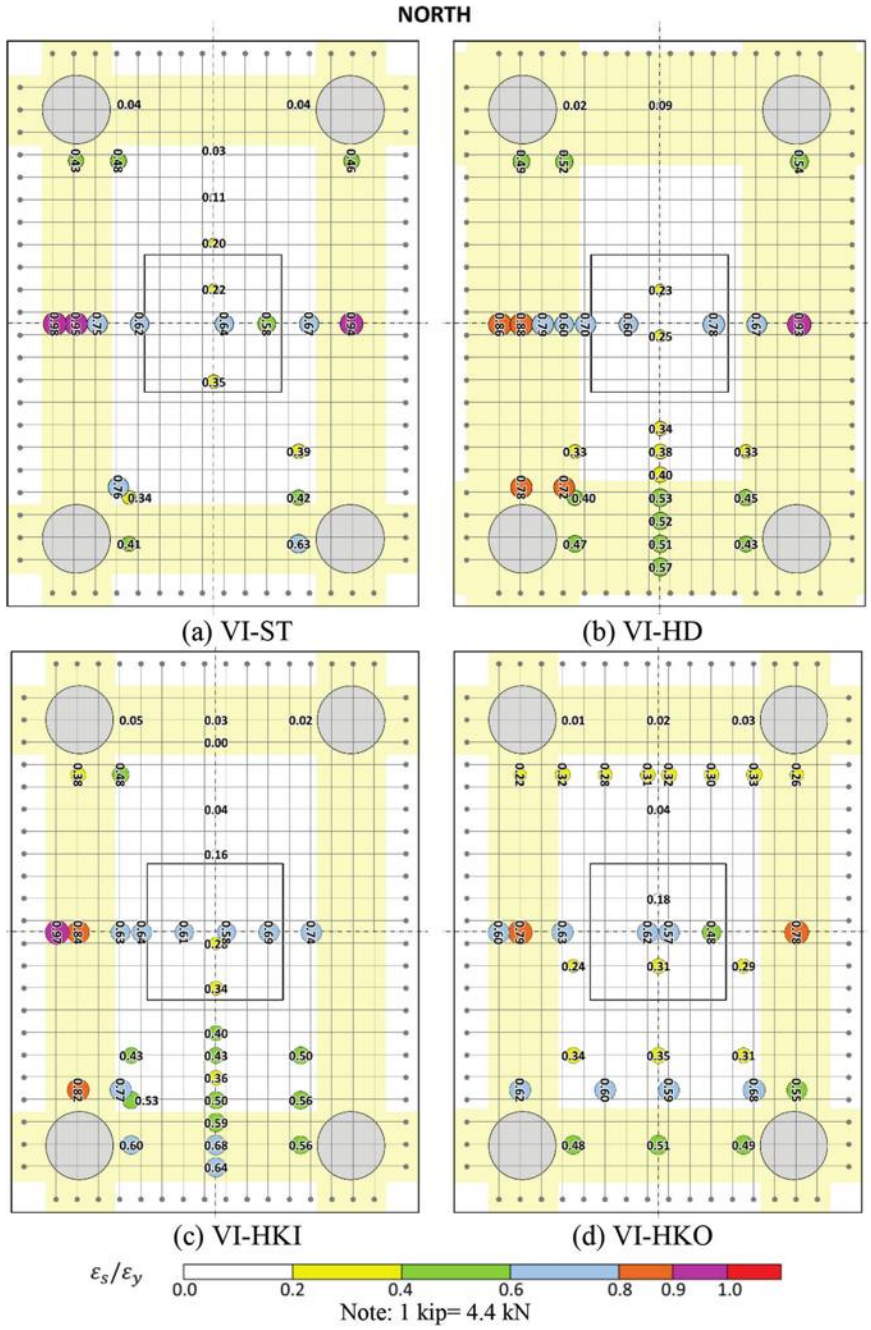

Fig. 17—Strain distribution in bottom mat reinforcement at P *= 2000 kip (8.9 MN).*

end of the column reinforcement induce the reinforcing bar stress increments that were observed in the lower portion of the embedment length in all anchorage types except for the outer-oriented hooked. In the straight bars, tensile bar stresses are developed by way of bond along the anchorage length, with relatively high bond stresses at the lower portion of the anchorage due to confining action of the struts. The inner-oriented hooked bar and headed bar provided a significant bar stress increment near the bottom end of the anchorage owing to the bearing action of the hook or head. The outer-oriented hooked bar did not activate a bearing/mechanical force transfer action because the direction of the bend radius was not oriented towards the diagonal strut flowing down to the bottom end of the column tie element. Instead, the tensile bar stresses for the column bars in VI-HKO are developed through bond within the upper half of the embedment length. Thus, based on the test results obtained, it is evident that hook orientation significantly affects the behavior of the column reinforcement embedded in drilled shaft footings. Although the outer-oriented hooked bar could develop its yield strength near the column interface, the negligible stress development near its bottom end indicates inefficient structural performance of the anchorage detail. In the perspective of the 3-D STM, the outer-oriented hooked reinforcement cannot transfer the diagonal strut forces funneling into the hooks to the vertical column tie. To ensure proper behavior of the hooked column reinforcement, the hook orientation should be oriented inwards to react against the diagonal strut starting at the compression face of the column. This finding is in line with the findings

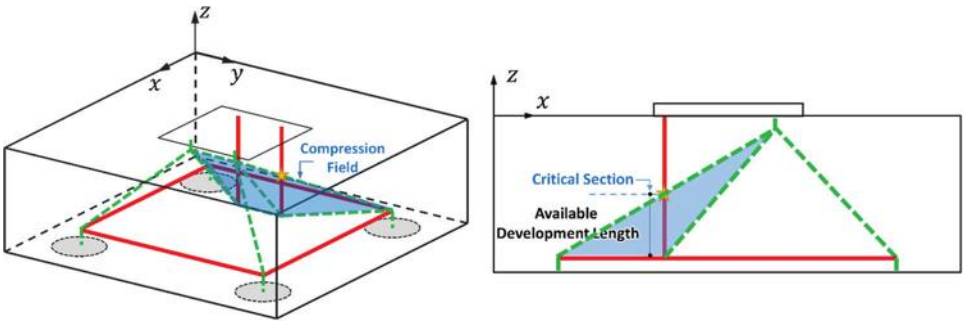

Fig. 18—Compression field formed by diagonal struts and proposed critical section of column reinforcement.

of Nilsson and Losberg[14] on the effect of hook orientation on the seismic behavior of beam-column joints.

It should be noted that the test results presented in this study were obtained from footing specimens with a very large amount of bottom mat reinforcement (0.96%) and relatively light column reinforcement (0.94%). Those amounts were determined to ensure that yielding of column bars would occur, as mentioned in a previous section. Actual footing designs will have less bottom mat reinforcement and may anchor larger amounts of column reinforcement. Nevertheless, such differences are not expected to influence the fundamental anchorage response of the column bars observed in these tests. If the reinforcement in the drilled shaft footing is properly designed using the STM, smaller amounts of bottom mat reinforcement should not hinder the anchorage capacity of the column bars. Larger amounts of column reinforcement will imply using larger bars and/or smaller bar separations, and its influence in the anchorage detail will be reflected in an increase of the required development length.

Critical section for anchorage length verification

This study identified that significant reinforcing bar tensile stress increments can be achieved throughout the embedment region of column reinforcement in properly anchored bars. Bar stresses are induced by the diagonal compressive field flowing down from the compression side of the column to the opposite support of the footing (idealized as a strut in Fig. 14(a)), which crosses the column vertical tie. Further, the widespread compression field is responsible for the diagonal cracks observed in Fig. 14(b) through (e) and can also be identified from the bottom mat reinforcing bar stress distribution (Fig. 17) which were developed over the entire width of the footing. Therefore, this study defines a large compression field influencing the embedded column reinforcement by assuming the field is bounded by idealized struts (Struts AB, AC, DE, and DF in Fig. 14(a)), as shown in Fig. 18. The large compression field performs the same role as an extended nodal zone even though the diagonal strut flowing down to the drilled shaft does not intersect the column tie element. Based on the defined compression field, the critical section of the column reinforcement can be defined in a simple way as the intersection of the diagonal struts and the column ties in the 3-D STM viewed from its side view, as illustrated in Fig. 18. As opposed to previous recommendations,[10-12] the proposed definition of the critical section allows consideration of bond forces along the development length of the column bars. Still, this criterion is conservative because it neglects the contribution of the observed bond stresses developing in the upper part of the embedment region.

The available lengths of the column reinforcement measured from the proposed critical section are compared with the minimum development lengths required for the different anchorage types in accordance with both ACI 318-19[1] and AASHTO LRFD[2] and summarized in Table 5. To determine the inclination of the struts, the nodal positions of the 3-D STM were determined based on the recommendations proposed by Williams et al.[12] The available length measured for the straight column reinforcement is shorter than the minimum development lengths computed from the provisions. Nevertheless, the straight column reinforcement was shown to yield during testing; therefore, arguably validates the proposed critical section.

Detailing recommendations for 90-degree hooked column reinforcement

Column reinforcement anchorage type can be determined from an anchorage check employing the proposed critical section. For drilled shaft footings designed with the 3-D STM, the results from this study would suggest that any anchorage type can be used if the available length satisfies the minimum development lengths required for the anchorage type. Nevertheless, it is envisioned that 90-degree hooked bars will be more generally employed in actual footing construction rather than straight or headed bars due to their ease of placement in the field.

Figure 19 presents different detailing options for the anchorage of hooked column reinforcement. Based on the test results, the detailing of the column reinforcement designed with 90-degree hooks needs to be determined from the internal force flow of drilled shaft footings. Considering constructability, hooked column reinforcement oriented outwards to the column is the conventional detailing practice for drilled shaft footings in construction projects. Although this detail can develop the yield strength of the bar if sufficient embedment length is provided, the experimental results of this study showed that its structural performance is inferior to that of inner-oriented hooked bars and even straight column reinforcement because the outward-oriented hook cannot activate any bearing action at its anchorage. The best structural performance would be obtained by placing all hook orientations inward to the column, but this detail can cause extreme congestion of the reinforcement at the

Table 5—Anchorage check based on proposed critical section

		Specimen ID			
		VI-ST	VI-HD	VI-HKO	VI-HKI
Anchorage types		Straight	Headed	Hooked (Orientation: outward)	Hooked (Orientation: inward)
Available length (l_a), in.		18.0			
AASHTO LRFD (2020)	Minimum development length (l_d), in.	27.5	N/A*	7.0	7.4
	l_a/l_d	0.65		2.57	2.43
ACI 318-19	Minimum development length (l_d), in.	27.5	7.0	13.8	15.0
	l_a/l_d	0.65	2.57	1.30	1.20

*Minimum development length for headed bars is not specified in AASHTO LRFD[2]; N/A is not available.

Note: 1 in. = 25.4 mm.

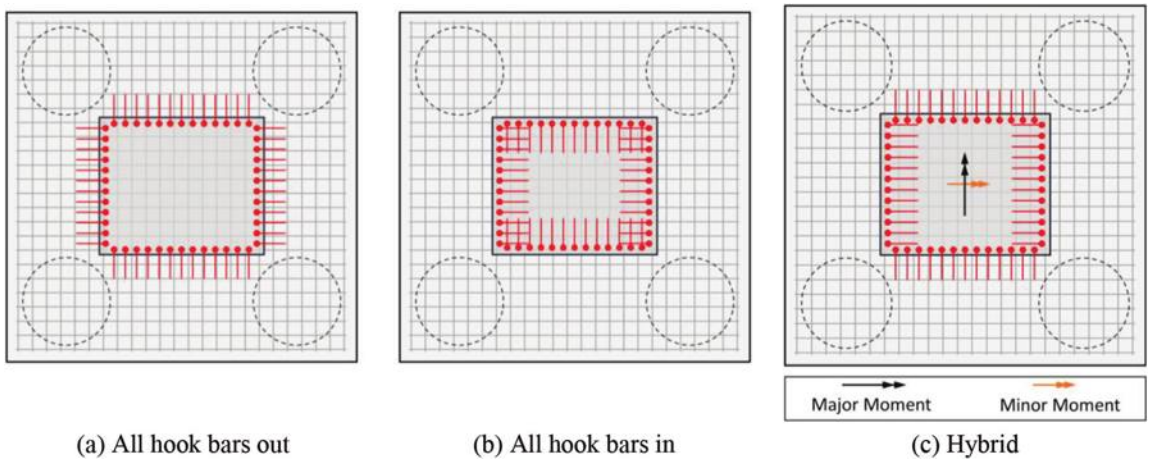

Fig. 19—Anchorage detailing options of 90-degree hooked column reinforcement in drilled shaft footings.

anchorage region of the column corners. Therefore, this study proposes a hybrid detailing for 90-degree hooked bars to achieve optimized structural performance and constructability by providing inner-oriented and outer-oriented hooked column reinforcement against the major and minor flexural moment, respectively. Nevertheless, actual footings are designed considering various loading cases which may not satisfy that the major flexural moment occurs always in the same direction. For those cases, the performance of the hybrid detail and potential weakening effect of outer-oriented hooked bars should be further investigated.

CONCLUSIONS

This paper investigated various anchorage details for vertical column reinforcement embedded in drilled shaft footings subjected to combined axial force and moderate uniaxial bending moment. Four drilled shaft footing specimens, employing four different column reinforcement anchorage details (straight, headed, inner-oriented 90-degree hooked, and outer-oriented 90-degree hooked), were fabricated and tested under eccentric vertical loads. The specimens were loaded beyond tension yielding of the column reinforcement.

The primary findings and conclusions obtained from large-scale testing are as follows:

1. All column bars were able to develop their full yield strength regardless of the anchorage type. However, column reinforcement force transfer actions were found to be dependent on the anchorage details provided at the ends of the column reinforcing bars.

2. Experimentally obtained stress profiles of the column bars and the sectional crack patterns from specimen cuts indicate that the diagonal struts flowing down to the drilled shaft and the bottom end of the column reinforcement induce significant tensile stresses in the vicinity of the bottom end of the column reinforcement for all anchorage types except for the outer-oriented hooked anchor, which are commonly employed anchorage details for drilled shaft footings.

3. The inner-oriented hooked bars and headed bars relied, to a large extent, on the bearing action of the hook or head to develop tensile yield capacity, whereas the straight and outer-oriented hooked bars developed their capacities solely through bond.

4. The outer-oriented hooked bar could not activate its bearing action in the hook because no stresses were developed near the hook end. This resulted in a relatively high-stress level developing in the central and upper portions of the embedment region.

5. Based on test results, a simple criterion is proposed to determine the critical section of the column reinforcement for a three-dimensional (3-D) strut-and-tie model (STM). The large compression field formed by the idealized diagonal struts in the base of the column can be considered to

perform the same role as an extended nodal zone for establishing the critical section of column tie elements.

Alternative column reinforcement detailing strategies can be employed to optimize reinforcement anchorage and constructability when 90-degree hooked column bars are employed. The proposed definition of the critical section for the column bars is simple, consistent with the current 3-D STMs in code provisions and provides a conservative estimation of the available development length of the bars according to the test results. Therefore, follow-up studies conducted with various design parameters (for example, footing geometry, column reinforcement size, and area) that can influence the behavior of the column reinforcement or cracking position due to the diagonal strut can solidify the proposal of this study.

AUTHOR BIOS

Yousun Yi *is a Postdoctoral Fellow in the Ferguson Structural Engineering Laboratory at The University of Texas at Austin, Austin, TX, where he received his PhD in civil engineering in 2022. His research interests include the strut-and-tie method and nonlinear analysis of reinforced concrete structures.*

Hyunsu Kim *is a Structural Specialist at COWI North America Inc. He received his BS and MS from Seoul National University, Seoul, South Korea, in 2008 and 2010, respectively; and his PhD from The University of Texas at Austin in 2022. His research interests include the refinement of the strut-and-tie method for drilled shaft footings and numerical analysis of concrete structures.*

Ryan A. Boehm *is a Project Engineer at Datum Engineers, Inc., Dallas, TX. She received her BS and MS from The University of Texas at Austin.*

Zachary D. Webb *is a Research Engineer at the Ferguson Structural Engineering Laboratory. He received his BS and MS in civil engineering from The University of Texas at Austin in 2007 and 2011, respectively. His research interests include the behavior and design of conventionally reinforced and prestressed concrete structures.*

ACI member **Jongkwon Choi** *is an Assistant Professor in the Department of Civil and Environmental Engineering at Hongik University, Seoul, South Korea. He received his BS and MS from Seoul National University and his PhD from The University of Texas at Austin. His research interests include the mechanical behavior, experiments, and analysis of reinforced concrete and prestressed concrete structures and structural assessment of aging concrete structures.*

ACI member **Juan Murcia-Delso** *is an Assistant Professor in the Department of Civil and Environmental Engineering at Universitat Politècnica de Catalunya - BarcelonaTech (UPC), Barcelona, Spain. He received his BS and MS from UPC, and his PhD from the University of California, San Diego, La Jolla, CA. He is a member of Joint ACI-ASCE Committee 408, Bond and Development of Steel Reinforcement. His research interests include the nonlinear behavior, design, and assessment of concrete structures.*

ACI member **Trevor D. Hrynyk** *is an Assistant Professor in the Department of Civil and Environmental Engineering at the University of Waterloo, Waterloo, ON, Canada. He is a member of Joint ACI-ASCE Committees 447, Finite Element Analysis of Reinforced Concrete Structures; 421, Design of Reinforced Concrete Slabs; and 445, Shear & Torsion. His research interests include nonlinear analysis of reinforced concrete structures, response under extreme loads, damage assessment, and finite element modeling.*

Oguzhan Bayrak, *FACI, is a University Distinguished Teaching Professor and Phil M. Ferguson Professor in the Department of Civil, Architectural, and Environmental Engineering at The University of Texas at Austin. He is a member of ACI Committees 341, Earthquake-Resistant Concrete Bridges, and E803, Faculty Network Coordinating Committee; and Joint ACI-ASCE Committees 441, Reinforced Concrete Columns, and 445, Shear and Torsion.*

ACKNOWLEDGMENTS

The authors wish to express their gratitude and sincere appreciation to the Texas Department of Transportation (TxDOT) for funding this study through Project 0-6953. The findings and suggestions reported in this paper are those of the authors and do not necessarily reflect the perspectives of TxDOT.

REFERENCES

1. ACI Committee 318, "Building Code Requirements for Structural Concrete (ACI 318-19) Commentary on Building Code Requirements for Structural Concrete (ACI 318R-19)," American Concrete Institute, Farmington Hills, MI, 2019, 628 pp.

2. AASHTO, "AASHTO LRFD Bridge Design Specifications," ninth edition, American Association of State Highway and Transportation Officials, Washington, DC, 2020, 1912 pp.

3. Sabnis, G. M., and Gogate, A. B., "Investigation of Thick Slab (Pile Cap) Behavior," *ACI Journal Proceedings*, V. 81, No. 1, Jan.-Feb. 1984, pp. 35-39.

4. Suzuki, K.; Otsuki, K.; and Tsubata, T., "Influence of Bar Arrangement on Ultimate Strength of Four-Pile Caps," *Transactions of the Japan Concrete Institute*, V. 20, 1998, pp. 195-202.

5. Suzuki, K.; Otsuki, K.; and Tsubata, T., "Experimental Study on Four-Pile Caps with Taper," *Transactions of the Japan Concrete Institute*, V. 21, 1999, pp. 327-334.

6. Suzuki, K.; Otsuki, K.; and Tsuchiya, T., "Influence of Edge Distance on Failure Mechanism of Pile Caps," *Transactions of the Japan Concrete Institute*, V. 22, 2000, pp. 361-367.

7. Suzuki, K., and Otsuki, K., "Experimental Study on Corner Shear Failure of Pile Caps," *Transactions of the Japan Concrete Institute*, V. 23, 2002, pp. 303-310.

8. Clarke, J. L., "Behaviour and Design of Pile Caps with Four Piles," Technical Report No. 42.489, Cement and Concrete Association, Waxham Spring, UK, 1973, 19 pp.

9. Miguel-Tortola, L.; Miguel, P. F.; and Pallarés, L., "Strength of Pile Caps under Eccentric Loads: Experimental Study and Review of Code Provisions," *Engineering Structures*, V. 182, 2019, pp. 251-267. doi: 10.1016/j.engstruct.2018.12.064

10. Klein, G. J., "Example 9: Pile Cap," *Examples for the Design of Structural Concrete with Strut-and-Tie Models*, SP-208, K. Reineck, ed., American Concrete Institute, Farmington Hills, MI, 2002, pp. 213-223.

11. Widianto, and Bayrak, O., "Example 11: Deep Pile Cap with Tension Piles," *Further Examples for the Design of Structural Concrete with Strut-and-Tie Models*, SP-273, K. Reineck and L. C. Novak, ed., American Concrete Institute, Farmington Hills, MI, 2011, pp. 169-190.

12. Williams, C.; Deschenes, D.; and Bayrak, O., "Strut-and-Tie Model Design Examples for Bridges," Report No. FHWA/TX-12/5-5253-01-1, Center for Transportation Research, The University of Texas at Austin, Austin, TX, 2012, 276 pp.

13. Yi, Y.; Kim, H.; Boehm, R. A.; Webb, Z. D.; Choi, J.; Wang, H.; Murcia-Delso, J.; Hrynyk, T. D.; and Bayrak, O., "3D Strut-and-Tie Modeling for Design of Drilled Shaft Footings," Report No. FHWA/TX-21/0-6953-R1, Center for Transportation Research, The University of Texas at Austin, Austin, TX, 2021, 466 pp.

14. Nilsson, I. H., and Losberg, A., "Reinforced Concrete Corners and Joints Subjected to Bending Moment," *Journal of the Structural Division*, ASCE, V. 102, No. 6, 1976, pp. 1229-1254. doi: 10.1061/JSDEAG.0004362

15. ASTM A706/A706M-16, "Standard Specification for Deformed and Plain Carbon-Steel Bars for Concrete Reinforcement," ASTM International, West Conshohocken, PA, 2016, 7 pp.

16. ASTM A615/A615M-20, "Standard Specification for Deformed and Plain Carbon-Steel Bars for Concrete Reinforcement," ASTM International, West Conshohocken, PA, 2020, 8 pp.

17. ASTM C39/C39M-21, "Standard Test Method for Compressive Strength of Cylindrical Concrete Specimens," ASTM International, West Conshohocken, PA, 2021, 8 pp.

18. ASTM A370-21, "Standard Test Methods and Definitions for Mechanical Testing of Steel Products," ASTM International, West Conshohocken, PA, 2021, 50 pp.

19. *fib*, "*fib* Model Code for Concrete Structures 2010," Wilhelm Ernst & Sohn, Germany, 2013, 434 pp.

ACI STRUCTURAL JOURNAL TECHNICAL PAPER

Title No. 120-S76

Behavior of NiTi Shape Memory Alloy- and Steel-Reinforced Shear Walls Repaired with Engineered Cementitious Composite

by Michael A. Soto-Rojas, Anca C. Ferche, and Dan Palermo

This paper presents the results of an experimental study investigating the response of two shear walls repaired with engineered cementitious composite (ECC). One of the walls was reinforced in the boundary regions within the plastic hinge with superelastic, nickel-titanium (NiTi) shape memory alloy (SMA) bars, while the companion wall was reinforced with deformed mild steel bars only. The repair method involved the removal of the heavily damaged concrete in the plastic hinge zone, replacement of ruptured and buckled steel reinforcement, placement of starter bars at the base of the walls, and casting of ECC to replace the removed concrete. The SMA bars were reused as they sustained no damage from the initial testing. Summarized in this paper are an assessment of the performance of the repaired walls and a comparison with the responses of the walls previously tested in their original condition. The experimental program highlights the enhanced performance of the composite system that integrates the self-centering capabilities of SMA bars and the distinctive tension strain hardening and ductility of ECC. The lateral strength was markedly increased, while the energy dissipation and recovery capacities, in general, were improved for the repaired walls compared to the original walls. The repaired steel-reinforced wall developed a peak lateral strength of 23% larger compared to the original wall, while the repaired SMA-reinforced wall had a 16% increase in peak lateral strength compared to the original specimen. The strength enhancement of the repaired walls led to higher dissipated energy throughout testing. For both sets of walls, the SMA-reinforced walls exhibited larger rotations compared to the steel-reinforced walls primarily on account of the lower stiffness of the SMA bars.

Keywords: energy dissipation; engineered cementitious composite (ECC); nickel-titanium (NiTi); recovery capacity; reinforced concrete; repair; shape memory alloys (SMAs); shear walls.

INTRODUCTION

Reinforced concrete structures designated as normal importance are designed to behave in the inelastic range during rare events such as high seismic loading, the primary objective being safeguarding against collapse and ensuring life safety. This is achieved through the design of plastic hinge regions that are controlled by the yielding of the reinforcement, resulting in significant residual deformations and damage.[1-3] Structures built in the major cities of Chile were designed based on relatively current codes,[4] and they experienced severe permanent damage during the 2010 earthquake.[5] A similar scenario occurred in Christchurch, New Zealand, during the 2011 earthquake.[6] This resulted in compromised, post-earthquake infrastructure in terms of structural integrity and functionality, leading to significant economic deficits.

The owners of structures damaged during design-level seismic events typically have two alternatives: demolition and replacement; or repair to recover the strength, stiffness, and ductility of the structure. The first alternative is highly disruptive and expensive, impacting the affected community for a significant period. The second alternative has the potential to be more desirable when the extent of damage is limited, and the repair operations are feasible and can be executed in a reasonable time frame.

Ductility capacity and energy dissipation are two primary characteristics well-designed reinforced concrete structures are expected to exhibit. In addition, ease of repair after rare loading events is preferable from a reliability perspective. The implementation of innovative materials such as shape memory alloy (SMA) bars and engineered cementitious composite (ECC) materials provide an opportunity to improve the post-earthquake state of structures while achieving the primary design objectives of preventing collapse and safeguarding against loss of life. By limiting the post-earthquake residual damage, demolition may be avoided, and repairs for a relatively immediate occupancy become possible. The combination of these two materials leads to self-centering behavior with improved damage tolerance.

Applications of SMAs in structural systems have received increased research focus during the past decade as a viable option to design resilient structures. The recentering ability of SMAs makes them attractive for structures expected to experience large deformations. SMAs dissipate energy through hysteretic damping and can reach strengths comparable to mild steel reinforcing bars. Disadvantages of SMA bars include high initial cost, smooth surface, low elastic modulus, and the need for couplers to connect with conventional bars. The most common type of SMA studied for structural applications, which was also used for this experimental program, is a nickel-titanium (NiTi) alloy consisting of approximately 56% nickel and 44% titanium. ECC materials are a special class of high-performance fiber-reinforced cement composites and consist typically of a mortar base

ACI Structural Journal, V. 120, No. 4, July 2023.
MS No. S-2022-238.R2, doi: 10.14359/51738745, received January 9, 2023, and reviewed under Institute publication policies.

matrix comprising sand, silica fume, cement, fly ash, and up to a 2% volumetric fraction of polyvinyl alcohol (PVA) fibers.[7,8] The tensile capacity varies between 4 and 6 MPa, and the response exhibits high ductility.

Experimental investigations on the use of SMA bars in concrete elements for new design and for the repair of concrete elements are limited and consist of applications for columns, beam-columns joints, beams, and shear walls.[9-17] Abdulridha and Palermo[9] and Morcos and Palermo[10,11] illustrated that substituting deformed longitudinal reinforcement with SMA bars in the boundary regions within the plastic hinge of a slender shear wall results in greater recentering capacity and reduced residual displacements. Cortés-Puentes et al.[12] repaired a previously tested SMA-reinforced shear wall by replacing the damaged reinforcing bars within the plastic hinge region with new segments and the damaged concrete with self-consolidating concrete (SCC). The response of the repaired wall under cyclic loading was comparable to its response in the original state in terms of strength, stiffness, and cracking pattern. Saiidi et al.[13] demonstrated substantial benefits such as self-centering and improved damage tolerance when using a combination of SMA longitudinal bars and ECC in the plastic hinge region of a column.

RESEARCH SIGNIFICANCE

The experimental study presented herein focused on the structural behavior of a composite system that integrates NiTi SMA, mild steel bars, and ECC to enhance the performance of a shear wall subjected to reversed cyclic loading. The investigation studied the applicability of ECC as part of a repair method for heavily damaged SMA- and steel-reinforced concrete shear walls that were previously tested. This study highlights the benefits of implementing ECC concrete and SMA reinforcement to enhance the post-repair behavior under simulated seismic loading by reducing the permanent deformation and damage typically experienced by shear walls. To the best of the authors' knowledge, this is the first study to test a hybrid SMA-steel-reinforced shear wall repaired with ECC. The results of this study will be of general interest to practicing structural engineers and standards committees, with the goal of accelerating the acceptance of high-performance design concepts and repair strategies incorporating NiTi SMA bars and ECC.

EXPERIMENTAL PROGRAM

The shear walls investigated in this study were previously tested by Morcos and Palermo[10] under a reversed cyclic lateral loading protocol. The experimental program undertaken by Morcos and Palermo[10] focused on characterizing the behavioral response and the self-centering capacity of a hybrid NiTi SMA-steel-reinforced shear wall compared to a steel-reinforced wall. The original wall identifiers were SWS-R for the steel-reinforced wall and SWN for the hybrid NiTi SMA-reinforced wall. The first two letters "SW" represent the structural element type (shear wall), followed by "S" to denote the steel wall with local repairs "-R." The "N" identifier following "SW" represents the hybrid NiTi SMA-steel-reinforced wall. The base of the original steel wall, SWS-R, experienced honeycombing regions that were locally repaired with SCC. After testing the original walls by Morcos and Palermo,[10] both walls were repaired and renamed RSWS-R and RSWN to differentiate between the original and repaired walls.

Original walls

Wall details—The original walls were designed based on the seismic provisions for ductile walls prescribed by CAN/CSA A23.3-04,[10,18] respecting the reinforcement limits specified by the design standard. (Note that the original walls were similar to the walls reported by Abdulridha and Palermo,[9] which were designed and constructed based on the requirements for ductile walls in CAN/CSA A23.3-04, the design standard that was current at the time.) The design of the SMA wall was similar to the steel-reinforced wall as no code provisions exist for SMA-reinforced structural components. The walls had identical nominal dimensions, the major difference consisting of the longitudinal reinforcement in the boundary zones. The walls had a rectangular cross section, an aspect ratio (height-to-length ratio) of 2.2, and were 2200 mm in height, 1000 mm in length, and 150 mm in thickness. This aspect ratio was selected to promote flexural-dominant behavior. The walls were cast above foundation beams that were 1600 mm long, 500 mm high, and 1000 mm wide, which facilitated the anchorage of the walls to the strong floor of the laboratory. Additionally, loading beams 1600 mm long, 400 mm high, and 400 mm wide were monolithically cast with the walls to distribute the applied lateral loading.

Within the web region, the walls contained two layers of 10M bars (11.3 mm diameter, 100 mm^2 area) spaced at 150 mm in both the vertical and horizontal directions. The boundary zones were reinforced with four vertical bars confined by 10M closed stirrups spaced at 75 mm within the plastic hinge region and 150 mm above it. The vertical reinforcing bars in the boundary zones of SWS-R consisted of continuous 10M bars. The boundary zones of SWN contained 12.7 mm diameter smooth SMA bars in the plastic hinge region, connected through mechanical couplers with No. 13 (12.7 mm diameter, 129 mm^2 area) bars extending above the plastic hinge region. The reinforcement details of Wall SWN are shown in Fig. 1. The SMA bars extended 900 mm within the plastic hinge region and 300 mm into the foundation beam. A noninvasive method of mechanical coupling, based on forging the bar ends and using threaded couplers, was employed to connect the SMA bars to the deformed No. 13 reinforcement. Additional details on the design and fabrication of the original walls can be found elsewhere.[10,19]

Damage characteristics—The original walls were tested under reversed cyclic lateral loading following a protocol established by FEMA 461[20] and ATC-24,[21] which consisted of applying increasing lateral displacements until failure. Wall SWS-R sustained a peak load of 125 kN at 23 mm lateral displacement in the positive direction of loading, and SWN reached a peak load of 121 kN at 98 mm lateral displacement in the negative direction of loading.

For both walls, the first cracks propagated along the base at a lateral displacement of 1.2 mm. For SWS-R, subsequent

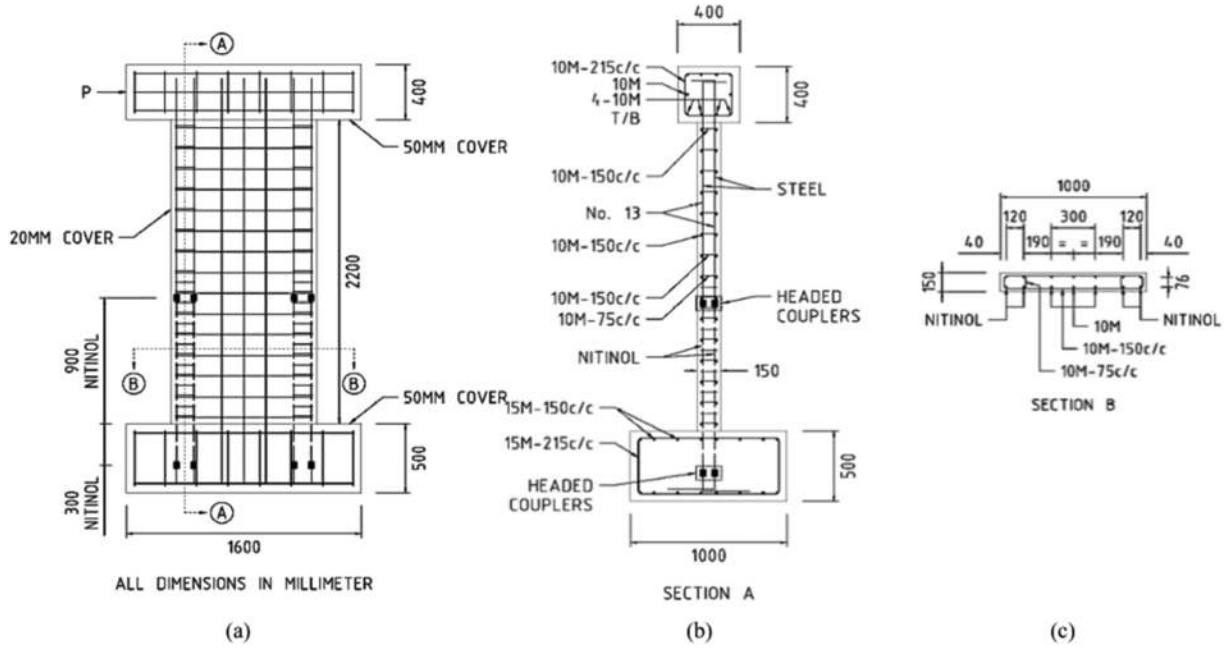

Fig. 1—Nominal dimensions and reinforcement details for Wall SWN: (a) elevation view; (b) section A-A; and (c) section B-B. (Taken from Morcos.[19])

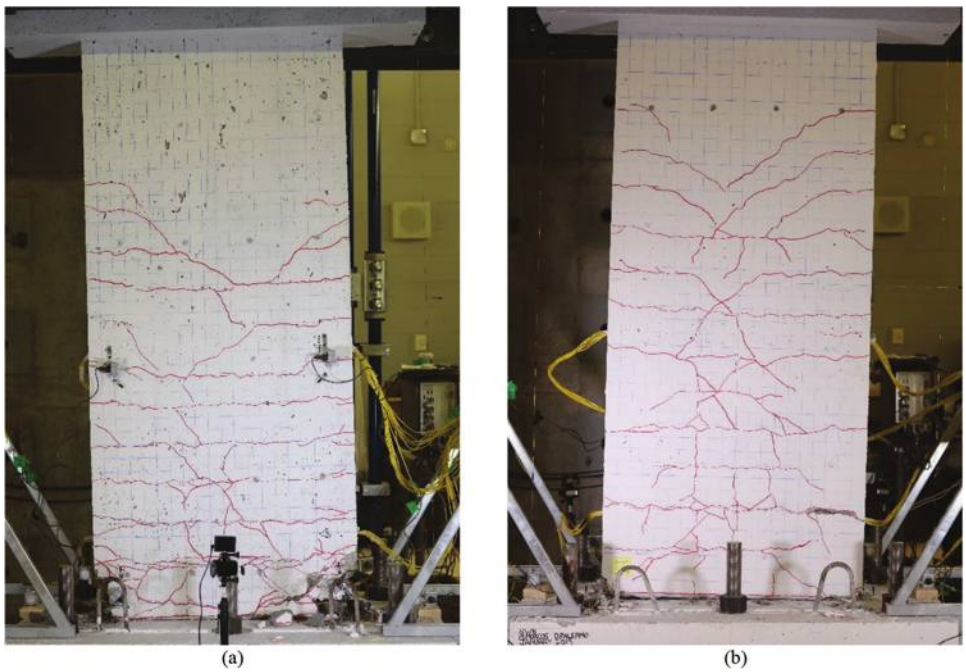

Fig. 2—Conditions of original walls after testing: (a) SWS-R; and (b) SWN. (Taken from Morcos.[19])

loading cycles led to the development of additional flexural cracks that propagated across the length of the wall and were spaced at approximately 150 mm over the height of the plastic hinge zone, as shown in Fig. 2(a). Additionally, flexural-shear cracks inclined at approximately 45 degrees developed. Crushing and spalling of concrete were pronounced around the toe regions of the wall. The loading cycles at an imposed lateral displacement of 72 mm led to the fracture of multiple vertical reinforcing bars in the boundary zones. Two bars fractured during the first positive excursion near the outer face, followed by the fracture of the two opposite bars during the negative excursion. The second positive cycle resulted in the fracture of the second row of reinforcing bars in the boundary zone, which concluded the test.

Wall SWN developed a crack pattern that was noticeably different compared to SWS-R, as shown in Fig. 2(b). One dissimilarity pertains to the propagation of flexural cracks, some of which did not extend over the entire length of the wall and remained confined to the web region. The spacing of the cracks within the web region was similar to that observed for SWS-R. Within the boundary zones, however, over the height of the plastic hinge region, the crack spacing was approximately twice the distance, approximately 300 mm. Additionally, three vertical cracks developed in the web, aligned with

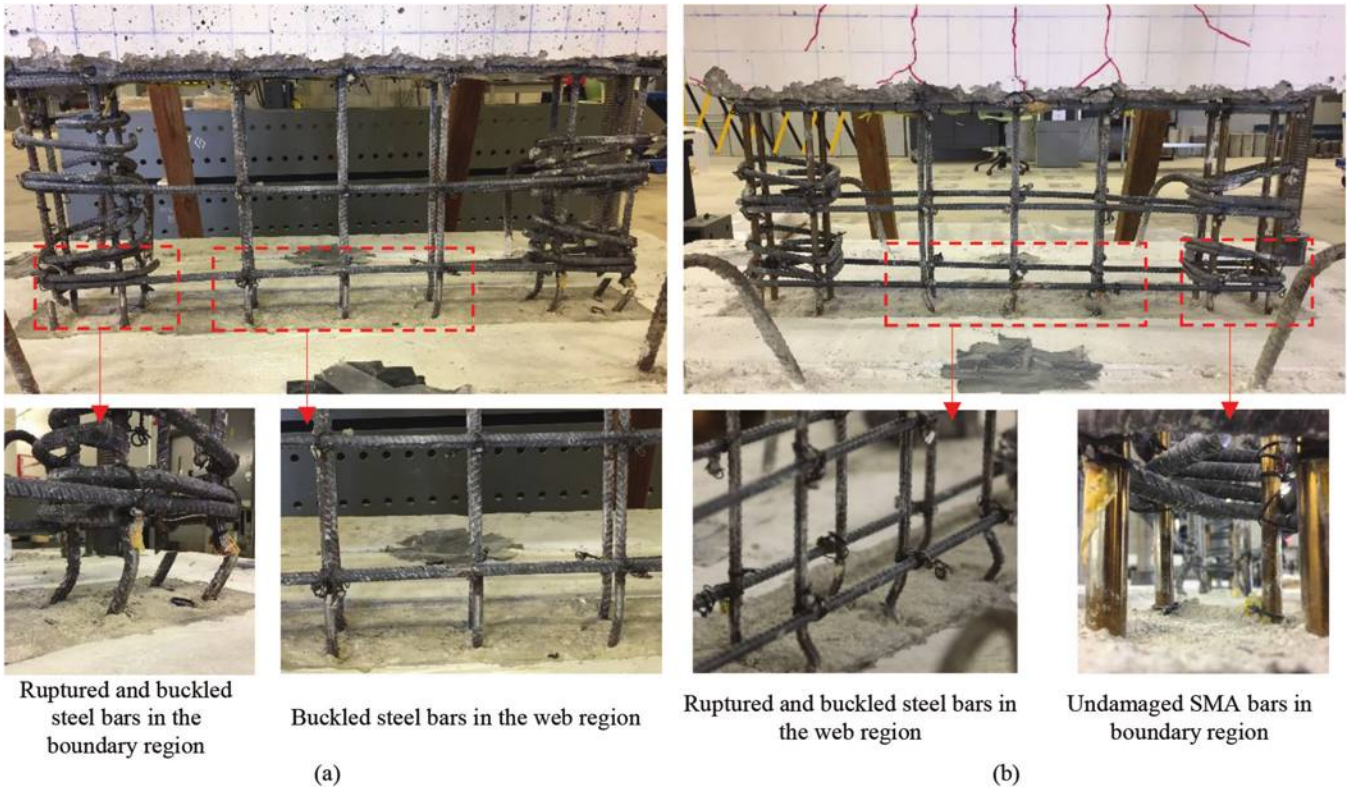

Fig. 3—First stage of concrete removal and damage of reinforcing bars: (a) SWS-R; and (b) SWN.

the position of the vertical reinforcing bars. As the loading progressed, one flexural crack along the base and another at 300 mm above the base became dominant, developing significantly larger widths compared to the rest of the cracks. Flexural-shear cracks also developed, extending up to 1900 mm from the base, approximately 300 mm higher compared to Wall SWS-R. At a lateral displacement of 72 mm, rocking of the wall about the dominant flexural crack along the base was pronounced. Crushing of concrete in the toe regions was observed, albeit not as severe as SWS-R. The vertical bars in the web, closest to the boundary region, ruptured during the first negative excursion at 108 mm displacement. The web reinforcing bars placed along the centerline of the wall ruptured during the first imposed lateral displacement of 120 mm in the negative direction. The second positive excursion at 120 mm resulted in the rupture of the web reinforcement closest to the left boundary zone; this led to the termination of the test. No damage was observed in the SMA bars.

Both walls developed similar strength capacities; their overall responses, however, were marked by several significant differences. Compared to SWS-R, Wall SWN had a lower yield secant stiffness owing primarily to the lower stiffness of the SMA bars relative to the steel bars. Additionally, the smooth surface of the SMA bars led to the development of wider flexural cracks and larger crack spacing in Wall SWN in comparison with Wall SWS-R. The failure mechanism experienced by Wall SWN was characterized by a markedly reduced degree of damage in terms of sliding of the base, concrete crushing, and distribution of cracking. Furthermore, the SMA bars in Wall SWN suffered no damage, remaining functional, while the steel bars in the boundary zones of SWS-R buckled and fractured. Further details on the performance of the original set of walls are available elsewhere (Morcos and Palermo[10] and Morcos[19]).

Repair procedure

The repair procedure consisted of the construction of a bracing system for the walls to facilitate the safe and complete removal of damaged concrete from the plastic hinge region, replacement and addition of steel reinforcing bars, construction of formwork, and casting of the ECC mixture. Damage above the plastic hinge region, specifically concrete cracking, was not remediated in the repair strategy.

Concrete removal—Concrete removal was performed in three stages that allowed for a progressive investigation of the extent of the damage. The initial stage consisted of removing concrete over a height of 300 mm, as shown in Fig. 3, which revealed extensive damage experienced by the steel reinforcement in the form of buckling and fracture, and no observable damage for the SMA bars. The second stage involved removing concrete from the boundary regions over the entire plastic hinge length (900 mm in height from the base). No additional damage to the reinforcing bars was observed over this length for either of the walls. In addition, the coupling mechanism that connected the SMA bars to the No. 13 bars had no visible damage. During the third and final stage, the concrete was removed from the entire plastic hinge region and over a depth of approximately 60 mm into the foundation beam, as shown in Fig. 4. The concrete removal from the foundation was necessary to provide sufficient height to couple the remaining existing bars with the replacement segments, and for the repair ECC to penetrate the foundation to form a shear key.

Fig. 4—Final stage of concrete removal: (a) SWS-R; and (b) SWN.

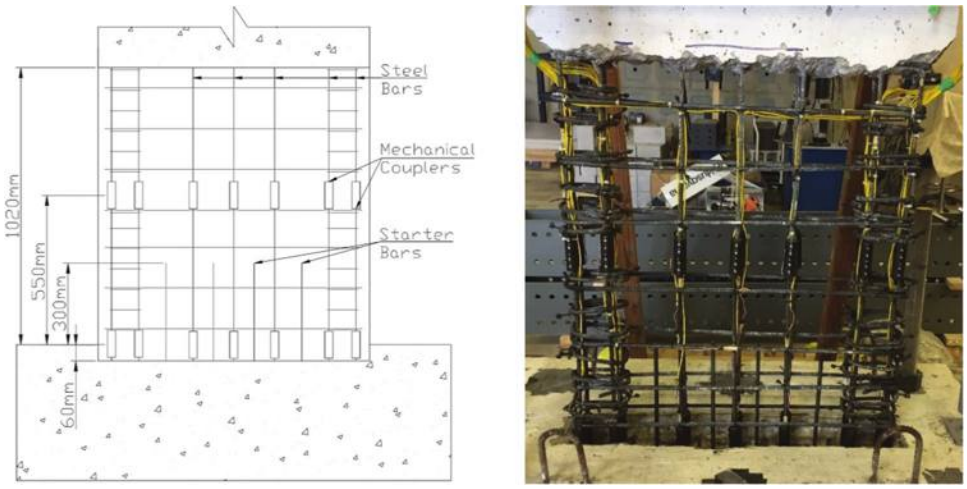

Fig. 5—Reinforcement layout of Wall RSWS-R in plastic hinge region.

The primary reasons for choosing this repair procedure were the extent of damage in the plastic hinge region and the opportunity to assess the behavior of the walls repaired with ECC in the plastic hinge region as part of a hybrid system. In addition, employing the same repair strategy for both walls permitted a direct comparison between their responses.

Replacement and addition of reinforcing bars—The damaged vertical steel reinforcing bars were removed and replaced with new segments of identical 10M bars. Shear-off mechanical couplers were used to connect the replacement segments to the remaining bars. In addition, four 10M starter bars, spaced at 150 mm along the base of the wall and extending 300 mm from the base, were provided in both walls to address the rocking and sliding observed at the base of the wall during testing of the original walls. Shown in Fig. 5 and 6 is the reinforcement layout within the repaired regions for RSWS-R and RSWN, respectively. For RSWS-R, all vertical bars were replaced, while for RSWN, only the vertical reinforcement in the web needed replacement as the SMA bars were undamaged. The ties in the boundary regions and the shear reinforcement of both walls were reused as no damage was observed.

First, the buckled and ruptured reinforcing bars were removed with an angle grinder, 500 mm from the base and slightly below the foundation level. The ends of the remaining reinforcing bars were then prepared with a belt sander to create a flat cross section to ensure a butt-end connection in the couplers with the replacement segments. Thereafter, the starter bars were installed. A rotary hammer was used to drill holes into the foundation, 12.5 mm in diameter and 125 mm in depth. The extent of drilling was based on the specifications required for the adhesive epoxy to ensure a proper bond. After the placement of the starter bars, the replacement segments of the vertical reinforcement were connected to the remaining bars using positional couplers. The couplers were 100 mm long and employed lock-shear

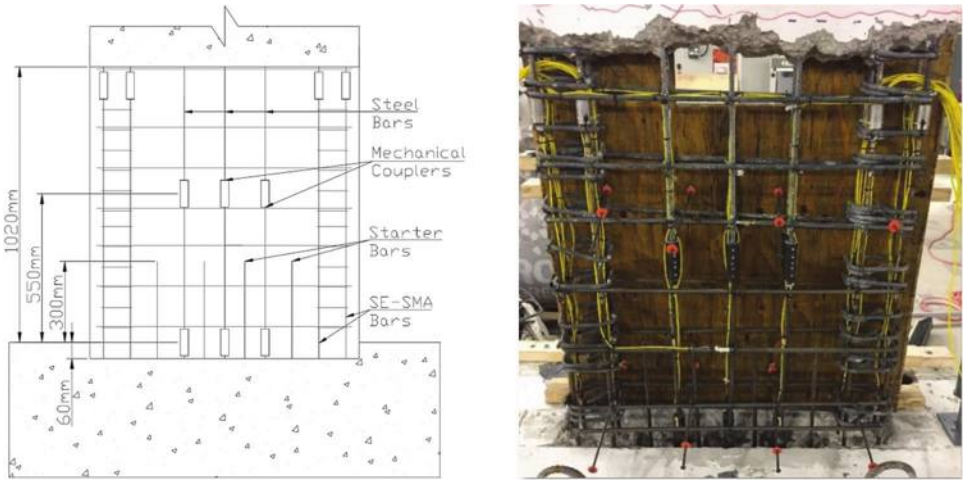

Fig. 6—Reinforcement layout of Wall RSWN in plastic hinge region.

Table 1—Mixture design proportions for 75 L batch

PVA fibers, kg									
ϕ = 0.10 mm	ϕ = 0.04 mm	Cement, kg	Fly ash, kg	Silica fume, kg	Slag, kg	Sand, kg	Water, kg	HRWRA, kg	Volume, L
0.94	0.94	30	50	8.25	3.38	33.38	23.33	0.75	75

bolts and serrated grip rails to mechanically splice the bars inserted from either end. An air impact wrench was used to tighten the bolts of the couplers.

Construction of formwork and casting of ECC—Plywood, 12.5 mm thick, was used as the main formwork component. Dimensional studs, 38 x 89 mm (2 x 4 in.), braced the plywood in the vertical and horizontal directions. In addition, snap ties were installed for additional resistance. A 200 x 300 mm opening was provided at the top of the formwork for concrete placement. The formwork design is illustrated in the Appendix, Fig. A.1.

The ECC was batched and mixed in-house, following a mixture design proposed by Eshghi,[22] with two modifications: the addition of smaller-diameter PVA fibers (ϕ = 0.04 mm) and the use of a different high-range water-reducing admixture (HRWRA) to obtain a flow between 200 and 250 mm, as per ASTM C1856/C1856M-17.[23] As such, two different types of PVA fibers were employed in this mixture, one with a 0.1 mm diameter and 1200 MPa tensile strength, and the other with a 0.04 mm diameter and 1560 MPa tensile strength. Both fiber types were 12 mm in length. Several trials were conducted to reach the final mixture design, summarized in Table 1. The objective was to achieve a mixture that provided post-cracking ductility,[24] while the compressive strength was not a controlling factor. The former was deemed critical for providing improved concrete damage control relative to the normal-strength concrete used in the original walls.

Casting deficiencies were encountered for Wall RSWS-R. The ECC was not adequately distributed along the top boundary of the plastic hinge, resulting in 50 mm gaps at both extremes of the wall, which gradually narrowed toward the center of the wall. To address this, SCC was cast in the affected areas. The curing procedure began immediately after formwork removal and was extended for 28 days. It consisted of covering the repaired regions of the walls with wet burlap sheets and a vapor barrier and watering every day until the end of the curing period. Figure 7 illustrates the repaired walls prior to testing.

Experimental setup and loading protocol

The experimental test setup is shown in Fig. A.2 in the Appendix and is the same as the setup used for the original walls, as designed by Morcos and Palermo.[10] Lateral loading was applied in a displacement-controlled mode through a single hydraulic actuator positioned along the centerline of the top beam of the walls. The actuator was attached to a steel bracket that was fixed to the strong wall. A lateral supporting frame was used to control out-of-plane displacements. It consisted of four vertical I-section steel columns bolted to the strong floor and connected to each other with four steel beams to provide a rigid restraining system, as shown in Fig. A.2. The lateral supporting frame was connected to the top beam of the walls through four casters placed on each lateral side of the steel beams.

The response of the walls was monitored and recorded with strain gauges, linear displacement transducers, and cable displacement potentiometers. The lateral and vertical displacements at different heights and the diagonal elongations in the plastic hinge zone of the repaired walls were measured. Additional details on the instrumentation are available elsewhere (Soto Rojas[24]).

The loading protocol for Walls RSWS-R and RSWN consisted of reverse cycles at multiples of the yield displacement (Δ_y) of Wall SWN to be consistent with the protocol applied to the original walls by Morcos and Palermo.[10] The approach was intended to evaluate the pre- and post-repair behavior of the walls under similar loading conditions. The yield displacement (Δ_y) of SWN was estimated from a preliminary pushover analysis to be 24 mm.[19] The loading cycles were divided into two groups: pre- and post-yield lateral displacement phases. The first loading phase

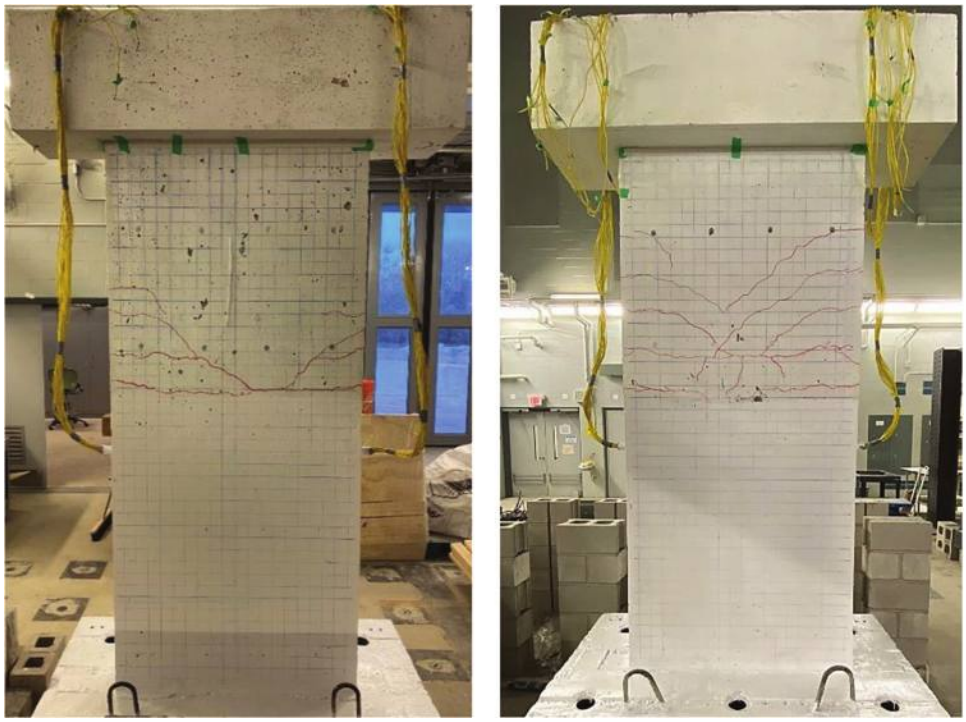

Fig. 7—Repaired walls prior to testing: (a) RSWS-R; and (b) RSWN.

consisted of three repetitions of seven targeted symmetrical displacements of $1/20\Delta_y$, $1/10\Delta_y$, $1/5\Delta_y$, $3/10\Delta_y$, $2/5\Delta_y$, and $1/2\Delta_y$ to reach the yield displacement Δ_y; thereafter, two repetitive cycles were imposed with displacement increments of $1/2\Delta_y$ until $5\Delta_y$ for Wall RSWS-R (following Wall SWS-R). Wall RSWN (following Wall SWN) continued with three repetitive cycles for each target displacement up to $2\Delta_y$ and two cycles per subsequent displacement level thereafter. (Note that based on preliminary numerical analysis, the yield displacement of SWS-R was approximated as one-half the yield displacement of SWN; therefore, the walls were subjected to three repetitions of loading up to two times their respective yield displacements.)

TEST RESULTS

Material properties

Concrete properties—The compressive strength of the ECC and SCC was evaluated from standard compression tests on 75 x 150 mm cylinders. The average compressive strength of three cylinders for the ECC was 64 MPa for RSWS-R and 63 MPa for RSWN on the day of testing the walls. The SCC in RSWS-R had an average compressive strength of 59 MPa.

Four-point bending tests were performed to characterize the flexural strength of the ECC on two prism specimens: Prism P1 with the dimensions of 75 x 75 x 250 mm, and Prism P2 with the dimensions of 75 x 75 x 500 mm. The prisms were cast from the ECC batch for Wall RSWS-R and were tested at the age of 28 days. The corresponding average 28-day compressive strength of three cylinders for the ECC was 49 MPa. Shown in Fig. 8 are the load-displacement responses, exhibiting a noticeable ductile behavior, characterized by a plateau stage at the initiation of cracking and prior to reaching the peak load. The descending branch of

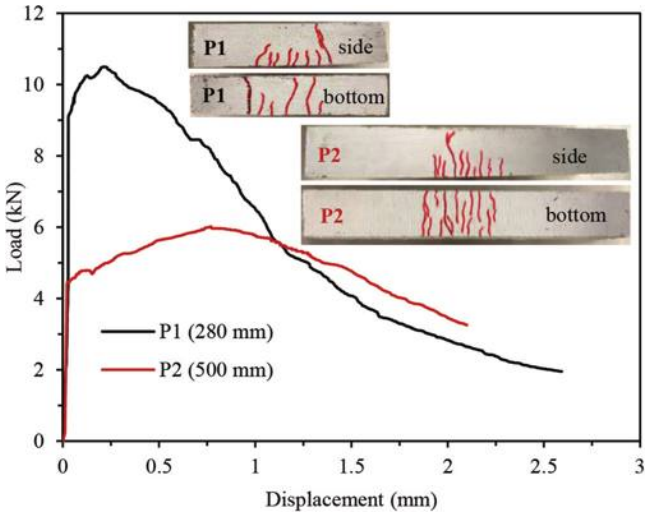

Fig. 8—Load versus midspan displacement of ECC flexural prisms and crack patterns at end of testing.

both prisms followed a gradual softening behavior. Additionally, both prisms developed a stiff initial response, where the first crack developed at 85% of the peak load for Prism P1 and 75% for Prism P2. The presence of the PVA fibers prevented a brittle failure mode; both prisms developed a localized dominant crack within the constant moment region and additional multiple finer cracks, as shown in Fig. 8. The fibers were able to bridge through and control the opening of the dominant crack, leading to the formation of other finer cracks. The maximum equivalent flexural strengths were 5.60 MPa for P1 and 6.42 MPa for P2; the corresponding midspan displacements were 0.22 mm for P1 and 0.77 mm for P2. (Note that the equivalent strengths were based on the gross section properties [Soto Rojas[24]]).

Table 2—Mechanical properties of reinforcing bars

Specimen ID	Bar	Yield strength, MPa	Modulus of elasticity, GPa	Tensile strength, MPa	Tensile strain, %	Rupture strain, %
SWS-R	10M*	428	197	558	14.7	17.4
SWN	10M*	435	186	564	14.0	15.8
SWN	No. 13*	463	203	627	12.3	16.5
SWN	SMA	338	42	1034	16.0†	16.0
RWS-R and RSWN	10M‡	430	175	537	16.4	26.2

*Mechanical properties following a repetition of the material tests. These updated properties differ from the values reported by Morcos,[19] Morcos and Palermo,[10] and Soto Rojas.[24]

†Strain at rupture.

‡Based on cyclic tensile test of one bar reported by Soto Rojas.[24]

Reinforcement properties—The mechanical properties of the 10M bars used in the repaired region of the walls were determined from standard coupon tests. Table 2 summarizes the properties of the reinforcing bars used in the original walls and the replacement bar segments used in the repair.

To assess the recovery capacity of the SMA bars, Morcos[19] performed a hybrid monotonic loading with a 6% strain cycle on an SMA bar used in Wall SWN. Shown in Fig. 9 is the comparison between the stress-strain response for the SMA bar and a 10M reinforcing bar used in the original walls. The superelasticity property of the SMA bar is evident; at a 6% strain, the SMA developed a stress of 495 MPa, and thereafter, when unloaded to zero stress, the SMA experienced a negligible plastic offset of 0.18% strain prior to reloading to failure. The SMA failed prematurely by rupture of the top conical head of the mechanical coupler used in the original SWN wall at a stress of 1034 MPa and a corresponding 16% strain.[19] At a 6% strain, the 10M steel bar was in the strain-hardening phase and at a stress level of 534 MPa. Unloading to zero stress, the steel bar experienced a residual strain of approximately 6%. Thereafter, the steel bar was loaded to failure, reaching a maximum tensile strength of 584 MPa at a corresponding strain of 16.6%.

Cracking characteristics

Figure 10 illustrates the cracking patterns after testing Walls RSWS-R and RSWN. The existing cracks from the initial testing are highlighted with red and the new cracks are marked with green. At 4.8 mm displacement (0.2% drift) Wall RSWN developed the first flexural crack in the repaired region, 425 mm above the base; the crack was 0.3 mm wide and 300 mm long. During the last repetition at 4.8 mm in the negative direction, a previously existing flexural crack located above the repaired region, 1250 mm from the base, widened and reached 0.25 mm in width. RSWS-R developed no cracks in the repaired region at this displacement level and the existing cracks did not experience growth.

Wall RSWS-R developed the first crack in the repaired region during the first cycle of 12 mm displacement (0.5% drift) in the negative direction; the crack was 250 mm long and surfaced 25 mm from the base of the wall. Another crack, 0.15 mm wide and 25 mm long, appeared during the second repetition in the positive direction at 250 mm from the base. In addition, two flexural-shear cracks, 0.15 mm in width, developed at 1550 and 1650 mm from the base of the wall.

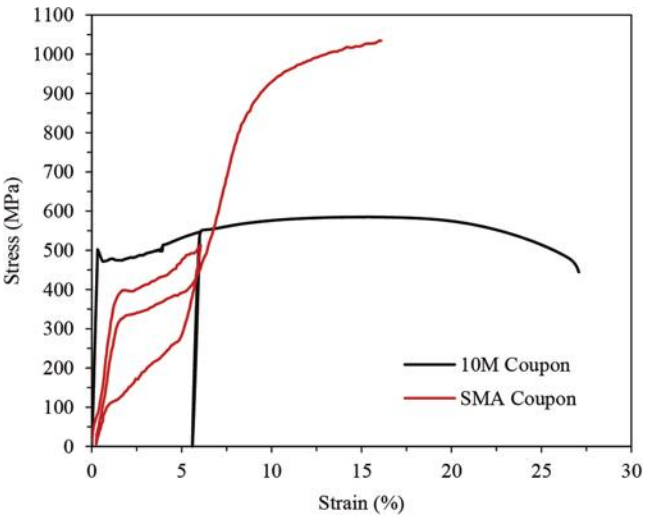

Fig. 9—Stress-strain response with 6% strain cycle of 10M steel and SMA bars. (Adapted from Morcos.[19])

Both walls developed major cracks at a displacement of 24 mm (1% drift). For Wall RSWS-R, a 3.0 mm wide flexural crack formed at 275 mm from the base. The negative excursions propagated this crack through the entire length of the wall. This localized damage was attributed to the change in the wall's stiffness at that location due to the presence of the starter bars and mechanical couplers. Additional shorter cracks developed on both sides of this major crack. Above the repaired region, three new 0.1 mm-wide shear cracks developed. Similarly, during the loading excursions at 24 mm lateral displacement, Wall RSWN developed a major 5.0 mm wide horizontal crack extending through the length of the wall, approximately 500 mm from the base. Two hairline shear cracks branched downward at a 45-degree angle from the major horizontal crack, and two existing hairline shear cracks located above the repaired region reopened and extended for an additional 5 mm.

As the displacement levels increased, the cracks for both walls experienced an increase in width, accompanied by visible pullout and rupture of the fibers. For Wall RSWS-R, the major horizontal crack extended along the entire length and through the thickness, dividing the wall into two sections that were mainly connected by the longitudinal steel reinforcement. During the loading cycles at 60 mm (2.5% drift), two longitudinal steel bars in the right boundary region of RSWS-R ruptured. At this displacement level, the cracks within the repaired region of the RSWN wall became wider

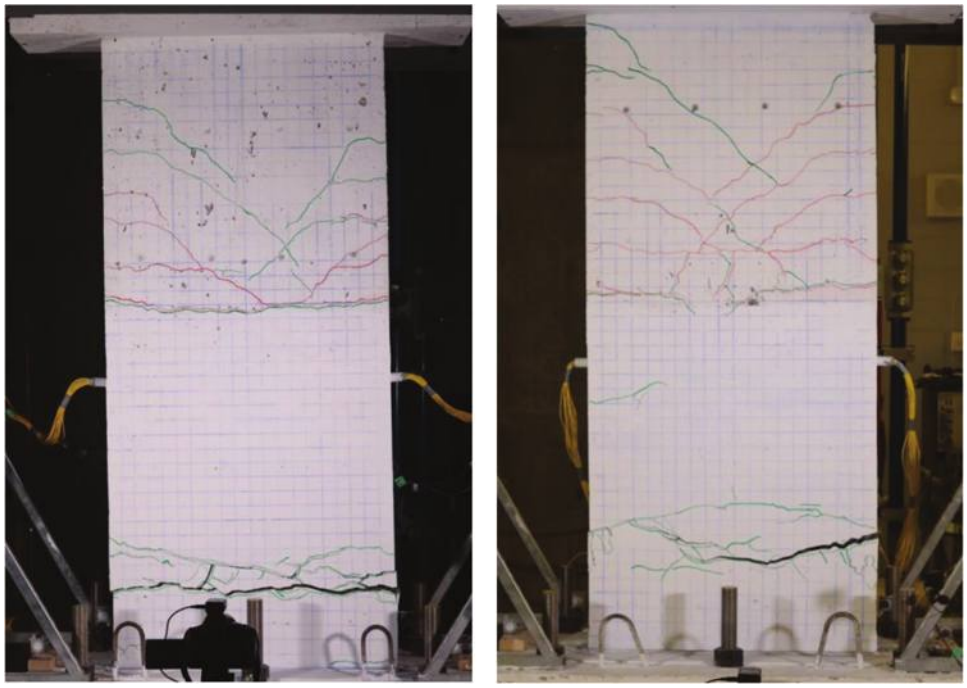

Fig. 10—Repaired walls after testing: (a) RSWS-R; and (b) RSWN.

without undergoing any propagation, with the major horizontal crack opening to 20 mm. Unlike the steel-reinforced wall, vertical cracks appeared on the right side of the wall and are attributed to debonding of the SMA bars. The same crack pattern was visible on the left side of the wall due to the loss of bond between the SMA bar and the surrounding concrete.

At the 72 mm displacement cycle (3% drift), testing of RSWS-R was terminated. The cracking characteristics did not change throughout this cycle, except for the dominant horizontal crack that extended to a width of 30 mm without recovery. Three longitudinal steel bars ruptured in the right boundary region by the end of the second repetition, while two bars ruptured in the left boundary region. At the end of testing, Wall RSWS-R experienced a lateral offset of approximately 20 mm along the dominant horizontal crack.

Testing of Wall RSWN proceeded with higher lateral displacements, up to 96 mm (4.0% drift). At 84 mm lateral displacement (3.5% drift), during the negative loading cycle, Wall RSWN experienced rupture of one longitudinal steel bar on the right side of the web region, adjacent to the SMA bars. The right side of the dominant horizontal crack widened to 31 mm. Testing was terminated at the end of the first cycle at 96 mm (4% drift). During loading to the positive direction, a longitudinal steel bar ruptured on the left side of the web region. Furthermore, in the final excursion in the negative direction, two longitudinal reinforcing bars located on the right side of the web region were ruptured.

Load-displacement response

The lateral load-displacement responses of the walls pre- and post-repair are illustrated in Fig. 11. The displacements were based on readings from the cable potentiometer installed at the midheight of the loading beam, which recorded measurements relative to the foundation. The performance of the repaired walls is marked by a higher lateral load resistance in comparison to the original walls and comparable displacement capacity. Wall RSWS-R dissipated more energy than Wall SWS-R, with slightly wider hysteretic curves characterized by the development of higher loads for the same displacements, as shown in Fig. 11(a). Similarly, a significant increase in the lateral strength was observed for Wall RSWN (Fig. 11(b)). Wall RSWN experienced a reduction in drift capacity relative to the original wall. No significant difference in pinching was observed in the repaired SMA wall in comparison to the original SMA wall.

Table 3 summarizes performance parameters for the original and repaired walls at the yield, peak, and ultimate points, calculated as an average from the positive and negative directions. Based on the reduced stiffness equivalent elastoplastic method,[25] the yield point was determined with a secant stiffness passing through the load-displacement response at 75% of the average nominal strength. The average yield load for Wall RSWS-R was 127 kN with a corresponding average yield displacement of 13.6 mm (0.6% drift). Wall RSWN had an average yield load of 123 kN and an average yield displacement of 30.9 mm (1.3% drift). Both walls had a nearly linear response prior to yielding, with Wall RSWN exhibiting a softer response due to the lower modulus of elasticity of the SMA bars compared to the steel reinforcement.

The post-yield behavior of Wall RSWS-R was marked by a steep development of load capacity prior to reaching the peak load. Conversely, Wall RSWN exhibited a sustained plateau with only a minor increase in load. In addition, the displacement recovery capacity of Wall RSWN was significantly more pronounced in comparison to RSWS-R; at the displacement level of 24 mm (1% drift), Wall RSWN experienced a residual displacement of 4.9 mm, while the residual displacement in Wall RSWS-R was 11 mm.

Table 3—Average performance points of original and repaired walls

Specimen ID	Yield			Peak			Ultimate		
	δ, mm	Drift, %	Load, kN	δ, mm	Drift, %	Load, kN	δ, mm	Drift, %	Load, kN
SWS-R	8.7	0.4	98	30.0	1.3	118	60	2.5	101
RSWS-R	13.6	0.6	127	29.3	1.2	145	56	2.3	128
SWN	45.0	1.9	93	91.0	3.8	118	103	4.3	113
RSWN	30.9	1.3	123	59.0	2.5	137	84	3.5	124

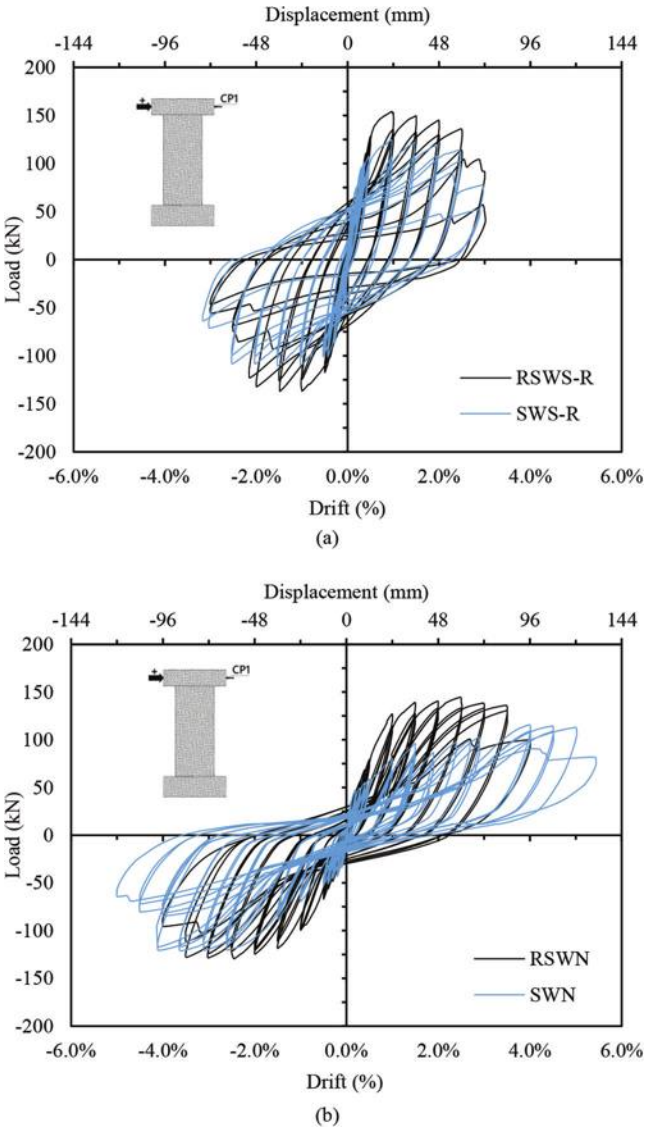

Fig. 11—Lateral load-displacement response of walls: (a) SWS-R and RSWS-R; and (b) SWN and RSWN.

Wall RSWS-R had an average peak lateral load capacity of 145 kN at an average displacement of 29 mm (1.2% drift). During loading to the positive direction at the first excursion of 24 mm (1% drift), RSWS-R developed a major crack located 300 mm above the base of the wall that corresponded to the peak load for the positive direction. The peak load in the negative direction occurred during the first repetition at 36 mm (1.5% drift) when a similar crack appeared on the opposite side. Wall RSWN had an average peak load of 137 kN with an average displacement of 59 mm (2.5% drift).

The post-peak response of both walls was dominated by the major cracks that developed above the starter bars. The ultimate point was established based on a 20% reduction in the lateral load capacity or the displacement cycle prior to the fracturing of the reinforcement. After the peak point, Wall RSWS-R experienced a gradual degradation of lateral load capacity, leading to an average ultimate load of 128 kN at an average displacement of 56 mm (2.3% drift), which represented the last cycle prior to rupturing of the longitudinal steel reinforcement in the boundary region. Wall RSWN sustained an average ultimate load of 124 kN with an average ultimate displacement of 84 mm (3.5%). The SMA bars located in the boundary region experienced no damage; however, the longitudinal steel reinforcing bars in the web region ruptured and marked the termination of the test.

DISCUSSION OF RESULTS

Envelope load-drift response

Figure 12 compares the lateral load-drift envelopes from the positive loading excursions of Walls SWS-R, RSWS-R, and RSWN and the negative loading excursion of Wall SWN. The negative loading envelope was chosen for Wall SWN to avoid discussing and comparing results obtained from the asymmetrical positive loading of this specimen. The envelopes were developed from the first repetition of each displacement level in the loading direction.

The original steel wall, SWS-R, exhibited a higher initial stiffness in comparison to the repaired companion wall RSWS-R; this difference is attributed to the existing damage above the plastic hinge region in RSWS-R. For the SMA-reinforced walls, the responses were relatively similar up to 48 kN lateral loading, after which they diverged significantly, with the repaired wall exhibiting markedly stiffer behavior. The initial stiffnesses, determined at 1.2 mm displacement (0.05% drift), were 32.4 and 24.4 kN/mm for Walls SWS-R and SWN, respectively. Walls RSWS-R and RSWN developed initial stiffnesses of 20.1 and 15.4 kN/mm, respectively.

It may be observed that the repaired steel wall experienced global yielding at a larger drift relative to the original wall. Conversely, the repaired SMA wall experienced a yield drift that was smaller than the original wall. However, the repaired walls exhibited a significant increase in the corresponding lateral strength at yielding. In the post-yielding regime, the repaired specimens, Walls RSWS-R and RSWN, sustained increased lateral loads in comparison with the original walls. The trend continued up to failure. It is noteworthy that, as shown in Fig. 12, the shapes of the envelopes are similar for RSWS-R and SWS-R. The envelope of RSWN exhibits a

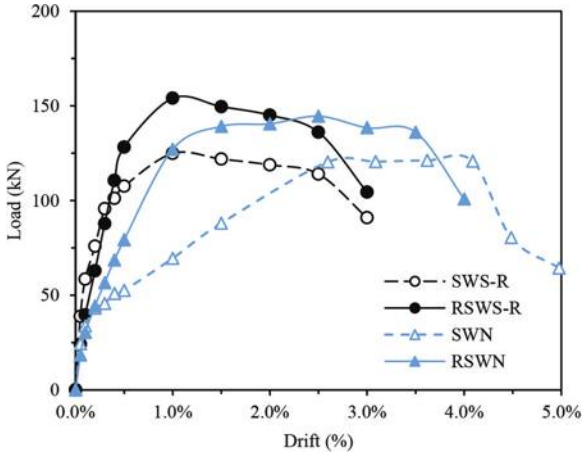

Fig. 12—Lateral load-drift envelopes of Walls SWS-R, RSWS-R, SWN, and RSWN.

response that can be satisfactorily characterized by bilinear behavior, whereas SWN provides a more pronounced trilinear response.

Cyclic rotation responses

The rotation responses were calculated from the vertical displacements recorded from the soffit of the top loading beam relative to the top of the foundation. The load-rotation behaviors are shown in Fig. 13. Overall, the SMA-reinforced walls exhibited larger rotations compared to the steel-reinforced walls. This behavior was observed for the original and repaired walls and is primarily attributed to the lower stiffness of the SMA bars and the development of dominant cracks. In addition, the SMA-reinforced walls were able to recover large rotations to a greater extent compared to the steel-reinforced walls due to the self-centering capacity of the SMA bars. The average rotation from the positive and negative loading cycles at yielding for Wall SWS-R was 5.5×10^{-3} rad, while the average rotation for SWN was 19.9×10^{-3} rad. The repaired Walls RSWS-R and RSWN exhibited 10.7×10^{-3} rad and 28.7×10^{-3} rad average rotations, respectively.

Wall RSWS-R sustained noticeably larger rotations compared to Wall SWS-R in the final loading cycles. This was due to the influence of ECC on the overall response, which led to the formation of a dominant crack in the repaired region and thus facilitated increased rotations. Repaired Wall RSWN also developed larger rotations compared to the original SWN wall, primarily due to the ECC material. At peak, Walls SWS-R and SWN developed average rotations of 12.3×10^{-3} rad and 36.7×10^{-3} rad, respectively. Repaired Walls RSWS-R and RSWN had average rotations of 20.1×10^{-3} rad and 45.6×10^{-3} rad, respectively. At ultimate, the original Wall SWS-R had a rotation of 21.7×10^{-3} rad, while SWN's rotation was 41.1×10^{-3} rad. The repaired Walls RSWS-R and RSWN at ultimate sustained 34.1×10^{-3} rad and 58.6×10^{-3} rad rotations, respectively.

Shear strain responses

The shear strains were calculated in the plastic hinge area following the approach suggested by Oesterle et al.[26]

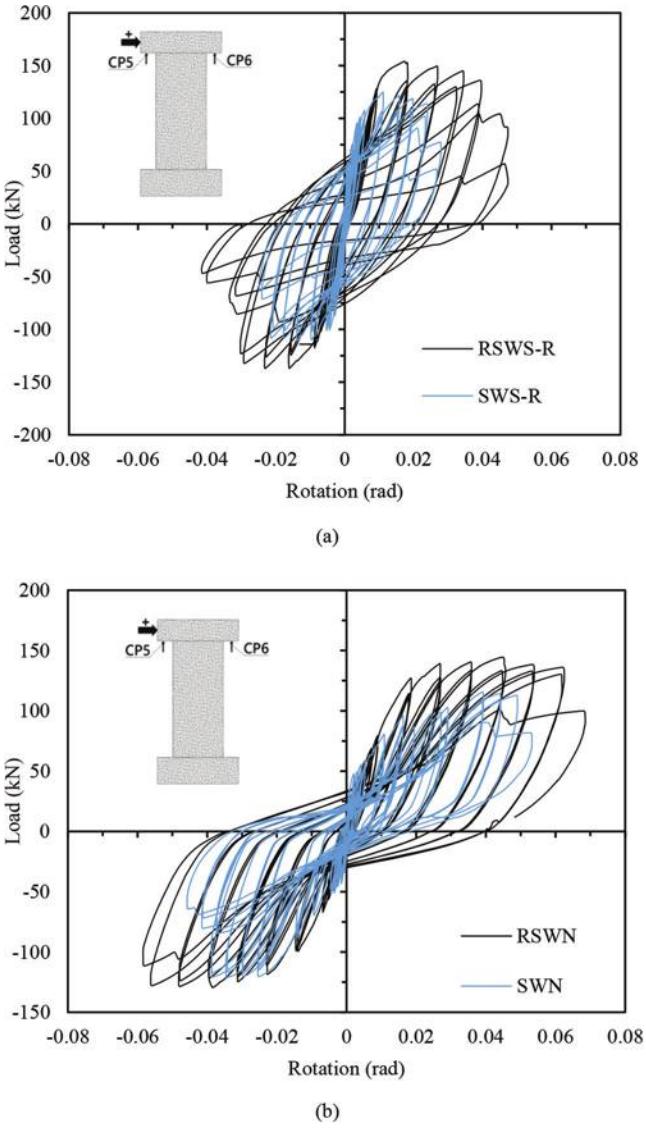

Fig. 13—Load-rotation responses of walls: (a) SWS-R and RSWS-R; and (b) SWN and RSWN.

$$\gamma = (\delta_1 d_1 - \delta_2 d_2)/2hl \quad (1)$$

where γ is the shear strain; d_1 and d_2 are the reference lengths of the cable potentiometers installed diagonally in the plastic hinge; δ_1 and δ_2 are the change in length of the diagonal cable potentiometers; and h and l are the vertical and horizontal projections of the cable potentiometers. The dimensions were the same for all walls, d_1 and d_2 were 1130 mm, and h and l were 800 mm. Figure 14 depicts the load-shear strain responses.

At yielding, the repaired walls experienced average shear strains of 1.5×10^{-3} rad for Wall RSWS-R and 4.4×10^{-3} rad for Wall RSWN. The original walls, SWS-R and SWN, developed at yielding average shear strains of 0.5×10^{-3} and 2.4×10^{-3} rad, respectively. At peak lateral load, Wall RSWN developed average shear strains of 6.75×10^{-3} rad compared to 4.0×10^{-3} rad for Wall RSWS-R. The original Walls SWN and SWS-R exhibited average shear strains at peak loads of 4.50×10^{-3} and 2.9×10^{-3} rad, respectively. As the lateral displacements increased, Wall RSWS-R experienced larger

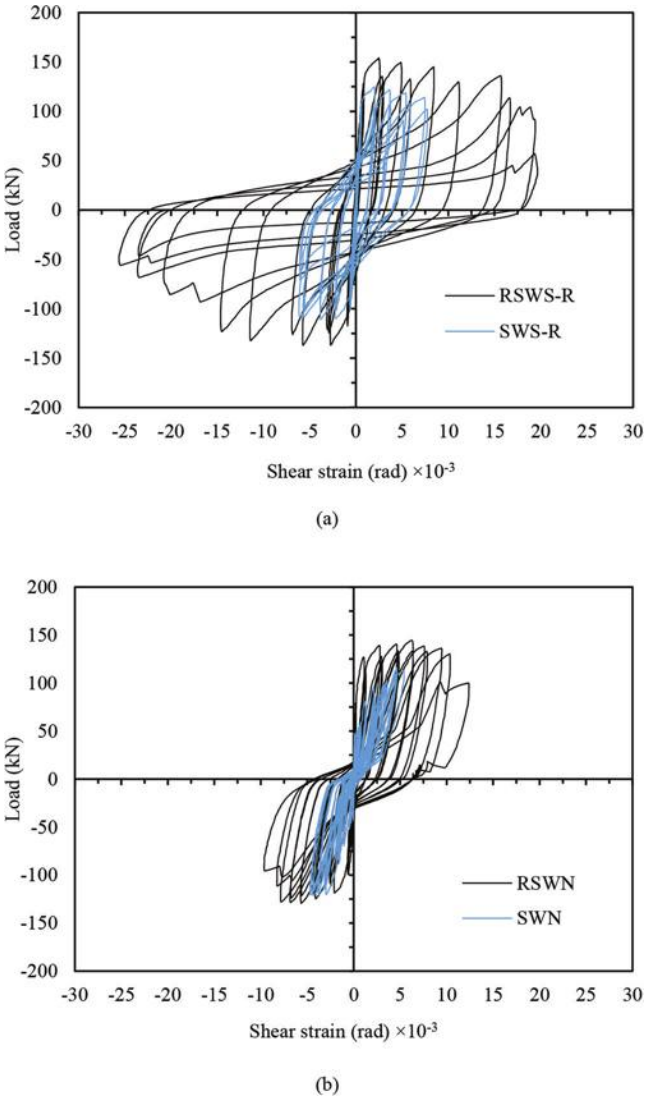

Fig. 14—Load-shear strain responses of walls: (a) SWS-R and RSWS-R; and (b) SWN and RSWN.

shear strains compared to Wall RSWN, reaching an ultimate average shear strain of 14.9×10^{-3} rad, while Wall RSWN was subjected to 9.1×10^{-3} rad. The ultimate average shear strains for SWS-R and SWN were 6.8×10^{-3} rad for Wall SWS-R and 4.6×10^{-3} rad for Wall SWN.

The repaired walls did not experience shear failure or significant shear damage, indicating that the shear capacity of ECC combined with the transverse reinforcement was not exceeded. The main difference between the repaired walls is denoted by the higher shear strain recovery capacity of the SMA wall, whereas the steel-reinforced wall sustained high residual shear strain. The recentering characteristics of the SMA bars promoted the symmetrical behavior of Wall RSWN, while the conventional steel wall experienced an asymmetrical response (ratcheting in one direction); similar responses were observed for the original walls. In addition, no accentuated pinching was observed in the walls, explained by the lack of shear cracks within the plastic hinge region. In comparison with the original walls, the repaired walls developed considerably larger shear distortions over the plastic hinge region, attributed mainly to the behavior of ECC and to the contribution of the starter bars. (Recall that the original walls experienced rocking at the base of the walls, which was controlled in the repaired walls.)

Energy dissipation

Figure 15 provides the load-displacement response of all walls at 36 mm (1.5% drift). The characteristics of the responses between each set of walls are similar, with the exception of higher loads measured for the repaired walls. The dissipated energy was calculated as the area encompassed by the loop of the first repetition of loading. At this displacement level, the energy dissipated by Wall RSWS-R was 6240 N·m, which represented 8% more energy than SWS-R, with a dissipated energy of 5765 N·m. Similarly, Wall RSWN dissipated 2700 N·m, a 22% increase over Wall SWN, with 2130 N·m of energy dissipated. The ECC used for the repaired walls contributed to a strength enhancement in the walls, leading to higher dissipated energy throughout testing. In addition, the starter bars shifted the critical section above the base of the wall, effectively reducing the lever arm and resulting in increased strength.

Figure 16 illustrates the energy dissipated at each drift level for the original and repaired walls. Up to a 0.5% drift, the energy dissipation for all the walls was comparable. Thereafter, it is evident that the repaired steel-reinforced wall dissipated more energy compared to the original wall. For the SMA walls, the difference in energy dissipation became more pronounced in the final loading cycles, with the repaired wall dissipating significantly more energy.

Recovery capacity

Figure 17 presents the recovery capacity-drift response of all the walls. The recovery capacity is calculated as the ratio of the difference between the peak displacement and the residual displacement to the peak displacement for each drift level. For Wall SWN, the negative loading direction was also included, due to a significant difference in response compared to the positive direction. For the remainder of the walls, the recovery capacity was similar for the positive and negative loading directions; as such, only the positive results are reported. The enhanced recovery attained by the repaired walls in the initial phase of testing was partly due to the preferred behavior of the ECC. In addition, the placement of the starter bars shifted the critical section away from the base of the wall, allowing for the characteristics of the ECC and SMA materials to better contribute to the response of the walls.

At the onset of testing, up to a 0.3% drift, the original and repaired steel-reinforced walls behaved in a similar manner. At a 0.4% drift, Wall SWS-R recovered 76% from the imposed displacement, while Wall RSWS-R recovered 85.4%. Similar behavior was experienced throughout testing; at a 1% drift, Wall SWS-R recovered 40.2%, whereas Wall RSWS-R recuperated 51.6%. At a 2% drift, Wall SWS-R recovered 29%, while Wall RSWS-R was able to retrieve 37.6%. The difference of approximately 10% in recovery capacities decreased as the walls approached failure.

The repaired SMA wall, RSWN, exhibited an improved recovery capacity up to a 1.5% drift, compared to both the

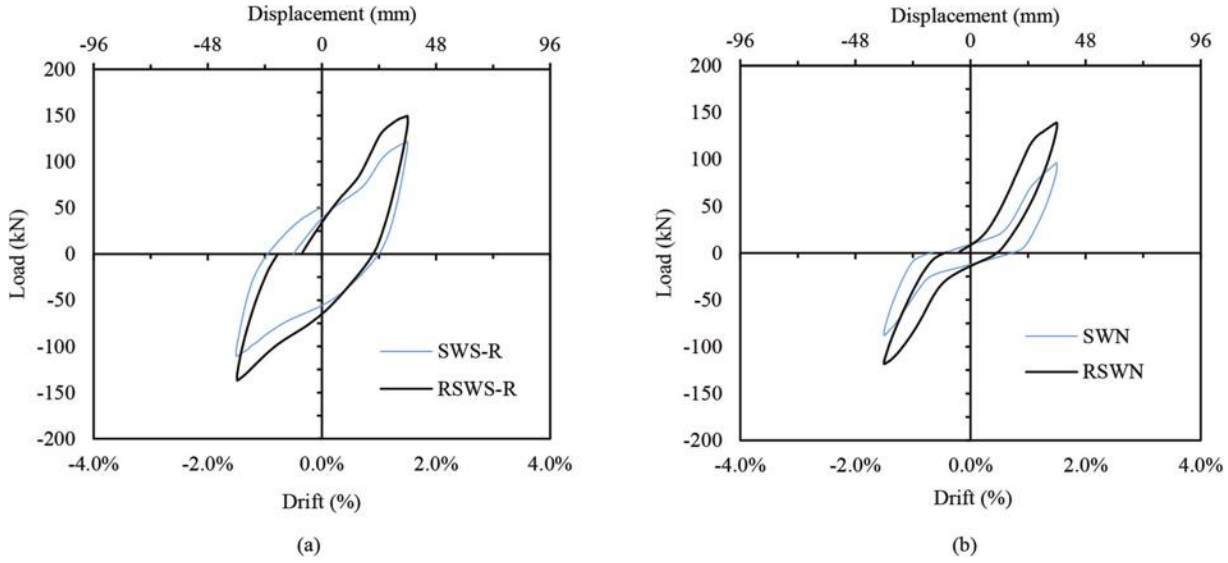

Fig. 15—Hysteretic response at 36 mm displacement (1.5% drift) of walls: (a) SWS-R and RSWS-R; and (b) SWN and RSWN.

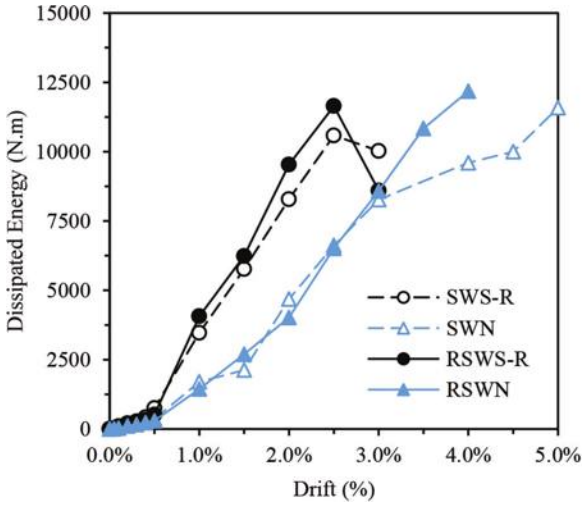

Fig. 16—Energy dissipated at different drift levels.

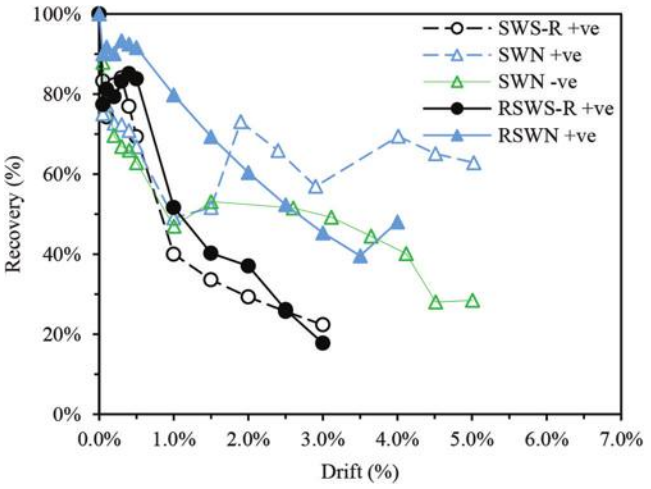

Fig. 17—Displacement recovery capacity-drift responses of walls: SWS-R and RSWS-R; and SWN and RSWN.

positive and negative responses of the original SWN wall. Thereafter, Wall SWN provided an enhanced recovery capacity in the positive loading direction compared to the repaired wall, which was maintained until failure. Compared to the recovery capacity of Wall SWN measured in the negative direction, the repaired wall exhibited a preferred response; the difference in recovery, however, was diminished as the walls approached failure, similar to the trend observed for the steel-reinforced walls. The primary reason behind the dissimilarity between the positive and negative loading responses for Wall SWN is attributed to the pronounced sliding at the base and rocking of the wall. Note that the increase of recovery for Wall RSWN at a 4% drift was the result of the fracturing of the longitudinal web bars, reducing the resistance to recovery.

Effect of starter bars

The addition of the starter bars in the web region of the repaired walls aimed to control the sliding of the walls along the cold joint between the ECC repair concrete and the existing concrete at the foundation level. In addition, the starter bars were used to prevent the rocking of the walls experienced by the original walls along their base. Controlling sliding and rocking resulted in a response that was controlled within the wall panel. This, in turn, ensured that the benefits of the ECC were realized. A cable potentiometer was installed 50 mm above the base of the walls to monitor the horizontal displacements throughout testing. The maximum lateral displacement was 0.38 mm for Wall RSWN and 0.31 mm for Wall RSWS-R. The negligible displacements validated that the addition of the starter bars eliminated sliding along the base of the walls. Furthermore, the starter bars eliminated the damage experienced by the original walls at the base. Figure 18 illustrates the state of the base of Walls SWN and RSWN at the end of testing. No significant cracking surfaced in the repaired walls along the height of the starter bars (300 mm) due to the high concentration of steel in this region, which created a rigid section, shifting the failure mode higher into the wall.

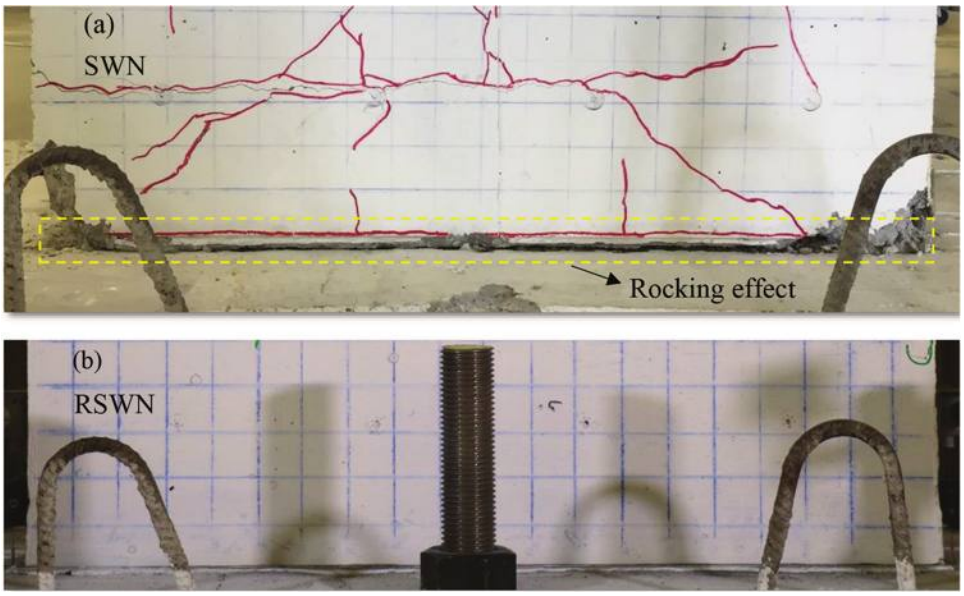

Fig. 18—State of base of walls at end of testing: (a) SWN; and (b) RSWN.

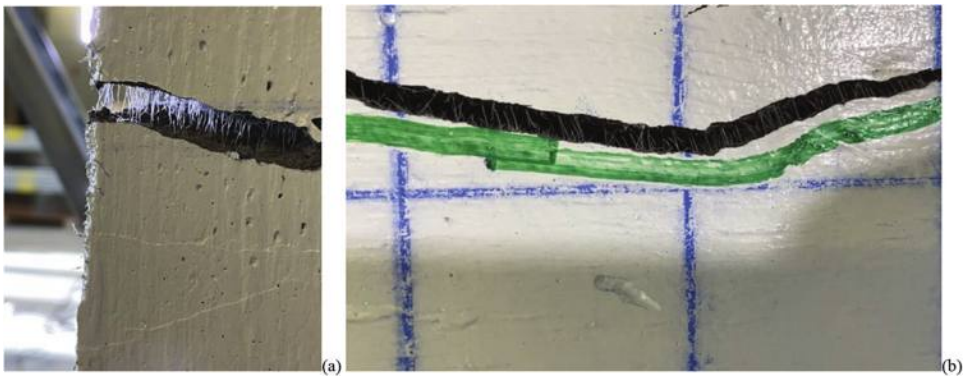

Fig. 19—Wall RSWN: Pulling out and fracturing of PVA fibers at localized cracks: (a) boundary zone; and (b) web region.

Failure modes

Figures 2 and 10 depict the crack patterns of the original and repaired walls at the end of testing. The influence of the ECC mixture is evident when comparing the state of the walls at failure. For the repaired wall, widespread cracking did not surface as was observed in the original walls (Fig. 2), and the formation of a more localized damage zone was evident (Fig. 10).

Replacing the conventional concrete with the ECC in the plastic hinge resulted in a delay in the damage experienced by the repaired walls at larger drifts. Moderate damage was detected up to a 1.5% drift for both repaired walls compared to a 0.5% drift for Wall SWS-R and a 0.3% drift for Wall SWN. This was associated with the effectiveness of the fibers in bridging the cracks at large displacements. The damage retention and crack recovery were sustained up to drifts of 2% for Wall RSWS-R and 2.5% for Wall RSWN. Thereafter, the fibers began pulling out from and fracturing at the localized major crack. The PVA fibers pulled out once the crack width exceeded the anchorage length of the fibers, approximately 6 mm. The major crack that formed in Wall RSWN at a height of 400 mm from the base illustrated the benefits of the fibers, which prevented the crack from widening up to drifts of 2.5%. Figure 19 is a close-up view of the PVA fibers pulling out and fracturing at the localized cracks located in the boundaries and web region of Wall RSWN. Note that similar behaviors were observed in both repaired walls.

CONCLUSIONS

Two previously tested shear walls were repaired and tested under reversed cyclic loading. One of the walls was reinforced with nickel-titanium (NiTi) superelastic bars in the boundary regions of the plastic hinge area, while the other wall contained steel reinforcement only. The repair involved the removal of heavily damaged concrete in the plastic hinge area, the replacement of ruptured and buckled steel reinforcement, the addition of starter bars, and the casting of engineered cementitious composite (ECC) to replace the concrete that was removed. The following conclusions are drawn from the experimental testing:

1. The repaired walls developed localized damage primarily within one-third of the plastic hinge region, as opposed to the original walls, which presented widespread cracking. The major benefit of localized damage relates to a potentially more accelerated repair process.

2. The lateral strength of the repaired walls was considerably higher compared to the original walls. The enhanced properties of the ECC were one of the main factors

contributing to the increase in capacity. Repaired Wall RSWS-R developed a peak lateral strength 23% larger compared to the original Wall SWS-R; both walls reached their peak strength at 30 mm lateral displacement. Wall RSWN had a 16% increase in peak lateral strength compared to SWN; the repaired wall developed its peak load at 66 mm lateral displacement, in comparison to 91 mm for SWN. The strength enhancement of the repaired walls led to generally higher dissipated energy.

3. The ultimate drift capacity of the repaired RSWS-R wall was marginally lower, 2.3% compared to 2.5% for SWS-R. A more pronounced reduction in ultimate drift was measured for Wall RSWN (3.5%) compared to SWN (4.3%).

4. Generally, enhanced recovery capacity was observed for the repaired walls compared to the original walls, primarily due to the enhanced behavior of ECC and the placement of the starter bars. (Note that this is true for the repaired shape memory alloy [SMA] wall relative to the negative direction of loading of the original wall.) The starter bars shifted the critical section away from the base of the wall, thus allowing for the ECC and SMA materials to better contribute to the response of the walls.

5. For both sets of walls, the SMA-reinforced walls exhibited larger rotations compared to the steel-reinforced walls on account of the lower stiffness of the SMA bars.

6. The repaired walls did not exhibit significant shear damage. Wall RSWN developed a higher shear strain recovery capacity compared to Wall RSWS-R, which sustained high residual shear strain. The recentering characteristics of the SMA bars promoted the symmetrical behavior of Wall RSWN, while the conventional steel wall experienced an asymmetrical response; similar responses were observed for the original walls.

In summary, the study presented herein demonstrates that NiTi SMA bars and ECC constitute a viable system for slender concrete shear walls. In general, the repair strategy enhanced the recovery and energy dissipation capacities, resulted in damage localization, and permitted the walls to exhibit enhanced shear distortion and rotation responses.

AUTHOR BIOS

Michael A. Soto-Rojas *is a Structural Engineer in Training with the Department of Highways and Public Works, Whitehorse, YT, Canada. He received his MASc from York University, Toronto, ON, Canada, in 2020. His research interests include engineered cementitious composites, shape memory alloys, and testing of concrete shear walls.*

Anca C. Ferche *is an Assistant Professor in the Department of Civil, Architectural and Environmental Engineering at The University of Texas at Austin, Austin, TX. She received her PhD from the University of Toronto, Toronto, ON, Canada, in 2020. Her research interests include performance assessment and analysis of reinforced concrete structures, concrete deterioration mechanisms, and rehabilitation of structures.*

Dan Palermo *is a Professor in the Department of Civil Engineering at York University. His research interests include seismic repair and retrofitting of concrete structures, nonlinear finite element modeling, seismic applications of shape memory alloys, ultra-high-performance steel fiber-reinforced concrete and engineered cementitious composites, tall masonry wall systems, and the response of structures to tsunami loading.*

ACKNOWLEDGMENTS

The authors acknowledge the funding provided by the Natural Sciences and Engineering Research Council of Canada (NSERC) through the Discovery Grants program (Grant: RGPIN-2017-05679).

REFERENCES

1. EN 1998-1:2004, "Eurocode 8: Design of Structures for Earthquake Resistance—Part 1: General Rules, Seismic Actions and Rules for Buildings," European Committee for Standardization, Brussels, Belgium, 2004, 231 pp.

2. FEMA P-1050, "NEHRP Recommended Seismic Provisions for New Buildings and Other Structures," Building Seismic Safety Council, Washington, DC, 2015.

3. Joint ACI-ASCE Committee 441, "High-Strength Concrete Columns: State of the Art (ACI 441R-96)," American Concrete Institute, Farmington Hills, MI, 1996, 13 pp.

4. ACI Committee 318, "Building Code Requirements for Structural Concrete (ACI 318-19) and Commentary (ACI 318R-19) (Reapproved 2022)," American Concrete Institute, Farmington Hills, MI, 2019, 624 pp.

5. Wallace, J. W.; Massone, L. M.; Bonelli, P.; Dragovich, J.; Lagos, R.; Lüders, C.; and Moehle, J., "Damage and Implications for Seismic Design of RC Structural Wall Buildings," *Earthquake Spectra*, V. 28, No. 1_suppl1, June 2012, pp. 281-299. doi: 10.1193/1.4000047

6. Elwood, K. J., "Performance of Concrete Buildings in the 22 February 2011 Christchurch Earthquake and Implications for Canadian Codes," *Canadian Journal of Civil Engineering*, V. 40, No. 8, Aug. 2013, pp. 759-776. doi: 10.1139/cjce-2011-0564

7. Pan, Z.; Wu, C.; Liu, J.; Wang, W.; and Liu, J., "Study on Mechanical Properties of Cost-Effective Polyvinyl Alcohol Engineered Cementitious Composites (PVA-ECC)," *Construction and Building Materials*, V. 78, Mar. 2015, pp. 397-404. doi: 10.1016/j.conbuildmat.2014.12.071

8. Mohammed, B. S.; Nuruddin, M. F.; Aswin, M.; Mahamood, N.; and Al-Mattarneh, H., "Structural Behavior of Reinforced Self-Compacted Engineered Cementitious Composite Beams," *Advances in Materials Science and Engineering*, V. 2016, 2016, Article No. 5615124, 12 pp. doi: 10.1155/2016/5615124

9. Abdulridha, A., and Palermo, D., "Behaviour and Modelling of Hybrid SMA-Steel Reinforced Concrete Slender Shear Wall," *Engineering Structures*, V. 147, Sept. 2017, pp. 77-89. doi: 10.1016/j.engstruct.2017.04.058

10. Morcos, M., and Palermo, D., "SMA-Reinforced Concrete Shear Walls Subjected to Reverse Cyclic Loading," *Proceedings of the Fifth International Conference on Smart Monitoring, Assessment and Rehabilitation of Civil Structures (SMAR 2019)*, Aug. 2019, Potsdam, Germany, 2019, 8 pp.

11. Morcos, M., and Palermo, D., "Numerical Modelling of Slender Superelastic-Shape Memory Alloy Reinforced Concrete Shear Walls," *Proceedings of 6th International Structural Specialty Conference (CSCE 2018)*, K. Arjomandi and A. El Damatty, eds., Fredericton, NB, Canada, June 2018, pp. 528-538.

12. Cortés-Puentes, L.; Zaidi, M.; Palermo, D.; and Dragomirescu, E., "Cyclic Loading Testing of Repaired SMA and Steel Reinforced Concrete Shear Walls," *Engineering Structures*, V. 168, Aug. 2018, pp. 128-141. doi: 10.1016/j.engstruct.2018.04.044

13. Saiidi, M. S.; O'Brien, M.; and Sadrossadat-Zadeh, M., "Cyclic Response of Concrete Bridge Columns Using Superelastic Nitinol and Bendable Concrete," *ACI Structural Journal*, V. 106, No. 1, Jan.-Feb. 2009, pp. 69-77.

14. Abdulridha, A.; Palermo, D.; Foo, S.; and Vecchio, F. J., "Behavior and Modeling of Superelastic Shape Memory Alloy Reinforced Concrete Beams," *Engineering Structures*, V. 49, Apr. 2013, pp. 893-904. doi: 10.1016/j.engstruct.2012.12.041

15. Saiidi, M. S., and Wang, H., "Exploratory Study of Seismic Response of Concrete Columns with Shape Memory Alloys Reinforcement," *ACI Structural Journal*, V. 103, No. 3, May-June 2006, pp. 436-443.

16. Youssef, M. A.; Alam, M. S.; and Nehdi, M., "Experimental Investigation on the Seismic Behavior of Beam-Column Joints Reinforced with Superelastic Shape Memory Alloys," *Journal of Earthquake Engineering*, V. 12, No. 7, 2008, pp. 1205-1222. doi: 10.1080/13632460802003082

17. Nehdi, M.; Alam, M. S.; and Youssef, M. A., "Seismic Behaviour of Repaired Superelastic Shape Memory Alloy Reinforced Concrete Beam-Column Joint," *Smart Structures and Systems*, V. 7, No. 5, 2011, pp. 329-348. doi: 10.12989/sss.2011.7.5.329

18. CAN/CSA A23.3-04 (R2010), "Design of Concrete Structures," CSA Group, Toronto, ON, Canada, 2004, 352 pp.

19. Morcos, M., "Seismic Behaviour of SMA-Reinforced Slender Concrete Shear Walls," master's thesis, York University, Toronto, ON, Canada, 2021, 446 pp.

20. FEMA 461, "Interim Testing Protocols for Determining the Seismic Performance Characteristics of Structural and Nonstructural Components," Applied Technology Council, Redwood City, CA, 2007, 138 pp.

21. ATC-24, "Guidelines for Cyclic Seismic Testing of Components of Steel Structures," Applied Technology Council, Redwood City, CA, 1992, 58 pp.

22. Eshghi, N., "Behaviour and Analysis of Strain Hardening Fiber Reinforced Cementitious Composites Under Shear and Flexure," MASc thesis, York University, Toronto, ON, Canada, 2018, 209 pp.
23. ASTM C1856/C1856M-17, "Standard Practice for Fabricating and Testing Specimens of Ultra-High Performance Concrete," ASTM International, West Conshohocken, PA, 2017, 4 pp.
24. Soto Rojas, M. A., "Behavior of Engineered Cementitious Composite-Repaired Superelastic-Shape Memory Alloy Reinforced Shear Walls," MASc thesis, York University, Toronto, ON, Canada, 2020, 289 pp.
25. Park, R., "State-of-the-Art Report: Ductility Evaluation from Laboratory and Analytical Testing," *Proceedings of the Ninth World Conference on Earthquake Engineering*, Tokyo-Kyoto, Japan, Aug. 1988, 12 pp.
26. Oesterle, R. G.; Fiorato, A. E.; Johal, L. S.; Carpenter, J. E.; Russell, H. G.; and Corley, W. G., "Earthquake Resistant Structural Walls - Tests of Isolated Walls," Portland Cement Association, Skokie, IL, 1976, 328 pp.

APPENDIX

The Appendix contains additional material supporting the discussion contained in the preceding journal paper.

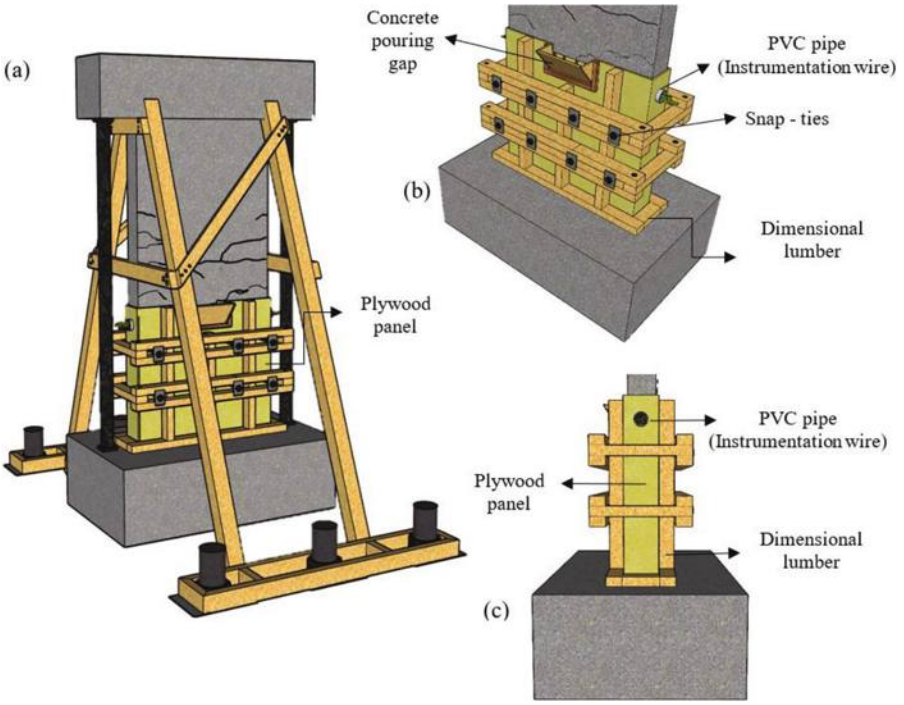

Fig. A1—Formwork design for plastic hinge.

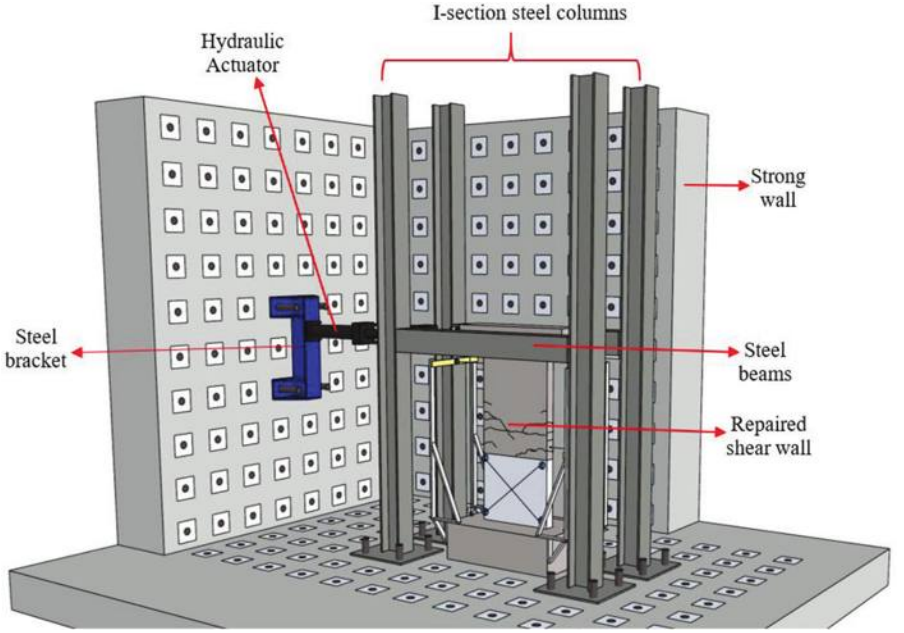

Fig. A2—Test setup assembly.

ARE YOU A RESEARCHER?

SIGN UP FOR ORCID TODAY!

ORCID provides a persistent digital identifier that distinguishes you from every other researcher and, through integration in key research workflows such as manuscript and grant submission, supports automated linkages between you and your professional activities, ensuring that your work is recognized.

Individuals may use ORCID services freely and it's as easy as **1-2-3**:

1. REGISTER
2. ADD YOUR INFO
3. USE YOUR ORCID ID

For more information and to register, visit:

WWW.ORCID.ORG

NEW Symposium Publications from ACI

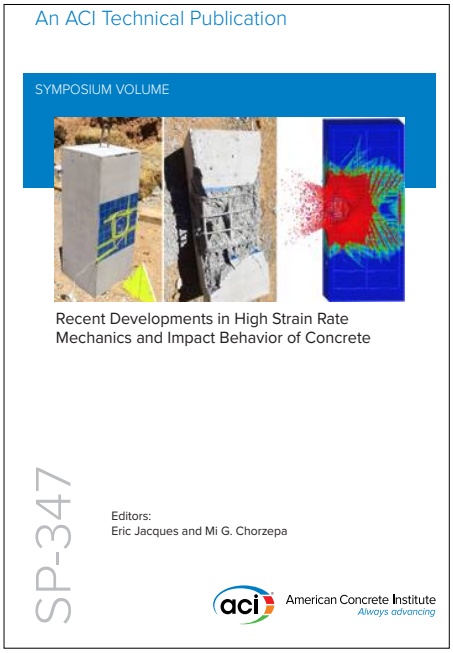

SP-347: Recent Developments in High Strain Rate Mechanics and Impact Behavior of Concrete

This Symposium Volume reports on the latest developments in the field of high-strain-rate mechanics and behavior of concrete subject to impact loads. This effort supports the mission of ACI Committee 370, Blast and Impact Load Effects, to develop and disseminate information on the design of concrete structures subjected to impact, as well as blast and other short-duration dynamic loads.

Available in PDF format: $69.50
(ACI members: $39.00) ($30.50 savings)

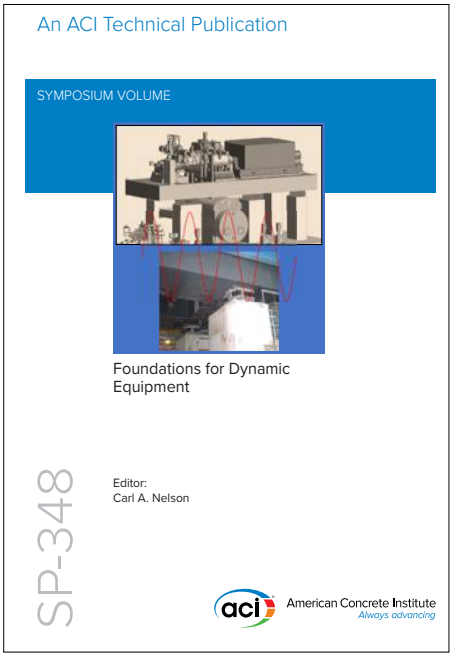

SP-348: Foundations for Dynamic Equipment

This special publication grew out of the Technical Session titled “Application of ACI 351-C Report on Dynamic Foundations,” held at the ACI Spring 2019 Convention in Québec City, Québec. Following this event, ACI Committee 351 decided to undertake a special publication with contributions from those session participants willing to develop their presentations into full-length papers. Three papers included in the current publication were contributed by these presenters and their coauthors, with six additional papers provided by others.

Available in PDF format: $69.50
(ACI members: $39.00) ($30.50 savings)

American Concrete Institute
+1.248.848.3700 • www.concrete.org

ACI STRUCTURAL JOURNAL TECHNICAL PAPER

Title No. 120-S77

Comparison of Strength-Assessment Methods for Shear-Critical Reinforced Concrete Rectangular Columns

by Maria C. Olaya, Mario E. Rodriguez, José I. Restrepo, and Luis H. Valdivieso

Shear failures are one of the most brittle modes of response in reinforced concrete columns subjected to earthquake-induced lateral drifts, notably if the failure occurs before the flexural strength is reached. Columns exhibiting this failure mode are termed shear-critical and are associated with the loss of the column's axial load-carrying capacity. Using a database of tests on 38 large-sized rectangular and square columns that exhibited this mode of failure, this paper reviews 10 methods published in the literature and compares their predictive capabilities. This paper shows significant differences between the methods, with the methods in Pan and Li (2013) and ASCE/SEI 41-13 being assessed as the most accurate.

Keywords: assessment methods; columns; earthquakes; lateral loading; shear failure; strength.

INTRODUCTION

Failure of shear-critical columns is one of the most undesirable behavioral modes in reinforced concrete structures. Such failures are inherently brittle and can lead to the loss of gravity load-carrying capacity. This paper defines shear-critical columns as those where the longitudinal strains in the extreme fiber in the concrete and the tensile strains in the longitudinal reinforcement induced by combined flexure and axial force at the column ends are lower than those used to compute the capacity. A more descriptive definition of this type of failure is given in the paper. Failures of this type are more commonly found in the aftermath of an earthquake in columns of older buildings that were subjected to double curvature when side swaying. An accurate assessment of the shear strength of columns of old buildings in seismic regions is needed to support a decision if a column should be retrofitted. This paper examines 10 methods that can be used to assess the strength of shear-critical columns, namely: 1) Priestley et al. (1994); 2) Bentz (2000); 3) Priestley et al. (2007); 4) Pan and Li (2013); 5) ASCE/SEI 41-13 (ASCE 2014); 6) Pujol et al. (2016); 7) ASCE/SEI 41-17 (ASCE 2017); 8) Hua et al. (2019); 9) ACI 318-19 (ACI Committee 318 2019) Method A; and 10) ACI 318-19 Method B. The methods proposed by Priestley et al. (1994, 2007), Bentz (2000), Pan and Li (2013), ASCE/SEI 41-13, ASCE/SEI 41-17, and Hua et al. (2019) have also been developed to capture flexure-shear failure in columns, which occurs after the column reaches its flexural strength. Such a failure mode is not examined in this paper.

RESEARCH SIGNIFICANCE

Many columns in older buildings in seismic regions could be classified as shear-critical. Shear-critical columns have a mode of response that is inherently brittle and whose failure compromises the columns' gravity load-carrying capacity. This paper examines the predictive capabilities of 10 methods that could be used to assess the strength of normalweight reinforced concrete shear-critical columns. Predicted shear strengths are compared with those measured for 38 large-scale square- and rectangular-section columns exhibiting such a failure mode.

PREDICTIVE SHEAR STRENGTH MODELS

This section briefly reviews 10 methods suitable for assessing the strength of shear-critical square and rectangular normalweight columns. The methods are presented in chronological order from the date the method was published.

Priestley et al. (1994) method

This method belongs to the family of superimposed parallel-angle truss and diagonal strut mechanisms of shear transfer (refer to Fig. 1) proposed simultaneously by Shohara and Kato (1981) and Minami and Wakabayashi (1981). These researchers fixed the angle of the truss to 45 degrees, and the angle of inclination of the diagonal strut α_S was determined from equilibrium following several assumptions made to find the share of the shear force carried by each mechanism. Ichinose (1992) and Watanabe and Ichinose (1992) made the angle of the parallel-angle truss a function of concrete compressive strength, the transverse reinforcement ratio, and its yield strength. They limited it to no less than 26 degrees, following the recommendation by Thürlimann (1979). As described next, Priestley et al. (1994) used an angle of inclination of 30 degrees to the vertical for the truss mechanism. This shear-transfer mechanism through a parallel-angle truss and a diagonal strut is straightforward and intuitive. However, overlapping two compressive stress fields having different orientations creates some conceptual difficulties. The nominal shear strength in the Priestley et al. (1994) method is given by the sum of three independent mechanisms

$$V_n = V_c + V_s + V_N \quad (1)$$

ACI Structural Journal, V. 120, No. 4, July 2023.

MS No. S-2022-266.R1, doi: 10.14359/51738722, received December 8, 2022, and reviewed under Institute publication policies.

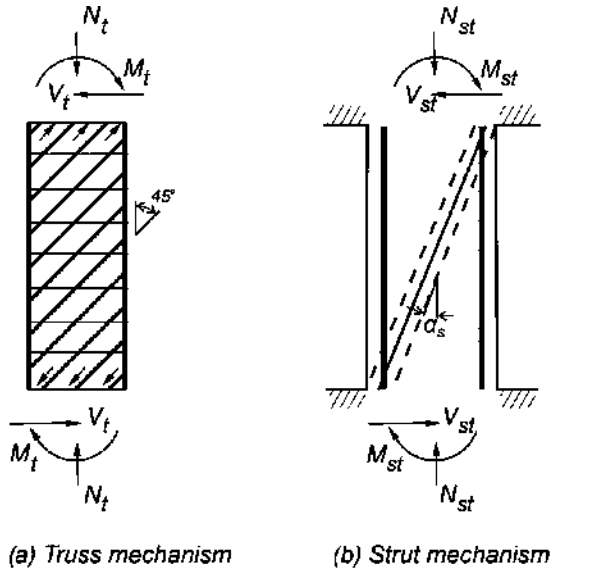

Fig. 1—Earliest truss-and-strut model of shear resistance with truss mechanism with compressive stress field inclined at 45 degrees and diagonal strut inclined at angle α_s with vertical. (Adapted from Shohara and Kato [1981].)

where V_c is the shear force carried by the concrete, whose magnitude depends on the ductility level; V_s is the shear force carried by the transverse reinforcement; and V_N is the shear force carried by the diagonal strut. The shear force sum $V_c + V_s$ is the contribution of the truss mechanism to shear resistance, as first envisioned by Shohara and Kato (1981) and Minami and Wakabayashi (1981).

In Eq. (1), the shear force carried by the concrete is given by

$$V_c = k_d\sqrt{f_c'}A_e \text{ (MPa)} \tag{2}$$

where parameter k_d depends on the displacement ductility and whether the columns are subjected to uniaxial or biaxial loading; and the effective shear area, A_e, is made equal to $0.8A_g$, where A_g is the gross area of the concrete section. For uniaxial loading, when the member displacement ductility is less than 2 or greater than 4, k_d equals 0.29 and 0.1, respectively. Factor k_d varies linearly in the range of ductility values from 2 to 4.

In rectangular columns, the shear force carried by the transverse reinforcement, V_s, to be used in Eq. (1) is

$$V_s = (A_v f_{yt} h'/s)\cot\theta \tag{3}$$

where A_v is the area of shear reinforcement within spacing s; f_{yt} is the yield strength of transverse reinforcement; θ is the angle of inclination of the diagonal compressive stress field to the vertical and was made equal to 30 degrees; h' is the distance between the perimeter hoop centers; and s is the center-to-center spacing of transverse reinforcement.

The contribution of the axial load component, V_N, is given by

$$V_N = N_u\tan\alpha_P = \frac{h-c}{2a_v}N_u \tag{4}$$

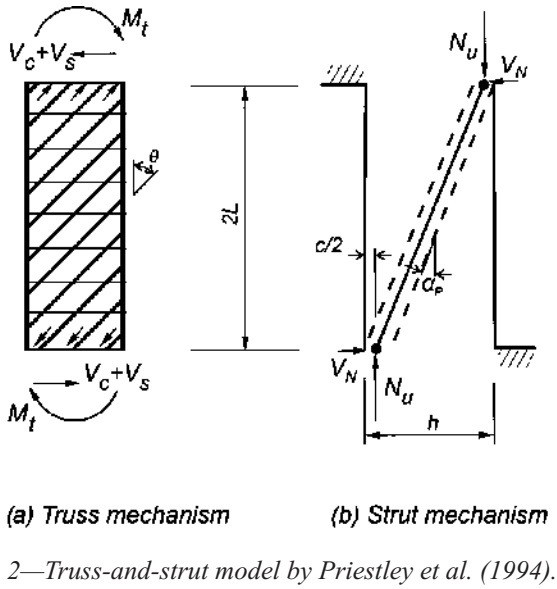

Fig. 2—Truss-and-strut model by Priestley et al. (1994).

where N_u is the axial load acting on the column, defined as positive in compression; h is the column depth; c is the flexural compression zone depth; and a_v is the shear span given by L for a cantilever column or the length of a column from the critical section to the point of inflection. In this method, the axial force N_u is assumed to act at $c/2$ at the column end, where the maximum bending moment occurs (refer to Fig. 2). A difficulty with this method is that the value of c has to be found by iterations using a section moment-curvature.

Response-2000 (Bentz 2000)

Response-2000 by Bentz (2000) is a program that adapts the Modified Compression Field Theory (Vecchio and Collins 1986) for calculating the force-displacement response of prismatic beams and columns. Among several other calculations, this program computes the nominal shear strength through numerical integration of the shear stresses in a sectional analysis. Response-2000 makes the kinematic assumption that plane sections remain plane, uses average stress-average strain constitutive material relationships, and incorporates a limit of the shear stresses at crack interfaces.

Priestley et al. (2007) method

In 2000, Kowalsky and Priestley modified the method proposed by Priestley et al. (1994) for circular columns, and in 2007, Priestley et al. extended it for application to rectangular columns. In this method, the nominal shear strength in a rectangular column is the sum of the three independent mechanisms given by Eq. (1), with changes to the shear strength contributed by the concrete, V_c, and the transverse reinforcement, V_s, as follows

$$V_c = \alpha\beta\left(0.29\sqrt{f_{ce}'}\right)A_e \text{ (MPa)} \tag{5}$$

$$V_s = \frac{A_v f_{yt}(h-c-c_o)}{s}\cot\theta \tag{6}$$

where $1 \le \alpha = 3 - (a_v/h) \le 1.5$; $\beta = 0.5 + 20\rho_l \le 1$; f_{ce}' is the expected concrete compressive strength; $\theta = 30$ degrees; c is the neutral axis depth; c_o is the cover to the centerline of

the perimeter hoop; and ρ_l is the ratio of the area of longitudinal reinforcement to the gross concrete area perpendicular to that reinforcement.

Pan and Li (2013) method

This method belongs to the family of superimposed truss and diagonal strut mechanisms of shear transfer previously discussed. However, in this method, the authors use a variable angle instead of a parallel truss, and they estimate the crack critical angle based on minimizing the external work caused by a unit shear force.

As in the Priestley et al. (1994) method, the nominal shear strength in this method is given by the sum of three components (refer to Eq. (1)). The shear force carried by the transverse reinforcement, V_s, is expressed by Eq. (3), where h' is replaced by d_v, defined as the effective shear depth taken as the flexural lever arm, which need not be taken less than $0.9d$. In Eq. (3), θ is defined as follows

$$\theta = \arctan\left(\frac{n\rho_v + \zeta_2\frac{\rho_v b_w d_v}{\rho_v A_g}}{1 + n\rho_v}\right)^{1/4} \quad (7)$$

where $n = E_s/E_c$; E_s and E_c are the modulus of elasticity of reinforcing steel and concrete, respectively; and parameter ζ_2 equals 0.57 and 1.57 for columns with fixed-fixed and fixed-pinned ends, respectively.

The shear force carried by the concrete in the truss model is

$$V_c = \beta b_w d_v \sqrt{f_c'} \text{ (MPa)} \quad (8)$$

where β is expressed as (Bentz et al. 2006)

$$\beta = \frac{0.40}{1 + 1500\varepsilon_x}\frac{1300}{1000 + s_{ze}} \quad (9)$$

where s_{ze} is the effective crack spacing; and ε_x is the longitudinal strain at the middepth of the cross section. Pan and Li (2013) express ε_x in Eq. (9) as a function of $V_c + V_s$, N_u, θ, E_s, and A_s (area of longitudinal tension reinforcement), leading to a closed-form solution for V_c.

For defining the contribution of the axial load component, V_N, Pan and Li (2013) equal the shear deformation produced by the truss model and that of the strut model; thus, they remove the incompatibility between the two mechanisms of shear transfer, making it conceptually clear

$$\frac{V_c + V_s}{K_t} = \frac{V_N}{K_a} \quad (10)$$

where K_a and K_t are the shear stiffness of the strut model and the truss model, respectively, and these coefficients are defined in Pan and Li (2013).

From Eq. (10), the contribution of the axial load component, V_N, is given by

$$V_N = (V_c + V_s)(K_a/K_t) \quad (11)$$

ASCE/SEI 41-13 (2014)

The assessment and retrofit standard ASCE/SEI 41-13 was adopted with some modifications from the Sezen and Moehle (2004) method for computing the shear strength of reinforced concrete rectangular columns. In these two methods, the nominal shear strength in a rectangular column is the sum of concrete and transverse reinforcement mechanisms

$$V_n = k_s(V_s + V_c) \quad (12)$$

where k_s is a shear strength factor that decreases with ductility and is equal to 1 in shear-critical columns.

In these methods, the contribution of the transverse reinforcement to the shear strength is given by the traditional "45-degree" truss

$$V_s = A_v f_{yt} d_e/s \quad (13)$$

where the depth d_e is the distance from the extreme fiber in compression to the resultant tensile force in the Sezen and Moehle (2004) method, whereas $d_e = 0.8h$ in ASCE/SEI 41-13. This is the only difference between these two methods.

The contribution of the concrete to the shear strength, V_c, is based on the assumption of diagonal tension failure, and it is assumed that this failure is related to the principal tensile stress acting in the column, σ_1, which, in an x-y plane, is defined as

$$\sigma_1 = \frac{\sigma_x + \sigma_y}{2} + \sqrt{\left(\frac{\sigma_x - \sigma_y}{2}\right)^2 + \tau^2} \quad (14)$$

where σ_x and σ_y are the normal stresses in the x- and y-directions, respectively, taken as positive in tension; and τ is the shear stress. This method assumes $\sigma_x = 0$ and makes $\sigma_y = -N_u/A_g$, where N_u is defined as positive in compression and equal to zero in tension, and A_g is the column gross-section area. With these definitions, Eq. (14) can be solved for τ as follows

$$\tau = \sigma_1\sqrt{1 + \frac{N_u}{\sigma_1 A_g}} \quad (15a)$$

Sezen and Moehle (2004) made the direct tensile strength of concrete $\sigma_1 = 0.5\sqrt{f_c'}$ MPa, which is in reasonable agreement with Gopalaratnam and Shah (1985) and Zheng et al. (2001) for normalweight concrete. As a result, the shear stress associated with the direct tensile strength of concrete is given by

$$\tau = 0.5\sqrt{f_c'}\sqrt{1 + \frac{N_u}{0.5\sqrt{f_c'}A_g}} \text{ (MPa)} \quad (15b)$$

V_c is defined as the product of the shear stress, τ, given by Eq. 15(b), and an effective concrete area equal to $0.8A_g$. Following the recommendation of Joint ASCE-ACI Task Committee 426 (1973), this method includes an empirical correction to relate Eq. (15) with V_c as follows

$$V_c = k_s\left[0.5\sqrt{f_c'}\sqrt{1 + \frac{N_u}{0.5\sqrt{f_c'}A_g}}\right]\frac{0.8A_g}{a_v/d_e} \text{ (MPa)} \quad (16)$$

where $a_v/d_e \in [2, 4]$ and $k_s = 1.0$ in shear-critical columns. In Eq. (16), ASCE/SEI 41-13 makes the effective shear area equal to $0.8A_g$.

Pujol et al. (2016) method

Pujol et al. (2016) used a Mohr-Coulomb failure criterion with a tension cutoff (Paul 1961) as the basis for the development of a method to compute the strength of shear-critical rectangular columns. The nominal shear strength in a shear-critical column is given by the product of a shear stress, τ_n, times a shear area A_{cc}

$$V_n = \tau_n A_{cc} \tag{17}$$

where A_{cc} is the core cross-sectional area defined by the centerline of the perimeter rectilinear hoops; and τ_n is a nominal shear strength given by the smaller of the stresses τ_1 and τ_2 computed for Limit 1 and Limit 2, respectively, in the Mohr-Coulomb failure criterion with a tension cutoff (refer to Fig. 3). These stresses are given by (to achieve consistency, some terms defined by Pujol et al. [2016] have been redefined in this paper)

$$\tau_1 = \frac{1}{2}\sqrt{\left[f'_{ceff} + \frac{k_c - 1}{k_c + 1}\left(\sigma_a + \sigma_t - f'_{ceff}\right) + \left(\sigma_a - \sigma_t\right)\right]\left[f'_{ceff} + \frac{k_c - 1}{k_c + 1}\left(\sigma_a + \sigma_t - f'_{ceff}\right) - \left(\sigma_a - \sigma_t\right)\right]} \tag{18}$$

$$\tau_2 = \sqrt{(\sigma_a + f_{te})(\sigma_t + f_{te})} \tag{19}$$

where f_{ceff}' is the effective compressive concrete strength defined by these researchers as $2/3f_c'$ on the basis of the work on concrete plasticity by Nielsen (1998); and k_c is a concrete confinement coefficient. Pujol et al. (2016) used $k_c = 4$ as a simplification of the term proposed by Richart et al. (1929) of $k_c = 4.1$. Using $k_c = 4$ defines the cohesion and friction parameters $k_1 = 1/4$ and $k_2 = 0.75$ in the Mohr-Coulomb failure criterion (refer to Fig. 3(b)). In Eq. (19), $f_{te} = 0.083\sqrt{f_c'}$ MPa is an effective concrete tensile strength assumed to act in a section not subjected to curvature. Finally, in Eq. (18) and (19), the mean transverse stress, σ_t, and the mean axial stress, σ_a, are given by

$$\sigma_t = p_{we} f_{yt} \tag{20}$$

where the ratio $p_{we} = A_v/(b_c s)$ is the cross-sectional area of transverse reinforcement A_v divided by the product of core width b_c times stirrup spacing s

$$\sigma_a = \frac{N_u + T_e}{A_{cc}} \tag{21}$$

Unlike the assumption made of no curvature for defining the effective tensile strength in concrete, the tension force T_e in this method is computed assuming the presence of curvature in the section, for which the authors give the following simplified equation

$$T_e = \frac{1}{4} A_{st} f_y \left(1 - \frac{N_u}{0.3 f_c' A_g}\right) \tag{22}$$

where A_{st} is the total cross-sectional area of longitudinal reinforcement.

ASCE/SEI 41-17 (2017) and New Zealand (MBIE 2018) methods

The shear strength equations in ASCE/SEI 41-17 and the New Zealand Seismic Assessment Guidelines (MBIE 2018) adopted the model proposed by Sezen and Moehle (2004) with some modifications. In these references, the equations are to be used with lower-bound or expected strengths. In

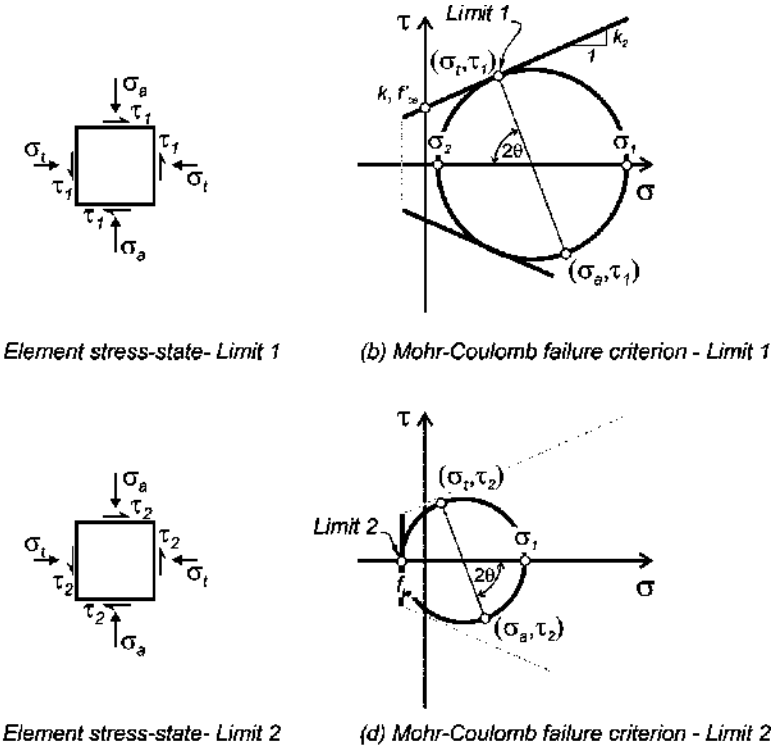

(a) Element stress-state- Limit 1 (b) Mohr-Coulomb failure criterion - Limit 1

(c) Element stress-state- Limit 2 (d) Mohr-Coulomb failure criterion - Limit 2

Fig. 3—Truncated Mohr-Coulomb failure criterion used in method proposed by Pujol et al. (2016).

the context of this paper, where methods are compared with a data set of test results, the actual mechanical properties of the concrete cylinder and yield strength of the reinforcement are known. For this reason, the equations are rewritten in terms of the nominal shear strength V_n as follows

$$V_n = k_s \left[\begin{array}{l} \alpha_{Col}\left(\frac{A_v f_y d_e}{s}\right) + \\ \left(\frac{0.5\sqrt{f_c'}}{a_v/d_e}\sqrt{1+\frac{N_u}{0.5A_g\sqrt{f_c'}}}\right)0.8A_g \end{array} \right] \text{(MPa)} \quad (23)$$

where all variables except α_{Col} were previously defined under the ASCE/SEI 41-13 method; and α_{Col} is a parameter that evaluates the effectiveness of the transverse reinforcement in resisting shear: $\alpha_{Col} = 1.0$ for $s/d_e \le 0.75$, $\alpha_{Col} = 0.0$ for $s/d_e \ge 1.0$, and α_{Col} varies linearly for s/d_e between 0.75 and 1.0.

Hua et al. (2019) method

The method proposed by Hua et al. (2019) determines the nominal shear strength as one given by three different shear-resisting mechanisms, namely: 1) the truss mechanism V_{truss}; 2) the diagonal tension mechanism, $V_{diag\text{-}tension}$; and 3) the strut-compression mechanism, $V_{strut\text{-}compression}$. According to this method, the nominal shear strength is the maximum of the strengths computed for the three mechanisms

$$V_n = max(V_{truss}, V_{diag\text{-}tension}, V_{strut\text{-}compression}) \quad (24)$$

where the shear resisted by the truss mechanism, V_{truss}, is given by

$$\text{If } V_s \ge 0.1V_{truss\text{-}tension},$$

$$V_{truss} = min\begin{cases} V_{truss\text{-}tension} = k_s\left(V_c + V_s\right) = \\ k_s\left[\left(\frac{f_{ct}}{a_v/d}\sqrt{1+\frac{N_u}{f_{ct}A_g}}\right)\alpha_1 A_g + \alpha_2 A_v f_{yt}\, d/s\right] \\ V_{truss\text{-}compression} = k_s\zeta f_c' A_g \alpha_3 \end{cases} \text{(MPa)} \quad (25)$$

$$\text{and if } V_s < 0.1V_{truss\text{-}tension},$$

$$V_{truss} = 0$$

taking $f_{ct} = 0.5\sqrt{f_c'}$ MPa, $\alpha_1 = 1.0$; $\alpha_2 = 0.9$; $\alpha_3 = 0.3$; $\zeta = 3.35/\sqrt{f_c'}$ MPa ≤ 0.52; and making $k_s = 1$ in shear-critical columns. Furthermore, this method defines d as the distance from the extreme compression fiber to the extreme longitudinal reinforcement in tension.

The shear resisted by the diagonal tension mechanism $V_{diag\text{-}tension}$ is given by

$$V_{diag\text{-}tension} = k_s V_c = k_s\left(\frac{f_{ct}}{a_v/d}\sqrt{1+\frac{N_u}{f_{ct}A_g}}\right)\alpha_1 A_g \text{ (MPa)} \quad (26)$$

The shear resisted by the strut-compression mechanism, $V_{strut\text{-}compression}$, is given by

$$V_{strut\text{-}compression} = \alpha_4 k_s K\zeta f_c' k d b_w \cos\theta_{str} \quad (27)$$

where b_w is the width of a rectangular column; $\alpha_4 = 1.2$; $\zeta = min(3.35/\sqrt{f_c'}, 0.52)$ (MPa) is the softening coefficient of cracked concrete in compression; and kd is the depth of flexural compression zone of an elastic column and is computed from Eq. (28)

$$kd = (0.25 + 0.85N_u/(A_g f_c'))h \quad (28)$$

In Eq. (27), K is given by

$$K = 1 + 0.9(F_{yh}/\zeta f_c' A_{str}) \le 1.67 \quad (29)$$

where $A_{str} = kdb_w$; and F_{yh} is the yield force of horizontal ties and is given by

$$F_{yh} = \frac{3}{4}\left(1 - \frac{h}{4a_v}\right)\left(\sum_{i=1}^{n_t} A_v^i f_{yt}\right) \quad (30)$$

where n_t is the total number of ties along length a_v.

Angle θ_{str} in Eq. (27) is given by

$$\theta_{str} = \tan^{-1}\left(\frac{l_u}{h - 2kd/3}\right) \quad (31)$$

Considering the two truss mechanisms defined by Hua et al. (2019), it can be shown that V_{truss} is always larger than $V_{diag\text{-}tension}$. Therefore, in this method, the shear strength of a column becomes the maximum of: 1) the shear resisted by the truss mechanism V_{truss}; and 2) the shear resisted by a strut-compression mechanism, $V_{strut\text{-}compression}$.

ACI 318-19 methods

The two design methods found in ACI 318-19 are included in this paper as assessment methods because these methods are used in some parts of the world for this purpose.

The nominal shear strength at a column section is calculated by

$$V_n = V_c + V_s \quad (32)$$

The column's cross section needs to satisfy

$$V_n \le V_c + 0.66\sqrt{f_c'} b_w d \text{ (MPa)} \quad (33)$$

For nonprestressed members and $A_v \ge A_{v,min}$, the nominal shear strength provided by concrete, V_c, is given by either Eq. (34a) for Method A or Eq. (34b) for Method B

$$V_c = \left[0.17\sqrt{f_c'} + \frac{N_u}{6A_g}\right] b_w d \text{ (MPa)} \quad (34a)$$

$$V_c = \left[0.66(\rho_w)^{1/3}\sqrt{f_c'} + \frac{N_u}{6A_g}\right] b_w d \text{ (MPa)} \quad (34b)$$

where $\rho_w = A_s/(b_w d)$; and A_s is the area of nonprestressed longitudinal tension reinforcement. In evaluating the paper's ACI 318-19 methods, A_s was computed as $3/8A_{st}$ (Restrepo and Rodriguez 2013). The axial stress $N_u/(6A_g)$ in Eq. (34) should not be taken greater than $0.05f_c'$ MPa, and the shear

strength provided by concrete, V_c, should not be taken greater than

$$V_c = 0.42\sqrt{f_c'}b_w d \text{ (MPa)} \quad (35)$$

Additionally, in this method, the shear strength provided by shear reinforcement V_s is given by

$$V_s = A_v f_{yt} d/s \quad (36)$$

According to ACI 318-19, the depth d is the distance from the extreme compression fiber to the centroid of the longitudinal reinforcement in tension, but the Code gives no equation to determine this depth. Guerrini and Restrepo (2018) proposed a simple expression to compute d, which was used in the evaluation of the ACI 318-19 methods in the paper

$$d = \left[0.65\left(0.76\frac{N_u}{A_g f_c'} + 0.28\right) + \frac{1}{2}\right]h \quad (37)$$

In evaluating the ACI 318-19 methods carried out later, ACI 318-19 Method A and Method B refer to the cases of computing V_n using Eq. (34a) and (34b), respectively.

COLUMN DATABASE

To compare the predictive capabilities of the different methods described previously, a database of 38 shear-critical columns was compiled from reversed cyclic tests reported by Ramirez and Jirsa (1980), Kuramoto and Minami (1992), Yoshimura and Nakamura (2002), Kabeyasawa et al. (2002), Tran (2010), Nakamura and Yoshimura (2014), Ou and Kurniawan (2015), Ghannoum et al. (2015), Li et al. (2019), and Huy et al. (2022). The brittle-most behavior in shear-critical columns is when failure occurs before flexural yielding—that is, when a column meets three criteria: 1) the column is subjected to double curvature and exhibits a distinct diagonal shear band at failure which passes through the point of inflection; 2) the maximum tensile strain in the longitudinal does not exceed $0.85\varepsilon_y$; and 3) the peak compressive strain does not exceed ε_c'. The latter two criteria are most often determined by analysis with peak compressive strain defined by Eq. (38) (Collins and Mitchell 1991)

$$\varepsilon_c' = \frac{f_c'}{E_c}\frac{n_1}{n_1 - 1} \text{ (MPa)} \quad (38)$$

where

$$n_1 = 0.8 + (f_c'/17) \text{ (MPa)} \quad (39)$$

The aforementioned definition implies that columns can also be shear-critical after yielding occurs at the column ends. An example of such columns is those whose density of transverse reinforcement is greater at the column ends than at the column midheight.

All columns in the database for this study were tested in double curvature. Because of possible size effects (Yu and Bažant 2011), only columns with a depth of at least 300 mm (11.8 in.) were selected for the database. Tables 1 and 2 list the key parameters of each of the columns. In Table 2, d_b is the nominal diameter of the longitudinal bar, d_{bt} is the nominal diameter of transverse reinforcement, ρ_v is the ratio of A_v to $b_w s$, and c_c is the clear cover of reinforcement. Figure 4 depicts the distribution of key variables, where it is evident that:

1. The 38 columns in the database have a low to moderate axial load ratio.
2. Twenty-eight columns have concretes with a measured cylinder compressive strength, $\hat{f}_c'$, lower than 42 MPa (6 ksi); and 10 columns have measured ultra-high-strength concrete $\hat{f}_c' \geq 90$ MPa (13.1 ksi).
3. Thirty-six columns have a depth between 300 and 600 mm (11.8 and 23.6 in.), with the distribution of depth in this range being rather uniform, and two columns are 800 mm deep (31.5 in.).
4. Twenty-six columns have longitudinal reinforcement with a measured yield strength $\hat{f}_y$ of 376 and 455 MPa (54.5 and 66.0 ksi), two columns have longitudinal reinforcement with a measured yield strength $\hat{f}_y \leq 355$ MPa (51.5 ksi), and 10 columns have longitudinal reinforcement with a measured yield strength of 735 MPa (106.6 ksi).
5. All the other variables (that is, f_{yt}, ρ_l, ρ_v, and a_v/h) have a distribution that is somewhat uniform or normal.

EVALUATION OF METHODS' PREDICTIVE CAPABILITIES

The box plots depicted in Fig. 5 summarize the 10 methods' predictive capabilities. The vertical axis in this figure is the ratio between the shear strength measured during testing versus the nominal shear strength predicted by a given method for the column database, or V_{test}/V_n. The median (that is, 50% percentile) of the ratios is shown with a thick horizontal line inside the box. The upper and lower ends of the box are the 25 and 75% quartiles. The depth of a box is the interquartile range (IQR), which indicates the magnitude of the spread. The whiskers above and below a box extend to either the farthest (that is, maximum or minimum) data point or 1.5 IQR from the quartile. When the latter condition controls, the most distant point is defined as an outlier and plotted with a black dot. Table 3 contains all the quantitative data supporting the box plots shown in Fig. 5. Because of space restrictions, the following paragraphs will largely compare the methods qualitatively.

In Fig. 5, the box plots computed for each method were sorted by the median computed for each method. Values of the median below unity indicate that the method overpredicts the experimental maximum shear force for at least 50% of the columns. That is, such a method has an unconservative bias. Conversely, values of the median above unity indicate that the method underpredicts the experimental maximum shear force for at least 50% of the columns, meaning that such a method has a conservative bias.

The median of the two methods by Priestley et al. (1994, 2007) and that of Hua et al. (2019) exhibit an unconservative bias and have the smallest IQR of all the methods examined herein. These methods will largely overpredict the shear force capacity of a column, as indicated by the ratios of V_{test}/V_n at the 25 and 75% quartiles. The two Priestley et al. methods do not state how the neutral axis depth, c, required in Eq. (4) and (16), is calculated. Here, this depth for each

Table 1—Relevant properties of rectangular test columns

No.	Designation	References	h, mm	b_w, mm	$\hat{f}_c'$, MPa	$\hat{f}_y$, MPa	$\hat{f}_{yt}$, MPa	ρ_l, %
1	CUS	Umehara and Jirsa (1982)*	406	229	34.9	441	414	3.1%
2	UNIT_1_1	Bett et al. (1985)*	305	305	29.9	462	414	2.4%
3	D1	Ousalem et al. (2004)*	300	300	27.7	447	398	1.7%
4	D11	Ousalem et al. (2004)*	300	300	28.1	447	398	2.3%
5	D12	Ousalem et al. (2004)*	300	300	28.1	447	398	2.3%
6	D13	Ousalem et al. (2004)*	300	300	26.1	447	398	2.3%
7	D16	Ousalem et al. (2004)*	300	300	26.1	447	398	1.7%
8	N-27C	Nakamura and Yoshimura (2002)*	300	300	26.5	380	375	2.7%
9	SC-1.7-0.20	Tran (2010)	350	350	27.5	408	393	2.1%
10	B-1	Kabeyasawa et al. (2002)	300	300	18.3	338	289	1.8%
11	A1	Nakamura and Yoshimura (2014)	450	450	28.0	383	399	1.1%
12	B4	Nakamura and Yoshimura (2014)	450	450	28.0	383	399	1.7%
13	C1	Nakamura and Yoshimura (2014)	450	450	28.0	376	399	2.3%
14	S100	Nakamura and Yoshimura (2014)	450	450	25.0	383	399	1.7%
15	120C-U	Ramirez and Jirsa (1980)	305	305	30.7	450	455	2.5%
16	2C	Yoshimura and Nakamura (2002)	300	300	25.2	396	392	2.6%
17	3C	Yoshimura and Nakamura (2002)	300	300	25.2	396	392	2.6%
18	2C13	Yoshimura and Nakamura (2002)	300	300	25.2	350	392	1.7%
19	2CUS	Umehara and Jirsa (1982)	410	230	42.0	441	414	3.0%
20	A-1	Ou and Kurniawan (2015)	600	600	92.5	735	862	3.6%
21	A-2	Ou and Kurniawan (2015)	600	600	99.9	735	862	3.6%
22	A-3	Ou and Kurniawan (2015)	600	600	96.9	735	862	3.6%
23	A-4	Ou and Kurniawan (2015)	600	600	107.1	735	862	3.6%
24	B-1	Ou and Kurniawan (2015)	600	600	108.3	735	862	3.6%
25	B-2	Ou and Kurniawan (2015)	600	600	125.0	735	862	3.6%
26	B-3	Ou and Kurniawan (2015)	600	600	112.9	735	862	3.6%
27	B-4	Ou and Kurniawan (2015)	600	600	121.0	735	862	3.6%
28	4DH	Li et al. (2019)	500	500	34.0	472	448	3.2%
29	4NL	Li et al. (2019)	500	500	29.7	472	448	3.2%
30	4NH	Li et al. (2019)	500	500	30.8	472	448	3.2%
31	3DL	Li et al. (2019)	500	500	34.5	472	448	3.2%
32	3DH	Li et al. (2019)	500	500	33.8	472	448	3.2%
33	3NL	Li et al. (2019)	500	500	33.5	472	448	3.2%
34	3NH	Li et al. (2019)	500	500	32.4	472	448	3.2%
35	C-S-L	Huy et al. (2022)	800	800	43.0	473	398	3.1%
36	C-FS-L	Huy et al. (2022)	800	800	41.0	473	398	3.1%
37	C62	Kuramoto and Minami (1992)	300	300	113.8	736	735	3.8%
38	C32	Kuramoto and Minami (1992)	300	300	113.8	736	735	3.8%
				Mean	50.9	511	521	2.8%
				Maximum	125.0	736	862	3.8%
				Minimum	18.3	338	289	1.1%

*Ghannoum et al. (2015) column database.

column in the database was determined with the program Response-2000 (Bentz 2000) at the maximum measured shear force of the column being assessed. It is interesting to observe in Fig. 5 that the revised Priestley et al. (2007) method shows no improvement over the original method.

Table 2—Relevant properties of rectangular test columns (continuation)

No.	Designation	$N_u/\left(A_g\hat{f}_c'\right)$	d_b, mm	d_{bt}, mm	s, mm	ρ_v, %	c_c, mm	a_v/h
1	CUS	0.16	19.0	6.0	89.0	0.56%	25.4	1.13
2	UNIT_1_1	0.10	19.1	6.4	210.0	0.17%	25.4	1.50
3	D1	0.22	12.7	6.0	50.0	0.38%	27.5	1.00
4	D11	0.21	12.7	6.0	150.0	0.13%	27.5	1.50
5	D12	0.21	12.7	6.0	150.0	0.13%	27.5	1.50
6	D13	0.23	12.7	6.0	50.0	0.38%	27.5	1.50
7	D16	0.23	12.7	6.0	50.0	0.38%	27.5	1.00
8	N-27C	0.27	16.0	6.0	100.0	0.19%	31.0	1.50
9	SC-1.7-0.20	0.18	20.0	6.0	125.0	0.13%	25.0	1.71
10	B-1	0.27	13.0	5.0	160.0	0.08%	28.5	1.50
11	A1	0.16	19.0	10.0	300.0	0.12%	40.5	1.00
12	B4	0.16	19.0	10.0	150.0	0.23%	40.5	1.00
13	C1	0.16	22.0	10.0	75.0	0.47%	39.0	1.00
14	S100	0.18	19.0	10.0	150.0	0.23%	40.5	1.00
15	120C-U	0.19	19.1	6.4	65.3	0.32%	25.4	1.50
16	2C	0.19	15.9	6.0	100.0	0.19%	31.0	1.00
17	3C	0.29	15.9	6.0	100.0	0.19%	31.0	1.00
18	2C13	0.19	12.7	6.0	100.0	0.19%	32.5	1.00
19	2CUS	0.27	19.0	6.0	89.0	0.28%	25.0	1.11
20	A-1	0.10	32.3	12.7	450.0	0.14%	40.0	1.50
21	A-2	0.10	32.3	12.7	450.0	0.14%	40.0	1.50
22	A-3	0.10	32.3	12.7	260.0	0.24%	40.0	1.50
23	A-4	0.10	32.3	12.7	260.0	0.24%	40.0	1.50
24	B-1	0.15	32.3	12.7	450.0	0.14%	40.0	1.50
25	B-2	0.18	32.3	12.7	450.0	0.14%	40.0	1.50
26	B-3	0.20	32.3	12.7	260.0	0.24%	40.0	1.50
27	B-4	0.20	32.3	12.7	260.0	0.24%	40.0	1.50
28	4DH	0.22	25.4	9.5	100.0	0.43%	30.0	2.00
29	4NL	0.08	25.4	9.5	300.0	0.10%	30.0	2.00
30	4NH	0.24	25.4	9.5	300.0	0.10%	30.0	2.00
31	3DL	0.07	25.4	9.5	100.0	0.43%	30.0	1.50
32	3DH	0.22	25.4	9.5	100.0	0.43%	30.0	1.50
33	3NL	0.07	25.4	9.5	300.0	0.10%	30.0	1.50
34	3NH	0.23	25.4	9.5	300.0	0.10%	30.0	1.50
35	C-S-L	0.09	32.3	6.4	350.0	0.02%	40.0	2.00
36	C-FS-L	0.10	32.3	6.4	120.0	0.13%	40.0	2.00
37	C62	0.17	19.0	6.0	80.0	0.47%	24.5	1.50
38	C32	0.33	19.0	6.0	80.0	0.47%	24.5	1.50
Mean		0.18				0.24%		1.43
Maximum		0.29				0.56%		2.00
Minimum		0.07				0.02%		1.00

The three methods to the right in Fig. 5 (that is, the two ACI 318 methods and Bentz's Response-2000 method) exhibit a conservative bias. When used for assessment purposes, these methods are likely to underpredict the maximum shear force, as indicated by the ratios of V_{test}/V_n at the 25 and 75% quartiles, all of which are greater than 1. As design tools, the two ACI 318 methods, combined with the design strength reduction factor, will result in a column shear design with a very

low probability of failing in shear before the column's flexural strength is reached and likely to ensure some ductility in the column's response. It is noted that ACI 318-19 Method B is Method A with a refinement (compare Eq. (34a) and (34b)). The refinement in Method B shows no improvement in predictability over Method A, and it actually worsens it; hence, it does justify its presence in the Code.

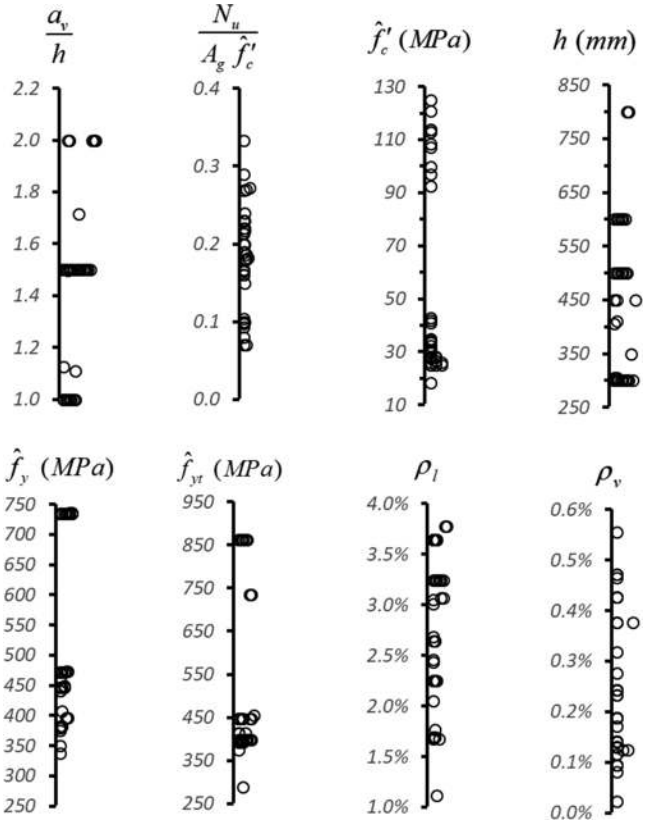

Fig. 4—Distribution of key variables in shear-critical column database.

The four methods with the lowest median bias are those by Pan and Li (2013), Pujol et al. (2016), ASCE/SEI 41-13, and ASCE/SEI 41-17. However, Pujol's and the ASCE/SEI 41-17 methods have some of the largest IQR and maximum-to-minimum data point ranges. In contrast, the methods by Pan and Li (2013) and ASCE/SEI 41-13 exhibit a reasonably small IQR of 16% and a maximum-to-minimum data point range of 43% and 50%, respectively. The median, mean, and standard deviation computed for the Pan and Li method were 0.92, 0.93, and 0.13, respectively, and for the ASCE/SEI 41-13 method were 1.09, 1.10, and 0.13, respectively.

Finally, it is also interesting to observe that, like in the previous cases where a refinement has been made to an original method, the ASCE/SEI 41-17 method—which is a refinement of the ASCE/SEI 41-13 method—does not enhance the predictability of the original method.

CONCLUSIONS

This paper reviewed 10 methods that can be used to predict the strength of shear-critical columns. Each method's predictive capabilities were analyzed against the shear strength measured for 38 square and rectangular normal-weight columns. The column database contained columns with a depth ranging between 300 and 800 mm (11.8 and 31.5 in.). A quantitative analysis of the results shows that the method of Pan and Li (2013) and the method incorporated into the standard ASCE/SEI 41-13 (2014) have the best predictive capabilities.

Two of the methods examined, those proposed by Priestley et al. (1994) and Sezen and Moehle (2004), have been revisited and refined in Priestley et al. (2007) and ASCE/SEI 41-17 (2017). This paper indicates that the refinements produce either a negligible improvement (in the case of Priestley et al.) or worsen the predictability (in the case of ASCE/SEI 41-17).

The two-column shear design methods in ACI 318-19 are often used in some parts of the world for assessing the shear

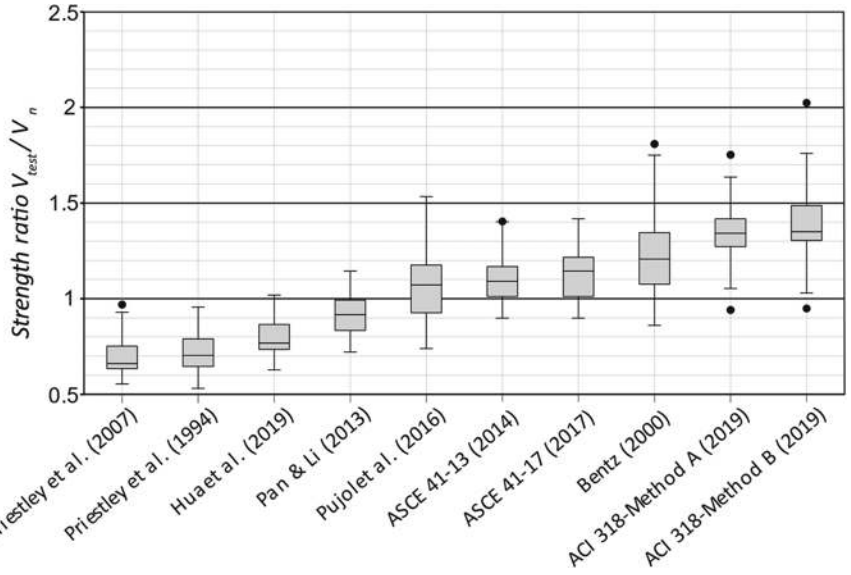

Fig. 5—Box plot diagram comparing experimental/predicted shear strength of 38 rectangular shear-critical columns predicted by 10 methods.

Table 3—V_{test} and V_{test}/V_n calculated using various methods

No.	Designation	V_{test}, kN	V_{test}/V_n									
			Priestley et al. (1994)	Bentz (2000)	Priestley et al. (2007)	Pan and Li (2013)	ASCE/SEI 41-13	Pujol et al. (2016)	ASCE/SEI 41-17	Hua et al. (2019)	ACI 318-19 A	ACI 318-19 B
1	CUS	323	0.53	1.19	0.55	0.72	0.90	0.84	0.90	0.64	1.07	1.08
2	UNIT_1_1	214	0.76	1.22	0.67	0.95	1.06	1.08	1.20	0.80	1.45	1.52
3	D1	327	0.68	1.16	0.72	0.94	1.17	1.16	1.17	0.84	1.36	1.44
4	D11	245	0.83	1.49	0.75	1.12	1.17	1.26	1.17	0.86	1.44	1.52
5	D12	251	0.85	1.47	0.77	1.14	1.20	1.29	1.20	0.88	1.47	1.56
6	D13	266	0.64	0.95	0.65	0.99	0.96	0.94	0.96	0.76	1.10	1.15
7	D16	340	0.71	1.13	0.75	0.99	1.23	1.22	1.23	0.93	1.41	1.50
8	N-27C	263	0.79	1.35	0.73	1.14	1.14	1.19	1.14	0.87	1.29	1.34
9	SC-1.7-0.20	294	0.80	1.43	0.80	1.13	1.16	1.14	1.16	0.89	1.39	1.49
10	B-1	175	0.82	1.54	0.76	1.07	1.11	1.32	1.11	0.87	*	*
11	A1	570	0.81	1.69	0.82	0.86	1.34	1.53	1.42	0.75	1.75	2.02
12	B4	578	0.70	1.29	0.71	0.84	1.15	1.22	1.15	0.65	1.46	1.57
13	C1	687	0.63	1.12	0.65	0.82	1.05	1.07	1.05	0.78	1.27	1.32
14	S100	522	0.65	1.16	0.66	0.77	1.07	1.12	1.07	0.66	1.32	1.43
15	120C-U	280	0.64	0.99	0.63	0.94	0.97	0.94	0.97	0.77	1.16	1.20
16	2C	222	0.67	1.15	0.63	0.74	1.07	1.12	1.07	0.63	1.33	1.38
17	3C	264	0.68	1.29	0.65	0.82	1.14	1.18	1.14	0.70	1.26	1.31
18	2C13	260	0.77	1.34	0.76	0.91	1.25	1.37	1.25	0.73	1.56	1.69
19	2CUS	400	0.67	1.25	0.66	0.88	1.16	1.07	1.16	0.65	1.35	1.35
20	A-1	1578	0.71	1.16	0.64	0.83	1.03	0.93	1.24	0.75	1.37	1.35
21	A-2	1638	0.71	1.16	0.64	0.84	1.03	0.93	1.23	0.75	1.36	1.34
22	A-3	1772	0.64	0.93	0.61	0.81	0.97	0.84	0.97	0.74	1.25	1.24
23	A-4	1781	0.62	0.90	0.59	0.79	0.93	0.81	0.93	0.70	1.20	1.19
24	B-1	2078	0.73	1.34	0.68	0.93	1.11	1.01	1.29	0.80	1.37	1.37
25	B-2	2298	0.70	1.34	0.65	0.88	1.07	0.97	1.21	0.76	1.40	1.40
26	B-3	2418	0.65	1.07	0.63	0.91	1.03	0.87	1.03	0.76	1.31	1.31
27	B-4	2528	0.65	1.09	0.64	0.92	1.03	0.87	1.03	0.76	1.34	1.34
28	4DH	772	0.56	0.86	0.66	0.89	0.94	0.74	0.94	0.77	0.94	0.95
29	4NL	467	0.80	1.34	0.85	0.93	1.22	0.95	1.22	0.93	1.48	1.48
30	4NH	661	0.83	1.50	0.89	1.14	1.30	1.08	1.30	0.97	1.27	1.29
31	3DL	766	0.64	0.91	0.63	0.81	0.98	0.91	0.98	0.78	1.29	1.29
32	3DH	845	0.57	0.91	0.59	0.85	0.91	0.81	0.91	0.70	1.03	1.04
33	3NL	471	0.74	1.26	0.62	0.75	0.99	0.94	0.99	0.71	1.46	1.46
34	3NH	699	0.78	1.42	0.69	0.95	1.12	1.13	1.12	0.87	1.33	1.35
35	C-S-L	1468	0.96	1.81	0.97	1.02	1.40	1.22	1.40	1.02	*	*
36	C-FS-L	1708	0.88	1.37	0.93	1.15	1.36	1.08	1.36	1.01	1.60	1.62
37	C62	758	0.71	1.07	0.70	1.13	1.15	0.97	1.15	0.91	1.39	1.39
38	C32	801	0.59	1.01	0.62	0.99	1.01	0.79	1.01	0.83	1.32	1.32
Mean			0.71	1.23	0.70	0.93	1.10	1.05	1.13	0.79	1.34	1.38
Standard deviation			0.09	0.22	0.10	0.13	0.13	0.18	0.14	0.10	0.34	0.36
Minimum			0.53	0.86	0.55	0.72	0.90	0.74	0.90	0.63	0.94	0.95
First quartile (25%)			0.64	1.07	0.63	0.83	1.00	0.92	1.00	0.73	1.27	1.29
Median			0.70	1.21	0.66	0.92	1.09	1.07	1.14	0.77	1.34	1.35
Third quartile (75%)			0.80	1.35	0.75	1.00	1.17	1.18	1.22	0.87	1.43	1.49
Maximum			0.96	1.81	0.97	1.15	1.40	1.53	1.42	1.02	1.75	2.02

*$A_v < A_{v,min}$.

assessment of rectangular columns. These methods yield the most conservative results of all the methods examined. One of the two methods is a refinement of the other method. The refinement did not yield any tangible improvement in the predictability, for which its presence in the Code as a design method does not seem justified.

AUTHOR BIOS

Maria C. Olaya *is an MS Student in structural engineering at UNAM. She received her BS in civil engineering from the Universidad Cooperativa de Colombia, Neiva, Colombia. Her research interests include seismic design and behavior of reinforced concrete structures.*

Mario E. Rodriguez, *FACI, is a Professor of structural engineering at the Universidad Nacional Autónoma de México (UNAM), Mexico City, Mexico. He received his BS in civil engineering from the Universidad Nacional de Ingeniería, Lima, Peru, and his PhD from UNAM. He is a member of ACI Committees 369, Seismic Repair and Rehabilitation, and 374, Performance-Based Seismic Design of Concrete Buildings. His research interests include seismic design and evaluation of reinforced concrete structures.*

José I. Restrepo, *FACI, is a Professor of structural engineering at the University of California San Diego, La Jolla, CA. He received his BS in civil engineering from the Universidad de Medellín, Medellín, Colombia, and his PhD from the University of Canterbury, Christchurch, New Zealand. He is a past recipient of the ACI Chester Paul Siess Award for Excellence in Structural Research. His research interests include reinforced and precast/prestressed concrete, particularly seismic design.*

Luis H. Valdivieso *is a Professor of mathematics at the Pontificia Universidad Católica del Perú (PUCP), Lima, Peru. He received his BS in statistics from PUCP, and his PhD from Katholieke Universiteit Leuven, Leuven, Belgium.*

ACKNOWLEDGMENTS

The second author gratefully acknowledges PASPA at Universidad Nacional Autónoma de México for the partial financial support of this study.

NOTATION

A_{cc}	=	core cross-sectional area
A_e	=	effective shear area
A_g	=	gross area of concrete section
A_s	=	area of longitudinal tension reinforcement
A_{st}	=	total area of longitudinal reinforcement
A_v	=	area of shear reinforcement within spacing s
a_v	=	shear span given by L for cantilever column
b_c	=	core width
b_w	=	width of rectangular column
c	=	flexural compression zone depth
c_c	=	clear cover of reinforcement
c_o	=	cover to centerline of perimeter hoop
d	=	distance from extreme compression fiber to centroid of longitudinal tension reinforcement
d_b	=	nominal diameter of longitudinal bar
d_{bt}	=	nominal diameter of shear reinforcement
d_e	=	effective depth
d_v	=	effective shear depth taken as flexural lever arm, which need not be taken less than $0.9d$
E_c	=	modulus of elasticity of concrete
E_s	=	modulus of elasticity of reinforcing steel
F_{yh}	=	yield force of horizontal ties
f_c'	=	specified compressive strength of concrete
f_{ce}'	=	expected compressive strength of concrete
f_{ceff}'	=	effective compressive strength of concrete
f_{ct}	=	direct tensile strength of concrete
f_{te}	=	effective tensile strength of concrete
f_y	=	specified yield strength of longitudinal reinforcement
f_{yt}	=	specified yield strength of shear reinforcement
$\hat{f}_c'$	=	measured compressive strength of concrete
$\hat{f}_y$	=	measured yield strength of longitudinal reinforcement
$\hat{f}_{yt}$	=	measured yield strength of shear reinforcement
h	=	column depth
h'	=	distance between perimeter hoop centers
K_a	=	shear stiffness of strut mechanism
K_t	=	shear stiffness of truss mechanism
kd	=	depth of flexural compression zone of elastic column
k_d	=	ductility-related factor
k_s	=	shear strength factor
k_1, k_2	=	cohesion and friction defining parameters
L	=	length of cantilever column
l_u	=	unsupported length of column
N_u	=	axial force
n	=	E_s/E_c
n_t	=	total number of ties along length a_v
p_{we}	=	ratio of A_v to $b_e s$
s	=	center-to-center spacing of shear reinforcement
s_{ze}	=	effective crack spacing
T_e	=	resultant tensile force
V_c	=	shear force carried by concrete
$V_{diag\text{-}tension}$	=	shear force carried by diagonal tension mechanism
V_N	=	shear force carried by diagonal strut
V_n	=	nominal shear strength
V_s	=	shear force carried by shear reinforcement
$V_{strut\text{-}compression}$	=	shear force carried by strut-compression mechanism
V_{test}	=	shear strength measured during testing
V_{truss}, $V_{truss\text{-}tension}$, $V_{truss\text{-}compression}$	=	shear forces carried by truss mechanism
α	=	factor accounting for aspect ratio
α_{Col}	=	parameter accounting for effectiveness of shear reinforcement
α_P	=	inclination of line joining centers of flexural compression at top and bottom in double bending column
α_S	=	angle of inclination of diagonal strut
β	=	factor accounting for longitudinal steel ratio
ε_c'	=	peak compressive strain
ε_x	=	longitudinal strain at middepth of cross section
ε_y	=	tensile strain at yielding of longitudinal reinforcement
θ	=	inclination between shear cracks and vertical column axis, made equal to 30 degrees
θ_{str}	=	inclination angle of diagonal compressive strut to horizontal axis
ρ_l	=	ratio of A_{st} to $b_w h$
ρ_v	=	ratio of A_v to $b_w s$
ρ_w	=	ratio of A_s to $b_w d$
σ_a	=	mean axial stress
σ_t	=	mean transverse stress
σ_x	=	normal stresses in x-direction
σ_y	=	normal stresses in y-direction
σ_1	=	principal tensile stress
τ	=	shear stress
τ_n	=	nominal shear strength given by smaller of stresses τ_1 and τ_2
τ_1	=	shear stress computed for Limit 1
τ_2	=	shear stress computed for Limit 2
ζ	=	softening coefficient of cracked concrete in compression

REFERENCES

ACI Committee 318, 2019, "Building Code Requirements for Structural Concrete (ACI 318-19) and Commentary (ACI 318R-19) (Reapproved 2022)," American Concrete Institute, Farmington Hills, MI, 624 pp.

ASCE/SEI 41-13, 2014, "Seismic Evaluation and Retrofit of Existing Buildings," American Society of Civil Engineers, Reston, VA.

ASCE/SEI 41-17, 2017, "Seismic Evaluation and Retrofit of Existing Buildings," American Society of Civil Engineers, Reston, VA.

Bentz, E. C., 2000, "Sectional Analysis of Reinforced Concrete Members," PhD thesis, Department of Civil Engineering, University of Toronto, Toronto, ON, Canada, 316 pp.

Bentz, E. C.; Vecchio, F. J.; and Collins, M. P., 2006, "Simplified Modified Compression Field Theory for Calculating Shear Strength of Reinforced Concrete Elements," *ACI Structural Journal*, V. 103, No. 4, July-Aug., pp. 614-624.

Bett, B. J.; Klingner, R. E.; and Jirsa, J. O., 1985, "Behavior of Strengthened and Repaired Reinforced Concrete Columns under Cyclic Deformations," PMFSEL Report No. 85-3, The University of Texas at Austin, Austin, TX, 82 pp.

Collins. M. P., and Mitchell, D., 1991, *Prestressed Concrete Structures*, Prentice Hall, Upper Saddle River, NJ.

Ghannoum, W.; Sivaramakrishnan, B.; Pujol, S.; Catlin, A. C.; Fernando, S.; Yoosuf, N.; and Wang, Y., 2015, "NEES: ACI 369 Rectangular Column Database," Network for Earthquake Engineering Simulation

(NEES), https://datacenterhub.org/resources/255/about. (last accessed Apr. 25, 2023)

Gopalaratnam, V. S., and Shah, S. P., 1985, "Softening Response of Plain Concrete in Direct Tension," *ACI Journal Proceedings*, V. 82, No. 3, May-June, pp. 310-323.

Guerrini, G., and Restrepo, J. I., 2018, "Extent of Plasticity in Reinforced Concrete Columns," *ACI Structural Journal*, V. 115, No. 5, Sept., pp. 1219-1230. doi: 10.14359/51702245

Hua, J.; Eberhard, M. O.; Lowes, L. N.; and Gu, X., 2019, "Modes, Mechanisms, and Likelihood of Seismic Shear Failure in Rectangular Reinforced Concrete Columns," *Journal of Structural Engineering*, ASCE, V. 145, No. 10, Oct., p. 04019096. doi: 10.1061/(ASCE)ST.1943-541X.0002365

Huy, P. P. A.; Yuen, T. Y. P.; Hung, C.-C.; and Mosalam, K. M., 2022, "Seismic Behaviour of Full-Scale Lightly Reinforced Concrete Columns under High Axial Loads," *Journal of Building Engineering*, V. 56, Sept., Article No. 104817.

Ichinose, T., 1992, "A Shear Design Equation for Ductile R/C Members," *Earthquake Engineering & Structural Dynamics*, V. 21, No. 3, pp. 197-214. doi: 10.1002/eqe.4290210302

Joint ASCE-ACI Task Committee 426, 1973, "The Shear Strength of Reinforced Concrete Members," *Journal of the Structural Division*, ASCE, V. 99, No. 6, June, pp. 1091-1187. doi: 10.1061/JSDEAG.0003532

Kabeyasawa, T.; Tasai, A.; and Igarashi, S., 2002, "An Economical and Efficient Method of Strengthening Reinforced Concrete Columns against Axial Load Collapse during Major Earthquake," *The Third U.S.-Japan Workshop on Performance-Based Earthquake Engineering Methodology for Reinforced Concrete Building Structures*, Seattle, WA, PEER Report 2002/02, pp. 399-412.

Kowalsky, M. J., and Priestley, M. J. N., 2000, "Improved Analytical Model for Shear Strength of Circular Reinforced Concrete Columns in Seismic Regions," *ACI Structural Journal*, V. 97, No. 3, May-June, pp. 388-396.

Kuramoto, H., and Minami, K., 1992, "Experiments on the Shear Strength of Ultra-High Strength Reinforced Concrete Columns," *Proceedings of the Tenth World Conference on Earthquake Engineering*, Madrid, Spain, pp. 3001-3006.

Li, Y.-A.; Weng, P.-W.; and Hwang, S.-J., 2019, "Seismic Performance of Reinforced Concrete Intermediate Short Columns Failed in Shear," *ACI Structural Journal*, V. 116, No. 3, May, pp. 195-206. doi: 10.14359/51713309

MBIE, 2018, "The Seismic Assessment of Existing Buildings - Part C: Concrete Buildings," Ministry of Business, Innovation and Employment; Earthquake Commission; New Zealand Society for Earthquake Engineering; Structural Engineering Society New Zealand; and New Zealand Geotechnical Society, Wellington, New Zealand, https://www.building.govt.nz/assets/Uploads/building-code-compliance/b-stability/b1-structure/seismic-assessment/c5-concrete-buildings.pdf. (last accessed Apr. 25, 2023)

Minami, K., and Wakabayashi, M., 1981, "Rational Analysis of Shear in Reinforced Concrete Columns," *IABSE Colloquium on Advanced Mechanics of Reinforced Concrete*, Final Report, Delft, the Netherlands, pp. 603-614.

Nakamura, T., and Yoshimura, M., 2002, "Gravity Load Collapse of Reinforced Concrete Columns with Brittle Failure Modes," *Journal of Asian Architecture and Building Engineering*, V. 1, No. 1, pp. 21-27. doi: 10.3130/jaabe.1.21

Nakamura, T., and Yoshimura, M., 2014, "Gravity Load Collapse of Reinforced Concrete Columns with Decreased Axial Load," *Second European Conference on Earthquake Engineering and Seismology (2nd ECEES)*, Istanbul, Turkey, pp. 5129-5139.

Nielsen, M. P., 1998, *Limit Analysis and Concrete Plasticity*, second edition, CRC Press, Boca Raton, FL.

Ou, Y.-C., and Kurniawan, D. P., 2015, "Shear Behavior of Reinforced Concrete Columns with High-Strength Steel and Concrete," *ACI Structural Journal*, V. 112, No. 1, Jan.-Feb., pp. 35-46. doi: 10.14359/51686822

Ousalem, H.; Kabeyasawa, T.; and Tasai, A., 2004, "Effect of Hysteretic Reversals on Lateral and Axial Capacities of Reinforced Concrete Columns," *The Fifth U.S.-Japan Workshop on Performance-Based Earthquake Engineering Methodology for Reinforced Concrete Building Structures*, Hakone, Japan, PEER Report 2003/11, pp. 211-221.

Pan, Z., and Li, B., 2013, "Truss-Arch Model for Shear Strength of Shear-Critical Reinforced Concrete Columns," *Journal of Structural Engineering*, ASCE, V. 139, No. 4, Apr., pp. 548-560.

Paul, B., 1961, "A Modification of the Coulomb-Mohr Theory of Fracture," *Journal of Applied Mechanics*, V. 28, No. 2, pp. 259-268. doi: 10.1115/1.3641665

Priestley, M. J. N.; Calvi, G. M.; and Kowalsky, M. J., 2007, *Displacement-Based Seismic Design of Structures*, IUSS Press, Pavia, Italy.

Priestley, M. J. N.; Verma, R.; and Xiao, Y., 1994, "Seismic Shear Strength of Reinforced Concrete Columns," *Journal of Structural Engineering*, ASCE, V. 120, No. 8, Aug., pp. 2310-2329. doi: 10.1061/(ASCE)0733-9445(1994)120:8(2310)

Pujol, S.; Hanai, N.; Ichinose, T.; and Sozen, M. A., 2016, "Using Mohr-Coulomb Criterion to Estimate Shear Strength of Reinforced Concrete Columns," *ACI Structural Journal*, V. 113, No. 3, May-June, pp. 459-468. doi: 10.14359/51688743

Ramirez, H., and Jirsa, J. O., 1980, "Effect of Axial Load on Shear Behavior of Short RC Columns under Cyclic Lateral Deformations," PMFSEL Report No. 80-1, The University of Texas at Austin, Austin, TX, 205 pp.

Response-2000, 2000, "Reinforced Concrete Sectional Analysis Using the Modified Compression Field Theory," by E. C. Bentz and M. P. Collins, University of Toronto, Toronto, ON, Canada.

Restrepo, J. I., and Rodriguez, M. E., 2013, "On the Probable Moment Strength of Reinforced Concrete Columns," *ACI Structural Journal*, V. 110, No. 4, July-Aug., pp. 681-690.

Richart, F. E.; Brandtzaeg, A.; and Brown, R. L., 1929, "The Failure of Plain and Spirally Reinforced Concrete in Compression," Bulletin No. 190, Engineering Experiment Station, University of Illinois at Urbana-Champaign, Urbana, IL, 74 pp.

Sezen, H., and Moehle, J. P., 2004, "Shear Strength Model for Lightly Reinforced Concrete Columns," *Journal of Structural Engineering*, ASCE, V. 130, No. 11, Nov., pp. 1692-1703. doi: 10.1061/(ASCE)0733-9445(2004)130:11(1692)

Shohara, R., and Kato, B., 1981, "Ultimate Strength of Reinforced Concrete Members under Combined Loading," *IABSE Colloquium on Advanced Mechanics of Reinforced Concrete*, Final Report, Delft, the Netherlands, pp. 701-716.

Thürlimann, B., 1979, "Plastic Analysis of Reinforced Concrete Beams," *IABSE Colloquium on Plasticity in Reinforced Concrete*, Introductory Report, Copenhagen, Denmark, pp. 71-90.

Tran, C. T. N., 2010, "Experimental and Analytical Studies on the Seismic Behavior of Reinforced Concrete Columns with Light Transverse Reinforcement," PhD thesis, School of Civil and Environmental Engineering, Nanyang Technological University, Singapore, 208 pp.

Umehara, H., and Jirsa, J. O., 1982, "Shear Strength and Deterioration of Short Reinforced Concrete Columns under Cyclic Deformations," PMFSEL Report No. 82-3, The University of Texas at Austin, Austin, TX, 273 pp.

Vecchio, F. J., and Collins, M. P., 1986, "The Modified Compression-Field Theory for Reinforced Concrete Elements Subjected to Shear," *ACI Journal Proceedings*, V. 83, No. 2, Mar.-Apr., pp. 219-231.

Watanabe, F., and Ichinose, T., 1992, "Strength and Ductility Design of RC Members Subjected to Combined Bending and Shear," *Concrete Shear in Earthquake*, T. C. C. Hsu and S. T. Mau, eds., Elsevier Applied Science, Amsterdam, the Netherlands, pp. 429-438.

Yoshimura, M., and Nakamura, T., 2002, "Axial Collapse of Reinforced Concrete Short Columns," *The Fourth U.S.-Japan Workshop on Performance-Based Earthquake Engineering Methodology for Reinforced Concrete Building Structures*, Toba, Japan, PEER Report 2002/21, pp. 187-198.

Yu, Q., and Bažant, Z. P., 2011, "Can Stirrups Suppress Size Effect on Shear Strength of RC Beams?" *Journal of Structural Engineering*, ASCE, V. 137, No. 5, May, pp. 607-617. doi: 10.1061/(ASCE)ST.1943-541X.0000295

Zheng, W.; Kwan, A. K. H.; and Lee, P. K. K., 2001, "Direct Tension Test of Concrete," *ACI Materials Journal*, V. 98, No. 1, Jan.-Feb., pp. 63-71.